Physics of Atomic Nuclei, Vol. 65, No. 9, 2002, pp. 1563–1568. Translated from Yadernaya Fizika, Vol. 65, No. 9, 2002, pp. 1603–1608.
Original Russian Text Copyright © 2002 by Penionzhkevich, Muzychka, Lukyanov, Kalpakchieva, Skobelev, Perelygin, Sobolev, Mikhailov, Ugryumov, Vincour, Dlouhy, Kostov, Mrazek, Poroshin.

Above-Barrier Enhancement of Fusion in the ^{6}He + ^{209}Bi Nuclear Reaction

Yu. E. Penionzhkevich, Yu. A. Muzychka, S. M. Lukyanov, R. Kalpakchieva, N. K. Skobelev, V. P. Perelygin, Yu. G. Sobolev, L. V. Mikhailov, V. Yu. Ugryumov, J. Vincour[1], Z. Dlouhy[1], L. Kostov[2], Ya. Mrazek[1], and N. O. Poroshin[3]

Laboratory of Nuclear Reactions, Joint Institute for Nuclear Research, Dubna, Moscow oblast, 141980 Russia

Received July 10, 2001; in final form, January 23, 2002

Abstract—The fission cross sections for the ^{6}He + ^{209}Bi reaction as functions of the ^{6}He-beam energy are measured. The experimental excitation functions for the reaction ^{209}Bi(^{6}He, $4n$)^{211}At are also presented. The ^{6}He secondary ion beam is obtained on the basis of the extracted-beam transport system of the U400-M accelerator (the Q4DQ spectrometer). A comparison of the experimental data obtained with available results for the ^{6}He + ^{209}Bi reaction shows that a pronounced enhancement of the fission cross sections in the above-barrier energy region is observed in the case of the reaction with the ^{6}He beam. In order to fit the results of theoretical calculations to the experimental data, it is necessary to reduce the Coulomb barrier by 15% (20%). This corresponds to an increase of 1.5 (1.6) fm in the parameter r_0 of the nuclear potential. *© 2002 MAIK "Nauka/Interperiodica"*.

INTRODUCTION

The main direction of studies with secondary radioactive beams is measurement of cross sections for reactions of exotic nuclei with target nuclei. These data present a basis for extracting information on the structure of nuclei far from the stability region and on the distribution of nuclear matter or nuclear radii. In particular, experimental evidence of the existence of a neutron halo (^{11}Li) or a skin (^{6}He) for neutron-rich nuclei was obtained [1, 2]. The reaction mechanism for such nuclei has its specific features caused by the existence of weakly bound valence protons. The explanation of the mechanism of these reactions requires going beyond simple one-dimensional models in which the interaction between colliding nuclei is implied to depend only on the distance between their centers. Valuable information is extracted from experiments studying subbarrier fusion in reactions induced by neutron-rich nuclei such as ^{6}He and ^{8}He. The choice of subbarrier fusion is motivated by the fact that, in this case, the basic channel associated with the penetration through the one-dimensional potential barrier turns out to be suppressed, so that it becomes possible to reveal other channels against this background. Measurements of the fusion cross sections are of interest within the region of beam energies above the Coulomb barrier, where the effect of weakly bound neutrons in the ^{6}He and ^{8}He nuclei on the fusion process must manifest itself in this case. The mechanisms of reactions in the above-barrier energy region may differ from those that play the main role at energies lower than the Coulomb barrier. It is worth noting that, in the above-barrier region, the situation is more complicated, since the exponential growth of the fusion cross section (which is associated with the necessity of overcoming the one-dimensional barrier) will hinder the manifestation of the contribution of other processes to that of fusion. Therefore, the choice of a channel for compound-nucleus decay that could be an indicator of the complete fusion of nuclei participating in the reaction is extremely important. We may hope that, in the case of the use of sufficiently heavy and weakly fissile nuclei as targets, such a channel could be the fission of an excited compound nucleus. In this case, nuclei with a reasonably high orbital angular momentum $l\hbar$ noticeably contribute to fission. Therefore, the increase in the fusion cross section, which is associated with an extension of the population of levels of compound nuclei being formed, will result in a noticeable enhancement of the fission cross section. In this case, the contribution of the partial cross sections to the

---

[1] Institute of Nuclear Studies, Řež, Czech Republic.

[2] Institute for Nuclear Research and Nuclear Energy, BG-1784 Sofia, Bulgaria.

[3] Moscow Engineering Physics Institute, Kashirskoe sh. 31, Moscow, 115409 Russia.

1063-7788/02/6509-1563$22.00 © 2002 MAIK "Nauka/Interperiodica"

cross section for the formation of a compound nucleus is proportional to $(2l + 1)$.

The fusion cross sections were calculated for the ^{11}Li + ^{208}Pb and ^{11}Li + ^{238}U reactions [3–5]. In those studies, special attention was paid to the influence that the breakup of ^{11}Li into ^{9}Li and two neutrons in the field of the target nucleus exerts on the fusion cross section. It was shown that the breakup process significantly affects the cross section for ^{11}Li fusion with a target nucleus at energies close to the Coulomb barrier, i.e., at a lower fusion probability. However, these reactions were not experimentally investigated because of the low intensity of secondary ^{11}Li-ion beams. Studies of fusion–fission reactions was first begun with secondary ^{6}He beams [6, 7]. Later, these investigations were continued with ^{6}He [8–10], ^{11}Be [11], and ^{38}S [12] beams. Some of the experimental data obtained imply an increase in the fusion and fission cross sections. The data of [8, 9] on the fusion cross sections in the subbarrier energy region are inconsistent. In the experimental studies [8] of ^{209}Bi fission induced by ^{6}He nuclei, the authors did not observe an increase in the cross section compared to ^{209}Bi fission induced by α particles. On the other hand, a strong increase in the cross section for the ^{209}Bi(^{6}He, $3n$) reaction in the subbarrier energy region was found in [9]. This fact made it possible to draw the conclusion that the fusion barrier for the ^{6}He + ^{209}Bi reaction decreases by 25%. The data of [11] on the cross sections for ^{11}Be fusion also have an ambiguous character. In the case of the ^{38}S + ^{181}Ta reaction, an enhancement of the fission cross section was observed in relation to the cross section for tantalum fission induced by ^{38}S nuclei. This could be explained by a decrease in the fusion-barrier height [12].

In performing these investigations, the choice of target nucleus is extremely important. This nucleus cannot be too light, since the fission cross section will be small in this case, so that such experiments will be complicated by relatively low ^{6}He-beam intensities available at the moment. At the same time, the target nucleus cannot be too heavy (e.g., uranium and heavier nuclei). This is associated both with the high probability of the neutron- and other-particle-induced fission of such target nuclei and with the fact that fission becomes the main decay mode for the compound nucleus at all values of l. In this case, revealing the influence of other channels on the probability of compound-nucleus formation becomes difficult. Nuclei close to lead, in particular, the ^{209}Bi nucleus, are the most suitable. For this nucleus, there also exists a detailed measurement (in a wide energy range) of the excitation function for fission induced by α particles, i.e., for the ^{209}Bi(^{4}He, f) reaction [13]. This is very important for the analysis of the experimental data obtained.

In the present study, we have measured the excitation function for bismuth-nucleus fission induced by a secondary ^{6}He-ion beam and the excitation function for the reaction accompanied by the evaporation of four neutrons. These measurements were performed in more detail in relation to our previous studies [6, 7], with higher statistics, and within a wider energy range.

EXPERIMENTAL METHOD

A secondary ^{6}He-ion beam was obtained in the ^{7}Li + ^{9}Be reaction at a ^{7}Li-beam energy of 35 MeV/A. The primary ^{7}Li-ion beam from the U400-M accelerator was focused onto a cooled Be target 3 mm thick. In order to separate reaction products that leave the target from primary-beam ions and to form secondary beams, use was made of the ion-optic beam-transport system of the U400-M accelerator (so-called Q4DQ spectrometer). The main characteristics of this system are presented in [14].

The employment of a system of four dipole and quadrupole magnets allowed us to obtain a ^{6}He-beam intensity not lower than 5×10^4 particle/s. For better purifying the ^{6}He beam from other secondary particles, slotted diaphragms and an additional charge-exchange 2-mm polypropylene foil (degrader) were installed between the dipole magnets. The control of the size of the secondary beam, while it was formed, and of its quality and beam monitoring were carried out by means of position-sensitive plate-parallel avalanche counters and semiconductor silicon detectors.

The application of this technique made it possible to purify the ^{6}He beam from other particles to a degree not worse than 98%. The secondary ^{6}He beam obtained did not vary its characteristics during a long-term operation of the accelerator. The content of admixtures in long-term experiments varied within 2 to 5%. The energy spread of the secondary beam was ±6 MeV.

Targets made of ^{209}Bi (700 μg/cm^2 thick) were installed in the secondary ^{6}He beam. These targets were produced by the method of vacuum sputtering of metallic bismuth onto a 2.5-μm polymeric backing. Fission fragments were recorded on-line by means of surface-barrier silicon detectors located around the targets. The overall geometric efficiency could reach 30% of the total solid angle. At low ^{6}He energies, plastic solid-state detectors were used to measure the excitation function and to detect fission fragments [6, 7].

ANALYSIS OF THE EXPERIMENTAL RESULTS

The excitation functions measured in the present study for both the fission of ^{215}At nuclei produced in the ^{6}He + ^{209}Bi reaction and the formation of ^{211}At nuclei in the ^{209}Bi(^{6}He, $4n$)^{211}At reaction are presented in Fig. 1. For the sake of comparison, the data from [7] for the fission of ^{209}Bi nuclei that is induced by α particles are shown in the same figure. It is worth mentioning that the excitation function for the ^{209}Bi(α, f) reaction measured by the same method as for ^{6}He is in good agreement with the data of [13]. In Fig. 1, the difference between the fission cross sections for the ^{4}He + ^{209}Bi and ^{6}He + ^{209}Bi reactions is clearly seen. In order to extract quantitative and, especially, qualitative information, we performed a comparative analysis of the results obtained in both reactions.

It is necessary to note that, in the analysis of these data, there arises the important question of the contribution of complete fusion and other channels to the fission of ^{209}Bi nuclei. In this reaction, fission, in addition to complete fusion, can also arise in the breakup of ^{6}He into two neutrons and an α particle with the subsequent capture of either the neutrons or the α particle, with a ^{211}Bi nucleus being formed in the first case. If we consider the case of the maximum energy of the ^{6}He beam, which, in our experiments, is ≈70 MeV, then the excitation energy of the ^{211}Bi nucleus is approximately equal to 33 MeV (24 MeV is the kinetic energy of the neutrons, and 9.7 MeV is the reaction Q value). In this case, only 0.0001 of all formed compound nuclei can undergo fission, which is a negligible quantity. At the same time, the capture of the α particle (also at the maximum energy of ^{6}He) leads to the formation of a ^{213}At nucleus with an excitation energy of ≈37 MeV (24 MeV is carried away by the neutrons, and 9.3 MeV is the α-particle binding energy in the ^{213}At nucleus). In this case, 2% of the ^{213}At nuclei undergo fission, and the cross section for this process is smaller than 5% of the measured fission cross section equal to 0.8 b. Naturally, this quantity is even smaller at lower ^{6}He energies. Thus, we can state that all fission events recorded in the irradiation of ^{209}Bi nuclei with ^{6}He ions arise upon the complete fusion of the nuclei participating in the reaction.

In the analysis of the experimental data, we used the ALICE–MP code [15]. The calculations of fission widths and evaporation widths according to this code are based on the classical Bohr–Wheeler formula and on the Weiskopf–Ewing formalism, respectively. In the calculation of the level density, the relations of the Fermi gas model with allowance for shell effects in the level-density parameter were employed [16]:

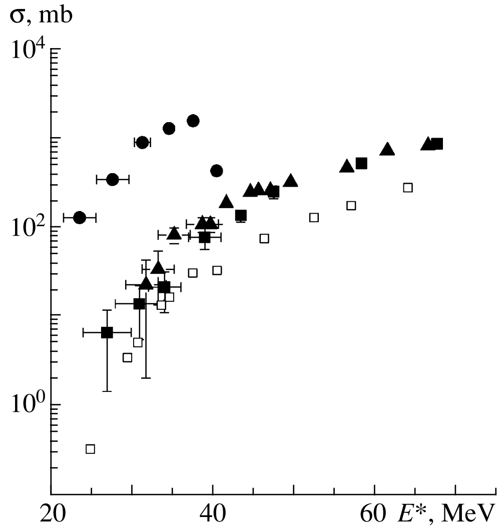

Fig. 1. Experimental excitation functions for the ^{6}He + ^{209}Bi and ^{4}He + ^{209}Bi reactions {data on the ^{6}He + ^{209}Bi fission channel from (■) our present study and (▲) [7], and data on the ^{4}He + ^{209}Bi fission channel from (□) [7, 13]} and for (●) the (^{6}He, $4n$) evaporation channel.

$$a_\nu(E^*) = \tilde{a}_\nu\{1 + [1 - \exp(-0.054E^*)]\Delta w_\nu(A, Z)/E^*\}.$$

Here, $a_\nu(E^*)$ is the level-density parameter in the evaporation channel for a particle ν at an energy E^*, $\tilde{a}_\nu$ is the asymptotic value of the level-density parameter in the evaporation channel for the same particle ν, E^* is the excitation energy of the compound nucleus, and Δw_ν is the shell correction to the mass of the nucleus formed after the emission of the particle ν (n, p, α).

We consider the level-density parameter a_f in the fission channel to be independent of the excitation energy and to be proportional to $\tilde{a}_\nu$. (In other words, we assume the shell correction at the saddle point to be negligible.) The fission barriers for the nuclei were calculated according to the formula

$$B_f(l) = CB_f^{\text{LD}}(l) + \Delta W_f,$$

where C is a free parameter, $B_f^{\text{LD}}(l)$ is the fission barrier in the Cohen–Plasil–Swiatecki model of a rotating liquid drop [17], and ΔW_f is the shell component of the fission barrier for the compound nucleus (it is equal to the modulus of the shell correction to the mass of its ground state). In calculating the fission barrier, we also ignored the small value of the shell correction at the saddle point.

In analyzing the experimental data and formulating conclusions that follow from our results, the values of the parameters used in the calculations play an

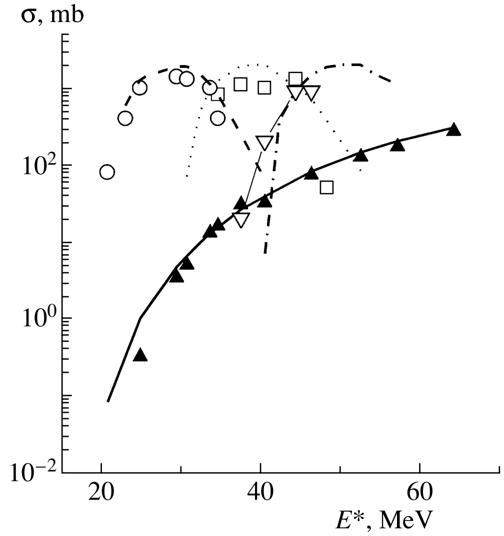

Fig. 2. Experimental excitation functions for the ^{6}He + ^{209}Bi reaction [data for the (▲) (α, f), (□) (α, $4n$), and (▽) (α, $5n$) channels], along with relevant theoretical results represented by solid, dashed, dotted, and dash-dotted lines, respectively.

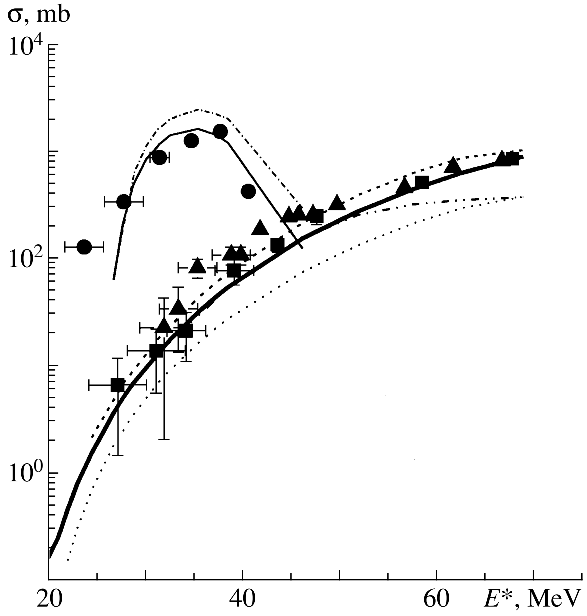

Fig. 3. Comparison of the experimental excitation functions for the (^{6}He, f) {according to (■) our present study and (▲) [7]} and (^{6}He, $4n$) {according to (•) [7]} reactions with the calculated results. The results of the calculations employing various values of the radius r_0 and of the angular momentum l are represented by the dotted ($r_0 =$ 1.29 fm, $l = 40$), dash-and-double-dot ($r_0 = 1.5$ fm, $l =$ 40), thick solid ($r_0 = 1.5$ fm, $l = 50$), and dashed ($r_0 =$ 1.5 fm, $l = 60$) lines. The best agreement with the experimental data is achieved for $r_0 = 1.5$ fm and $l = 50$–60 (thick solid and dashed lines). The results calculated for the (^{6}He, $4n$) reaction are represented by thin solid ($r_0 = 1.29$ fm) and dashed-dotted ($r_0 = 1.5$ fm) lines.

important role. Therefore, we consider the situation for these parameters in more detail. In calculating reaction cross sections associated with the evaporation of particles and cross sections for the fission of excited nuclei, we use two sets of parameters. One set determines the production cross section for the compound nucleus and is connected with the geometric size of the nuclear part of the interaction potential (radius parameter r_0) and its shape (diffuseness d of the potential and its depth V). Numerous calculations that were performed here to determine compound-nucleus-production cross sections for reactions with different particles (from ^{7}Li to ^{48}Ca) and targets (from Ca to Cf) showed that, in all cases under consideration, we can use the same set of parameters, namely, $r_0 = 1.29$ fm, $V = 67$ MeV, and $d = 0.4$ fm.

The other set of parameters determines the competition of the fission and evaporation channels for the produced compound nucleus. The density of nuclear levels in the fission and evaporation channels depends on the values of these parameters. In our calculations, these were the ratio $\tilde{a}_f/\tilde{a}_\nu$ of the asymptotic values of the level densities in the fission and evaporation channels and the free parameter C in the formula for the fission barrier.

Furthermore, we compared the calculated results with experimental data related to the excitation functions for fission and evaporation reactions over a wide range of nuclei. This analysis made it possible to conclude that, in all cases, we may use the fixed ratio $\tilde{a}_f/\tilde{a}_\nu = 1$. Moreover, the excitation-energy dependence of the ratio Γ_n/Γ_f of the fission to the evaporation decay width for compound nuclei according to data obtained in reactions induced by ^{22}Ne ions in ^{194,196,198}Pt targets [18] was analyzed on the basis of the statistical model. It was shown that the above value of the ratio $\tilde{a}_f/\tilde{a}_\nu$ yields results consistent with the experimental data. Thus, this parameter has a fixed value, too.

The parameter C determining the contribution of the liquid-drop component to the fission barrier has no fixed value. It varies with the charge number Z and the mass number A of the compound nucleus. It is of importance that it varies very smoothly and monotonically. This allows us to determine rather reliably its value for a particular compound nucleus according to the values obtained for nearby nuclei. The value of the parameter C is 0.8 for heavy astatine isotopes.

Thus, none of the above parameters is free in the analysis of the experimental data obtained in the present study for the ^{6}He + ^{209}Bi reaction.

There is yet another parameter that plays an important role in calculations of the fission cross sections. This is the critical angular momentum l_{cr} that, at sufficiently high energies (when l_{cr} becomes lower than the maximum angular momentum $l_{\max}$), determines the number of partial waves leading to the formation of a compound nucleus. The above parameters (r_0, d, V, and $\tilde{a}_f/\tilde{a}_\nu$) either remain constant in a sufficiently wide region of nuclei or very smoothly vary with Z and A (parameter C). Therefore, the cross sections for a definite reaction were calculated by using the parameters obtained from the analysis of other reactions leading to the production of compound nuclei with sufficiently close values of Z and A (apart from the parameter l_{cr}). On the basis of rather general considerations concerning the mechanism of compound-nucleus formation, we may suppose that l_{cr} has a square-root dependence on energy, as well as on the mass of the particle inducing the reaction. Of course, this statement is true provided that, in going over from one particle to another, there is no abrupt change in properties [e.g., variations of the fusion-channel radius that are not proportional to $(A_1^{1/3} + A_2^{1/3})$].

Before analyzing the experimental data on fission that were obtained in the ^{6}He + ^{209}Bi reaction, we performed calculations for the ^{4}He + ^{209}Bi reaction, for which there exists a detailed measurement of the excitation function for fission [7, 13], as well as for evaporation of three, four, and five neutrons [19]. This allowed us, first, to verify the applicability of the parameter values used and, second, to perform a comparative analysis of the data for both reactions. The latter would make it possible to reveal special features of the ^{6}He + ^{209}Bi reaction.

Figure 2 presents the experimental and calculated excitation functions for the (α, f), $(\alpha, 3n)$, $(\alpha, 3n)$, $(\alpha, 4n)$, and $(\alpha, 5n)$ channels of the ^{4}He + ^{209}Bi reaction. As was mentioned above, the only free parameter of the calculation was l_{cr}. Agreement between the experimental and calculated cross-section values at $E^* = 69.2$ MeV ($E_{\mathrm{lab}} = 80$ MeV) was obtained for l_{cr} equal to 35. It should be noted that the parameter $l_{\max}$ determined by the height of the Coulomb barrier becomes equal to this value at $E_{\mathrm{lab}} = 68$ MeV ($E^* = 46.7$ MeV) and begins to play a significant role at $E_{\mathrm{lab}} = 68$ MeV ($E^* = 57.5$ MeV). We may assume that, in a greater part of the energy range under consideration, the number of partial waves leading to compound-nucleus production is determined by the nuclear interaction potential. The good agreement between the calculated and experimental data demonstrated the applicability of the approach used above to calculating reactions induced by such light particles as helium isotopes and confirmed the validity of our set of parameters.

With this set of parameters, the calculations of the excitation functions for the fission and evaporation of four neutrons in the ^{6}He + ^{209}Bi reaction were carried out. The experimental excitation functions for the (^{6}He, f) and (^{6}He, $4n$) reactions and the calculated results are shown in Fig. 3. The dotted curve corresponds to the standard parameter set. It can be seen that, for ^{6}He (in contrast to ^{4}He, for which good agreement was obtained with these parameters), the calculated fission excitation function falls considerably short of the experimental one. At the same time, good agreement is observed for the reaction accompanied by the evaporation of four neutrons (thin solid curve). It is noteworthy that the calculated and experimental fission excitation functions are virtually parallel to each other over the entire energy range under consideration, the tendency of approaching each other being absent.

It should be noted that, for the highest excitation energy of $E^* = 70$ MeV, the value of $l_{\mathrm{cr}} = 40$, which nearly coincides with $l_{\max}$, was used in the calculations. Therefore, a simple increase in l_{cr} did not improve the agreement (the increase in l_{cr} to 50 changes the quantity σ_f at the extreme point only by 15%). Therefore, a decrease in the Coulomb barrier height is the only way to increase the cross section for compound-nucleus formation and, hence, the fission cross section. Within the one-dimensional model, this can be achieved by increasing the interaction radius. Indeed, the increase in the value of r_0 to 1.5 or 1.6 fm (and of l_{cr} to 50) leads to perfect agreement between the experimental and calculated fission excitation functions (see Fig. 3). This corresponds to lowering the Coulomb barrier by 15–20% ($r_0 = 1.5$–1.6 fm). In this case, the results for the evaporation reaction ($4n$) vary rather weakly. This is quite natural since partial waves characterized by relatively low values of $l \leq 30$–35 mainly contribute to the cross section for evaporation reactions at energies not far from the excitation-function maximum.

The increase of 15% in the interaction radius in going over from ^{4}He to ^{6}He (or even of 20%) is hardly associated with the geometric size of the ^{6}He nucleus itself. Probably, this is associated with the manifestation of the enhancement of the above-barrier fusion caused by the influence of other channels on the fusion process. The questions related to the type of these channels and their contribution need additional investigations. However, the pair of weakly bound neutrons in the ^{6}He nucleus may play here a decisive role.

ACKNOWLEDGMENTS

We are grateful to Yu.Ts. Oganessian and M.G. Itkis for enlightening discussions on the results presented here. We also are indebted to the service group of the U400-M cyclotron for providing an intense primary ^{7}Li beam.

This work was carried out in the framework of the special financial support of Bulgaria and the Czech Republic to JINR and was also supported by INTAS (grant no. 00-00463) and the Russian Foundation for Basic Research (project no. 01-02-22001).

REFERENCES

1. I. Tanihata *et al.*, Phys. Rev. Lett. **55**, 2676 (1985).
2. I. Tanihata *et al.*, Phys. Lett. B **289**, 261 (1992).
3. M. Takigawa *et al.*, Phys. Rev. C **47**, R2470 (1993).
4. C. Dasso *et al.*, Nucl. Phys. A **597**, 473 (1996).
5. M. S. Hussein *et al.*, Phys. Rev. C **46**, 377 (1992); Nucl. Phys. A **588**, 85c (1995).
6. N. K. Skobelev *et al.*, JINR Rapid Commun., No. [61]-93, 36 (1993).
7. Yu. E. Penionzhkevich *et al.*, Nucl. Phys. A **588**, 258c (1995); A. S. Fomichev *et al.*, Z. Phys. A **351**, 129 (1995).
8. J. J. Kolata *et al.*, Phys. Rev. C **57**, R6 (1998); P. A. De Young *et al.*, Phys. Rev. C **58**, 3442 (1998).
9. J. J. Kolata *et al.*, Phys. Rev. Lett. **81**, 4580 (1998); Phys. Rev. Lett. **84**, 5058 (2000).
10. M. Trotta *et al.*, Phys. Rev. Lett. **84**, 2342 (2000).
11. A. Yoshida *et al.*, Phys. Lett. B **389**, 457 (1996).
12. K. E. Zyromski *et al.*, Phys. Rev. C **55**, R562 (1997).
13. A. V. Ignatyuk, M. G. Itkis, *et al.*, Yad. Fiz. **40**, 625 (1984) [Sov. J. Nucl. Phys. **40**, 400 (1984)].
14. S. M. Lukyanov *et al.*, Soobshch. Ob'edin. Inst. Yad. Issled., No. R13-218-2000 (Dubna, 2001).
15. Yu. A. Muzychka and B. I. Pustyl'nik, in *Proceedings of the International School—Workshop on Physics of Heavy Ions, Alushta, 1983,* No. D7-83-644 (Ob'edin. Inst. Yad. Issled., Dubna, 1983), p. 420.
16. A. V. Ignatyuk, G. N. Smirenkin, and A. S. Tishin, Yad. Fiz. **21**, 485 (1975) [Sov. J. Nucl. Phys. **21**, 255 (1975)].
17. S. Cohen, F. Plasil, and W. J. Swiatecki, Ann. Phys. (N.Y.) **82**, 557 (1974).
18. A. N. Andreev, D. D. Bogdanov, V. I. Chepigin, *et al.*, Nucl. Phys. A **620**, 229 (1997).
19. S. S. Rattan, N. Chakravarty, A. Ramaswami, and R. J. Singh, Radiochim. Acta **55**, 7 (1991).

Translated by G. Merzon

Physics of Atomic Nuclei, Vol. 65, No. 9, 2002, pp. 1569–1574. Translated from Yadernaya Fizika, Vol. 65, No. 9, 2002, pp. 1609–1614.
Original Russian Text Copyright © 2002 by Kuznetsov, Byalkowski, Ivanov, Kalpakchieva, Kugler, Kukhtina, Kushniruk, Maslov, Mikhailov, Negoita, Penionzhkevich, Poroshin, Skobelev, Smirnov, Sobolev, Ugryumov.

NUCLEI
Experiment

Total Cross Sections for ^{4,6}He + ^{28}Si Reactions Measured at 10–28 MeV/A

I. V. Kuznetsov[1], E. Byalkowski[2], M. P. Ivanov[1], R. Kalpakchieva[1]*, A. Kugler[3], I. N. Kukhtina[1], V. F. Kushniruk[1], V. A. Maslov[1], L. Mikhailov[3], F. Negoita[4], Yu. E. Penionzhkevich[1], N. O. Poroshin[5], N. K. Skobelev[1], V. I. Smirnov[1], Yu. G. Sobolev[1], and V. Yu. Ugryumov[1]

Received July 10, 2001; in final form, October 15, 2001

Abstract—New results on the energy dependence of the total cross section (σ_R) for ^{6}He scattering on ^{28}Si in the incident energy range 10–28 MeV/A are obtained. The α-particle-production cross sections for the ^{28}Si(^{6}He, ^{4}He)X channel are measured as well. The secondary beam of ^{6}He with an intensity of up to 5×10^4 particle/s was generated by bombarding a thick beryllium target with $\sim$ 32-MeV/A ^{7}Li ions. In the energy region below 17 MeV/A, σ_R increases sharply. The experimental dependences of the total cross sections are compared with the results of σ_R calculations using the double-folding potential within the optical model. The energy dependence of σ_R for ^{6}He differs from that for the neighboring nuclei, which can be associated with the structural features of the former nucleus. The energy spectra of α particles produced in the ^{6}He interactions with silicon indicate two mechanisms of their production: transfer reaction and ^{6}He breakup in the field of the ^{28}Si nucleus. © *2002 MAIK "Nauka/Interperiodica"*.

INTRODUCTION

Extensive experimental and theoretical studies of the cross section (σ_I) for the interaction of radioactive nuclei with stable nuclei—or the total cross section for these reactions (σ_R)—were initiated by Tanihata *et al.* [1]. It was just in this study that a conclusion about substantial extension of the neutron-density distribution in the neutron-rich isotopes of such nuclei was drawn on the basis of the analysis of the cross sections for the interaction of ^{3,4,6,8}He isotopes with Be, C, and Al targets at 790 MeV/A. After this study [1], it also became evident that experiments measuring σ_I or σ_R by using the radioactive beams even at low intensity are promising for obtaining information on the size and the structure of unstable nuclei.

Subsequent measurements of σ_I or σ_R were performed with extension of the energy range of bombarding particles, as well as with extension of the diversity of their mass and atomic numbers. A review of experimental data on the total cross sections and the interaction cross sections for light exotic nuclei can be found in [2].

Among neutron-rich exotic nuclides, the ^{6}He nucleus stands out owing to the fact that, possessing a relatively normal size ($R_{\mathrm{rms}} = 2.52$ fm) [3], it can be represented as a compact inert ^{4}He-core surrounded by two loosely bound neutrons. The properties of the ground state of ^{6}He can be properly simulated using either the macroscopic three-cluster model [4] or the microscopic model [5]. The energy dependence of the total cross section for ^{6}He + ^{28}Si reaction measured in the range 20–60 MeV/A [6] appeared to be weak, which was in conflict with theoretical predictions.

In order to study in detail the behavior of the total cross section of the ^{6}He + ^{28}Si reaction and to extend the energy range to lower interaction energies, we measured σ_R in the range from 10 to 28 MeV/A, decreasing energy in smaller steps as compared to those used in [6]. The total cross sections for ^{4}He production in the ^{6}He breakup channel and in the reaction of neutron transfer on silicon were measured as well. We obtained the total cross sections for the ^{4}He + ^{28}Si reaction at two energies, which complement the data presented in [7].

EXPERIMENTAL PROCEDURE

The secondary beam of ^{6}He ions was obtained at the U400-M accelerator of the Laboratory of Nu-

---

[1] Joint Institute for Nuclear Research, Dubna, Moscow oblast, 141980 Russia.

[2] Institute of Nuclear Physics, Krakow, Poland.

[3] Nuclear Physics Institute, Řež, CZ-250 68 Czech Republic.

[4] Institute of Atomic Physics, Bucharest, Romania.

[5] Moscow State Engineering Physics Institute (Technical University), Kashirskoe sh. 31, Moscow, 115409 Russia.

*e-mail: `kalpak@sungraph.jinr.ru`

clear Reactions (JINR, Dubna) by irradiating a thick beryllium target (140 mg/cm^2) with ~240-MeV ^{7}Li ions. To separate the ^{6}He ions and to focus them onto the silicon target studied, the standard dipole and quadrupole elements of the ion-optical system of the main channel of the cyclotron were used. Additional purification of the ^{6}He beam from admixtures was achieved by inserting of a polypropylene plate between two pairs of the dipole magnets; this plate decreased in a different way the energy of the secondary particles. The main admixtures (up to 10% of the total intensity) are deuterium and tritium ions.

The energy dependence of the total reaction cross sections was measured by the well-known method based on the use of a multilayer silicon telescope [8, 9]. The detectors of the telescope simultaneously served as a target, detecting the reaction products and decreasing the energy of the ^{6}He ions. The operating detector cross section area was ~3 cm^2, and the total telescope length was 10 cm. Immediately in front of the telescope was installed a 2-cm-thick aluminum diaphragm 12 mm in diameter, and a ring silicon detector with an inner diameter of 10 mm was placed behind the diaphragm. Thus, the secondary beam striking the telescope had a transverse size of ~ 10 mm. The telescope detectors were of various thickness in the range from 400 to 1200 μm; the thickness was measured to within ± 3 μm. The energy calibration was carried out using α decay of a ^{226}Ra source, as well as using the specific energy losses of ^{6}He ions with various initial energies (135, 181, and 193 MeV). All recording channels (11 channels were for the energy deposition, one channel for the ring detector, and one channel for the time of flight) were equipped with the standard set of electronics. A pulse from the preamplifier or the time-to-code converter was fed to the spectrometric amplifier and then to the analog-to-digital converter (ADC). Startup of all ADCs was effected by a scheme which analyzed fast signals from the first and second detectors.

Further processing of the accumulated data and determination of the reaction cross sections were performed by the following scheme. First, the events connected with ^{6}He ions were separated from the accumulated data. For this purpose, the following conditions were applied to data sorting: a narrow energy deposition range in the first detector, a narrow range of the time of flight, and no dE signal from the ring detector. Figure 1*a* shows the two-dimensional matrices of energy depositions ($dE_i \cdot dE_k$) in the sequential pairs of the detectors for the case when the initial energy of ^{6}He ions was $E_0 = 193.0 \pm 1.9$ MeV.

Dark spots, standing out on the matrices, correspond to the energy deposition of ^{6}He ions only due to the ionization losses. The events outside the spots correspond to the ^{6}He nuclear interaction with silicon in the given pair of detectors. To determine the number of events associated with the nuclear interactions, a contour was drawn around the elastic peak (spot), and then the events lying outside this contour were separated. When passing over to the next pair, we set the conditions of the presence of events inside the contour of the previous pair and outside the contour around the studied pair. Figure 1*b* demonstrates the two-dimensional matrices for the events associated only with the nuclear reactions in the fourth and fifth detectors, in which the "loci" of ^{4}He originating from ^{6}He in the interaction with silicon are clearly seen. The α particles ejected from ^{6}He ions as a result of their breakup or the neutron transfer reactions on silicon possess sufficient energy to penetrate into the last three detectors. Figure 1*b* demonstrates the contour on the dE_8–dE_9 matrix, which was used to separate α particles from the nuclear reaction products in the fourth and fifth detectors and to determine their number.

Figure 2*a* shows the energy spectrum of all the reaction products observed in these detectors. The narrow peak in the region of 90–100 MeV is explained by the charge exchange reaction ^{28}Si(^{6}He, ^{6}Li)^{28}Al. The energy of ^{6}Li almost coincides with the energy of ^{6}He; however, too high an energy deposition in the fifth detector leading to saturation of the amplifier causes distortion of the total spectrum of ^{6}Li. Figure 2*b* shows the energy spectrum of ^{4}He produced in the pair of the detectors indicated above. The peak at a lower energy corresponds to α particles produced in the ^{6}He breakup channel; the peak at a higher energy complies with the neutron transfer reactions.

On the basis of the measured total number of events associated with the nuclear reactions (Figs. 2*a* and 2*b*), the known thickness of the detectors, and the number of ^{6}He ions striking detectors 4 and 5, we determined the total reaction cross section as

$$\sigma_R\,[mb] = \frac{2 \times 10^8 N}{LI},$$

where N is the number of events in the nuclear reactions, L is the total thickness of the fourth and fifth detectors in microns, and I is the number of ^{6}He ions incident on the detectors.

The same procedure of determination of the total reaction cross section and the cross section of the reaction with the α-particle production was applied to the other pairs of detectors.

The proposed procedure of determination of the reaction cross section by means of the detector pairs was used because the energy depositions from α particles adjoin closely those from noninteracting ^{6}He

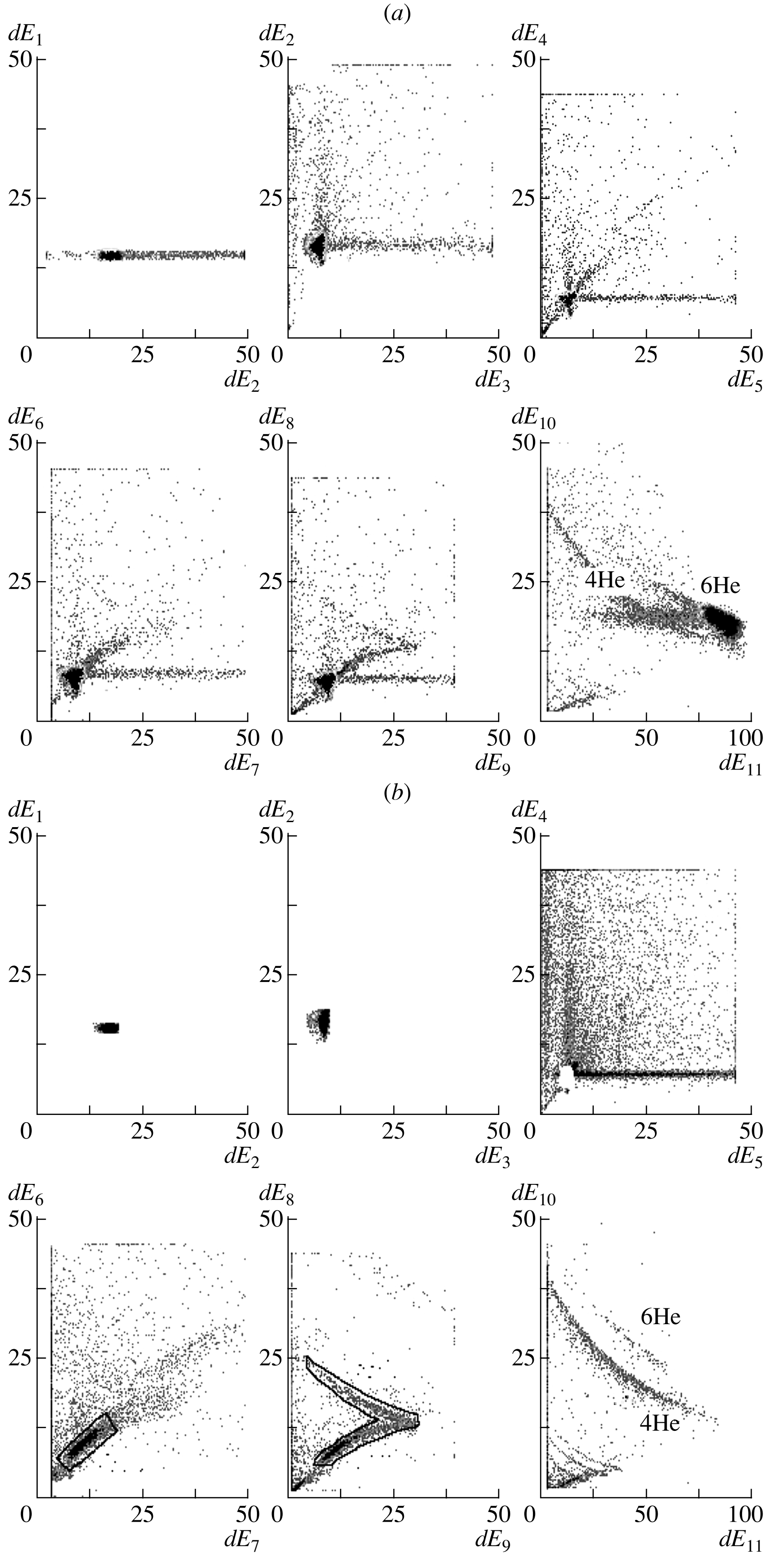

Fig. 1. Energy deposition (MeV) in the telescope detectors.

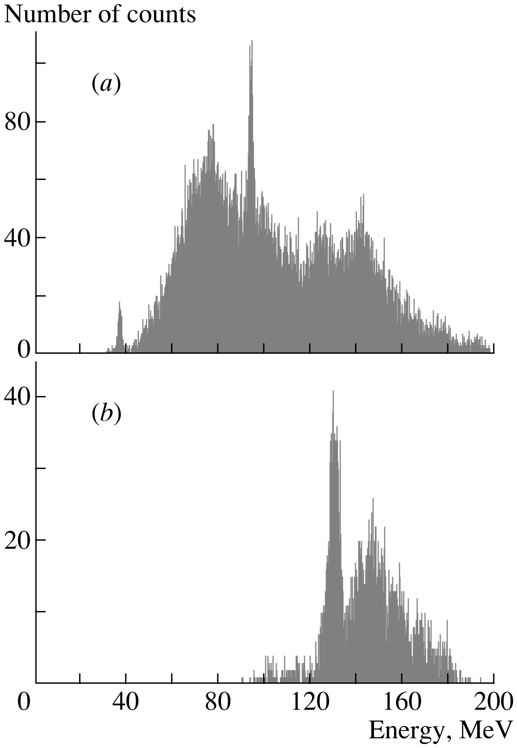

Fig. 2. The energy spectra (*a*) of all reaction products observed in detectors 4 and 5 and (*b*) of α particles from reaction ^{28}Si (^{6}He, ^{4}He) in the same pair of detectors.

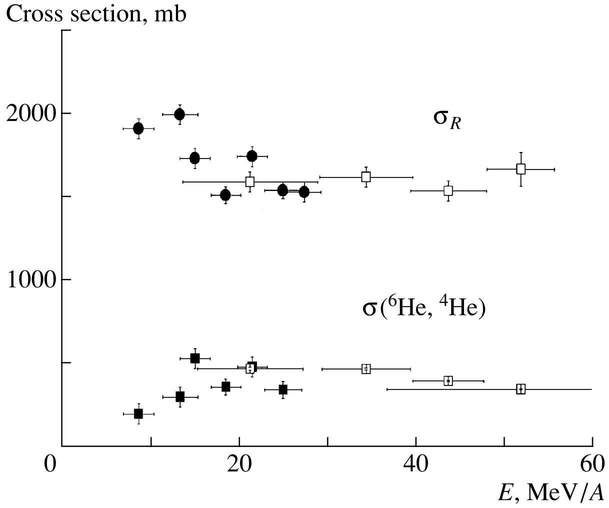

Fig. 3. The total reaction cross sections of ^{6}He (σ_R) and the cross sections of the reaction ^{28}Si (^{6}He, ^{4}He) measured in this study (closed circles) and reported in [6] (open circles).

(Fig. 1*b*). Therefore, separation of the reaction products by one-dimensional spectra from the detector used results in large measurement uncertainties.

EXPERIMENTAL RESULTS

Figure 3 shows the reaction cross sections determined in our measurements (closed circles) and the similar data from [6] (open circles). As can be seen from Fig. 3, our data on σ_R coincide with the data from [6] to within the experimental uncertainty in the energy range from 15 to 30 MeV/A. At the energies below 15 MeV/A used in our experiment, a sharp increase in σ_R is observed.

The cross sections of reactions with the α particle produced in the ^{28}Si(^{6}He, ^{4}He)X channel measured in our experiments also differ only slightly from the data from [6] within the overlapping energy range (Fig. 3). However, a nonregularity is observed for the energy dependences of these cross sections as well as for the variation of σ_R; in this case, the cross section decreases at energies below 15 MeV/A.

The widths of the energy intervals (Fig. 3) used in the measurements were determined by the detector thickness and by the E_0 initial energy of ^{6}He ions. Some values of the intervals overlapped because the experiments were performed at different E_0. The uncertainties of σ_R were ±3%, as determined by the statistical errors, by uncertainty of the measured detector thickness, and mainly by the accuracy of separation of the events caused by the nuclear interactions in the given pair of detectors. The uncertainties were higher in determining the cross section of the reaction ^{28}Si (^{6}He, ^{4}He)X, where they amounted to ±6%.

DISCUSSION

In our view, a comparison of the energy dependence of the total cross section of ^{6}He interaction with ^{28}Si to the similar dependences for the neighboring nuclei is of interest. Figure 4 shows the total reaction cross sections for ^{4}He, ^{6}Li, and ^{8}He together with the data for ^{6}He. The values of σ_R for ^{4}He presented in Fig. 4 are taken from [7] and marked with open squares. The results of our measurements are indicated by black circles. The procedure used for measuring σ_R in [7] differed from that used in our study. Nevertheless, good agreement is observed between these data (Fig. 4). The σ_R values of the ^{6}Li + ^{28}Si reaction are taken from [10]. It should be noted that the σ_R values marked with open triangles in Fig. 4 were obtained from data on the elastic scattering of ^{6}Li on ^{28}Si [10]. The results on the direct σ_R measurement presented in [6, 9] do not contradict the data from [10]. The σ_R values for ^{8}He were taken from [6].

Comparison of the experimental dependences of the total reaction cross sections presented in Fig. 4 clearly indicates the "anomalous" behavior of the σ_R excitation function for ^{6}He in comparison to the neighboring nuclei—that is, an almost invariable value within the range from 20 to 60 MeV/A and a sharp increase in the region of $\sim$15 MeV/A.

Solid curves in Fig. 4 show the results of calculation of the total reaction cross sections based on the semimicroscopic approach [11] using a double-convolution potential within the framework of the optical model for the analysis of σ_R. The interaction potential of two colliding nuclei is presented in the form

$$U(\mathbf{R}) = U^E(\mathbf{R}) + U^D(\mathbf{R}), \quad (1)$$

where $U^D(\mathbf{R})$ is the "direct" double-convolution potential:

$$U^D(\mathbf{R}) = \int\int \rho^{(1)}(\mathbf{r}_1) V^D(\mathbf{s}) \rho^{(2)}(\mathbf{r}_2) d\mathbf{r}_1 d\mathbf{r}_2. \quad (2)$$

Here, $V^D(\mathbf{s})$ is the "direct" component of the effective interaction with $\mathbf{s} = \mathbf{r}_2 - \mathbf{r}_1$ and ρ^i $(i = 1, 2)$ are the densities of the colliding nuclei. The main contribution to the exchange potential $U^E(\mathbf{R})$ is due to the single-nucleon exchange described within the formalism of the density matrix

$$U^E(\mathbf{R}) = \int\int \rho^{(1)}(\mathbf{r}_1, \mathbf{r}_1 + \mathbf{s}) V^E(\mathbf{s}) \quad (3)$$
$$\times \rho^{(2)}(\mathbf{r}_2, \mathbf{r}_2 - \mathbf{s}) \exp\left(i\frac{\mathbf{k}\cdot(\mathbf{R})\mathbf{s}}{\eta}\right) d\mathbf{r}_1 d\mathbf{r}_2.$$

Here, $V^E(\mathbf{s})$ is the exchange component of the effective interaction $\rho^i(\mathbf{r}, \mathbf{r}')$ are the density matrices of the colliding nuclei $(i = 1, 2)$ and $\mathbf{K}(\mathbf{R})$ is the local momentum determined by the relation

$$\mathbf{K}^2(\mathbf{R}) = \frac{2m\eta}{\hbar^2}(E - U(\mathbf{R}) - V_{\mathrm{C}}(\mathbf{R})), \quad (4)$$

where $\eta = A_1A_2/(A_1 + A_2)$, A_i $(i = 1, 2)$ being the mass numbers of the nuclei, and $V_{\mathrm{C}}(\mathbf{R})$ is the Coulomb potential. The initial data for the calculation of the double-convolution potential are the effective nucleon–nucleon forces and the densities of the colliding nuclei. The proton and neutron densities can be parametrized or calculated within the framework of the nuclear structure models. The total optical potential must comprise both the real part and the imaginary part, the latter being responsible for the absorption of the incident particle in the inelastic channels. Thus, the total potential is

$$U_t(\mathbf{R}) = U(\mathbf{R}) + i\left[N_w U(\mathbf{R}) - \alpha R \frac{dU(\mathbf{R})}{dR}\right], \quad (5)$$

where $U(\mathbf{R})$ includes the direct and exchange parts and the imaginary part has two parameters (N_w and α). For the calculations of the reaction cross sections based on potential (5) to have a predicting power, it is necessary to determine the N_w and α parameters from the analysis of the angular distributions of elastic scattering measured at the same energy as the total reaction cross sections. The table gives the root-mean-square radii of the proton, neutron, and matter distributions that served as the basis for the calculations of the cross sections.

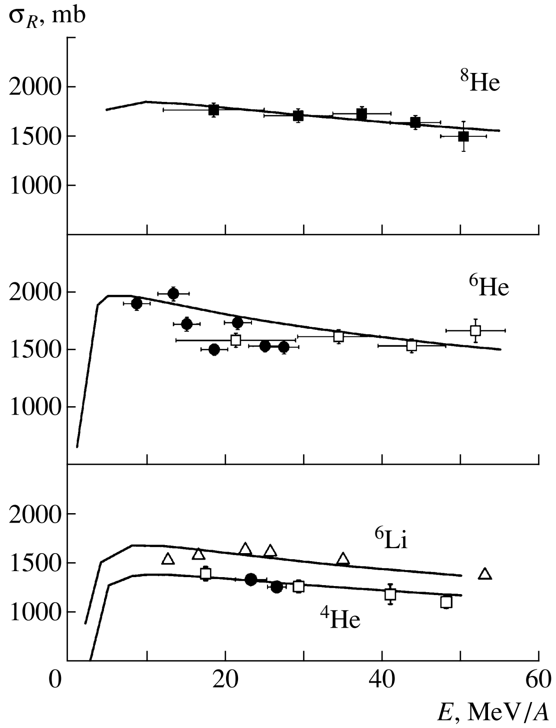

Fig. 4. Total reaction cross sections for ^{4}He [(□) [7]; (●) this study], ^{6}Li (△) [10], ^{8}He (■) [6], and ^{6}He [(●) this study; (□) [6]].

Figure 4 demonstrates that the theoretical calculations of the energy dependence of σ_R for ^{4,8}He and ^{6}Li are in reasonable agreement with the experimental results. However, variation of the parameters of the ^{6}He density or fitting of the N_w and α parameters in potential (5) do not result in satisfactory description of the behavior of the σ_R excitation function for ^{6}He.

Root-mean-square radii of the distribution of protons, neutrons, and matter (in fm)

Nucleus	R^p_{rms}	R^n_{rms}	R^m_{rms}
^{4}He	1.57	1.57	1.57
^{6}He	2.04	2.79	2.56
^{8}He	1.98	2.92	2.72
^{6}Li	2.37	2.38	2.36

CONCLUSION

The total cross sections of the reaction ^{6}He + ^{28}Si measured in this study for the energy range not studied previously complement the available data. The sharp increase in σ_R is observed in the energy range below 17 MeV/A. The energy spectra of α particles produced in the ^{6}He interaction with silicon indicate two mechanisms of their production: transfer reactions and ^{6}He breakup in the field of the ^{28}Si nucleus. The energy dependence of σ_R for ^{6}He, different from that for the neighboring nuclei, is probably caused by the structural features of this nucleus. The observed behavior of σ_R indicates the necessity of an experimental study of the σ_R variations in a wide energy range up to the Coulomb barrier in more detail.

ACKNOWLEDGMENTS

We are grateful to Yu.Ts. Oganessian and M.G. Itkis for stimulating discussions and to the technical staff of the U400-M cyclotron for obtaining an intense incident beam of ^{7}Li ions.

This work was performed within the special purpose program of the JINR collaboration with the Czech Republic and Bulgaria and was supported by the Russian Foundation for Basic Research (project no. 01-02-22001); the work of one of authors (I.N.K.) was supported by the Russian Foundation for Basic Research (project no. 00-01-00617).

REFERENCES

1. I. Tanihata, H. Hamagaki, O. Hashimoto, *et al.*, Phys. Lett. B **160B**, 380 (1985).
2. O. M. Knyazkov, I. N. Kukhtina, and S. A. Fayans, Fiz. Élem. Chastits At. Yadra **30**, 870 (1999) [Phys. Part. Nucl. **30**, 369 (1999)].
3. I. Tanihata, T. Kobayashi, *et al.*, Phys. Lett. B **206**, 592 (1988).
4. M. V. Zhukov, B. V. Danilin, *et al.*, Phys. Rep. **231**, 151 (1993).
5. D. Baye, L. Desorger, D. Guillain, and D. Herschkowitz, Phys. Rev. C **54**, 2563 (1996).
6. R. E. Warner *et al.*, Phys. Rev. C **54**, 1700 (1996).
7. A. Ingemarsson, J. Nyberg, P. U. Renberg, *et al.*, Nucl. Phys. A **676**, 3 (2000).
8. R. E. Warner *et al.*, Phys. Rev. C **52**, R1166 (1995).
9. I. V. Kuznetsov, M. P. Ivanov, R. Kalpakchieva, *et al.*, Izv. Akad. Nauk, Ser. Fiz. **63**, 992 (1999).
10. F. Carstoiu and M. Lassaut, Nucl. Phys. A **597**, 269 (1996).
11. O. M. Knyazkov, I. N. Kukhtina, and S. A. Fayans, Yad. Fiz. **61**, 827 (1998) [Phys. At. Nucl. **61**, 744 (1998)].

Translated by E. Kozlovskiĭ

Physics of Atomic Nuclei, Vol. 65, No. 9, 2002, pp. 1575–1587. From Yadernaya Fizika, Vol. 65, No. 9, 2002, pp. 1615–1628.
Original English Text Copyright © 2002 by Ponomarev, Solov'ev.

NUCLEI
Theory

Advanced Adiabatic Approach to Superlow-Energy Inelastic Collisions of Mesic Atoms in Excited States*

L. I. Ponomarev and E. A. Solov'ev[1]

Russian Research Centre Kurchatov Institute, pl. Kurchatova 1, Moscow, 123182 Russia

Received April 12, 2001; in final form, October 15, 2001

Abstract—The advanced adiabatic approach previously proposed for describing collision problems in atomic physics is extended to the specific case of mesic-atom collisions in the excited states $n \geq 2$. The method and the algorithm of the calculations are described. The calculations of the charge-exchange and Coulomb deexcitation rates in collisions of $(p\mu)_n, (d\mu)_n$, and $(t\mu)_n$ muonic atoms in the excited states $n = 3, 4, 5$ with the hydrogen isotopes p, d, t are presented in comparison with the conventional adiabatic approach. © *2002 MAIK "Nauka/Interperiodica".*

1. INTRODUCTION

There are several problems in muonic physics, weak-interaction physics, and especially in physics of muon-catalyzed fusion which need the cross section of different collision processes of mesic hydrogen isotope atoms in the excited states $n \leq 6$, particularly

charge exchange

$$(a\mu)_n + b \xrightarrow{\lambda^{\mathrm{ex}}_{nn'}} (b\mu)_{n'} + a; \quad (1)$$

Coulomb deexcitation

$$(a\mu)_n + b \xrightarrow{\lambda^{\mathrm{C}}_{nn'}} (a\mu)_{n'} + b, \quad n' < n; \quad (2)$$

Stark mixing

$$(a\mu)_{nl} + b \xrightarrow{\lambda^{\mathrm{St}}_{n}} (a\mu)_{nl'} + b. \quad (3)$$

Here, $(a, b) = (p, d, t)$, and collision energy $0.001 \leq \varepsilon \leq 100$ eV.

This problem was first formulated in the classical paper by Leon and Bethe [1], but it has not yet been solved properly. At present, processes (1)–(3) are becoming of special interest in the problem of muon-catalyzed fusion (μCF), particularly for the description of μCF kinetics.

Initially, muonic atoms $(a\mu)_{nl}$ are formed in the quantum states (nl), $n \lesssim (m_\mu/m_e)^{1/2} \approx 14$. Then, the distributions $\rho_{nl}(\varepsilon)$ over the states (nl) and kinetic energy ε are determined by the collision processes (1)–(3) as well as the Auger transitions

$$(a\mu)_n + \mathrm{H}_2 \to (a\mu)_{n'} + \mathrm{H}_2^+ + e \quad (4)$$

and radiative transitions

$$(a\mu)_{nl} \to (a\mu)_{n'l'} + \gamma. \quad (5)$$

The final results of μCF cascade $(nl) \to (1s\sigma)$ are the distribution $\rho_{1s}(\varepsilon)$ in the ground state and the x-ray intensities $Y_{nl,n'l'}$ of process (5).

There are no rigorous quantum-mechanical calculations of processes (1)–(3) for $n > 2$. Here, we will apply the advanced adiabatic approach (AAA method) [2, 3] for the calculations of the cross sections of these processes. The first applications of the AAA method for processes (1)–(3) were presented in [4–8]. However, these calculations were performed not for the pure Coulomb three-body systems in processes (1)–(3) but for the screened Coulomb centers chosen in the static form [9].

In what follows, we will present the self-consistent method of calculation of the rates of processes (1) and (2) based on the AAA method modified to the specific case of low-energy mesic-atom collisions.

2. ADIABATIC REPRESENTATION

The main and only difference of processes (1)–(3) from the analogous atomic processes is the muon mass $m_\mu = 206.769 m_e$, which leads nevertheless to an essential modification of the codes developed for the description of atomic collisions.

As a consequence of the mass ratio $m_\mu/m_e \approx 200$, the Bohr radius in mesic atomic physics is much

---

*This article was submitted by the authors in English.

[1] Macedonian Academy of Science and Art, Skopje, Macedonia; permanent address: Research Coordinative Center on the Problems of Muon Catalyzed Fusion and Exotic Quantum Systems (MUCATEX), Moscow, Russia.

1063-7788/02/6509-1575$22.00 © 2002 MAIK "Nauka/Interperiodica"

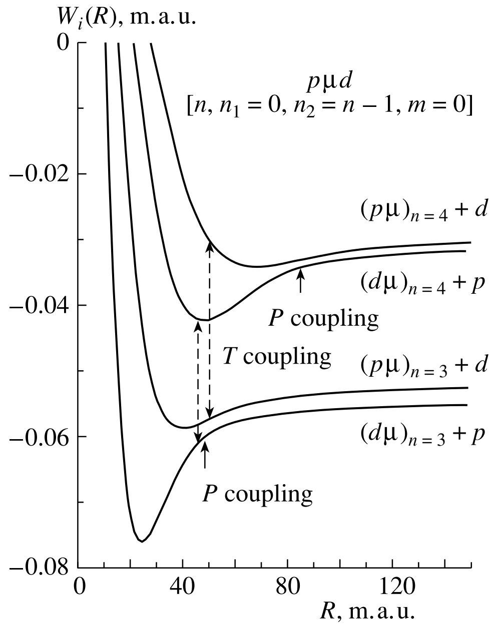

Fig. 1. Selected terms and illustration of inelastic transitions via hidden crossings in the system $p\mu d$. The locations of hidden crossings are marked by arrows.

smaller ($a_\mu = a_0 m_e/m_\mu = 2.56 \times 10^{-11}$ cm) and the unit of energy is much higher ($E_\mu = 2\text{Ry}(m_\mu/m_e) = 5606$ eV). Hence, the typical energy in mesic atomic collisions ($\sim$1 eV) corresponds to superlow energy ($\sim$0.005 eV) in atomic collisions. In the collision-energy range $\varepsilon \leq 100$ eV, all processes (1)–(3) are deep adiabatic ($v/\alpha c \lesssim 0.1$) and the relative motion of nuclei with reduced mass $M \sim 10 m_\mu$ takes place in the static potential formed by the averaged muon motion.

Contrary to atomic collisions, where the classical description of the relative nuclear motion is appropriate, the low-energy mesic atomic collisions (1)–(3) at $n > 2$ should be considered as semiclassical [9], and impact-parameter approximation is inadequate in this case due to the small number of partial waves ($J \lesssim 10$).

All the peculiarities of mesic atomic processes mentioned above are taken into account in the method of calculation described below.

The Hamiltonian $\hat{H}$ of the problem in Jacobi coordinates $(\mathbf{R}, \mathbf{r})$ has the form (in mesic atomic units, m.a.u., $\hbar = e = m_\mu = 1$)

$$\hat{H} = -\frac{1}{2M}\Delta_{\mathbf{R}} - \frac{1}{2m^*}\Delta_{\mathbf{r}} - \frac{Z_a}{r_a} - \frac{Z_b}{r_b} + \frac{Z_a Z_b}{R}. \tag{6}$$

Here, $\mathbf{R}$ is the vector of the internuclear distance, $\mathbf{r}$ is the coordinate of muon referred to the c.m. of nuclei, $M = (1/M_a + 1/M_b)^{-1}$ is the reduced mass of two nuclei ($M_a \geq M_b$), Z_a and Z_b are the charges of nuclei a and b, and $m^* = [1 + 1/(M_a + M_b)]$ is the reduced mass of muon moving around nuclei.

The wave functions $\Psi(\mathbf{r}, \mathbf{R})$ describing reactions (1)–(3) obey the Schrödinger equation

$$(\hat{H} - E)\Psi(\mathbf{r}, \mathbf{R}) = 0, \tag{7}$$

where E is the total energy of the three-body problem. Due to the adiabatic nature of reactions (1)–(3), the wave function $\Psi(\mathbf{r}, \mathbf{R})$ can be expanded in the solutions $\varphi_{jp}(\mathbf{r}; R)$ of the Coulomb two-center problem [10]

$$\Psi(\mathbf{r}, \mathbf{R}) = \sum_{jp} \varphi_{jp}(\mathbf{r}; R)\frac{1}{R}\chi^J_{jp}(R) D_{Jm}(\varphi, \Theta, \Phi). \tag{8}$$

Here, J is the total angular momentum of the three-body problem; $D_{Jm}(\varphi, \Theta, \Phi)$ is the Wigner function; $\chi^J_{jp}(R)$ is the radial part of the wave function describing the relative nuclear motion; $\varphi_{jp}(\mathbf{r}; R)$ is the complete set of the solutions of the Coulomb two-center problem

$$\hat{h}\varphi_{jp}(\mathbf{r}; R) = E_j(R)\varphi_{jp}(\mathbf{r}; R), \quad \hat{h} = -\frac{1}{2m^*}\Delta_{\mathbf{r}} - \frac{Z_a}{r_a} - \frac{Z_b}{r_b}, \tag{9}$$

describing the motion of particle with effective mass m^* at fixed nuclei separated at the distance R; $jp = [nn_1n_2m]_p$ is the set of parabolic quantum numbers specifying the quantum state of the muon motion (p is the state parity: g—gerade, u—ungerade). The adiabatic energy potential curves $E_j(R)$ represent the energy of muon in the state j as a function of R.

After averaging of Eq. (7) over the coordinates $\mathbf{r}$ of muon motion and angular variables (φ, Θ, Φ), processes (1)–(3) are described by the infinite set of ordinary differential equations

$$\frac{1}{2M}\frac{d^2\chi_i(R)}{dR^2} + \left[E - W_i(R) - \frac{J(J+1)}{2MR^2}\right] \times \chi^J_i(R) = \frac{1}{2M}\sum_j U_{ij}(R)\chi^J_j(R), \tag{10}$$

where $W_i(R) = E_i(R) + Z_aZ_b/R$ is effective potential for internuclear motion and $U_{ij}(R)$ are the nonadiabatic coupling potentials.

In the limit $R \to \infty$, the adiabatic terms $E_j(R)$ converge to the energy of the isolated atoms $(a\mu)_j$ and $(b\mu)_j$ with the relative accuracy $\sim M^{-1}$ only [10], because the effective mass m^* in Eq. (9) is different from the reduced masses $m_a = M_a/(1 + M_a)$ and

$m_b = M_b/(1+M_b)$ of atoms $(a\mu)$ and $(b\mu)$. To incorporate the corresponding isotopic corrections that play the important role in processes (1)–(3), the standard adiabatic approach should be modified according to [11], using the coordinates $(\mathbf{q}, \mathbf{Q})$ instead of Jacobi pair $(\mathbf{r}, \mathbf{R})$ according to the formulas

$$\mathbf{q} = \frac{1}{2}\left(\sqrt{m_a} + \sqrt{m_b}\right)\mathbf{R}_\mu - \frac{1}{2}\left(\sqrt{m_a}\mathbf{R}_a + \sqrt{m_b}\mathbf{R}_b\right), \tag{11}$$

$$\mathbf{Q} = \left(\sqrt{m_a} - \sqrt{m_b}\right)\mathbf{R}_\mu - \left(\sqrt{m_a}\mathbf{R}_a - \sqrt{m_b}\mathbf{R}_b\right),$$

where m_a and m_b are the reduced masses of mesic atoms $(a\mu)$ and $(b\mu)$. Then, the Coulomb three-body Hamiltonian in the coordinates $(\mathbf{q}, \mathbf{Q})$ takes the form

$$\hat{H} = -\frac{1}{4}\left(1 + \sqrt{m_a m_b}\right)\Delta_{\mathbf{q}} \tag{12}$$

$$- \left(1 - \sqrt{m_a m_b}\right)\Delta_{\mathbf{Q}} - \frac{\sqrt{m_a}Z_a}{|\mathbf{q}+\mathbf{Q}/2|} - \frac{\sqrt{m_b}Z_b}{|\mathbf{q}-\mathbf{Q}/2|}$$

$$+ \frac{\sqrt{m_a m_b}Z_a Z_b}{|\left(\sqrt{m_a}+\sqrt{m_b}\right)\mathbf{Q}/2 - \left(\sqrt{m_a}-\sqrt{m_b}\right)\mathbf{q}|},$$

which formally coincides with the Hamiltonian of the three-body problem with two identical heavy quasiparticles with masses $\left(1-\sqrt{m_a m_b}\right)^{-1} \gg 1$ and the light-particle mass $m = 2\left(1+\sqrt{m_a m_b}\right)^{-1} \approx 1$. (The small q corrections in the internuclear repulsion potential are out of the leading order of the adiabatic approximation.) It means that transformation (11) converts the asymmetry in masses M_a and M_b into asymmetry in charges: $Z_a \to \sqrt{m_a}Z_a$ and $Z_b \to \sqrt{m_b}Z_b$. The eigenvalues $E_j(Q)$ of the modified Hamiltonian (12) converge at $R \to \infty$ to the correct binding energies of mesic atoms $(a\mu)$ and $(b\mu)$ with the accuracy $O(M^{-2})$. This is enough for further consideration.

Transformation (11) destroys the (g, u) symmetry of the solutions $\varphi_{jp}(\mathbf{r}; R)$, and the pair of terms $E_{jg}(R)$ and $E_{ju}(R)$ degenerate for $R \to \infty$, after transformation (11), split into the pair $E_{ja}(Q)$ and $E_{jb}(Q)$, which, for $Q \approx R + (m/M)r \to \infty$, $r \ll R$, represent the energies of isolated atoms $(a\mu)_j$ and $(b\mu)_j$, respectively, with the accuracy $\sim M^{-2}$ (their ratio is represented exactly).

Quasiresonance charge-exchange process (1) at $n' = n$ is described in this case as the transition from the potential curve $(p\mu)_n + d$ to the curve $(d\mu)_n + p$, and Coulomb deexcitation $n \to n'$ (2) is described as the transitions from the potential curve $(p\mu)_n + d$ to the curves $(p\mu)_{n'} + d$ or $(d\mu)_{n'} + p$, respectively (see Figs. 1 and 2, where transient points are marked by arrows).

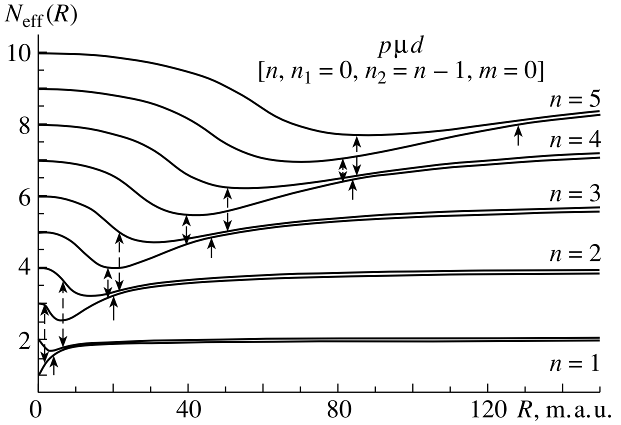

Fig. 2. Functions $N_{\text{eff}}(R) = (-E_j(R))^{-1/2}$ for the system $p\mu d$. P-type hidden crossings are marked by solid arrows, and T-type ones are marked by the dashed two side arrows.

3. PROBABILITY OF NONADIABATIC TRANSITIONS

The boundary conditions for the system of equations (10) in the case of the initially populated ith channel for $R \to \infty$ have the form

$$\chi_j^J(R) = \begin{cases} (-1)^{J+1}e^{-ip_iR} + S_{ii}^J e^{ip_iR}, & i = j \\ S_{ji}^J e^{ip_jR}, & i \neq j, \end{cases} \tag{13}$$

where $p_j = [2M(E - E_j(\infty))]^{1/2} = (2M\varepsilon)^{1/2}$ is the asymptotic momenta, S_{ji}^J are the S-matrix elements for the transition $i \to j$, and ε is the collision energy. The cross sections of inelastic processes are

$$\sigma_{ij} = \frac{\pi}{p_i^2}\sum_{J=0}(2J+1)|S_{ji}^J|^2. \tag{14}$$

In the leading order of adiabatic approximation, the coupling terms $(2M)^{-1}U_{ij}(R)$ in Eqs. (10) can be neglected and solutions $\chi_j^J(R)$ can be presented in the semiclassical form[2)]

$$\chi_j^J(R) = C_j\left[p_j^J(R)\right]^{-1/2}\exp\left\{i\int\limits_{R_0}^{R} p_j^J(R')dR'\right\}, \tag{15}$$

where

$$p_j^J(R) = \left[2M\left(E - \frac{W_j(R)}{R} - \frac{(J+1/2)^2}{2MR^2}\right)\right]^{1/2}.$$

In the adiabatic approach, the inelastic transitions are located in the vicinity of the quasicrossings of the

---

[2)] This solution is valid at $n \geq 2$ and $R \gtrsim 2M$ [9] due to the relations $p_n(R)dp_n^{-1}(R)/dR \ll 1$ at $R \gg 1$ and $E_n(R) \approx 3n(n_1 - n_2)/(2MR^2)$.

adiabatic potential curves. The quasicrossing of the terms $E_i(R)$ and $E_j(R)$ at $R = R_q = \mathrm{Re}R_c$ reflects the exact crossing of terms $E_i(R_c) = E_j(R_c) = E_c$ in the complex plane R at $R = R_c$, and the unique analytic surface $E(R) = \{E_i(R)\}$ in Eq. (9) has the root branch point

$$E_{i,j}(R) = E_c \pm \mathrm{const} \times (R - R_c)^{1/2}. \qquad (16)$$

The distribution and location of quasicrossings are illustrated in Fig. 2, where effective quantum numbers $N_{\mathrm{eff}}(R) = (-2E_j(R)/(Z_a + Z_b))^{-1/2}$ of the system $p\mu d$ are presented.[3)] The quasicrossings of terms in this picture are marked by the arrows.

To obtain the transition probability, one should continue asymptotic expression (15) into the complex R plane. This asymptotic expression is valid everywhere except for the small region Ω around a complex branch point R_c where the operator of nonadiabatic coupling $U_{ij}(R)$ has a singularity and the right-hand side of Eq. (10) gives the contribution to the leading order of adiabatic approximation. Inside Ω, it is necessary to find a solvable system of equations (the so-called comparison system) which takes into account the singularities of $U_{ij}(R)$ at the point R_c explicitly. The amplitude of the transition probability is obtained by matching the solution of the comparison system to the asymptotic expression given by (15) at the boundary of the region Ω. The final expression for the transition probability p_{ij} between i and j adiabatic states reads [12]

$$P^J_{ij} = |S^J_{ji}|^2 = e^{-2\Delta^J_{ij}}, \qquad (17)$$

$$\Delta^J_{ij} = \left| \mathrm{Im} \int\limits_{\mathrm{Re}R_c}^{R_c} \left[p^J_i(R) - p^J_j(R)\right] dR \right|. \qquad (18)$$

In the case of many quasicrossings, the density matrix can be represented as $\hat\rho^{\mathrm{in}} = \{\rho_{ij}\}, \rho_{ij} = \delta_{ij}$. The evolution of the system in the collision process from $R = \infty$ to the turning point $R = R_0$ and back to $R \to \infty$ can be presented in the matrix form

$$\begin{aligned}\hat\rho^{\mathrm{out}} &= \hat P_1 \hat P_2 \ldots \hat P_{N-1} \hat P^2_N \hat P_{N-1} \ldots \hat P_2 \hat P_1 \hat\rho^{\mathrm{in}} \qquad (19)\\ &= \hat{\mathbf{P}}^T \hat{\mathbf{P}} \hat\rho^{\mathrm{in}},\\ \hat{\mathbf{P}} &= \hat P_N \hat P_{N-1} \ldots \hat P_1,\end{aligned}$$

where N is the number of passed quasicrossings. The transient matrix $\hat P_q$ at the quasicrossing point R_q of two terms $E_\alpha(R)$ and $E_\beta(R)$ has the form [3]

$$\begin{aligned}\left(\hat P_q\right)_{ij} &= \delta_{ij}(1 - \delta_{i\alpha})(1 - \delta_{i\beta}) + (1 - P_{\alpha\beta}) \qquad (20)\\ &\times (\delta_{i\alpha}\delta_{j\alpha} + \delta_{i\beta}\delta_{j\beta}) + P_{\alpha\beta}(\delta_{i\alpha}\delta_{j\beta} + \delta_{i\beta}\delta_{j\alpha}).\end{aligned}$$

The probability of finding the system in the state j coming from the state i is equal to

$$P_{ij} = \left(\hat\rho^{\mathrm{out}}\right)_{ij}. \qquad (21)$$

In the case of one quasicrossing in the two-state system, expressions (19) take the well-known form

$$\hat\rho^{\mathrm{in}} = \begin{pmatrix} 1 & 0 \\ 0 & 1 \end{pmatrix}; \qquad (22)$$

$$\hat\rho^{\mathrm{out}} = \begin{pmatrix} (1 - p_{12})^2 + p^2_{12} & 2p_{12}(1 - p_{12}) \\ 2p_{12}(1 - p_{12}) & (1 - p_{12})^2 + p^2_{12} \end{pmatrix};$$

$$P_{12} = \left(\hat P^2_1 \rho^{\mathrm{in}}\right)_{12} = 2p_{12}(1 - p_{12});$$

$$p_{12} = \exp\{-2\Delta_{12}\}.$$

4. THE HIDDEN CROSSINGS

The quasicrossings are evident and visible on the graphs of terms if $\mathrm{Im}R_c$ is small enough, i.e., the complex crossing point R_c is located near the real axis R. Usually, these quasicrossings correspond to the resonant subbarrier penetrations in the asymptotic region $R \gg 1$. Nonadiabatic transitions at these points are well known as Landau–Zener transitions. This is quite a rare case, however, and, as a rule, hidden crossings (HC) take place.

There are four types of HC: S, T, P, and Q series [2].

(i) S series consists of an infinite set of branch points connecting pairwise the states (N, l, m) and $(N + 1, l, m)$ of the two-center problem (in the united atom classification). It means that the quasicrossed terms differ from each other in "quasiradial" quantum numbers n_1 by unity: $n_1 \leftrightarrow n_1 + 1$. This series reflects the rearrangement of the topology of the wave function from the two-center geometry of quasimolecule to the one-center geometry of united atom at the moment of formation of the centrifugal barrier.

The values R^S_c are located in the small domain of the R plane according to the relation $\mathrm{Re}R^S_{c,N} > \mathrm{Re}R^S_{c,N+1}$ with limiting value $R^S_{c,\infty}$ [3],

$$R^S_{c,\infty} = \frac{(l + 1/2)^2}{Z_a + Z_b} \exp\left\{ i\frac{\pi(m + 1)}{2l + 1} \right\}. \qquad (23)$$

(ii) T series connects the states (N, l, m) and $(N + 2, l + 2, m)$ in the symmetric case $Z_a = Z_b$. In this

---

[3)] In the limit $R \to 0$, $N_{\mathrm{eff}}(R) \to N$, where N is the principal quantum number in the united atom classification of terms $E_j(R)$. At $Z_a = Z_b = 1$, $j = (Nlm)$, $N = n_1 + l + m + 1$, $l = 2n_2$ or $l = 2n_2 + 1$ for g and u terms, respectively.

case, only the terms with the same parity and the same quantum numbers n_1 are connected and quantum numbers n_2 differ by unity: $n_2 \leftrightarrow n_2 + 1$.

The position of the T branch points can be estimated by the asymptotic expression [3]

$$R_c^{T^{\pm}} = n\left[6n_2 + 3m + 3 + i(6 \mp 2)\right], \qquad (24)$$

where $n = n_1 + n_2 + m + 1$ and $(\pm)$ parity W is related to (g, u) parity I by the relation $I = We^{im\pi}$.

T series reflects changing the muon motion with changing the internuclear distance near the top of the potential barrier separating nuclei: at $R < \mathrm{Re}R_c^T$, the muon belongs to both centers; at $R > \mathrm{Re}R_c^T$, muon motion is located near one of the nuclei and its wave function can be represented approximately by the symmetric and antisymmetric superposition of the solutions of the one-center separated atom problem (at the value $R = \mathrm{Re}R_c^T$, the energy of the system coincides with the top of the potential barrier in the angular equation of the two-center problem).

(iii) P series connects the states (N, l, m) and $(N + 1, l + 1, m)$ of the system with the slightly different charges Z_a and Z_b, which appear, for example, as a result of isotopic transformation (11). The P series connects the terms $E_{ia}(R)$ and $E_{ib}(R)$ with the same set of parabolic quantum numbers $[nn_1n_2m]$ due to subbarrier penetration. They are located in the region where the resonance defect $\Delta E = E_{ib}(\infty) - E_{ia}(\infty) = (m_a - m_b)/2n^2$ is comparable with the splitting $\Delta E_{gu}(R)$ of the terms $E_{ig}(R)$ and $E_{iu}(R)$ in the symmetric system $Z_a = Z_b$. The lower term $E_{ia}(R)$ belongs to the heavier atom $(a\mu)_i$ and corresponds at $M_a = M_b$ to the symmetric g state $(l = 2n_2)$, and the upper term $E_{ib}(R)$ of the atom $(b\mu)_i$ corresponds to the u state $(l = 2n_2 + 1)$. At $R < \mathrm{Re}R_c$, we can ignore the isotopic defect; at $R > R_q$, the isotopic defect dominates, the approximate (g, u) symmetry disappears, and the adiabatic states are localized at one of the atoms $(a\mu)_i$ or $(b\mu)_i$. The position R_c^P of the P-series branch points can be estimated from the relation [13]

$$\frac{m_a - m_b}{2n^2} = \Delta E_{gu}(R) = 2(2R/n)^{n-\Delta} \qquad (25)$$
$$\times \left[n^3 n_2!(n_2 + m)!\right]^{-1} \exp(n - R/n).$$

The P series has a special structure in this case, and the transition probability P_{ij} is calculated with the Rosen–Zener–Demkov formula, which differs from the standard Landau–Zener one [14, 15]:

$$P_{ij} = \sum_{k=1}^{\infty} (-1)^k e^{-2k\Delta_{ij}} = \frac{e^{-\Delta_{ij}}}{2\mathrm{ch}\Delta_{ij}}. \qquad (26)$$

(iv) Q series connects the same states (N, l, m) and $(N + 1, l + 1, m)$, but it appears when Z_a and Z_b began to differ significantly. Its physical origin is the same as the T series.

The sequence of the branching points R_c of the different series at $Z_a \approx Z_b$ for the same energy curve is the following:

$$\mathrm{Re}R_c^S < \mathrm{Re}R_c^Q < \mathrm{Re}R_c^P. \qquad (27)$$

5. ALGORITHM OF THE CALCULATIONS

The numerical code for the calculations of the cross sections of processes (1) and (2) is based on the automated program package ARSENY [16]. It includes the following subprograms:

(i) Calculations of the terms $E_j(R)$ of the two-center problem for the parabolic states $jp = [n\, n_1\, n_2\, m]_p, n = n_1 + n_2 + m + 1, n \leq 5, p = (g, u)$. In the united atom classification, this basis includes 110 adiabatic states (N, l, m) with the principal quantum numbers $N \leq 10$.

(ii) Search for all the branch points $R_c = \mathrm{Re}R_c + i\mathrm{Im}R_c$ of the HC in the complex plane R connecting pairwise terms $E_i(R_c) = E_j(R_c)$.

Calculations of the corresponding Stückelberg parameters $\Delta_{ij}^J(R_c)$, and S_{ji}^J matrix elements (17).

Calculations of the cross sections $\sigma_{ij}(\varepsilon)$ for the selective transitions $i \to j$ and total cross sections $\sigma_{nn'}(\varepsilon)$.

For the selective transition $i \to j$, $i = [nn_1\, n_2m]$, $j = [n'n_1'n_2'm]$, the Stückelberg parameter Δ_{ij}^J is calculated by Eq. (18):

$$\Delta_{ij}^J = \left|\mathrm{Im} \int\limits_{\mathrm{Re}R_c}^{R_c} \left[p_i^J(R) - p_j^J(R)\right] dR\right|.$$

The values $\Delta_{ij}^J(\varepsilon)$ for the system $p\mu d$ as a function of collision energy ε at $J = 0$ are plotted in Fig. 3.

The selective cross sections $\sigma_{ij}(\varepsilon)$ are determined by the equation

$$\sigma_{ij}(\varepsilon) = \frac{\pi}{p_i^2} \sum_{J=0}^{\infty} (2J + 1) P_{ij}^J, \qquad (28)$$

where ε is the impact energy, $p_i = [2M(E - E_i(\infty))]^{1/2} = (2M\varepsilon)^{1/2}$ is the momentum in the entrance channel i, and P_{ij}^J is determined by

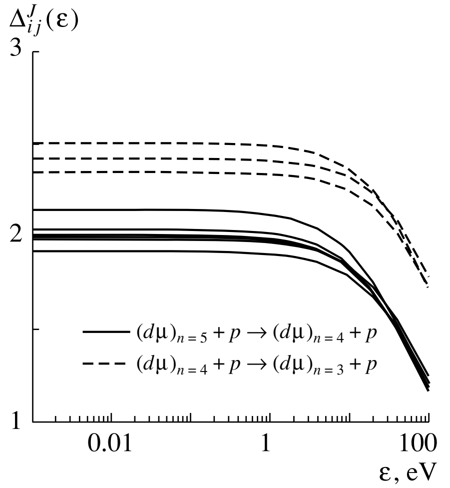

Fig. 3. Stückelberg parameters $\Delta^J_{ij}(\varepsilon)$ at $J = 0$ as a function of energy: $\Delta^0_{ij}(\varepsilon) \approx \text{const}$ at $\varepsilon \lesssim 1$ eV.

(17). The averaged cross sections $\sigma_{nn'}(\varepsilon)$ for the transitions $n \to n'$ are equal to[4)]

$$\sigma_{nn'}(\varepsilon) = \sum_{n_1,n_2,n'_1,n'_2,m} \frac{2-\delta_{0m}}{n^2}\sigma_{ij}(\varepsilon). \qquad (29)$$

The transition rates are defined at liquid-hydrogen density $\rho_0 = 4.25 \times 10^{22}$ cm^{-3} by the relation

$$\lambda_{nn'} = \sigma_{nn'} v \rho_0, \qquad (30)$$

where v is the relative velocity in collisions (1)–(3).

The calculation scheme can be illustrated in Figs. 1 and 2, where terms $E_i(R)$ with $m = 0$ and $\Delta = -(n-1)$ at $n \leq 5$ are plotted. HC of P and T types are marked by arrows. Only these two types of quasicrossings give the contributions to the cross sections σ_{ij} of the processes (1) and (2). At low collision energies under consideration, only attractive terms at $R \gg 1$

$$E_i(R) \approx -\frac{1}{2n^2} + \frac{3}{2R} n\Delta + \cdots$$

with $\Delta = n_1 - n_2 < 0$ contribute to σ_{ij}. From 110 terms $E_i(R)$ of the basis set at $n \leq 5$, only 14 are attractive ($\Delta < 0$). They are connected by the branch points (13 of them are P-type and 25 are T-type). Figure 2 demonstrates the transition from terms $E_i(R)$ with $m = 0$, $\Delta = -(n-1)$. It is clear that quasiresonant charge–exchange reaction (1) is ruled only by the P-type branch points: six for transition $(n = 5) \to (n' = 5, 4, 2$, and one for the transitions from $n = 4, 3$, and 2, respectively (see Table 1). The Coulomb deexcitations (2) are ruled by the T-type branch points only. The combination of the P- and T-type hidden crossings is of importance

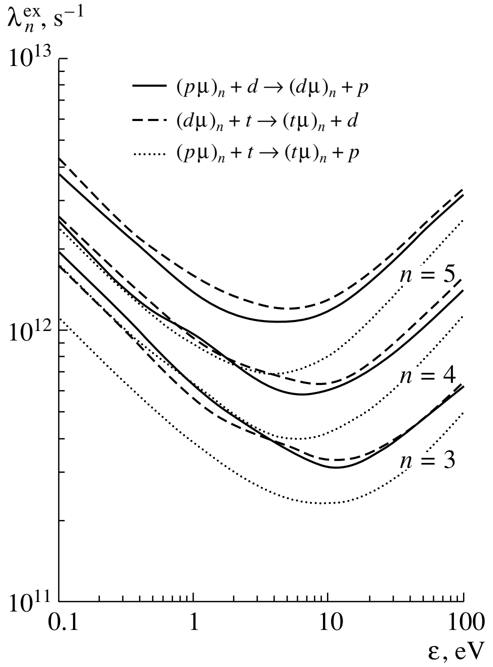

Fig. 4. Rates $\lambda^{\text{ex}}_n(\varepsilon)$ of the resonance charge exchange (1) as a function of collision energy ε.

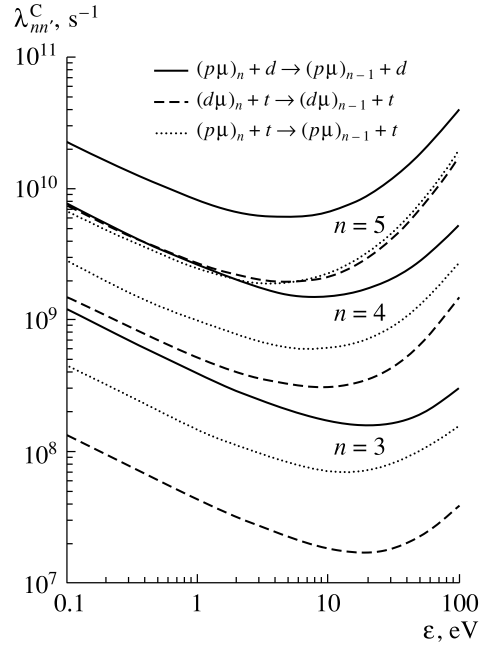

Fig. 5. Rates $\lambda^{\text{C}}_{nn'}$ of the nonsymmetric Coulomb deexcitations (2) from the heavier mesic atom to the lighter one.

[4)] Equation (29) is also valid for symmetrical systems ($p\mu p$, etc.). In this case, however, the asymptotic atomic states $|ia\rangle$ and $|ib\rangle$ are formed as a superposition of the two-center states: $|ia\rangle = (|ig\rangle + |iu\rangle)/\sqrt{2}$, $|ib\rangle = (|ig\rangle - |iu\rangle)/\sqrt{2}$.

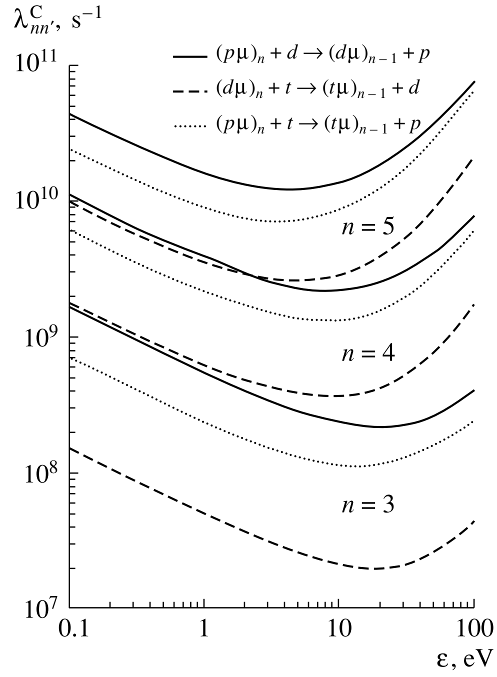

Fig. 6. Rates $\lambda^{C}_{nn'}$ of the nonsymmetric Coulomb deexcitations (2) from the lighter mesic atom to the heavier one.

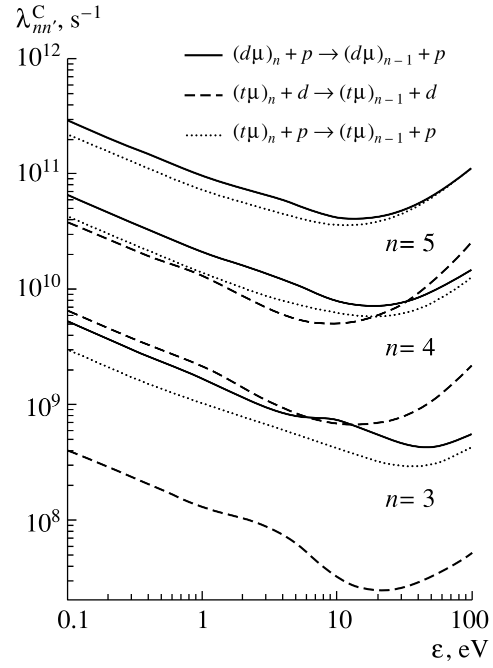

Fig. 7. Rates $\lambda^{C}_{nn'}$ of the symmetrical deexcitations (2).

for the reactions

$$(p\mu)_n + d \to (d\mu)_{n'} + p, \quad n \neq n'. \qquad (31)$$

It is quite easy to trace the path through the transient points R_q for any reaction $n \to n'$ corresponding to the selective transitions $[nn_1n_2m] \to [n'n'_1n'_2m]$ and to extract the most essential of them which make the main contributions to the transition probabilities P_{ij}. For example, in the case of the reaction (31) at $n = 5$, the main contribution gives the quasicrossing point of T type, which connects the states $i = [5040]$ and $j = [4030]$ with parameters $R_q \approx 83$, $\Delta_{ij} \simeq 2$ (see Fig. 2). For the reaction

$$(d\mu)_n + p \to (d\mu)_{n'} + p \qquad (32)$$

from $n = 4$ to $n' = 3$, only T-type quasicrossings are significant at $R \approx 45$.

6. ESTIMATIONS

Relations (16)–(21) and (28)–(30) give the complete scheme for the calculation of all the cross sections $\sigma_{ij}(\varepsilon)$ and $\sigma_{nn'}(\varepsilon)$ at collision energy ε. At ε high enough, we can also use the impact parameter language for the presentation of the results. In this case,

$$\frac{\pi}{p^2}\sum_J (2J+1) \to 2\pi \int_0^{\rho_m} \rho\, d\rho, \qquad (33)$$

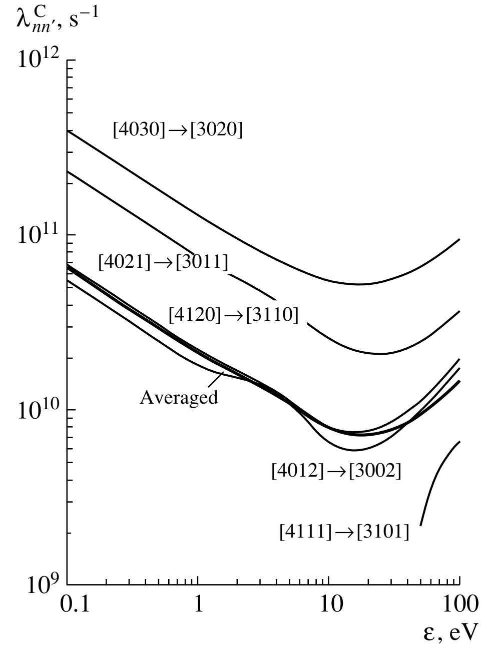

Fig. 8. Partial and total rates of Coulomb deexcitations $[nn_1n_2m] \to [n'n'_1n'_2m]$ for the process $(d\mu)_{n=4} + p \to (d\mu)_{n=3} + p$.

where the maximal impact parameter ρ_m is determined from the relations

$$\rho_m = \min\{\rho_{iq}, \rho_{jq}\}, \qquad (34)$$

Table 1. HC parameters for the system $(d\mu)_n + p$ at $\varepsilon = 1$ eV for the transitions $[nn_1n_2m] \to [n'n_1'n_2'm]$ (initial shell $n = 4$)

$[n, n_1, n_2, m]$	$[n', n_1', n_2', m]$	Type of HC	G	R_q	$\Delta_0(J=0)$	J_m
$4030(d\mu)$	$3020(d\mu)$	T	385.5	46.0	2.411	18
$3020(d\mu)$	$3020(p\mu)$	P	535.7	46.0	0.279	0
$3011(d\mu)$	$3011(p\mu)$	P	442.4	37.7	0.190	0
$4031(d\mu)$	$3011(d\mu)$	T	294.3	36.2	2.338	13
$3110(d\mu)$	$3110(p\mu)$	P	329.0	29.3	0.190	0
$4120(d\mu)$	$3110(d\mu)$	T	166.4	28.2	2.491	7
$3002(d\mu)$	$3002(p\mu)$	P	301.4	26.7	0.194	0
$4012(d\mu)$	$3002(d\mu)$	T	150.5	26.0	2.490	7
$2010(d\mu)$	$2010(p\mu)$	P	489.2	21.5	0.146	0
$3020(d\mu)$	$2010(d\mu)$	T	319.3	20.4	2.564	0
$3101(d\mu)$	$3101(p\mu)$	P	167.6	19.5	0.217	0
$2001(d\mu)$	$2001(p\mu)$	P	333.4	15.0	0.138	0
$3011(d\mu)$	$2001(d\mu)$	T	191.5	13.4	2.461	0
$2100(d\mu)$	$2100(p\mu)$	P	177.5	9.6	0.137	0
$1000(d\mu)$	$1000(p\mu)$	P	297.6	6.0	0.112	0
$2010(d\mu)$	$1000(d\mu)$	T	91.6	4.8	3.786	0

$$\rho_{iq} = R_q \left[1 - \frac{W_i(R_q)}{\varepsilon}\right]^{1/2},$$
$$\varepsilon = E - E_i(\infty),$$
$$W_i(R) = \frac{Z_a + Z_b}{R} + E_i(R) - E_i(\infty)$$

with the additional condition $R_q \geq R_0$, where $R_q = \mathrm{Re} R_c$ and R_0 is the turning point for the motion in the potential $W_i(R)$. (It is evident that $P_{ij} = 0$ at $R_q < R_0$.) The number J_m of the partial waves in the sum (28) can be estimated from the relation

$$J_m = \mathrm{ent}\left(\sqrt{2M\varepsilon}\rho_m - 1/2\right). \qquad (35)$$

We can also determine the focusing factor

$$G = \frac{\rho_m}{R_q}, \qquad (36)$$

which reflects the amplification of the inelastic cross sections comparing to the "geometrical" cross sections at straight-line collisions:

$$\sigma_{ij} = \pi\rho_m^2 P_{ij} = \pi R_q^2 G^2 P_{ij}. \qquad (37)$$

At low collision energy, G factors are large (Table 1).

The described method allows one to perform semianalytic calculations of the cross sections σ_{ij} using the simple approximation of the Stückelberg parameter, which follows from (15), (18), and (33):

$$\Delta_{ij}^J(\rho) = \Delta_0 + \Delta_1 \left(\frac{\rho}{\rho_m}\right)^2, \qquad (38)$$

where ρ_m is determined by (34), and Δ_0 and Δ_1 can be calculated from (18). Finally, we obtain the simple estimate for the cross section determined by a single HC:

$$\sigma = 2\pi \int_0^{\rho_m} 2e^{-2\Delta(\rho)} \left(1 - e^{-2\Delta(\rho)}\right) \rho d\rho \qquad (39)$$
$$= \frac{\pi\rho_m^2}{\Delta_1}\xi(1-\xi) = \frac{\pi}{\Delta_1}(GR_q)^2 \xi(1-\xi),$$
$$\xi = e^{-2\Delta_0}\left(1 - e^{-2\Delta_1}\right).$$

For example, the partial Coulomb deexcitation rate [4030] → [3020] in $(d\mu)_n + p$ collision at $\varepsilon = 1$ eV is equal to $\lambda = 1.30 \times 10^{11}\ \mathrm{s}^{-1}$. According to Table 1, it is determined by the T-type HC at $R_q = 46$ with parameters $G = 385.5$ and $\Delta_0 = 2.41$. Having $\Delta_1 = 1.06$ from (18), we can find from (39) a very reasonable estimate for this rate $\tilde{\lambda} = 1.44 \times 10^{11}\ \mathrm{s}^{-1}$.

Table 2. Charge-transfer (1) and deexcitation (2) rates (in s^{-1}) in $(p\mu)_n + d$ collisions (J_m is the number of partial waves)

ε, eV	Charge transfer			Deexcitation		J_m
	$n' = n$	$n' = n - 1$	$n' = n - 2$	$n' = n - 1$	$n' = n - 2$	
0.001	1.86×10^{13}	1.68×10^{10}	6.76×10^{5}	1.21×10^{10}	5.38×10^{5}	8
0.004	9.29×10^{12}	8.40×10^{9}	3.38×10^{5}	6.04×10^{9}	2.69×10^{5}	8
0.01	5.88×10^{12}	5.31×10^{9}	2.14×10^{5}	3.82×10^{9}	1.70×10^{5}	8
0.04	2.94×10^{12}	2.66×10^{9}	1.07×10^{5}	1.91×10^{9}	8.52×10^{4}	8
0.1	1.95×10^{12}	1.68×10^{9}	6.78×10^{4}	1.21×10^{9}	5.40×10^{4}	8
0.5	8.80×10^{11}	7.63×10^{8}	3.07×10^{4}	5.49×10^{8}	2.44×10^{4}	8
1.0	6.29×10^{11}	5.48×10^{8}	2.20×10^{4}	3.95×10^{8}	1.75×10^{4}	8
5.0	3.65×10^{11}	2.88×10^{8}	1.10×10^{4}	2.08×10^{8}	8.78×10^{3}	9
10.0	3.14×10^{11}	2.41×10^{8}	8.85×10^{3}	1.74×10^{8}	7.04×10^{3}	11
50.0	4.72×10^{11}	2.63×10^{8}	8.14×10^{3}	1.92×10^{8}	6.49×10^{3}	17
100.0	6.22×10^{11}	4.10×10^{8}	1.07×10^{4}	3.03×10^{8}	8.59×10^{3}	23
$n = 4$						
0.001	2.53×10^{13}	1.13×10^{11}	2.89×10^{8}	7.67×10^{10}	2.17×10^{8}	11
0.004	1.26×10^{13}	5.66×10^{10}	1.44×10^{8}	3.83×10^{10}	1.08×10^{8}	11
0.01	8.00×10^{12}	3.58×10^{10}	9.14×10^{7}	2.43×10^{10}	6.85×10^{7}	11
0.04	4.00×10^{12}	1.79×10^{10}	4.58×10^{7}	1.22×10^{10}	3.43×10^{7}	11
0.1	2.54×10^{12}	1.14×10^{10}	2.90×10^{7}	7.72×10^{9}	2.18×10^{7}	11
0.5	1.18×10^{12}	5.21×10^{9}	1.33×10^{7}	3.54×10^{9}	9.96×10^{6}	11
1.0	9.68×10^{11}	3.99×10^{9}	9.64×10^{6}	2.71×10^{9}	7.23×10^{6}	11
5.0	5.88×10^{11}	2.29×10^{9}	5.22×10^{6}	1.56×10^{9}	3.92×10^{6}	13
10.0	6.03×10^{11}	2.24×10^{9}	4.52×10^{6}	1.53×10^{9}	3.40×10^{6}	15
50.0	1.02×10^{12}	4.18×10^{9}	7.79×10^{6}	2.83×10^{9}	5.90×10^{6}	25
100.0	1.42×10^{12}	7.94×10^{9}	1.52×10^{7}	5.34×10^{9}	1.16×10^{6}	34
$n = 5$						
0.001	3.75×10^{13}	4.34×10^{11}	5.12×10^{9}	2.22×10^{11}	3.31×10^{9}	17
0.004	1.87×10^{13}	2.17×10^{11}	2.56×10^{9}	1.11×10^{11}	1.65×10^{9}	17
0.01	1.19×10^{13}	1.37×10^{11}	1.62×10^{9}	7.04×10^{10}	1.05×10^{9}	17
0.04	5.94×10^{12}	6.89×10^{10}	8.13×10^{8}	3.53×10^{10}	5.25×10^{8}	17
0.1	3.77×10^{12}	4.38×10^{10}	5.17×10^{8}	2.25×10^{10}	3.34×10^{8}	17
0.5	1.85×10^{12}	2.13×10^{10}	2.45×10^{8}	1.09×10^{10}	1.57×10^{8}	17
1.0	1.39×10^{12}	1.63×10^{10}	1.89×10^{8}	8.22×10^{9}	1.20×10^{8}	17
5.0	1.08×10^{12}	1.24×10^{10}	1.39×10^{8}	6.13×10^{9}	8.71×10^{7}	19
10.0	1.18×10^{12}	1.39×10^{10}	1.49×10^{8}	6.68×10^{9}	9.23×10^{7}	22
50.0	2.31×10^{12}	3.75×10^{10}	4.00×10^{8}	1.84×10^{10}	2.53×10^{8}	44
100.0	3.19×10^{12}	7.85×10^{10}	9.58×10^{8}	4.10×10^{10}	6.22×10^{8}	61

Table 3. Charge-transfer (1) and deexcitation (2) rates (in s^{-1}) in $(d\mu)_n + p$ collisions (J_m is the number of partial waves)

ε, eV	Charge transfer			Deexcitation		J_m
	$n' = n$	$n' = n - 1$	$n' = n - 2$	$n' = n - 1$	$n' = n - 2$	
0.001	0	3.76×10^{10}	1.05×10^{6}	5.27×10^{10}	1.32×10^{6}	10
0.004	0	1.88×10^{10}	5.25×10^{5}	2.64×10^{10}	6.60×10^{5}	10
0.01	0	1.19×10^{10}	3.32×10^{5}	1.67×10^{10}	4.17×10^{5}	10
0.04	0	5.95×10^{9}	1.66×10^{5}	8.34×10^{9}	2.09×10^{5}	10
0.1	0	3.77×10^{9}	1.05×10^{5}	5.28×10^{9}	1.32×10^{5}	10
0.5	0	1.70×10^{9}	4.73×10^{4}	2.38×10^{9}	5.94×10^{4}	10
1.0	0	1.21×10^{9}	3.37×10^{4}	1.69×10^{9}	4.23×10^{4}	10
5.0	0	5.74×10^{8}	1.60×10^{4}	8.02×10^{8}	2.01×10^{4}	10
10.0	0	5.23×10^{8}	2.25×10^{4}	7.30×10^{8}	2.83×10^{4}	10
50.0	3.27×10^{11}	3.12×10^{8}	1.20×10^{4}	4.30×10^{8}	1.50×10^{4}	15
100.0	5.40×10^{11}	4.09×10^{8}	1.36×10^{4}	5.56×10^{8}	1.70×10^{4}	21
			$n = 4$			
0.001	0	3.41×10^{11}	9.62×10^{8}	6.48×10^{11}	1.29×10^{9}	18
0.004	0	1.71×10^{11}	4.81×10^{8}	3.24×10^{11}	6.45×10^{8}	18
0.01	0	1.08×10^{11}	3.04×10^{8}	2.05×10^{11}	4.08×10^{8}	18
0.04	0	5.40×10^{10}	1.52×10^{8}	1.03×10^{11}	2.04×10^{8}	18
0.1	0	3.42×10^{10}	9.65×10^{7}	6.50×10^{10}	1.29×10^{8}	18
0.5	0	1.55×10^{10}	4.37×10^{7}	2.95×10^{10}	5.86×10^{7}	18
1.0	0	1.11×10^{10}	3.14×10^{7}	2.12×10^{10}	4.21×10^{7}	18
5.0	0	5.83×10^{9}	1.59×10^{7}	1.10×10^{10}	2.13×10^{7}	18
10.0	3.09×10^{11}	4.10×10^{9}	1.08×10^{7}	7.98×10^{9}	1.44×10^{7}	19
50.0	8.48×10^{11}	4.96×10^{9}	1.24×10^{7}	9.39×10^{9}	1.64×10^{7}	23
100.0	1.28×10^{12}	8.33×10^{9}	2.11×10^{7}	1.49×10^{10}	2.77×10^{7}	34
			$n = 5$			
0.001	0	1.22×10^{12}	1.84×10^{10}	2.85×10^{12}	3.06×10^{10}	25
0.004	0	6.10×10^{11}	9.19×10^{9}	1.43×10^{12}	1.53×10^{10}	25
0.01	0	3.86×10^{11}	5.82×10^{9}	9.02×10^{11}	9.67×10^{9}	25
0.04	0	1.94×10^{11}	2.91×10^{9}	4.53×10^{11}	4.85×10^{9}	25
0.1	0	1.23×10^{11}	1.85×10^{9}	2.88×10^{11}	3.08×10^{9}	25
0.5	0	5.63×10^{10}	8.47×10^{8}	1.31×10^{11}	1.41×10^{9}	25
1.0	0	4.15×10^{10}	6.17×10^{8}	9.67×10^{10}	1.03×10^{9}	25
5.0	0	2.37×10^{10}	3.47×10^{8}	5.41×10^{10}	5.74×10^{8}	26
10.0	7.09×10^{11}	1.83×10^{10}	2.64×10^{8}	4.19×10^{10}	4.38×10^{8}	27
50.0	2.05×10^{12}	3.06×10^{10}	4.53×10^{8}	6.37×10^{10}	7.23×10^{8}	42
100.0	3.03×10^{12}	5.70×10^{10}	9.32×10^{8}	1.13×10^{11}	1.45×10^{9}	60

Table 4. Partial rates (in s^{-1}) of transitions $[nn_1n_2m] \to [n'n'_1n'_2m]$ for Coulomb deexcitation (2) $(n = 4) \to (n' = 3)$

ε, eV	$[4030] \to [3020]$	$[4120] \to [3110]$	$[4021] \to [3011]$	$[4012] \to [3002]$	Total rate of $(n = 4) \to (n' = 3)$, s^{-1}
$(p\mu)_n + d \to (p\mu)_{n'} + d$					
0.001	0.755×10^8	0.181×10^{12}	0.367×10^{12}	0.156×10^{12}	7.67×10^{10}
0.004	0.378×10^8	0.906×10^{11}	0.183×10^{12}	0.780×10^{11}	3.83×10^{10}
0.01	0.239×10^8	0.573×10^{11}	0.116×10^{12}	0.494×10^{11}	2.43×10^{10}
0.04	0.120×10^8	0.287×10^{11}	0.581×10^{11}	0.247×10^{11}	1.22×10^{10}
0.1	0.762×10^7	0.182×10^{11}	0.369×10^{11}	0.157×10^{11}	7.72×10^9
0.5	0.353×10^7	0.840×10^{10}	0.169×10^{11}	0.721×10^{10}	3.54×10^9
1.0	0.261×10^7	0.615×10^{10}	0.133×10^{11}	0.526×10^{10}	2.71×10^9
5.0	0.244×10^7	0.349×10^{10}	0.782×10^{10}	0.292×10^{10}	1.56×10^9
10.0	0.296×10^7	0.345×10^{10}	0.757×10^{10}	0.293×10^{10}	1.53×10^9
50.0	0.147×10^{10}	0.631×10^{10}	0.117×10^{11}	0.548×10^{10}	2.83×10^9
100.0	0.569×10^{10}	0.120×10^{11}	0.195×10^{11}	0.106×10^{11}	5.34×10^9
$(d\mu)_n + p \to (d\mu)_{n'} + p$					
0.001	0.399×10^{13}	0.675×10^{12}	0.231×10^{13}	0.548×10^{12}	6.48×10^{11}
0.004	0.200×10^{13}	0.338×10^{12}	0.115×10^{13}	0.274×10^{12}	3.24×10^{11}
0.010	0.126×10^{13}	0.214×10^{12}	0.730×10^{12}	0.173×10^{12}	2.05×10^{11}
0.040	0.632×10^{12}	0.107×10^{12}	0.365×10^{12}	0.867×10^{11}	1.03×10^{11}
0.1	0.400×10^{12}	0.678×10^{11}	0.231×10^{12}	0.550×10^{11}	6.50×10^{10}
0.5	0.181×10^{12}	0.308×10^{11}	0.105×10^{12}	0.249×10^{11}	2.95×10^{10}
1.0	0.130×10^{12}	0.222×10^{11}	0.751×10^{11}	0.180×10^{11}	2.12×10^{10}
5.0	0.674×10^{11}	0.114×10^{11}	0.377×10^{11}	0.110×10^{11}	1.10×10^{10}
10.0	0.550×10^{11}	0.806×10^{10}	0.257×10^{11}	0.663×10^{10}	7.98×10^9
50.0	0.660×10^{11}	0.113×10^{11}	0.245×10^{11}	0.982×10^{10}	9.39×10^9
100.0	0.957×10^{11}	0.198×10^{11}	0.370×10^{11}	0.176×10^{11}	1.49×10^{10}

Table 5. Partial rates (in s^{-1}) of transitions $[nn_1n_2m] \to [n'n_1'n_2'm]$ for charge exchange (1) at $(n = 4) \to (n' = 3)$

ε, eV	$[4030] \to [3020]$	$[4120] \to [3110]$	$[4021] \to [3011]$	$[4012] \to [3002]$	Total rate of $(n = 4) \to (n' = 3)$, s^{-1}
$(p\mu)_n + d \to (d\mu)_{n'} + p$					
0.001	0.226×10^{8}	0.267×10^{12}	0.538×10^{12}	0.233×10^{12}	1.13×10^{11}
0.004	0.113×10^{8}	0.134×10^{12}	0.269×10^{12}	0.116×10^{12}	5.65×10^{10}
0.01	0.715×10^{7}	0.846×10^{11}	0.170×10^{12}	0.736×10^{11}	3.57×10^{10}
0.04	0.358×10^{7}	0.424×10^{11}	0.853×10^{11}	0.369×10^{11}	1.79×10^{10}
0.1	0.228×10^{7}	0.269×10^{11}	0.542×10^{11}	0.234×10^{11}	1.13×10^{10}
0.5	0.106×10^{7}	0.124×10^{11}	0.248×10^{11}	0.107×10^{11}	5.21×10^{9}
1.0	0.780×10^{6}	0.907×10^{10}	0.195×10^{11}	0.783×10^{10}	3.98×10^{9}
5.0	0.730×10^{6}	0.512×10^{10}	0.115×10^{11}	0.432×10^{10}	2.29×10^{9}
10.0	0.890×10^{6}	0.504×10^{10}	0.111×10^{11}	0.433×10^{10}	2.24×10^{9}
50.0	0.461×10^{10}	0.893×10^{10}	0.166×10^{11}	0.784×10^{10}	3.90×10^{9}
100.0	0.175×10^{11}	0.164×10^{11}	0.267×10^{11}	0.147×10^{11}	7.29×10^{9}
$(d\mu)_n + p \to (p\mu)_{n'} + d$					
0.001	0.120×10^{13}	0.452×10^{12}	0.154×10^{13}	0.364×10^{12}	3.41×10^{11}
0.004	0.601×10^{12}	0.226×10^{12}	0.769×10^{12}	0.182×10^{12}	1.70×10^{11}
0.01	0.380×10^{12}	0.143×10^{12}	0.487×10^{12}	0.115×10^{12}	1.07×10^{11}
0.04	0.190×10^{12}	0.716×10^{11}	0.244×10^{12}	0.576×10^{11}	5.40×10^{10}
0.1	0.120×10^{12}	0.454×10^{11}	0.154×10^{12}	0.365×10^{11}	3.41×10^{10}
0.5	0.546×10^{11}	0.206×10^{11}	0.699×10^{11}	0.166×10^{11}	1.55×10^{10}
1.0	0.392×10^{11}	0.149×10^{11}	0.502×10^{11}	0.120×10^{11}	1.11×10^{10}
5.0	0.204×10^{11}	0.772×10^{10}	0.253×10^{11}	0.731×10^{10}	5.83×10^{9}
10.0	0.167×10^{11}	0.546×10^{10}	0.173×10^{11}	0.445×10^{10}	4.10×10^{9}
50.0	0.205×10^{11}	0.793×10^{10}	0.172×10^{11}	0.684×10^{10}	4.78×10^{9}
100.0	0.303×10^{11}	0.144×10^{11}	0.268×10^{11}	0.127×10^{11}	7.73×10^{9}

7. RESULTS AND DISCUSSION

The results of calculations are presented in Figs. 4–8 and Tables 2–5.

The rates of the quasi-resonance charge-exchange reaction (1) $n \to n$ are one order of magnitude higher than the rates of the Coulomb deexcitation (2) ones in the case of reaction $(d\mu)_n + p \to (d\mu)_{n-1} + p$ and two orders of magnitude less than the rates of reaction $(p\mu)_n + d \to (d\mu)_{n-1} + p$. The highest rate of the Coulomb deexcitation partial transitions $[nn_1n_2m] \to [n'n_1'n_2'm']$ at $n = 4$ is the rate of transition $[4030] \to [3020]$, which is determined by the T-type HC at $R_q = 46$.

The energy dependence

$$\sigma_{ij}(\varepsilon) \sim \mathrm{const}/\varepsilon \qquad (40)$$

at $\varepsilon < 1$ eV is determined mainly by G factor (36) and follows from (28) because $P_{ij} \approx \mathrm{const}$ at $\varepsilon \to 0$.

The described method is adequate at $n > 2$ only because at $n \leq 2$ the contribution of the polarization potential $\sim R^{-4}$ becomes significant in comparison with the adiabatic terms. The interference effects, which are important at small n, are also not taken into account in the presented method. In both cases, it is necessary to use rigorous *ab initio* methods, e.g., the adiabatic hyperspherical approach [17, 18], which is now in progress. At $n = 3$, they can be mutually calibrated.

The method is illustrated on the collision processes of muon atomic physics, but after simple scaling the obtained results also describe the collision processes involving $a\pi^-$-, aK^--, and $a\bar{p}$-hydrogen isotope exotic atoms ($a = p, d, t$).

We did not take into account the screening effects, which are especially significant at low collision energy for $n \gtrsim 5$. Such calculations were done before [4–7] and we concentrated on the methodical aspects of the solution of the pure Coulomb three-body problem without any additional complications related to particular experiments.

The HC method gives an effective tool for obtaining reliable numerical results, but at the same time it provides a transparent picture of inelastic transitions (in strong contrast to fully numerical approaches). Again, it is unique in providing not only a calculational prescription for quantum-mechanical transitions but also a direct insight into the fundamental dynamics of inelastic processes. Therefore, it is a perfect method complementary to exact but highly involved numerical ones and an indispensable tool in the analysis of the results of such methods.

ACKNOWLEDGMENTS

We are grateful to Dr. A. Kravtsov and Dr. A. Mikhaĭlov for fruitful discussions and Prof. J. Pop-Jordanov and the Macedonian Academy of Art and Sciences, and INTAS (grant no. 1032) for financial support.

REFERENCES

1. M. Leon and H. Bethe, Phys. Rev. **127**, 636 (1962).
2. E. A. Solov'ev, Usp. Fiz. Nauk **157**, 437 (1989) [Sov. Phys. Usp. **32**, 228 (1989)].
3. E. A. Solov'ev, in *The Physics of Electronic and Atomic Collisions,* Ed. by L. J. Dube *et al.* (American Institute of Physics, New York, 1995), p. 471.
4. V. V. Gusev, L. I. Ponomarev, and E. A. Solov'ev, Hyperfine Interact. **82**, 53 (1993).
5. A. V. Kravtsov and A. I. Mikhailov, Zh. Éksp. Teor. Fiz. **107**, 1473 (1995) [JETP **80**, 822 (1995)].
6. L. I. Ponomarev and E. A. Solov'ev, Pis'ma Zh. Éksp. Teor. Fiz. **64**, 129 (1996) [JETP Lett. **64**, 135 (1996)]; Pis'ma Zh. Éksp. Teor. Fiz. **68**, 9 (1998) [JETP Lett. **68**, 7 (1998)].
7. A. V. Kravtsov, Hyperfine Interact. **119**, 45 (1999).
8. L. I. Ponomarev and E. A. Solov'ev, Hyperfine Interact. **119**, 55 (1999).
9. L. I. Men'shikov and L. I. Ponomarev, Z. Phys. D **2**, 1 (1986).
10. S. I. Vinitsky and L. I. Ponomarev, Fiz. Élem. Chastits At. Yadra **13**, 1336 (1982) [Sov. J. Part. Nucl. **13**, 557 (1982)].
11. E. A. Solov'ev, Yad. Fiz. **43**, 775 (1986) [Sov. J. Nucl. Phys. **43**, 492 (1986)].
12. E. C. G. Stückelberg, Helv. Phys. Acta **5**, 369 (1932).
13. P. T. Greenland, J. Phys. B **11**, 3563 (1978).
14. N. Rosen and C. Zener, Phys. Rev. **40**, 502 (1932).
15. Yu. N. Demkov, Zh. Éksp. Teor. Fiz. **45**, 195 (1963) [Sov. Phys. JETP **18**, 138 (1963)].
16. E. A. Solov'ev, in *Proceedings of Workshop on Hidden Crossings in Ion–Atom Collisions and in the Other Nonadiabatic Transitions* (Harvard Smithonian Center for Astrophysics, Cambridge, 1991).
17. V. V. Gusev *et al.*, Few-Body Syst. **9**, 137 (1990).
18. D. I. Abramov, V. V. Gusev, and L. I. Ponomarev, Yad. Fiz. **60**, 1259 (1997) [Phys. At. Nucl. **60**, 1133 (1997)]; Yad. Fiz. **64**, 1442 (2001) [Phys. At. Nucl. **64**, 1364 (2001)].

Physics of Atomic Nuclei, Vol. 65, No. 9, 2002, pp. 1588–1595. Translated from Yadernaya Fizika, Vol. 65, No. 9, 2002, pp. 1629–1636.
Original Russian Text Copyright © 2002 by Kosenko, Ivanyuk, Pashkevich.

NUCLEI
Theory

Multidimensional Langevin Approach to Describing the ^{18}O + ^{208}Pb Fusion–Fission Reaction

G. I. Kosenko, F. A. Ivanyuk[1], and V. V. Pashkevich[2]
Omsk State University, pr. Mira 55A, Omsk, 644077 Russia

Received Received July 17, 2001; in final form, February 4, 2002

Abstract—The fusion–fission reaction is treated as a multistep process. Langevin equations are used to describe the evolution of the system at each reaction stage. The parameters of the fusion process are calculated at the first stage. The results obtained in the input channel are employed as initial conditions in calculating the features of the fission process. The cross sections for fusion and fission are successfully described, and the cross sections for the formation of evaporation residues are estimated. In addition, the procedure used makes it possible to describe the mass distribution of fission fragments and the fragment-mass dependence of the multiplicity of prefission neutrons and to determine the mass–energy distribution of fission fragments. From the calculations, it follows that all the fission features of the reaction in question can be reproduced without considering the formation of a classical compound nucleus. The reaction times are so long that it is impossible to separate experimentally such events from the case of true fission through a compound nucleus. *© 2002 MAIK "Nauka/Interperiodica".*

1. INTRODUCTION

For a long time, the nuclear fission and fusion processes had been treated separately. To a considerable extent, this was motivated by the fact that experimental investigations dealt primarily with the fusion of nuclei with light ions, in which case it was assumed that the light projectile is very fast absorbed by the target nucleus. As the projectiles used became heavier, the situation changed significantly [1]; presently, when experimentalists have already implemented the acceleration of uranium nuclei, the separation of the fusion and the fission process does not seem justified.

The model of a dinuclear system [2] is one of the versions of such an analysis. In this model, it is assumed that objects constituting the system formed retain their individual features. In [2], the parameters of the input channel are included in the consideration through the probability of the formation of a dinuclear system, this quantity, which is determined on the basis of the optical model, being thus the only piece of information about the input channel in the memory of the system. Without discussing the advantages and disadvantages of the model in question, we only note that different approaches are employed within this model in taking into account information concerning the input channel and in performing a further analysis of the fission process.

In this context, the models developed by Gonchar [3] and by Pomorski [4] seem more appealing. The inclusion of input-channel parameters (angular-momentum dependence of the probability of compound-nucleus formation) [5] and a further consideration of the evolution of the system formed [3] are based on the same approach. However, the model of a dinuclear system starts from the instant at which the nuclei involved come into contact, while the models proposed in [3, 4] skip this instant altogether. Having determined the angular-momentum distribution of product nuclei, the authors of those models use it to calculate the parameters of the fission process; thereby, they describe the evolution of the system from the ground state without addressing the question of how this system has found its way to the ground state. We deem that this results in the loss of a considerable amount of information about the evolution of the system.

In the present study, we aim at filling this gap—namely, at considering the evolution of a system involved in the fusion–fission reaction within a unified approach based on Langevin equations. For a test, we will take the ^{18}O + ^{208}Pb reaction, because there is a vast body of experimental data on this reaction and because the spherical shape of the participant nuclei facilitates the calculations.

2. DESCRIPTION OF THE MODEL

In treating the fusion–fission reaction, we break down our calculations here into two steps. At the

---

[1] Institute for Nuclear Research, National Academy of Sciences of Ukraine, pr. Nauki 47, Kiev, 252028 Ukraine.

[2] Joint Institute for Nuclear Research, Dubna, Moscow oblast, 141980 Russia.

first step, we consider the process through which the colliding nuclei come into contact. Using information obtained at the first step, we then proceed to analyze the evolution of the system formed. Unfortunately, there is no appropriate nuclear-shape parametrization that would make it possible to treat the two stages simultaneously; therefore, we employ an individual form of parametrization for each step. The calculation of the evolution process at each such step is performed for a large number of collisions. In the discussion that follows, each specific collision is referred to as a trajectory.

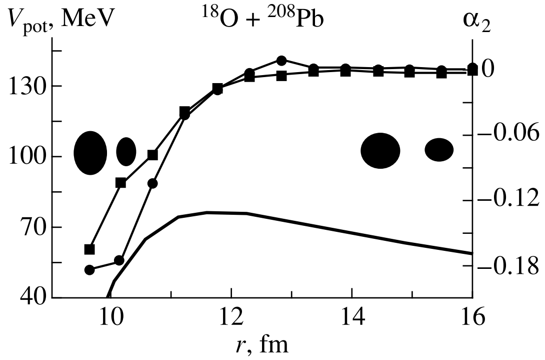

Fig. 1. Dependence of (thick curve) the potential energy of colliding ions (left scale along the ordinate) on the distance r between them and r dependence of the mean values of the deformations of (curve connecting boxes) the target ion and (curve connecting circles) the projectile ion (right scale along the ordinate). Also shown schematically are the shapes of the ions (on the right) at large distances and (on the left) at the instant close to that at which they come into contact.

2.1. Equations of Motion

For dynamical equations, we take Langevin equations. In order to describe the fusion process, we use the equations [6]

$$\frac{dr}{dt} = \frac{p_r}{m}, \tag{1}$$

$$\frac{dp_r}{dt} = -\frac{\partial V(r,\boldsymbol{\alpha})}{\partial r} - \frac{L^2}{mr^3} - K_r^r\frac{dr}{dt} - \sum_j K_r^j\frac{\pi_j}{D_j} + \xi, \tag{2}$$

$$\frac{d\alpha_i}{dt} = \frac{\pi_i}{D_i}, \tag{3}$$

$$\frac{d\pi_i}{dt} = -\frac{\partial V(r,\boldsymbol{\alpha})}{\partial \alpha_i} - K_i^r\frac{p_r}{m} - \sum_j K_i^j\frac{\pi_j}{D_j} - C_i\alpha_i - \frac{1}{2}\xi. \tag{4}$$

Here, r is the distance between the centers of colliding nuclei; p_r is the momentum conjugate to this variable; m is the reduced mass; $V(r,\boldsymbol{\alpha})$ is the interaction energy of the nuclei, which includes the Coulomb and the nuclear part (the Gross–Kalinowski potential $V_{\rm GK}$ [7] is taken for the nuclear part); and K_i^j are the friction parameters with respect to the corresponding degrees of freedom. The second pair in the above set of equations describes changes in the shapes of colliding nuclei, with α_i and π_i being, respectively, collective coordinates describing the shape of a nucleus and the momenta conjugate to them (the index i distinguishes the target and the projectile); D_i and C_i are, respectively, the inertial and the friction parameters for the coordinates that describe nuclear shapes (these parameters were determined within the liquid-drop model). The quantity ξ takes into account random effects on the system—that is fluctuations. The fluctuations depend on the excitation energy of intrinsic degrees freedom; therefore, they are equal to zero at the initial instant. As the nuclei approach each other, part of the kinetic energy is converted into the internal energy because of friction; this leads to the emergence and growth of fluctuations.

The set of Eqs. (1)–(4) does not include an equation that would describe the variation of the angular momentum L of the system. In our calculations, we assumed that this angular momentum is constant for each specific trajectory.

For a mononuclear system, the set of equations in question takes the form [8]

$$\frac{dq_i}{dt} = \mu_{ij}p_j, \tag{5}$$

$$\frac{dp_i}{dt} = -\frac{\partial V(\mathbf{q})}{\partial q_i} - \frac{1}{2}p_jp_k\frac{\partial \mu_{jk}}{\partial q_i} - \gamma_{ij}\mu_{jk}p_k + \xi_i, \tag{6}$$

where $\mathbf{q}$ are collective coordinates describing the shape of this mononuclear system; $\mathbf{p}$ are the momenta conjugate to them; μ_{jk} and γ_{jk} are, respectively, the inertial and the friction parameters. For a mononuclear system, these parameters were calculated in [9] on the basis of the linear-response model. We believe that, here and below, it is more appropriate to refer to the system in question as a mononuclear system rather than as a compound nucleus. This is because the use of the latter term tacitly assumes the occurrence of a spherical nucleus in the ground state, but, in our calculations, such a situation is not frequently realized.

2.2. Collective Coordinates

The deformation of colliding nuclei has a pronounced effect on the process through which these

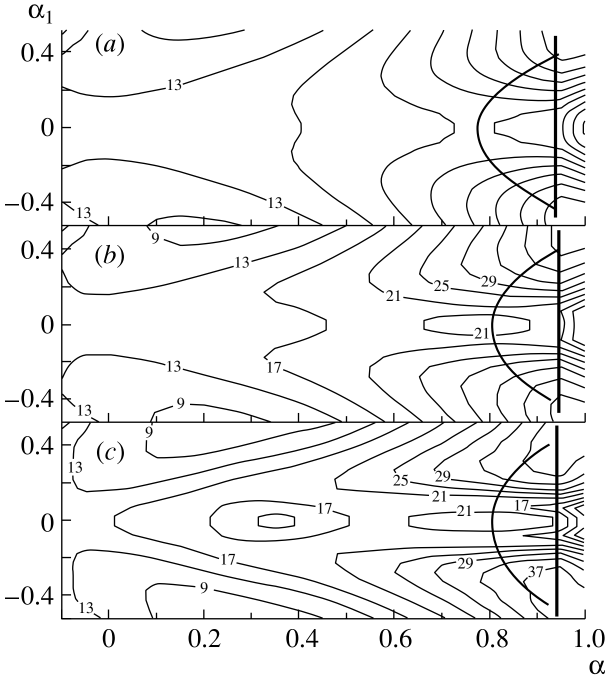

Fig. 2. Potential-energy chart for the ^{226}Th nucleus in terms of the coordinates α and α_1. The coordinate α_4 is fixed at -0.18. The potential-energy surfaces are given at various values of the temperature of the system: (*a*) 1.5, (*b*) 1.0. and (*c*) 0.5 MeV. The vertical line represents the stability line, while the thick curve corresponds to the ridge line.

nuclei come into contact; therefore, it is necessary to parametrize their shapes. For this purpose, we use Legendre polynomials of second degree; that is,

$$R_i(x) = \lambda^{-1}R_0(1 + \alpha_{2i}P_2(x)),$$

where R_0 is the radius of a spherical nucleus, the index i distinguishes the target and the projectile, the quantity α_{2i} specifies the deformation of an ion, and λ is a normalization factor that is determined from the volume-conservation condition. In considering the evolution of the system, it is assumed that the symmetry axes of colliding ions coincide (see Fig. 1); that is, the rotation of the ions is disregarded. As a result, the fusion cross section is somewhat reduced [10], but we believe that this approximation is quite reasonable.

At the stage where the participant nuclei have already come into contact and where they are considered as a discrete unit, their shape is described in terms of Cassinian ovals [11]; that is,

$$\rho_s(x) = \frac{1}{\sqrt{2}}[(R^4 + 2sR^2(2x^2-1) + s^2)^{1/2} - R^2(2x^2-1) - s]^{1/2},$$

$$z(x) = \frac{\operatorname{sign}(x)}{\sqrt{2}}[(R^4 + 2sR^2(2x^2-1) + s^2)^{1/2} + R^2(2x^2-1) + s]^{1/2}, \quad (7)$$

$$R(x) = \lambda^{-1}R_0(1 + \alpha_1 P_1(x) + \alpha_4 P_4(x)),$$

$$s = \varepsilon R_0^2,$$

$$\varepsilon = \frac{1}{4}(\alpha-1)\left[\left(1+\sum_{m=1,4}\alpha_m\right)^2 + \left(1+\sum_{m=1,4}(-1)^m\alpha_m\right)^2\right] + \frac{1}{2}(\alpha+1)\left[1+\sum_{m=1,4}(-1)^m\alpha_{2m}(2m-1)!!/(2^m m!)\right]^2,$$

where the coordinates α, α_1, and α_4 are taken for variables specifying the shape $\rho_s(x)$ of the relevant mononuclear system. They define, respectively, elongation (the configuration is spherical at $\alpha = 0$ and is that of two tangent fragments at $\alpha = 1$), asymmetry, and the dimension of the neck between fragments. The quantity s is the square of the distance between the focus of Cassinian ovals and the origin of coordinates. We will consider only axisymmetric shapes that are obtained by rotating ρ_s about the symmetry axis (z axis).

Thus, we use three parameters both in calculating collision dynamics and in calculating the evolution of the resulting simply connected system. These are the distance r between the centers of colliding ions and their deformations α_i in the first case and the parameters α, α_1, and α_4 in the second case.

2.3. Potential Energy

In calculating fusion dynamics, the interaction of the ions involved was described in terms of the Gross–Kalinowski potential [7]

$$V_{\mathrm{GK}} = \frac{1}{2}(V_{12} + V_{21}), \quad (8)$$

$$V_{12} = \int V_1(\mathbf{r} - \mathbf{r}', \alpha_1)\rho_2(\mathbf{r}', \alpha_2)d\mathbf{r}',$$

$$V_i(\mathbf{r}, \alpha_i) = \frac{V_p}{1 + \exp\left(\frac{r - R_p(\alpha_i, x)}{a_p}\right)},$$

$$R_p(\alpha_i, x) = 1.25A_i^{1/3}(1 + \alpha_i P_2(x)) \ \text{[fm]},$$

$$\rho_i(\mathbf{r}, \alpha_i) = \frac{\rho_0}{1 + \exp\left(\frac{r - R_d(\alpha_i, x)}{a_d}\right)},$$

$$\rho_0 = 0.17 \ \text{fm}^{-3}, \quad a_d = 0.54 \ \text{fm},$$

$$R_d(\alpha_i, x) = (1 + \alpha_i P_2(x)) \times (1.12A_i^{1/3} - 0.86A_i^{-1/3}) \ \text{[fm]}.$$

The parameters of the potential $V_i(\mathbf{r}, \alpha_i)$ (V_p and a_p) were chosen in accordance with [12]. In the dynamical calculations, we used a mesh of dimensions $100 \times 41 \times 41$ ($r \times \alpha_p \times \alpha_t$).

In computing the nuclear potential energy, we took into account shell corrections by means of a procedure similar to that in [13]. As the system in question undergoes evolution, part of its energy associated with collective degrees of freedom is converted into energy associated with intrinsic degrees of freedom. This process, which leads to the damping of shell effects, was taken into account by the method proposed in [14].

Figure 2 shows the potential-energy chart in terms of the coordinates α and α_1 at a fixed value of the deformation parameter α_4, which, as was indicated above, determines the thickness of the neck of our mononuclear system. It can be seen that, with increasing temperature (the data in Fig. 2 are presented for its values of 0.5, 1.0, and 1.5 MeV), the potential energy is smoothed out, becoming ever more similar to the liquid-drop potential energy—in particular, there appears one fission valley instead of two. Thus, we can conclude that, depending on the internal excitation of the system, the mass distribution of fission fragments will be either asymmetric or symmetric, but an intermediate shape of it may also be realized.

2.4. Transition from Calculating the Fusion Cross Section to Calculating the Parameters of the Fission Process

At the first stage, we solve Eqs. (1)–(4), whereby we obtain information about the input channel. This information includes the probability that a mononuclear system is formed, the excitation energy of the system at the instant of touching, and the deformations of fragments. Data obtained by considering the input channel are displayed in Fig. 3.

For the case of the laboratory energy of 90 MeV, Fig. 3*a* shows the initial-angular-momentum dependence of the excitation energy at the instant when colliding ions come into contact. Here, we can clearly see that, for each specific value of the angular momentum, we have a distribution featuring a maximum. With increasing angular momentum, the energy value corresponding to this maximum tends to zero. This reflects the fact that the rotational energy of the system increases in this case.

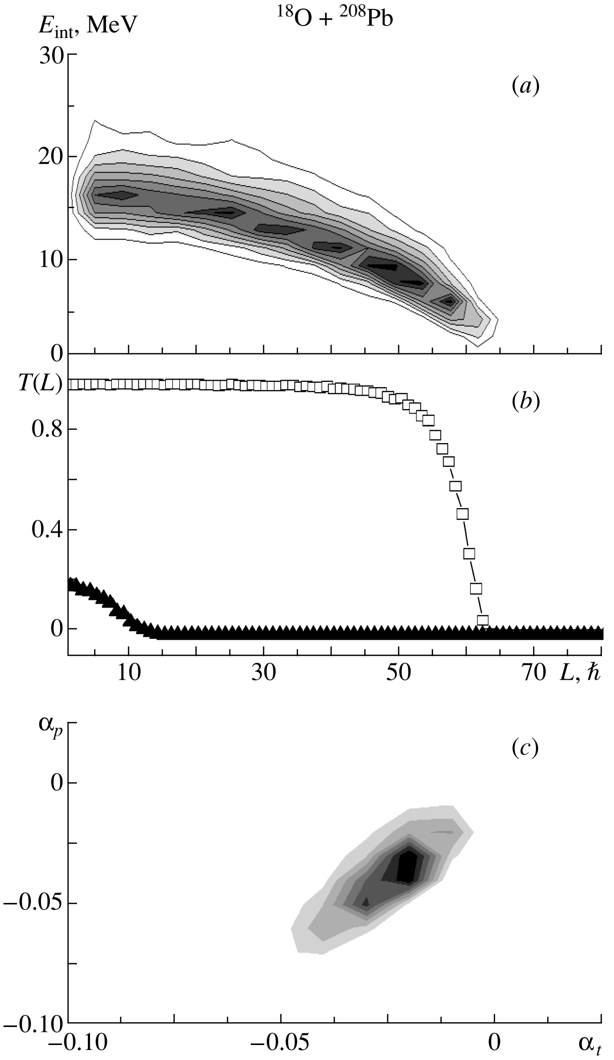

Fig. 3. (*a*) Internal excitation energy of the mononuclear system at the instant when colliding ions touch each other and (*b*) coefficient of touching versus the initial angular momentum at $E_{\text{lab}} =$ (▲) 78 and (□) 90 MeV; (*c*) distribution of the deformations of the target and the projectile at the instant of touching (the deformation of the projectile and the deformation of the target are plotted along the ordinate and the abscissa, respectively). These distributions are used to determine the initial conditions in calculating the evolution of the mononuclear system formed.

Figure 3*b* presents the probability of touching as a function of the initial angular momentum. Here, we can clearly see the distinction between the fusion process occurring at an energy considerably exceeding the barrier height and the fusion process occurring at an energy approximately equal to the barrier height. The graph starting from unity corresponds to the projectile-ion energy equal to 90 MeV. At the projectile-ion energy of 78 MeV, the probability of touching is very small, in which case the maximum does not exceed 0.2. In either case, the inclusion of fluctuations leads to a smooth decrease in the fission probability from a maximum value to zero.

The distribution of the deformations of colliding nuclei at the instant of touching is given in Fig. 3*c*. These deformations are negative, which corresponds to oblate shapes. The mean values of the deformations

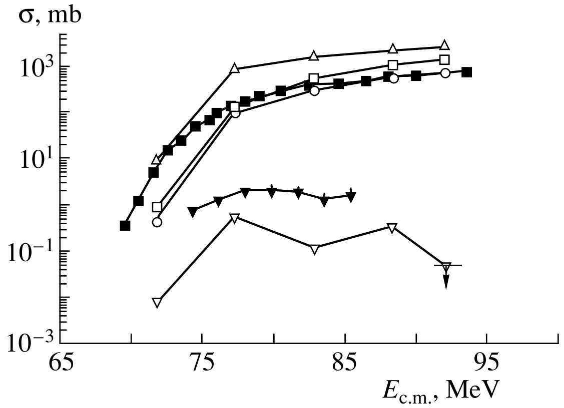

Fig. 4. (△) Cross section for the formation of a mononuclear system, (□) fusion cross section, and (○) fission cross section versus the c.m. energy of the projectile ion; (▽) cross section for events in which no decay processes occurred within 500×10^{-21} s. Closed symbols represent experimental data from [15]: (■) cross section for fusion and (▼) cross section for the formation of evaporation residues in the ^{16}O $+^{208}$ Pb reaction, which is similar to that studied here.

in question are shown in Fig. 1 versus the distance of the ions approaching each other. Proceeding to calculate the evolution of the mononuclear system formed, we chose the initial angular momentum, the excitation energy of the system, and the deformations of colliding ions (it is these deformations that determine the shape of the mononuclear system formed) by the Neumann method ("hit-and-miss" method) on the basis of the distributions displayed in Fig. 3. All these data were initial conditions for Eqs. (5) and (6)—namely, the initial angular momentum determines the rotational energy of the system, while the initial excitation energy specifies the temperature of the system and, hence, the degree of damping of shell effects. In addition, we assumed that the energy associated with collective degrees of freedom is given by

$$E_{\rm kin} = E_{\rm tot} - V_{\rm pot} - E_{\rm int},$$

where $E_{\rm tot}$ is the total energy of the system as determined from the energy-balance equation on the basis of the initial energy of colliding ions, $V_{\rm pot}$ is the potential energy of the system (it is determined by collective coordinates—that is, by the shape of the mononuclear system formed), and $E_{\rm int}$ is the internal excitation energy of the system.

3. RESULTS AND DISCUSSION

For the case of spherical colliding nuclei, the thick curve in Fig. 1 depicts the interaction energy as a function of the distance between them (left scale along the ordinate). When the projectile nuclei are deformed, the potential changes slightly. The curves connecting symbols illustrate changes suffered by the mean deformation of the projectile nuclei as they approach the target (right scale along the ordinate), the curve connecting circles (boxes) corresponding to a lighter (heavier) nucleus. It can clearly be seen that, far off the barrier, there are virtually no deformations or they are positive. Upon passing the barrier, the deformations become negative; that is, the ions assume an oblate shape. Of course, this leads to an increase in the Coulomb energy. The longer the distance that the ion travels on passing the barrier, the greater the values that the deformations take; it is noteworthy that, in contrast to the case where the deformations of the ions are disregarded (that is, colliding nuclei are taken to be spherical), the point at which the ions come into contact can be achieved in the calculations very rarely, if at all. In our calculations, we therefore went over to a mononuclear system as soon as the ions approached at a distance that was shorter than the half-sum of the diffuseness parameters of the potentials V_i, a_p. The cross section obtained in this way was identified with the cross section for touching—that is, with the cross section for the formation of the mononuclear system. In Fig. 4, the values of these cross sections are represented by upward oriented open triangles.

In the course of ensuing evolution, the system being considered can undergo breakup almost immediately or can walk for some time over the surfaces depicted in Fig. 2. Depending on the results of these walks, we will obtain (see Fig. 4) either the fusion cross section (open squares) or the fission cross section (open circles). In Fig. 4, closed boxes represent the experimental values of the fusion cross section from [15].

It can be seen that the values obtained for the fusion cross section and for the fission cross section agree with experimental data only at high projectile energies. As the projectile energy approaches the fission barrier in magnitude, the effect of tunneling through the barrier comes into play. In our calculations, this possibility was disregarded (recall that the model developed in [6] takes into account only subbarrier processes).

The problem of separating fission events from events of pure fusion (quasifission) is of interest and importance in itself. The results displayed in Fig. 4 were obtained in the following way. The entire region of deformations of the mononuclear system was broken down into two parts. The first part—that from the line of touching ($\alpha = 1$) to the stability line (see Fig. 2)—reflects the position in which the system loses hydrodynamic stability [16]; that is, the system moving from the ground state ($\alpha = 0$) can undergo disintegration into two fragments at any instant of time as soon as it intersects the stability line. But if

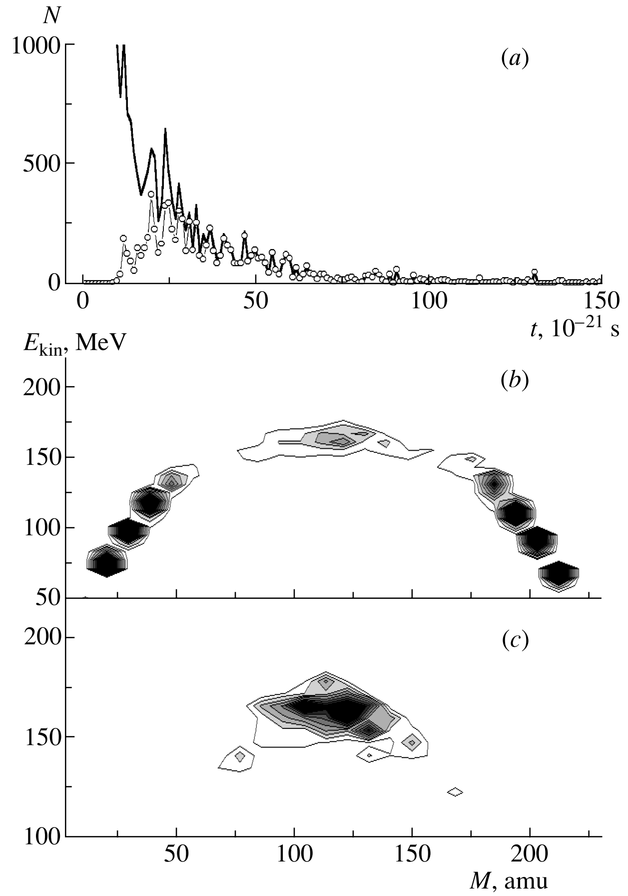

Fig. 5. (*a*) Distribution of events with respect to the reaction time: (thick curve) all events and (curve connecting circles) only fission events; (*b*) mass–energy distribution of reaction products (it corresponds to the thick curve in Fig. 5*a*); and (*c*) same distribution as in Fig. 5*b*, but only for fission events (this distribution corresponds to the curve connecting circles in Fig. 5*a*).

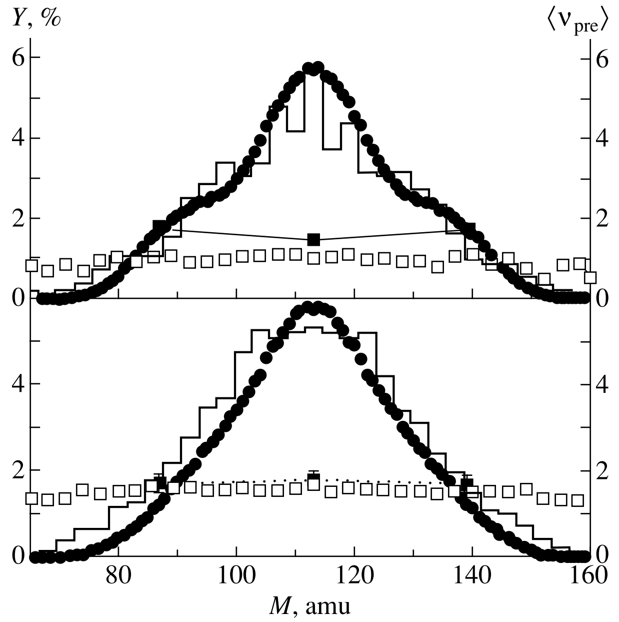

Fig. 6. Mass distribution of fission fragments (left scale along the ordinate) according to (●) experimental data from [18] and (histogram) our calculations, along with the neutron multiplicity (right scale along the ordinate) as a function of the fragment mass according to (■) experimental data from [18] and (□) our calculations. The results presented in the upper (lower) panel correspond to $E_{\rm lab} = 78\,(90)$ MeV.

the system traverses the stability line, moving from the point of touching at $\alpha = 1$, it becomes, on the contrary, stable with respect to disintegration into parts. Thus, we deem that all trajectories that traverse the stability line $\alpha \sim 0.94$ lead to fusion. If trajectories traverse the line $\alpha = 0.83$, the respective events are assumed to be fission events. We note that this value of α corresponds to the position of the fission barrier if one moves from the ground state and to the fusion barrier if one moves from the point of touching. If the system underwent disintegration prior to reaching the deformation value of $\alpha = 0.94$, this event is, in all probability, that of transfer reactions or that of some other fast processes (for example, reactions of deep-inelastic transfer). At this stage, we are not interested in such processes.

In order to identify, as fission events, events featuring deformations more compact than that of $\alpha = 0.83$, one needs some arguments. We can adduce a few of them.

The first argument in favor of such an identification is provided by the mass–energy distribution of fission fragments. Figure 5 displays such a distribution prior to (Fig. 5*b*) and after (Fig. 5*c*) the selection of fission events. In addition, Fig. 5*a* shows the distribution of events with respect to the time of the process (from the instant of touching to the instant of fragment separation). The mass–energy distribution in Fig. 5*b* and the thick curve in Fig. 5*a* (time dependence) reflect the full pattern—that is, all events. This full pattern is then subjected to selections which consist in rejecting events where the minimum value of the deformation is greater than $\alpha = 0.83$. As a result, the pattern changes drastically—all events featuring a high asymmetry of fragments have not passed the above selections (the respective mass–energy distribution is shown in Fig. 5*c*), and only the central section of the distribution has survived. But distributions of precisely this type are obtained in experiments that study mass–energy distributions of fission fragments [17]. Concurrently, short-lived events disappear from the distribution with respect to reaction times (curve connecting circles in Fig. 5*a*)—there remained only times longer than 10×10^{-21} s.

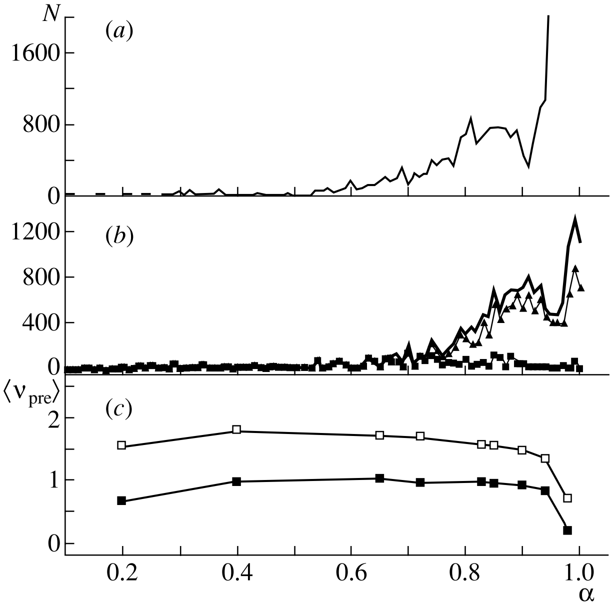

Fig. 7. Distribution of events versus the minimal value of the attained deformations for (*a*) all events of disintegration and (*b*) events featuring neutron evaporation [in this panel, the thick curve, the curve connecting triangles, and the curve connecting boxes represent data for, respectively, all neutrons ($\alpha_{\min} < 1.0$), neutrons emitted by systems characterized by $\alpha_{\min} < 0.94$, and neutrons emitted by systems characterized by $\alpha_{\min} < 0.64$; (*c*) mean number of neutrons per decay event versus α at $E_{\text{lab}} =$ (□) 90 and (■) 78 MeV.

We note that there are virtually no events whose duration is longer than 150×10^{-21} s. A few events that could not reach the scission point could be assessed very roughly as those that have led to evaporation residues (in Fig. 4, the corresponding cross sections are represented by open inverted triangles).

The next argument can be inferred from the mass distribution of fission fragments (left scale along the ordinate in Fig. 6) and from the neutron multiplicity corresponding to it (right scale along the ordinate in this figure). Figure 6 shows mass distributions of fission fragments and neutron multiplicities for two values of the projectile-ion energy. The histogram and open boxes represent the results of the calculations, while closed circles (mass distribution) and curves connecting closed boxes (neutron multiplicity) correspond to experimental data from [18]. It can be seen that, at the laboratory energy of 90 MeV (lower panel), the agreement is fairly good both for the mass distribution and for the neutron multiplicity. Not only is this agreement qualitative, but it is also quantitative. At the energy value of 78 MeV (upper panel), the agreement is poorer. Here, the projectile energy is nearly equal to the barrier height in the input channel. It can be seen from Fig. 4 that, in this case, the value that we obtained for the cross section for touching is smaller than the experimental cross section for fusion. All this suggests that tunneling through the barrier must be taken into account at such energies. Nonetheless, the mass distribution obtained at $E_{\text{lab}} = 78$ MeV reproduces experimental data rather well. At this energy value, the influence of shell effects is already noticeable; in addition, the distribution exhibits shoulders corresponding to an asymmetric disintegration. The neutron multiplicity calculated for this case falls short of experimental data; it even fails to reproduce a qualitative pattern. According to the calculations, the multiplicity is virtually independent of the masses of the fragments, whereas, in experiments, a modest minimum in the neutron multiplicity is observed for symmetric fission. Possibly, better agreement would be attained upon taking into account the tunneling effect in the input channel.

Figure 7*a* displays the distribution of all decay events with respect to the minimum deformation. Figure 7*b* shows the multiplicity of neutrons emitted at a given deformation; here, the thick curve, the curve connecting triangles, and the curve connecting boxes were calculated for, respectively, all events involving neutron emission, events featuring deformations less than $\alpha = 0.94$, and events where $\alpha < 0.64$. Figure 7*c* gives the mean number of neutrons per decay as a function of α at two values of E_{lab}. As follows from the data presented in Fig. 7*b*, the bulk of neutrons are evaporated in the region near the barrier. This is because the majority of the trajectories do not pass behind the barrier. If one considers events characterized by a minimal deformation such that $\alpha < 0.64$, it can be seen that, for them, there is also a modest maximum in the barrier region. By and large, the probability of neutron evaporation is rather uniformly distributed along the deformation. But if we address the neutron multiplicity per fission event, we can see from Fig. 7*c* that, from $\alpha = 0.94$, this multiplicity undergoes virtually no changes; hence, a considerable part of the trajectories do not pass behind the barrier.

4. CONCLUSION

Within a unified approach, we have calculated both the fusion and the fission cross section; in addition, we have estimated the cross section for the formation of evaporation residues. We have also obtained the mass–energy distribution of reaction products, the multiplicity of prefission neutrons as a function of the fragment mass, and the mass-number dependence of the fragment yield. A comparison of these theoretical results with experimental data has revealed that this approach provides satisfactory agreement with these data at projectile-ion energies above the fusion barrier.

An analysis of the results obtained in the present study has led to the conclusion that, even if the system being considered was unable to reach the state of a classical compound nucleus, the final pattern showed absolutely no difference from that in which a compound nucleus was present. In addition, it has been found that, in the process of evolution, the majority of the nuclei do not reach deformations more compact than that at the saddle-point configuration. The motion of the nuclei from the point of touching to the ground state was accompanied by the emission of a considerable number of neutrons in the barrier region. Because of the loss of energy through this emission, the system could overcome the barrier and decayed into fragments, not reaching the ground state. In order to reach the ground state, the system must possess a considerable amount of energy for passing the saddle-point configuration. By way of example, we indicate that, in synthesizing superheavy elements, experiments where the system being studied emitted three to four neutrons prior to reaching the ground state proved to be successful.

Of course, we are aware that our result was obtained in studying a specific system and that further investigations are required. Moreover, the agreement with experimental data in the energy region near the Coulomb barrier is rather poor. Our further plans include undertaking efforts aimed at improving a theoretical description in this region.

ACKNOWLEDGMENTS

We are indebted to all those who showed interest in this study—above all, to the directorate of the Laboratory of Nuclear Reactions at the Joint Institute for Nuclear Research and, personally, to Yu.Ts. Oganessian and M.G. Itkis, whose support made possible the existence of the present collaboration. G.I. Kosenko is grateful to the directorate of RIKEN, where a major part of our calculations were performed, and, in particular, to S. Yamaji; his thanks are also due to the Yukawa Institute for Theoretical Physics (Kyoto), where part of this work was done, and to Y. Abe of this institution for his permanent interest in this study and stimulating discussions. We gratefully acknowledge the constructive criticism of A.Ya. Rusanov, who inspired us to perform three-dimensional calculations rather than two-dimensional ones, and the enlightening discussions with V.S. Salamatin, D.V. Vanin, G.D. Adeev, Y. Aritomo, T. Wada, R.S. Kurmanov, A.A. Goverdovsky, and F. Hanappe during the preparation of this article.

This work was supported by INTAS (grant no. 11929).

REFERENCES

1. V. V. Volkov, *Nuclear Reactions of Deep-Inelastic Transmission* (Énergoatomizdat, Moscow, 1982).
2. N. V. Antonenko *et al.*, Phys. Lett. B **319**, 425 (1993); N. V. Antonenko *et al.*, Fiz. Élem. Chastits At. Yadra **25**, 1379 (1994) [Phys. Part. Nucl. **25**, 583 (1994)]; G. G. Adamian, N. V. Antonenko, and R. V. Jolos, Nucl. Phys. A **584**, 205 (1995); A. Diaz-Torres *et al.*, Phys. Rev. C **64**, 024604 (2001).
3. I. I. Gonchar, Fiz. Élem. Chastits At. Yadra **26**, 932 (1995) [Phys. Part. Nucl. **26**, 394 (1995)].
4. K. Pomorski *et al.*, Nucl. Phys. A **679**, 25 (2000).
5. P. Fröbrich and J. Marten, Nucl. Phys. A **545**, 854 (1992).
6. P. Fröbrich and S. Y. Xu, Nucl. Phys. A **477**, 143 (1988).
7. D. H. E. Gross and H. Kalinowski, Phys. Rep. **45**, 175 (1978).
8. Y. Abe, C. Gregoire, and H. Delagrange, J. Phys. (Paris) **47**, C329 (1986).
9. H. Hofmann, Phys. Rep. **284**, 137 (1997); F. A. Ivanyuk *et al.*, Phys. Rev. C **55**, 1730 (1997).
10. P. Fröbrich and G. Grawert, Nucl. Phys. A **451**, 338 (1986).
11. V. V. Pashkevich, Nucl. Phys. A **169**, 275 (1971); **477**, 1 (1988).
12. P. Fröbrich, Phys. Rep. **116**, 337 (1984).
13. J. Damgaard *et al.*, Nucl. Phys. A **135**, 432 (1969).
14. A. V. Ignatyuk, G. N. Smirenkin, and A. S. Tishin, Yad. Fiz. **21**, 485 (1975) [Sov. J. Nucl. Phys. **21**, 255 (1975)].
15. E. Vulgaris *et al.*, Phys. Rev. C **33**, 2017 (1986).
16. U. Brosa, S. Grossmann, and A. Müller, Phys. Rep. **197**, 167 (1990).
17. M. G. Itkis and A. Ya. Rusanov, Fiz. Élem. Chastits At. Yadra **29**, 389 (1998) [Phys. Part. Nucl. **29**, 160 (1998)].
18. I. V. Pokrovski *et al.*, in *Proceedings of the International Conference on Nuclear Physics "Nuclear Shells—50," Dubna, Russia, 1999,* Ed. by Yu. Ts. Oganessian and R. Kalpakchieva (World Sci., Singapore, 2000), p. 105.

Translated by A. Isaakyan

Physics of Atomic Nuclei, Vol. 65, No. 9, 2002, pp. 1596–1608. Translated from Yadernaya Fizika, Vol. 65, No. 9, 2002, pp. 1637–1649.
Original Russian Text Copyright © 2002 by Karpov, Adeev.

NUCLEI
Theory

Langevin Description of the Charge Distribution of Fragments Originating from the Fission of Excited Nuclei

A. V. Karpov and G. D. Adeev

Omsk State University, pr. Mira 55A, Omsk, 644077 Russia

Received June 19, 2001; in final form, January 24, 2002

Abstract—The charge distribution of fragments originating from the fission of the ^{236}U compound nucleus is calculated within a stochastic approach based on Langevin equations. The elongation coordinate, the neck-thickness coordinate, and the charge-asymmetry coordinate are chosen as collective variables. The friction parameter of the charge mode is calculated on the basis of two nuclear-viscosity mechanisms, that of one-body and that of two-body dissipation. It is shown that the Langevin approach is applicable to studying isobaric distributions. In addition, the charge distribution in question is studied as a function of the excitation energy of the compound nucleus and as a function of the coefficient of two-body viscosity. *© 2002 MAIK "Nauka/Interperiodica".*

1. INTRODUCTION

In the last two decades, the approach based on the set of multidimensional Langevin equations [1–6] has been the most popular method for solving problems of nuclear dynamics, including those that are associated with the fission of highly excited compound nuclei. In theoretical investigations into these realms, preference was given to this approach primarily because Langevin equations can be efficiently solved to a preset accuracy by using conventional numerical schemes. It is obvious that, in developing a theoretical approach to problems of the fission process (in particular, a Langevin approach), it is necessary to adapt it in such a way as to meet the demand for describing as vast a body of experimental data as is possible. This will make it possible to assess the degree of universality of the approach used and to reconstruct the dynamic pattern of the fission process in minute detail. As a matter of fact, all the aforesaid furnishes a sufficient motivation for solving the set of Langevin equations for as many collective variables as is possible. However, the introduction of each new collective variable increases dramatically the volume of relevant computations and, consequently, the machine time. This is the reason why, until recently, only one- (see [7, 8]) and two-dimensional problems were comprehensively investigated within the Langevin approach. Two-dimensional calculations enable one to obtain either energy distributions for symmetric fission [2, 9, 10] or the mass distribution of fission fragments that corresponds to the most probable kinetic energy [3, 4]. However, the latest studies in these realms resulted in formulating a model that makes it possible to analyze, on the basis of three-dimensional Langevin equations, such features of the fission of highly excited nuclei as mass–energy distributions of fission fragments, multiplicities of prefission light particles, and fission times [5, 6].

The charge distribution of fragments, which is an important feature of the fission process indeed, has not yet been investigated within the Langevin approach. This is partly due to the paucity of experimental information about the isobaric distribution of fragments originating from the fission of excited compound nuclei. Moreover, a reliable model for calculating transport coefficients of the charge mode has yet to be developed.

In view of this, we aim here primarily at demonstrating the applicability of the Langevin approach to describing charge distributions and at revealing general regularities in the evolution of the charge degree of freedom. On the basis of three-dimensional Langevin equations, we explore the charge distribution of fission fragments by considering the reaction $^{4}\mathrm{He} + {}^{232}\mathrm{Th} \to {}^{236}\mathrm{U}$, where the excitation energy of the compound nucleus formed varies in the range $E^* = 39$–160 MeV. We investigate the charge distribution for the case of disintegration into fragments of equal masses. The mass parameter and the friction parameter of the charge mode are calculated on the basis of the hydrodynamic model. In addition, an attempt is made to employ, in dynamical calculations, the one-body nuclear-viscosity mechanism to describe energy dissipation associated with the evolution of the charge mode.

2. DESCRIPTION OF THE MODEL

2.1. Parametrization of the Nuclear Shape and Collective Coordinates

It was indicated above that, in studying the isobaric distribution, we perform our calculations for the symmetric fission of the ^{236}U nucleus. The popular $\{c, h, \alpha\}$ parametrization [11] is used here for the profile function $\rho_s(z)$, whose rotation about the symmetry axis specifies the shape of the nuclear surface. In the symmetric case ($\alpha = 0$) considered here, the equation of the nuclear surface in terms of cylindrical coordinates has the form

$$\rho_s^2(z) = \begin{cases} \left(c^2 - z^2\right)\left(A_s + Bz^2/c^2\right), & B \geq 0 \\ \left(c^2 - z^2\right) A_s \exp(Bcz^2), & B < 0, \end{cases} \quad (1)$$

where ρ_s is a polar radius of a point at the surface of the nucleus being considered and z is the coordinate along its symmetry axis. The quantities A_s and B are expressed in terms of the nuclear-shape parameters (c, h) as [2, 11]

$$A_s = \begin{cases} c^{-3} - \dfrac{B}{5}, & B \geq 0 \\ -\dfrac{4}{3}\dfrac{B}{\exp(Bc^3) + \left(1 + \dfrac{1}{2Bc^3}\right)\sqrt{-\pi Bc^3}\,\mathrm{erf}(\sqrt{-Bc^3})}, & B < 0; \end{cases}$$

$$B = 2h + \frac{c-1}{2}, \quad (2)$$

where c is the elongation parameter (the length of a nucleus in units of the radius R_0 of the initial sphere is $2c$) and h characterizes the change in the neck thickness at a given elongation.

The convenience in implementing a numerical algorithm for solving Langevin equations and its ability to tackle specific problems often depends on the choice of collective coordinates. In the model proposed here, the first two collective coordinates describe the evolution of the nuclear shape. In our calculations, these are geometric parameters of the nuclear shape [(c, h)]. The third coordinate $\eta_Z = (Z_R - Z_L)/(Z_R + Z_L)$, where Z_R and Z_L are the charges of, respectively, the right- and the left-hand fragment, specifies the distribution of the charge among fission fragments. Here and below, the subscripts R and L label quantities referring to the right- and the left-hand fragment. The variable η_Z was often used as a charge coordinate [12, 13]; in our opinion, it is the most convenient. We note that, in [14], Strutinsky emphasized the advantages of the mass-asymmetry coordinate $\eta_A = (A_R - A_L)/(A_R + A_L)$, whose structure is identical to the structure of the charge coordinate η_Z chosen here.

2.2. Equations of Motion

Within the stochastic approach developed in [1, 7, 15], the evolution of collective degrees of freedom is treated as the motion of a Brownian particle in a heat bath formed by single-particle degrees of freedom of a nucleus. In the case of three collective coordinates, the set of coupled Langevin equations has the form

$$\dot{q}_i = \mu_{ij} p_j, \quad (3)$$

$$\dot{p}_i = -\frac{1}{2} p_j p_k \frac{\partial \mu_{jk}}{\partial q_i} - \frac{\partial F}{\partial q_i} - \gamma_{ij}\mu_{jk}p_k + \theta_{ij}\xi_j,$$

where $i, j, k = 1, 2, 3$; $\mathbf{q} = (c, h, \eta_Z)$ is the set of collective coordinates; $\mathbf{p} = (p_c, p_h, p_{\eta_Z})$ is the set of momenta conjugate to them; m_{ij} ($\|\mu_{ij}\| = \|m_{ij}\|^{-1}$) is the tensor of inertia; γ_{ij} is the tensor of friction; $F(\mathbf{q})$ is the free energy of the system being considered; $\theta_{ij}\xi_j$ is a random force; and ξ_i is a random quantity that possesses the following statistical properties:

$$\langle \xi_i \rangle = 0, \quad (4)$$
$$\langle \xi_i(t_1)\xi_j(t_2) \rangle = 2\delta_{ij}\delta(t_1 - t_2).$$

In (4) and below, the angular brackets mean averaging over the statistical ensemble.

The amplitude θ_{ij} of the random force is related to the diffusion tensor D_{ij} by the equation

$$D_{ij} = \theta_{ik}\theta_{kj}. \quad (5)$$

The eigenvalues and the eigenvectors of the diffusion matrix D_{ij}, which are used [7] to calculate the random force, were determined by the Jacobi method [16]. As to the diffusion tensor, it was found from the Einstein relation

$$D_{ij} = T\gamma_{ij}. \quad (6)$$

We emphasize that the charge mode is finite; in Eq. (6), it is therefore necessary to employ, instead of temperature T, the effective temperature T_Z^* [17] that takes into account quantum oscillations in the charge coordinate and which is given by

$$T_Z^* = \frac{\hbar\omega_Z}{2}\coth\left(\frac{\hbar\omega_Z}{2T}\right), \quad (7)$$

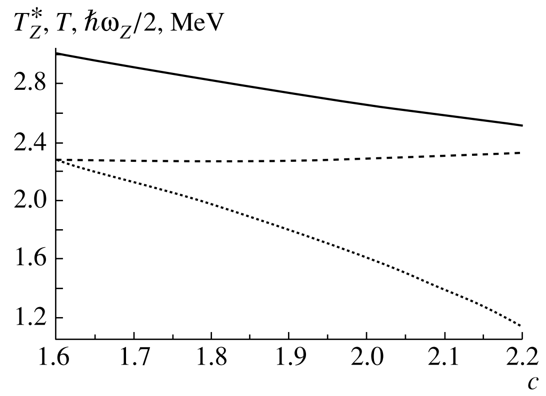

Fig. 1. Dependences of various quantities on the fission coordinate c along the mean trajectory: (solid curve) effective temperature of the nucleus for the charge degree of freedom according to the calculation by formula (7), (dashed curve) thermodynamic temperature of the nucleus as given by Eq. (11), and (dotted curve) half the energy of charge-density oscillations ($\hbar\omega_Z/2$). The calculations have been performed for $E^* = 110$ MeV.

where ω_Z is the frequency of oscillations in η_Z. We note that, in contrast to what occurs in the case of a charge distribution, investigation of mass distributions does not require introducing the effective temperature with respect to the mass-asymmetric coordinate because, for this collective mode, the frequency of oscillations is much less than the temperature T of the heat bath [18]. In that case ($T \gg \hbar\omega_A/2$, where ω_A is the frequency of oscillations in the mass-asymmetric coordinate), the effective temperature T_A^* is approximately equal to the temperature T. As is shown in Fig. 1, the frequency of oscillations in the charge mode is so great over the entire interval of descent from the saddle to the scission point along the mean trajectory that the temperature T of the heat bath and the quantity $\hbar\omega_Z$ are on the same order of magnitude. In calculating the random-force component along the coordinate η_Z, it is therefore necessary to use the effective temperature. By a mean trajectory, we imply that which is obtained by averaging Langevin trajectories over the ensemble. Upon averaging of this type, the random force appearing in the set of Eqs. (3) vanishes by virtue of relations (4), with the result that the set of Langevin equations reduces to a set of generalized Hamilton's equations. Our calculations have revealed that the use of the effective temperature T_Z^* instead of the thermodynamic temperature T leads to an increase of 15% in the variance of the charge distribution.

A numerical integration of the set of Eqs. (3) was performed on the basis of the first-order Heuen scheme [7]. For the initial values of the collective coordinates, we took the coordinates corresponding to the ground state of the compound nucleus ($c = 1$, $h = 0, \eta_Z = 0$); also, we set the initial momentum p_{η_Z} to zero and assumed that the initial distributions with respect to the momenta p_c and p_h are equilibrium. The angular-momentum distribution was borrowed from [7]. The integration of the stochastic Langevin Eqs. (3) was terminated as soon as a dynamical trajectory intersected the scission surface defined by the condition

$$\left(\frac{\partial^2 V(\mathbf{q})}{\partial h^2}\right)_{c,\eta_Z} = 0. \tag{8}$$

As a scission criterion, we used here the condition that the neck radius is $0.3R_0$, in which case the equality in (8) is satisfied identically. From the physical point of view, fulfillment of relation (8) means that the system loses stability with respect to variations in the neck thickness.

Obviously, the concept of charge transfer between the fragments is meaningful only in the case where one can unambiguously separate one fragment from another, but this is possible only if the nuclear shape features a neck. In our dynamical calculations, the evolution of the charge degree of freedom therefore began as soon as the nucleus being considered developed a neck; as to shapes involving no neck, only the coordinates specifying the shape of the nuclear surface (coordinates c and h) evolved for them. In the ^{236}U nucleus, a neck appeared immediately upon traversing the ridge separating the ground-state region from the fission valley. This brings about the question of whether it is wise to begin dynamical calculations from the ground state. (Would it not be more appropriate to start from the ridge, for example?) Our choice of initial conditions was motivated by the desire to take fully into account the evaporation of light prescission particles—and especially neutrons—which, as is well known, has a pronounced effect on the distributions of fission fragments. In [19], it was shown that the overwhelming majority of prescission neutrons (more than half of them) are evaporated from the ground-state region of the nucleus before it reaches the ridge, and this is the reason why it is desirable to choose initial conditions in the ground state of the compound system. In discussing methods for calculating the potential energy and transport coefficients, we will hereafter imply that there is a neck in the nuclear shape.

In the case of excited nuclear systems, it is of course necessary to use, in determining the conservative force, a thermodynamic potential (free energy, as a rule) [20, 21] instead of the potential energy. Within the Fermi gas model, the free-energy functional is given by

$$F(\mathbf{q}) = V(\mathbf{q}) - a(\mathbf{q})T^2, \tag{9}$$

where $V(\mathbf{q})$ is the potential energy and $a(\mathbf{q})$ is the level-density parameter. In calculating the density of excited levels, we took into account the effect of the nuclear deformation on the level-density parameter; that is, we represented it as

$$a(\mathbf{q}) = \alpha A + \beta A^{2/3} B_s(\mathbf{q}), \qquad (10)$$

where the values of $\alpha = 0.073$ MeV^{-1} and $\beta = 0.095$ MeV^{-1} were borrowed from [22] and where $B_s(\mathbf{q})$ is the collective-coordinate dependent functional of the surface energy of a nucleus that is represented as a liquid drop with a sharp boundary [11, 23]. As will be described below in discussing the calculation of the potential energy, the surface-energy functional is independent of the charge coordinate within our model. It follows that the use of the free energy, instead of the potential energy, in calculating the conservative force affects only the evolution of the nuclear-shape coordinate. As to the conservative-force component along the coordinate η_Z, it is determined exclusively by the dependence of the potential energy of the charge coordinate.

The heat-bath temperature T used in our calculations was determined within the Fermi gas model as

$$T = (E_{\text{int}}/a(\mathbf{q}))^{1/2}, \qquad (11)$$

where E_{int} is the excitation energy of internal degrees of freedom. Over the entire interval of the evolution of the nucleus from the ground state to the scission point, we checked fulfillment of the energy-conservation law in the form

$$E^* = V(\mathbf{q}) + E_{\text{int}} + E_{\text{coll}} + E_{\text{evap}}(t), \qquad (12)$$

where E_{coll} is the kinetic energy of the motion along the collective coordinates and E_{evap} is the energy fraction carried away by evaporated prescission particles by the instant t. In order to take into account the discrete character of the evaporation of prescission light particles and photons, our dynamical model was combined, according to the method described in [24], with the statistical evaporation branch of the calculations.

2.3. Potential Energy

In calculating the potential energy on the basis of the liquid-drop model, it is usually assumed that the charge density is constant over the entire volume of the nucleus. It is obvious, however, that, because of the Coulomb repulsion of the protons of the nucleus, the intranuclear nucleons are redistributed in such a way that the charge density is greater at the nuclear periphery than in the interior of the nucleus. The simplest solution to the problem of the form of the charge-density function was proposed in [25], where the charge density was approximated by a linear function of the coordinate z (coordinate along the symmetry axis). The problem of the charge distribution in a nucleus was comprehensively studied in [26, 27], where use was made of variational methods, the analysis in [27] being based on two versions of the liquid-drop model. From experimental data on the charge distribution that are presented in [28, 29], one can conclude that the polarizability of nuclear matter is rather small; on this basis, we assumed, for a first approximation, that the charge density takes different values in the different would-be fragments, but that it is constant within each of them [30]; that is,

$$\rho^p(\mathbf{r}) = \begin{cases} \rho^p_R, & \mathbf{r} \in V_R, \\ \rho^p_L, & \mathbf{r} \in V_L, \end{cases} \qquad (13)$$

where V_R and V_L are the volumes of, respectively, the right- and the left-hand fragment. Although the representation of the charge density in the form (13) is a rough approximation, it enables us to avoid introducing additional parameters (like the charge-polarization parameter [25]) and to describe the distribution of the charge among the fragments in terms of simple formulas that admit a straightforward interpretation.

From the condition requiring that nuclear liquid be incompressible, it follows that the sum of the proton- and the neutron-liquid density is constant; that is,

$$\rho^p_R + \rho^n_R = \rho^p_L + \rho^n_L = \rho^p_0 + \rho^n_0 = \rho, \qquad (14)$$

where $\rho^p_0 = Z/(4\pi R_0^3/3)$ and $\rho^n_0 = N/(4\pi R_0^3/3)$ are the densities of, respectively, protons and neutrons in the case of a uniform charge distribution over the entire nucleus and ρ is the intranuclear-nucleon density. The quantities ρ^p_R and ρ^p_L are related to the charge coordinate η_Z by the equation

$$\rho^p_R = \rho^p_0 \frac{(k+1)}{2k}(1 + \eta_Z), \qquad (15)$$
$$\rho^p_L = \rho^p_0 \frac{(k+1)}{2}(1 - \eta_Z),$$

where $k = A_R/A_L$ is the ratio of the masses of nascent fragments. The corresponding neutron densities ρ^n_R and ρ^n_L can easily be found on the basis of Eqs. (14) and (15).

We assume that the potential energy of a nucleus is the sum of the symmetry energy, the Coulomb energy, the surface energy, and the energy associated with the rotation of this nucleus as a discrete unit. The parameters of the liquid-drop model were set to the values chosen by Myers and Swiatecki [31]. We note that the surface energy was taken to be independent of the charge-asymmetry coordinate η_Z. This assumption is inevitable in view of the ambiguity in breaking down the symmetry energy into the volume and the surface component.

For an arbitrary nuclear shape, the symmetry energy can be calculated under the assumption that this energy is uniformly distributed over the entire nucleus, in which case we have [32]

$$V_{\rm sym} = a_{\rm sym} \int \frac{[\rho^n(\mathbf{r}) - \rho^p(\mathbf{r})]^2}{\rho} dV, \qquad (16)$$

where $a_{\rm sym} = 23.7$ MeV is the symmetry-energy coefficient. Under the assumption that the neutron and the proton density are constant within each of the fragments, the symmetry energy can be represented as

$$V_{\rm sym} = \frac{a_{\rm sym}}{\rho} \left[(\rho_R^n - \rho_R^p)^2 V_R + (\rho_L^n - \rho_L^p)^2 V_L\right]. \quad (17)$$

It is rather difficult to calculate the Coulomb energy for the case where the charge distribution over the nuclear volume is not uniform. But for a uniform charge distribution in each of the fragments, this problem is significantly simplified; its solution is given by the relation

$$V_{\rm C}(\mathbf{q}) = \frac{E_{\rm C}^0}{(\rho_0^p)^2} \left[(\rho_R^p - \rho_L^p) \right. \qquad (18)$$
$$\left. \times\, (\rho_R^p B_{\rm C}^R(\mathbf{q}) - \rho_L^p B_{\rm C}^L(\mathbf{q})) + \rho_R^p \rho_L^p B_{\rm C}(\mathbf{q})\right],$$

where $E_{\rm C}^0$ is the Coulomb energy of the initial spherical nucleus, while $B_{\rm C}$, $B_{\rm C}^R$, and $B_{\rm C}^L$ are the Coulomb energies (in units of the Coulomb energy of the corresponding spherical nucleus) of the entire nucleus and of the would-be fragments having a constant charge density.

From (17) and (18), it can be found that the potential energy as a function of the charge-asymmetry parameter η_Z can be represented as

$$V(c, h, \eta_Z, J) = V(c, h, \langle\eta_Z\rangle, J) \qquad (19)$$
$$+ \frac{C_{\eta_Z}}{2}(\eta_Z - \langle\eta_Z\rangle)^2,$$

where J is the angular momentum of the compound nucleus. The mean value of the charge-asymmetry parameter, $\langle\eta_Z(c, h)\rangle$, is the point of a local minimum of the potential energy at given values of the shape parameters (c, h). It should be noted that $\langle\eta_Z\rangle = 0$ is the case of symmetric fission considered here. The quantity

$$C_{\eta_Z} = \left.\frac{\partial^2 V(c, h, \eta_Z)}{\partial \eta_Z^2}\right|_{\eta_Z = \langle\eta_Z\rangle}$$

is the stiffness of the nucleus in the coordinate η_Z. For this stiffness, relations (17) and (18) yield

$$C_{\eta_Z} = \left(\frac{(k+1)Z}{kA}\right)^2 \left(2a_{\rm sym}kA + \frac{2E_{\rm C}^0}{(1-\delta)^2} \right. \qquad (20)$$
$$\left. \times \left[(1+k)(B_{\rm C}^R + kB_{\rm C}^L) - kB_{\rm C}\right]\right),$$

where $\delta = (N - Z)/A$. The stiffness computed by formula (20) depends only slightly on the nuclear deformation since the main contribution to it comes from the symmetry energy [first term in (20)]. An order-of-magnitude estimate of the stiffness is $C_{\eta_Z} = (7–8) \times 10^3$ MeV.

2.4. Inertia Parameter of the Charge Mode

The calculation of transport coefficients is one of the most important problems in nuclear dynamics. For problems involving the charge degree of freedom, the calculation of transport coefficients is complicated by the fact that two collective coordinates (c and h) are associated with variations in the nuclear shape, while the third coordinate (η_Z) is associated with the redistribution of charge in the nucleus being considered, the physical nature of this coordinate being totally different from that of the shape coordinates. In view of the above, it is obvious that a model for describing the charge components of the mass and the friction tensor must be different from a model for describing the other components of these tensors. In choosing a method for calculating the inertia- and the friction-tensor components corresponding to the coordinates of the nuclear shape, we relied on rich experience accumulated through investigations in these realms (in particular, on our experience gained in studying mass–energy distributions within Langevin dynamics [5, 6] and on the conclusions on nuclear viscosity that were drawn in [6]). The inertia-tensor components m_{cc}, m_{ch}, and m_{hh} were computed by the Werner–Wheeler method based on the hydrodynamic model of the irrotational flow of incompressible nuclear liquid [33], while the corresponding components of the friction tensor were treated within the model of surface one-body dissipation [34–36] with allowance for the reduction of the contribution from the wall formula, the corresponding reduction factor being set to $k_s = 0.25$ [6, 37, 38]. The problem of determining the transport coefficients associated with the charge mode is much more involved. A reliable approach to studying the interplay of charge transfer between fission fragments and variations in the nuclear shape has yet to be developed. In view of this, the off-diagonal inertia-tensor components $m_{c\eta_Z}$ and $m_{h\eta_Z}$ and the corresponding components of the friction tensor were set to zero.

Let us now discuss a method for computing the mass factor $m_{\eta_Z\eta_Z}$ associated with the charge mode. As was noted above, the hydrodynamic approach (Werner–Wheeler method) was successfully employed in calculating the mass tensor for the shape coordinates; for this reason, the hydrodynamic model was applied for the charge degree of freedom as well. By way of example, we indicate that, in [39], the mass parameter was determined by the formula

$$m_{\eta_Z\eta_Z}(c,h) = \frac{C_{\eta_Z}(c,h)}{\omega_1^2(c,h)}, \qquad (21)$$

where ω_1 is the frequency of longitudinal dipole oscillations that is obtained by solving the Helmholz equation for charge-density fluctuations [32, 40].

For the case of an inviscid liquid flowing through a round hole of radius r_N between two touching fragments of spherical shape, it was found in [41] that the inertia parameter associated with the charge mode can be represented as

$$m_{\eta_Z\eta_Z}(c,h) = \frac{\pi}{6} r_0^3 m \frac{ZA^2}{N}\frac{1}{r_N}, \qquad (22)$$

where r_0 is the nuclear-radius parameter; m is the nucleon mass; A is the mass number of the nucleus undergoing fission; and Z and N are the numbers of, respectively, protons and neutrons in it.

The fact that the neck connecting the fragments has a nonzero length was ignored in deriving expression (22). Moreover, viscosity plays an important role in our model. In [42], it was shown that, for a flow of a viscous incompressible liquid through a cylindrical neck of radius r_N and length l, the mass parameter of the charged mode is given by

$$m_{\eta_Z\eta_Z}(c,h) = \frac{m}{3\pi\rho}\frac{ZA^2}{N}\frac{(l+2r_N)}{r_N^2}, \qquad (23)$$

where ρ is the density of intranuclear nucleons.

We have compared the results produced by formulas (21)–(23). The values of the mass parameter according to (21) were borrowed from [39], where the mass parameter as a function of the distance between the centers of mass of the would-be fragments is given for a few fixed values of the neck-thickness parameter h. The results are presented in Fig. 2 at the neck-thickness parameter set to $h = 0$ (the line $h = 0$ roughly approximates the bottom of the fission value [11]). The mass-parameter values in the figure correspond to large values of the elongation parameter c in the region of nuclear deformations from the saddle to the scission point. All three dependences exhibit a characteristic increase in the inertia parameter $m_{\eta_Z\eta_Z}$ as the nucleus approaches the scission point. From Fig. 2, it can also be seen that formulas (21) and (23) yield close values of $m_{\eta_Z\eta_Z}$, but that formula (22) leads to values falling considerably short of these.

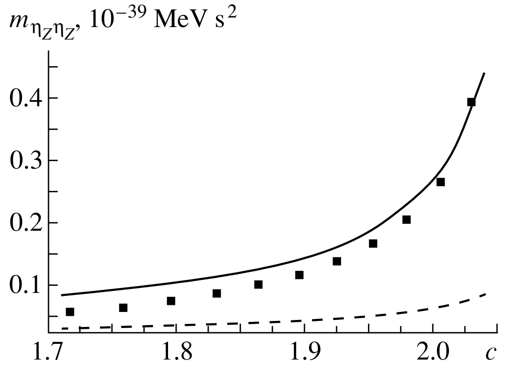

Fig. 2. Inertia parameter as a function of the fission coordinate c at the neck-thickness parameter of $h = 0$: (solid curve) mass parameter $m_{\eta_Z\eta_Z}$ calculated by formula (23) [42], (dashed curve) results of the calculation by formula (22) [41], and (closed boxes) results of the calculation by formula (21) according to [39].

In our opinion, formula (21) is the most consistent. However, it is rather difficult in practice to calculate the frequencies of isovector dipole oscillations. It should be emphasized that, from our analysis of the above three formulas, it follows that formulas (21) and (23) yield close values of the mass parameter $m_{\eta_Z\eta_Z}$ over the entire region of the nuclear-deformation parameters (c, h) that is of interest to us. Taking the aforesaid into account, we calculate below the mass parameter of the charge mode on the basis of (23). In order to apply this formula, it is necessary to know the neck radius r_N and the neck length l at fixed values of c and h. To specify them, the nuclear shape in the region of deformations featuring a pronounced neck was approximated by two spherical fragments connected by a cylindrical neck of radius r_N. The centers of the spheres were taken to coincide with the centers of mass of the nascent fragments, their radii R_R and R_L being determined from the condition of nuclear-volume conservation. The neck length is then given by $l = R - R_R - R_L$, where R is the distance between the centers of mass of the would-be fragments.

2.5. Friction Parameter of the Charge Mode

In theoretically studying isobaric distributions, the friction coefficient $\gamma_{\eta_Z\eta_Z}$ was frequently assumed (see, for example, [39, 43]) to be a variable parameter that is independent of coordinates. This is, however, a rough approximation, because it is necessary to take into account the dependence of the friction parameter of the charge mode on the deformation of the nucleus. In the present study, the coordinate dependence of the friction parameter $\gamma_{\eta_Z\eta_Z}$ was taken into account by two methods—that is, under the assumption of the one-body dissipation mechanism and under the assumption of the two-body dissipation mechanism. The simplest procedure for assessing the friction parameter is that which relies on the hydrodynamic model where one studies energy dissipation accompanying the motion of a viscous incompressible liquid in a pipe (neck connecting nascent fragments) of length l and radius r_N. In this case, the velocity field obtained by solving the Navier–Stokes equation has a nonvanishing component only along the z axis (symmetry axis of the nucleus) [44]; that is,

$$u(\mathbf{r}) = u_z(\mathbf{r}) = \frac{\Delta p}{4\nu_0 l}(r_N^2 - r^2), \tag{24}$$

where Δp is the pressure drop between the ends of the pipe and ν_0 is the coefficient of dynamical viscosity. In the general case of a flow of a viscous incompressible liquid, the kinetic energy of the liquid and the rate of kinetic-energy dissipation are given by

$$E_{\rm kin} = \frac{m\rho}{2}\int u^2 dV, \tag{25}$$

$$\dot{E}_{\rm kin} = -\frac{\nu_0}{2}\int\left(\frac{\partial u_i}{\partial x_k} - \frac{\partial u_k}{\partial x_i}\right)^2 dV,$$

where it is implied that integration is performed over the pipe (neck) volume and where i and k are Cartesian subscripts. For the velocity field given by relation (24), the kinetic energy of the liquid has the form

$$E_{\rm kin} = \frac{\pi m\rho(\Delta p)^2 r_N^6}{96\nu_0^2 l}, \tag{26}$$

while the rate of kinetic-energy dissipation is

$$\dot{E}_{\rm kin} = -\frac{\pi(\Delta p)^2 r_N^4}{8\nu_0 l}. \tag{27}$$

From (26) and (27), we find that the reduced coefficient of friction for the charge mode has the form

$$\beta_{\eta_Z\eta_Z} = \frac{\gamma_{\eta_Z\eta_Z}}{m_{\eta_Z\eta_Z}} = -\frac{\dot{E}_{\rm kin}}{2E_{\rm kin}} = \frac{6\nu}{r_N^2}, \tag{28}$$

where ν is the coefficient of kinematic viscosity. It is obvious that, in the hydrodynamic model, the friction coefficient for the charge mode is dependent on the approach used to calculate the inertia parameter $m_{\eta_Z\eta_Z}$ and is determined by the formula $\gamma_{\eta_Z\eta_Z} = m_{\eta_Z\eta_Z}\beta_{\eta_Z\eta_Z}$. The value of $\nu = 13.5 \times 10^{21}$ fm^2 s^{-1} was extracted from experimental data on the widths of giant dipole resonances [45]. We used this value of the coefficient ν as an input in our dynamical calculations that assume the two-body mechanism of nuclear viscosity, since isovector dipole oscillations along the symmetry axis make a dominant contribution to the redistribution of charge among the fragments.

In calculating the friction parameter of the charge degree of freedom, it is of particular interest to apply the model of one-body viscosity. In this model, it is considered in the one-body mechanism of viscosity that a nucleus is a system of fermions and that, by virtue of the Pauli exclusion principle, the range of intranuclear nucleons is as large as the nuclear size. We note that, in studying the fission of excited nuclei, the one-body mechanism of viscosity has not yet been used as a mechanism of energy dissipation associated with the charge mode (however, it was successfully employed in exploring the widths of giant dipole resonances [46, 47]). The classical formula expressing the rate of collective-energy dissipation within a modified version of the model of one-body viscosity can be written in the following conventional form [35]:

$$-\dot{E}_{\rm kin} = m\rho\bar{v}\Bigg[\oint_{\Sigma_L}(\dot{\mathbf{n}} - \mathbf{Q}_L)^2 d\Sigma + \oint_{\Sigma_R}(\dot{\mathbf{n}} - \mathbf{Q}_R)^2 d\Sigma + \frac{1}{4}(2u_\parallel^2 + u_\perp^2)\Delta\sigma + \frac{16}{9}\frac{1}{\rho^2\Delta\sigma}\dot{N}_1^2\Bigg]. \tag{29}$$

Here, m is the particle mass; ρ is the density of particles in a nucleus; $\bar{v}$ is the mean velocity of their motion; $\dot{\mathbf{n}}$ is the normal velocity of the nuclear-surface element $d\Sigma$; $\mathbf{Q}_{R(L)}$ is the velocity of the right-hand (left-hand) fragment as a discrete unit with respect to the center of mass of the whole system; $\Delta\sigma$ is the area of the window (the neck between two would-be fragments); $u_{||}$ and $u_\perp$ are the components of the velocity of the relative motion of would-be fragments, respectively, along the normal to the window $\Delta\sigma$ and in the plane orthogonal to this normal; and N_1 is the number of particles in one of the fragments (for example, in the right-hand one). The quantity $\dot{E}_{\rm kin}$ is related to the friction tensor by the well-known equation $\sum_{i,j}\gamma_{ij}\dot{q}_i\dot{q}_j = -\dot{E}_{\rm kin}$, where $\{q_i\}$ is the set of collective coordinates.

Here, we would like to make some comments that are necessary for applying the model of one-body viscosity to the charge mode. The idea underlying the derivation of the formula for the friction parameter of the charge mode consists in applying expression (29) to the proton and the neutron liquid individually and in representing the total rate of energy dissipation as the sum of the contributions from the proton and the neutron subsystem; that is, $\dot{E}_{\rm kin} = \dot{E}_{\rm kin}^p + \dot{E}_{\rm kin}^n$. In implementing this procedure, we impose the condition that number of nucleons is constant in each fragment. In addition, we must fix the shape parameters, since we are going to calculate the rate of collective-energy dissipation associated with charge transfer between nascent fragments and not with variations in the nuclear shape. A similar procedure for calculating the friction parameter was used in [47]. The first two terms in expression (29) represent the wall formula for each of the nascent fragments. For the charge degree of freedom, the wall formula must describe energy dissipation for the case where the neutron and the proton liquid move with respect to each other within would-be fragments. Indeed, it was shown in [47] that the result produced by the wall formula for the charge mode is proportional to $\dot{D}_{pn}^2$, where D_{pn} is the distance between the centers of mass of the proton and the neutron liquid. Since we do not consider oscillations of the charge density within the fragments and since we have assumed that the charge density is constant, $D_{pn} \equiv 0$ in each of the fragments; therefore, the term expressing the result given by the wall formula for the charge mode vanishes identically.

In the case of the charge mode, the term describing energy dissipation associated with the relative motion of the fragments—the window formula [third term in formula (29)]—has the form

$$-\dot{E}_{\text{kin}}^{\text{window}} = \dot{D}_p^2 \frac{m\rho}{2} \frac{Z}{NA} [N\bar{v}_p + Z\bar{v}_n]\Delta\sigma, \qquad (30)$$

where D_p is the distance between the centers of mass of the proton subsystems of nascent fragments and $\bar{v}_p$ and $\bar{v}_n$ are the mean velocities of, respectively, protons and neutrons within the nucleus. At a fixed nuclear deformation, D_p is constant—in particular, it does not depend on the ratio of the numbers of protons in the fragments. In this case, $\dot{D}_p \equiv 0$, and the corresponding term in the formula for the case of one-body dissipation is also equal to zero. We note that the first three terms in expression (29) will vanish for any time-independent charge distribution of the form $\rho^p(\mathbf{r}) = \rho_0^p f(\mathbf{r})$, where ρ_0^p is the density of protons in the case of a uniform charge distribution over the volume of the nucleus and $f(\mathbf{r})$ is an arbitrary function of the radius vector of a point within the nucleus. It is clear, however, that the exchange of protons and neutrons between the fragments leads to a deviation of the charge density from the equilibrium value; as a result, damped oscillations tending to restore the disturbed equilibrium arise in the fragments.

For the concept of equilibrium density [see Eq. (13)] to be used in the model adopted here, it is therefore necessary that the characteristic time over which the proton-liquid oscillations relative to the neutron liquid within the fragments are damped be much less than the relaxation time in the charge mode η_Z. The simple expression $R/\bar{v}$, where $\bar{v}$ is the mean velocity of intranuclear nucleons and R is the nuclear radius, was obtained in [46] for the time over which charge-density oscillations are damped in a spherical nucleus. If the radius of one of the fragments (R_R or R_L) is taken for R, the result for the time of relaxation of proton-liquid oscillations relative to the neutron liquid within one of the fragments will be (0.8–1.0) × 10^{-22} s; for the coordinate η_Z, the characteristic time of damping is $\tau_{\eta_Z} \simeq 4 \times 10^{-22}$ s (see Fig. 5 below and the discussion of τ_{η_Z} in Section 3). By virtue of this relationship between the corresponding relaxation times, the charge distribution in a nucleus can be taken to be steady-state and the charge-density function can be assumed to feature no explicit time dependence.

Thus, it turns out that, in the absence of proton-liquid oscillations relative to the neutron liquid within the fragments, a nonzero contribution comes only from the last term in (29); this term, which was

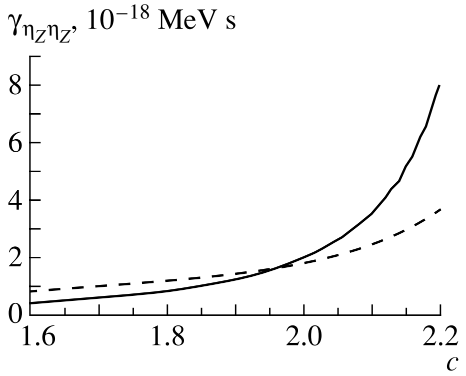

Fig. 3. Friction parameter of the charge mode versus the elongation parameter c along the mean trajectory under the assumption of (solid curve) the two-body viscosity mechanism ($\nu = 13.5 \times 10^{21}$ fm^2 s^{-1}) and (dashed curve) the one-body viscosity mechanism.

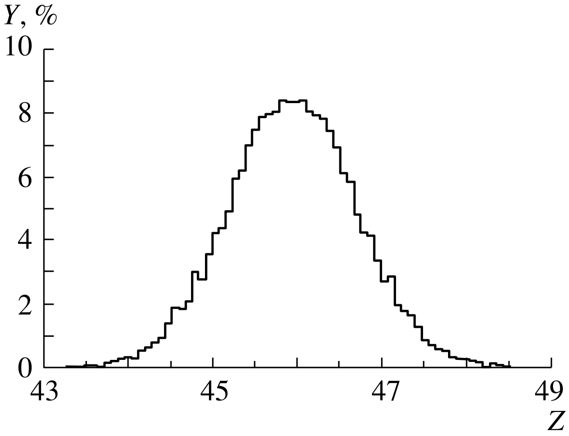

Fig. 4. Charge yield obtained in our dynamical calculations employing the two-body mechanism of nuclear viscosity in the charge degree of freedom ($\nu = 13.5 \times 10^{21}$ fm^2 s^{-1}). The calculations were performed for the reaction ^{4}He + ^{232}Th → ^{236}U at the excitation energy of $E^* = 110$ MeV. The yield was normalized by 200%.

obtained in [35, 36] as a term that is additional to the original formula of the model of one-body viscosity [34], takes into account the reaction of the system against variations in the mass asymmetry. In the case of the charge degree of freedom, it describes energy dissipation associated with the relative change in the number of protons in the fragments without any variations in the nuclear shape. Within the model of one-body viscosity, we obtained the following expression for the friction parameter of the charge mode:

$$\gamma_{\eta_Z\eta_Z} = \frac{4m}{9\rho}\frac{AZ}{N}[N\bar{v}_p + Z\bar{v}_n]\frac{1}{\Delta\sigma}. \qquad (31)$$

Figure 3 shows the friction parameter of the charge mode as a function of the elongation parameter c for both the two- and the one-body viscosity mechanism (solid and dashed curves, respectively). From expression (31), it can be seen that, in the case of the one-body viscosity mechanism, the parameter $\gamma_{\eta_Z\eta_Z}$ is determined exclusively by the neck thickness; therefore, $\gamma_{\eta_Z\eta_Z} \sim 1/r_N^2$ for $r_N \to 0$ (that is, as the nucleus approaches the scission point). As to the two-body mechanism, the inertia parameter computed by formula (23) is proportional to $1/r_N^2$ when the neck radius tends to zero, whence it follows that, in the case of two-body viscosity, the friction parameter behaves as $1/r_N^4$ for $r_N \to 0$. Indeed, it can be seen from Fig. 3 that, at deformation characteristic of the saddle point, the two-body mechanism of nuclear viscosity yields friction-parameter values smaller than those for the one-body mechanism, but that, as the nucleus being considered approaches the scission point, the quantity $\gamma_{\eta_Z\eta_Z}$ as given by the two-body mechanism increases sharply, becoming, at this point, more than twice as great as $\gamma_{\eta_Z\eta_Z}$ values computed by formula (31). We would like to emphasize yet another important distinction between the two mechanisms of nuclear viscosity—namely, the formula corresponding to two-body viscosity involves a variable parameter (coefficient of viscosity ν), but there are no variable parameters within the one-body model.

3. RESULTS OF THE CALCULATIONS

It was indicated in the Introduction that, in the present study, the charge distribution of fission fragments is explored by considering the example of the symmetric fission of the compound nucleus ^{236}U formed in the reaction ^{232}Th + ^{4}He → ^{236}U. The calculations were performed for two mechanisms of nuclear viscosity (that of one-body dissipation and that of two-body dissipation). A typical histogram of the charge distribution calculated under the assumption of the two-body mechanism of viscosity in the coordinate η_Z is shown in Fig. 4 for the case where the excitation energy of the compound nucleus is $E^* =$ 110 MeV. From this figure, it can clearly be seen that the charge distribution obtained in our theoretical calculations has the form of a Gaussian function, the corresponding mean value being $\langle Z\rangle = Z/2$. This result is in qualitative agreement with experimental data.

Previously the isobaric charge distribution for the fission of the same compound nucleus of ^{236}U was studied theoretically in [39, 43] on the basis of the Fokker–Planck equation. In those studies, however, the coefficient of friction for the charge mode was taken to be independent of collective coordinates and was a variable parameter. For low excitation energies, there is a vast body of experimental data on the variances of charge distributions for the ^{236}U nucleus. By way of example, we recall the well-known experimental fact [48, 49] that, in the thermal-neutron-induced fission of ^{235}U nuclei, the charge variance σ_Z^2 is independent of the excitation energy and is equal to 0.4 ± 0.05. This behavior of the charge variance σ_Z^2 suggests that, at low excitation energies, the formation of the charge distribution is governed by quantum processes. It is also well known that, in this energy region, experimental data on σ_Z^2 are closely reproduced by the expression arising in the statistical limit and having the form

$$\sigma^2_{Z\mathrm{stat}}(E_{\mathrm{int}}) = \frac{T_Z^*(\langle\mathbf{q}_{\mathrm{sc}}\rangle)}{C_Z(\langle\mathbf{q}_{\mathrm{sc}}\rangle)}, \qquad (32)$$

where $C_Z(\langle\mathbf{q}_{\mathrm{sc}}\rangle) = 4C_{\eta_Z}(\langle\mathbf{q}_{\mathrm{sc}}\rangle)/Z^2$ and $\langle\mathbf{q}_{\mathrm{sc}}\rangle$ are the coordinates of the mean scission point. If $T \ll \hbar\omega_Z/2$, then $T_Z^* \simeq \hbar\omega_Z/2$, which explains invariability of the charge variance at low energies. Our dynamical model cannot be applied to describing low-energy fission because shell effects and effects of nucleon pairing are disregarded there in calculating the potential energy and transport coefficients. Nonetheless, we can compute the quantity $\sigma^2_{Z\mathrm{stat}}$ and compare the result with experimental data. At the excitation energy of 6.4 MeV (which corresponds to ^{235}U fission by thermal neutrons), we obtained the value of $\sigma^2_{Z\mathrm{stat}} = 0.35$, which is in good agreement with experimental data.

Let us now proceed to consider the results of our dynamical calculations. We begin by discussing characteristic times for the charge mode of the nucleus. As a characteristic time, a dissipating system features the relaxation time [50] in the corresponding collective coordinate; that is,

$$\tau_{\eta_Z} = \begin{cases} 2\tilde{\beta}_{\eta_Z}^{-1}, & \omega_{\eta_Z} \geq \tilde{\beta}_{\eta_Z}/2 \\ \left[\tilde{\beta}_{\eta_Z}/2 - (\tilde{\beta}_{\eta_Z}^2/4 - \omega_{\eta_Z^2})^{1/2}\right]^{-1}, & \omega_{\eta_Z} < \tilde{\beta}_{\eta_Z}/2, \end{cases} \tag{33}$$

where $\tilde{\beta}_{\eta_Z} = \beta_{\eta_Z} + \dot{m}_{\eta_Z\eta_Z}/m_{\eta_Z\eta_Z}$ is the generalized coefficient of damping for the charge mode. In (33), the first case (that of $\omega_{\eta_Z} \geq \tilde{\beta}_{\eta_Z}/2$) corresponds to the regime of damped oscillations, while the second case ($\omega_{\eta_Z} < \tilde{\beta}_{\eta_Z}/2$) corresponds to the regime of aperiodic damping. The results obtained by calculating τ_{η_Z} are displayed in Fig. 5 for both mechanisms of viscosity. From this figure, we can see that the curve representing the relaxation time for the two-body mechanism of viscosity differs significantly from the curve calculated for the relaxation time under the assumption of one-body viscosity in η_Z. In the case of the one-body mechanism, the nuclear system in question is in the regime of damped oscillations over the entire interval of descent from the saddle to the scission point, whereas, in the case of two-body viscosity, there occurs a transition into the aperiodic-damping regime at the final state of this descent.

Moreover, the relaxation time τ_{η_Z} calculated under the assumption of the one-body mechanism remains constant, in contrast to what occurs in the case of two-body viscosity, over the entire interval of descent from the saddle to the scission point. This is because, in the case of the one-body mechanism of friction, the inertia coefficient and the friction coefficient for the charge mode are proportional to $1/r_N^2$; therefore, the generalized coefficient of damping $\tilde{\beta}_{\eta_Z}$ does not change along the mean trajectory (the ratio $\dot{m}_{\eta_Z\eta_Z}/m_{\eta_Z\eta_Z}$ is much less than β_{η_Z}). Within the two-body mechanism, the reduced coefficient of friction [see relation (28)] depends strongly on the neck thickness; therefore, τ_{η_Z} will also feature a pronounced coordinate dependence if viscosity in the charge mode is associated with the two-body mechanism. As can be seen from Fig. 5, the minimum value of the relaxation times for the charge mode is $\tau_{\eta_Z} = (0.3–0.4) \times 10^{-21}$ s. This is only two to three times longer than the relaxation times for internal degrees of freedom, so that the Markov approximation in solving stochastic Langevin equations is at the margin of safety here. But even if Langevin equations in the Markov approximation are inapplicable to studying the evolution of the charge mode, generalized Langevin equations including memory effects, which lead to the emergence of retarded friction (see, for example, the original study of Ayik *et al.* [51] and the review article of Abe *et al.* [1]), can be employed to study this evolution.

It is of great interest to study the variance of the charge distribution versus the excitation energy. First of all, this is necessary for comparing results obtained within the two mechanisms of viscosity and for drawing thereby definitive conclusions on the mechanism of nuclear viscosity in the charge coordinate. In addition, our estimates demonstrate that the relaxation times for processes involving the charge coordinate are much shorter than characteristic times for modes associated with variations in the nuclear-surface shape (see also [27]). On this basis, one may expect that statistical equilibration with respect to the charge mode will occur not only at low but also at high excitation energies. Figure 6 shows the variance of the charge distribution versus the internal excitation energy of the nucleus at the scission point. The curve in Fig. 6 represents the variance $\sigma^2_{Z\mathrm{stat}}$ as a function of E_{int}. In plotting this curve, we have considered that, according to our calculations and the results presented in [52], the neck length is virtually independent of the nuclear deformation.

On the basis of the data presented in Fig. 6, we can draw the following conclusions. First, the calculated variance of the isobaric distribution exhibits a characteristic growth with excitation energy. Second, the calculations employing the different mechanisms of viscosity yield values of the variance that agree with each other within the statistical error, which is associated with the fact that the number of Langevin trajectories is bounded (there were about 10^4 trajectories in our calculations). Thus, we can state that, within our model, the variance of the charge distribution is

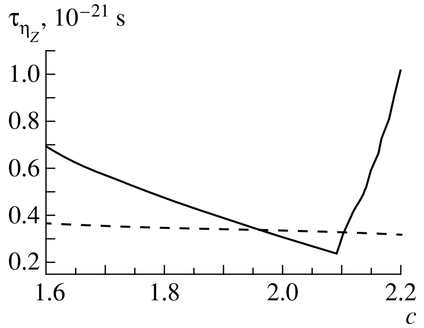

Fig. 5. Relaxation times for the charge mode versus the elongation coordinate c for (solid curve) the two-body ($\nu = 13.5 \times 10^{21}$ fm^2 s^{-1}) and (dashed curve) the one-body mechanism of viscosity.

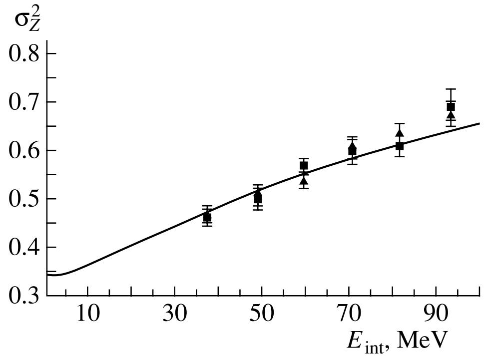

Fig. 6. Variance σ_Z^2 of the isobaric distribution as a function of the internal excitation energy of the compound nucleus at the scission point: (closed boxes) results of the calculation that assumes the two-body mechanism of viscosity in the charge mode ($\nu = 13.5 \times 10^{21}$ fm^2 s^{-1}), (closed triangles) results of the calculation that assumes the one-body mechanism of viscosity, and (solid curve) statistical limit at the mean scission point [see formula (32) and the comments to it].

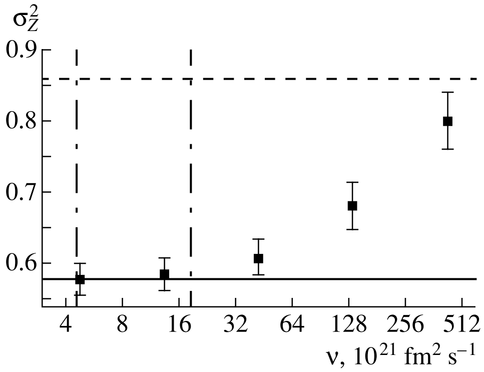

Fig. 7. Variance σ_Z^2 of the charge distribution versus the coefficient of two-body viscosity, ν, at the excitation energy of $E^* = 110$ MeV. The solid and the dashed line represent, respectively, the statistical limit and the limit of frozen initial conditions. The vertical dash-dotted lines bound the interval of values of the coefficient of two-body viscosity from [18, 33, 54]. Points correspond to our calculated values.

insensitive to the mechanism of nuclear viscosity. It is noteworthy that, for the same reaction of ^{232}Th fission induced by helium ions, the charge distribution was studied in [53] at excitation energies ranging between 20 and 57 MeV. It was found there that the charge distribution has a Gaussian form whose variance is independent of the excitation energy up to 39 MeV. Our dynamical calculations at an excitation energy of 39 MeV yield $\sigma_Z^2 = 0.46$, which is in agreement with the result quoted in [53], where values in the range $\sigma_Z^2 = 0.45$–0.50 were obtained over the entire energy range under study. Third, it can be seen from Fig. 6 that the variance σ_Z^2 obtained on the basis of our calculations shows but very modest deviations from the statistical-limit curve passing through experimental data on the charge variance at the excitation energies of $E^* = 6.4$ and 39 MeV. Therefore, we can draw the following important conclusion: statistical equilibration with respect to the charge coordinate occurs both at low and at high energies.

The second derivative $d^2\sigma^2_{Z\rm stat}/dE^2_{\rm int}$ carries important information about the mechanism that governs the formation of the charge distribution. We found that the entire energy range can be broken down into two parts: $E_{\rm int} < 20$ MeV and $E_{\rm int} > 20$ MeV. Within the first interval, we have $d^2\sigma^2_{Z\rm stat}/dE^2_{\rm int} > 0$, which means that, over this interval, quantum fluctuations play a dominant role in the formation of the charge distribution. Within the second interval, we have $d^2\sigma^2_{Z\rm stat}/dE^2_{\rm int} < 0$; there, fluctuations associated with the charge mode are predominantly of a thermal origin.

In discussing the calculation of the friction tensor, we have already mentioned that the friction parameter of the charge mode behaves differently for the different mechanisms of nuclear viscosity (this distinction becomes especially pronounced as the nucleus approaches the scission point). However, our dynamical calculations have revealed the mechanism of nuclear viscosity has virtually no effect on the width of the charge distribution. Therefore, it is natural to expect that σ_Z^2 depends only slightly on the coefficient of kinematic viscosity ν, which is the only free parameter of the model. In order to investigate this issue, we have calculated the variance of the charge distribution over the wide interval $\nu = (4.75$–$475)$ fm^2 s^{-1}. The results of these calculations are displayed in Fig. 7 on a logarithmic scale. The behavior of the variance of the isobaric distribution as a function of the coefficient ν can be explained in the following way. In the case of high friction in the coordinates c and h and low friction in the coordinate η_Z, statistical equilibration in the charge coordinate has time to occur at any point of a stochastic trajectory. A totally different situation becomes prevalent as viscosity in the charge mode increases—namely, memory effects come into play that consist in that the nuclear system in question memorizes the values of the charge coordinate that it had prior to going over to this regime. Indeed, it can be seen from Fig. 7 that the variance of the charge distribution fits in the statistical-limit line (solid line) at low values of the coefficient of viscosity, but that, as the coefficient ν increases, the variance σ_Z^2 grows, approaching the limit of frozen initial conditions (dashed line). By the limit of frozen initial conditions, we mean the ratio $T_Z^*(\mathbf{q}_{\rm sd})/C_Z(\mathbf{q}_{\rm sd})$, where $\mathbf{q}_{\rm sd}$ are the coordinates of the saddle point. From Fig. 7, it can also be seen that the variance σ_Z^2 grows very slowly as the viscosity parameter changes (indeed, an increase in the coefficient ν by two orders of magnitude leads to only a 50% increase in the variance). It is precisely this circumstance that explains an extremely low sensitivity of the variance σ_Z^2 to the nuclear-viscosity mechanism in our calculations.

Previously, the mechanism of two-body viscosity was widely used in studying mass–energy distributions of fission fragments, and some conclusions were drawn on the value of the coefficient of friction. In [33, 54], the mean kinetic energy of fission fragments was calculated over a broad range of values of the fissility parameter $Z^2/A^{1/3}$; the values found there for this coefficient from fits of the results of those calculations to experimental data are $\nu = (6.7 \pm 2.2) \times 10^{21}$ fm^2 s^{-1} [33] and $\nu = (14.1 \pm 4.5) \times 10^{21}$ fm^2 s^{-1} [54]. On the basis of the Fokker–Planck equation, mass–energy distributions of fragments originating from the nuclear-fission process were studied in [18], and it was found there that the ν value at which the results of those dynamical calculations reproduce experimental data most closely is $\nu = (11.2 \pm 3.7) \times 10^{21}$ fm^2 s^{-1}. The above values of ν were found by rescaling the values of the coefficient of dynamic viscosity ν_0 that were obtained in [18, 33, 54]; this rescaling was performed under the assumption that the nuclear-radius constant is $r_0 = 1.2249$ fm [31], the corresponding nuclear density having the standard value of 1.344×10^{-45} MeV s^2 fm^{-5}. It can easily be seen that the coefficient of friction found for the charge mode from the calculation of the widths of giant dipole resonances has a value (13.5×10^{21} fm^2 s^{-1}) that is astonishingly close to the ν value extracted from the analysis of the parameters of mass–energy distributions. From Fig. 7, it also follows that values from the interval $(4 \leq \nu \leq 20) \times 10^{21}$ fm^2 s^{-1} lead to good agreement with the result in the statistical limit and, hence, with the experimental values of σ_Z^2.

4. CONCLUSIONS

A model has been proposed for describing the charge distribution of fragments originating from the symmetric fission of excited nuclei, and the charge distribution and its features have been calculated for the compound nucleus ^{236}U. The friction parameter of the charge mode has been calculated for two mechanisms of viscosity, that of one-body dissipation and that of two-body dissipation. The main results of this study can be summarized as follows:

(i) The proposed model, which is based on the use of a set of three-dimensional Langevin equations, provides a fairly good description of the charge distribution of fragments originating from the fission of highly excited nuclei. In particular, the calculated variances σ_Z^2 have characteristic values that are very close to those obtained experimentally.

(ii) Over a wide interval of excitation energies, the two viscosity mechanisms used—the one-body and the two-body one characterized by the coefficient of $\nu = 13.5 \times 10^{21}$ fm^2 s^{-1}—lead to close values of σ_Z^2. This is a consequence of a weak sensitivity of the width of the isobaric distribution to the magnitude of nuclear viscosity.

(iii) A comparison of the results of our dynamical calculations with experimental data makes it possible to conclude that statistical equilibration in the charge mode occurs not only at low but also at high excitation energies. The statistical limit is reached both for the one-body mechanism of nuclear viscosity and for the two-body mechanism characterized by values of the coefficient of two-body viscosity in the range $(4 \leq \nu \leq 20) \times 10^{21}$ fm^2 s^{-1}.

(iv) For $\nu > 30 \times 10^{21}$ fm^2 s^{-1}, the results obtained by studying the variance σ_Z^2 as a function of the parameter of two-body viscosity indicate that memory effects play an important role in the formation of the isobaric distribution and that the strength of this influence grows with increasing friction in the charge mode.

To summarize the above, we emphasize once again that only for the symmetric disintegration of a nucleus into fragments have we performed dynamical calculations of the charge distribution. It would be of interest to study the mass–charge distribution; for this, it is necessary either to introduce the fourth coordinate (that of mass asymmetry) in the model or to choose, as collective coordinates of the three-dimensional model, the mass-asymmetry coordinate, the charge-asymmetry coordinate, and the third coordinate that would describe the elongation of the nucleus being considered and eventually its disintegration into fragments.

REFERENCES

1. Y. Abe, S. Ayik, P.-G. Reinhard, and E. Suraud, Phys. Rep. **275**, 49 (1996).
2. J. Bao, Y. Zhuo, and X. Wu, Z. Phys. A **352**, 321 (1995).
3. D. V. Vanin, G. I. Kosenko, and G. D. Adeev, Phys. Rev. C **59**, 2114 (1999).
4. D. V. Vanin, P. N. Nadtochy, G. I. Kosenko, and G. D. Adeev, Yad. Fiz. **63**, 1957 (2000) [Phys. At. Nucl. **63**, 1865 (2000)].
5. P. N. Nadtochy, A. V. Karpov, D. V. Vanin, and G. D. Adeev, Yad. Fiz. **64**, 926 (2001) [Phys. At. Nucl. **64**, 861 (2001)].
6. A. V. Karpov, P. N. Nadtochy, D. V. Vanin, and G. D. Adeev, Phys. Rev. C **63**, 054610 (2001).

7. P. Fröbrich and I. I. Gontchar, Phys. Rep. **292**, 131 (1998).
8. I. I. Gontchar, L. A. Litnevsky, and P. Fröbrich, Comput. Phys. Commun. **107**, 223 (1997).
9. T. Wada, N. Carjan, and Y. Abe, Nucl. Phys. A **538**, 283c (1992).
10. G.-R. Tillack *et al.*, Phys. Lett. B **296**, 296 (1992).
11. M. Brack *et al.*, Rev. Mod. Phys. **44**, 320 (1972).
12. R. K. Gupta, W. Scheid, and W. Greiner, Phys. Rev. Lett. **35**, 353 (1975); R. K. Gupta, Fiz. Élem. Chastits At. Yadra **8**, 717 (1977) [Sov. J. Part. Nucl. **8**, 289 (1977)].
13. U. Brosa and H. J. Krappe, Nukleonika **24**, 389 (1979).
14. V. M. Strutinskiĭ, Zh. Éksp. Teor. Fiz. **45**, 1900 (1963) [Sov. Phys. JETP **18**, 1298 (1964)].
15. H. A. Kramers, Physica (Utrecht) **7**, 284 (1940).
16. V. V. Voevodin and G. Kim, *Computational Methods and Programming* (Mosk. Gos. Univ., Moscow, 1962).
17. L. D. Landau and E. M. Lifshitz, *Course of Theoretical Physics,* Vol. 5: *Statistical Physics* (Nauka, Moscow, 1976; Pergamon, Oxford, 1980), Part 1.
18. G. D. Adeev, I. I. Gonchar, V. V. Pashkevich, *et al.*, Fiz. Élem. Chastits At. Yadra **19**, 1229 (1988) [Sov. J. Part. Nucl. **19**, 529 (1988)].
19. P. N. Nadtochy, A. V. Karpov, and G. D. Adeev, Yad. Fiz. **65**, 832 (2002) [Phys. At. Nucl. **65**, 799 (2002)].
20. A. Bohr and B. R. Mottelson, *Nuclear Structure* (Benjamin, New York, 1975; Mir, Moscow, 1977), Vol. 2.
21. A. V. Ignatyuk, *Statistical Properties of Excited Nuclei* (Énergoatomizdat, Moscow, 1983).
22. A. V. Ignatyuk, M. G. Itkis, V. N. Okolovich, *et al.*, Yad. Fiz. **21**, 1185 (1975) [Sov. J. Nucl. Phys. **21**, 612 (1975)].
23. S. Cohen and W. J. Swiatecki, Ann. Phys. (N.Y.) **22**, 406 (1963).
24. N. D. Mavlitov, P. Fröbrich, and I. I. Gontchar, Z. Phys. A **342**, 195 (1992).
25. R. W. Hasse, Pramana **11**, 441 (1978); R. W. Hasse and W. D. Myers, *Geometrical Relationships of Macroscopic Nuclear Physics* (Springer-Verlag, Berlin, 1988).
26. M. G. Mustafa, H. W. Schmitt, and U. Mosel, Nucl. Phys. A **178**, 9 (1971).
27. G. D. Adeev, Fiz. Élem. Chastits At. Yadra **23**, 1572 (1992) [Sov. J. Part. Nucl. **23**, 684 (1992)].
28. E. K. Hyde, I. Perlman, and G. T. Seaborg, *The Nuclear Properties of the Heavy Elements,* Vol. 3: *Fission Phenomena* (Prentice-Hall, Englewood Cliffs, 1964; Atomizdat, Moscow, 1969); R. Vandenbosh and J. R. Huizenga, *Nuclear Fission* (Academic, New York, 1973).
29. D. C. Hofman and M. H. Hofman, Annu. Rev. Nucl. Sci. **24**, 151 (1974).
30. G. D. Adeev, L. A. Filipenko, and P. A. Cherdantsev, Yad. Fiz. **23**, 30 (1976) [Sov. J. Nucl. Phys. **23**, 15 (1976)].
31. W. D. Myers and W. J. Swiatecki, Ark. Fys. **36**, 343 (1967).
32. J. M. Eisenberg and W. Greiner, *Nuclear Theory,* Vol. 1: *Nuclear Models* (North-Holland, Amsterdam, 1970; Atomizdat, Moscow, 1975).
33. K. T. R. Davies, A. J. Sierk, and J. R. Nix, Phys. Rev. C **13**, 2385 (1976).
34. J. Blocki *et al.*, Ann. Phys. (N.Y.) **113**, 330 (1978).
35. J. Randrup and W. J. Swiatecki, Nucl. Phys. A **429**, 105 (1984).
36. H. Feldmeier, Rep. Prog. Phys. **50**, 915 (1987).
37. J. R. Nix and A. J. Sierk, in *Proceedings of the International School-Seminar on Heavy Ion Physics, Dubna, USSR, 1986,* Ed. by M. I. Zarubina and E. V. Ivashkevich (Joint Inst. for Nuclear Research, Dubna, 1987), p. 453.
38. *Proceedings of the 6th Adriatic Conference on Nuclear Physics: Frontiers of Heavy Ion Physics, Dubrovnik, Yugoslavia, 1987,* Ed. by N. Cindro, R. Caplar, and W. Greiner (World Sci., Singapore, 1990), p. 333.
39. G. D. Adeev, I. I. Gonchar, and L. A. Marchenko, Yad. Fiz. **42**, 42 (1985) [Sov. J. Nucl. Phys. **42**, 25 (1985)].
40. W. E. Undegraff and D. S. Onley, Nucl. Phys. A **161**, 191 (1971).
41. U. Brosa and H. J. Krappe, Z. Phys. A **287**, 65 (1978); U. Brosa and D. H. E. Gross, Z. Phys. A **294**, 217 (1980).
42. E. S. Hernandez, W. D. Myers, J. Randrup, and B. Remaud, Nucl. Phys. A **361**, 483 (1981).
43. B. Martschew and K. Pomorski, Acta Phys. Pol. B **13**, 747 (1982).
44. L. D. Landau and E. M. Lifshitz, *Course of Theoretical Physics,* Vol. 6: *Fluid Mechanics* (Nauka, Moscow, 1986; Pergamon, New York, 1987).
45. R. W. Hasse and P. Nerud, J. Phys. G **2**, L101 (1976).
46. W. D. Myers, W. J. Swiatecki, T. Kodama, *et al.*, Phys. Rev. C **15**, 2032 (1977).
47. B. Bush and Y. Alhassid, Nucl. Phys. A **531**, 27 (1991).
48. F. Gönnenwein, in *Nuclear Fission Process,* Ed. by C. Wagemans (CRC Press, Boca Raton, 1991), p. 287.
49. H. G. Clerc, W. Lang, H. Wohlfarth, *et al.*, in *Proceedings of the Fourth Symposium on the Physics and Chemistry of Fission, Jülich, 1979* (IAEA, Vienna), Vol. 2, p. 65; W. Lang, H. G. Clerc, H. Wohlfarth, *et al.*, Nucl. Phys. A **345**, 34 (1980).
50. G. D. Adeev, I. I. Gonchar, V. V. Pashkevich, and O. I. Serdyuk, Yad. Fiz. **50**, 1242 (1989) [Sov. J. Nucl. Phys. **50**, 774 (1989)].
51. S. Ayik, E. Suraud, J. Stryjewski, and M. Belkacem, Z. Phys. A **337**, 413 (1990).
52. M. Asghar, Z. Phys. A **296**, 79 (1980).
53. J. A. McHugh and M. C. Michel, Phys. Rev. **172**, 1160 (1968).
54. K. T. R. Davies, R. A. Managan, J. R. Nix, and A. J. Sierk, Phys. Rev. C **16**, 1890 (1977).

Translated by A. Isaakyan

Physics of Atomic Nuclei, Vol. 65, No. 9, 2002, pp. 1609–1615. From Yadernaya Fizika, Vol. 65, No. 9, 2002, pp. 1650–1656.
Original English Text Copyright © 2002 by Ladygin, Ladygina.

Angular Dependences of the Tensor Analyzing Powers in the $dd \to {}^3\mathrm{He}n$ Reaction at Intermediate Energies*

V. P. Ladygin and N. B. Ladygina

Joint Institute for Nuclear Research, Dubna, Moscow oblast, 141980 Russia

Received June 20, 2001

Abstract—The tensor analyzing powers A_{yy}, A_{xx}, and A_{xz} in the $dd \to {}^3\mathrm{He}n$ reaction at intermediate energies are considered in the framework of the one-nucleon-exchange approximation. Their strong sensitivity to the ${}^3\mathrm{He}$ and deuteron spin structure at short distances is shown. © *2002 MAIK "Nauka/Interperiodica".*

1. INTRODUCTION

The structure of light nuclei has been extensively investigated over the last few decades using both electromagnetic and hadron probes. The spin structure of these nuclei at short internucleonic distances (or at large internal momenta) is of special interest. One-nucleon-exchange (ONE) reactions like $dp \to pd$, $d^3\mathrm{He} \to p^4\mathrm{He}$, or $d^3\mathrm{He} \to {}^3\mathrm{He}d$ are the simplest processes with large momentum transfer and, therefore, can be used as a tool for investigating the structure of the deuteron and ${}^3\mathrm{He}$ at short distances. In the framework of the ONE approximation, the polarization observables of the above reactions are defined by the D/S-wave ratios of these nuclei.

A significant amount of data for the deuteron spin structure at short distances have been accumulated over the last years. Recently, the tensor analyzing power T_{20} and the polarization transfer coefficient κ_0 in backward elastic scattering, $dp \to pd$, has been measured at Saclay and Dubna [1, 2]. The tensor and vector analyzing powers A_{yy}, A_{xx}, A_{xz}, A_y^d [3, 4], and A_y^p [5] have been measured in dp elastic scattering over a wide range of angles at intermediate energies at the RIKEN and KVI. The polarization transfer coefficients K_{yy}^y, K_{xx}^y, and K_{xz}^y have been evaluated at 270 MeV at backward angles [4]. Another binary reaction, $d^3\mathrm{He} \to p^4\mathrm{He}$, has been investigated at the RIKEN using both polarized deuteron and ${}^3\mathrm{He}$ at energies up to 270 MeV [6, 7]. All the data are sensitive to the deuteron spin structure at short distances. For instance, T_{20} for both the $dp \to pd$ and the $d^3\mathrm{He} \to p^4\mathrm{He}$ reactions has a large negative value reflecting the negative sign of the D/S-wave ratio in the deuteron. The tensor analyzing power T_{20} in $d^3\mathrm{He}$ backward elastic scattering has been measured at 140, 200, and 270 MeV [8]. The sign of T_{20} is positive in accordance with the sign of D/S-wave ratio in ${}^3\mathrm{He}$ [9].

However, the polarization observables and the ONE predictions using standard deuteron and ${}^3\mathrm{He}$ wave functions strongly differ even at relatively small internal momenta of ~200 MeV/c. Such a discrepancy may be due to the nonadequate description of the light nucleus spin structure at short distances, as well as to the importance of mechanisms other than ONE reactions. In particular, the spin structure of the three-nucleon forces when all three nucleons are involved in the interaction may be overlooked [10]. Therefore, the new polarization data sensitive to the spin structure of deuteron and ${}^3\mathrm{He}$ are of great importance.

The $dd \to {}^3\mathrm{H}p({}^3\mathrm{He}n)$ process also falls into the class of ONE reactions. This reaction can be described by the sum of two diagrams according to the symmetry of the initial state. The analysis of the polarization phenomena in the $dd \to {}^3\mathrm{He}n$ reaction in the collinear geometry, where ${}^3\mathrm{He}$ and beam deuteron have the same direction of the momentum in the c.m., was performed in [11]. Under these kinematical conditions, one of the two diagrams is strongly suppressed (by several orders of magnitude) by the fast decrease in the deuteron and ${}^3\mathrm{He}$ wave functions with increasing relative momenta (at incident deuteron momenta higher than 200 MeV/c). The tensor analyzing power T_{20} due to the polarization of the beam deuteron is defined by the D/S-wave ratio of the ${}^3\mathrm{He}$ wave function. A more exhaustive analysis [12] performed for the collinear geometry shows, for instance, that the tensor analyzing power T_{20} is completely defined by the deuteron or ${}^3\mathrm{He}$ spin structure when ${}^3\mathrm{He}$ is emitted in the backward or forward direction

---

*This article was submitted by the authors in English.

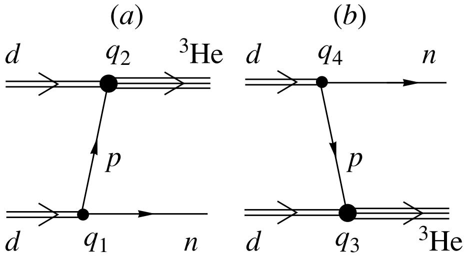

Fig. 1. The ONE diagrams for $dd \to {}^3\mathrm{He}n$: t-channel diagram (a) and u-channel diagram (b). Momenta q_{1-4} are defined in the text.

in the c.m., respectively. Therefore, the $dd \to {}^3\mathrm{He}n$ reaction can be used to study both the deuteron and the ^{3}He spin structure at short distances.

The goal of this paper is to predict the angular behavior of the tensor analyzing powers A_{yy}, A_{xx}, and A_{xz} in the $dd \to {}^3\mathrm{He}n({}^3\mathrm{H}p)$ reaction proposed for the measurements at RIKEN [13]. In the next section, the tensor analyzing powers are calculated in the framework of ONE. The results are discussed in Section 3. The conclusions are drawn in the last section.

2. ONE-NUCLEON-EXCHANGE APPROXIMATION

Within the framework of ONE, the $dd \to {}^3\mathrm{He}n$ process can be described by the sum of two diagrams (Fig. 1) according to the symmetry of the initial state of the reaction.

The deuteron wave function (DWF) in the momentum space can be represented in the following form [14]:

$$\Phi_d(\mathbf{p}) = \frac{i}{\sqrt{2}}\frac{1}{\sqrt{4\pi}}\psi_p^{\alpha+}\Bigg[\Bigg((u_1(p)(\boldsymbol{\sigma}\cdot\boldsymbol{\xi}) \quad (1)$$
$$-\frac{w_1(p)}{\sqrt{2}}(3(\hat{\mathbf{p}}\cdot\boldsymbol{\xi})(\boldsymbol{\sigma}\cdot\hat{\mathbf{p}}) - (\boldsymbol{\sigma}\cdot\boldsymbol{\xi}))\Bigg)\sigma_y\Bigg]_{\alpha\beta}\psi_n^{\beta+},$$

where ψ_p and ψ_n are the proton and neutron spinors, respectively; $\boldsymbol{\xi}$ is the deuteron polarization vector defined in the standard manner:

$$\boldsymbol{\xi}_1 = -\frac{1}{\sqrt{2}}(1, i, 0), \quad \boldsymbol{\xi}_{-1} = \frac{1}{\sqrt{2}}(1, -i, 0), \quad (2)$$
$$\boldsymbol{\xi}_0 = (0, 0, 1);$$

$\mathbf{p}$ is the relative proton–neutron momentum inside the deuteron; $\hat{\mathbf{p}} = \mathbf{p}/|\mathbf{p}|$ is the unit vector in the $\mathbf{p}$ direction; and $u_1(p)$ and $w_1(p)$ are the S and D components of the DWF.

To describe the $\langle dp|{}^3\mathrm{He}\rangle$ vertex, we use the expression suggested by Germond and Wilkin [15]:

$$\Phi_\tau(\mathbf{k}) = \frac{1}{\sqrt{2}}\frac{1}{\sqrt{4\pi}}\psi_\tau^{\alpha+}\Bigg[u_2(k)(\boldsymbol{\sigma}\cdot\boldsymbol{\xi}) \quad (3)$$
$$-\frac{w_2(k)}{\sqrt{2}}(3(\hat{\mathbf{k}}\cdot\boldsymbol{\xi})(\boldsymbol{\sigma}\cdot\hat{\mathbf{k}}) - (\boldsymbol{\sigma}\cdot\boldsymbol{\xi}))\Bigg]_{\alpha\beta}\psi_p^{\beta},$$

where $u_2(k)$ and $w_2(k)$ are the S and D components of the ^{3}He wave function, $\mathbf{k}$ is the relative proton–deuteron momentum inside ^{3}He, $\hat{\mathbf{k}} = \mathbf{k}/|\mathbf{k}|$ is the unit vector in the $\mathbf{k}$ direction, and ψ_τ is the ^{3}He spinor.

In view of expressions (1) and (3), the matrix element for the $dd \to {}^3\mathrm{He}n$ process can be written as

$$\mathcal{M} = \frac{1}{4\pi}\frac{i}{2}\psi_\tau^{\alpha+}F_{\alpha\beta}\psi_n^{\beta+} = \frac{1}{4\pi}\frac{i}{2}\psi_\tau^{\alpha+} \quad (4)$$
$$\times\Bigg[\Bigg(u_2(q_2)(\boldsymbol{\sigma}\cdot\boldsymbol{\xi}_2) - \frac{w_2(q_2)}{\sqrt{2}}(3(\hat{\mathbf{q}}_2\cdot\boldsymbol{\xi}_2)(\boldsymbol{\sigma}\cdot\hat{\mathbf{q}}_2) - (\boldsymbol{\sigma}\cdot\boldsymbol{\xi}_2))\Bigg)\Bigg)$$
$$\times\Bigg(u_1(q_1)(\boldsymbol{\sigma}\cdot\boldsymbol{\xi}_1) - \frac{w_1(q_1)}{\sqrt{2}}(3(\hat{\mathbf{q}}_1\cdot\boldsymbol{\xi}_1)(\boldsymbol{\sigma}\cdot\hat{\mathbf{q}}_1) - (\boldsymbol{\sigma}\cdot\boldsymbol{\xi}_1))\Bigg)\sigma_y$$
$$+\Bigg(u_2(q_3)(\boldsymbol{\sigma}\cdot\boldsymbol{\xi}_1) - \frac{w_2(q_3)}{\sqrt{2}}(3(\hat{\mathbf{q}}_3\cdot\boldsymbol{\xi}_1)(\boldsymbol{\sigma}\cdot\hat{\mathbf{q}}_3) - (\boldsymbol{\sigma}\cdot\boldsymbol{\xi}_1))\Bigg)$$
$$\times\Bigg(u_1(q_4)(\boldsymbol{\sigma}\cdot\boldsymbol{\xi}_2) - \frac{w_1(q_4)}{\sqrt{2}}(3(\hat{\mathbf{q}}_4\cdot\boldsymbol{\xi}_2)(\boldsymbol{\sigma}\cdot\hat{\mathbf{q}}_4) - (\boldsymbol{\sigma}\cdot\boldsymbol{\xi}_2))\Bigg)\sigma_y\Bigg]_{\alpha\beta}\psi_n^{\beta+}.$$

In accordance with the definition of the arguments of the deuteron and ^{3}He wave functions, we have for momenta $\mathbf{q}_i$

$$\mathbf{q}_1 = \frac{\mathbf{p}_1}{2} - \mathbf{k}_1, \qquad \mathbf{q}_2 = \mathbf{p}_2 - \frac{2}{3}\mathbf{k}_2, \qquad (5)$$
$$\mathbf{q}_3 = \mathbf{p}_1 - \frac{2}{3}\mathbf{k}_2, \qquad \mathbf{q}_4 = \frac{\mathbf{p}_2}{2} - \mathbf{k}_1.$$

Here, $\mathbf{p}_1$ and $\mathbf{p}_2$ correspond to the target and beam deuteron momenta, and $\mathbf{k}_1$ and $\mathbf{k}_2$ are the momenta of the final neutron and ^{3}He, respectively.

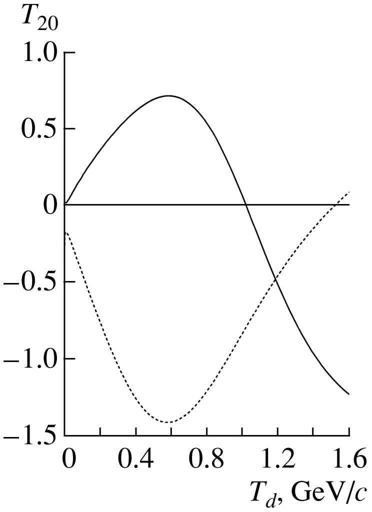

Fig. 2. Tensor analyzing power T_{20} in the $dd \to {}^3\mathrm{He}n$ reaction for the collinear geometry. The curves are the results of ONE calculations using the Urbana ^{3}He wave function [19] and Paris DWF [18] for the emission of ^{3}He at 0° (solid curve) and 180° (dashed curve) in the c.m.

We use a right-handed coordinate system defined in accordance with the Madison convention [16]. This system is specified by a set of three orthogonal vectors $\mathbf{z}$, $\mathbf{y}$, and $\mathbf{x}$, where $\mathbf{z} = \mathbf{p}_2/|\mathbf{p}_2|$, $\mathbf{y}$ is taken to be orthogonal to the scattering plane ($\mathbf{y} = [\mathbf{p}_2 \times \mathbf{k}_2]/|\mathbf{p}_2 \times \mathbf{k}_2|$), and $\mathbf{x} = \mathbf{y} \times \mathbf{z}$.

We define the tensor analyzing power A_{ij} due to polarization of the beam for $dd \to {}^3\mathrm{He}n({}^3\mathrm{H}p)$ in terms of spin operators Q_{ij} for deuterons as [17]

$$A_{ij} = \frac{\mathrm{tr}(\mathcal{M} Q_{ij} \mathcal{M}^+)}{\mathrm{tr}(\mathcal{M}\mathcal{M}^+)}. \tag{6}$$

Here, only three tensor analyzing powers, A_{yy}, A_{xx}, and A_{xz}, are independent [17]. The corresponding matrices Q_{ij} have the form

$$Q_{yy} = \frac{1}{2}\begin{pmatrix} -1 & 0 & -3 \\ 0 & 2 & 0 \\ -3 & 0 & -1 \end{pmatrix}, \quad Q_{xx} = \frac{1}{2}\begin{pmatrix} -1 & 0 & 3 \\ 0 & 2 & 0 \\ 3 & 0 & -1 \end{pmatrix}, \tag{7}$$

$$Q_{xz} = \frac{3}{\sqrt{8}}\begin{pmatrix} 0 & 1 & 0 \\ 1 & 0 & -1 \\ 0 & -1 & 0 \end{pmatrix}.$$

The expressions for A_{yy}, A_{xx}, and A_{xz} obtained with formulas (4) and (6) are given in the Appendix. The numerical results are discussed in the next section.

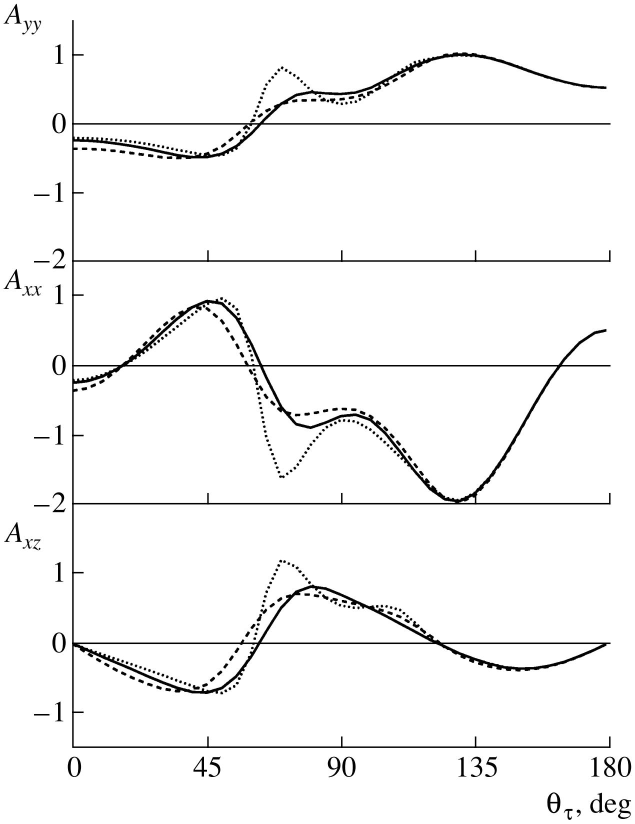

Fig. 3. Tensor analyzing power A_{yy}, A_{xx}, and A_{xz} in the $dd \to {}^3\mathrm{He}n$ reaction at 200 MeV. The curves are the results of ONE calculations using the Paris DWF [18] and ^{3}He wave functions from [19] (solid curve), [20] (dashed curve), and [21] (dotted curve).

3. NUMERICAL RESULTS AND DISCUSSION

In the collinear geometry with ^{3}He emitted at 0° or 180° in the c.m., the tensor analyzing powers A_{yy} and A_{xx} are equal. As mentioned above, the diagrams presented in Figs. 1*a* and 1*b* dominate for the forward and backward ^{3}He emission, respectively. Hence, the tensor analyzing powers $T_{20} = -\sqrt{2}\,A_{yy}$ due to the beam deuteron polarization at 0° and 180° are defined by the D/S-wave ratios in the ^{3}He and deuteron, respectively, and can be expressed as [12]

$$T_{20}(0^\circ) = \frac{1}{\sqrt{2}} \frac{2\sqrt{2}u_2(q_2)w_2(q_2) - w_2^2(q_2)}{u_2^2(q_2) + w_2^2(q_2)}, \tag{8}$$

$$T_{20}(180^\circ) = \frac{1}{\sqrt{2}} \frac{2\sqrt{2}u_1(q_4)w_1(q_4) - w_1^2(q_4)}{u_1^2(q_4) + w_1^2(q_4)}.$$

Here, the momenta q_2 and q_4 are defined according to Eq. (5) (see also Fig. 1).

The behavior of the tensor analyzing powers $T_{20}(0^\circ)$ and $T_{20}(180^\circ)$ in the $dd \to {}^3\mathrm{He}n$ reaction

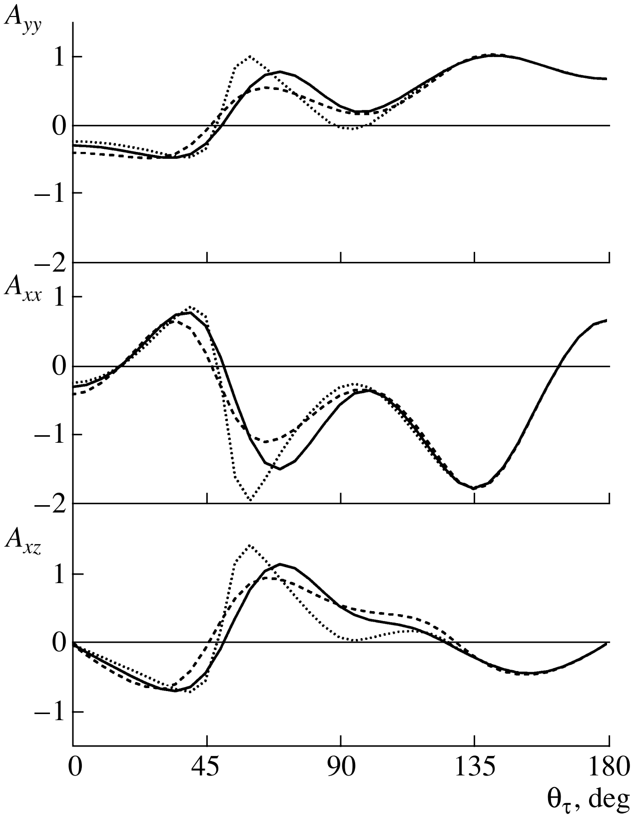

Fig. 4. The same as in Fig. 3 at 270 MeV.

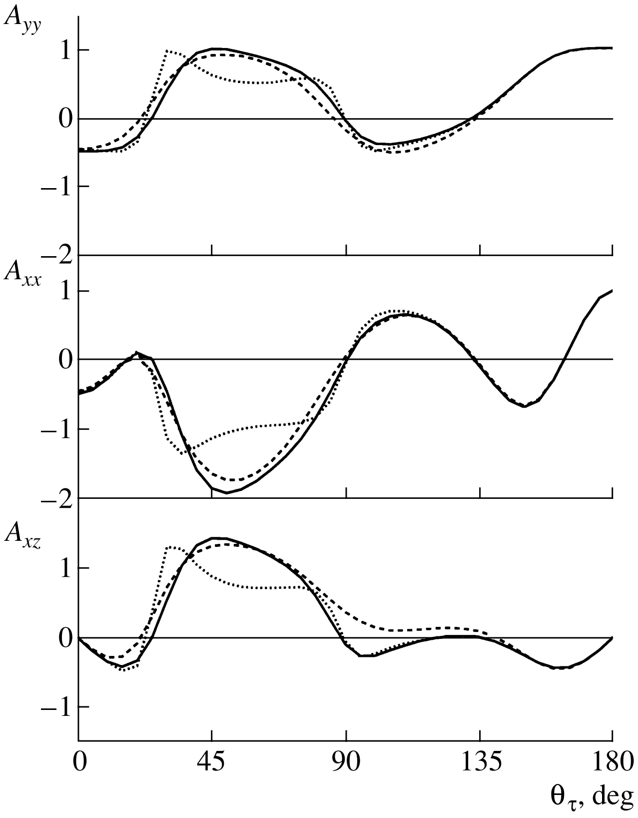

Fig. 5. The same as in Fig. 3 at 600 MeV.

versus initial deuteron energy is presented in Fig. 2 by the solid and dashed curves, respectively. The calculations were performed within the ONE approximation (see Fig. 1) using the Paris DWF [18] and Urbana ^{3}He wave function [19] (with Germond–Wilkin parametrization [15]). The relative sign of the S and D waves of ^{3}He is taken to be positive according to [9]. One can see the strong energy dependence of T_{20}. The positive and negative sign of T_{20} for the forward and backward kinematics at intermediate energies clearly demonstrates the sensitivity to the D/S-wave ratios in the ^{3}He and deuteron, respectively. The highest values of $|T_{20}|$ for both kinematics are expected at $\sim$600 MeV. T_{20} at 0° and 180° changes sign at $\sim$1000 and $\sim$1500 MeV, respectively.

The measurement of the tensor analyzing powers in the $dd \to {}^3\mathrm{He}n$ reaction at nonzero emission angles provides the probing of higher relative momenta in the ^{3}He and deuteron with respect to collinear geometry. For instance, the momentum range up to $\sim$600 MeV/c in the ^{3}He can be probed in the forward kinematics at 270 MeV at the RIKEN [13].

The dependences of the tensor analyzing powers A_{yy}, A_{xx}, and A_{xz} in the $dd \to {}^3\mathrm{He}n$ reaction at 200 and 270 MeV on the ^{3}He scattering angle in the c.m. are shown in Figs. 3 and 4, respectively. The solid, dashed, and dotted curves are the ONE predictions using ^{3}He wave functions from papers [19], [20], and [21] (with parameters taken from [22]), respectively. All calculations were performed with the use of the Paris DWF [18]. One can see the strong sensitivity to the ^{3}He spin structure when ^{3}He is emitted in the forward hemisphere in the c.m. and the strong variation of the tensor analyzing powers with angle. The dependence of A_{yy}, A_{xx}, and A_{xz} on the DWF at 90° or larger angles is insignificant.

The largest values of $|T_{20}|$ in the collinear geometry are expected at $\sim$ 600 MeV. The ONE predictions for the angular behavior of A_{yy}, A_{xx}, and A_{xz} at 600 MeV are given in Fig. 5. The notation for the curves are the same as in Figs. 3 and 4. A_{yy} and A_{xx} at 0° have a negative value of about -0.5 and are virtually independent of the ^{3}He wave function used. These observables reach a maximal value of $+1$ at backward kinematics. The tensor analyzing power A_{xz} is more sensitive to the ^{3}He wave function near 90° than A_{xx} and A_{yy}. Note that the angular range where the analyzing powers are most sensitive to the

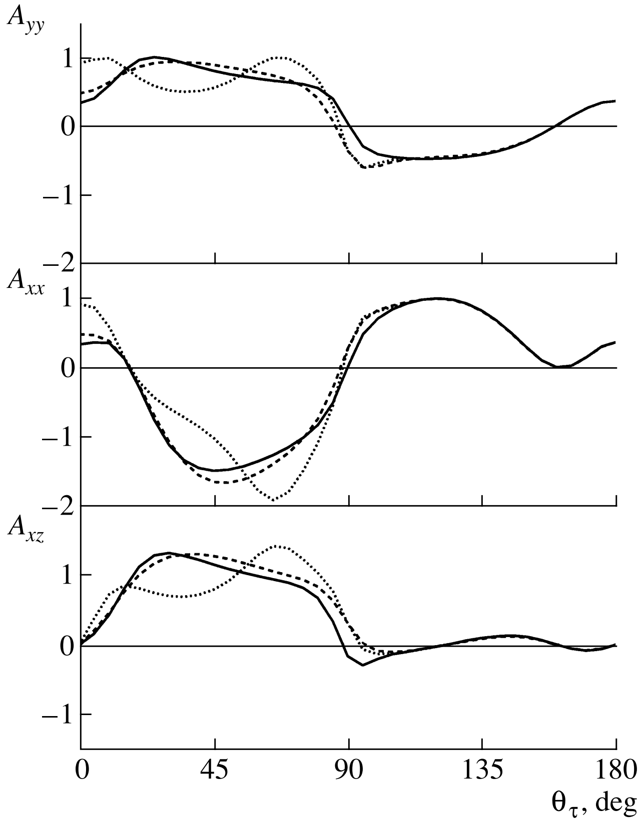

Fig. 6. The same as in Fig. 3 at 1200 MeV.

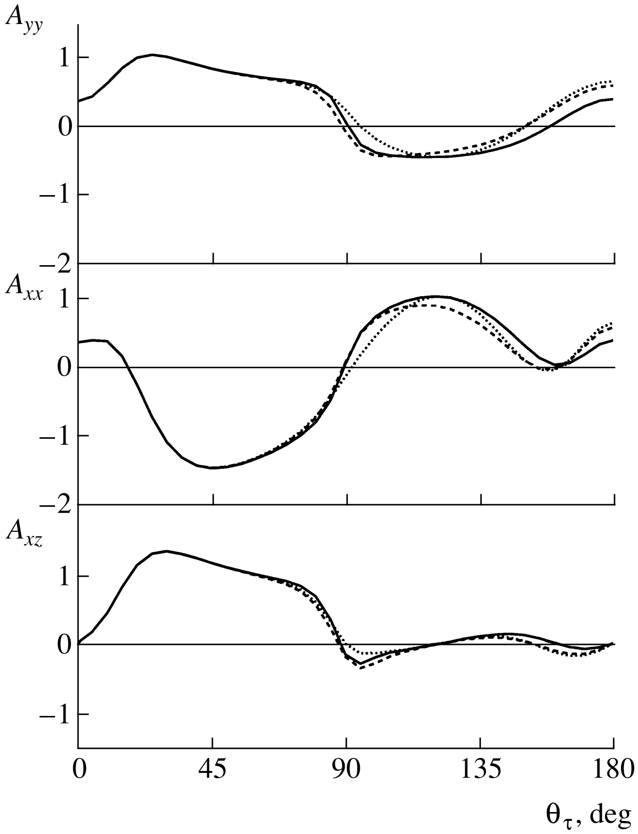

Fig. 7. Tensor analyzing power A_{yy}, A_{xx}, and A_{xz} in the $dd \to {}^3\mathrm{He}n$ reaction at 1200 MeV. The curves are the results of ONE calculations using the Urbana ^{3}He wave function [19] and Paris [18] (solid curve), Bonn B (dashed curve), and Bonn C (dotted curve) [23] DWFs.

^{3}He spin structure changes with energy. The sensitivity is observed in the angular ranges of 45°–90°, 35°–90°, and 15°–90° at 200, 270, and 600 MeV, respectively. The energy variation of the angular range sensitive to the ^{3}He spin structure is easy to understand. Larger angles in the c.m. correspond to higher internal momenta in ^{3}He. Since the behavior of the ^{3}He wave functions differs at internal momenta higher than 250 MeV/c, these momenta will be probed at decreasing angles as the initial energy increases.

The behavior of the tensor analyzing powers A_{yy}, A_{xx}, and A_{xz} at 1200 MeV is shown in Fig. 6. The notation is the same as in Figs. 3–5. One can see the strong sensitivity of all the analyzing powers to the ^{3}He spin structure in the forward hemisphere. Note that the sign of A_{yy}, A_{xx}, and A_{xz} at small angles is positive, while, at 200, 270, and 600 MeV, it is negative. This reflects the change in the D/S-wave ratio sign in the ^{3}He wave function. A_{xz} is very small in the backward hemisphere.

In principle, the analyzing powers in the GeV range may depend significantly on the deuteron spin structure, especially, in the backward hemisphere. Figure 7 demonstrates the results of the calculations for A_{yy}, A_{xx}, and A_{xz} at 1200 MeV performed in terms of ONE using the Urbana ^{3}He wave function [19] and different DWFs. The solid, dashed, and dotted curves were obtained with the use of the Paris [18], Bonn B, and Bonn C [23] DWFs, respectively. One can see the minor dependence of the analyzing powers on the DWF in the backward hemisphere.

The spherical tensor analyzing powers T_{20}, T_{21}, and T_{22} are related to the Cartesian ones as

$$T_{20} = -\frac{1}{\sqrt{2}}(A_{xx} + A_{yy}), \tag{9}$$
$$T_{21} = -\frac{1}{\sqrt{3}}A_{xz},$$
$$T_{22} = \frac{1}{2\sqrt{3}}(A_{xx} - A_{yy}).$$

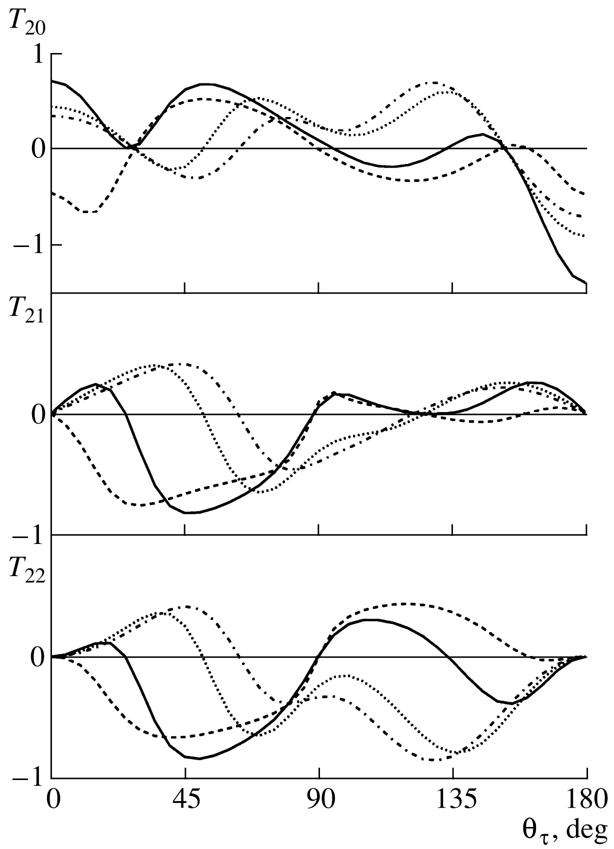

Fig. 8. Tensor analyzing power T_{20}, T_{21}, and T_{22} in the $dd \to {}^3\mathrm{He}n$ reaction. The dot-and-dash, dotted, solid, and dashed curves and the results of ONE calculations at the initial energies 200, 270, 600, and 1200 MeV, respectively, using the Urbana ^{3}He wave function [19] and Paris DWF [18].

The behavior of T_{20}, T_{21}, and T_{22} in the $dd \to {}^3\mathrm{He}n$ reaction at different initial energies is shown in Fig. 8. The curves were obtained in terms of ONE using the Urbana ^{3}He [19] and Paris deuteron [18] wave functions. The dot-and-dash, dotted, solid, and dashed curves represent the results of calculations at initial energies of 200, 270, 600, and 1200 MeV, respectively. One can see the strong energy dependence of the angular distributions of these observables. T_{20} at 0° is positive at three low energies and changes sign at 1200 MeV. T_{20} is negative at 180° at all the four energies. $|T_{20}|$ achieves maximal values in the collinear geometry at 600 MeV. There are two points where T_{20} crosses zero regardless of the energy, namely, at ∼25° and ∼150° in the c.m. The tensor analyzing powers T_{21} and T_{22} vary significantly with angle. They are positive at small angles at three low energies and change sign at 1200 MeV. All the analyzing powers cross zero at ∼90° at 600 and 1200 MeV.

The strong energy dependence of the tensor analyzing powers in the $dd \to {}^3\mathrm{He}n$ reaction within the ONE approximation reflects their sensitivity to the internal structure of the ^{3}He and deuteron, because different energies correspond to different internal momentum ranges.

4. CONCLUSIONS

The tensor analyzing powers A_{yy}, A_{xx}, and A_{xz} in the $dd \to {}^3\mathrm{He}n$ reaction within the ONE approximation are considered. Their high sensitivity to the spin structure of the ^{3}He and deuteron, especially, at intermediate energies, is found.

The measurements of these observables are being planned at the RIKEN at energies up to 270 MeV [13]. The measurements of T_{20} at 0° in the GeV range are proposed for the LHE–JINR Accelerator Complex [24]. The measurements of the angular dependence of A_{yy} at intermediate energies will be possible at the COSY with the ANKE facility providing a polarized deuteron beam.

ACKNOWLEDGMENTS

We are grateful to the participants of the R308n experiment at the RARF. Special thanks are due to Prof. A.I. Malakhov, Prof. H. Sakai, and Dr. T. Uesaka for their permanent help and stimulating discussions.

APPENDIX

The analyzing powers A_{yy}, A_{xx}, and A_{xz} in the $dd \to {}^3\mathrm{He}n$ reaction can be written as

$$A_{ij} = A_{ij}^{(a)} + A_{ij}^{(b)} + 2A_{ij}^{(\mathrm{inter})}, \qquad (\mathrm{A.1})$$

where $A_{ij}^{(a)}$, $A_{ij}^{(b)}$, and $A_{ij}^{(\mathrm{inter})}$ are defined below. These terms in the first approximation are the contributions of the diagrams shown in Figs. 1*a* and 1*b* and of their interference, respectively.

$A_{ij}^{(a)}$ can be expressed as

$$A_{yy}^{(a)} = 2\mathcal{N}^{-1}(3a_1^2(q_1) + 2a_1(q_1)b_1(q_1) + b_1^2(q_1))(2a_2(q_2)b_2(q_2) + b_2^2(q_2)), \qquad (\mathrm{A.2})$$

$$A_{xx}^{(a)} = 2\mathcal{N}^{-1}(3a_1^2(q_1) + 2a_1(q_1)b_1(q_1) + b_1^2(q_1))(2a_2(q_2)b_2(q_2) + b_2^2(q_2))(1 - 3(\hat{\mathbf{q}}_2 \cdot \hat{\mathbf{x}})^2), \qquad (\mathrm{A.3})$$

$$A_{xz}^{(a)} = -6\mathcal{N}^{-1}(3a_1^2(q_1) + 2a_1(q_1)b_1(q_1) + b_1^2(q_1))(2a_2(q_2)b_2(q_2) + b_2^2(q_2))(\hat{\mathbf{q}}_2 \cdot \hat{\mathbf{x}})(\hat{\mathbf{q}}_2 \cdot \hat{\mathbf{z}}). \qquad (\mathrm{A.4})$$

The normalization factor $\mathcal{N}$ corresponds to the matrix element square summed over all particle spin projections and is written as

$$\mathcal{N} = \mathrm{tr}(\mathcal{M}\mathcal{M}^+)$$

$$
\begin{aligned}
&= 2[3a_1^2(q_1) + 2a_1(q_1)b_1(q_1) + b_1^2(q_1)] \\
&\times [3a_2^2(q_2) + 2a_2(q_2)b_2(q_2) + b_2^2(q_2)] \\
&+ 2[3a_1^2(q_4) + 2a_1(q_4)b_1(q_4) + b_1^2(q_4)] \\
&\times [3a_2^2(q_3) + 2a_2(q_3)b_2(q_3) + b_2^2(q_3)] \\
&+ 4a_1(q_4)a_2(q_2)[3a_1(q_1)a_2(q_3) + a_2(q_3)b_1(q_1) \\
&+ a_1(q_1)b_2(q_3) + b_2(q_3)b_1(q_1)(\hat{\mathbf{q}}_1 \cdot \hat{\mathbf{q}}_3)^2] \qquad (A.5) \\
&+ 4a_2(q_2)b_1(q_4)[a_1(q_1)a_2(q_3) \\
&+ a_2(q_3)b_1(q_1)(\hat{\mathbf{q}}_1 \cdot \hat{\mathbf{q}}_4)^2 + a_1(q_1)b_2(q_3)(\hat{\mathbf{q}}_3 \cdot \hat{\mathbf{q}}_4)^2 \\
&+ b_1(q_1)b_2(q_3)(\hat{\mathbf{q}}_1 \cdot \hat{\mathbf{q}}_3)(\hat{\mathbf{q}}_1 \cdot \hat{\mathbf{q}}_4)(\hat{\mathbf{q}}_3 \cdot \hat{\mathbf{q}}_4)] \\
&+ 4a_1(q_4)b_2(q_2)[a_1(q_1)a_2(q_3) \\
&+ a_2(q_3)b_1(q_1)(\hat{\mathbf{q}}_1 \cdot \hat{\mathbf{q}}_2)^2 + a_1(q_1)b_2(q_3)(\hat{\mathbf{q}}_2 \cdot \hat{\mathbf{q}}_3)^2 \\
&+ b_1(q_1)b_2(q_3)(\hat{\mathbf{q}}_1 \cdot \hat{\mathbf{q}}_2)(\hat{\mathbf{q}}_1 \cdot \hat{\mathbf{q}}_3)(\hat{\mathbf{q}}_2 \cdot \hat{\mathbf{q}}_3)] \\
&+ 4b_1(q_4)b_2(q_2)[a_1(q_1)a_2(q_3)(\hat{\mathbf{q}}_2 \cdot \hat{\mathbf{q}}_4)^2 \\
&+ a_2(q_3)b_1(q_1)(\hat{\mathbf{q}}_1 \cdot \hat{\mathbf{q}}_2)(\hat{\mathbf{q}}_1 \cdot \hat{\mathbf{q}}_4)(\hat{\mathbf{q}}_2 \cdot \hat{\mathbf{q}}_4) \\
&+ a_1(q_1)b_2(q_3)(\hat{\mathbf{q}}_2 \cdot \hat{\mathbf{q}}_3)(\hat{\mathbf{q}}_2 \cdot \hat{\mathbf{q}}_4)(\hat{\mathbf{q}}_3 \cdot \hat{\mathbf{q}}_4) \\
&+ b_1(q_1)b_2(q_3)(\hat{\mathbf{q}}_1 \cdot \hat{\mathbf{q}}_3)(\hat{\mathbf{q}}_1 \cdot \hat{\mathbf{q}}_4)(\hat{\mathbf{q}}_2 \cdot \hat{\mathbf{q}}_3)(\hat{\mathbf{q}}_2 \cdot \hat{\mathbf{q}}_4)] \\
&- 4b_1(q_1)b_2(q_2)b_1(q_4)b_2(q_3)(\hat{\mathbf{q}}_1 \cdot \hat{\mathbf{q}}_3)(\hat{\mathbf{q}}_2 \cdot \hat{\mathbf{q}}_4) \\
&\times [(\hat{\mathbf{q}}_1 \cdot \hat{\mathbf{q}}_4)(\hat{\mathbf{q}}_2 \cdot \hat{\mathbf{q}}_3) - (\hat{\mathbf{q}}_1 \cdot \hat{\mathbf{q}}_2)(\hat{\mathbf{q}}_3 \cdot \hat{\mathbf{q}}_4)].
\end{aligned}
$$

Here, $\hat{\mathbf{q}}_{1-4}$ are the unit vectors in the directions of the momenta $\mathbf{q}_{1-4}$ defined in Eq. (5); $\hat{\mathbf{x}}$, $\hat{\mathbf{y}}$, and $\hat{\mathbf{z}}$ are the unit vectors of the coordinate system; and a_1, b_1, a_2, and b_2 can be expressed through combinations of the S and D components of the deuteron and ^{3}He wave functions:

$$
\begin{aligned}
a_{1,2}(q) &= u_{1,2}(q) + w_{1,2}(q)/\sqrt{2}, \qquad (A.6) \\
b_{1,2}(q) &= -3w_{1,2}(q)/\sqrt{2}.
\end{aligned}
$$

The terms $A_{ij}^{(b)}$ have the following forms:

$$
\begin{aligned}
A_{yy}^{(b)} &= 2\mathcal{N}^{-1}(3a_2^2(q_3) + 2a_2(q_3)b_2(q_3) \qquad (A.7) \\
&+ b_2^2(q_3))(2a_1(q_4)b_1(q_4) + b_1^2(q_4)), \\
A_{xx}^{(b)} &= 2\mathcal{N}^{-1}(3a_2^2(q_3) + 2a_2(q_3)b_2(q_3) \qquad (A.8) \\
&+ b_2^2(q_3))(2a_1(q_4)b_1(q_4) + b_1^2(q_4))(1 - 3(\hat{\mathbf{q}}_4 \cdot \hat{\mathbf{x}})^2), \\
A_{xz}^{(b)} &= -6\mathcal{N}^{-1}(3a_2^2(q_3) + 2a_2(q_3)b_2(q_3) \qquad (A.9) \\
&+ b_2^2(q_3))(2a_1(q_4)b_1(q_4) + b_1^2(q_4))(\hat{\mathbf{q}}_4 \cdot \hat{\mathbf{x}})(\hat{\mathbf{q}}_4 \cdot \hat{\mathbf{z}}).
\end{aligned}
$$

The interference term $A_{ij}^{(\mathrm{inter})}$ can be written in the general form for all the three tensor analyzing powers as

$$
\begin{aligned}
A_{ij}^{(\mathrm{inter})} &= 2\mathcal{N}^{-1}[\delta_{mn}\delta_{kl} + \delta_{ml}\delta_{kn} - \delta_{mk}\delta_{nl}] \qquad (A.10) \\
&\times \left[\delta_{m'k'}\delta_{ij} - \frac{3}{2}\delta_{m'i}\delta_{k'j} - \frac{3}{2}\delta_{m'j}\delta_{k'i}\right] \\
&\times [a_2(q_2)a_1(q_4)\delta_{mm'}\delta_{kk'} + a_2(q_2)b_1(q_4)\delta_{mm'}\hat{q}_4^k\hat{q}_4^{k'} \\
&+ a_1(q_4)b_2(q_2)\delta_{kk'}\hat{q}_2^m\hat{q}_2^{m'} + b_1(q_4)b_2(q_2)\hat{q}_2^m\hat{q}_4^k\hat{q}_2^{m'}\hat{q}_4^{k'}] \\
&\times [a_1(q_1)a_2(q_3)\delta_{kl} + a_2(q_3)b_1(q_1)\hat{q}_1^n\hat{q}_1^l \\
&+ a_1(q_1)b_2(q_3)\hat{q}_3^l\hat{q}_3^n + b_1(q_1)b_2(q_3)(\hat{\mathbf{q}}_1 \cdot \hat{\mathbf{q}}_3)\hat{q}_1^n\hat{q}_3^l].
\end{aligned}
$$

Here, all summations over dummy discrete indices are implied.

REFERENCES

1. V. Punjabi, R. Abegg, S. Belostotsky, *et al.*, Phys. Lett. B **350**, 178 (1995).
2. L. S. Azhgirey, E. V. Chernykh, A. P. Kobushkin, *et al.*, Phys. Lett. B **391**, 22 (1997); Yad. Fiz. **61**, 494 (1998) [Phys. At. Nucl. **61**, 432 (1998)].
3. N. Sakamoto, H. Okamura, T. Uesaka, *et al.*, Phys. Lett. B **367**, 60 (1996).
4. H. Sakai, K. Sekiguchi, H. Witala, *et al.*, Phys. Rev. Lett. **84**, 5288 (2000).
5. R. Bieber, W. Glöckle, J. Golak, *et al.*, Phys. Rev. Lett. **84**, 606 (2000).
6. T. Uesaka, H. Sakai, H. Okamura, *et al.*, Phys. Lett. B **467**, 199 (1999).
7. T. Uesaka, H. Sakai, H. Okamura, *et al.*, Few-Body Syst. Suppl. **12**, 497 (2000).
8. M. Tanifuji, S. Ishikawa, Y. Iseri, *et al.*, Phys. Rev. C **61**, 024 602 (2000).
9. A. M. Eiro and F. D. Santos, J. Phys. G **16**, 1139 (1990).
10. W. Glöckle, H. Witala, D. Hüber, *et al.*, Phys. Rep. **274**, 107 (1996).
11. V. P. Ladygin and N. B. Ladygina, Yad. Fiz. **59**, 828 (1996) [Phys. At. Nucl. **59**, 789 (1996)].
12. V. P. Ladygin and N. B. Ladygina, Nuovo Cimento A **112**, 855 (1999).
13. V. P. Ladygin, N. B. Ladygina, H. Sakai, and T. Uesaka, Part. Nucl. Lett. **59** (100), 74 (2000).
14. W. W. Buck and F. Gross, Phys. Rev. D **20**, 2361 (1979).
15. J.-F. Germond and C. Wilkin, J. Phys. G **14**, 181 (1988).
16. *Proceedings of the Third International Symposium on Polarization Phenomena in Nuclear Reactions, Madison, 1970,* Ed. by H. H. Barshall and W. Haeberli, p. XXV.
17. H. O. Ohlsen, Rep. Prog. Phys. **35**, 717 (1972).
18. M. Lacombe, B. Loiseau, R. Vinh Mau, *et al.*, Phys. Lett. B **101B**, 139 (1981).
19. R. Schiavilla, V. R. Pandharipande, and R. B. Wiringa, Nucl. Phys. A **449**, 219 (1986).
20. J.-M. Laget, J. F. Lecolley, and F. Lefebvres, Nucl. Phys. A **370**, 479 (1981).
21. F. D. Santos, A. M. Eiro, and A. Barosso, Phys. Rev. C **19**, 238 (1979).
22. Yu. N. Uzikov, Fiz. Élem. Chastits At. Yadra **29**, 1010 (1998) [Phys. Part. Nucl. **29**, 417 (1998)].
23. R. Machleidt, K. Holinde, and C. Elster, Phys. Rep. **149**, 1 (1987).
24. V. P. Ladygin and N. B. Ladygina, JINR Rapid Commun., No. 4[72]-95, 19 (1995).

Physics of Atomic Nuclei, Vol. 65, No. 9, 2002, pp. 1616–1627. Translated from Yadernaya Fizika, Vol. 65, No. 9, 2002, pp. 1657–1668.

Investigation of Quasimolecular States in ^{24}Mg* through the Analysis of the Angular $d\alpha$ Correlations in the ^{12}C(^{14}N, d)^{24}Mg(α)^{20}Ne Reaction

T. L. Belyaeva[1], **N. S. Zelenskaya, and M. Aguero Granados**[1]

Research Institute of Nuclear Physics, Moscow State University, Moscow, Russia

Received June 22, 2001; in final form, December 19, 2001

Abstract—Theoretical analysis of the differential cross sections and angular correlation functions in the ^{12}C(^{14}N, d)^{24}Mg*(α)^{20}Ne reaction at the energy of the incident nitrogen ions $E_{\rm lab} = 29$–42 MeV is performed in the models of the direct transfer of ^{12}C cluster and the compound nucleus. Amplitudes of the reduced widths for the excited quasimolecular states like $^{12}\mathrm{C} \otimes ^{12}\mathrm{C}^*$ in the ^{24}Mg nucleus are obtained. The effect of various states of the relative motion of nuclei in the $^{12}\mathrm{C} + ^{12}\mathrm{C}^*$ configuration on the angular $d\alpha$-correlation functions is studied. © *2002 MAIK "Nauka/Interperiodica"*.

1. INTRODUCTION

At present, there exists a large volume of the experimental and theoretical information on the differential cross sections and angular correlation functions (ACF) in the reactions induced by semiheavy ions with the production of excited final nuclei. An analysis of these data shows that investigation of the particle–particle angular correlations in reactions of the direct transfer of α particles can be used to determine both the spin characteristics of strongly excited α cluster states and the parameters of the internuclear interaction potential in the excited states.

Investigation of the angular correlations in the reactions involving multinucleon transfer opens new possibilities for the study of the quasimolecular states of the nuclei with high spin values and for a more detailed investigation of the reaction mechanisms and the spectroscopy of excited states containing 2α and 3α clusters.

Experimental investigations of the angular $d\alpha$-correlation functions in the ^{12}C(^{14}N, d) × ^{24}Mg*(α)^{20}Ne reaction at $E_{^{14}\mathrm{N}}(\mathrm{lab}) = 29$–$42$ MeV [1, 2] convincingly demonstrated the possibility of the direct transfer of a 12-nucleon cluster upon the excitation of one (13.45 MeV, 6^+) of the states of the ^{24}Mg nucleus. The oscillating (proportional to the squared Legendre polynomial of the sixth order) ACF structure discovered in [1, 2] for the small deuteron emission angle was related to the presence of quasimolecular configurations of the type $^{12}\mathrm{C} \otimes ^{12}\mathrm{C}^*$ in this state of the ^{24}Mg nucleus. The previous measurements of the differential cross sections for the ^{12}C(^{14}N, d)^{24}Mg* reaction [3] and a theoretical analysis using the Hauser–Feshbach formalism of the compound nucleus (CN) model [4] showed that such calculations describe on the average the behavior of the experimental cross sections. An analysis of the deuteron angular distributions together with the angular $d\alpha$-correlation functions in the CN model [5] confirmed the conclusion that the CN contribution is important; at the same time, this analysis demonstrated a smooth, rather than polynomial, behavior of the angular $d\alpha$-correlation functions for the 13.45 MeV, 6^+ state in ^{24}Mg for all forward deuteron emission angles.

Calculations performed by the method of distorted waves with exact allowing for the finite interaction region (EFRDWBA and MIVOKOR) [6, 7] for the direct carbon transfer mechanism showed that the angular distributions calculated in this model exhibit a rich angular structure and in some cases provide for a better description of the experimental data than does the CN model. Recent EFRDWBA calculations [8] allowing for the direct transfer of ^{12}C (cluster breakdown mechanism) and ^{10}B (heavy breakdown mechanism) confirmed that the main features of the angular distributions of deuterons for the ground state and the first excited state (1.37 MeV, 2^+) in ^{24}Mg are well reproduced in the one-step mechanisms of the cluster transfer with an allowance for excitation of the intermediate nucleus. Nevertheless, the spectroscopic amplitudes calculated in [8] in the translation-invariant shell model for the ground and the first excited states in ^{24}Mg should be increased by a factor greater than 10^2 in order to obtain quantitative agree-

---

[1] Mexican Independent University, Estado, Mexico.

ment between theoretical and experimental cross sections.

This paper is aimed at the further theoretical investigation of the problem of quasimolecular states in the ^{24}Mg nucleus and their effect on the reaction characteristics. We analyzed the differential cross section and the angular $d\alpha$-correlation functions for the $^{12}\mathrm{C}(^{14}\mathrm{N}, d)^{24}\mathrm{Mg}^*(\alpha)^{20}\mathrm{Ne}$ reaction in the model of the direct transfer of the massive cluster ^{12}C and in the model of the compound nucleus in order to obtain a most complete description of the experimental data and to understand the role of various reaction mechanisms. The analysis made it possible to explain why the oscillating structure of the experimental ACF is observed for only one individual level of the ^{24}Mg nucleus and was never observed [1] for other strongly excited states of this nucleus with a similar structure. We studied the role of various quasimolecular states in ^{24}Mg in the process of the direct transfer of a 12-nucleon cluster and estimated the spectroscopic amplitudes through the comparison of the calculation results with the experiment.

2. METHOD OF CALCULATION OF THE PARTICLE–PARTICLE ANGULAR CORRELATION FUNCTIONS

2.1. General Formalism

Let us consider a binary nuclear reaction $a(I_a) + A(I_A) \to B^*(I_f) + b(I_b)$ with the production of an excited nucleus B^* and a particle b in the final state. The second stage of this reaction is the decay $B^*(I_f) \to C^*(I_0) + c(I_2)$ of the nucleus B^* with the spin I_f into the nucleus C^* with the spin I_0 and the secondary particle c emitted with the spin I_2.

According to the general formalism [9–11], the ACF $W(I_f; \Omega_b, \Omega_c)$ is determined as the probability of the simultaneous registration of the particle b in the direction Ω_b and the particle c in the direction Ω_c and can be represented in the form

$$W(I_f; \Omega_b, \Omega_c) = \sum_{kq} \rho_{kq}(I_f; \Omega_b) \varepsilon^*_{kq}(I_f, I_0, I_2; \Omega_c), \tag{1}$$

where $0 < k < 2I_f$ and $q = -k, \ldots, k$. In (1), the spin tensors $\rho_{kq}(I_f; \Omega_b)$ of the density matrix $\rho_{I_f}(M_f, M'_f; \Omega_b)$ of the nucleus $B^*(I_f)$ and the spin tensors $\varepsilon_{kq}(I_f, I_0, I_2; \Omega_c)$ of the matrix $\varepsilon_{I_f}(\Omega_c)$ of the efficiency of registration of the final system $C^*(I_0) + c(I_2)$ are defined in the standard way [9, 10].

For the nonpolarized particles and nuclei in the initial state, the spin density matrix of the nucleus B^* in the state with the spin I_f and its projection M_f can be written [11] in terms of the operator T_{if} of the system transition from the initial state $|i\rangle$ to the final state $|f\rangle$:

$$\rho_{I_f}(M_f, M'_f, \Omega_b) = \frac{1}{(2I_a + 1)(2I_A + 1)} \tag{2}$$
$$\times \sum_{M_a M_A M_b M'_b} T_{if, M_a M_A M_b M_f}(\Omega_b) T^*_{if, M_a M_A M'_b M'_f}(\Omega_b).$$

The density matrix (2) is normalized to the differential cross section by the condition

$$\mathrm{tr}\rho_{I_f}(M_f, M'_f; \Omega_b) = \frac{d\sigma}{d\Omega} = \rho_{00}. \tag{3}$$

We consider a special case when the spin state of the residual system $C^*(I_0) + c(I_2)$ is fixed as the ground state, that is $I_0 = I_2 = 0$. In this case, the efficiency tensor $\varepsilon_{kq}(I_f; \Omega_c)$ assumes the simplest form,

$$\varepsilon_{kq}(I_f; \Omega_c) \tag{4}$$
$$= (-1)^{I_f}(2I_f + 1)(4\pi(2k + 1))^{-1/2}$$
$$\times \langle I_f 0 I_f 0 | k0 \rangle Y^*_{kq}(\Omega_c),$$

and the expression for the ACF acquires the following form [11, 12]:

$$W(I_f; \Omega_b, \Omega_c) = \frac{(2I_f + 1)^{1/2}}{(2I_a + 1)(2I_A + 1)} \tag{5}$$
$$\times \sum_{M_f M'_f} (-1)^{I_f} Y^*_{I_f M_f}(\Omega_c) Y_{I_f M'_f}(\Omega_c)$$
$$\times \sum_{M_a M_A M_b} \left| T_{if, M_a M_A M_b M_f}(\Omega_b) \right|^2.$$

Therefore, expression (5) makes it possible to calculate the ACF in any theoretical model, provided that the form of the matrix element T_{if} of the transition operator is known. We shall consider two complementary models: the model of direct nuclear reactions in the MIVOKOR formalism [13] and the model of compound nucleus in the modified Hauser–Feshbach formalism [14, 15].

2.2. Angular Correlation Functions in the MIVOKOR Formalism

In the general case, the ACF calculation in MIVOKOR (EFRDWBA) is based on the transformation of expression (2) for the density matrix of the nucleus $B^*(I_f)$ and its spin tensors $\rho_{kq}(I_f; \Omega_b)$ using an expression for the matrix element T_{if} of the operator of transition between the initial and the final states in the reaction $A(a, b)B$ written in MIVOKOR [13, 16]. We shall apply a standard scheme of the summation of the total momenta:

$$\mathbf{I}_f = \mathbf{I}_1 + \mathbf{I}_A, \mathbf{I}_a = \mathbf{I}_2 + \mathbf{I}_b, \tag{6}$$

$$\mathbf{l} = \mathbf{\Lambda}_1 + \mathbf{\Lambda}_2,$$

where $\mathbf{l}$ is the angular-momentum transfer; $\mathbf{\Lambda}_1$ and $\mathbf{\Lambda}_2$ are the orbital angular momenta of the relative motion of the nuclei in the vertices $B \to X + A$ and $a \to X + b$; and $\mathbf{I}_1$ and $\mathbf{I}_2$ are the total angular-momentum in the input and output channels, respectively.

In the simplest case, when the residual nucleus C and the emitted particle c are spinless, we can use expression (4). The ACF assumes the form

$$W(I_f; \Omega_b, \Omega_c) = \frac{(2I_f + 1)^{1/2}}{(2I_A + 1)} \tag{7}$$
$$\times \sum_{I_2 M_2 M_A} \left| \sum_{M_f} T^{I_f M_f}_{I_2 M_2 M_A}(\Omega_b) Y^*_{I_f M_f}(\Omega_c) \right|^2,$$

where

$$T^{I_f M_f}_{I_2 M_2 M_A}(\Omega_b) \tag{8}$$
$$= \sum_{I_1 M_1} (2I_1 + 1)^{1/2} \langle I_A M_A I_1 M_1 \mid I_f M_f \rangle$$
$$\times \sum_{l m_l} i^l \langle I_2 - M_2 I_1 M_1 \mid l m_l \rangle$$
$$\times \sum_{\Lambda_1 \Lambda_2 I_X E_X} (-1)^{l + \Lambda_1 + \Lambda_2} \Theta_{l \Lambda_1 \Lambda_2 I_1 I_2 I_X}$$
$$\times \beta_{l m_l \Lambda_1 \Lambda_2 I_X E_X}(\Omega_b).$$

In (8), the kinematic factors $\beta_{l m_l \Lambda_1 \Lambda_2 I_X E_X}(\Omega_b)$ are the overlap integrals of the input $\chi^{(+)}(\mathbf{K}_a \cdot \mathbf{r}_a)$ and output $\chi^{(-)}(\mathbf{K}_b \cdot \mathbf{r}_b)$ distorted waves, the wave functions of the relative motion $\Psi_{n_1 \Lambda_1 M_{\Lambda 1}}(\mathbf{r}_{XA})$, $\Psi_{n_2 \Lambda_2 M_{\Lambda_2}}(\mathbf{r}_{Xb})$ (we use index 1 for the vertex $B \to X + A$ and index 2 for the vertex $a \to X + b$), and the interaction potential V. The structural factor $\Theta_{l \Lambda_1 \Lambda_2 I_1 I_2 I_X}$ for the direct processes can be written in the form

$$\Theta_{l \Lambda_1 \Lambda_2 I_1 I_2 I_X} = (-1)^{I_X} \frac{u(I_1 \Lambda_1 I_2 \Lambda_2 : I_X l)}{\sqrt{2I_X + 1}} \tag{9}$$
$$\times \Theta^{B \to X + A}_{\Lambda_1 I_1 I_X} \Theta^{a \to X + b}_{\Lambda_2 I_2 I_X},$$

where $\Theta^{B \to X + A}_{\Lambda_1 I_1 I_X}$ and $\Theta^{a \to X + b}_{\Lambda_2 I_2 I_X}$ are the amplitudes of the reduced decay widths of the nuclei B and a through the $X + A$ and $X + b$ channels, respectively.

Let us calculate the structural factor (9) in the scheme of summation of the total momenta (6) for the case when the transferred nucleus X is a massive cluster possessing excited states. For this purpose, it is necessary to introduce a summation schemes for the orbital angular momenta,

$$\mathbf{L}_f = \mathbf{L}_X + \mathbf{\Lambda}_1 + \mathbf{L}_A = \mathbf{L}_X + \mathbf{L}_1, \tag{10}$$
$$\mathbf{L}_a = \mathbf{L}_X + \mathbf{\Lambda}_2 + \mathbf{L}_b = \mathbf{L}_X + \mathbf{L}_2,$$

and a summation scheme for the total momenta,

$$\mathbf{I}_f = \mathbf{I}_X + \mathbf{\Lambda}_1 + \mathbf{I}_A = \mathbf{I}_X + \mathbf{J}_1 = \mathbf{I}_1 + \mathbf{I}_A, \tag{11}$$
$$\mathbf{I}_a = \mathbf{I}_X + \mathbf{\Lambda}_2 + \mathbf{I}_b = \mathbf{I}_X + \mathbf{J}_2 = \mathbf{I}_2 + \mathbf{I}_b,$$

where $\mathbf{L}_a, \mathbf{L}_b, \mathbf{L}_A, \mathbf{L}_f$, and $\mathbf{L}_X$ are the orbital angular momenta of the corresponding nuclei and $\mathbf{I}_X$ is the total momentum of the transferred nucleus.

Then, the reduced width amplitude $\Theta^{a \to X + b}_{\Lambda_2 I_2 I_X}$, which enters (9), can be presented in the following form:

$$\Theta^{a \to X + b}_{\Lambda_2 I_2 I_X} = \sum_{J_2} u(I_b \Lambda_2 I_a I_X : J_2 I_2) \Theta^{a \to X + b}_{\Lambda_2 I_X J_2}, \tag{12}$$

where the cluster spectroscopic amplitude of the reduced width that separates the heavy cluster X in the nucleus a is defined in the standard way (see, e.g., [17, 18]):

$$\Theta^{a \to X + b}_{\Lambda_2 I_X J_2} = \begin{pmatrix} N_a \\ N_X \end{pmatrix}^{1/2} \left(\frac{a}{X}\right)^{N_{\Lambda_2}/2} \tag{13}$$
$$\times \sum_{[f_i] L_i S_i T_i, i = a, b, X} \mathbf{a}^{J_a T_a}_{[f_a] L_a S_a} \mathbf{a}^{J_X T_X}_{[f_X] L_X S_X} \mathbf{a}^{J_b T_b}_{[f_b] L_b S_b}$$
$$\times (-1)^{\Lambda_2 + I_X + I_b - I_a} u(\Lambda_2 L_b J_2 S_b : L_2 I_b)$$
$$\times K(\Lambda_2 L_b; L_2) \langle T_X M_{T_X} T_b M_{T_b} \mid T_a M_{T_a} \rangle$$
$$\times \begin{pmatrix} L_X & S_X & I_X \\ L_2 & S_b & J_2 \\ L_a & S_a & I_a \end{pmatrix}$$
$$\times \langle N_a [f_a] L_a S_a T_a \mid N_X [f_X] L_X S_X T_X;$$
$$N_2 [f_b] L_2 S_b T_b \rangle.$$

In (13), $\mathbf{a}^{J_i T_i}_{[f_i] L_i S_i}$ are the intermediate coupling coefficients; $K(\Lambda_2 L_b; L_2)$ are the generalized Talmi–Moshinsky–Smirnov coefficients [17, 18], which factorize the wave function of the b nucleons with the orbital angular momentum L_2 into the product of the wave function $\Psi_{n_2 \Lambda_2 M_{\Lambda_2}}(\mathbf{r}_{Xb})$ of the relative motion with the orbital momentum Λ_2 and the wave function of the internal motion with the main quantum number n_b and the orbital momentum L_b (here, $n_2 + n_b = N_2$).

2.3. Spin Tensors of the Density Matrix in the Statistical Model of Compound Nucleus

The modified CN model [14, 15] considered in this paper makes it possible to allow for the arbitrary spins of the nuclei participating in the reaction, spin–orbit

Table 1. The reduced width amplitudes of the $^{14}\mathrm{N} \rightarrow {}^{12}\mathrm{C} + d$ vertex

I_X	I_2	Λ_2	$\Theta_{\Lambda_2 I_X I_2}^{^{14}\mathrm{N} \rightarrow {}^{12}\mathrm{C}+d}$
0	0	0	0.326
	2	2	0.736
2	2	0	0.883
	0	2	0.415
	1	2	−0.533
	2	2	0.198

interaction of the nuclei in the initial and the final channels, and the interference of the incoming and outgoing partial distorted waves.

According to the main statement of the CN model, the matrix element T_{if} of the transition operator between the initial and the final states of the $a + A = C = b + B$ reaction in the asymptotic region of the compound nucleus assumes the form

$$T_{if} = \langle \Psi_f \mid \Psi_C \rangle \langle \Psi_C \mid \Psi_i \rangle , \tag{14}$$

where Ψ_i, Ψ_f, and Ψ_C are the wave functions of the initial, final, and intermediate states, respectively.

We define the summation rules for the angular momenta as

$$\begin{aligned} \mathbf{I}_1 = \mathbf{I}_a + \mathbf{I}_A, \mathbf{I}_2 = \mathbf{I}_b + \mathbf{I}_f, \\ \mathbf{I}_C = \mathbf{I}_1 + \mathbf{L}_a = \mathbf{I}_2 + \mathbf{L}_b, \end{aligned} \tag{15}$$

where $\mathbf{l}_a$ and $\mathbf{l}_b$ are the orbital angular momenta of the relative motion of particles in the input and output channels and $\mathbf{I}_C$ is the spin of the compound nucleus.

Following [14], we first obtain an expression for the density matrix $\rho_{I_f}(M_f, M_f'; \Omega_b)$ allowing for one quasistationary state (resonance) of the compound nucleus and then pass to a quasicontinuous spectrum of the compound nucleus through the summation over all resonances in the interval of averaging. In the reference frame with the z axis directed along the incident beam and $\varphi_b = 0$, the expression for the spin tensors of the density matrix of the final nucleus assumes the form [14, 15]

$$\begin{aligned} \rho_{kq}(I_f; \Omega_b) = \frac{(2I_f + 1)^{1/2}}{2{K_a}^2 (2I_A + 1)(2I_a + 1)} \\ \times \sum_{I_1 I_2 I_2' I_C l_a l_b l l' m_l m_l'} (-1)^{2I_C + I_f + I_b} \\ \times (2I_C + 1)^2 \left[(2I_1 + 1)(2I_2 + 1)\right]^{1/2} \\ \times w(I_f I_2 I_f I_2' : I_b k)(-1)^{m_l + I_1 + I_2 + I_2'} \\ \times \left[(2l + 1)(2l' + 1)(2l_a + 1)(2l_b + 1)\right]^{1/2} \\ \times \langle l m_l l' - m_l' \mid kq \rangle \langle l_a 0 l_b - m_l \mid l m_l \rangle \\ \times \langle l_a' 0 l_b' - m_l' \mid l' m_l' \rangle w(I_2 l I_2' l' : I_1 k) \\ \times w(I_1 l_a I_2 l_b : I_C l) w(I_1 l_a' I_2' l_b : I_C l') \\ \times P_{l_b m_l}(\theta_b) P_{l_b' m_{l'}}(\theta_b) \frac{\mathcal{T}_{l_a I_1}^{I_C} \mathcal{T}_{l_b I_2}^{I_C}}{G(I_C)}, \end{aligned} \tag{16}$$

where the penetrability coefficients $\mathcal{T}_{lI}^{I_C}$ are calculated in the optical model of the elastic scattering and the total width $G(I_C)$ includes all energy-allowed decay channels of the compound nucleus:

$$G(I_C) = \sum_{n l_b} \sum_{I_2 = |l_b - I_C|}^{l_b + I_C} \sum_{I_f' = |I_2 - I_b|}^{I_2 + I_b} \left[\sum_{E_f'}^{E_c} \mathcal{T}_{l_b I_2}^{I_C} + \int_{E_c}^{E_f^*} \mathcal{T}_{l_b I_2}^{I_C} \rho(E_f^*, I_f') dE_f^* \right] . \tag{17}$$

In (17), n is the number of open channels; E_f^* is the energy of the excited level of the final nucleus $\widetilde{B}^*$ in the $\widetilde{b} + \widetilde{B}^*$ channel; E_c is the energy edge of the continuous spectrum of the nucleus $\widetilde{B}^*$.

Using expressions (4), (16), and (17), it is possible to calculate the ACF using expression (1).

3. $^{12}\mathrm{C}(^{14}\mathrm{N}, d)^{24}\mathrm{Mg}^*(\alpha)^{20}\mathrm{Ne}$ REACTION

3.1. Reduced Width Amplitudes

We begin the analysis of the reaction in the MIVOKOR formalism with the calculation of the reduced widths for the $^{14}\mathrm{N} \rightarrow {}^{12}\mathrm{C} + d$ vertex, since the values obtained in some of the previous papers clearly disagree with each other. We calculated the reduced width amplitudes (RWAs) for the $^{14}\mathrm{N} \rightarrow {}^{12}\mathrm{C} + d$ vertex in the case with the transfer of the $^{12}\mathrm{C}$ in the ground and the first excited state (4.433 MeV, 2^+). The calculation was based on the formalism considered in the Section 2.2 using the summation scheme of the total momenta (6), (10), (11) and allowing for the transfer of a massive cluster possessing a number of excited states. Allowing for the transfer of the higher excitations (for example, in the 14.05 MeV, 4^+ state, as was done in [8]) requires a more correct calculation of the wave functions

Table 2. Parameters of the optical potentials and the interaction potentials in the bound states of the nuclei ^{14}N and ^{24}Mg

Channel	V, MeV	R, fm	a_R, fm	W, MeV	R_W, fm	a_W, fm	$R_{\rm Coul}$, fm
$^{12}{\rm C} + ^{14}{\rm N}$	100	5.59	0.48	27	5.92	0.26	6.58
$d + ^{24}{\rm Mg}$	50	4.33	0.59	16	4.33	0.59	4.33
$d + ^{12}{\rm C}$		2.97	0.65				2.97
$^{12}{\rm C} + ^{12}{\rm C}$		4.235	0.7				4.235

Note: $\mathcal{V} = Vf(r) + Wf(r) + V_{\rm Coul}$, $f(r) = \left[1 + \exp\left(\dfrac{r - R_n A^{1/3}}{a_n}\right)\right]^{-1}$, $n = V, W$.

for the quasistationary states $^{12}{\rm C} \otimes\ ^{12}{\rm C}^*$, because in this case the binding energy becomes positive even for the ground state of ^{24}Mg. In other words, it is necessary to allow for the decay width of the state (see, for example, the ACF calculation for the $^{12}{\rm C}(^7{\rm Li}, t)^{16}{\rm O}^*(\alpha)^{12}{\rm C}$ reaction [19], where the higher quasistationary states in ^{16}O were described by wave functions of the Gamow type).

According to (12), we calculated the reduced widths using the complete basis set of the wave functions for the nuclei ^{12}C and ^{14}N, namely, three components of the wave function of ^{14}N, three components of the wave function of ^{12}C in the ground state, and four components in the excited state 4.433 MeV, 2^+ (we took the intermediate coupling coefficients $\mathbf{a}^{J_iT_i}_{[f_i]L_iS_i}$ from [20]). We also used the fractional parentage coefficients of deuteron tabulated in [21]. Table 1 displays the calculated $\Theta^{a\to X+b}_{\Lambda_2 I_X I_2}$ for the $^{14}{\rm N} \to\ ^{12}{\rm C} + d$ vertex.

It should be emphasized that the differential cross section of the reaction in the MIVOKOR formalism is the incoherent sum with respect to the total momenta I_1, I_2 and the transferred angular momentum l, while expressions (7) and (8) for the ACF contain incoherent summation with respect to the total momentum I_1, its projection M_1, and the angular-momentum transfer l. In both cases, the matrix element of the reaction includes the coherent summation with respect to the total momentum I_2 and its projection M_2, and the coherent summation with respect to the total momentum I_X of the intermediate nucleus and the orbital momenta of the relative motion Λ_1 and Λ_2.

In our calculations, the reduced width amplitude $\Theta^{B\to X+A}_{\Lambda_1 I_X I_1}$ for the $^{24}{\rm Mg}^* \to\ ^{12}{\rm C} + ^{12}{\rm C}^*$ vertex, which enters the spectroscopic factor $\Theta_{l\Lambda_1\Lambda_2 I_1 I_2 I_X}$, was a free parameter determined from the fit to the experimental data.

3.2. Differential Cross Sections

We analyzed the reaction $^{12}{\rm C}(^{14}{\rm N}, d)^{24}{\rm Mg}^*$ at two different energies of the ^{14}N ions $E_{\rm lab} = 29$ and 35 MeV for various excited states of ^{24}Mg. The calculations were performed in the modified CN model by the program package CNCOR [15]. The main details and the calculation parameters were discussed in the previous paper [5]. Many investigations emphasized the important role of the critical angular momentum $J_{\rm cr}$ for the formation of the compound nucleus ^{26}Al in the calculation of the cross section magnitude in the CN model. When the value of $J_{\rm cr}$ was chosen approximately equal to $J_{\rm gr}$ ($J_{\rm gr}$ is the angular momentum corresponding to the penetrability coefficients in the input channel equal to $\sim$0.5 [4]), the reaction cross sections calculated in the CN model for the most part of levels exceeded the experimental values. Since the critical angular momentum $J_{\rm cr}$ is determined by the maximum orbital angular momentum $l_a^{\rm max}$ in the input channel and characterizes the probability of formation of the compound nucleus at $l_a < l_a^{\rm max}$, it seems to be reasonable that $J_{\rm cr}$ depends not only on the incident ion energy, but also on the probability of the existence of the competing channel, for example, the direct breakdown channel, which gives the maximum contribution at $l_a^{\rm max} \lesssim l_a \lesssim l_a^{\rm gr}$. We used $J_{\rm cr} \approx J_{\rm gr} \simeq 13$ for the 5.23 MeV, 3^+ level in ^{24}Mg at $E_{^{14}{\rm N}} = 35$ MeV, because the formation of this level owing to the direct processes is forbidden by the selection rules. For the other levels, we selected $J_{\rm cr} < J_{\rm gr}$ depending on the value of $E_{^{14}{\rm N}}$ (lab).

Calculations in the MIVOKOR formalism were performed by the program package OLYMP-5 [22, 15], modified to allow for the summation with respect to the total momentum I_X of the excited states of the intermediate nucleus X and the total momenta I_1 and I_2. Table 2 displays the parameters of the optical potentials and the interaction potentials.

Figures 1 and 2 present the calculation results for the differential cross sections of the reaction $^{12}{\rm C}(^{14}{\rm N}, d)^{24}{\rm Mg}^*$ for various excited states of the

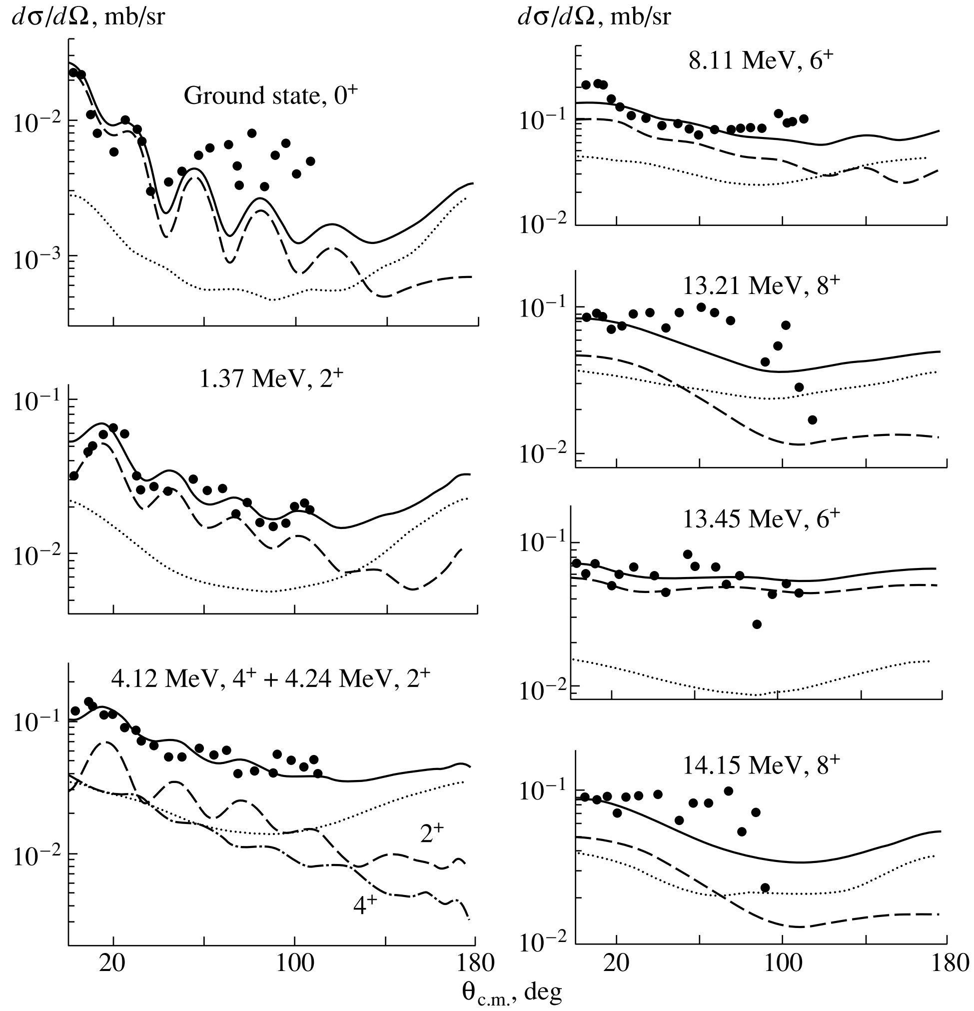

Fig. 1. The angular distributions of deuterons in the $^{12}C(^{14}N, d)^{24}Mg^*$ reaction at the energy $E_{^{14}N}(\mathrm{lab}) = 29$ MeV. The dashed (dashed-dotted) curves show the contribution of the mechanism of the direct transfer of the ^{12}C cluster; the dotted curves show the contribution of the CN mechanism. The solid curve is the incoherent sum of the contributions from both mechanisms. The points represent the experimental data [6].

^{24}Mg nucleus at $E_{^{14}N}(\mathrm{lab}) = 29$ and 35 MeV. The experimental data for these energies are taken from [6] and [3], respectively. The data have high statistical accuracy—the statistical errors usually do not exceed the size of the points in the figures. Theoretical cross sections represent the incoherent sums of the cross sections calculated in the statistical CN model and in the model of the direct transfer (the breakdown mechanism) of the ^{12}C nucleus in the ground and the first excited state ($E^* = 4.433$ MeV, 2^+). Note that the cross sections with excitation of the 4.12 MeV, 4^+ and 4.24 MeV, 2^+ states are experimentally forbidden. While comparing these cross section with the experiment, we calculated each cross section separately and then summed the obtained results. Since we studied the quasimolecular states $^{12}C \otimes\ ^{12}C^*$, we omitted the calculations allowing for the heavy breakdown mechanism, that is, the direct transfer of the nucleus ^{10}B: in this case, the excited states in ^{24}Mg are formed owing to the configurations $^{14}N \otimes\ ^{10}B$.

The contribution of the direct transfer of the ^{12}C nucleus to the cross section of the reaction with the production of the ground state ^{24}Mg is dominating compared to the contribution of the CN mechanism. The former contribution reaches approximately 80–85% in the forward angular region of the deuteron emission, 65–85% in the region of medium emission angles, and slightly decreases when the energy of the incident ions increases from 29 to 35 MeV. At large deuteron emission angles, the contribution of the direct transfer mechanism decreases to 25–50% of the total reaction cross section. For the cross sections with the production of the excited states of ^{24}Mg, the contribution of the direct transfer mechanism also exceeds that of the CN mechanism in the region of

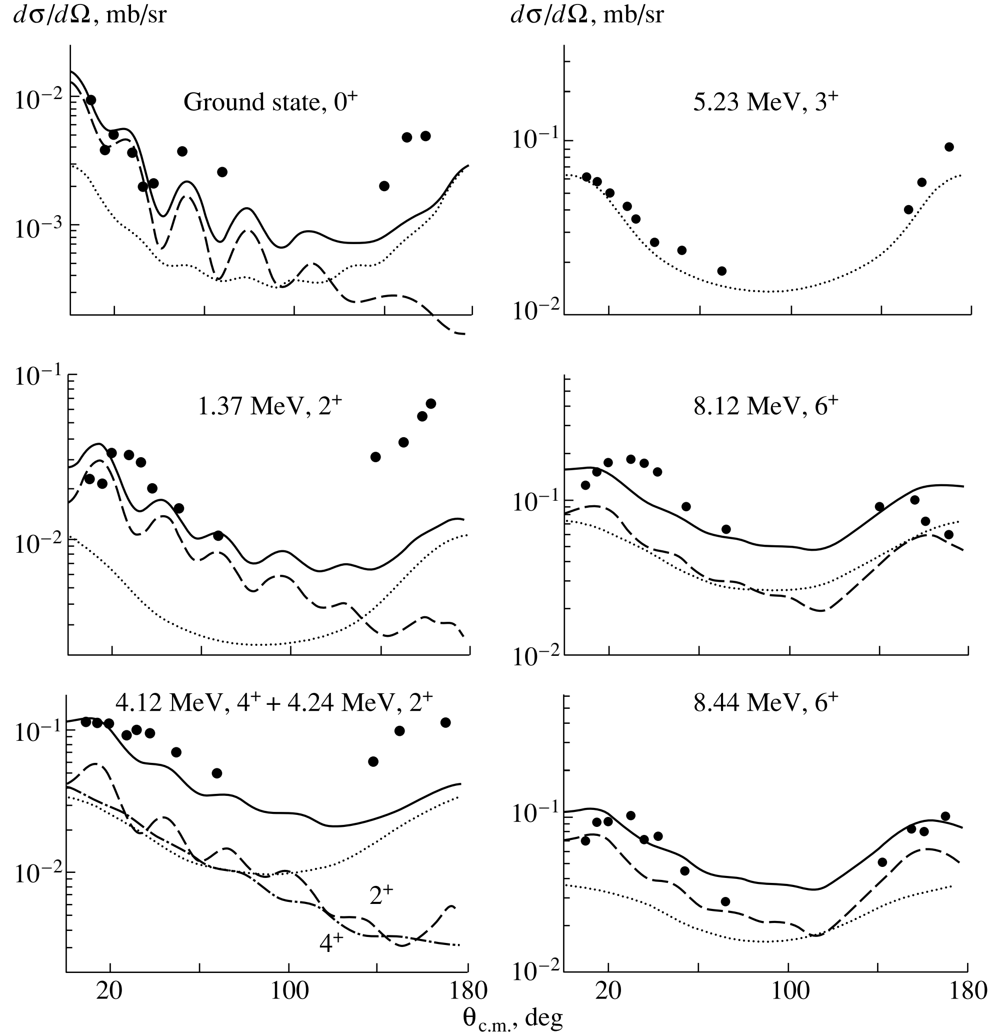

Fig. 2. The angular distributions of deuterons in the $^{12}C(^{14}N, d)^{24}Mg^*$ reaction at the energy $E_{^{14}N}$(lab) = 35 MeV. The notations are the same that in Fig. 1. The points represent the experimental data [3].

forward angles and reaches 70% for the 2^+ level, 50–70% for the 4^+ and 6^+ levels, and 55–60% for the 8^+ level. In the region of medium angles, the contribution of the direct transfer mechanism is comparable with the contribution of the CN mechanism and reaches 70% for the 2^+ level, 40–50% for the 4^+ level, 50–65% for the 6^+ level, and 35–45% for the 8^+ level. At large deuteron emission angles, the CN mechanism dominates. The 13.45 MeV, 6^+ level is distinguished by the significant excess of the contribution from the direct transfer mechanism over the contribution from the CN mechanism. For this level, the direct transfer mechanism gives 80 to 85% of the cross section for the forward, medium, and large deuteron emission angles.

Table 3 presents the reduced width amplitudes $\Theta_{\Lambda_1 I_1 I_X}^{^{24}Mg^* \to\, ^{12}C + ^{12}C^*}$ obtained as a result of the comparison of the calculated cross sections with the experimental data.

An analysis of the results of calculation of the differential cross section leads to the following conclusions.

The reduced width amplitudes $\Theta_{\Lambda_1 I_1 I_X}^{^{24}Mg^* \to\, ^{12}C + ^{12}C^*}$ for the quasimolecular states $^{12}C \otimes {}^{12}C^*$ have sufficiently high values comparable with RWA of the deuteron in the ^{14}N nucleus (see Tables 1 and 3). The RWA difference for the 13.45 MeV, 6^+ level at the nitrogen ion energies $E_{\rm lab} = 29$ [6] and 33 MeV [2] (see Table 3) is related to the fact that the experimental cross sections reported in various papers differ from each other by a factor of more than 3.

For the lowest states of ^{24}Mg with $I^\pi = 0^+, 2^+$, 4^+, the configurations in which the transfer of ^{12}C occurs in the ground state and in the first excited state (4.433 MeV, 2^+) give comparable contributions. In

Table 3. The reduced width amplitudes of the $^{24}\mathrm{Mg}^* \to {}^{12}\mathrm{C} + {}^{12}\mathrm{C}^*$ vertex for various energies of the incident ^{14}N ions

I^π, $E^*_{^{24}\mathrm{Mg}}$, MeV	I_1	Λ_1	I_X	E_{lab}, MeV		
				29	35*	42
0^+, ground state	0	0	0	0.84	0.84	
$2^+, 1.37$	2	2	0	0.66	0.66	
	2	0	2	0	0	
	2	2	2	0.66	0.66	
	2	4	2	−0.2	−0.2	
$2^+, 4.24$	2	2	0	0.66	0.66	
	2	0	2	0	0.2	
	2	2	2	0.66	0.66	
	2	4	2	−0.2	−0.2	
4^+, 4.12	4	4	0	0.35	0.35	
	4	2	2	0.35	0.35	
	4	4	2	0.35	0.35	
	4	6	2	0	0.35	
$6^+, 8.11$; $6^+, 8.44$	6	6	0	0	0	0
	6	4	2	0.447	0.447	0
	6	6	2	0.447	0.447	0.447
	6	8	2	0.447	0.447	0.447
$6^+, 13.25$	6	6	0	0	0	0
	6	4	2	0.114	0.28	0
	6	6	2	0.114	0.28	0.28
	6	8	2	0	0	0.56
$8^+, 14.15$	8	8	0	0		
	8	6	2	0.26		
	8	8	2	0.26		
	8	10	2	0		

* The RWA for the 13.24 MeV, 6^+ level are obtained at $E_{\mathrm{lab}} = 33$ MeV.

particular, for $I_X = 2$, all allowed momenta of the relative motion $\mathbf{\Lambda}_1 = \mathbf{I}_f + \mathbf{2}$ of nuclei in the $^{12}\mathrm{C} + {}^{12}\mathrm{C}^*$ configuration are usually important. For the strongly excited quasimolecular states of ^{24}Mg ($I^\pi = 6^+, 8^+$), the role of configurations featuring the transfer of the intermediate ^{12}C nucleus in the ground state becomes insignificant, and the main contribution comes from the configurations with the transfer of $^{12}\mathrm{C}^*(2^+)$. In this case, the highest allowed momenta of the relative motion Λ_1 of the nuclei in the $^{12}\mathrm{C} + {}^{12}\mathrm{C}^*$ configuration become dominating with increasing energy of the incident ions.

It should be emphasized that the analysis of the differential cross sections is insufficient for obtaining reliable information about the higher quasistationary states in ^{24}Mg and should be supplemented by an analysis of the angular correlation functions.

3.3. The Angular $d\alpha$-Correlation Functions

We calculated the ACFs for all excited states of the ^{24}Mg nucleus with the excitation energy exceeding the energy of the 4.12 MeV, 4^+ level allowing for the coherent summation with respect to the momenta $l, \Lambda_1, \Lambda_2, I_X$ (Figs. 3–6). A specific feature of ACFs in this reaction is a strong dependence of their shape on the incident ion energy and on the structure (wave function and weights of various configurations) of the excited state of the final ^{24}Mg nucleus. Investigation of the ACFs at various energies enables sufficiently reliable estimation of the contributions from various states of the relative motion of $^{12}\mathrm{C} \otimes {}^{12}\mathrm{C}^*$ in ^{24}Mg. If the levels of ^{24}Mg possess a given quasimolecular structure, then, starting from the 8.11 MeV, 6^+ level, the relative binding energy of the carbon nuclei becomes positive; that is, these states become quasistationary. In these cases, we performed calculations with an effective negative value of the binding energy $\epsilon = -0.01$ MeV.

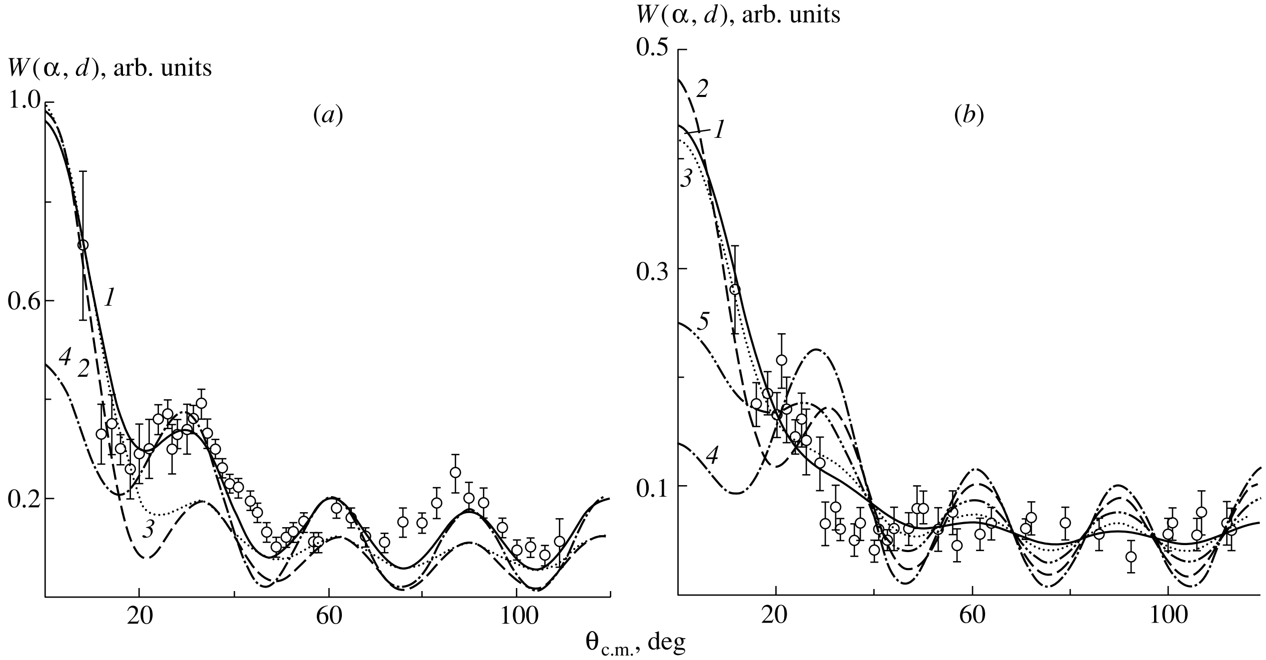

Fig. 3. The angular $d\alpha$-correlation functions in the $^{12}\mathrm{C}(^{14}\mathrm{N}, d)^{24}\mathrm{Mg}^*(\alpha)^{20}\mathrm{Ne}$ reaction at the energy $E_{^{14}\mathrm{N}}(\mathrm{lab}) = 33$ (*a*) and 42 MeV (*b*) for the excited state 13.24 MeV, 6^+ in $^{24}\mathrm{Mg}$ at the zero deuteron emission angle in the c.m. reference frame. The curves were calculated in the model of the direct transfer of the $^{12}\mathrm{C}$ cluster with $I_X = 2$ for various ratios between contributions of the configurations $^{12}\mathrm{C}\otimes{}^{12}\mathrm{C}^*$ with different momenta of the relative motion: (*a*) $\Theta_{\Lambda_1=4} : \Theta_{\Lambda_1=6} : \Theta_{\Lambda_1=8} = 1 : 1 : 0$ (*1*), 1 : 1 : 1 (*2*), 0 : 1 : 1 (*3*), and 0 : 1 : 0 (*4*); (*b*) $\Theta_{\Lambda_1=4} : \Theta_{\Lambda_1=6} : \Theta_{\Lambda_1=8} = 0 : 1 : 2$ (*1*), 1 : 1 : 1 (*2*), 0 : 1 : 1 (*3*), 0 : 1 : 0 (*4*), and 1 : 1 : 0 (*5*). The points correspond to the experimental data [2].

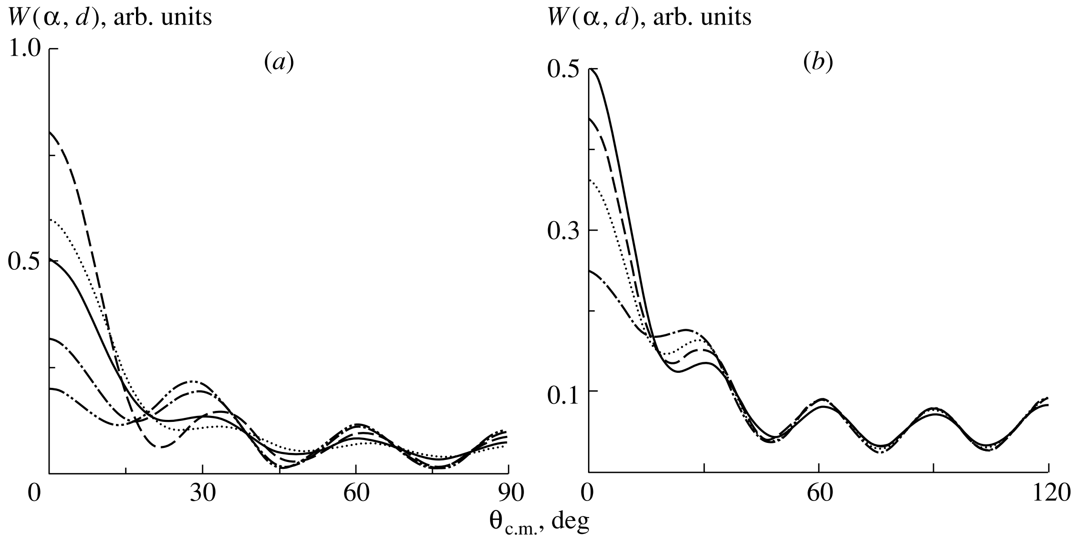

Fig. 4. The angular $d\alpha$-correlation functions for the 13.24 MeV, 6^+ state in $^{24}\mathrm{Mg}$, calculated in the model of the direct transfer of the $^{12}\mathrm{C}$ cluster with various contributions of the $^{12}\mathrm{C} \otimes {}^{12}\mathrm{C}^*$ configurations with different momenta of the relative motion: (*a*) the curves correspond to the RWA ratios $\Theta_{\Lambda_1=4} : \Theta_{\Lambda_1=6} : \Theta_{\Lambda_1=8} = 1 : 1 : 0$ (solid), 1 : 1 : 1 (dash), 0 : 1 : 1 (dot), 0 : 1 : 0 (dash–dot), $0{:}1(I_X = 0, 2){:}0$ (dash with double dots), $E_{^{14}\mathrm{N}}(\mathrm{lab}) = 29$ MeV; (*b*) $\Theta_{\Lambda_1=4} = 0.114$, $\Theta_{\Lambda_1=6} = 0.114$, $\Theta_{\Lambda_1=8} = 0$, the curves correspond to $E_{^{14}\mathrm{N}}(\mathrm{lab}) = 29$ (solid), 33 (dash), 35 (dot); 42 MeV (dash–dot).

Figure 3 displays the ACFs for the 13.24 MeV, 6^+ level (the experimental data are taken from [2]) for two energies of the nitrogen ions $E_{\mathrm{lab}} = 33$ (*a*) and 42 MeV (*b*), calculated with various RWA values $\Theta^{^{24}\mathrm{Mg}\to{}^{12}\mathrm{C}+{}^{12}\mathrm{C}^*}_{\Lambda_1 I_1 I_X}$ taken from Table 3. Since the RWA

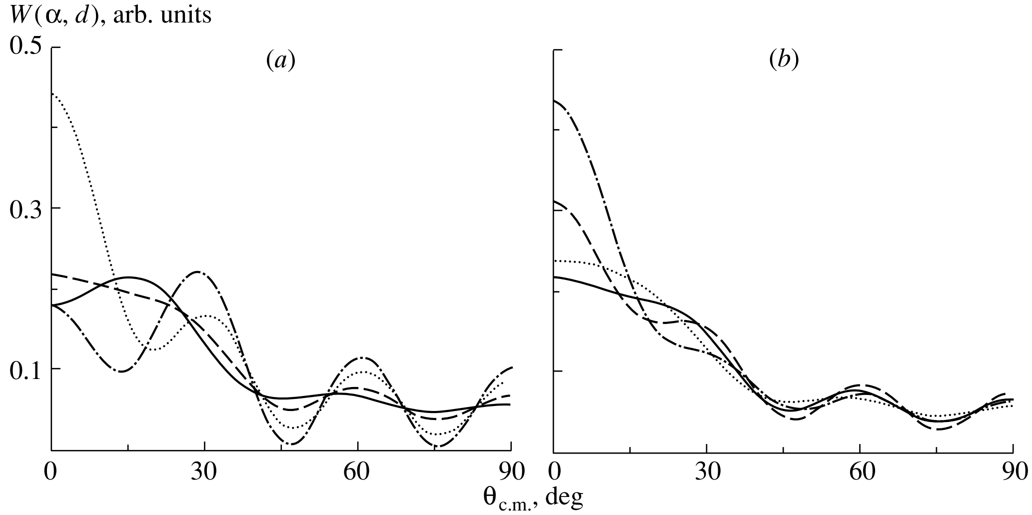

Fig. 5. The angular $d\alpha$-correlation functions for the 8.11 MeV, 6^+ state in ^{24}Mg calculated in the model of the direct transfer of the ^{12}C cluster with various contributions of the $^{12}\mathrm{C} \otimes {}^{12}\mathrm{C}^*$ configurations with different momenta of the relative motion: (*a*) the curves correspond to the RWA ratios $\Theta_{\Lambda_1=4} : \Theta_{\Lambda_1=6} : \Theta_{\Lambda_1=8} = 2 : 1 : 1$ (solid), 1 : 1 : 1 (dash), 0 : 1 : 1 (dot), 0 : 1 : 0 (dash–dot), $E_{^{14}\mathrm{N}}$(lab) = 29 MeV; (*b*) $\Theta_{\Lambda_1=4} = \Theta_{\Lambda_1=6} = \Theta_{\Lambda_1=8} = 0.447$, $E_{^{14}\mathrm{N}}$(lab) = 29 MeV (solid), 33–35 MeV (dash), 42 MeV (dot); $\Theta_{\Lambda_1=4} = 0$, $\Theta_{\Lambda_1=6} = \Theta_{\Lambda_1=8} = 0.447$, $E_{^{14}\mathrm{N}}$(lab) = 42 MeV (dash–dot).

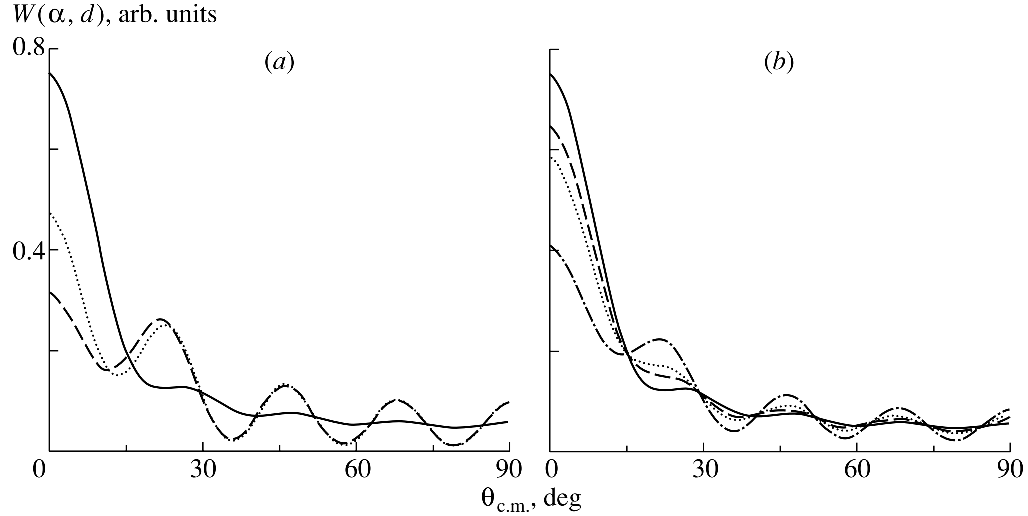

Fig. 6. The angular $d\alpha$-correlation functions for the 13.21 MeV, 8^+ state in ^{24}Mg, calculated in the model of the direct transfer of the ^{12}C cluster with various contributions from the $^{12}\mathrm{C} \otimes {}^{12}\mathrm{C}^*$ configurations with different momenta of the relative motion: (*a*) the curves correspond to the RWA ratios $\Theta_{\Lambda_1=6} : \Theta_{\Lambda_1=8} : \Theta_{\Lambda_1=10} = 1 : 1 : 0$ (solid), 0 : 1 : 0 (dash), $1 : 1(I_X = 0, 2) : 0$ (dot), $E_{^{14}\mathrm{N}}$(lab) = 29 MeV; (*b*) $\Theta_{\Lambda_1=6} = 0.26$, $\Theta_{\Lambda_1=8} = 0.26$, $\Theta_{\Lambda_1=10} = 0$, $E_{^{14}\mathrm{N}}$(lab) = 29 (solid), 33 (dash), 35 (dot), 42 MeV (dash–dot).

are determined as the calculated parameters from the comparison of the corresponding differential cross sections with experiment, their values automatically allow for a difference in the experimental excitation cross sections of this level at different energies of the nitrogen ions observed in [2] and mentioned in the preceding section. The shape of the ACF significantly changes depending on the RWA ratio characterizing the contributions of various momenta of the relative motion of the carbon nuclei in the quasimolecular $^{12}\mathrm{C} \otimes {}^{12}\mathrm{C}^*$ configuration.

Figure 4 displays the ACFs for the same level calculated for $E_{\mathrm{lab}} = 29$ MeV with various RWAs (*a*) and various energies of the nitrogen ions in the interval 29–42 MeV (*b*) with the RWA from Table 3. The ACF oscillations observed experimentally at 29 and 33 MeV appear only when the coherent sum of two states with $\Lambda_1 = 4, 6$ at $I_X = 2$ are accounted for. As the ion energy increases to 42 MeV, the ACF oscillations become smoothed owing to an increase in the contribution of the higher momenta $\Lambda_1 = 6, 8$ of the relative motion allowed by the selection rules.

Figures 5 and 6 present the ACFs for the 8.11 MeV, 6^+ and 13.21 MeV, 8^+ levels. Their shapes also strongly depend on the contribution of different momenta of the relative motion Λ_1 (Figs. 5*a* and 6*a*) and on the incident ion energy (Figs. 5*b* and 6*b*). An analysis of the calculation results leads to the conclusion that the absence of the oscillating polynomial structure of ACFs for the 8.11 and 8.44 MeV, 6^+ levels is probably related to the equal contributions of all momenta of the relative motion $\Lambda_1 = 4$, 6, 8 allowed by the selection rules. As the energy of the nitrogen ions increases to 42 MeV, the maximum of the ACF in the forward direction for these states grows, but no oscillations of the type $|P_6(\cos\theta)|^2$ appear.

The calculated ACFs for the 13.21 and 14.15 MeV, 8^+ levels may exhibit a polynomial form, in particular, when the ion energy increases up to 42 MeV. Unfortunately, no experimental data were available for these levels to be compared to the calculated ACFs.

4. CONCLUSION

The results of investigation of the differential cross sections and the angular $d\alpha$-correlation functions in the $^{12}\mathrm{C}(^{14}\mathrm{N}, d)^{24}\mathrm{Mg}^*(\alpha)^{20}\mathrm{Ne}$ reaction at the nitrogen ion energies $E_{\mathrm{lab}} = 29$–42 MeV demonstrated the possibility of simultaneous description of these characteristics of the reaction for a broad spectrum of excited states in ^{24}Mg, starting from the ground state and up to the highly excited states $I_f^\pi = 6^+, 8^+$ by the mechanism of the direct transfer of the 12-nucleon cluster (^{12}C nucleus). For this reaction, induced by semiheavy nitrogen ions, the contribution of the mechanism of the direct transfer of the ^{12}C cluster dominates over the CN contribution in the forward hemisphere of the deuteron emission for the production of all excited states of ^{24}Mg, where the direct transfer mechanism is not forbidden by the selection rules. Our calculations confirmed the conclusion that the quasimolecular configurations like $^{12}\mathrm{C} \otimes {}^{12}\mathrm{C}^*$ in ^{24}Mg play an important role in the understanding of the reaction mechanism. We showed that the relation between the contributions of various orbital momenta of the relative motion of the carbon nuclei (which can accept several values depending on the spin of the excited state of the transferred nucleus) determines specific features of the behavior of the differential cross sections and the angular correlation functions and, in particular, forms the polynomial shape of the ACF. The corresponding reduced width amplitudes obtained from a comparison of the theoretical and experimental cross sections and ACFs acquire rather large values. This is indicative of a significant probability of the formation of the quasimolecular states in the ^{24}Mg nucleus. The constancy of the obtained RWAs at the nitrogen ion energies of 29 and 35 MeV confirms reliability of the applied approach. At the same time, an increase of the calculation energy up to 42 MeV results in a change of the ratio between the contributions of various momenta and in an increase in the contribution of the highest allowed momenta of the relative motion of nuclei in the $^{12}\mathrm{C} + {}^{12}\mathrm{C}^*$ configuration.

In conclusion, we would like to attract the attention of experimenters and theoreticians to the further investigation of strongly excited cluster and quasimolecular states in the nuclei of the $2s1d$ shell, in particular, by studying the angular correlation functions. This requires, first of all, the development of adequate theoretical methods for the calculation of the reduced widths of massive clusters.

REFERENCES

1. K. R. Artemov, V. Z. Goldberg, M. S. Golovkov, *et al.*, Phys. Lett. B **149**, 325 (1984).
2. R. W. Zurmuhle, Z. Liu, D. R. Benton, *et al.*, Phys. Rev. C **49**, 2549 (1994).
3. C. Volant, M. Conjeaud, S. Harar, *et al.*, Nucl. Phys. A **238**, 120 (1975).
4. H. V. Klapdor, H. Reiss, G. Rosnerb, and M. Schrader, Nucl. Phys. A **244**, 157 (1975); H. V. Klapdor, H. Reiss, and G. Rosner, Nucl. Phys. A **262**, 157 (1976).
5. T. L. Belyaeva, N. S. Zelenskaya, and N. V. Odintsov, Izv. Akad. Nauk, Ser. Fiz. **58** (11), 112 (1994).
6. K. P. Artemov, M. S. Golovkov, V. Z. Gol'dberg, *et al.*, Yad. Fiz. **44**, 579 (1986) [Sov. J. Nucl. Phys. **44**, 373 (1986)].
7. T. L. Belyaeva and N. S. Zelenskaya, Izv. Akad. Nauk, Ser. Fiz. **52**, 942 (1988).
8. S. B. Sakuta, D. L. Ukrainskiĭ, and Yu. M. Chuvil'skiĭ, Yad. Fiz. **62**, 2019 (1999) [Phys. At. Nucl. **62**, 1873 (1999)].
9. L. C. Biedenharn and M. E. Rose, Rev. Mod. Phys. **25**, 729 (1953); L. C. Biedenharm and J. D. Louck, *Angular Momentum in Quantum Mechanics* (Addison-Wesley, New York, 1981).
10. L. Goldfarb, in *Nuclear Reactions,* Ed. by P. M. Endt and M. Demeur (North-Holland, Amsterdam, 1959; Gosatomizdat, Moscow, 1962), Vol. 1.
11. N. S. Zelenskaya and I. B. Teplov, Nucl. Phys. A **406**, 306 (1983); N. S. Zelenskaya and I. B. Teplov, *Adjectives of Excited States of Nuclei and Angular Correlation in Nuclear Reactions* (Énergoatomizdat, Moscow, 1995).
12. T. L. Belyaeva and N. S. Zelenskaya, Fiz. Élem. Chastits At. Yadra **29**, 262 (1998) [Phys. Part. Nucl. **29**, 107 (1998)].

13. N. S. Zelenskaya and I. B. Teplov, Fiz. Élem. Chastits At. Yadra **11**, 342 (1980) [Sov. J. Part. Nucl. **11**, 126 (1980)]; *Exchange Processes in Nuclear Reactions* (Mosk. Gos. Univ., Moscow, 1985).
14. N. A. Bogdanova, N. S. Zelenskaya, and I. B. Teplov, Yad. Fiz. **51**, 986 (1990) [Sov. J. Nucl. Phys. **51**, 631 (1990)].
15. T. L. Belyaeva, N. S. Zelenskaya, and N. V. Odintsov, Comput. Phys. Commun. **73**, 161 (1992); T. L. Belyaeva, N. A. Bogdanova, N. S. Zelenskaya, and N. V. Odintsov, Preprint NIIYaF MGU-92-40/289 (Institute of Nuclear Physics, Moscow State University, Moscow, 1992).
16. N. Austern, Phys. Rev. B **136**, 1743 (1964); N. Austern, R. M. Drisko, E. C. Halbert, and G. R. Satchler, Phys. Rev. B **133**, 3 (1964); G. R. Satchler, Nucl. Phys. **55**, 1 (1964).
17. V. G. Neudachin and Yu. F. Smirnov, *Nucleon Clusters in Light Nuclei* (Nauka, Moscow, 1969).
18. N. S. Zelenskaya and I. B. Teplov, Izv. Akad. Nauk, Ser. Fiz. **44**, 960 (1980).
19. T. L. Belyaeva, N. S. Zelenskaya, and N. V. Odintsov, Yad. Fiz. **56** (9), 50 (1993) [Phys. At. Nucl. **56**, 1179 (1993)].
20. A. N. Boyarkina, *Structure of the p-Shell Nuclei* (Mosk. Gos. Univ., Moscow, 1973).
21. J. B. Elliott, J. Hope, and H. A. Jahn, Philos. Trans. R. Soc. London, Ser. A **246**, 241 (1953).
22. I. B. Teplov, N. S. Zelenskaya, and T. L. Belyaeva, State Fond of Algorithms and Programs, No. 50850000734 (Moscow, 1985).

Translated by M. Kobrinsky

Physics of Atomic Nuclei, Vol. 65, No. 9, 2002, pp. 1628–1633. Translated from Yadernaya Fizika, Vol. 65, No. 9, 2002, pp. 1669–1675.
Original Russian Text Copyright © 2002 by Agababyan, Ajvazyan, Ammosov, Atayan, Grigoryan, Gulkanyan, Ivanilov, Karamyan, Korotkov.

ELEMENTARY PARTICLES AND FIELDS
Experiment

Study of the Mechanisms of Cumulative-Proton Production in Neutrino–Nucleus Interactions

N. M. Agababyan[1], G. Ajvazyan[2], V. V. Ammosov, M. Atayan[2], N. Grigoryan[2], G. Gulkanyan[2]*, A. A. Ivanilov, G. Karamyan[2], and V. A. Korotkov**

Institute for High Energy Physics, Protvino, Moscow oblast, 142284 Russia

Received July 18, 2001; in final form, November 8, 2001

Abstract—The mechanisms of cumulative proton production are studied on the basis of data from the SCAT propane–freon bubble chamber exposed to a wideband neutrino beam at the Serpukhov accelerator. Kinematic correlations between the cumulative proton and muon, as well as pair correlations of the final protons, are analyzed. The former correlations are predicted by the two-nucleon correlation mechanism (TCM), whereas the latter are caused by the mechanism of secondary pion absorption (SPA) in the nucleus. It is shown that the TCM contribution to the cumulative proton production is most significant in the peripheral interactions (about 50%). The SPA contribution accounts for about a quarter of the inclusive cross section of cumulative proton production. *© 2002 MAIK "Nauka/Interperiodica".*

1. INTRODUCTION

In particle–nucleus interactions, cumulative protons (CPs) can be produced by direct (spectator) or multistage mechanisms. In accordance with the former, CP production is caused by interaction of the incident particle with multinucleon or multiquark clusters in the nucleus [1–3]. The simplest spectator process is that according to the two-nucleon correlation mechanism (TCM) [2], which implies certain kinematic correlations between secondary leptons and cumulative protons with a momentum reflecting the properties of the nuclear wave function at small distances. These correlations were observed in the interactions of (anti)neutrinos with the neon nucleus [4–6], in which the TCM contribution to CP production was estimated for the peripheral interactions [6]. In the nonperipheral interactions, as well as in the neutrino interactions with heavy nuclei, the TCM contribution was insignificant [7, 8]. In these interactions, CP production is caused mainly by the secondary interactions within the nucleus, that is, by the multistage mechanisms.

The main multistage mechanism is secondary pion absorption (SPA) on a quasi-deuteron pair, which results in certain kinematic correlations between two final protons. At present, the SPA contribution is estimated only for the hadron–nucleus interactions [9–12].

Our article is concerned with the study of the aforementioned mechanisms of CP production in the interactions of neutrinos with nuclei of a propane–freon mixture at energies $E_\nu = 3$–30 GeV. The experimental procedure is described in Section 2. The invariant cross spectra of CPs are presented in Section 3. The contributions of the TCM and SPA mechanisms to CP production are estimated in Sections 4 and 5, respectively.

2. EXPERIMENTAL PROCEDURE

The experiment was performed in the SCAT bubble chamber [13], exposed to a wideband neutrino beam obtained with 70-GeV primary protons from the Serpukhov accelerator. The chamber was filled with a propane–freon mixture containing 87 vol % propane (C_3H_8) and 13 vol % freon (CF_3Br) with the percentage of nuclei $H : C : F : Br = 67.9 : 26.8 : 4.0 : 1.3\%$. The density of the mixture was 0.55 g/cm^3, the radiation length was $X_0 = 50$ cm, and the nuclear interaction length was 149 cm. The total chamber volume and the fiducial one were 6.5 m^3 and 1.73 m^3, respectively. A 20-kG uniform magnetic field was provided within the operating chamber volume.

We selected the interaction events caused by a charged beam current with a muon momentum of $p_\mu > 0.5$ GeV/c. A negatively charged particle with the greatest transverse momentum among the particles not exhibiting secondary interaction in

---

[1] Joint Institute for Nuclear Research, Dubna, Moscow oblast, 141980 Russia.

[2] Yerevan Physics Institute, ul. Brat'ev Alikhanyan 2, Yerevan, 375036 Armenia.

*e-mail: `gulkan@jerewan1.yerphi.am`

**e-mail: `ivanilov@mx.ihep.su`

1063-7788/02/6509-1628$22.00

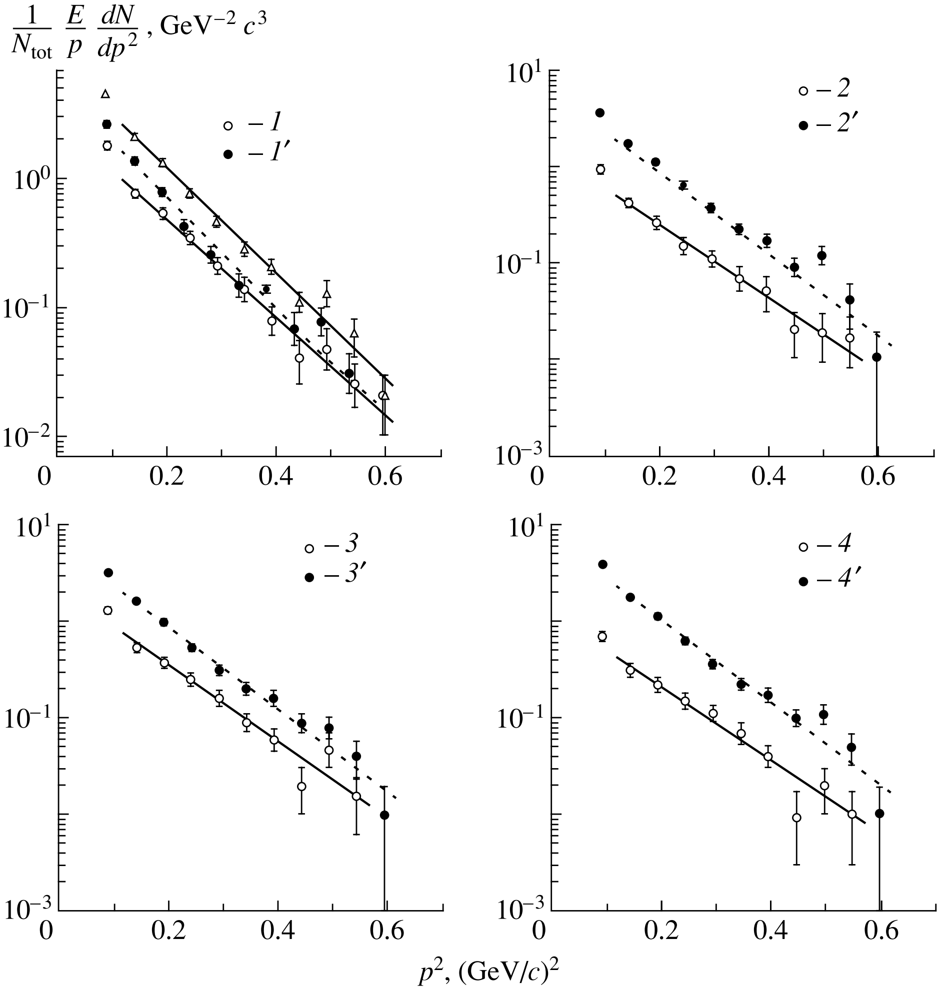

Fig. 1. Invariant spectrum of cumulative protons for all events with CPs (△) and the peripheral and nonperipheral events (samples *1–4* and *1′–4′*, respectively). For the notation, see the text and table.

the chamber was considered to be a muon. Other negatively charged particles were considered to be π^- mesons. Protons with the momenta below 0.6–0.65 GeV/c and a fraction of protons with momentum up to 0.8 GeV/c were identified by their stopping in the chamber. The rest of the positively charged particles were considered to be π^+ mesons. The mean probability of γ-quantum conversion in the chamber was 0.67.

When the neutrino energy was determined, we took into account the charged particles and the γ quanta with a relative error of the momentum measurement $\Delta p/p < 27\%$ and $\Delta p/p < 100\%$, respectively. Introducing corrections for unseen γ quanta, neutrons, and tracks with high relative error of the momentum measurement, we selected events with neutrino energies within the range of 3 GeV $\leq E_\nu \leq$ 30 GeV. The total number of these events was $N_{\rm tot} =$ 7927; the mean neutrino energy was $\langle E_\nu \rangle = 9.0$ GeV; the mean square transferred momentum was $\langle Q^2 \rangle =$ 2.2 GeV^2. Then, we selected events containing at least one CP, that is, the proton with an escape angle of $\vartheta > 90°$ with respect to the neutrino beam direction and with a momentum of $p > 0.24$ GeV/c (the latter constraint was introduced to suppress the contribution of "evaporation" protons). As a result, 1399 events were selected, which contained 1699 cumulative protons.

3. INVARIANT SPECTRA OF CUMULATIVE PROTONS

Figure 1 shows the invariant spectrum of CPs (triangles), corrected for the losses of protons with the momentum of $0.6 < p < 0.8$ GeV/c caused by escape from the chamber. This spectrum can be described by an exponential function $\exp(-bp^2)$ with the slope $b = 9.4 \pm 0.4$ (GeV/c)$^{-2}$; to within the experimental error, this parameter agrees with the measurements performed with hadron, photon, and neutrino beams

The number of cumulative protons ($\overleftarrow{p}$); the slope of the invariant spectrum (b); the correlation parameter (β); the contribution of the two-nucleon correlations ($\beta_{\rm TCM}$)

Sample	Number of CP	b, $({\rm GeV}/c)^{-2}$	β	$\beta_{\rm TCM}$
All CP events	1699	9.5 ± 0.4	0.43 ± 0.06	$0.36 \pm 0.05 \pm 0.07$
(*1*) $1\overleftarrow{p} + (\leq 1)\overrightarrow{p}$	678	8.9 ± 0.6	0.56 ± 0.09	$0.46 \pm 0.08 \pm 0.09$
(*1′*) all events except for (*1*)	1021	9.9 ± 0.6	0.35 ± 0.08	$0.29 \pm 0.07 \pm 0.06$
(*2*) $1\overleftarrow{p} + 0\overrightarrow{p}$	353	8.9 ± 0.9	0.54 ± 0.15	$0.45 \pm 0.12 \pm 0.09$
(*2′*) all events except for (*2*)	1346	9.8 ± 0.5	0.39 ± 0.07	$0.33 \pm 0.06 \pm 0.07$
(*3*) quasi-two-nucleon events	484	9.1 ± 0.7	0.58 ± 0.12	$0.49 \pm 0.10 \pm 0.10$
(*3′*) all events except for (*3*)	1215	9.9 ± 0.5	0.35 ± 0.07	$0.29 \pm 0.06 \pm 0.06$
(*4*) quasi-deuteron events	285	8.8 ± 0.9	0.75 ± 0.15	$0.62 \pm 0.13 \pm 0.12$
(*4′*) all events except for (*4*)	1414	9.9 ± 0.5	0.37 ± 0.07	$0.31 \pm 0.06 \pm 0.06$

Note: $\overrightarrow{p}$ is proton escaping into the forward hemisphere.

within a wide range of incident energies from several GeV to several hundred GeV (see [12] and references therein).

It should be expected that the relative contributions of different mechanisms of CP production can vary according to the degree of peripherality of the νA interactions. Figure 1 compares the invariant spectra of various samples of events enriched by the peripheral and nonperipheral interactions.

The following criteria were used to select the peripheral interactions: (*1*) events in which CP was accompanied by no more than one noncumulative proton; (*2*) events in which CP was not accompanied by other protons; (*3*) quasi-two-nucleon events, corresponding topologically to neutrino interactions with (pn) and (pp) pairs, in which there was no more than one proton in addition to CP in the final state and the total charge of the final particles (including muon) was $q = 1$ or 2; (*4*) quasi-deuteron events with $q = 1$ from the sample of quasi-two-nucleon events.

The samples *1′–4′* of the nonperipheral events were obtained by eliminating the corresponding peripheral events from the total sample.

The slopes of the invariant spectra of the above samples are summarized in table. To within the experimental error, the values of parameter b are in agreements with each other for all the samples. However, there is some evidence that the spectra of peripheral events drop at a somewhat slower rate with increasing p than do the spectra of the nonperipheral events.

4. CONTRIBUTION OF TWO-NUCLEON CORRELATION MECHANISM

According to TCM, CP are produced due to the interaction of a primary lepton with a correlated nucleon pair, in which the particle momenta are equal in magnitude and opposite in direction. The neutrino is scattered on the nucleon with the momentum directed into the forward hemisphere, while the spectator nucleon escapes into the backward hemisphere with an initial momentum $\mathbf{p}$ due to disruption of the bond between nucleons of the pair. Neutrino scattering on the nucleon moving forward causes an experimentally observed effect of a shift to lower values of the distribution versus the Bjorken variable x and that versus $v \equiv xy = (E_\mu - p_\mu^L)/m$. The latter variable is determined by the kinematic parameters of the muon—the energy E_μ and the longitudinal momentum p_μ^L—and does not require separately measuring the scaling variables x and $y = (E_\nu - E_\mu)/E_\nu$. In this case, the mean value $\langle v_\alpha \rangle$ of the variable v appears to be a linearly decreasing function of the kinematic variable $\alpha = (E - p^L)/m$ of the cumulative proton [2, 6] (where E, p^L, and m are the CP energy, longitudinal momentum, and mass, respectively):

$$\langle v_\alpha \rangle / \langle v \rangle = 2 - \alpha. \tag{1}$$

Here, $\langle v \rangle$ is the mean value of the variable v in the inclusive scattering process, which is determined by averaging over all events without CP (in our experiment, $\langle v\rangle = 0.138$).

The dependence (1) is confirmed by experimental data on the (anti)neutrino scattering on deuterons [6]. In the case of a complex target nucleus, the correlation can be decreased by proton rescattering in the nucleus.

Figure 2 shows the plots of $\langle v_\alpha\rangle/\langle v\rangle$ versus α for all the events considered above, and its approximation by the linear expression

$$\langle v_\alpha\rangle/\langle v\rangle = (1+\beta) - \beta\alpha. \qquad (2)$$

The values of the parameter β characterizing the kinematic correlation between scattered leptons and CPs are listed in table. These data indicate that the degree of correlation is higher for the peripheral events than for the nonperipheral ones and reaches a maximum for the quasi-deuteron events.

Previously, the β parameter was obtained for the νNe ($\bar\nu$Ne) interactions at a minimum momentum of $p^{\min} = 0.35$ GeV/c [6]. The values of $\beta = 0.36 \pm 0.19$ (0.24 ± 0.20) and $\beta = 0.90 \pm 0.26$ (0.69 ± 0.24) were obtained for the total sample and for the peripheral events without protons other than CP, respectively. These values are comparable with the values obtained from our data at $p^{\min} = 0.35$ GeV/c: $\beta = 0.44 \pm 0.06$ for the total sample and $\beta = 0.79 \pm 0.14$ for the sample without accompanying protons.

The relative contribution of TCM to CP production can be estimated using the values of the parameter β presented in table. If we assume that the observed correlations are determined completely by TCM and there are no correlations in the competitive mechanisms, then the relative contributions will be equal to $\beta_{\rm TCM} = \beta$ and $\beta_0 = 1-\beta$, respectively. However, since some of the competitive mechanisms can make a certain contribution as well, the β value determines the upper limit of the relative contribution of TCM, that is, $\beta^{\max}_{\rm TCM} = \beta$. Such processes include multinucleon correlations (involving three or more nucleons) with a weaker dependence [2]:

$$\frac{\langle v_\alpha\rangle}{\langle v\rangle} = \frac{\bar k - \alpha}{\bar k - 1}, \qquad (3)$$

where $\bar k \ge 3$ is the effective number of correlated nucleons from the cluster of which CP escapes. Since the probability of multinucleon correlations is considerably lower than that of the two-nucleon correlations, it can be expected that their total relative contribution is such that $\beta_{\bar k} < \beta_{\rm TCM}$. If CP are produced via the three mechanisms considered above ($\beta_{\rm TCM} + \beta_{\bar k} + \beta_0 = 1$), then the measured parameter β is determined as

$$\beta = \beta_{\rm TCM} + \frac{1}{\bar k - 1}\beta_{\bar k}, \qquad (4)$$

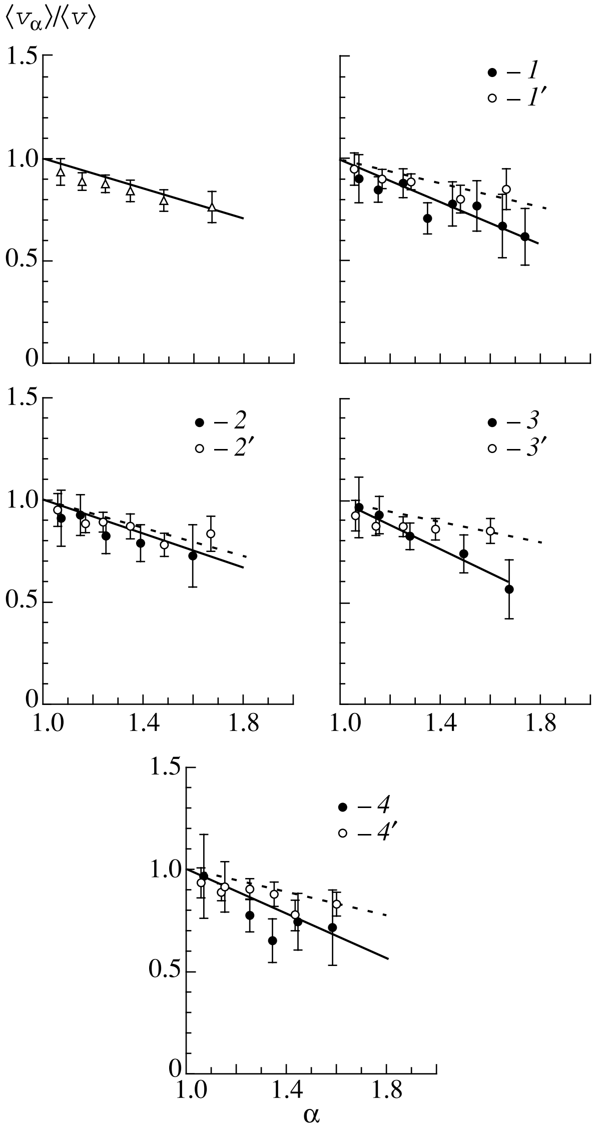

Fig. 2. The plots of $\langle v_\alpha\rangle/\langle v\rangle$ versus α for all events with CP ($\triangle$) and the peripheral and nonperipheral events (samples *1–4* and *1′–4′*, respectively). The notation is presented in the text and table.

from which it follows that $\beta^{\min}_{\rm TCM} = \frac{2}{3}\beta$ (at $\beta_{\bar k} < \beta_{\rm TCM}$ and $\bar k \ge 3$). Combining the upper and lower limits, $\beta^{\max}_{\rm TCM}$ and $\beta^{\min}_{\rm TCM}$, the parameter can be estimated as $\beta_{\rm TCM} = \frac{5}{6}(\beta \pm \Delta\beta) \pm \frac{1}{6}\beta$. This expression takes into account both the statistical uncertainty $\Delta\beta$ and the maximum scattering $\pm\frac{1}{6}\beta$ between the upper and lower limits (the last column of table).

The estimates of the TCM contribution presented in the table do not allow for the fact that a proton produced in the primary interaction event can exhibit rescattering in the nucleus causing attenuation of the

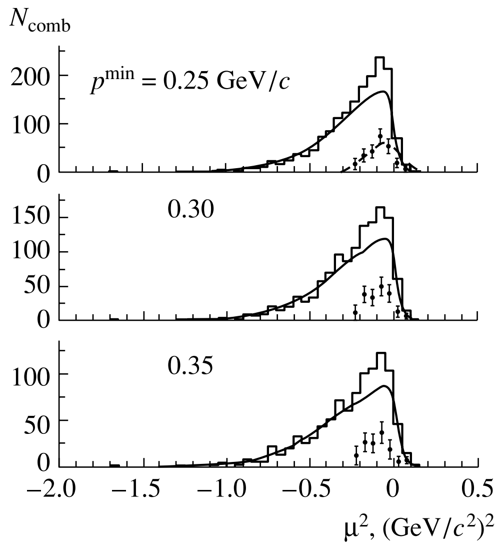

Fig. 3. A distribution with respect to μ^2 for the pairs of protons with the minimum momenta of 0.25, 0.30, and 0.35 GeV/c (the notation is explained in the text).

correlation between $\langle v_\alpha \rangle$ and α. The mean potential proton range in the nucleus is equal to $\bar{l} \simeq 0.75\bar{R}$, where $\bar{R} = 3.6$ fm for the neutrino interacting with a mixture of the C, F, and Br nuclei possessing the mean atomic number $\bar{A} = 27$. For the mean free proton range in the nucleus $\lambda = 5$ fm [14, 15], the rescattering probability is about 0.4. Thus, the estimates of β_{TCM} presented in the table can be underestimated at about 40% for both the total sample and the samples of the nonperipheral interactions. This correction must be substantially lower for the peripheral interactions because of a smaller mean potential proton range and owing to the fact that a secondary interaction can result in an increasing number of protons in the final state, which will correspond topologically to the kind of nonperipheral interactions.

As can be seen from the table, TCM dominates in the quasi-deuteron sample. For this sample, the invariant CP spectrum is characterized by slope parameter $b(pn) = 8.8 \pm 0.9$ (GeV/c)$^{-2}$. Taking into account that the competitive mechanisms (a small admixture of which can be present in the sample of quasi-deuteron events) are characterized by slightly higher values of the slope, then $b(\text{TCM}) \leq b(pn)$ is expected for the TCM slope. A comparison of b(TCM) to a similar parameter of the cumulative (spectator) protons produced in the (anti)neutrino interactions with a free deuteron [6] ($b(d) = 12.8 \pm 2.0$ (GeV/c)$^{-2}$) indicates that the probability of the high-momentum component is greater by a factor of $\exp(p^2/q_0^2)$ for the quasi-deuteron than for the deuteron ($q_0 = 0.50 \pm 0.14$ GeV/c).

5. CONTRIBUTION OF SECONDARY PION ABSORPTION

The basic two-stage mechanism of CP production is absorption of relatively low-energy pions ($p_\pi \leq 0.5$ GeV/c), produced in the primary νN interaction, by a pair of intranuclear nucleons:

$$\pi(NN) \to \overleftarrow{p}N, \tag{5}$$

where one of the protons ($\overleftarrow{p}$) escapes into the backward hemisphere. In a particular case of π^+ meson absorption on a free deuteron ($\pi^+ d \to pp$), the value

$$\mu^2 = (T_1 + T_2)^2 - (\mathbf{p}_1 + \mathbf{p}_2)^2 \tag{6}$$

does not depend on the pion momentum and is equal to $\mu^2 = m_\pi^2$. Here, $T_1, T_2, \mathbf{p}_1$, and $\mathbf{p}_2$ are the kinetic energies and momenta of the final protons. In the case of absorption of the intermediate pion by a pair nucleons bound in the nucleus, the distribution with respect to μ^2 can be shown to have a maximum with a width of $\gamma \approx 2|\mathbf{p}_d(\mathbf{p}_1 + \mathbf{p}_2)|$, which is shifted from m_π^2 to lower values by $\delta \approx 2\Delta E(T_1 + T_2) + p_d^2$, where ΔE is the mean binding energy and p_d is the mean value of the Fermi momentum of the nucleon pair in the nucleus (see the dashed curve in Fig. 3 calculated for the nucleus with $A = 27$ [12]).

We should note that the minimum proton momentum in reaction (5) on a deuteron at rest is equal to $p^{\min} = 0.37$ GeV/c, whereas this value decreases due to the Fermi motion to $p^{\min} = 0.2$–0.25 GeV/c. Therefore, studying the SPA mechanism, we selected events of the reaction

$$\nu A \to \overleftarrow{p} + p + X, \tag{7}$$

containing besides CP at least one proton with a momentum $p > 0.25$ GeV/c flying out into the front hemisphere. The minimum CP momentum was varied between 0.25 and 0.35 GeV/c.

Figure 3 shows the distributions with respect to μ^2 for reaction (7). The solid curves correspond to the combinatorial background obtained by combining protons from various events which fly into the forward and backward hemispheres. The background curve is normalized to the experimental histogram within the range $\mu^2 < -0.25$ (GeV/c^2)^2, where the expected SPA contribution is negligibly small. A difference between the background and experimental distributions has just the same shape as the calculated dashed curve; therefore, it can be related to the SPA mechanism (over the whole range $\mu^2 > -0.25$ (GeV/c^2)^2). The contribution of this mechanism to the inclusive cross section of CP production with momenta $p > p^{\min}$ was $\alpha(\text{SPA}) = 0.15 \pm 0.02$, 0.16 ± 0.02, and 0.14 ± 0.02 at $p^{\min} = 0.25$, 0.3, and 0.35 GeV/c, respectively. We should note that these values are appreciably smaller than the ones in the hadron-nucleus interactions [9–12]: $\alpha(\text{SPA})$ falls within the range between 0.21 ± 0.03 and 0.26 ± 0.04 at $p^{\min} = 0.25$ GeV/c for the light nuclei with $12 \leq A \leq 27$. Such discrepancy is caused probably by the fact that the mean potential length $\bar{l}_\pi$ of the pion passage through the nucleus is slightly shorter for the neutrino interactions than that for the hadron interactions.

The SPA probability can be expected to decrease with increasing peripherality of the interaction—that is, with decreasing $\bar{l}_\pi$. For a sample of relatively peripheral interactions, when there is one pair of nucleons in the final state—that is, when the X state on the right-hand side of expression (7) does not contain identified protons—$\alpha(\text{SPA}) = 0.09 \pm 0.05$ is obtained. It does not contradict the expected attenuation of the role of the SPA mechanism.

Up to this point, we considered SPA corresponding to process (5) with two protons in the final state—that is, $\pi^+(pn) \to \overleftarrow{p}p$ and $\pi^0(pp) \to \overleftarrow{p}p$. It is evident that other processes with CP and neutron production can take place: $\pi^+(nn) \to \overleftarrow{p}n$, $\pi^0(pn) \to \overleftarrow{p}n$, $\pi^-(pp) \to \overleftarrow{p}n$. According to the estimates [9], the contribution of these processes amounts to $\sim 60\%$ of the contribution of process (5) with two protons in the final state. Thus, the total contribution of the SPA mechanism to the inclusive cross section of CP production can be estimated as $\alpha_{NN}(\text{SPA}) = 1.6\alpha(\text{SPA}) = 0.24 \pm 0.03$.

As was mentioned in the preceding section, the estimates based on the observed kinematic correlations can be underestimated, since these correlations can be violated noticeably because of the processes of intranuclear rescattering. Protons produced in reaction $\pi(NN) \to \overleftarrow{p}p$ escape mainly at large angles; their rescattering causes mainly a decrease in the angle of expansion—that is, spreading of the distribution with respect to μ^2 towards negative values and consequent depression of the observed effect.

CONCLUSION

The mechanisms of cumulative proton production due to the interactions of high-energy neutrinos with nuclei are studied. Kinematic correlations, between CP and scattered lepton, caused by the mechanism of two-nucleon correlations, are observed, as well as the correlations, between coupled protons of the pair, which are caused by the mechanism of secondary-pion absorption.

Estimates of the relative contribution of TCM to CP production are obtained. This contribution is $0.36 \pm 0.05 \pm 0.07$ in inclusive production of CPs and increases in the peripheral interactions. In particular, TCM dominates in the quasi-deuteron sample ($\beta_{\text{TCM}} = 0.62 \pm 0.13 \pm 0.12$), which enables one to extract information on the high-momentum component in the quasi-deuteron, its probability being higher by a factor of $\exp(p^2/q_0^2)$ than that in the free deuteron ($q_0 = 0.50 \pm 0.14$ GeV/c). The contribution of the SPA mechanism with due regard to all processes $\pi(NN) \to \overleftarrow{p}N$ is 0.24 ± 0.03 of the inclusive cross section of CP production. This value is noticeably smaller than that for the hadron interactions with the nucleus with $A = 27$.

Both considered mechanisms are responsible for about a half of the inclusive cross section of the CP production: $\beta(\text{TCM} + \text{SPA}) = 0.52 \pm 0.06 \pm 0.14$. In the peripheral interactions, a dominant fraction of CP is produced via these mechanisms.

REFERENCES

1. A. M. Baldin, Fiz. Élem. Chastits At. Yadra **8**, 429 (1977) [Sov. J. Part. Nucl. **8**, 175 (1977)].
2. L. L. Frankfurt and M. I. Strikman, Phys. Rep. **76**, 215 (1981); **160**, 235 (1988).
3. C. E. Carlson *et al.*, Phys. Rev. D **63**, 117 301 (2001).
4. J. P. Berge *et al.*, Phys. Rev. D **18**, 1367 (1978).
5. V. I. Efremenko *et al.*, Phys. Rev. D **22**, 2581 (1980).
6. E. Matsinos *et al.*, Z. Phys. C **44**, 79 (1989).
7. V. V. Ammosov, D. S. Baranov, G. Yu. Grabosh, *et al.*, Yad. Fiz. **43**, 1186 (1986) [Sov. J. Nucl. Phys. **43**, 759 (1986)].
8. D. S. Baranov, V. I. Ermolaev, A. A. Ivanilov, *et al.*, Yad. Fiz. **40**, 1454 (1984) [Sov. J. Nucl. Phys. **40**, 923 (1984)].
9. V. M. Asaturyan, G. R. Gulkanyan, and A. G. Khudaverdyan, Yad. Fiz. **45**, 1059 (1987) [Sov. J. Nucl. Phys. **45**, 657 (1987)]; V. M. Asaturyan, G. R. Gulkanyan, and A. G. Khudaverdyan, Nucl. Phys. A **496**, 770 (1989).
10. D. Armutliĭski, A. P. Gasparyan, V. G. Grishin, *et al.*, Yad. Fiz. **46**, 1712 (1987) [Sov. J. Nucl. Phys. **46**, 1023 (1987)].
11. M. A. Alimov *et al.*, Phys. Rev. D **46**, 45 (1992).
12. N. M. Agababyan *et al.*, Z. Phys. C **66**, 385 (1995).
13. V. V. Ammosov, *et al.*, Fiz. Élem. Chastits At. Yadra **23**, 648 (1992) [Sov. J. Part. Nucl. **23**, 283 (1992)].
14. A. Nadasen *et al.*, Phys. Rev. C **23**, 1023 (1981).
15. J. W. Negele and K. Yazaki, Phys. Rev. D **15**, 71 (1977).

Translated by E. Kozlovskiĭ

Physics of Atomic Nuclei, Vol. 65, No. 9, 2002, pp. 1634–1642. Translated from Yadernaya Fizika, Vol. 65, No. 9, 2002, pp. 1676–1684.
Original Russian Text Copyright © 2002 by Vysotsky, Gaidaenko, Novikov.

ELEMENTARY PARTICLES AND FIELDS
Theory

On Lepton-Pair Production in Neutrino–Nucleus Collisions

M. I. Vysotsky, I. V. Gaidaenko, and V. A. Novikov

Institute of Theoretical and Experimental Physics,
Bol'shaya Cheremushkinskaya ul. 25, Moscow, 117259 RussiaInstitute of Theoretical and Experimental Physics,
Bol'shaya Cheremushkinskaya ul. 25, Moscow, 117259 Russia

Received October 1, 2001

Abstract—A calculation of the cross section for the reaction $\nu\gamma \to \nu\mu^+\mu^-$, which is induced by the neutrino magnetic moment, is described in detail. The expression obtained for this cross section is used to determine the asymptotic behavior of the cross section for the reaction $\nu N \to \nu N\mu^+\mu^-$ by the Weiszäcker–Williams method. It is shown that, upon going over from the nucleus involved to a structureless particle (for example, an electron), the resulting expression is doubled owing to integration with respect to the virtual-photon momentum over the region $m_\mu \ll Q \ll E_\nu$, where the Weiszäcker–Williams approximation is not applicable. The method developed here makes it possible to obtain straightforwardly the known asymptotic expressions for the cross sections describing the reactions $eN \to eN\mu^+\mu^-$ and $e^+e^- \to W^+W^-e^+e^-$. *© 2002 MAIK "Nauka/Interperiodica".*

1. INTRODUCTION

The main objective of this article is to describe in greater detail the results that were previously presented in a concise form in [1] and which were obtained by studying the question of whether it is possible to deduce constraints on the neutrino magnetic moment from data of the CHARM II and CCFR experiments, where the experimentalists observed the production of muon pairs in the scattering of muon neutrinos on target nuclei. A great number of theoretical studies have been devoted to the process $\nu N \to \nu N l^+ l^-$ since the early 1960s (see, for example, [2–13]). Interest in this reaction is explained by the fact that it admits a thorough theoretical analysis. In experiments of the type being discussed, attention is given primarily to the production of muon pairs. For example, the process $\nu_\mu N \to \nu_\mu N\mu^+\mu^-$ was first observed in the neutrino experiment of the CHARM collaboration [14]. Subsequent experiments [15–17] (CHARM II, CCFR, NUTEV) confirmed that the relevant experimental data are in agreement with the predictions of the Standard Model. Among other things, it was established in [16], at a 99% confidence level, that, in this process, neutrino interaction is due not only to the charged but also to the neutral current—specifically, the number of relevant events observed experimentally was one-half as great as that which is predicted by the theory that takes into account only the charged current. Within the Standard Model, this can be explained by the interference between charged and neutral currents. Presently, experimentalists are to address the problem of testing other neutrino features, including the neutrino magnetic moment. The Standard Model predicts a nonzero value of the neutrino magnetic moment (provided that the neutrino has a nonzero mass); that is,

$$\mu_\nu = \frac{3eG_{\rm F}m_\nu}{8\pi^2\sqrt{2}}, \qquad (1)$$

where $G_{\rm F}$ is the Fermi constant and μ_ν and m_ν are the neutrino magnetic moment and the neutrino mass, respectively.

If one takes the present-day constraint on the mass of the muon neutrino, $m_{\nu_\mu} < 0.19$ MeV [18], the resulting limit on its magnetic moment, $\mu_{\nu_\mu} < 6 \times 10^{-14}\mu_{\rm B}$, is much less than that obtained from experiments studying $\nu_\mu e$ scattering, $\mu_{\nu_\mu} < 7 \times 10^{-10}\mu_{\rm B}$ [18]. It was shown in [1] that, according to the results of the CHARM II and CCFR experiments, the constraint on μ_{ν_μ} is even more lenient, $\mu_{\nu_\mu} < 4 \times 10^{-8}\mu_{\rm B}$. It is obvious that the current state of the art in particle experiments will give no way to measure the neutrino magnetic moment if its value is on the same order of magnitude as that which is predicted by the Standard Model. Nonetheless, it is advisable to perform such experiments since the discovery of a large magnetic moment of the neutrino would suggest the presence of new physics.

2. CONTRIBUTION OF THE NEUTRINO MAGNETIC MOMENT TO MUON-PAIR PRODUCTION IN NEUTRINO–PHOTON SCATTERING

In this section, differential and total cross sections for muon-pair production in neutrino–photon scat-

1063-7788/02/6509-1634$22.00 © 2002 MAIK "Nauka/Interperiodica"

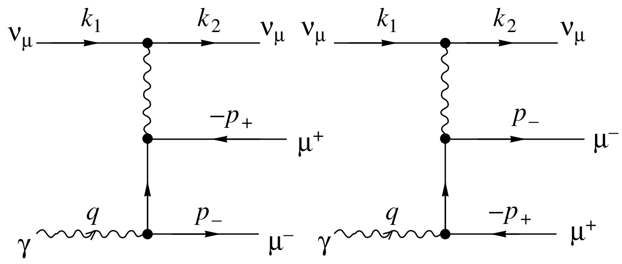

Fig. 1.

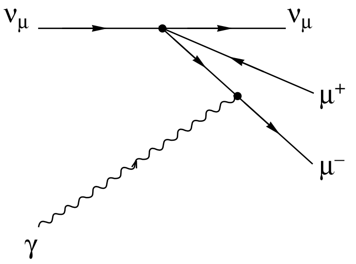

Fig. 2.

tering will be obtained for the case where the neutrino has a nonzero magnetic moment. We assume that the neutrino is a Dirac particle having both a left- and a right-handed component. The process of interest is described by two diagrams (see Fig. 1).

It is noteworthy that the cross section for this process does not interfere with the Standard Model cross section (Fig. 2), because the neutrino changes helicity here.

The neutrino electromagnetic vertex has the form

$$V=\mu_\nu\bar{\nu}\sigma_{\alpha\beta}\nu A_\alpha q_\beta,\quad \sigma_{\alpha\beta}=\frac{1}{2}(\gamma_\alpha\gamma_\beta-\gamma_\beta\gamma_\alpha),\tag{2}$$

where A_α is the 4-potential of an electromagnetic field. Hereafter, we use the following notation: $\alpha=e^2/(4\pi)$ is the fine-structure constant; μ_ν is the neutrino magnetic moment; $g_{\alpha\beta}=(+,-,-,-)$ is the metric tensor in Minkowski space; k_1 and k_2 are, respectively, the initial and the final neutrino momentum, $k_1^2=k_2^2=0$; p_- and p_+ are the momenta of μ^- and μ^+, respectively; q is the real-photon momentum, $-q^2=Q^2=0$; $k=k_1-k_2$ is the virtual-photon momentum; $k_s=k_1+k_2, k_s^2=-k^2=2k_1k_2$, and $k_sk=0$; $P=p_++p_-+k_2=k_1+q, P^2=s$; $p_1=p_--k=q-p_+$ and $p_2=-p_++k=p_--q$ are the momenta of virtual fermion lines; $p=k+q=p_++p_-$; $k=(\omega,\mathbf{k}),p=(\varepsilon,\mathbf{p}),q=(q_0,\mathbf{q})$; $\kappa_i=m^2-p_i^2$, where m is the muon mass; $\kappa_1=2p_+q-q^2$ and $\kappa_2=2p_-q-q^2$; $l=(p_++p_-)^2=p^2$ is the muon-pair invariant mass squared; $t=2kq=\kappa_1+\kappa_2=l-k^2-q^2$; v is the velocity of the product muons in their c.m. frame, $v=|\mathbf{p}'_+|/\varepsilon'_+=\sqrt{1-4m^2/l}$ (the momenta and energies in the $\mu^+\mu^-$ c.m. frame are primed, while those in the c.m. frame of colliding particles are unprimed); $\kappa_{1,2}=(t/2)(1\pm\hat{v}\cos\theta')=t(1\pm\hat{v}x)/2$; $x=\cos\theta', \mathbf{q}'\cdot\mathbf{p}'_-=\cos\theta'\cdot|\mathbf{q}'|\cdot|\mathbf{p}'_-|$, and $\hat{v}^2/v^2=1-4k^2q^2/t^2$; and $do'_\pm=2\pi dx$ is a solid-angle element in the $\mu^+\mu^-$ c.m. frame.

The cross section is calculated by the formula

$$\sigma=\frac{1}{2}\frac{1}{4k_1q}\sum_{f,i}\int|M_{fi}|^2d\tau_3^{(f)},\tag{3}$$

where the factor 1/2 appears because of averaging over the initial state of the photon involved.

Below, we present the expressions for the quantities appearing in (3):

$$4k_1q=2(s+Q^2)=2s;\tag{4}$$

$$\begin{aligned}d\tau_3^{(f)}&=d\tau_2(\mu^+\mu^-)\frac{d\mathbf{k}_2}{2\omega_2(2\pi)^3}\\&=\frac{1}{(4\pi)^2}\frac{1}{2s}dldtv\frac{do'_\pm}{4\pi}\end{aligned}\tag{5}$$

is the phase space of the final state;

$$d\tau_2(\mu^+\mu^-)=\frac{1}{8\pi}v\frac{do'_\pm}{4\pi}\tag{6}$$

is the phase space of the product lepton pair;

$$\sum_{f,i}|M_{fi}|^2=\mu_\nu^2T^{(\nu)}_{\alpha\beta}\frac{1}{(k^2)^2}e^2T^{(\mu)}_{\alpha\beta,\sigma\lambda}e^2(-g_{\sigma\lambda})\tag{7}$$

is the square of the matrix element, where the factors involved are given by

$$T^{(\nu)}_{\alpha\beta}=\mathrm{tr}\left[\hat{k}_2\sigma_{\alpha\mu}k^\mu\hat{k}_1k^\nu\sigma_{\nu\beta}\frac{1+\gamma_5}{2}\right]=k_s^2k_s^\alpha k_s^\beta,\tag{8}$$

$$T^{(\mu)}_{\alpha\beta,\lambda\sigma}=\mathrm{tr}[(\hat{p}_-+m)\,Q_{\alpha\lambda}\,(\hat{p}_+-m)\,Q_{\sigma\beta}],\tag{9}$$

$$Q_{\alpha\lambda}=\gamma_\alpha\frac{1}{\hat{p}_1-m}\gamma_\lambda+\gamma_\lambda\frac{1}{\hat{p}_2-m}\gamma_\alpha,\tag{10}$$

$$\begin{aligned}T^{(\nu)}_{\alpha\beta}\frac{1}{(k^2)^2}T^{(\mu)}_{\alpha\beta,\sigma\lambda}(-g_{\sigma\lambda})&=-4\frac{k_1^\alpha k_1^\beta}{k_s^2}T^{(\mu)}_{\alpha\beta,\lambda\lambda}\\&=16\left\{\left[-\left(\frac{2k_1p_-}{\kappa_2}+\frac{2k_1p_+}{\kappa_1}\right)\right.\right.\\&\left.+\frac{s\left(s-k_s^2\right)-2\cdot2k_1p_+\cdot2k_1p_-}{\kappa_1\kappa_2}\right]\\&+\frac{2m^2}{k_s^2}\left[\left(\frac{2k_1p_-\left(s-2k_1p_+\right)}{\kappa_1^2}\right.\right.\\&\left.+\frac{2k_1p_+\left(s-2k_1p_-\right)}{\kappa_2^2}\right)\end{aligned}\tag{11}$$

$$\left.\left.-\frac{k_s^2+2\cdot 2k_1p_+\cdot 2k_1p_-}{\kappa_1\kappa_2}\right]\right\}.$$

Upon integration with respect to the angles appearing in the element $do'_\pm$ (see Appendix), we obtain [1]

$$\begin{aligned}\frac{d^2\sigma}{dtdl} = \frac{\alpha^2\mu_\nu^2}{\pi s^2}\Bigg\{&\ln\left(\frac{1+v}{1-v}\right)\Bigg\{\frac{1}{t}\left(-s-2m^2\right) \\ &+\frac{1}{t^2}\left(s^2+2sl+2m^2(4s+l)\right) \\ &+\frac{1}{t^3}\left(-2sl(s+l)+2m^2(-4s^2-6sl+4m^2s)\right) \\ &+v\Bigg\{\frac{1}{t}(s+l)+\frac{1}{t^2}\left(-(s+l)^2-6sl\right) \\ &+\frac{1}{t^3}\left(8sl(s+l)+4m^2sl\right) \\ &+\frac{1}{t^4}\left(-8s^2l^2-4m^2s^2l\right)\Bigg\}\Bigg\}.\end{aligned} \tag{12}$$

Expression (12) can be recast into a more comprehensible form if we consider that the tensor $\int T^{(\mu)}_{\alpha\beta,\lambda\lambda}do'_\pm$ can be expressed in terms of two scalar functions T_1 and T_2 depending on the variables t, l, and m^2 rather on s; that is,[1]

$$\begin{aligned}\int T^{(\mu)}_{\alpha\beta,\lambda\lambda}v\frac{do'_\pm}{4\pi} &= T_1\cdot\left(g^{\alpha\beta}-\frac{k^\alpha k^\beta}{k^2}\right) \\ &+T_2\cdot\left(\frac{p^\alpha p^\beta}{(pk)^2}k^2+\frac{k^\alpha k^\beta}{k^2}-\frac{p^\alpha k^\beta+k^\alpha p^\beta}{(pk)}\right) \\ &\times\left(\frac{l+k^2}{l-k^2}\right)^2,\end{aligned} \tag{13}$$

where $2pk = l+k^2, l-k^2 = t$.

By using this expression and the relation $2pk_s = 2s-t$, we can straightforwardly obtain

$$-\frac{k_s^\alpha k_s^\beta}{k_s^2}\int T^{(\mu)}_{\alpha\beta,\lambda\lambda}v\frac{do'_\pm}{4\pi} = -T_1+T_2\frac{(2s-t)^2}{t^2}, \tag{14}$$

$$\frac{d^2\sigma}{dldt} = \frac{\alpha^2\mu_\nu^2}{32\pi s^2}\left[-T_1+T_2\cot\frac{(2s-t)^2}{t^2}\right]. \tag{15}$$

It can easily be seen that expression (12) features precisely this dependence on s. A comparison of formulas (12) and (15) makes it possible to determine the functions T_1 and T_2. the results are given by

$$\begin{aligned}T_2 = 8\Bigg\{&\ln\left(\frac{1+v}{1-v}\right)\left(1-\frac{2(l+4m^2)}{t}+\frac{2(l^2+6m^2l-4m^4)}{t^2}\right) \\ &-v\left(1-\frac{8l}{t}+\frac{(8l^2+4m^2l)}{t^2}\right)\Bigg\},\end{aligned} \tag{16}$$

$$T_1-T_2 = 32\frac{t-l}{t}\left\{\frac{2m^2}{t}\ln\left(\frac{1+v}{1-v}\right)-v\frac{l}{t}\right\}.$$

Finally, we integrate (12) first with respect to t ($l < t < s$) and then with respect to l ($4m^2 < l < s$). For the differential cross section with respect to the invariant mass of the product muon pair and for the total cross section, this yields [1]

$$\begin{aligned}\frac{d\sigma}{dl} = \frac{\alpha^2\mu_\nu^2}{2\pi l}\Bigg\{&\ln\left(\frac{1+v}{1-v}\right) \\ &\times\Bigg[\frac{4}{3}+2\frac{l}{s}\ln\left(\frac{l}{s}\right)-2\frac{l^2}{s^2}+\frac{2}{3}\frac{l^3}{s^3}-\frac{16}{3}\frac{m^4}{l^2} \\ &+4\frac{m^2}{s}+8\frac{m^4}{sl}+\frac{4m^2l}{s^2}\ln\left(\frac{l}{s}\right) \\ &-\frac{4m^2l}{s^2}-\frac{8}{3}\frac{m^4l}{s^3}\Bigg] \\ &+v\Bigg[\frac{2}{3}-6\frac{l}{s}+6\frac{l^2}{s^2} \\ &-\frac{2}{3}\frac{l^3}{s^3}+2\left(\frac{l}{s}+\frac{l^2}{s^2}\right)\ln\left(\frac{s}{l}\right) \\ &-\frac{4}{3}\frac{m^2}{l}\left(\frac{2s^3-3ls^2+l^3}{s^3}\right)\Bigg]\Bigg\},\end{aligned} \tag{17}$$

$$\begin{aligned}\sigma = \frac{\alpha^2\mu_\nu^2}{2\pi}\Bigg\{&\Bigg\{\frac{1}{2}\ln\left(\frac{1+v_m}{1-v_m}\right)\ln\left(\frac{s}{m^2}\right) \\ &+F\left(-\frac{1+v_m}{2}\right)-F\left(-\frac{1-v_m}{2}\right)\Bigg\} \\ &\times\left[\frac{4}{3}+r+\frac{r^2}{4}\right]+\ln\left(\frac{1+v_m}{1-v_m}\right) \\ &\times\left[-\frac{19}{9}+r-\frac{r^2}{4}+\frac{7}{72}r^3\right] \\ &+v_m\left[\frac{46}{27}+\frac{17}{27}r+\frac{7}{36}r^2\right]\Bigg\} \\ =\frac{\alpha^2\mu_\nu^2}{3\pi}\Bigg\{&\ln^2\frac{s}{m^2}-\frac{19}{6}\ln\frac{s}{m^2}\end{aligned} \tag{18}$$

---

[1] The tensor $\int T^{(\mu)}_{\alpha\beta,\lambda\sigma}do'_\pm$ describes lepton-pair production in the scattering of two virtual photons. Apart from a factor, it coincides with the tensor $W_{\alpha\beta,\lambda\sigma}$ introduced in [19], where the tensor $W_{\alpha\beta,\lambda\sigma}$ was expressed in terms of eight scalar functions—this corresponds to the most general case. In this section, we consider the case where one of the photons is real ($q_2^2 = 0$), so that the functions T_1 and T_2 are linear combinations of the functions $W_{TT}|_{q_2^2=0}$ and $W_{ST}|_{q_2^2=0}$ used in [19]. In particular, T_1 coincides, apart from a factor, with $W_{TT}|_{q_2^2=0}$.

$$+\frac{23}{9}-\frac{\pi^2}{3}+O\left(\frac{m^2}{s}\ln^2\left(\frac{s}{m^2}\right)\right)\Bigg\},$$

where $r = 4m^2/s = 1 - v_m^2$ and

$$F(s)=\int\limits_0^s \ln(1+x)\frac{dx}{x} \qquad (19)$$

is the Spens function.

Thus, the cross section in question varies at high energies in proportion to $\ln^2 s$ [1]:

$$\sigma=\frac{\alpha^2\mu_\nu^2}{3\pi}\ln^2(\frac{s}{m^2}). \qquad (20)$$

3. LEADING CORRECTION TO THE CROSS SECTION FOR THE REACTION $\nu N \to \mu^+\mu^-\nu N$ FROM THE NEUTRINO MAGNETIC MOMENT: WEISZÄCKER–WILLIAMS APPROXIMATION

The cross section calculated in the preceding section for neutrino–photon scattering makes it possible to obtain the leading contribution to the cross section for neutrino scattering on a nucleus. For this purpose, we write the exact formula expressing the cross section for scattering on a nucleus in terms of the cross section for scattering on a virtual photon emitted by this nucleus, scattering on the nucleus being considered to be elastic. We have

$$\sigma_{\nu N\to\nu N\mu^+\mu^-}=\frac{1}{2\omega_1}\int a^{00}\frac{(Ze)^2}{(q^2)^2}\frac{d\mathbf{q}}{(2\pi)^3}. \qquad (21)$$

Here, Z is the charge of the nucleus and a^{00} is the (0, 0) component of the tensor $a^{\alpha\beta}$ that is taken in the rest frame of the nucleus and which is used to represent the cross section for scattering on the virtual photon in the form

$$\sigma_{\nu\gamma^*\to\nu\mu^+\mu^-}=\frac{1}{4k_1q}a^{\alpha\beta}e^\alpha e^\beta, \qquad (22)$$

where e^α is the polarization of the virtual photon.

The tensor $a^{\alpha\beta}$ depends on two dimensionless parameters Q^2/s and m^2/s ($Q^2 = -q^2 \neq 0$). The gauge-invariance condition $a^{\alpha\beta}q_\beta = 0$ makes it possible to express $a^{\alpha\beta}$ in terms of two scalar functions as

$$a^{\alpha\beta}=a_1\cdot\left(-g^{\alpha\beta}+\frac{q^\alpha q^\beta}{q^2}\right) \qquad (23)$$
$$+a_2\cdot\left(\frac{s-Q^2}{s+Q^2}\right)^2\left(\frac{P^\alpha q^\beta+q^\alpha P^\beta}{Pq}\right.$$
$$\left.-\frac{q^\alpha q^\beta}{q^2}-\frac{P^\alpha P^\beta}{(Pq)^2}\cdot q^2\right),$$

where $2Pq = s - Q^2$.

The factor $((s - Q^2)/(s + Q^2))^2$ eliminates a spurious pole at $s = Q^2$. There is no pole at $q^2 = 0$ either, so that we have

$$a_2\left(\frac{Q^2}{s},\frac{m^2}{s}\right) \qquad (24)$$
$$=a_1\left(\frac{Q^2}{s},\frac{m^2}{s}\right)\left(1+O\left(\frac{Q^2}{s}\right)\right).$$

Using relation (23) and considering that, in our case (Q is much less than the nuclear mass, and there is only a momentum transfer to the nucleus), $q^0 = 0$ and $P^0 = k_1^0 = \omega_1$, we obtain

$$a^{00}=-a_1+a_2\frac{4\omega_1^2Q^2}{(s+Q^2)^2} \qquad (25)$$
$$=a_1\left(\frac{Q^2}{s},\frac{m^2}{s}\right)\tan^2\theta\cdot\left(1+O\left(\frac{Q^2}{s}\right)\right),$$

where θ is the angle between the vectors $\mathbf{k}_1$ and $\mathbf{q}$ in the rest frame of the nucleus: $s = 2k_1q + q^2 = -2\omega_1 Q\cos\theta - Q^2$ and $\cos\theta = -(s + Q^2)/(2\omega_1 Q)$.

The function $a_1(0, m^2/s)$ can easily be expressed in terms of the cross section for scattering on the virtual photon as

$$\sigma_r=\frac{1}{2s}a_1\left(0,\frac{m^2}{s}\right). \qquad (26)$$

Let us now use the condition that scattering on the nucleus is elastic. It is well known that the nuclear form factor decreases fast at momentum transfers of about the inverse nuclear radius. In (21), we must therefore perform integration with respect to Q up to $Q_{\max} \approx 1/R_A \approx m_\pi A^{-1/3} \sim m$ (R_A is the nuclear radius, and A is the total number of nucleons in the nucleus). Owing to the condition $Q^2_{\max}/s \leq Q^2_{\max}/(4m^2) \lesssim 1$, we can expand the function $a^{00}(Q^2/s, m^2/s)$ for $Q < Q_{\max}$ in a series in Q^2 [see (34)]; that is,

$$a_1\left(\frac{Q^2}{s},\frac{m^2}{s}\right) \qquad (27)$$
$$=a_1\left(0,\frac{m^2}{s}\right)\left(1+O\left(\frac{Q^2}{s}\right)+O\left(\frac{Q^2}{4m^2}\right)\right)$$
$$=a_1\left(0,\frac{m^2}{s}\right)\left(1+O\left(\frac{Q^2}{4m^2}\right)\right),$$

$$a^{00}=a_1\left(0,\frac{m^2}{s}\right)\tan^2\theta\left(1+O\left(\frac{Q^2}{4m^2}\right)\right) \qquad (28)$$
$$=2s\sigma_r\tan^2\theta\left(1+O\left(\frac{Q^2}{4m^2}\right)\right).$$

Substituting this expression into (21), we obtain the cross section for scattering on the nucleus in the form

$$\sigma_{\nu N\to\nu N\mu^+\mu^-} = \frac{2Z^2\alpha}{\pi} \tag{29}$$

$$\times \int\limits_{4m^2}^{s_{\max}} \sigma_r(s) s ds \int\limits_{s/(2\omega_1)}^{Q_{\max}} \frac{dQ}{Q(s+Q^2)^2}\left(1-\cos^2\theta\right)$$

$$\times\left(1+O\left(\frac{Q^2}{4m^2}\right)\right)$$

$$= \frac{2Z^2\alpha}{\pi}\int\limits_{4m^2}^{s_{\max}} \sigma_r(s)\frac{ds}{s}\left[\ln\left(\frac{2\omega_1 Q_{\max}}{s}\right)+O\left(1\right)\right],$$

where $s_{\max} = 2\omega_1 Q_{\max} - Q_{\max}^2 \approx 2\omega_1 Q_{\max}$ if $\omega_1 \gg m$.

That we discarded terms of orders Q^2/s and $\cos\theta$ in the integral with respect to dQ—such terms do not contribute to the leading logarithmic asymptotic behavior—corresponds to the Weizsäcker–Williams approximation [20–23]. To a logarithmic accuracy, formula (29) can be represented in the form

$$\sigma_{\nu N\to\nu N\mu^+\mu^-} = \frac{2Z^2\alpha}{\pi}\int\limits_{m}^{\omega_1}\sigma_r(s)\ln\left(\frac{\omega_1}{\omega}\right)\frac{d\omega}{\omega}, \tag{30}$$

where, by definition, $s = m\omega$. In the Weizsäcker–Williams reference frame, where the neutrino energy is m, ω is the energy of virtual photons from the cloud of a fast nucleus and $dn/d\omega = (2Z^2\alpha/\pi)(1/\omega)\times \ln(\omega_1/\omega)$ is their spectral density.

It should be noted that the disregard of $O(1)$ terms against $\ln(\omega_1/\omega)$ is legitimate only in the case where σ_r does not grow with energy in proportion to s^n, where $n > 0$. In our case, σ_r grows as a logarithm, whence it follows that, upon integration with respect to s, the term $\ln(\omega_1/\omega)$ yields an extra power of $\ln(\omega_1/m)$ [1]; that is,

$$\sigma_{\nu N\to\nu N\mu^+\mu^-} = \frac{2Z^2\alpha}{\pi}\int\limits_{m}^{\omega_1}\frac{\alpha^2\mu_\nu^2}{3\pi} \tag{31}$$

$$\times\ln^2\left(\frac{s}{m^2}\right)\ln\left(\frac{\omega_1}{\omega}\right)\frac{d\omega}{\omega} = \frac{Z^2\alpha^3}{18\pi^2}\mu_\nu^2\ln^4\left(\frac{\omega_1}{m}\right).$$

Expression (31) was used in [1] to deduce a constraint on the muon-neutrino magnetic moment on the basis of data from the CHARM II and CCFR neutrino experiments reported in [15] and [16], respectively. The limits on μ_{ν_μ} that were obtained in [1],

$$\mu_{\nu_\mu} \lesssim 6.5\times10^{-8}\mu_{\rm B} \text{ according to the CHARM II data,} \tag{32}$$

$$\mu_{\nu_\mu} \lesssim 4.0\times10^{-8}\mu_{\rm B} \text{ according to the CCFR data,} \tag{33}$$

appeared to be approximately two orders of magnitude greater than those that follow from experiments that studied $\nu_\mu e$ scattering [18]. In order to strengthen the above constraints on the neutrino magnetic moment by two orders of magnitude, it is necessary to improve the accuracy of cross-section measurements by four orders of magnitude. But for this, an eight order of magnitude enlargement of statistics is required ($\Delta\sigma \sim 1/\sqrt{N}$), which is hardly possible at present.

The Weiszäcker–Williams approximation used here is valid for the case of scattering on a nucleus, where the nuclear form factor cuts off the region of integration with respect to Q at $Q_{\max}$. If there is no such cutoff (for example, in the case of scattering on an electron), integration with respect to Q must be performed up to ω_1. In this case, the expansion in (28) is no longer correct since the quantity σ_r must be replaced by the cross section for scattering on a virtual photon at $Q > m$. The calculations demonstrate that, if we include the region $m < Q < \omega_1$, the cross section appears to be twice as large as that given by (31) (if the form factor of a particle is independent of Q). In calculating the cross section for this reaction with allowance for $Q^2 \neq 0$ (virtual initial photon), integration is actually performed with respect to $\hat{\ell} = l + Q^2$ rather than with respect to l (see Appendix); therefore, the quantity $\hat{\ell}_{\rm min} = 4m^2 + Q^2$ will be the cutoff parameter for the cross section describing the reaction $\gamma^*\nu \to \nu l^+l^-$ [compare with (20)]; that is,

$$\sigma_{\gamma^*\nu\to\nu l^+l^-} = \frac{\alpha^2\mu_\nu^2}{3\pi}\ln^2\frac{\hat{s}}{4m^2+Q^2}, \tag{34}$$

where $\hat{s} = s + Q^2$. [As a matter of fact, this formula represents an interpolation between (20) and (A.17).]

In order to obtain the contribution to the cross section from the region $2m < Q < 2\omega_1$, it is sufficient to use the first equality in (29). The result is

$$\sigma^{(2)} = \frac{2Z^2\alpha}{\pi}\int\limits_{2m}^{2\omega_1}\frac{dQ}{Q}\int\limits_{Q^2}^{2\omega_1 Q}\frac{d\hat{s}}{\hat{s}}\sigma_{\gamma^*\nu\to\nu l^+l^-}(\hat{s}) \tag{35}$$

$$= \frac{Z^2\alpha^3}{18\pi^2}\mu_\nu^2\ln^4\left(\frac{\omega_1}{m}\right).$$

One can see that, if we distract our attention from the nuclear form factor for the time being, the total cross section will be the sum of expressions (31) and (35). This differs radically from the case where a lepton pair is produced in the scattering of two charged particles and where the region $Q > m$ is not logarithmic. This is because, in charged-particle scattering on a virtual photon, the cross section behaves as $1/\hat{\ell}_{\min}$, so that, at $Q > m$, an extra power of Q^2 from $\hat{\ell}_{\min}$ cuts off the logarithmic integral $\int dQ/Q$. It should be emphasized that, at $Q > m$, the Weiszäcker–Williams approximation is not valid.

4. CONCLUSION

We have demonstrated that the cross section for the lepton-pair production in a reaction where a neutral particle having a nonzero magnetic moment is scattered on a nucleus grows with energy in proportion to $\ln^4 E$. It is well known [19, 24] that the cross section for a similar process induced by the scattering of two charged particles grows with energy only in proportion to $\ln^3 E$. This can easily be tested by considering the example of the reaction $eN \to e\mu^+\mu^- N$ and by using the results obtained here. The entire procedure reduces to making the substitution $\mu_\nu^2 T_{\alpha\beta}^{(\nu)} \to e^2 T_{\alpha\beta}^{(e)}/2$, where

$$T_{\alpha\beta}^{(e)} = tr\left[(\hat{k}_2 + m_e)\gamma_\alpha(\hat{k}_1 + m_e)\gamma_\beta\right] \qquad (36)$$
$$= 2\left[2(k_1^\alpha k_2^\beta + k_2^\alpha k_1^\beta) + k^2\gamma^{\alpha\beta}\right].$$

The analog of formula (15) for the reaction $\gamma e \to \mu^+\mu^- e$ has the form

$$\left(\frac{d^2\sigma}{dldt}\right)_{\gamma e \to \mu^+\mu^- e} = \frac{\alpha^3}{4s^2}\frac{1}{-k^2} \qquad (37)$$
$$\times \left[T_1\left(\frac{4m^2}{t}, \frac{k^2}{t}\right) + \frac{2s(s-t)}{t^2}T_2\left(\frac{4m^2}{t}, \frac{k^2}{t}\right)\right],$$

where $-k^2 = t - l$.

This expression has a nonintegrable singularity for $-k^2 \to 0$; therefore, we must take into account the electron mass m_e. In the case of $m_e \ll m$, we have

$$(-k^2)_{\min} \approx m_e^2 \frac{l^2}{s(s-l)}. \qquad (38)$$

By integrating expression (37), we can prove that, at high energies, the cross section for the process $\gamma e \to \mu^+\mu^- e$ varies in proportion to $\ln s$:

$$\sigma_{\gamma e \to \mu^+\mu^- e} = \frac{\alpha^3}{4s^2}\int\limits_{4m^2}^{s} dl \int\limits_{l+(-k^2)_{\min}}^{s} \frac{dt}{-k^2}\frac{2s^2}{t^2} \qquad (39)$$
$$\times \left(1 + O\left(\frac{t}{s}\right)\right) T_2\left(\frac{4m^2}{l}, 0\right)\left(1 + O\left(\frac{k^2}{t}\right)\right)$$
$$\to \frac{\alpha^3}{4m^2}\ln\left(\frac{s}{m_e m}\right)\int\limits_1^\infty \frac{dx}{x^2}T_2\left(\frac{1}{x}, 0\right)$$
$$= \frac{28\alpha^3}{9m^2}\ln\frac{s}{m_e m}\Big), \text{for } s \to \infty.$$

Accordingly, the cross section for the process $eN \to eN\mu^+\mu^-$ grows in proportion to $\ln^3 E_e$ (see [24, 19]); that is,

$$\sigma_{eN \to eN\mu^+\mu^-} \qquad (40)$$
$$= \int \sigma_{\gamma e \to \mu^+\mu^- e}(\omega)\frac{2Z^2\alpha}{\pi}\frac{d\omega}{\omega}\ln\left(\frac{E_e}{\omega}\right)$$
$$\to \frac{28}{27\pi}\frac{Z^2\alpha^4}{m^2}\ln^3\left(\frac{E_e}{m}\right),$$

where $s = \omega m$ and E_e is the energy of the electron incident on the nucleus in the c.m. frame of the nucleus.

In conclusion, we would like to note that, in the literature, there is an example of a $2 \to 4$ process ($e^+e^- \to e^+e^-W^+W^-$) whose cross section has the $\ln^4 E$ asymptotic behavior [19, 25]. There, however, the mechanism is totally different from that considered in the present article. The point is that, for $E \gg m_W$, the cross section for the reaction $\gamma\gamma \to W^+W^-$ approaches a constant [19, 25],

$$\sigma_{\gamma\gamma \to W^+W^-} \approx \frac{8\pi\alpha^2}{m_W^2}, \qquad (41)$$

while the cross section $\sigma_{\gamma\gamma \to \mu^+\mu^-}$ decreases with energy in proportion to $(\ln E^2)/E^2$. Formula (37) enables us to prove that the cross section $\sigma_{e^+e^- \to e^+e^-W^+W^-}$ does indeed have the $\ln^4 E$ asymptotic behavior. By using the relation

$$\sigma_{\gamma\gamma \to X} = \frac{\pi\alpha^2}{2l}T_1\left(\frac{4m^2}{l}, 0\right) \qquad (42)$$

to express T_i in (37) in terms of the cross section $\sigma_{\gamma\gamma \to W^+W^-}$ ($X = W^+W^-$), we obtain

$$\left(\frac{d^2\sigma}{dldt}\right)_{\gamma e \to W^+W^- e} = \frac{\alpha^3}{4s^2}\frac{1}{-k^2}\left[1 + \frac{2s(s-t)}{t^2}\right] \qquad (43)$$
$$\times \frac{2l}{\pi\alpha^2}\sigma_{\gamma\gamma \to W^+W^-}\left(1 + O\left(\frac{k^2}{t}\right)\right)$$
$$= \frac{\alpha}{\pi}\cdot\frac{1}{l}\left(1 - \frac{l}{s} + \frac{l^2}{2s^2}\right)\frac{1}{-k^2}$$
$$\times \sigma_{\gamma\gamma \to W^+W^-}\left(1 + O\left(\frac{k^2}{t}\right)\right).$$

Under the condition $\ln(s/m_e^2) \gg \ln(s/m_W^2) \gg 1$, the factor $\ln(s/m_e^2)$ can be isolated in the integrals

$\int dk^2/k^2$ and $\int dq^2/q^2$; that is,

$$\int \frac{dl\,dt}{-k^2}\left(1+O\left(\frac{k^2}{t}\right)\right) \tag{44}$$

$$= \left(\ln\left(\frac{s}{m_e^2}\right)+O\left(\ln\frac{s}{m_W^2}\right)\right)\int dl.$$

As a result, the expression for $\sigma_{e^+e^-\to e^+e^-W^+W^-}$ takes the form (see [19, 25])

$$\sigma_{e^+e^-\to e^+e^-W^+W^-} \tag{45}$$

$$\approx \left(\frac{\alpha}{\pi}\ln\left(\frac{s}{m_e^2}\right)\right)^2 \int\limits_{4m_W^2}^{s} \frac{ds'}{s'}\left(1-\frac{s'}{s}+\frac{s'^2}{2s^2}\right)$$

$$\times \int\limits_{4m_W^2}^{s'} \frac{dl}{l}\left(1-\frac{l}{s'}+\frac{l^2}{2s'^2}\right)\sigma_{\gamma\gamma\to W^+W^-}(l)$$

$$\approx \left(\frac{\alpha}{\pi}\right)^2 \ln^2\left(\frac{s}{m_e^2}\right)\sigma_{\gamma\gamma\to W^+W^-}(s)$$

$$\times \int\limits_{4m_W^2}^{s}\frac{ds'}{s'}\int\limits_{4m_W^2}^{s'}\frac{dl}{l} = \frac{4\alpha^4}{\pi m_W^2}\ln^2\left(\frac{s}{m_e^2}\right)\ln^2\left(\frac{s}{m_W^2}\right).$$

ACKNOWLEDGMENTS

We are grateful to L.B. Okun and A.N. Rozanov for stimulating discussions and enlightening advice.

This work was supported by the Russian Foundation for Basic Research (project no. 00-15-96562).

APPENDIX

Integrals over the Phase Space of a Lepton Pair

In Section 2, we integrated the matrix element over the the phase space of the product lepton pair. In this section of the Appendix, we present expressions for all integrals required for this.

Let us recall that the phase space of a lepton pair has the form

$$d\tau_2(l^+l^-) = \frac{1}{8\pi}v\frac{do'_\pm}{4\pi}. \tag{A.1}$$

The integrals presented below correspond to the case of $q^2=0$:

$$\int \frac{do'_\pm}{4\pi} = 1, \tag{A.2}$$

$$\int v\frac{do'_\pm}{4\pi}\frac{t}{\kappa_i} = \ln\left(\frac{1+v}{1-v}\right), \tag{A.3}$$

$$\int v\frac{do'_\pm}{4\pi}\frac{t^2}{\kappa_1\kappa_2} = 2\ln\frac{1+v}{1-v}, \tag{A.4}$$

$$\int \frac{do'_\pm}{4\pi}\frac{t^2}{\kappa_i^2} = \frac{l}{m^2}, \tag{A.5}$$

$$\int v\frac{do'_\pm}{4\pi}\frac{2k_1p_+}{\kappa_1} = \frac{sl}{t^2}\ln\left(\frac{1+v}{1-v}\right) + \left(-\frac{2sl}{t^2}+\frac{s+l}{t}-1\right)v, \tag{A.6}$$

$$\int v\frac{do'_\pm}{4\pi}\frac{2k_1p_-\cdot t}{\kappa_1^2} = \left(\frac{2sl}{t^2}-\frac{s+l}{t}+1\right)\ln\left(\frac{1+v}{1-v}\right) + \frac{1}{m^2}\cdot\left(-\frac{sl^2}{t^2}+\frac{(s+l)l}{t}-l\right)v, \tag{A.7}$$

$$\int v\frac{do'_\pm}{4\pi}\frac{2k_1p_-\cdot 2k_1p_+}{\kappa_1\kappa_2} = 2sl\left(1+\frac{2m^2}{l}\right) \times\left(-\frac{sl}{t^4}+\frac{s+l}{t^3}-\frac{1}{t^2}\right)\ln\left(\frac{1+v}{1-v}\right) + \left(\frac{6s^2l^2}{t^4}-\frac{6sl(s+l)}{t^3} + \frac{6sl+(s+l)^2}{t^2}-\frac{2(s+l)}{t}+1\right)v, \tag{A.8}$$

$$\int v\frac{do'_\pm}{4\pi}\frac{2k_1p_-\cdot 2k_1p_+}{\kappa_1^2} \tag{A.9}$$

$$= \left(\frac{6s^2l^2}{t^4}-\frac{6sl(s+l)}{t^3}+\frac{6sl+(s+l)^2}{t^2} - \frac{2(s+l)}{t}+1\right)\ln\left(\frac{1+v}{1-v}\right) + \left(sl\left(8+\frac{4m^2}{l}\right) \times\left(-\frac{sl}{t^4}+\frac{s+l}{t^3}-\frac{1}{t^2}\right) + \left(-\frac{(s+l)^2}{t^2}+\frac{2(s+l)}{t}-1\right)\right)v.$$

The relation $2k_1p_+ + 2k_1p_- = s+k^2$ is also useful.

4.1. Cross Section for the Reaction $\gamma^*\nu\to\nu\mu^+\mu^-$ at High Virtualities γ^*

Below, we present a derivation of formula (34).

We begin by indicating that, at $-q^2=Q^2\neq 0$, expression (15) takes the form

$$\frac{d^2\sigma}{dl\,dt} = \frac{\alpha^2\mu_\nu^2}{32\pi\hat{s}^2}\left[-\hat{T}_1+\hat{T}_2\frac{(2\hat{s}-t)^2}{t^2}\right], \tag{A.10}$$

where $\hat{s}=2k_1q=s+Q^2$; $t=2kq=l-q^2-k^2=\hat{\ell}-k^2$; $\hat{\ell}=l+Q^2$; and the function $\hat{T}_i$ depends on the variables $4m^2/t, l/t$, and Q^2/t. Thus, we have

$$\sigma = \frac{\alpha^2\mu_\nu^2}{8\pi}\int\limits_{4m^2}^{s} dl \int\limits_{\hat{\ell}}^{\hat{s}+Q^2(s-l)/s} \frac{dt}{t^2} \tag{A.11}$$
$$\times\left(1+O\left(\frac{t}{\hat{s}}\right)\right)\hat{T}_2\left(\frac{4m^2}{t},\frac{l}{t},\frac{Q^2}{t}\right).$$

The function $\hat{T}_2$ cannot be expanded in a series in Q^2/t since it has the logarithmic singularity $\ln(\hat{\ell}/Q^2)$. In order to demonstrate this, we note that the doubly logarithmic behavior of the total cross section is due to $O(\hat{s}^2/\kappa_1\kappa_2)$ terms in the matrix element [see (11)], $O(\hat{s}t/\kappa_1\kappa_2)$ leading only to corrections of order $\sim\ln s$. On the basis of expression (11), we conclude that the leading contribution comes from the term

$$\frac{(\hat{s}+k^2)^2 - 2\cdot 2k_1p_+\cdot 2k_1p_-}{\kappa_1\kappa_2} \tag{A.12}$$
$$= \frac{(2k_1p_+)^2+(2k_1p_-)^2}{\kappa_1\kappa_2} = \lambda\cdot\frac{(\hat{s}+k^2)^2}{\kappa_1\kappa_2}$$
$$= \lambda\frac{\hat{s}^2}{\kappa_1\kappa_2}\left(1+O\left(\frac{k^2}{\hat{s}}\right)\right),$$

the function λ changing within the interval $1/2 \le \lambda \le 1$. Since, for $Q^2 \neq 0$, we have $\kappa_i = t(1\pm\hat{v}x)/2$, where

$$\frac{\hat{v}^2}{v^2} = 1 - \frac{4k^2q^2}{t^2}, \tag{A.13}$$

expression (A.12) can be reduced to the following form upon averaging over the phase space of the lepton pair:

$$\int v\frac{do'_\pm}{4\pi}\cdot\frac{(2k_1p_+)^2+(2k_1p_-)^2}{\kappa_1\kappa_2} \tag{A.14}$$
$$= \frac{v}{\hat{v}}\bar{\lambda}\frac{\hat{s}^2}{t^2}2\ln\left(\frac{1+\hat{v}}{1-\hat{v}}\right)\left(1+O\left(\frac{k^2}{\hat{s}}\right)\right).$$

We note that the function $\bar{\lambda}$ depends on the same variables as the quantity $\hat{T}_i$ and changes within the interval $1/2 \le \bar{\lambda} \le 1$ and that, at $m^2 = Q^2 = 0$, $\bar{\lambda}\ln[(1+\hat{v})/(1-\hat{v})]$ reduces to the analogous term in the expression for the function $T_2/8$ [see (16)]:

$$\bar{\lambda}\left(\frac{4m^2}{t},\frac{l}{t},\frac{Q^2}{t}\right)\bigg|_{m^2=Q^2=0} \tag{A.15}$$
$$= \bar{\lambda}\left(0,\frac{l}{t},0\right) = 1 - \frac{2l}{t} + \frac{2l^2}{t^2}.$$

In the region $2m < Q < 2\omega_1$, the function $\hat{T}_2$ can therefore be represented in the form

$$\hat{T}_2 = 8\frac{v}{\hat{v}}\cdot\bar{\lambda}\left(0,\frac{l}{t},0\right)\left(\ln\left(\frac{1+\hat{v}}{1-\hat{v}}\right)+O(1)\right) \tag{A.16}$$
$$\times\left(1+O\left(\frac{Q^2}{t}\right)\right).$$

Substituting (A.16) into (A.11), we obtain the expression for σ at $Q \gg m$ in the form

$$\sigma = \frac{\alpha^2\mu_\nu^2}{8\pi}\int\limits_{Q^2}^{\hat{s}}\frac{d\hat{\ell}}{\hat{\ell}}\int\limits_{1}^{\hat{s}/\hat{\ell}}\frac{dy}{y^2}\left(1+O\left(y\frac{\hat{\ell}}{\hat{s}}\right)\right) \tag{A.17}$$
$$\times 8\frac{v}{\hat{v}}\left(\ln\left(\frac{\hat{\ell}}{Q^2}\right)+\ln\left(\frac{y^2}{y-1}\right)+O(1)\right)$$
$$\times\bar{\lambda}\left(0,\frac{1}{y},0\right)\left(1+O\left(\frac{Q^2}{t}\right)\right)$$
$$= \frac{\alpha^2\mu_\nu^2}{\pi}\left[\int\limits_{Q^2}^{\hat{s}}\frac{d\hat{\ell}}{\hat{\ell}}\ln\left(\frac{\hat{\ell}}{Q^2}\right)\int\limits_{1}^{\infty}\frac{dy}{y^2}\bar{\lambda}\left(0,\frac{1}{y},0\right)\right.$$
$$\left.+O\left(\ln\left(\frac{\hat{s}}{Q^2}\right)\right)\right] = \frac{\alpha^2\mu_\nu^2}{3\pi}\left[\ln^2\left(\frac{\hat{s}}{Q^2}\right)\right.$$
$$\left.+O\left(\ln\left(\frac{\hat{s}}{Q^2}\right)\right)\right].$$

REFERENCES

1. I. V. Gaidaenko, V. A. Novikov, and M. I. Vysotsky, hep-ph/0007204; Phys. Lett. B **497**, 49 (2001).
2. A. M. Badalyan and Chzhou Guan-chzhao, Zh. Éksp. Teor. Fiz. **38**, 664 (1960) [Sov. Phys. JETP **11**, 477 (1960)].
3. M. A. Kozhushner and E. P. Shabalin, Zh. Éksp. Teor. Fiz. **41**, 949 (1961) [Sov. Phys. JETP **14**, 676 (1962)].
4. I. Yu. Kobzarev and L. B. Okun', Zh. Éksp. Teor. Fiz. **41**, 1205 (1961) [Sov. Phys. JETP **14**, 859 (1962)].
5. E. P. Shabalin, Zh. Éksp. Teor. Fiz. **43**, 175 (1962) [Sov. Phys. JETP **16**, 125 (1963)].
6. W. Czyz and J. D. Walecka, Phys. Lett. **8**, 77 (1964).
7. W. Czyz, G. G. Sheppey, and J. D. Walecka, Nuovo Cimento **34**, 404 (1964).
8. M. S. Marinov, Yu. P. Nikitin, Yu. P. Orevkov, and E. P. Shabalin, Yad. Fiz. **3**, 678 (1966) [Sov. J. Nucl. Phys. **3**, 497 (1966)].
9. A. É. Asratyan and M. A. Kubantsev, Yad. Fiz. **25**, 1051 (1977) [Sov. J. Nucl. Phys. **25**, 558 (1977)].
10. R. W. Brown, R. H. Hobbs, J. Smith, and N. Stanko, Phys. Rev. **6**, 3273 (1972).
11. K. Fujikawa, Phys. Rev. D **8**, 1623 (1973).
12. A. E. Asratyan, Preprint No. ITEP-113, ITEP (Moscow, 1979).
13. R. Belusevic and J. Smith, Phys. Rev. D **37**, 2419 (1988).
14. F. Bergsma *et al.*, Phys. Lett. B **122B**, 185 (1983).

15. G. Geiregat *et al.*, Phys. Lett. B **245**, 271 (1990).
16. S. R. Mishra *et al.*, Phys. Rev. Lett. **66**, 3117 (1991).
17. T. Adams *et al.*, hep-ex/9811012.
18. Particle Data Group (D. E. Groom *et al.*), Eur. Phys. J. C **15**, 25 (2000).
19. V. M. Budnev, I. F. Ginzburg, G. V. Meledin, and V. G. Serbo, Phys. Rep. C **15**, 181 (1975).
20. C. Weizsäcker, Z. Phys. B **88**, 612 (1934).
21. E. Williams, Phys. Rev. **45**, 729 (1934).
22. I. Ya. Pomeranchuk and I. M. Shmuskevich, Nucl. Phys. **23**, 452 (1961).
23. V. N. Gribov, V. A. Kolkunov, L. B. Okun', and V. M. Shekhter, Zh. Éksp. Teor. Fiz. **41**, 1839 (1961) [Sov. Phys. JETP **14**, 1308 (1962)].
24. L. D. Landau and E. M. Lifshitz, Phys. Z. Sowjetunion **6**, 244 (1934).
25. O. P. Sushkov, V. V. Flambaum, and I. B. Khriplovich, Yad. Fiz. **20**, 1016 (1974) [Sov. J. Nucl. Phys. **20**, 537 (1975)].

Translated by A. Isaakyan

Physics of Atomic Nuclei, Vol. 65, No. 9, 2002, pp. 1643–1656. Translated from Yadernaya Fizika, Vol. 65, No. 9, 2002, pp. 1685–1700.
Original Russian Text Copyright © 2002 by Almaliev, Kopytin, Shikhalev.

ELEMENTARY PARTICLES AND FIELDS
Theory

Off-Shell Behavior of the Scattering Amplitude and the Structure of NN Potentials

A. N. Almaliev, I. V. Kopytin, and M. A. Shikhalev[*]

Voronezh State University, Universitetskaya pl. 1, Voronezh, 394893 Russia

Received July 18, 2001; in final form, December 6, 2001

Abstract—We perform calculations and comparative analysis of the off-shell scattering matrices and related $pp \to pp\gamma$ reaction observables for various types of NN potentials—with forbidden states and with short-range repulsion. The emphasis is on studying the effects of the shape and depth of the central part of forbidden-state potentials on the behavior of the above quantities and on establishing the role of meson-exchange components in the NN interaction. We show that, when using potentials that give a good description of phase shifts and the proper behavior of the scattering matrix for low momentum transfers, the reaction $pp \to pp\gamma$ does not allow the choice between the potentials to be made, at least up to a proton energy of 400 MeV in the laboratory frame. © *2002 MAIK "Nauka/Interperiodica".*

1. INTRODUCTION

Progress in many fields of strong-interaction physics depends on the understanding of the internal mechanisms underlying a particular phenomenon. One of the most fundamental and, perhaps, most accessible processes that are capable of uncovering the mechanisms of subhadron dynamics and that have a direct bearing on the properties of nuclei and nuclear matter is NN interaction.

Since the discovery of vector mesons, single-boson exchange models (among recent papers, see, e.g., [1, 2]) have acquired the greatest popularity. In these models, a set of exchange processes involving the various types of mesons included in parametrization corresponds to the NN potential. More advanced multiboson exchange models [3, 4] also include two-meson exchange processes and take into account the contribution from Δ degrees of freedom. All meson-exchange models describe elastic scattering of nucleons well at low energies (up to 350 MeV in the laboratory frame, lab) and, qualitatively, up to energies ~1 GeV [3, 5]. They can also account for such subtle effects as the violation of charge symmetry, charge independence, etc. [6]. At the same time, these models have a number of drawbacks. There is no doubt that the meson picture becomes inadequate at collision energies when subhadron degrees of freedom, including quark ones, come into play. In addition, meson-exchange models are internally inconsistent even at low energies. Therefore, they may be considered, from the viewpoint of quantum chromodynamics (QCD), only as an efficient method for describing NN interactions. Finally, yet another major drawback is the use of phenomenological form factors and coupling constants of some mesons (e.g., ω and σ mesons). In general, the cutoff parameters in the form factors prove to be significantly overestimated compared to those inferred directly from experiments on meson—nucleon dynamics and from QCD predictions. As a result, using meson-exchange potentials to describe more complex processes than elastic NN scattering cannot be considered to be strictly justified (e.g., for processes that require allowance for meson-exchange currents). In recent years, all these factors have stimulated the development of NN-interaction models that, while based on QCD methods, included quark degrees of freedom and the corresponding symmetries. Among these, the various versions of the quark cluster model (QCM) became most popular.

Chiral invariance is known to be one of the heuristic symmetry principles of nonperturbative low-energy chromodynamics. Its spontaneous violation results in a certain type of interaction between quarks through scalar and pseudoscalar Goldstone bosons; while interacting with a QCD vacuum, the quarks themselves acquire a constituent mass. The advantage of the constituent quark model is that only a few physically meaningful parameters can be used to describe processes involving hadrons. The latter favorably distinguishes them from the phenomenological parameters of meson-exchange potentials.

Among major achievements of the models in which, apart from confinement, the interaction between quarks is effected by Goldstone meson exchange, we can point out the justification of the weak

---

[*] e-mail: `shehalev@phys.vsu.ru`

spin–orbit splitting and the proper sequence of levels with negative and positive parity in the hadron spectrum [7]. Based on the QCM [8, 9], it was also shown that, if antisymmetrization in quark variables is taken into account, the pseudoscalar interaction leads to short-range repulsion, which was previously thought to be the result of single-gluon exchange between quarks. This gave grounds to diminish the role of the single-gluon interaction and, thus, to explain the large mass difference between the $N(939)$ nucleon and its chiral partner $N^*(1535)$. Unfortunately, the QCM-based description of elastic NN scattering at collision energies below the π-meson production threshold is still qualitative. The problem is that, because of the weak spin–orbit interaction (there are no vector mesons and the single-gluon-exchange interaction is suppressed), the model is incapable of reproducing the strong splitting in the ^3P_J channel. In addition, the mixing parameters ϵ_1 and ϵ_2 in this model can be reproduced only at very low nucleon energies [9], suggesting that there is another physical mechanism responsible for the additional tensor short-range interaction.

Based on the theoretical-group approach, the authors of [10] proposed a slightly different NN-interaction model for a six-quark ($6q$) system. The essence of this model lies in different dynamics of the quark configurations $|s^4p^2[42]_xL = 0, 2\rangle$, $|s^3p^3[33]_xL = 1, 3\rangle$ and $|s^6[6]_xL = 0\rangle$, $|s^5p^1[51]_xL = 1\rangle$. Whereas the first two configurations have a cluster structure and are projected mainly on the NN channel, the third and fourth configurations, being the most symmetric, have the structure of a quark bag with a large weight of the $\Delta\Delta$ and CC (color dipole) states. As a result, the NN scattering wave function has a short-range node, which results from the condition for orthogonality of the cluster wave function and the wave function of the $6q$ compound state. It follows from QCM-based calculations [8, 9] that allowance for the coupling between the NN and $\Delta\Delta$ channels gives rise to additional short-range attraction. However, this coupling is weak, and, therefore, the effect is marginal. The possible existence of $\Delta\Delta$ dibaryons with spins $S = 0$ and 3 [11], which are strongly coupled with the channels $\Delta\Delta \to NN\pi\pi$ and $\Delta\Delta \to N\Delta\pi$ and which have large widths, also follows from the QCM. In addition, because of the increase in the density (or temperature) of $6q$ states with maximum symmetry $|s^6\rangle$ and $|s^5p^1\rangle$, chiral symmetry can be partially restored. This gives rise to additional attraction in the $6q$ system and, as a result, to stabilization of the above configurations [12]. In this case, the QCM may prove to be unsuitable for describing these states. In other words, the transitions $|s^4p^2\rangle \to |s^6\rangle + \sigma$ (or ρ), $NN \to \Delta\Delta\pi\pi$ ($\Delta\Delta\sigma$ or $\Delta\Delta\rho$), and $NN \to N\Delta \to \Delta\Delta\pi$ (the σ and ρ mesons are $\pi\pi$ resonances with $J = 0$ and 1, respectively) can give rise to strong short-range ($r < 1$ fm) attraction in the NN system. The model in which a virtual σ or ρ meson acting as a stimulator for transitions from the $|s^4p^2\rangle$ ($|s^3p^3\rangle$) configuration to the $|s^6\rangle$ ($|s^5p^1\rangle$) configuration is emitted simultaneously with the transition $NN \to \Delta\Delta$ is a microscopic basis for the so-called forbidden-state potentials (FSPs) [10, 13–15].

Of course, apart from short-range quark effects, realistic NN potentials must also take into account ordinary single- and two-meson exchange mechanisms. Basically, the approach based on the hadron quark structure and meeting the chiral symmetry requirements allows only a few parameters to be used to describe a broad range of phenomena. However, the resulting NN potentials are rather complex in structure (nonlocal, energy-dependent), which significantly hampers their use, in particular, when studying the properties of systems with a few nucleons. Therefore, NN potentials that are simple enough and, at the same time, take into account the principal interaction mechanisms underlying a particular microscopic model are of particular interest. In this case, of course, one has to introduce a large number of phenomenological parameters that are the result of excluding particular mechanisms or degrees of freedom from analysis. Thus, the NN potentials for single-boson exchange with short-range repulsion are merely an efficient means of describing the underlying QCM and the multiboson exchange model. If a FSP, for example, the Moscow potential [10, 13]) is used, then the emphasis is on the existence in a two-nucleon system of a deep attractive interaction in S and P waves, which is an effective reflection of the strong coupling between the $|s^4p^2\rangle(|s^3p^3\rangle)$ and $|s^6\rangle(|s^5p^1\rangle)$ $6q$ configurations. In order to emphasize the influence of this effect on the observables of a two-nucleon system and to reduce the number of fitting parameters, we exclude all single- and multiboson exchange mechanisms, except, perhaps, the single-pion one, from an explicit analysis. As a result, this potential is very simple in form and describes well elastic NN scattering up to 300 MeV and basic parameters of the deuteron. This success is perceived as one of the most convincing arguments for the microscopic model that underlies these potentials.

It is well known that even complete knowledge of the elastic scattering amplitude and deuteron properties is not enough to unambiguously determine the type of strong interaction. To completely establish the properties of the potential requires investigating the off-shell behavior of the scattering amplitude, i.e., to consider reactions involving more than two particles.

One of the most reliable sources of information on the off-shell behavior of the NN interaction can be bremsstrahlung (BS) $NN \to NN\gamma$, because in this case we have only two strongly interacting particles in the final state. The reaction $pp \to pp\gamma$ was investigated previously (see, e.g., [16]) in an effort to discriminate between the various meson-exchange and phenomenological short-range repulsive core potentials (RCPs). The result was disappointing: the differences in the BS observables were too small to be determined experimentally. This is because the scattering amplitude for RCPs exhibit approximately the same off-shell behavior attributable to a similar type of long- and medium-range interaction and to a weak sensitivity of the NN wave functions to a specific short-range potential [17]. It would probably be of greater interest to compare RCPs and FSPs in describing the reaction $NN \to NN\gamma$. The short-range node in the wave functions for forbidden state potentials causes a significant increase in the mean kinetic energy of a two-nucleon system and an increase in the importance of components with large momentum transfer. Since the short-range wave functions for RCPs virtually become zero, it becomes possible to discriminate between FSPs and RCPs [18].

Here, we perform calculations and comparative analysis of the off-shell scattering matrices and related BS observables in the reaction $pp \to pp\gamma$ for several types of NN potentials (FSPs and RCPs) in an effort to discriminate between them. This is done both for standard potentials and for specially selected ones in order to determine the role of the meson-exchange NN-interaction components that are commonly excluded from the FSPs and such key parameters as the shape and depth of the central part of the potential. All calculations for the reaction $pp \to pp\gamma$ are performed in momentum representation and in coplanar geometry. We show that, in contrast to the results from [18], where the Moscow potential of 1992 (MP92) [13] was taken as a FSP, when using potentials that give a good description of phase shifts and the proper behavior of the scattering matrix for low momentum transfers (which is determined mainly by single-pion exchange), the reaction $pp \to pp\gamma$ does not allow the choice between RCPs and FSPs to be made, at least up to proton energies $E_{\text{lab}} \simeq 400$ MeV in the laboratory frame.

2. FORMALISM

In many problems involving hadrons, the interaction between particles must be taken into account in all orders of perturbation theory. This implies that calculating the scattering t matrix is a more direct method of obtaining information on the dynamics of a particular process than a direct investigation of the potentials alone. The differences in the off-shell behavior of the NN scattering amplitudes may be due to different structures of the corresponding NN potentials and different approximations used to deduce the scattering t matrix for a specific NN potential. For all the potentials used here, except the Bonn potential, the scattering t matrix in the c.m. frame of two protons satisfies the Lippmann–Schwinger equation. For the Bonn potential, the t matrix satisfies the Logunov–Tavkhelidze equation [19]. This equation is a three-dimensional quasi-potential reduction to the four-dimensional relativistic Bethe–Salpeter equation. However, the t matrix derived in this way can also be expressed in terms of the solution to the Lippmann–Schwinger equation with a normal nonrelativistic coupling with scattering phases [2].

2.1. The NN Scattering t Matrix

If we use the partial-wave decomposition of the t matrix

$$\langle \mathbf{q}'|t^{\pm}(p)|\mathbf{q}\rangle = (4\pi)^2 \tag{1}$$

$$\times \sum_{\substack{JST\\LL'M}} i^{L-L'}\mathcal{Y}^{JM}_{L'S}(\hat{\mathbf{q}}')t^{JST\pm}_{L'L}(q',q;p)\mathcal{Y}^{JM\dagger}_{LS}(\hat{\mathbf{q}})P^T,$$

where P^T is the isospin projection operator,

$$\mathcal{Y}^{JM}_{LS}(\hat{\mathbf{q}}) = \sum_{M_L M_S} C^{JM}_{LM_L SM_S} Y_{LM_L}(\hat{\mathbf{q}})|SM_S\rangle,$$

S and M_S is the total spin of the NN system and its projection, $C^{JM}_{LM_LSM_S}$ is the Clebsch–Gordan coefficient, and $\hat{\mathbf{q}}$ specifies the direction of momentum $\mathbf{q}$: $\hat{\mathbf{q}} = \mathbf{q}/|\mathbf{q}|$, and a similar decomposition of the NN-interaction potential $V(\mathbf{q}', \mathbf{q})$, then the partial-wave Lippmann–Schwinger equation for $t^{JST\pm}_{L'L}$ can be represented as

$$t^{JST\pm}_{L'L}(q',q;p) = V^{JST}_{L'L}(q',q) \tag{2}$$

$$+ \frac{2m}{\pi}\sum_l \lim_{\eta\to 0}\int\limits_0^\infty \frac{V^{JST}_{L'l}(q',p')t^{JST\pm}_{lL}(p',q;p)}{p^2 - p'^2 \pm i\eta}p'^2\,dp'.$$

Here, $t^{JST\pm}_{L'L}(q',q;p)$ is the partial scattering matrix specified by the boundary conditions with incoming $(-)$ or outgoing $(+)$ waves; $V^{JST}_{L'L}(q',q)$ is the partial NN potential; J, L, and T mean, respectively, the total and orbital angular momenta and the isospin state of the two-nucleon system. The momentum p is related to the proton kinetic energy in the laboratory frame by $p^2 = mE_{\text{lab}}/2$, where m is the proton mass (below, we use the system of units with $\hbar = c = 1$) and the momenta q' and q can take on off-shell values. Since the potential $V(q', q)$ is Hermitian, it follows from (2) that $[t^{JST-}_{L'L}(q',q;p)]^* = t^{JST+}_{L'L}(q',q;p)$.

The two-particle elastic scattering amplitude is determined by the on-shell t-matrix element (1)

$$f(\mathbf{q}', \mathbf{q}) = -\frac{m}{4\pi}\langle \mathbf{q}'|t^+(p)|\mathbf{q}\rangle,$$

where $q' = q = p$.

For the scattering of two identical particles (e.g., two protons), we restrict our analysis to the isovector channel $T = 1$. In this case, the antisymmetrized scattering matrix takes the form

$$\langle \mathbf{q}', SM'_S|t^+(p)|\mathbf{q}, SM_S\rangle = 2(4\pi)^2 \tag{3}$$

$$\times \sum_{\substack{JLL'\\(S+L\ \text{even})}} \sum_{M} i^{L-L'} C^{JM}_{L'M-M'_S SM'_S} Y_{L'M-M'_S}(\hat{\mathbf{q}}')$$

$$\times\, t^{JS\pm}_{L'L}(q', q; p) C^{JM}_{LM-M_S SM_S} Y^*_{LM-M_S}(\hat{\mathbf{q}}).$$

The t matrix, which is not real, can be directly obtained in principle from Eq. (2). However, in order not to deal with complex-valued quantities, it is more convenient to use the following standard relation from a practical point of view:

$$\lim_{\eta\to+0}(p^2-p'^2 \pm i\eta)^{-1} = P\left(\frac{1}{p^2-p'^2}\right) \mp i\pi\delta(p^2-p'^2),$$

where P means taking the principal-value integral. In this case, instead of the t matrix, we can calculate a real quantity, the K matrix, which satisfies the integral equation

$$K^{JST}_{L'L}(q', q; p) = V^{JST}_{L'L}(q', q) \tag{4}$$

$$+\,\frac{2m}{\pi}\sum_l P\int_0^\infty \frac{V^{JST}_{L'l}(q', p')K^{JST}_{lL}(p', q; p)}{p^2-p'^2}p'^2\,dp'.$$

The sought-for t matrix is then related to the K matrix by the Heitler equation

$$t^{JST+}_{L'L}(q', q; p) = K^{JST}_{L'L} - imp\sum_{ll'} K^{JST}_{L'l}(q', p; p)$$

$$\times [I + imp\,K(p, p; p)]^{-1}_{ll'} K^{JST}_{l'L}(p, q; p),$$

where I means the unit matrix $\delta_{ll'}$ and $K(p, p; p)$ means the matrix $K^{JST}_{ll'}(p, p; p)$.

For an NN system, both particles have spin 1/2 and the interaction conserves the total angular momentum J and parity. Consequently, in the state with total angular momentum J, tensor forces can couple only the states with orbital angular momenta $L = J+1$ and $J-1$. For uncoupled (in L) states, the phase shifts $\delta_L(p)$ can be expressed directly in terms of the K matrix:

$$K_L(p) \equiv K^{JST}_{LL}(p, p; p) = -\frac{\tan\delta_L(p)}{mp}.$$

For the states coupled by tensor forces, we use the parametrization of Stapp *et al.* [20]. Defining

$$K = \begin{bmatrix} K_- & K_0 \\ K_0 & K_+ \end{bmatrix}, \quad \Sigma = mp(K_- - K_+),$$

$$\Delta = mp(K_- + K_+), \quad \mathcal{L} = m^2p^2(K_-K_+ - K_0^2),$$

$$\tan 2\sigma = -\frac{\Delta}{1-\mathcal{L}} \quad \text{and} \quad \tan 2\tau = -\frac{\Sigma}{1+\mathcal{L}},$$

we obtain the following relations for the phase shifts δ_- and δ_+ (which correspond to the states with $L = J-1$ and $L = J+1$) and the mixing parameter ϵ_J:

$$\delta_- = \sigma + \tau, \quad \delta_+ = \sigma - \tau,$$

$$\tan 2\epsilon_J = -\frac{2mpK_0}{\sqrt{(1+\mathcal{L})^2 + \Sigma^2}}.$$

2.2. The Amplitude and Differential Cross Section for the $pp \to pp\gamma$ *Process*

The BS process in pp collisions was considered in terms of the potential model previously (see, e.g., [16, 18, 21–25]). In this case, the problem in question can be solved on the basis of two different approaches, which must basically yield identical results.

In the first approach, the wave functions of a two-nucleon system can be derived from the solution to the Schrödinger equation in coordinate representation. Subsequently, these functions are used to calculate the matrix elements of the operator for the interaction with an electromagnetic field [18, 21]. This method allows one to easily take into account the Coulomb interaction between protons and automatically includes double rescattering diagrams. However, we use the second approach in our calculations. It is based on the formalism of the momentum representation. In this case, the BS amplitude is factorized into the nucleon–nucleon part (t matrix), the two-nucleon propagator, and the electromagnetic vertex part [16, 23–25]. Computationally, this approach is more convenient than the first one (e.g., it facilitates the use of nonlocal NN potentials). In addition, it allows the BS observables to be directly expressed in terms of the off-shell NN-scattering t matrix.

To simplify the problem, we disregard meson-exchange currents and Δ degrees of freedom. Their inclusion will not significantly change our results, although, of course, it would be necessary in a quantitative comparison of theory with experiment [24, 26]. We also ignore the Coulomb interaction between protons. Its role was assessed in [27], and it was shown that it could be ignored at proton energies near the π-meson production threshold, where the $^1S_0$ wave contribution is suppressed.

The BS dynamics is contained in the invariant matrix element

$$M_{fi} = \langle \widetilde{p}_{1f}, \widetilde{p}_{2f}; S'M'_S | V_{\rm em} | \widetilde{p}_{1i}, \widetilde{p}_{2i}; SM_S \rangle, \qquad (5)$$

where $\widetilde{p}_{1i}, \widetilde{p}_{2i}, \widetilde{p}_{1f}, \widetilde{p}_{2f}$ are, respectively, the initial and final proton 4-momenta ($\widetilde{p} = (p_0, \mathbf{p})$) and $V_{\rm em}$ is the operator for the interaction of the two-nucleon system with an electromagnetic field. The Pauli exclusion principle imposes standard constraints on the wave functions of the *pp* system, more specifically,

$$|\widetilde{p}_1, \widetilde{p}_2\rangle = (-1)^{S+1} |\widetilde{p}_2, \widetilde{p}_1\rangle. \qquad (6)$$

Because of momentum transfer to the photon, the frame in which the matrix element (5) is calculated cannot be simultaneously the c.m. frame for the initial and final states of the NN system. Besides, for the relativistic description of a two-body system, introducing the relative momentum $\widetilde{p} = \frac{1}{2}(\widetilde{p}_1 - \widetilde{p}_2)$ and the c.m. momentum $P_{\rm c.m.} = \widetilde{p}_1 + \widetilde{p}_2$ does not lead to a trivial separation of the two-particle wave function into the wave function of the relative motion and the c.m. wave function. However, the following representation is known to be admissible:

$$|\mathbf{p}_1, \mathbf{p}_2\rangle = |\mathbf{P}_{\rm c.m.}\rangle \otimes e^{-i\chi(\mathbf{P}_{\rm c.m.})} |\mathbf{p}\rangle, \qquad (7)$$

in which the dependence of the wave function for the relative motion on the c.m. motion is taken into account by the boost generator $\chi(\mathbf{P}_{\rm c.m.})$. Given (7), the matrix element (5) can be represented as

$$M_{fi} = \langle \widetilde{p}_f; S'M'_S | \widetilde{V}_{\rm em} | \widetilde{p}_i; SM_S \rangle, \qquad (8)$$

where

$$\widetilde{V}_{\rm em} = V_{\rm em} + i[\chi(\mathbf{P}^{(f)}_{\rm c.m.}) V_{\rm em} - V_{\rm em} \chi(\mathbf{P}^{(i)}_{\rm c.m.})] + O\left(\frac{1}{m^4}\right); \qquad (9)$$

$\widetilde{p}_i$ and $\widetilde{p}_f$ are the initial and final relative proton 4-momenta, respectively; and $P^{(i)}_{\rm c.m.} - P^{(f)}_{\rm c.m.} = k$, k is the photon 4-momentum. As was shown in [24], the term in the square brackets in (9) may be discarded if we pass to the so-called averaged barycentric frame in which

$$\mathbf{p}_{1i} + \mathbf{p}_{2i} - \frac{\mathbf{k}}{2} = 0 = \mathbf{p}_{1f} + \mathbf{p}_{2f} + \frac{\mathbf{k}}{2}. \qquad (10)$$

Since we calculate here the matrix element (8) in the averaged c.m. frame (10), we use the approximation $\widetilde{V}_{\rm em} = V_{\rm em}$. The passage between different frames is made through the Lorentz transformations.

The scattering t matrix is related to the wave function of the two-nucleon system by

$$\langle \widetilde{q} | \widetilde{p}, P_{\rm c.m.}; SM_S \rangle = (2\pi)^4 \delta^4(\widetilde{p} - \widetilde{q}) |SM_S\rangle \qquad (11)$$
$$+ iG\left(\frac{1}{2}P_{\rm c.m.} - \widetilde{q}\right) G\left(\frac{1}{2}P_{\rm c.m.} + \widetilde{q}\right)$$
$$\times \sum_{M'_S} |SM'_S\rangle \langle \widetilde{q}; SM'_S | t(P_{\rm c.m.}) | \widetilde{p}; SM_S \rangle,$$

where $G(\widetilde{p})$ means the single-particle Dirac Green's function. The relative proton energy in the c.m. frame is $p_0 = 0$. However, after interaction, the particles may prove to be off the energy shell and, in general, $q_0 \neq 0$. The latter implies the existence of delay effects in the NN interaction.

It is well known that the single-particle Dirac Green's function can be decomposed into components with positive and negative energies:

$$G(\widetilde{p}) = \frac{m}{E_p} \left[\frac{\Lambda_+(\mathbf{p})}{p_0 - E_p + i\eta} + \frac{\Lambda_-(\mathbf{p})}{p_0 + E_p - i\eta} \right],$$

where $E_p = \sqrt{\mathbf{p}^2 + m^2}$ and Λ_+ and Λ_- are the projection operators on the states with positive and negative energies, respectively. Here, we do not take into account the contribution of the states with negative energy. For this purpose, we would have to resort to the relativistic description of NN interaction, including when using FSPs, which presently seems to be impossible. We also ignore delay effects in the NN interaction; i.e., we set $q_0 = 0$ in the t-matrix element in (11). In this case, in the c.m. frame of two nucleons, the t-matrix element is given by relations (2) and (3). Only the NN-scattering matrix for the Bonn potential, which is calculated from the Logunov–Tavkhelidze equation [2], constitutes an exception.

Substituting (11) into (8) and using the conservation of 4-momentum at the electromagnetic vertex, we obtain the following expression for the BS amplitude after the integration over q_0 (the dependence on q_0 is retained in the Green's functions):

$$M_{fi} = \sum_\nu \Bigg\{ \frac{m}{E_{\mathbf{p}_i - \frac{\mathbf{k}}{2}}} \frac{\left\langle \mathbf{p}_i - \frac{\mathbf{k}}{2}; S'\nu | t^-(p_f) | \mathbf{p}_f; S'M'_S \right\rangle^* \left\langle S'\nu | V^{(1)}_{\rm em} \left(\mathbf{p}_i - \frac{\mathbf{k}}{2}, \mathbf{p}_i + \frac{\mathbf{k}}{2} \right) | SM_S \right\rangle}{2(E_{p_f} - E_{\mathbf{p}_i - \frac{\mathbf{k}}{2}})} \qquad (12)$$
$$+ \frac{m}{E_{\mathbf{p}_i + \frac{\mathbf{k}}{2}}} \frac{\left\langle \mathbf{p}_i + \frac{\mathbf{k}}{2}; S'\nu | t^-(p_f) | \mathbf{p}_f; S'M'_S \right\rangle^* \left\langle S'\nu | V^{(2)}_{\rm em} \left(-\mathbf{p}_i - \frac{d\mathbf{k}}{2}, -\mathbf{p}_i + \frac{\mathbf{k}}{2} \right) | SM_S \right\rangle}{2\left(E_{p_f} - E_{\mathbf{p}_i + \frac{\mathbf{k}}{2}}\right)}$$

$$+\frac{m}{E_{\mathbf{p}_f+\frac{\mathbf{k}}{2}}}\frac{\left\langle S'M'_S|V_{\rm em}^{(1)}\left(\mathbf{p}_f-\frac{\mathbf{k}}{2},\mathbf{p}_f+\frac{\mathbf{k}}{2}\right)|S\nu\right\rangle\left\langle \mathbf{p}_f+\frac{\mathbf{k}}{2};S\nu|t^+(p_i)|\mathbf{p}_i;SM_S\right\rangle}{2\left(E_{p_i}-E_{\mathbf{p}_f+\frac{\mathbf{k}}{2}}\right)}$$

$$+\frac{m}{E_{\mathbf{p}_f-\frac{\mathbf{k}}{2}}}\frac{\left\langle S'M'_S|V_{\rm em}^{(2)}\left(-\mathbf{p}_f-\frac{\mathbf{k}}{2},-\mathbf{p}_f+\frac{\mathbf{k}}{2}\right)|S\nu\right\rangle\left\langle \mathbf{p}_f-\frac{\mathbf{k}}{2};S\nu|t^+(p_i)|\mathbf{p}_i;SM_S\right\rangle}{2\left(E_{p_i}-E_{\mathbf{p}_f-\frac{\mathbf{k}}{2}}\right)}$$

$$+\sum_{\nu'}\lim_{\eta\to 0}\int\frac{d^3q}{(2\pi)^3}\frac{m}{E_q}\frac{m}{E_{\mathbf{q}}-\frac{\mathbf{k}}{4}}\frac{m}{E_{\mathbf{q}+\frac{\mathbf{k}}{4}}}\left\langle \mathbf{q}-\frac{\mathbf{k}}{4};S'\nu'|t^-(p_f)|\mathbf{p}_f;S'M'_S\right\rangle^*$$

$$\left.\times\frac{\left\langle S'\nu'|V_{\rm em}^{(1)}\left(\mathbf{q}-\frac{\mathbf{k}}{2},\mathbf{q}+\frac{\mathbf{k}}{2}\right)|S\nu\right\rangle\left\langle \mathbf{q}+\frac{\mathbf{k}}{4};S\nu|t^+(p_i)|\mathbf{p}_i;SM_S\right\rangle}{4\left(E_{p_i}-E_{\mathbf{q}+\frac{\mathbf{k}}{4}}+i\eta\right)\left(E_{p_f}-E_{\mathbf{q}-\frac{\mathbf{k}}{4}}+i\eta\right)}\right\}.$$

Here, $p_{i,f}$ means $|\mathbf{p}_{i,f}|$. In deriving (12), we used the equality

$$\langle\mathbf{p}_f;SM'_S|[t^-(p_f)]^\dagger|\mathbf{p}_i;SM_S\rangle$$
$$=\langle\mathbf{p}_i;SM_S|t^-(p_f)|\mathbf{p}_f;SM'_S\rangle^*.$$

The first four terms in (12) correspond to the direct and exchange diagrams for single scattering. The last term describes double rescattering. Using symmetry properties of the wave function for a two-proton system (6), we can express the rescattering term, where a photon is emitted by proton 2, via the term in which a photon is emitted by particle 1. Subsequently, for the antisymmetrized t matrices, the diagram with photon emission by proton 1 alone may be substituted for the antisymmetrized sum of all rescattering diagrams (some aspects of calculating the rescattering diagram are given in Appendix A).

The operator $V_{\rm em}^{(i)}$ is the Dirac operator for the interaction of the ith nucleon with an electromagnetic field. In the transverse gauge, it is

$$V_{\rm em}^{(i)}(\mathbf{q}_-,\mathbf{q}_+)$$
$$=\boldsymbol{\epsilon}_\lambda\left\langle\overline{u}(\mathbf{q}_-)\left|\frac{\mathbf{p}}{m}+\frac{\mu_p}{4m}[\boldsymbol{\gamma}^{(i)},\gamma^{\nu(i)}]k_\nu\right|u(\mathbf{q}_+)\right\rangle.$$

Here, $\boldsymbol{\epsilon}_\lambda$ is the photon polarization vector; μ_p is the proton magnetic moment (in units of the nuclear magneton $\mu_p = 2.793$); $\mathbf{q}_\pm = \mathbf{p}\pm\mathbf{k}/2$ and the bispinor

$$|u(\mathbf{q})\rangle=\sqrt{\frac{E_q+m}{2m}}\begin{pmatrix}1\\ \dfrac{\boldsymbol{\sigma}\mathbf{q}}{E_q+m}\end{pmatrix}$$

($\boldsymbol{\sigma}$ is the Pauli matrix). For the Dirac matrices γ^ν, we use definitions from [28]. As was shown in [23], relativistic corrections to the operator $V_{\rm em}$ appreciably affect the BS spectrum near the maximum photon energy, where the off-shell effects in the NN interaction are strongest.

Formally, the amplitude M_{fi} in (8) was determined in the averaged c.m. frame (10). In practice, however, the scattering t matrices are always calculated in the c.m. frame of two protons. In our case, there are two such systems that differ by the photon momentum $\mathbf{k}$. Each t matrix in (12) was calculated in its own c.m. frame. As a result, the first two terms in (12) are written in the final c.m. frame, while the third and fourth terms are written in the initial c.m. frame Strictly speaking, this is possible only when the t matrices themselves are Lorentz-invariant. This implies that they must be solutions to the relativistic Bethe–Salpeter equation or a quasipotential reduction to it (e.g., the t matrix for the Bonn potential [2]) but not to the Lippmann–Schwinger equation (2) with a nonrelativistic NN potential, as in most cases [1, 10].

The cross section for the reaction $pp\to pp\gamma$ in the laboratory frame is given by

$$\frac{d^5\sigma}{d\Omega_1 d\Omega_2 d\theta_\gamma}=\frac{\alpha m^3 p_{1f}^2 p_{2f}^2}{(2\pi)^4 p_{1i}E_{p_{1f}}E_{p_{2f}}N_a}\left|\widetilde{M}_{fi}\right|^2,\quad(13)$$

where α is the fine-structure constant ($\alpha = 1/137.04$). The angles $\Omega_1\equiv(\theta_1,\varphi_1)$ and $\Omega_2\equiv(\theta_2,\varphi_2)$ specify the direction of the protons flying apart, and θ_γ is the angle at which a γ-ray photon is emitted (the z axis is chosen along the incident beam, the protons escape on both sides of the beam, and the angle θ_γ is counted off in the same sense as θ_1). In coplanar geometry, the phase factor N_a is

$$N_a=-\frac{p_{1f}}{E_{p_{1f}}}\sin(\theta_\gamma+\theta_2)+\frac{p_{2f}}{E_{p_{2f}}}\sin(\theta_\gamma-\theta_1)$$
$$+\sin(\theta_1+\theta_2).$$

Parameters of the potentials

$^{2S+1}L_J$	FSP1		FSP2		FSP3		FSP4	
	V_0, MeV	β, fm^{-1}	V_0, MeV	β, fm^{-2}	V_0, MeV	β, fm^{-2}	V_0, MeV	β, fm^{-2}
$^1S_0$			−1450	1.7			−18300	10
$^3P_0$	−4065	2.92	−1108	1.07	−3000	3.3	−6900	3.3
$^3P_1$	−3860	2.93	−1054	1.06	−2800	3.3	−6700	3.3
$^3P_2$	−10950	5.1	−2780	3.0	−2780	3.0	−6800	6.45

Specifying the angles θ_1, θ_2, and θ_γ completely fixes the kinematics of the coplanar process and allows us to calculate the final proton momenta p_{1f} and p_{2f} and the photon momentum k for a known incident proton momentum p_{1i}. Since we are not concerned with polarization observables, the cross section in (13) must be summed over the final proton spin states, averaged over the initial proton spin states, and summed over the photon polarization states, i.e.,

$$\left|\widetilde{M}_{fi}\right|^2 = \frac{1}{4}\sum_{SM_S}\sum_{S'M'_S}\sum_{\lambda}|M_{fi}|^2 .$$

3. CALCULATIONS AND DISCUSSION

We calculated the scattering matrices [Eqs. (2) and (4)] and bremsstrahlung observables [Eq. (13)] for the reaction $pp \to pp\gamma$ for several types of potentials, FSPs and RCPs. Since, as was noted in the Introduction, all potentials with short-range repulsion yield similar results, we used the Nijmegen potential (NijmI in the notation of [1]) as a representative of this family. Some difficulties arose with the selection of forbidden-state potentials. Although several versions of such potentials are currently available (see, e.g., [10, 13, 14]), apart from advantages, they all have drawbacks. One of the first potentials, MP92 [13], has already been used previously [18] with a similar aim to find differences in the $pp \to pp\gamma$ reaction observables calculated with the MP92 and RCP. However, MP92 has a significant flaw—it unsatisfactorily reproduces elastic NN-scattering phases, particularly in the $^3PF_2$ channel. As we show below, this can be attributed to the following: an incomplete allowance for the meson-exchange mechanisms (only single-pion exchange was included in MP92) and the same depth of the potential well at short range in $^3P_2$ and $^3F_2$ waves. Note that the latter requires has no physical justifications and can be justified only by an attempt to reduce the number of input parameters. To improve the situation in P and F waves, a different parametrization was introduced in [10], the Moscow potential of 1999 (MP99). It has the following structure:

$$V = V_{\rm sep} + V_c + V_{\rm LS} + V_{\rm OPE},$$

where V_c, $V_{\rm LS}$, and $V_{\rm OPE}$ are respectively, the central, spin–orbit, and one-pion parts of the NN interaction, $V_{\rm sep}$ is the separable orthogonalizing pseudopotential $V_{\rm sep} = \kappa|\varphi\rangle\langle\varphi|(\kappa \to \infty)$, which imposes the additional condition for orthogonality of the scattering wave functions to the forbidden states $|\varphi\rangle$ in S and P waves. The functions $|\varphi\rangle$ reflect the structure of the $6q$ compound state ($|s^6\rangle$ and $|s^5p^1\rangle$ configurations) and have a Gaussian radial dependence. A peculiarity of MP99 compared to MP92 is the small depth of the central part in the P wave; it is an order of magnitude smaller than that for MP92. It can be verified that given the spin–orbit interaction in this wave, MP99, becomes repulsive altogether. Although the wave functions of both potentials have a short-range node (which makes it necessary to use $V_{\rm sep}$ in MP99), their amplitudes differ significantly. A shallow depth for the P wave in MP99 was probably chosen because it was impossible to reproduce well the phase shifts with a deep potential based on a common parametrization of all ^3P_J waves. If, however, we proceed from the microscopic model, which is the basis for all FSPs and which was briefly described in the Introduction, then there is no particular reasons to use the universal parametrization of ^3P_J waves. In our calculations, we use MP99, although, as was pointed out above, it can be attributed to the family of deep attractive potentials with a reservation. Below, however, while studying the effects of the shape and depth of the potentials on the off-shell behavior of the scattering matrix, we are not bound by the condition that the parameters of the central part of the potential be the same for all ^3P_J and $^3F_2$ waves.

In principle, there are several more parametrizations of the deep attractive potentials in S and P waves that describe the corresponding phase shifts

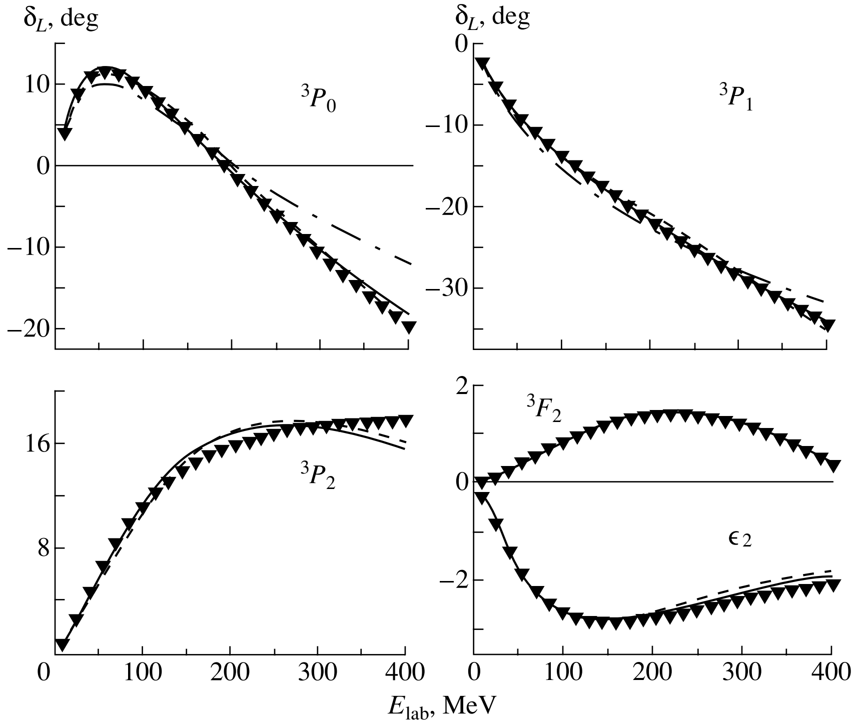

Fig. 1. Phase shifts for elastic *pp* scattering. The solid, dashed, and dash-dotted lines represent FSP1, FSP2, and FSP3, respectively; ▼ represents the NijmI potential [1].

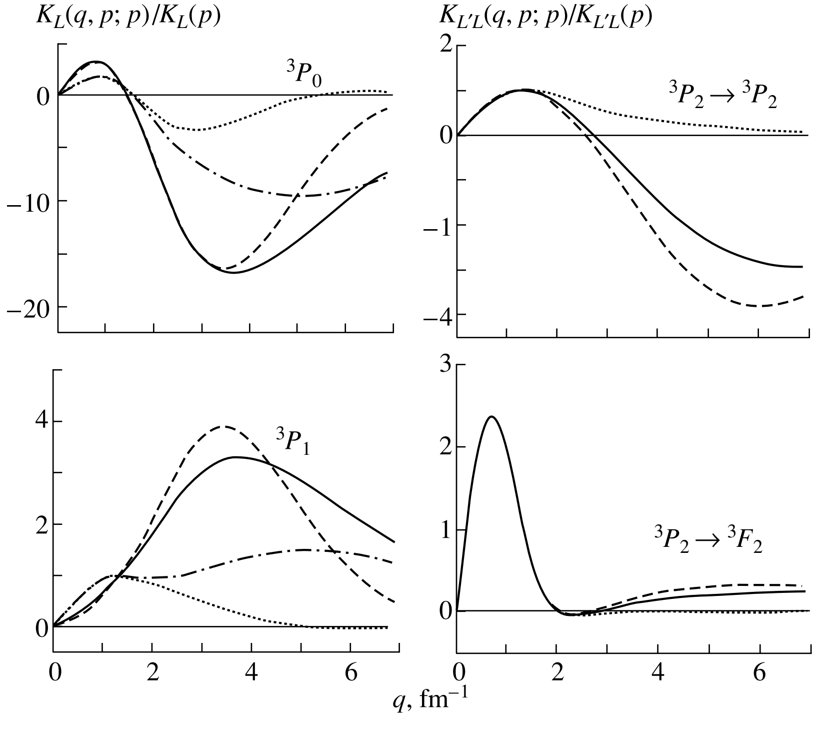

Fig. 2. The ratio of the off-shell K matrix to the on-shell K matrix; p is the momentum that corresponds to the scattering energy $E_{\text{lab}} = 150$ MeV. The solid, dashed, dash-dotted, and dotted lines represent, FSP1, FSP2, FSP3, and NijmI, respectively.

well [14]. However, their significant drawback is that the tensor interaction in the P wave is ignored (i.e., the term $V_{\rm OPE}$ is absent in the potentials). At the same time, the BS observables in pp collisions are known to be sensitive to this type of interaction, particularly to nondiagonal (in orbital quantum number) matrix elements, and, hence, $V_{\rm OPE}$ must be included in the potential. Therefore, we will not calculate the scattering matrices and BS observables directly with the potentials from [14] but first will modify them. Let us introduce two potentials, $V = V_c + V_{\rm LS} + V_{\rm OPE}$, which differ by the central part V_c. We parametrize them as follows: $V_{\rm LS}$ and $V_{\rm OPE}$ are left the same as those in MP99, while V_c is taken in an exponential form $V_c = V_0 \exp(-\beta r)$ in the former case (the corresponding potential is called FSP1) and in a Gaussian form $V_c = V_0 \exp(-\beta r^2)$ in the latter case (FSP2). The parameters V_0 and β for ^3P_J waves are given in the table. They are comparable in magnitude with the analogous parameters of the potentials from [14] with the same radial dependence of the central part. Since the principal interaction mechanism in waves with $L \geq 2$ is assumed to be meson exchange, to describe them, we take the NijmI potential, whose parametrization for these waves is theoretically more justified than, for example, in MP99. In particular, this implies that our potentials have different parametrizations in $^3P_2$ and $^3F_2$ waves. As a result, the $^3F_2$ phase and the mixing parameter ϵ_2 are reproduced much better than for MP92. Note also the large depth of the potential well in the $^3P_2$ wave in FSP1. An attempt to obtain the correct phases and mixing parameter in this channel with a smaller depth of V_0 failed. The phase shifts for these two potentials and for the Nijmegen potential are shown in Fig. 1 (for clarity, we ignore the insignificant phase difference by π for FSPs and RCPs, in accordance with the Levinson theorem). We see that very close scattering phases correspond to all three potentials.

We chose a real quantity, the K matrix (4), as the parameter that describes the off-shell behavior of a two-nucleon system [for PM99, we used relation (A.5) from Appendix B to calculate the K matrix). Figure 2 shows off-shell parameters of the scattering amplitudes. We see that for $^3P_0$ and $^3P_1$ waves, the scattering amplitudes are similar for FSP1 and FSP2 but differ significantly for NijmI even in the range of low momenta q. This range is determined by the behavior of the potential at medium and long ranges, where the interaction is effected by meson exchange. At the same time, the behavior of the K matrix at large $q (q > 2\ {\rm fm}^{-1})$ is determined by the short-range ($r < 1$ fm) wave function of the NN system and is naturally different for RCPs and FSPs. It emerged that the scattering amplitudes for FSP1 and FSP2 are almost the same as those for similar exponential and Gaussian potentials from [14] at any q, despite the presence of the term $V_{\rm OPE}$ in them. In addition, the wave functions of forbidden states in the P wave calculated with these potentials are exponential in form, while calculations based on the nucleon quark structure yield a Gaussian dependence. It thus follows that FSP1, FSP2, and the potentials from [14] poorly describe the long- and medium-range NN interactions. As a result, this circumstance must manifest itself in BS observables. Indeed, as we see from Fig. 3, using the differential BS cross section of FSP1 leads to a significant excess of the theoretical results compared to both experimental data [29] and the results obtained for potentials with short-range repulsion and MP99. In this case, the BS cross section includes all partial pp amplitudes with a total angular momentum up to $J = 6$, while those of them that are not included in the FSP parametrization are the scattering amplitudes for NijmI.

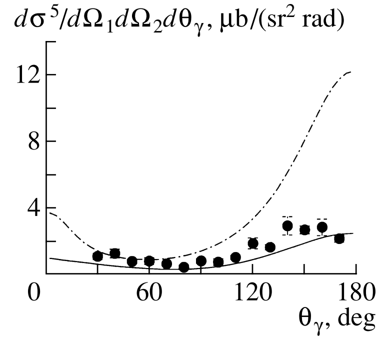

Fig. 3. Differential BS cross section versus photon escape angle in the laboratory frame at proton energy in the beam $E_{\rm lab} = 280$ MeV and at detection angles $\theta_1 = 12°$ and $\theta_2 = 12.4°$. The solid and dash-dotted line represent NijmI and FSP1, respectively. The experimental data were taken from [29]. The curves for MP99 and the Bonn potential [2] visually do not differ from the results for NijmI.

Let us try to rectify the situation by noting that the scattering phases are stable when the parameters V_0 and β are varied simultaneously. For example, we can make the potential well narrower but deeper. Let us now choose a slightly different parametrization of the central part in the P wave for a Gaussian potential (see FSP3 in the table) while leaving the parametrization for the $^3P_2$ wave unchanged (as for FSP2). As a result, the parameters for all ^3P_J waves prove to be comparable in magnitude. The phases calculated with FSP3 are also shown in Fig. 1. We see that they agree with experiment slightly worse than for FSP1 and FSP2, but the off-shell scattering amplitude (Fig. 2) has the proper behavior at low momenta.

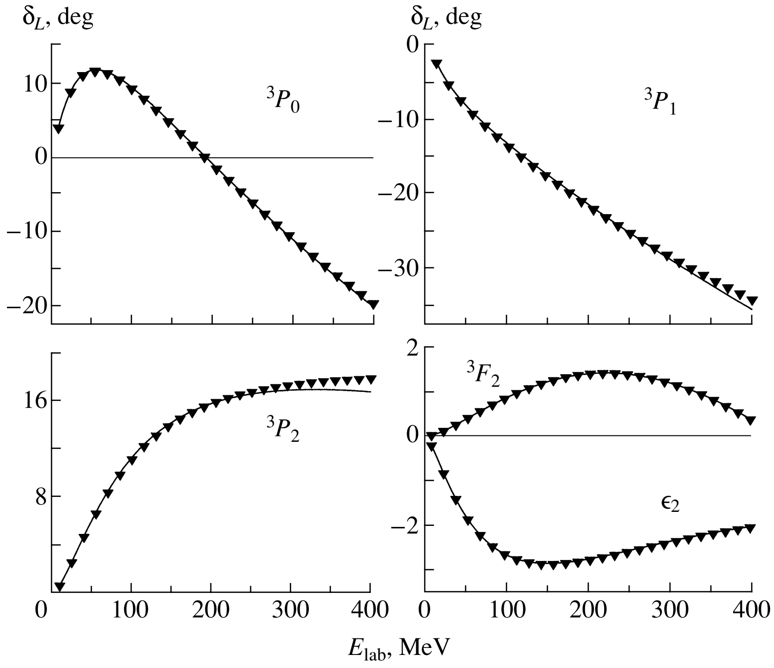

Fig. 4. Phase shifts for elastic *pp* scattering phases. The solid line and ▼ represent FSP4 and NijmI, respectively.

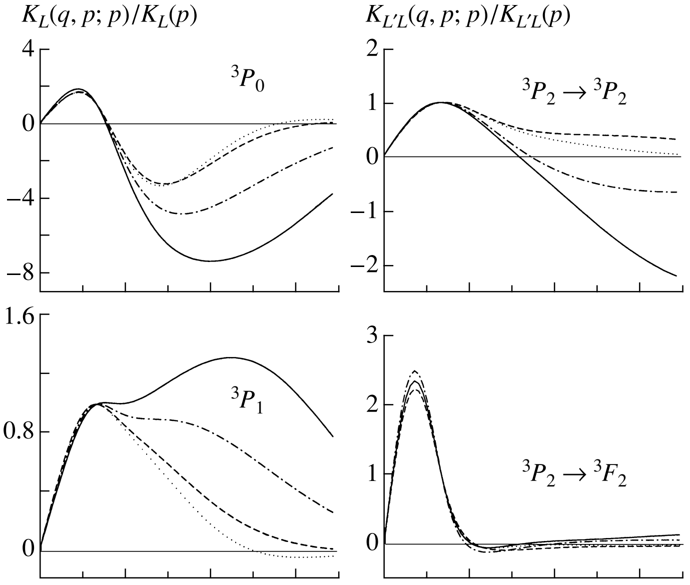

Fig. 5. The ratio of the off-shell K matrix to the on-shell K matrix; p is the momentum that corresponds to the scattering energy $E_{\rm lab} = 150$ MeV. The solid, dashed, dash-dotted, and dotted lines represent, respectively, FSP4, the Bonn potential [2], MP99, and NijmI.

The unsatisfactory reproduction of the phase shifts by FSP3 (particularly noticeable for the $^3P_0$ wave) stems from the fact that only single-pion exchange is taken into account in describing the long- and medium-range behavior of the potential. It may well be that this is not enough. Let us try to rectify the situation by introducing the following simple NN-interaction model: $V = V_c + V_{\rm me}$ (we designate it as FSP4). Here, V_c is the Gaussian central deep attractive potential and $V_{\rm me}$ is the meson-exchange potential (in our case, NijmI). Parameters for V_c in the ^3P_J channel are also given in the table. The calculated

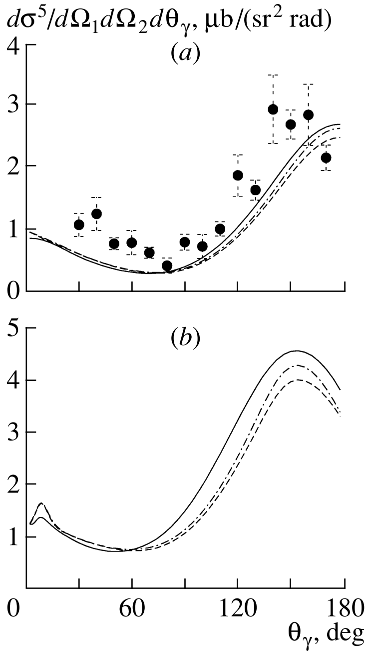

Fig. 6. Differential BS cross section versus photon escape angle in the laboratory frame: (a) at proton energies in the beam $E_{\text{lab}} = 280$ MeV and detection angles $\theta_1 = 12°$ and $\theta_2 = 12.4°$; (b) at proton energies $E_{\text{lab}} = 400$ MeV and detection angles $\theta_1 = 8°$ and $\theta_2 = 15°$. The solid, dashed, and dash-dotted lines represent FSP4, NijmI, and the Bonn potential, respectively. The experimental data were taken from [29].

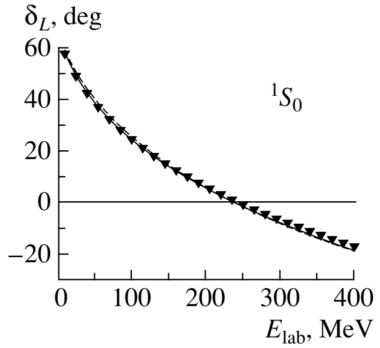

Fig. 7. $^1S_0$ phase shift for elastic pp scattering. The solid and dashed lines represent FSP4 and FSP2, respectively; ▼ represents NijmI.

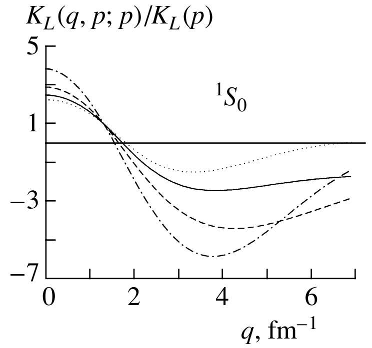

Fig. 8. The ratio of the off-shell K matrix to the on-shell K matrix for the $^1S_0$ channel; p is the momentum that corresponds to the scattering energy $E_{\text{lab}} = 150$ MeV. The solid, dashed, dash-dotted, and dotted lines represent, respectively, FSP4, MP99, FSP2, and NijmI.

phases for FSP4 are shown in Fig. 4. We see that the $^3P_0$ and $^3P_2$ phase shifts are now reproduced appreciably better. Figure 5 shows the off-shell behavior of the scattering amplitudes for FSP4, MP99, and the Bonn charge-dependent potential [2]. As we see from comparison of the results, the components with large momentum transfer increase appreciably in importance for FSP3 and FSP4. At the same time, because of the suppressed oscillations of the MP99 wave function at short range, the off-shell scattering matrices in the P wave for MP99 and RCP are virtually identical.

The BS observables at proton energies up to 400 MeV in the laboratory frame are determined mainly by the medium- and long-range potential structure. This implies that they are sensitive to off-shell effects in the range of low q, where the scattering amplitudes for FSP4 and RCP differ only slightly. In Fig. 6, the calculated differential cross sections for the reaction $pp \to pp\gamma$ [Eq. (13)] are plotted against photon escape angle for various potentials at various proton energies. Note that, in our kinematics, small angles θ_1 and θ_2 correspond to the emission of the hardest photons. We see that all theoretical curves are very close and satisfactorily reproduce the available experimental data [29]. This implies that we cannot choose between the various potentials by using the reaction $pp \to pp\gamma$ alone.

Since MP99 in the $^1S_0$ wave, in contrast, for example, to NijmI, has the form of a deep attractive potential, we may conclude that the scattering amplitudes cannot be distinguished in the BS observables from the S wave. This result agrees with the results from [16], where it was argued that, in coplanar geometry and at sufficiently high proton energies, the contribution of S and D waves is suppressed and P waves play a major role.

The parameters of MP92 used in [18] in the P wave are intermediate between the parameters of FSP2 and FSP3. In this case, the difference in the differential BS cross sections for FSP2 and RCP clearly shows up even at proton energies $E_{\text{lab}} = 280$ MeV; for MP92 and RCP, they begin to manifest themselves only at proton energies $E_{\text{lab}} =$ 350–450 MeV. They are the same in nature as those for FSP2.

For the $^1S_0$ wave, we can perform a similar analysis as for ^3P_J waves. The FSP2 and FSP4 parameters for the $^1S_0$ wave are also given in the table; for FSP2, they are approximately the same as for MP92 or the Gaussian potential from [14]. For FSP4, the node of the scattering wave functions orthogonal to the forbidden state lies approximately at a distance of 0.35 fm, in agreement with models for the nucleon structure [30]. Naturally, the depth of V_0 depends on the shape and parametrization of the meson-exchange part of the potential. Figures 7 and 8 show, respectively, the calculated off-shell scattering phases and amplitudes in the $^1S_0$ wave for FSP2, FSP4, and NijmI. We see from Fig. 8 that the scattering amplitude for FSP4 is much closer to the amplitude for RCP than that for MP99 and FSP2. Here, the same conclusions as for the P wave can be reached: even the reactions with protons in which the S wave plays a prominent role may not reveal the differences between FSP4 and RCP.

4. CONCLUSION

As follows from our analysis, the reaction $pp \to pp\gamma$ at proton energies up to 400 MeV does not allow the choice between potentials with and without a core to be made, in contrast, for example, to the $\alpha\alpha$ and αt systems, where this is apparently possible [31]. In all likelihood, the point is that the dynamics underlying the pp, $\alpha\alpha$, and αt interactions is different. In a pp system, the deep attractive potential is attributable to mechanisms related to the quark structure of nucleons and, therefore, it is of a short-range nature ($r < 1$ fm). At the same time, the BS observables for proton energies at which the potential model is valid are determined by the medium- and long-range NN-interaction structure. An explicit allowance for meson-exchange mechanisms was shown to be important in constructing realistic NN potentials. We estimated the depth and width of the attractive well at which the scattering amplitude has the proper off-shell behavior for low momentum transfer. In the course of our study, we found that a Gaussian dependence of the central part of potentials with short-range repulsion is preferred to an exponential dependence, because the latter leads to an irregular forbidden-state wave function. Note also that the information obtained from testing potentials by using the phase shifts alone will definitely be ambiguous.

Extending the range of proton energies under study to several GeV would be of great interest in testing various NN-interaction models. In this case, however, apart from the naturally arising inelastic processes, the various contact diagrams underlying the chosen microscopic model should be taken into account to quantify the results obtained. Their important role has recently been pointed out in [32]. In other words, if it is necessary to test the structure of a short-range interaction, in particular, to choose between the attractive and repulsive mechanisms, then one should not use the simple model of a local interaction (e.g., a local optical potential). Strictly speaking, it is suitable only for describing elastic scattering phases. The nonlocal mechanisms that can affect the parameters of various processes through NN interaction (e.g., the BS observables) will manifest themselves via various kinds of contact diagrams; disregarding them can significantly distort the results obtained.

ACKNOWLEDGMENTS

We are grateful to V.G. Neudatchin and Yu.M. Chuvil'sky for interest and helpful discussions.

APPENDIX A

The double rescattering diagrams are difficult to calculate, because the integrand in (12) has a pole singularity. It corresponds to the emergence of both protons on the energy shell before or after photon emission.

The rescattering term from (12) can be concisely written as

$$M_{fi}^{\rm res} = (2\pi)^{-3} \int q^2\, dq\, d\cos\theta\, d\varphi \frac{A_{fi}}{G_1 G_2}, \qquad (A.1)$$

where $G_1 = 2\left(E_{p_f} - E_{\mathbf{q}-\frac{\mathbf{k}}{4}} + i\eta\right)$ and $G_2 = 2\left(E_{p_i} - E_{\mathbf{q}+\frac{\mathbf{k}}{4}} + i\eta\right)$, and the quantity A_{fi} includes the rest, including the summation over ν and ν'.

The integral in (A.1) is most convenient to calculate in a coordinate system with the $\mathbf{z}$ axis directed along the motion of the emitted photon, i.e., $\mathbf{z} \parallel \mathbf{k}$. In this case, the quantities G_1 and G_2 are independent of the angle φ, which allows the integration over φ in (A.1) to be performed analytically.

Let us define the quantity $F_{fi} \equiv \int d\varphi A_{fi}$. Expression (A.1) can then be written as

$$M_{fi}^{\rm res} = \int\limits_{-1}^{1} d\cos\theta \int\limits_{0}^{\infty} dq \frac{H_{fi}(\mathbf{q})}{G_i(\mathbf{q}) G_f(\mathbf{q})}, \qquad (A.2)$$

where

$$H_{fi}(\mathbf{q}) = \frac{q^2}{4(2\pi)^3}\left(E_{p_f} + E_{\mathbf{q}-\frac{\mathbf{k}}{4}}\right)\left(E_{p_i} + E_{\mathbf{q}+\frac{\mathbf{k}}{4}}\right) F_{fi},$$

$$G_i(\mathbf{q}) = p_i^2 - \left(\mathbf{q} + \frac{\mathbf{k}}{4}\right)^2 + i\eta,$$

$$G_f(\mathbf{q}) = p_f^2 - \left(\mathbf{q} - \frac{\mathbf{k}}{4}\right)^2 + i\eta.$$

The following momenta q correspond to the poles in (A.2):

$$q_i^{\pm} = -\frac{k}{4}\cos\theta \pm \sqrt{p_i^2 - \frac{k^2}{16}\sin^2\theta} = -\frac{k}{4}\cos\theta \pm \Delta_i,$$

$$q_f^{\pm} = \frac{k}{4}\cos\theta \pm \sqrt{p_f^2 - \frac{k^2}{16}\sin^2\theta} = \frac{k}{4}\cos\theta \pm \Delta_f.$$

The poles at $q = q_i^-, q_f^-$ can appear in integral (A.2) only at small proton escape angles θ_1 and θ_2 in the laboratory frame and, simultaneously, at small photon escape angles $\theta_\gamma < 2^\circ$. In the kinematics used here, no poles of this kind appear, which allows integral (A.2) to be split into only two parts:

$$\int\limits_0^\infty dq \frac{H_{fi}(\mathbf{q})}{G_i(\mathbf{q})G_f(\mathbf{q})} = \int\limits_{a_1}^{a_2} dq \ldots + \int\limits_{b_1}^{b_2} dq \ldots ,$$

where the interval $[a_1; a_2]$ contains the pole q_i^+ and the interval $[b_1; b_2]$ contains the pole q_f^+. In that case,

$$\int\limits_{a_1}^{a_2} dq \frac{H_{fi}(\mathbf{q})}{G_i(\mathbf{q})G_f(\mathbf{q})} \tag{A.3}$$

$$= P\int\limits_{a_1}^{a_2} dq \frac{1}{G_i(\mathbf{q})}\left[\frac{H_{fi}(\mathbf{q})}{G_f(\mathbf{q})} - \frac{H_{fi}(\mathbf{q}_i^+)}{G_f(\mathbf{q}_i^+)}\right] + P\int\limits_{a_1}^{a_2} dq$$

$$+ \frac{1}{2\Delta_i}\frac{H_{fi}(\mathbf{q}_i^+)}{G_f(\mathbf{q}_i^+)}\left[\ln\left|\frac{(a_2 - q_i^-)(a_1 - q_i^+)}{(a_2 - q_i^+)(a_1 - q_i^-)}\right| - i\pi\right],$$

$$\int\limits_{b_1}^{b_2} dq \frac{H_{fi}(\mathbf{q})}{G_i(\mathbf{q})G_f(\mathbf{q})}$$

$$= P\int\limits_{b_1}^{b_2} dq \frac{1}{G_f(\mathbf{q})}\left[\frac{H_{fi}(\mathbf{q})}{G_i(\mathbf{q})} - \frac{H_{fi}(\mathbf{q}_f^+)}{G_i(\mathbf{q}_f^+)}\right] + P\int\limits_{a_1}^{a_2} dq$$

$$+ \frac{1}{2\Delta_f}\frac{H_{fi}(\mathbf{q}_f^+)}{G_i(\mathbf{q}_f^+)}\left[\ln\left|\frac{(b_2 - q_f^-)(b_1 - q_f^+)}{(b_2 - q_f^+)(b_1 - q_f^-)}\right| - i\pi\right].$$

Here, $\mathbf{q}_i^+$ and $\mathbf{q}_f^+$ mean the vectors with magnitudes q_i^+ and q_f^+ and with the same direction as the vector $\mathbf{q}$.

APPENDIX B

If the NN potential $V = V^{\mathrm{sep}} + V^r$ contains the separable part V^{sep}, i.e.,

$$V^{\mathrm{sep}}_{L'L}(q', q) = \kappa\varphi_{L'}(q')\varphi_L(q)\delta_{L'L},$$

then the Lippmann–Schwinger equation for the K matrix (4) can be represented as

$$K_{L'L}(q', q; p) = \kappa\varphi_{L'}(q')\varphi_L(q)\delta_{L'L} + V^r_{L'L}(q', q) \tag{A.4}$$

$$+ \frac{2m}{\pi}\kappa\varphi_{L'}(q')P\int\limits_0^\infty \frac{\varphi_{L'}(p')K_{L'L}(p', q; p)}{p^2 - p'^2}p'^2 dp'$$

$$+ \frac{2m}{\pi}\sum_l P\int\limits_0^\infty \frac{V^r_{L'l}(q', p')K_{lL}(p', q; p)}{p^2 - p'^2}p'^2 dp'.$$

Here, $V^r_{L'L}$ is the remaining inseparable part of the potential. If, however, $\kappa \to \infty$, which is the case for MP99, then expression (A.4) becomes computationally inconvenient. In this case, the following important property of the separable potentials can be used: the possibility of exactly solving the problem of scattering in two-particle systems. Hence, we derive the following expression for the K matrix from Eq. (A.4):

$$K_{L'L}(q', q; p) = \frac{\kappa\varphi_{L'}(q')}{1 - \kappa I_{1L'}}\big(\varphi_L(q)\delta_{L'L} + I_{2L'L}(q)\big) + V^r_{L'L}(q', q) \tag{A.5}$$

$$+ \frac{2m}{\pi}\sum_l P\int\limits_0^\infty \frac{\left(V^r_{L'l}(q', p') + \frac{\kappa\varphi_{L'}(q')}{1 - \kappa I_{1L'}}I_{2L'l}(p')\right)K_{lL}(p', q; p)}{p^2 - p'^2}p'^2 dp',$$

where

$$I_{1L} = \frac{2m}{\pi}P\int\limits_0^\infty \frac{|\varphi_L(p')|^2}{p^2 - p'^2}p'^2\, dp',$$

$$I_{2L'L}(q) = \frac{2m}{\pi}P\int\limits_0^\infty \frac{\varphi_{L'}(p')V^r_{L'L}(p', q)}{p^2 - p'^2}p'^2\, dp'.$$

We can now pass to the limit $\kappa \to \infty$ in Eq. (A.5) and then solve it by the same methods as those used to solve the standard Lippmann–Schwinger equation (4).

REFERENCES

1. V. G. J. Stoks, R. A. M. Klomp, C. P. F. Terheggen, and J. J. de Swart, Phys. Rev. C **49**, 2950 (1994).
2. R. Machleidt, Phys. Rev. C **63**, 024 001 (2001).
3. R. Machleidt, K. Holinde, and Ch. Elster, Phys. Rep. **149**, 1 (1987); R. Machleidt, Adv. Nucl. Phys. **19**, 189 (1989).
4. Th. A. Rijken and V. G. J. Stoks, Phys. Rev. C **54**, 2851 (1996).
5. T.-S. H. Lee, Phys. Rev. C **29**, 195 (1984); T.-S. H. Lee and A. Matsuyama, Phys. Rev. C **36**, 1459 (1987); T. Ueda, Y. Ikegami, and K. Tada, Few-Body Syst. **18**, 133 (1995).
6. R. Machleidt and I. Slaus, J. Phys. G **27**, R69 (2001).
7. L. Ya. Glozman, Nucl. Phys. A **663**, 103c (2000).
8. D. Bartz and Fl. Stancu, Phys. Rev. C **63**, 034 001 (2001).
9. D. R. Entem, F. Fernández, and A. Valcarce, Phys. Rev. C **62**, 034 002 (2000).
10. V. I. Kukulin, V. N. Pomerantsev, and A. Faessler, Phys. Rev. C **59**, 3021 (1999).
11. Q. B. Li and P. N. Shen, J. Phys. G **26**, 1207 (2000).
12. P. Rehberg, L. Bot, and J. Aichelin, Nucl. Phys. A **653**, 415 (1999); T. Hatsuda and T. Kunihiro, Phys. Rep. **247**, 221 (1994).
13. V. I. Kukulin and V. N. Pomerantsev, Prog. Theor. Phys. **88**, 159 (1992).
14. S. B. Dubovichenko, Yad. Fiz. **60**, 499 (1997) [Phys. At. Nucl. **60**, 425 (1997)].
15. V. I. Kukulin, I. T. Obukhovsky, V. N. Pomerantsev, and A. Faessler, Yad. Fiz. **64**, 1748 (2001) [Phys. At. Nucl. **64**, 1667 (2001)]; V. I. Kukulin, I. T. Obukhovsky, V. N. Pomerantsev, and A. Faessler, J. Phys. G **27**, 1851 (2001).
16. V. Herrmann and K. Nakayama, Phys. Rev. C **45**, 1450 (1992); A. Katsogiannis and K. Amos, Phys. Rev. C **47**, 1376 (1993); M. Jetter and H. V. von Geramb, Phys. Rev. C **49**, 1832 (1994).
17. M. K. Srivastava and D. W. L. Sprung, Adv. Nucl. Phys. **8**, 121 (1975).
18. V. G. Neudatchin, N. A. Khokhlov, A. M. Shirokov, and V. A. Knyr, Yad. Fiz. **60**, 1086 (1997) [Phys. At. Nucl. **60**, 971 (1997)]; N. A. Khokhlov, V. A. Knyr, V. G. Neudatchin, and A. M. Shirokov, Phys. Rev. C **62**, 054 003 (2000).
19. A. A. Logunov and A. N. Tavkhelidze, Nuovo Cimento **29**, 380 (1963); R. Blankenbecler and R. Sugar, Phys. Rev. **142**, 1051 (1966).
20. H. P. Stapp, T. J. Ypsilantis, and N. Metropolis, Phys. Rev. **105**, 302 (1957).
21. L. Heller and M. Rich, Phys. Rev. C **10**, 479 (1974).
22. V. R. Brown, P. L. Anthony, and J. Franklin, Phys. Rev. C **44**, 1296 (1991).
23. R. L. Workman and H. W. Fearing, Phys. Rev. C **34**, 780 (1986); V. Herrmann and K. Nakayama, Phys. Rev. C **46**, 2199 (1992).
24. J. A. Eden and M. F. Gari, Phys. Rev. C **53**, 1102 (1996).
25. G. H. Martinus, O. Scholten, and J. A. Tjon, Phys. Rev. C **56**, 2945 (1997).
26. M. Jetter and H. W. Fearing, Phys. Rev. C **51**, 1666 (1995); F. de Jong, K. Nakayama, and T.-S. H. Lee, Phys. Rev. C **51**, 2334 (1995); G. H. Martinus, O. Scholten, and J. A. Tjon, Phys. Rev. C **58**, 686 (1998).
27. A. Katsogiannis, K. Amos, M. Jetter, and H. V. von Geramb, Phys. Rev. C **49**, 2342 (1994).
28. J. D. Bjorken and S. D. Drell, *Relativistic Quantum Mechanichs* (McGraw-Hill, New York, 1964).
29. K. Michaelian, P. Kitching, D. A. Hutcheon, *et al.*, Phys. Rev. D **41**, 2689 (1990).
30. L. Ya. Glozman and D. O. Riska, Phys. Rep. **268**, 263 (1996).
31. I. V. Kopytin, M. A. Dolgopolov, and A. A. Khuskivadze, Yad. Fiz. **61**, 630 (1998) [Phys. At. Nucl. **61**, 558 (1998)]; I. V. Kopytin, A. S. Kornev, and A. A. Khuskivadze, Izv. Akad. Nauk, Ser. Fiz. **63**, 1005 (1999).
32. H. W. Fearing, Few-Body Syst. Suppl. **12**, 263 (2000); H. W. Fearing and S. Scherer, Phys. Rev. C **62**, 034 003 (2000).

Translated by V. Astakhov

Physics of Atomic Nuclei, Vol. 65, No. 9, 2002, pp. 1657–1672. From Yadernaya Fizika, Vol. 65, No. 9, 2002, pp. 1701–1716.
Original English Text Copyright © 2002 by Volkov, Yudichev.

First Radial Excitations of Scalar-Meson Nonet and the Glueball*

M. K. Volkov and V. L. Yudichev

Joint Institute for Nuclear Research, Dubna, Moscow oblast, 141980 Russia

Received March 27, 2001; in final form, November 27, 2001

Abstract—In a nonlocal $U(3) \times U(3)$ chiral quark model with the local 't Hooft interaction, the first radial excitations of scalar mesons are described. Simple Lorentz-covariant form factors, having a polynomial form in the momentum space, are used for the description of radially excited states. Due to the chiral symmetry, the form factors for scalar states coincide with those for pseudoscalars. As a result, using the experimental values for the masses of pseudoscalar mesons, we predict the mass spectrum of the ground and radially excited scalar-meson states. The scalar glueball is introduced into the effective meson Lagrangian by means of the dilaton model. It is shown that 19 scalar states with masses from 0.4 to 1.7 GeV can be interpreted as two scalar nonets and a glueball. Strong decay widths of scalar mesons are calculated. The state $f_0(1500)$ is shown to be the most probable candidate for the scalar glueball. *© 2002 MAIK "Nauka/Interperiodica".*

1. INTRODUCTION

The description of scalar mesons with masses from 0.4 to 1.7 GeV is an actual and complex problem attracting the attention of many physicists in recent years [1–4]. The final solution of this problem has not yet been found. It is complicated by the fact that, in this interval of masses, there exists a scalar glueball which is noticeably mixed with scalar–isoscalar quarkonia. In [5–7], we for the first time suggested interpreting 18 scalar mesons, lying in the mass interval under consideration, as two meson nonets: the ground nonet of scalar quarkonia (with masses below 1 GeV) and the nonet of their first radial excitations (with masses greater than 1 GeV). However, here, an additional scalar-meson state [8] has been seen experimentally. The origin of this extra, 19th, state is supposed as connected to the scalar glueball. Two possible candidates for the glueball are often argued: $f_0(1500)$ and $f_0(1710)$ [1, 2, 4–7, 9–11]. Our present paper is devoted to solving the problem of identification of the true glueball state with one of these states. This is to be done by introducing the scalar glueball into the effective meson Lagrangian investigated in [5–7].

A nonlocal $U(3) \times U(3)$ quark model of the Nambu–Jona-Lasinio (NJL) type was first suggested in [12, 13] to describe the ground and radially excited nonets of pseudoscalar and vector mesons. Next, in [5–7], this model was used to study scalar-meson nonets. Its Lagrangian was completed by the 't Hooft interaction to describe the singlet–octet mixing in the scalar and pseudoscalar sectors. For the description of excited states, simple Lorentz-covariant form factors of a polynomial form were used. To investigate the first radial excitations, polynomials of the second order by momentum sufficed. The form factor was chosen in a form which allowed us to reproduce all low-energy theorems in the chiral limit and the mechanism of spontaneous chiral symmetry breaking (SCSB) [12]. This model was applied for the description of strong decays of radially excited scalar, pseudoscalar, and vector mesons [5–7, 14].

The chiral symmetry allowed us to use the same form factors for both the pseudoscalar and scalar mesons. As a result, using the masses of excited pseudoscalar meson states, we predicted the mass spectrum of radially excited states of scalar mesons. We also showed that 18 scalar-meson states with masses from 0.4 to 1.7 GeV can be considered as two scalar meson nonets: the ground and first radially excited [5–7]. The state $f_0(1710)$ was considered as a quarkonium (the radial excitation of $f_0(980)$). A calculation of widths for the strong decay modes of these mesons and subsequent matching of them with experimental data corroborated our conclusions concerning the quark nature of the 18 states. Meanwhile, the state $f_0(1500)$ happened to be beyond our model, and its description required introducing a glueball into the model.

To solve the problem of describing the glueball, simple models that describe the ground scalar quarkonia states only with the glueball were constructed in [9–11]. There, we introduced a glueball into a $U(3) \times U(3)$ quark Lagrangian with the 't Hooft interaction by means of the dilaton model. The

---

*This article was submitted by the authors in English.

dilaton model has often been used for this purpose by many authors [1, 15–17].

The mixing of the glueball with scalar isoscalar quarkonia was described, and widths of the main modes of their strong decays were calculated. Our calculations showed that, among the most probable candidates for the glueball, states $f_0(1500)$ and $f_0(1710)$, the state $f_0(1500)$ better meets the assumption that it is the glueball rather than $f_0(1710)$. However, the final decision must be made after including radially excited states and taking into account mixing between five scalar–isoscalar states (four quarkonia and a glueball) and describing their decays.

Methods used in [5–7] and in [9, 10] are unified in the present paper to construct an extended nonlocal $U(3)\times U(3)$ model with the glueball, allowing us to describe all 19 scalar-meson states in the interval of masses concerned. After calculating the widths of the strong decay modes of scalar mesons, we once more saw that the most probable candidate for the glueball is the state $f_0(1500)$. Meanwhile, the glueball gets noticeably mixed with the states $f_0(400–1200)$ and $f_0(1370)$, mostly composed of u and d quarks, and is almost not represented in $f_0(980)$ and $f_0(1710)$, containing mostly s quarks. Isovector and strange states change little after introducing the glueball. Therefore, the results obtained here for isovectors and strange mesons are close to those derived in [5–7], where the glueball was not considered. All changes are connected with new value of the constant K which, unlike papers [5–7], is fixed in our paper not only by masses of η and η' but also by the lower experimental bound for the mass of the lightest scalar–isoscalar state $f_0(400–1200)$.

The structure of our paper is as follows. In Section 2, a nonlocal chiral quark model of the NJL type with the six-quark 't Hooft interaction is bosonized to construct an effective meson Lagrangian. In Section 3, the meson Lagrangian is extended by introducing a scalar glueball as a dilaton on the basis of scale invariance. The gap equations, the divergence of the dilatation current, and quadratic terms of the effective meson Lagrangian are derived in Section 4. There, we also diagonalize quadratic terms. Numerical estimates of the model parameters are given in Section 5. In Section 6, the widths for the main modes of strong decays of scalar mesons are calculated. The discussion over the obtained results is given in Section 7. A detailed description of how to calculate the quark loop contribution to the width of strong decays of scalar mesons is given in the Appendix.

2. $U(3)\times U(3)$ LAGRANGIAN FOR QUARKONIA

We start from an effective $U(3)\times U(3)$ quark Lagrangian of the following form (see [5–7]):

$$L = L_{\rm free} + L_{\rm NJL} + L_{\rm tH}, \tag{1}$$

$$L_{\rm free} = \bar{q}(i\hat{\partial} - m^0)q, \tag{2}$$

$$L_{\rm NJL} = \frac{G}{2}\sum_{n=1}^{N}\sum_{a=1}^{9}[(j^a_{{\rm S},n})^2 + (j^a_{{\rm P},n})^2], \tag{3}$$

$$L_{\rm tH} = -K\left\{\det[\bar{q}(1+\gamma_5)q] + \det[\bar{q}(1-\gamma_5)q]\right\}, \tag{4}$$

where $L_{\rm free}$ is the free quark Lagrangian with q and $\bar{q}$ being u, d, or s-quark fields; m^0 is a current quark mass matrix with diagonal elements: m^0_u, m^0_d, m^0_s ($m^0_u \approx m^0_d$). The term $L_{\rm NJL}$ contains nonlocal four-quark vertices of the NJL type which have the current-to-current form. The quark currents are defined in accordance with [5–7, 12, 13]:

$$j^a_{{\rm S(P)},n}(x) = \int d^4x_1 d^4x_2 \bar{q}(x_1) \times F^a_{{\rm S(P)},n}(x;x_1,x_2)q(x_2), \tag{5}$$

where the subscript S is for scalar, and P for pseudoscalar, currents. The term $L_{\rm tH}$ is the six-quark 't Hooft interaction, which is supposed as local, so no form factor is introduced into $L_{\rm tH}$.

For $n>1$, currents (5) are nonlocal due to form factors $F^a_{{\rm S(P)},n}$. This way of introducing nonlocality allows us to consider radially excited meson states, which is impossible in the standard local NJL model. In general, the number of radial excitations N is infinite, but we restrict ourselves to $N=2$, leaving only the ground and first radially excited states, because extending this model by involving heavier particles is not valid for this class of models.

Let us define the form factors in the momentum space.

$$F^a_{{\rm S(P)},n}(x;x_1,x_2) = \int \frac{d^4P}{(2\pi)^4}\frac{d^4k}{(2\pi)^4}\exp\left[\frac{i}{2}\Big((P+k)(x-x_1) + (P-k)(x-x_2)\Big)\right]F^a_{{\rm S(P)},n}(k|P), \tag{6}$$

where P is the total momentum of a meson and k is the relative momentum of quarks inside the meson. As it was mentioned in the Introduction, here we follow papers [5–7, 12, 13], where the form factors

$F^a_{\mathrm{S(P)},n}(k|P)$ are chosen in the momentum space as follows:

$$F^a_{\mathrm{S},n}(k|P) = \tau_a c_a f^a_n(k_\perp), \tag{7}$$
$$F^a_{\mathrm{P},n}(k|P) = i\gamma_5 \tau_a c_a f^a_n(k_\perp),$$

and the functions f^a_n $(n = 1, 2)$ are

$$f^a_1(k_\perp) = 1, \quad f^a_2(k_\perp) = 1 + d_a|k_\perp|^2. \tag{8}$$

These depend on the transverse relative momentum of the quarks:

$$k_\perp = k - \frac{P \cdot k}{P^2}P. \tag{9}$$

In the rest frame of a meson $P = (M, \mathbf{0})$, the vector $k_\perp$ equals $(0, \mathbf{k})$; thereby the form factors can be considered as functions of 3-dimensional momentum. Further calculations will be carried out in this particular frame. The matrices τ_a are expressed via the Gell-Mann λ_a matrices as follows:

$$\tau_a = \lambda_a \quad (a = 1, \ldots, 7), \tag{10}$$
$$\tau_8 = (\sqrt{2}\lambda_0 + \lambda_8)/\sqrt{3}, \quad \tau_9 = (-\lambda_0 + \sqrt{2}\lambda_8)/\sqrt{3}.$$

Here, $\lambda_0 = \sqrt{2/3}\,\mathbf{1}$, with $\mathbf{1}$ being the unit matrix.

Each form-factor function contains a slope parameter d_a which is fixed by special conditions given in Section 4 (see Eq. (55) below). The arbitrary parameter c_a can be absorbed by the four-quark interaction constant G. As a result, we obtain arbitrary constants $\bar{G}_a = c_a^2 G$, where only four constants $\bar{G}_1$, $\bar{G}_4$, $\bar{G}_8$, and $\bar{G}_9$ are free because the following relations take place:

$$\bar{G}_1 = \bar{G}_2 = \bar{G}_3, \quad \bar{G}_4 = \bar{G}_5 = \bar{G}_6 = \bar{G}_7. \tag{11}$$

Thus, the term L_{NJL} (see (3)) can be rewritten for the ground and first radially excited states in the following form:

$$L_{\mathrm{NJL}} = \frac{G}{2}\sum_{a=1}^{9}[(j^a_{\mathrm{S},1})^2 + (j^a_{\mathrm{P},1})^2] \tag{12}$$
$$+ \frac{1}{2}\sum_{a=1}^{9}\bar{G}_a[(\tilde{j}^a_{\mathrm{S},2})^2 + (\tilde{j}^a_{\mathrm{P},2})^2],$$

where

$$j^a_{\mathrm{S(P)},2} = c_a \tilde{j}^a_{\mathrm{S(P)},2}. \tag{13}$$

As follows from our further calculations (see Section 4), we have only three different form factor functions:

$$f^1_2 = f^2_2 = f^3_2 = f^8_2 = f^u_2 = 1 + d_u\mathbf{k}^2, \tag{14}$$
$$f^4_2 = f^5_2 = f^6_2 = f^7_2 = f^{us}_2 = 1 + d_{us}\mathbf{k}^2,$$
$$f^9_2 = f^s_2 = 1 + d_s\mathbf{k}^2.$$

The values of constants d_u, d_s, and d_{us} are given in Section 5. As a consequence of such a definition of form factor functions, all arbitrariness connected with introducing form factors reveals itself only in mass definitions (see (63) below), while the interaction of excited mesons is free of arbitrary parameters.

Instead of Lagrangian (1), it is convenient to use its equivalent form containing only four-quark vertices whose interaction constants take into account the 't Hooft interaction. Using the method described in [5–7, 9, 18–20], we obtain

$$L = \bar{q}(i\hat{\partial} - \bar{m}^0)q \tag{15}$$
$$+ \frac{1}{2}\sum_{a,b=1}^{9}\left[G^{(-)}_{ab} j^a_{\mathrm{S},1} j^b_{\mathrm{S},1} + G^{(+)}_{ab} j^a_{\mathrm{P},1} j^b_{\mathrm{P},1}\right]$$
$$+ \frac{1}{2}\sum_{a=1}^{9}\bar{G}_a\left[\tilde{j}^a_{\mathrm{S},2}\tilde{j}^a_{\mathrm{S},2} + \tilde{j}^a_{\mathrm{P},2}\tilde{j}^a_{\mathrm{P},2}\right],$$

where

$$G^{(\pm)}_{11} = G^{(\pm)}_{22} = G^{(\pm)}_{33} = G \pm 4Km_s\mathcal{J}^\Lambda_{0,1}[1], \tag{16}$$
$$G^{(\pm)}_{44} = G^{(\pm)}_{55} = G^{(\pm)}_{66} = G^{(\pm)}_{77} = G \pm 4Km_u\mathcal{J}^\Lambda_{0,1}[1],$$
$$G^{(\pm)}_{88} = G \mp 4Km_s\mathcal{J}^\Lambda_{0,1}[1], \quad G^{(\pm)}_{99} = G,$$
$$G^{(\pm)}_{89} = G^{(\pm)}_{98} = \pm 4\sqrt{2}Km_u\mathcal{J}^\Lambda_{0,1}[1],$$
$$G^{(\pm)}_{ab} = 0 \quad (a \neq b; \quad a, b = 1, \ldots, 7),$$
$$G^{(\pm)}_{a8} = G^{(\pm)}_{a9} = G^{(\pm)}_{8a} = G^{(\pm)}_{9a} = 0 \quad (a = 1, \ldots, 7),$$

and $\bar{m}^0$ is a diagonal matrix composed of modified current quark masses,

$$\bar{m}^0_u = m^0_u - 32Km_u m_s\mathcal{J}^\Lambda_{0,1}[1]\mathcal{J}^\Lambda_{0,1}[1], \tag{17}$$
$$\bar{m}^0_s = m^0_s - 32Km_u^2\mathcal{J}^\Lambda_{1,0}[1]^2, \tag{18}$$

introduced here to avoid double counting of the 't Hooft interaction in gap equations (see [9, 20]). Here, m_u and m_s are constituent quark masses. All integrals that appear in the paper are defined via the functional $\mathcal{J}$:

$$\mathcal{J}^\Lambda_{l,n}[f] = -i\frac{N_c}{(2\pi)^4}\int d^4k\frac{f(\mathbf{k})\theta(\Lambda^2 - \mathbf{k}^2)}{(m_u^2 - k^2)^l(m_s^2 - k^2)^n}, \tag{19}$$

where $f(\mathbf{k})$ is a product of form factor functions, e.g., $f^u_2(\mathbf{k})f^u_2(\mathbf{k})$, and $N_c = 3$ is the number of colors. Since the integral is divergent for some values of l and n, it is regularized by a 3-dimensional cutoff Λ.

After bosonization of Lagrangian (15), we obtain

$$\tilde{\mathcal{L}}(\bar{\sigma}, \phi) = \tilde{L}_G(\bar{\sigma}, \phi) - i\mathrm{tr}\ln\Big\{i\hat{\partial} - \bar{m}^0 \tag{20}$$
$$+ \sum_{n=1}^{2}\sum_{a=1}^{9}\tau_a g_{a,n}(\bar{\sigma}_{a,n} + i\gamma_5\sqrt{Z}\phi_{a,n})f^a_n\Big\},$$

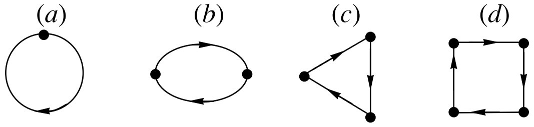

Fig. 1. The set of diagrams contributing to the effective meson Lagrangian. Tadpoles (*a*) determine gap equations, polarization diagrams (*b*) give kinetic and mass terms, triangle diagrams (*c*) and boxes (*d*) describe the interaction of mesons.

where

$$\begin{aligned}\tilde{L}_G(\bar\sigma,\phi) \qquad (21)\\ = -\frac{1}{2}\sum_{a,b=1}^{9} g_{a,1}\bar\sigma_{a,1}\left(G^{(-)}\right)^{-1}_{ab} g_{b,1}\bar\sigma_{b,1}\\ -\frac{Z}{2}\sum_{a,b=1}^{9} g_{a,1}\phi_{a,1}\left(G^{(+)}\right)^{-1}_{ab} g_{b,1}\phi_{b,1}\\ -\sum_{a=1}^{9}\frac{g^2_{a,2}}{2\bar G_a}(\sigma^2_{a,2}+\phi^2_{a,2}),\end{aligned}$$

and $\bar\sigma$ and ϕ are the scalar and pseudoscalar boson fields. As follows from our further calculations of quark-loop diagrams, the vacuum expectation values (VEVs) of fields $\bar\sigma_{8,1}$ and $\bar\sigma_{9,1}$ are not equal to zero, while $\langle\bar\sigma_{a,1}\rangle_0 = 0$, $a = 1,\ldots,7$. This is connected to the existence of tadpole diagrams (Fig. 1*a*) for the ground meson states. Therefore, it is necessary to introduce new fields $\sigma_{a,n}$ with zero VEVs $\langle\sigma_{8,n}\rangle_0 = \langle\sigma_{9,n}\rangle_0 = 0$ using the following relations:

$$\begin{aligned}g_{8,1}\bar\sigma_{8,1} - \bar m^0_u &= g_{8,1}\sigma_{8,1} - m_u, \qquad (22)\\ g_{9,1}\bar\sigma_{9,1} + \frac{\bar m^0_s}{\sqrt{2}} &= g_{9,1}\sigma_{9,1} + \frac{m_s}{\sqrt{2}}.\end{aligned}$$

VEVs taken from (22) give gap equations connecting current and constituent quark masses (see (53) and (54) in Section 4). This is a consequence of SCSB. As a result, we obtain [9, 18]

$$\begin{aligned}\mathcal{L}(\sigma,\phi) = L_G(\sigma,\phi) - i\,\mathrm{tr}\ln\Bigg\{i\hat\partial - m + \sum_{n=1}^{2} \qquad (23)\\ \times\sum_{a=1}^{9}\tau_a g_{a,n}(\sigma_{a,n} + i\gamma_5\sqrt{Z}\phi_{a,n})f^a_n\Bigg\}\\ = L_{\mathrm{kin}}(\sigma,\phi) + L_G(\sigma,\phi) + L_{\mathrm{loop}}(\sigma,\phi).\end{aligned}$$

The term $L_G(\sigma,\phi)$ is

$$\begin{aligned}L_G(\sigma,\phi) = -\frac{1}{2}\sum_{a,b=1}^{9}(g_{a,1}\sigma_{a,1} - \mu_a + \bar\mu^0_a) \qquad (24)\\ \times\left(G^{(-)}\right)^{-1}_{ab}(g_{b,1}\sigma_{b,1} - \mu_b + \bar\mu^0_b)\\ -\frac{Z}{2}\sum_{a,b=1}^{9} g_{a,1}\phi_{a,1}\left(G^{(+)}\right)^{-1}_{ab} g_{b,1}\phi_{b,1}\\ -\sum_{a=1}^{9}\frac{g^2_{a,2}}{2\bar G_a}(\sigma^2_{a,2}+\phi^2_{a,2}).\end{aligned}$$

Here, we introduced, for convenience, the constants μ_a and $\bar\mu^0_a$ defined as follows: $\mu_a = 0$, $a = 1,\ldots,7$, $\mu_8 = m_u$, $\mu_9 = -m_s/\sqrt{2}$ and $\bar\mu^0_a = 0$, $a = 1,\ldots,7$, $\bar\mu^0_8 = \bar m^0_u$, $\bar\mu^0_9 = -\bar m^0_s/\sqrt{2}$.

The term $L_{\mathrm{kin}}(\sigma,\phi)$ contains the kinetic terms and, in the momentum space, has the following form:

$$\begin{aligned}L_{\mathrm{kin}}(\sigma,\phi) = \frac{P^2}{2}\sum_{n,j=1}^{2} \qquad (25)\\ \times\sum_{a=1}^{9}\Big(\sigma_{a,n}\Gamma^a_{\mathrm{S},nj}\sigma_{a,j} + \phi_{a,n}\Gamma^a_{\mathrm{P},nj}\phi_{a,j}\Big),\end{aligned}$$

where

$$\begin{aligned}\Gamma^a_{\mathrm{S(P)},11} = \Gamma^a_{\mathrm{S(P)},22} = 1, \qquad (26)\\ \Gamma^a_{\mathrm{S(P)},12} = \Gamma^a_{\mathrm{S(P)},21} = \gamma^a_{\mathrm{S(P)}},\end{aligned}$$

$$\gamma^a_{\mathrm{S}} = \begin{cases}\dfrac{\mathcal{J}^{\Lambda}_{2,0}[f^u_2]}{\sqrt{\mathcal{J}^{\Lambda}_{2,0}[1]\mathcal{J}^{\Lambda}_{2,0}[f^u_2 f^u_2]}} & (a = 1,2,3,8,)\\ \dfrac{\mathcal{J}^{\Lambda}_{1,1}[f^{us}_2]}{\sqrt{\mathcal{J}^{\Lambda}_{1,1}[1]\mathcal{J}^{\Lambda}_{1,1}[f^{us}_2 f^{us}_2]}} & (a = 4,5,6,7)\\ \dfrac{\mathcal{J}^{\Lambda}_{0,2}[f^s_2]}{\sqrt{\mathcal{J}^{\Lambda}_{0,2}[1]\mathcal{J}^{\Lambda}_{0,2}[f^s_2 f^s_2]}} & (a = 9),\end{cases} \qquad (27)$$

$$\gamma^a_{\mathrm{P}} = \gamma^a_{\mathrm{S}}\sqrt{Z}. \qquad (28)$$

The term $L_{\mathrm{loop}}(\sigma,\phi)$ is a sum of one-loop (see Fig. 1) quark contributions[1], from which the kinetic term was subtracted:

$$\begin{aligned}L_{\mathrm{loop}}(\sigma,\phi) = L^{(1)}_{\mathrm{loop}}(\sigma) + L^{(2)}_{\mathrm{loop}}(\sigma,\phi) \qquad (29)\\ + L^{(3)}_{\mathrm{loop}}(\sigma,\phi) + L^{(4)}_{\mathrm{loop}}(\sigma,\phi),\end{aligned}$$

where the superscript in brackets stands for the degree of fields. Thus, $L^{(1)}_{\mathrm{loop}}$ (Fig. 1*a*) contains terms linear in the field σ; $L^{(2)}_{\mathrm{loop}}$ (Fig. 1*b*), the quadratic ones; and so on. For example[2],

$$L^{(1)}_{\mathrm{loop}}(\sigma) = 8m_u g_{8,1}\mathcal{J}^{\Lambda}_{1,0}[1]\sigma_{8,1} \qquad (30)$$

---

[1] Here, we retain only the terms of order of fields not higher than 4 (corresponding diagrams are shown in Fig. 1).

[2] Here, the expressions (32) and (33) for Yukawa coupling constants were used.

$$- 4\sqrt{2}m_s g_{9,1}\mathcal{J}_{0,1}^{\Lambda}[1]\sigma_{9,1},$$

$$L_{\text{loop}}^{(2)}(\sigma,\phi) = 4\sum_{a=1}^{3} g_{a,1}^2 \mathcal{J}_{1,0}^{\Lambda}[1] \tag{31}$$
$$\times (\sigma_{a,1}^2 + Z\phi_{a,1}^2) + 2\sum_{a=4}^{7} g_{a,1}^2 (\mathcal{J}_{1,0}^{\Lambda}[1] + \mathcal{J}_{0,1}^{\Lambda}[1])$$
$$\times (\sigma_{a,1}^2 + Z\phi_{a,1}^2) + 4g_{8,1}^2\mathcal{J}_{1,0}^{\Lambda}[1](\sigma_{8,1}^2 + Z\phi_{8,1}^2)$$
$$+ 4g_{9,1}^2\mathcal{J}_{0,1}^{\Lambda}[1](\sigma_{9,1}^2 + Z\phi_{9,1}^2)$$
$$+ 4\sum_{a=1}^{3} g_{a,2}^2 \mathcal{J}_{1,0}^{\Lambda}[f_2^a f_2^a](\sigma_{a,2}^2 + \phi_{a,2}^2)$$
$$+ 2\sum_{a=4}^{7} g_{a,2}^2 (\mathcal{J}_{1,0}^{\Lambda}[f_2^a f_2^a] + \mathcal{J}_{0,1}^{\Lambda}[f_2^a f_2^a])$$
$$\times (\sigma_{a,2}^2 + \phi_{a,2}^2) + 4g_{8,2}^2\mathcal{J}_{1,0}^{\Lambda}[f_2^8 f_2^8](\sigma_{8,2}^2 + \phi_{8,2}^2)$$
$$+ 4g_{9,2}^2\mathcal{J}_{0,1}^{\Lambda}[f_2^9 f_2^9](\sigma_{9,2}^2 + \phi_{9,2}^2)$$
$$- 2\sum_{i,j=1}^{2}\Bigg[m_u^2 \sum_{a=1}^{3} \sigma_{a,i}\Gamma_{\text{S},ij}^{a}\sigma_{a,j}$$
$$+ \left(\frac{m_u + m_s}{2}\right)^2 \sum_{a=4}^{7} \sigma_{a,i}\Gamma_{\text{S},ij}^{a}\sigma_{a,j}$$
$$+ m_u^2\sigma_{8,i}\Gamma_{\text{S},ij}^{8}\sigma_{8,j} + m_s^2\sigma_{9,i}\Gamma_{\text{S},ij}^{9}\sigma_{9,j}\Bigg].$$

The total expressions for $L_{\text{loop}}^{(3)}$ and $L_{\text{loop}}^{(4)}$ are too lengthy; therefore, we do not show them here. Instead, we will extract parts from them when they are needed (see, e.g., the Appendix).

The Yukawa coupling constants $g_{a,i}$ describing the interaction of quarks and mesons appear as a result of renormalization of meson fields (see [5–7, 12, 13, 21] for details):

$$g_{a,1}^2 = [4\mathcal{J}_{2,0}^{\Lambda}[1]]^{-1} \quad (a = 1,2,3,8), \tag{32}$$
$$g_{a,1}^2 = [4\mathcal{J}_{1,1}^{\Lambda}[1]]^{-1} \quad (a = 4,5,6,7),$$
$$g_{9,1}^2 = [4\mathcal{J}_{0,2}^{\Lambda}[1]]^{-1};$$

$$g_{a,2}^2 = [4\mathcal{J}_{2,0}[f_2^u f_2^u]]^{-1} \quad (a = 1,2,3,8), \tag{33}$$
$$g_{a,2}^2 = [4\mathcal{J}_{1,1}[f_2^{us} f_2^{us}]]^{-1} \quad (a = 4,5,6,7),$$
$$g_{9,2}^2 = [4\mathcal{J}_{0,2}[f_2^s f_2^s]]^{-1}.$$

For the pseudoscalar meson fields, π–A_1 transitions lead to the factor Z, describing an additional renormalization of pseudoscalar meson fields, with M_{A_1} being the mass of the axial-vector meson (see [13, 21]):

$$Z = \left(1 - \frac{6m_u}{M_{A_1}^2}\right)^{-1} \approx 1.46. \tag{34}$$

For the radially excited pseudoscalar states, a similar renormalization also takes place, but in this case the renormalization factor turns out to be approximately equal to unity, so it is omitted in our calculations (see [13]).

3. INTRODUCING THE DILATON

According to the prescription described in [9, 10], we introduce the dilaton field into Lagrangian (23) as follows: the dimensional model parameters G, Λ, m_u, m_s, and K are replaced by the following rule: $G \to G(\chi_c/\chi)^2$, $\Lambda \to \Lambda(\chi/\chi_c)$, $m_{u(s)} \to m_{u(s)}(\chi/\chi_c)$, $K \to K(\chi_c/\chi)^5$, where χ is the dilaton field with VEV χ_c. We also define the field χ' as the difference $\chi' = \chi - \chi_c$ that has zero VEV. Below, the effective meson Lagrangian is expanded in terms of χ' when calculating the mass terms and vertices describing the interaction of mesons.

The current quark masses break scale invariance and, therefore, should not be multiplied by the dilaton field. The modified current quark masses $\bar{m}_a^0$ are also not multiplied by the dilaton field. Finally, we come to the Lagrangian

$$\bar{\mathcal{L}}(\sigma,\phi,\chi) = L_{\text{kin}}(\sigma,\phi) + \bar{L}_G(\sigma,\phi,\chi) \tag{35}$$
$$+ \bar{L}_{\text{loop}}(\sigma,\phi,\chi) + \mathcal{L}(\chi) + \Delta L_{\text{an}}(\sigma,\phi,\chi).$$

The term $L_{\text{kin}}(\sigma,\phi)$ remains unchanged, as it is already scale-invariant.

Here, the term $\bar{L}_G(\sigma,\phi,\chi)$ is

$$\bar{L}_G(\sigma,\phi,\chi) = -\frac{1}{2}\left(\frac{\chi}{\chi_c}\right)^2 \tag{36}$$
$$\times \sum_{a,b=1}^{9}\left(g_{a,1}\sigma_{a,1} - \mu_a\frac{\chi}{\chi_c} + \bar{\mu}_a^0\right)\left(G^{(-)}\right)_{ab}^{-1}$$
$$\times \left(g_{b,1}\sigma_{b,1} - \mu_b\frac{\chi}{\chi_c} + \bar{\mu}_b^0\right)$$
$$- \frac{Z}{2}\left(\frac{\chi}{\chi_c}\right)^2 \sum_{a,b=1}^{9} g_{a,1}\phi_{a,1}\left(G^{(+)}\right)_{ab}^{-1} g_{b,1}\phi_{b,1}$$
$$- \left(\frac{\chi}{\chi_c}\right)^2 \sum_{a=1}^{9}\frac{g_{a,2}^2}{2\bar{G}_a}(\sigma_{a,2}^2 + \phi_{a,2}^2).$$

Expanding (36) in a power series of χ, we can extract a term that is of order χ^4. It can be absorbed by the term in the pure dilaton potential (see (39) below), which has the same degree of χ. This does not bring substantial changes, because such terms are scale-invariant and therefore do not contribute to the divergence of the dilatation current (see (59) below). This would lead only to a redefinition of constants χ_0 and B of potential (39).

The term $L_{\rm loop}(\sigma,\phi)$ after introducing dilaton fields takes the form

$$\bar{L}_{\rm loop}(\sigma,\phi,\chi) = L^{(1)}_{\rm loop}(\sigma)\left(\frac{\chi}{\chi_c}\right)^3 \tag{37}$$

$$+ L^{(2)}_{\rm loop}(\sigma,\phi)\left(\frac{\chi}{\chi_c}\right)^2 + L^{(3)}_{\rm loop}(\sigma,\phi)\frac{\chi}{\chi_c} + L^{(4)}_{\rm loop}(\sigma,\phi).$$

The term $\mathcal{L}(\chi)$ in (35) is the pure dilaton Lagrangian

$$\mathcal{L}(\chi) = \frac{P^2}{2}\chi^2 - V(\chi) \tag{38}$$

with the potential

$$V(\chi) = B\left(\frac{\chi}{\chi_0}\right)^4\left[\ln\left(\frac{\chi}{\chi_0}\right)^4 - 1\right], \tag{39}$$

which has a minimum at $\chi = \chi_0$, and the parameter B represents the vacuum energy when there are no quarks. The kinetic term is given in the momentum space, P being the momentum of the dilaton.

Note that Lagrangian (23) implicitly contains a term $L_{\rm an}$ that is induced by gluon anomalies:

$$L_{\rm an}(\bar\sigma,\phi) = -h_\phi\phi_0^2 + h_\sigma\bar\sigma_0^2, \tag{40}$$

where ϕ_0 and $\bar\sigma_0$ ($\langle\bar\sigma_0\rangle_0 \neq 0$) are pseudoscalar and scalar meson isosinglets, respectively; h_ϕ, h_σ are constants; $\phi_0 = \sqrt{2/3}\phi_{8,1} - \sqrt{1/3}\phi_{9,1}$, $\bar\sigma_0 = \sqrt{2/3}\bar\sigma_{8,1} - \sqrt{1/3}\bar\sigma_{9,1}$, where $\phi_{8,1}$ and $\bar\sigma_{8,1}$ ($\langle\bar\sigma_{8,1}\rangle_0 \neq 0$) consist of u quarks; and $\phi_{9,1}$, $\bar\sigma_{9,1}$ ($\langle\bar\sigma_{9,1}\rangle_0 \neq 0$), of s quarks. In our model, the 't Hooft interaction is responsible for the appearance of these terms.

The term $L_{\rm an}$ breaks scale invariance. However, when the procedure of the scale invariance restoration is applied to Lagrangian (23), the term $L_{\rm an}$ also becomes scale-invariant. To avoid this, one should subtract this part in the scale-invariant form and add it in a scale-breaking (SB) form. This is achieved by including the term $\Delta L_{\rm an}$:

$$\Delta L_{\rm an}(\sigma,\phi,\chi) \tag{41}$$

$$= -L_{\rm an}(\bar\sigma,\phi)\left(\frac{\chi}{\chi_c}\right)^2 + L^{\rm SB}_{\rm an}(\sigma,\phi,\chi).$$

Let us define the scale-breaking term $L^{\rm SB}_{\rm an}$. The coefficients h_σ and h_ϕ in (40) can be determined by comparing them with the terms in (24) that describe the singlet—octet mixing[3]. We obtain

$$h_\phi = -\frac{3}{2\sqrt{2}}g_{8,1}g_{9,1}Z\left(G^{(+)}\right)^{-1}_{89}, \tag{42}$$

$$h_\sigma = \frac{3}{2\sqrt{2}}g_{8,1}g_{9,1}\left(G^{(-)}\right)^{-1}_{89}. \tag{43}$$

If these terms were to be made scale-invariant, one should insert $(\chi/\chi_c)^2$ into them. However, as the gluon anomalies break scale invariance, we introduce the dilaton field into these terms in a more complicated way. The inverse matrix elements $\left(G^{(+)}\right)^{-1}_{ab}$ and $\left(G^{(-)}\right)^{-1}_{ab}$,

$$\left(G^{(+)}\right)^{-1}_{89} = \frac{-4\sqrt{2}m_uK\mathcal{J}^\Lambda_{1,0}[1]}{G^{(+)}_{88}G^{(+)}_{99} - \left(G^{(+)}_{89}\right)^2}, \tag{44}$$

$$\left(G^{(-)}\right)^{-1}_{89} = \frac{4\sqrt{2}m_uK\mathcal{J}^\Lambda_{1,0}[1]}{G^{(-)}_{88}G^{(-)}_{99} - \left(G^{(-)}_{89}\right)^2}, \tag{45}$$

are determined by two different interactions. The numerators are fully defined by the 't Hooft interaction, which leads to anomalous terms (40) breaking scale invariance; therefore, we do not introduce dilaton fields here. The denominators are determined by the constant G describing the NJL four-quark interaction, and the dilaton field is inserted into it, according to the prescription given above. Finally, we come to the following form of $L^{\rm SB}_{\rm an}$:

$$L^{\rm SB}_{\rm an}(\sigma,\phi,\chi) = \Bigg[-h_\phi\phi_0^2 \tag{46}$$

$$+ h_\sigma\left(\sigma_0 - F_0\frac{\chi}{\chi_c} + F_0^0\right)^2\Bigg]\left(\frac{\chi}{\chi_c}\right)^4,$$

$$F_0 = \frac{\sqrt{2}m_u}{\sqrt{3}g_{8,1}} + \frac{m_s}{\sqrt{6}g_{9,1}}, \tag{47}$$

$$F_0^0 = \frac{\sqrt{2}\bar m_u^0}{\sqrt{3}g_{8,1}} + \frac{\bar m_s^0}{\sqrt{6}g_{9,1}}.$$

From it, we immediately obtain the term $\Delta L_{\rm an}$:

$$\Delta L_{\rm an}(\sigma,\phi,\chi) \tag{48}$$

$$= \left[h_\phi\phi_0^2 - h_\sigma\left(\sigma_0 - F_0\frac{\chi}{\chi_c} + F_0^0\right)^2\right]$$

$$\times\left(\frac{\chi}{\chi_c}\right)^2\left[1 - \left(\frac{\chi}{\chi_c}\right)^2\right].$$

---

[3] The singlet—octet mixing is fully determined by the 't Hooft interaction.

4. EQUATIONS

One of the principal requirements for an effective meson Lagrangian with a glueball is that the terms linear in σ and χ' should be absent in the effective Lagrangian. This leads to the equations

$$\frac{\delta\bar{\mathcal{L}}}{\delta\sigma_{8,1}}\Bigg|_{\substack{\phi=0\\ \sigma=0\\ \chi=\chi_c}} = \frac{\delta\bar{\mathcal{L}}}{\delta\sigma_{9,1}}\Bigg|_{\substack{\phi=0\\ \sigma=0\\ \chi=\chi_c}} = \frac{\delta\bar{\mathcal{L}}}{\delta\chi}\Bigg|_{\substack{\phi=0\\ \sigma=0\\ \chi=\chi_c}} \qquad (49)$$

$$= \frac{\delta\bar{\mathcal{L}}}{\delta\sigma_{8,2}}\Bigg|_{\substack{\phi=0\\ \sigma=0\\ \chi=\chi_c}} = \frac{\delta\bar{\mathcal{L}}}{\delta\sigma_{9,2}}\Bigg|_{\substack{\phi=0\\ \sigma=0\\ \chi=\chi_c}} = 0.$$

Gap equations follow from them. For the ground states of quarkonia ($\sigma_{a,1}$) and the dilaton field χ', we obtain

$$(m_u - \bar{m}_u^0)\left(G^{(-)}\right)^{-1}_{88} - \frac{m_s - \bar{m}_s^0}{\sqrt{2}} \qquad (50)$$

$$\times\left(G^{(-)}\right)^{-1}_{89} - 8m_u\mathcal{J}_{1,0}^{\Lambda}[1] = 0,$$

$$(m_s - \bar{m}_s^0)\left(G^{(-)}\right)^{-1}_{99} - \sqrt{2}(m_u - \bar{m}_u^0) \qquad (51)$$

$$\times\left(G^{(-)}\right)^{-1}_{98} - 8m_s\mathcal{J}_{0,1}^{\Lambda}[1] = 0,$$

$$4B\left(\frac{\chi_c}{\chi_0}\right)^3\frac{1}{\chi_0}\ln\left(\frac{\chi_c}{\chi_0}\right)^4 \qquad (52)$$

$$+\frac{1}{\chi_c}\sum_{a,b=8}^{9}\bar{\mu}_a^0\left(G^{(-)}\right)^{-1}_{ab}(\bar{\mu}_b^0 - 3\mu_b)$$

$$-\frac{2h_\sigma}{\chi_c}\left(F_0 - F_0^0\right)^2 = 0.$$

Using (17) and (18), one can rewrite Eqs. (50) and (51) in the well-known form [20] (see Fig. 2):

$$m_u^0 = m_u - 8Gm_u\mathcal{J}_{1,0}^{\Lambda}[1] \qquad (53)$$

$$-32Km_um_s\mathcal{J}_{1,0}^{\Lambda}[1]\mathcal{J}_{0,1}^{\Lambda}[1],$$

$$m_s^0 = m_s - 8Gm_s\mathcal{J}_{0,1}^{\Lambda}[1] - 32K(m_u\mathcal{J}_{1,0}^{\Lambda}[1])^2. \quad (54)$$

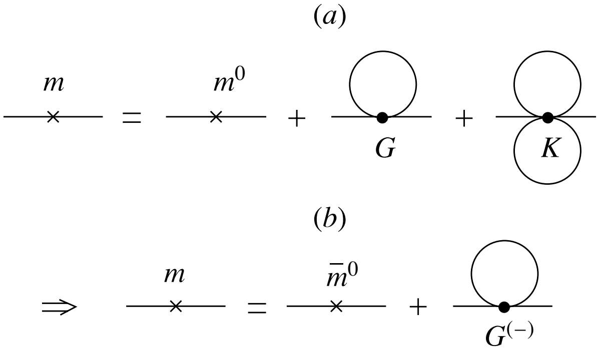

Fig. 2. The set of diagrams defining gap equations. In the figure, 2(b) the six-quark interaction is taken into account in the matrix of constants $G^{(-)}$. In order to avoid double counting of the contribution of the 't Hooft interaction, the current quark masses m^0 are replaced by the modified masses $\bar{m}^0$.

For excited states ($\sigma_{a,2}$), we require that the corresponding gap equations have the trivial solution $\langle\sigma_{a,2}\rangle_0 = 0$. This is one of the possible particular solutions of equations (49). An advantage of such a solution is that in this case the quark condensates and constituent quark masses remain unchanged after introducing radially excited states. This solution surely exists if the tadpole diagram (Fig. 1a) for the excited scalar is equal to zero (see [7, 12]). This leads to the condition

$$\mathcal{J}_{1,0}^{\Lambda}[f_2^u] = \mathcal{J}_{0,1}^{\Lambda}[f_2^s] = 0. \qquad (55)$$

In addition to these conditions, we impose a third:

$$\mathcal{J}_{1,0}^{\Lambda}[1 + d_{us}\mathbf{k}^2] + \mathcal{J}_{0,1}^{\Lambda}[1 + d_{us}\mathbf{k}^2] = 0, \qquad (56)$$

which fixes the constant d_{us}. The calculation of the second variation of the effective potential will prove that the solution that we have chosen gives the minimum of the potential.

In addition to the gap equations, a Ward identity for the divergence of dilation current, coming from QCD, should be taken into account. The identity reads

$$\langle\partial_\mu S^\mu\rangle = \mathcal{C}_g - \sum_{q=u,d,s} m_q^0\langle\bar{q}q\rangle_0, \qquad (57)$$

where

$$\mathcal{C}_g = \left(\frac{11N_c}{24} - \frac{N_{\mathrm{f}}}{12}\right)\left\langle\frac{\alpha}{\pi}\left(G^a_{\mu\nu}\right)^2\right\rangle_0 \qquad (58)$$

and N_f is the number of flavors; $\langle\frac{\alpha}{\pi}(G^a_{\mu\nu})^2\rangle_0$ and $\langle\bar{q}q\rangle_0$ are the gluon and quark condensates with α being the QCD constant of strong interaction.

Let us now consider VEVs of the divergence of the dilatation current S^μ [9, 15] calculated from the potential of Lagrangian (35):

$$\langle\partial_\mu S^\mu\rangle = \Bigg[\sum_{i=1}^{2}\sum_{a=1}^{9}\left(\sigma_{a,n}\frac{\partial V}{\partial\sigma_{a,n}} + \phi_{a,n}\frac{\partial V}{\partial\phi_{a,n}}\right) \qquad (59)$$

$$+ \chi\frac{\partial V}{\partial\chi} - 4V\Bigg]\Bigg|_{\substack{\phi=0\\ \sigma=0\\ \chi=\chi_c}} = 4B\left(\frac{\chi_c}{\chi_0}\right)^4$$

$$- 2h_\sigma\left(F_0 - F_0^0\right)^2 - \sum_{q=u,d,s}\bar{m}_q^0\langle\bar{q}q\rangle_0.$$

Here, $V = V(\chi) + \bar{V}(\sigma,\phi,\chi)$, and $\bar{V}(\sigma,\phi,\chi)$ is the potential part of Lagrangian $\bar{\mathcal{L}}(\sigma,\phi,\chi)$ (see (35)) that does not contain the pure dilaton potential (39). In the expression given in (59), the relation of the quark condensates to integrals $\mathcal{J}_{1,0}^{\Lambda}[1]$ and $\mathcal{J}_{0,1}^{\Lambda}[1]$,

$$4m_u\mathcal{J}_{1,0}^{\Lambda}[1] = -\langle\bar{u}u\rangle_0 = -\langle\bar{d}d\rangle_0, \qquad (60)$$

$$4m_s\mathcal{J}_{0,1}^{\Lambda}[1] = -\langle\bar{s}s\rangle_0,$$

and the gap equation connecting these integrals with constants $G_{ab}^{(-)}$ (see (50) and (51)) were used. Comparing (59) with the QCD expression (57), one can see that the term $\sum m_q^0\langle\bar{q}q\rangle_0$ on the right-hand side of (57) is canceled by the corresponding contribution from current quark masses on the right-hand side of (59). Equating the right-hand sides of (59) and (57),

$$\mathcal{C}_g - \sum_{q=u,d,s} m_q^0\langle\bar{q}q\rangle_0 = 4B\left(\frac{\chi_c}{\chi_0}\right)^4 \qquad (61)$$

$$- 2h_\sigma\left(F_0 - F_0^0\right)^2 - \sum_{q=u,d,s}\bar{m}_q^0\langle\bar{q}q\rangle_0,$$

we obtain the correspondence

$$\mathcal{C}_g = 4B\left(\frac{\chi_c}{\chi_0}\right)^4 + \sum_{a,b=8}^{9}\left(\bar{\mu}_a^0 - \mu_a^0\right)\left(G^{(-)}\right)_{ab}^{-1} \qquad (62)$$

$$\times\left(\mu_b - \bar{\mu}_b^0\right) - 2h_\sigma\left(F_0 - F_0^0\right)^2,$$

where $\mu_a^0 = 0$ $(a = 1,\ldots,7)$, $\mu_8^0 = m_u^0$, and $\mu_9^0 = -m_s^0/\sqrt{2}$. To derive (62), Eqs. (50), (51), and (60) were used; the quark condensates were expressed through model parameters. This equation relates the gluon condensate, whose value is taken from other sources (see, e.g., [22]), to the model parameter B. The next step is to investigate gap equations.

To determine the masses of quarkonia and of the glueball, let us consider the part of Lagrangian (35) which is quadratic in fields σ and χ' (including the kinetic terms). We denote it by $L^{(2)}$:

$$L^{(2)}(\sigma,\phi,\chi') = \frac{1}{2}\sum_{n,j=1}^{2}\Bigg[\sum_{a=1}^{3}(P^2 - 4m_u^2)\sigma_{a,n} \qquad (63)$$

$$\times\Gamma_{\mathrm{S},nj}^{a}\sigma_{a,j} + \sum_{a=4}^{7}(P^2 - (m_u + m_s)^2)\sigma_{a,n}$$

$$\times\Gamma_{\mathrm{S},nj}^{a}\sigma_{a,j} + (P^2 - 4m_u^2)\sigma_{8,n}\Gamma_{\mathrm{S},nj}^{8}\sigma_{8,j}$$

$$+ (P^2 - 4m_s^2)\sigma_{9,n}\Gamma_{\mathrm{S},nj}^{9}\sigma_{9,j}\Bigg]$$

$$- \frac{1}{2}g_{8,1}^2\left[\left(G^{(-)}\right)_{88}^{-1} - 8\mathcal{J}_{1,0}^{\Lambda}[1]\right]\sigma_{8,1}^2$$

$$- \frac{1}{2}g_{9,1}^2\left[\left(G^{(-)}\right)_{99}^{-1} - 8\mathcal{J}_{0,1}^{\Lambda}[1]\right]\sigma_{9,1}^2$$

$$- \frac{1}{2}g_{8,2}^2\left[1/\bar{G}_8 - 8\mathcal{J}_{1,0}^{\Lambda}[f_2^u f_2^u]\right]\sigma_{8,2}^2$$

$$- \frac{1}{2}g_{9,2}^2\left[1/\bar{G}_9 - 8\mathcal{J}_{0,1}^{\Lambda}[f_2^s f_2^s]\right]\sigma_{9,2}^2$$

$$- g_{8,1}g_{9,1}\left(G^{(-)}\right)_{89}^{-1}\sigma_{8,1}\sigma_{9,1} - \frac{M_g^2\chi'^2}{2}$$

$$+ \sum_{a,b=8}^{9}\frac{\bar{\mu}_a^0}{\chi_c}(G^{(-)})_{ab}^{-1}g_{b,1}\sigma_{b,1}\chi'$$

$$+ \frac{4h_\sigma(F_0 - F_0^0)}{\chi_c\sqrt{3}}\left(\sigma_{9,1} - \sigma_{8,1}\sqrt{2}\right)\chi',$$

where

$$M_g^2 = \frac{1}{\chi_c^2}\Bigg(4\mathcal{C}_g + \sum_{a,b=8}^{9}\bar{\mu}_a^0\left(G^{(-)}\right)_{ab}^{-1} \qquad (64)$$

$$\times\left(2\bar{\mu}_b^0 - \mu_b\right) + \sum_{a,b=8}^{9}4\mu_a^0\left(G^{(-)}\right)_{ab}^{-1}\left(\mu_b - \bar{\mu}_b^0\right)$$

$$- 4h_\sigma F_0^2 + 4h_\sigma(F_0^0)^2\Bigg)$$

is the glueball mass squared before taking into account mixing effects. Here, the gap equations and Eq. (62) are taken into account.

From this Lagrangian, after diagonalization, we obtain the masses of five scalar–isoscalar meson states: σ_{I}, σ_{II}, σ_{III}, σ_{IV}, and σ_{V} and a matrix of mixing coefficients b that connects the nondiagonalized fields $\sigma_{8,1}$, $\sigma_{9,1}$, $\sigma_{8,2}$, $\sigma_{9,2}$, χ' with the physical ones σ_{I}, σ_{II}, σ_{III}, σ_{IV}, σ_{V}:

$$\begin{pmatrix} \sigma_{8,1} \\ \sigma_{9,1} \\ \sigma_{8,2} \\ \sigma_{9,2} \\ \chi' \end{pmatrix} = \begin{pmatrix} b_{\sigma_{8,1}\sigma_{\rm I}} & b_{\sigma_{8,1}\sigma_{\rm II}} & b_{\sigma_{8,1}\sigma_{\rm III}} & b_{\sigma_{8,1}\sigma_{\rm IV}} & b_{\sigma_{8,1}\sigma_{\rm V}} \\ b_{\sigma_{9,1}\sigma_{\rm I}} & b_{\sigma_{9,1}\sigma_{\rm II}} & b_{\sigma_{9,1}\sigma_{\rm III}} & b_{\sigma_{9,1}\sigma_{\rm IV}} & b_{\sigma_{9,1}\sigma_{\rm V}} \\ b_{\sigma_{8,2}\sigma_{\rm I}} & b_{\sigma_{8,2}\sigma_{\rm II}} & b_{\sigma_{8,2}\sigma_{\rm III}} & b_{\sigma_{8,2}\sigma_{\rm IV}} & b_{\sigma_{8,2}\sigma_{\rm V}} \\ b_{\sigma_{9,2}\sigma_{\rm I}} & b_{\sigma_{9,2}\sigma_{\rm II}} & b_{\sigma_{9,2}\sigma_{\rm III}} & b_{\sigma_{9,2}\sigma_{\rm IV}} & b_{\sigma_{9,2}\sigma_{\rm V}} \\ b_{\chi'\sigma_{\rm I}} & b_{\chi'\sigma_{\rm II}} & b_{\chi'\sigma_{\rm III}} & b_{\chi'\sigma_{\rm IV}} & b_{\chi'\sigma_{\rm V}} \end{pmatrix} \begin{pmatrix} \sigma_{\rm I} \\ \sigma_{\rm II} \\ \sigma_{\rm III} \\ \sigma_{\rm IV} \\ \sigma_{\rm V} \end{pmatrix}. \qquad (65)$$

The values of matrix elements are given in Table 1.

For the isovector states we introduce physical states: the ground a_0 and radially excited $\hat{a}_0$. The corresponding mixing coefficients are represented as elements of a matrix connecting the physical fields a_0, $\hat{a}_0$ with the fields a_{01}, a_{02} before mixing:

$$\begin{pmatrix} a_{01} \\ a_{02} \end{pmatrix} = \begin{pmatrix} b_{a_{01}a_0} b_{a_{01}\hat{a}_0} \\ b_{a_{02}a_0} b_{a_{02}\hat{a}_0} \end{pmatrix} \begin{pmatrix} a_0 \\ \hat{a}_0 \end{pmatrix}. \qquad (66)$$

Their values are $b_{a_{01}a_0} = 0.918$, $b_{a_{02}a_0} = 0.138$, $b_{a_{01}\hat{a}_0} = 0.761$, $b_{a_{02}\hat{a}_0} = -1.18$. The mixing of strange scalar meson states is described as follows:

$$\begin{pmatrix} K^*_{01} \\ K^*_{02} \end{pmatrix} = \begin{pmatrix} b_{K^*_{01}K^*_0} b_{K^*_{01}\hat{K}^*_0} \\ b_{K^*_{02}K^*_0} b_{K^*_{02}\hat{K}^*_0} \end{pmatrix} \begin{pmatrix} K^*_0 \\ \hat{K}^*_0 \end{pmatrix}. \qquad (67)$$

The values of matrix elements are $b_{K^*_{01}K^*_0} = 0.866$, $b_{K^*_{02}K^*_0} = 0.232$, $b_{K^*_{01}\hat{K}^*_0} = 0.750$, $b_{K^*_{02}\hat{K}^*_0} = -1.12$. Here, the physical states are K^*_0 and its radial excitation $\hat{K}^*_0$. The states K^*_{01} and K^*_{02} correspond to the nondiagonalized Lagrangian.

After the diagonalization, we obtain the kinetic and mass terms of the effective Lagrangian in a diagonal form. Expressions for the quadratic terms in the case of isovector and strange mesons are given in [5–7].

5. MODEL PARAMETERS AND NUMERICAL ESTIMATES

The basic parameters of our model are G, Λ, m_u, and m_s. They are fixed by the pion weak decay constant $F_\pi = 93$ MeV, the ρ-meson decay constant $g_\rho \approx 6.14$, and the masses of pion and kaon [21, 23, 24]. To fix Λ and m_u, the Goldberger–Treiman relation $g_u F_\pi \sqrt{Z} = m_u$ and the equation $g_\rho = \sqrt{6} g_u$ are used. The parameter G is determined by the pion mass; and m_s, by the kaon mass. Their values do not change after the radially excited states [5–7, 12, 13] and the dilaton fields are introduced [9, 10]:

$$m_u = 280 \text{ MeV}, \quad m_s = 417 \text{ MeV}, \qquad (68)$$

$$\Lambda = 1.03 \text{ GeV}, \quad G = 3.202 \text{ GeV}^{-2}.$$

To have a correct description of η and η', one should fix the 't Hooft interaction constant by the masses of η and η'. The lower bound for the lightest scalar–isoscalar meson mass is also taken into account here. As a result, for the model masses we obtain $M_\eta \approx 500$ MeV, $M_{\eta'} \approx 870$ MeV, and for K,

$$K = 4.4 \text{ GeV}^{-5}. \qquad (69)$$

After introducing the radially excited states, there appear new parameters: the slope parameters d_a and the arbitrary parameters c_a. The constants d_a are not arbitrary and are fixed by conditions (55) and (56):

$$d_u = -1.77 \text{ GeV}^{-2}, \quad d_s = -1.72 \text{ GeV}^{-2}, \qquad (70)$$
$$d_{us} = -1.75 \text{ GeV}^{-2}.$$

The parameters c_a are absorbed by the four-quark interaction constants $\bar{G}_a$ and influence only masses of mesons. They are fixed from experiment by masses of excited pseudoscalar meson states. As a result, we obtain

$$\bar{G}_1 = 4.45 \text{ GeV}^{-2}, \quad \bar{G}_4 = 5.12 \text{ GeV}^{-2}, \qquad (71)$$
$$\bar{G}_8 = 4.64 \text{ GeV}^{-2}, \quad \bar{G}_9 = 5.09 \text{ GeV}^{-2}.$$

Due to the chiral symmetry of Lagrangian (3), the same values of the form-factor parameters are used both for the scalar and pseudoscalar mesons, which allows us to predict masses of excited scalar states[4].

After the dilaton is introduced, three new parameters χ_0, χ_c, and B appear. To fix the new parameters, one should use Eqs. (62) and (52) and the physical glueball mass. As a result, we find for χ_0 and B that

$$\chi_0 = \chi_c \exp\Bigg\{ -\Bigg[\sum_{a,b=8}^{9} \bar{\mu}^0_a \left(G^{(-)}\right)^{-1}_{ab} (3\mu_b - \bar{\mu}^0_b) \qquad (72)$$

$$+ 2h_\sigma \left(F_0 - F^0_0\right)^2 \Bigg] \Big/ 4 \Bigg[\mathcal{C}_g - \sum_{a,b=8}^{9} (\bar{\mu}^0_a - \mu^0_a)$$

---

[4] The excited meson K' is an exception. Insofar as the experimental status of the excited K' meson is unclear, we use the experimental value of the mass of $K^*_0(1430)$ to determine $\bar{G}_4$ and predict the mass of K'.

Table 1. Elements of the matrix b, describing mixing in the scalar–isoscalar sector. The singlet–octet and quarkonia–glueball mixing effects are taken into account

	σ_{I}	σ_{II}	σ_{III}	σ_{IV}	σ_{V}
$\sigma_{8,1}$	0.973	0.137	0.393	0.548	0.048
$\sigma_{8,2}$	−0.064	0.204	−0.978	−0.647	−0.047
$\sigma_{9,1}$	−0.225	0.876	0.160	0.011	0.628
$\sigma_{9,2}$	0.025	0.146	0.136	−0.082	−1.09
χ'	−0.266	0.095	−0.495	0.813	−0.116

$$\times \left(G^{(-)}\right)^{-1}_{ab} (\mu_b - \bar{\mu}_b^0) + 2h_\sigma \left(F_0 - F_0^0\right)^2 \Bigg] \Bigg\},$$

$$B = \frac{1}{4}\Bigg(\mathcal{C}_g - \sum_{a,b=8}^{9} (\bar{\mu}_a^0 - \mu_a^0) \left(G^{(-)}\right)^{-1}_{ab} \tag{73}$$

$$\times (\mu_b - \bar{\mu}_b^0) + 2h_\sigma \left(F_0 - F_0^0\right)^2 \Bigg) \left(\frac{\chi_0}{\chi_c}\right)^4 .$$

We adjust the parameter χ_c, so that the mass of the scalar meson state σ_{IV} would be close to 1500 MeV ($\chi_c = 219$ MeV).[5)] For the constants χ_0 and B we have $\chi_0 = 203$ MeV, $B = 0.007$ GeV^4. We found that, if the state $f_0(1710)$ is supposed as the glueball, the result turns out to be in worse agreement with experiment (see the Conclusion). The masses of scalar mesons calculated in our model, together with their experimental values, are given in Table 2.

6. STRONG DECAYS OF SCALAR ISOSCALAR MESONS

Once all parameters are fixed, we can estimate the decay widths for the main modes of strong decays of scalar mesons: $\sigma_l \to \pi\pi$, $K\bar{K}$, $\eta\eta$, $\eta\eta'$, and 4π (2σ, $\sigma 2\pi \to 4\pi$), where $l =$ I, II, III, IV, and V; decays of excited isovectors: $\hat{a}_0 \to \eta\pi$, $\hat{a}_0 \to \eta\pi$, $\hat{a}_0 \to K\bar{K}$; and of strange mesons: $\hat{K}_0^* \to K\pi$.

Note that, in the energy region under consideration (up to 1.7 GeV), we work on the brim of the validity of exploiting the chiral symmetry and scale invariance that were used to construct our effective Lagrangian. Thus, our results should be considered rather as qualitative.

Table 2. The model and experimental masses of scalar–isoscalar meson states

	Theory	Experiment [8]
σ_{I}	400	408 [25], 387 [26]
σ_{II}	1070	980 ± 10
σ_{III}	1320	1200–1500
σ_{IV}	1550	1500 ± 10
σ_{V}	1670	1712 ± 5
$\hat{a}_0$	1530	1474 ± 19
$\hat{K}_0^*$	1430	1429 ± 6

Let us start with the decay of a scalar–isoscalar meson into a pair of pions. The corresponding amplitude has the form

$$A_{\sigma_l \to \pi\pi} = A^{(1)}_{\sigma_l \to \pi\pi} + A^{(2)}_{\sigma_l \to \pi\pi}, \tag{74}$$

where the first part comes from contact terms of Lagrangian (35) that describe the decay of the glueball into pions. These terms come from $\bar{L}_G(\sigma, \phi, \chi)$ and $(\chi/\chi_c)^2 L^{(2)}_{\mathrm{loop}}(\sigma, \phi)$ (see (36) and (37)). They turn into the pion mass term if $\chi = \chi_c$. Expanding around $\chi = \chi_c$ in terms of χ' and choosing the term linear in χ', we obtain, after the mixing effects are taken into account, the following:

$$A^{(1)}_{\sigma_l \to \pi\pi} = -\frac{M_\pi^2}{\chi_c} b_{\chi' \sigma_l}, \tag{75}$$

where M_π is the pion mass and $b_{\chi'\sigma_l}$ is a mixing coefficient (see (65) and Table 1). The second contribution $A^{(2)}_{\sigma_l \to \pi\pi}$ describes the decay of the quarkonium part of σ_l and is determined by triangle quark loop diagrams (see Figs. 1*c* and 3). For details of their calculation see the Appendix. As a result, we obtain the following widths for decays of scalar isoscalar-mesons into two pions (in MeV):

$$\begin{aligned} \Gamma_{\sigma_{\mathrm{I}} \to \pi\pi} &\approx 600, \\ \Gamma_{\sigma_{\mathrm{II}} \to \pi\pi} &\approx 36\ (20), \\ \Gamma_{\sigma_{\mathrm{III}} \to \pi\pi} &\approx 680\ (480), \\ \Gamma_{\sigma_{\mathrm{IV}} \to \pi\pi} &\approx 100, \\ \Gamma_{\sigma_{\mathrm{V}} \to \pi\pi} &\approx 0.3. \end{aligned} \tag{76}$$

To calculate decay widths, we used the model masses of scalar mesons. For the state σ_{II}, hereafter we give in brackets the values obtained for its experimental mass. Concerning the state σ_{III}, the values in brackets correspond to calculations performed for the lowest experimental limit for its mass (1200 MeV). Note that for the experimental masses, the widths are

---

[5)] To reach closer agreement with experimental data in the description of strong decays of σ_{IV}, we chose the model value of $M_{\sigma_{\mathrm{IV}}} = 1550$ MeV (mass + halfwidth).

noticeably smaller than those derived for the model masses.

Decays of scalar–isoscalar mesons into kaons are described by the amplitude,

$$A_{\sigma_l\to K\bar K} = A^{(1)}_{\sigma_l\to K\bar K} + A^{(2)}_{\sigma_l\to K\bar K}, \qquad (77)$$

where $A^{(1)}_{\sigma_l\to K\bar K}$ originates from the same source as $A^{(1)}_{\sigma_l\to\pi\pi}$ and is determined by the kaon mass,

$$A^{(1)}_{\sigma_l\to K\bar K} = -\frac{2M_K^2}{\chi_c}b_{\chi'\sigma_l}, \qquad (78)$$

while the other part $A^{(2)}_{\sigma_l\to K\bar K}$ again comes from quark loop diagrams (see the Appendix). The decay widths thereby are[6] (in MeV)

$$\begin{aligned}\Gamma_{\sigma_{\rm III}\to K\bar K} &\approx 260\ (125),\\ \Gamma_{\sigma_{\rm IV}\to K\bar K} &\approx 28, \qquad (79)\\ \Gamma_{\sigma_{\rm V}\to K\bar K} &\approx 250.\end{aligned}$$

The state $\sigma_{\rm I}$ cannot decay into kaons, as it is below the threshold.

The amplitude describing decays of scalar–isoscalar mesons into $\eta\eta$ has a more complicated form, because it contains a contribution from $\Delta L_{\rm an}$. The singlet–octet mixing between pseudoscalar–isoscalar states should also be taken into account here. Using the expression for the fields $\phi_{8,1}$ and $\phi_{9,1}$ through the physical ones η and η',

$$\phi_{8,1} = b_{\phi_{8,1}\eta}\eta + b_{\phi_{8,1}\eta'}\eta' + \ldots, \qquad (80)$$

$$\phi_{9,1} = b_{\phi_{9,1}\eta}\eta + b_{\phi_{9,1}\eta'}\eta' + \ldots, \qquad (81)$$

where ... stand for the excited η and η', which we do not need here and therefore omit. The mixing coefficients for the scalar–pseudoscalar meson states were calculated in [5–7]. In the current calculation, their values changed a little because the parameter K varied; thus, $b_{\phi_{8,1}\eta} = 0.777$, $b_{\phi_{8,1}\eta'} = -0.359$, $b_{\phi_{9,1}\eta} = 0.546$, $b_{\phi_{9,1}\eta'} = 0.701$. Thus, we obtain for the amplitude

$$A_{\sigma_l\to\eta\eta} = A^{(1)}_{\sigma_l\to\eta\eta} + A^{(2)}_{\sigma_l\to\eta\eta} + A^{(3)}_{\sigma_l\to\eta\eta}. \qquad (82)$$

Here the contact term $A^{(1)}_{\sigma_l\to\eta\eta}$ has the form

$$A^{(1)}_{\sigma_l\to\eta\eta} = -\frac{M_\eta^2}{\chi_c}b_{\chi'\sigma_l}. \qquad (83)$$

The second term $A^{(2)}_{\sigma_l\to\eta\eta}$ comes from a quark loop calculation (see the Appendix), and the third term $A^{(3)}_{\sigma_l\to\eta\eta}$ originates from $\Delta L_{\rm an}$ (see (48)):

$$A^{(3)}_{\sigma_l\to\eta\eta} = \frac{2h_\phi}{3\chi_c}\left(\sqrt{2}b_{\phi_{8,1}\eta} - b_{\phi_{9,1}\eta}\right)^2. \qquad (84)$$

As result, we obtain the following decay widths (in MeV):

$$\begin{aligned}\Gamma_{\sigma_{\rm III}\to K\bar K} &\approx 260\ (125),\\ \Gamma_{\sigma_{\rm IV}\to K\bar K} &\approx 28, \qquad (85)\\ \Gamma_{\sigma_{\rm V}\to K\bar K} &\approx 250.\end{aligned}$$

The state $\sigma_{\rm V}$ can also decay into $\eta\eta'$. The corresponding amplitude is

$$A_{\sigma_l\to\eta\eta'} = A^{(2)}_{\sigma_l\to\eta\eta'} + A^{(3)}_{\sigma_l\to\eta\eta'}. \qquad (86)$$

The contact term $A^{(1)}_{\sigma_l\to\eta\eta'}$ is absent here. The term $A^{(2)}_{\sigma_l\to\eta\eta'}$ comes from quark loop diagrams, as usual, and the last term has the form

$$A^{(3)}_{\sigma_l\to\eta\eta'} = \frac{4h_\phi}{3\chi_c}\left(\sqrt{2}b_{\phi_{8,1}\eta} - b_{\phi_{9,1}\eta}\right) \qquad (87)$$
$$\times\left(\sqrt{2}b_{\phi_{8,1}\eta'} - b_{\phi_{9,1}\eta'}\right).$$

The decay width is approximately equal to 100 MeV.

The scalar-meson states $\sigma_{\rm III}$, $\sigma_{\rm IV}$, and $\sigma_{\rm V}$ can decay into four pions. This decay can occur via intermediate scalar mesons. Similar calculations for $f_0(1500)$ were performed in our previous works [9, 10]. Insofar as our calculations are qualitative, we consider here, instead of the direct processes that involve $\sigma_{\rm I}$ resonances, simpler decays: into $2\sigma_{\rm I}$ and $\sigma_{\rm I}2\pi$ as final states. Our investigation has shown that the result thus obtained can be a good estimate for the decay into 4π.

Let us consider decays into $2\sigma_{\rm I}$. Its amplitude can be divided into two parts:

$$A_{\sigma_l\to\sigma_{\rm I}\sigma_{\rm I}} = A^{(1)}_{\sigma_l\to\sigma_{\rm I}\sigma_{\rm I}} + A^{(2)}_{\sigma_l\to\sigma_{\rm I}\sigma_{\rm I}}. \qquad (88)$$

To calculate the first term $A^{(1)}_{\sigma_l\to\sigma_{\rm I}\sigma_{\rm I}}$, one should first take, from the effective meson Lagrangian, the terms that contain only scalar meson fields in the third power before taking into account mixing effects. The corresponding vertices have the form

$$a_1\chi'^3 + a_2\chi'^2\sigma_{8,1} + a_3\chi'\sigma_{8,1}^2 + a_4\chi'\sigma_{8,2}^2, \qquad (89)$$

where the coefficients a_k are given in the Appendix (see (A.20)–(A.23)). These vertices come from $\bar L_G$, $\mathcal{L}(\chi)$, and $\Delta L_{\rm an}$ (see Eqs. (36), (38), and (48)). We neglected here the terms with $\sigma_{9,i}$ fields which represent quarkonia made of s quarks, because we are interested in decays into pions that do not contain s quarks.

Up to this moment, the contribution $A^{(1)}_{\sigma_l\to\sigma_{\rm I}\sigma_{\rm I}}$ was considered. As to the term $A^{(2)}_{\sigma_l\to\sigma_{\rm I}\sigma_{\rm I}}$ in (88) connected

---

[6] The decay of $\sigma_{\rm II}$ into kaons occurs almost at the threshold; therefore, we cannot give a reliable estimate for this process.

Table 3. The partial and total decay widths (in MeV) of scalar–isoscalar meson states

Decays	$f_0(400\text{–}1200)$ $(\sigma_{\rm I})$	$f_0(980)$ $(\sigma_{\rm II})$	$f_0(1370)$ $(\sigma_{\rm III})$	$f_0(1500)$ $(\sigma_{\rm IV})$	$f_0(1710)$ $(\sigma_{\rm V})$	$a_0(1250)$ $(\hat{a}_0)$	$K_0^*(1430)$ $(\hat{K}_0^*)$
$\pi\pi$	600	36 (20)	680 (480)	100	0.3	–	–
$K\bar{K}$	–	–	260 (125)	28	250	160	–
$\eta\eta$	–	–	62 (26)	4	20	–	–
$\eta\eta'$	–	–	–	–	100	–	–
$4\pi(2\sigma_{\rm I})$	–	–	40	200	1	–	–
$\eta\pi$	–	–	–	–	–	250	–
$\eta'\pi$	–	–	–	–	–	36	–
$K\pi$	–	–	–	–	–	–	200
$K3\pi$ ($K_0^*\pi\pi$, $K_0^*\sigma_{\rm I}$, $K\pi\sigma_{\rm I}$)	–	–	–	–	–	–	~50
$\Gamma_{\rm tot}$	600	$> 40 (> 20)^a$	1040 (670)	330	370	450	250
$\Gamma_{\rm tot}^{\rm exp}$	600–1200	40–100	200–500	112±10	133 ± 14	265 ± 13	287 ± 23

Note: ^{a} for the meson state $\sigma_{\rm II}$, a decay into kaons is possible, which we did not calculate here, because its mass is at the threshold. We show only the lowest limit for its total decay width allowing for decay into kaons that can increase the total decay width. The value is given for the model mass 1070 MeV. Next, in brackets, we also give the decay width calculated for the experimental mass 980 MeV. In the case of $\sigma_{\rm III}$, two values are given for its model mass and (in brackets) for the lowest bound for its experimental mass (1200 MeV).

with quark loops, its calculation is given in the Appendix. As a result, we obtain the following decay widths (in MeV):

$$\Gamma_{\sigma_{\rm III}\to\sigma_{\rm I}\sigma_{\rm I}} \approx 40, \qquad (90)$$
$$\Gamma_{\sigma_{\rm IV}\to\sigma_{\rm I}\sigma_{\rm I}} \approx 200,$$
$$\Gamma_{\sigma_{\rm V}\to\sigma_{\rm I}\sigma_{\rm I}} \approx 1.$$

Four pions in the final state can also be produced through the process with one $\sigma_{\rm I}$ resonance ($\sigma_l \to \sigma_{\rm I}2\pi \to 4\pi$). To estimate this process, we calculate the decay into $\sigma 2\pi$ as a final state. The amplitude again can be divided into two parts:

$$A_{\sigma_l\to\sigma_{\rm I}2\pi} = A^{(1)}_{\sigma_l\to\sigma_{\rm I}2\pi} + A^{(2)}_{\sigma_l\to\sigma_{\rm I}2\pi}. \qquad (91)$$

The first term has the form

$$\begin{aligned} A^{(1)}_{\sigma_l\to\sigma_{\rm I}2\pi} &= -\frac{M_\pi^2}{\chi_c^2} b_{\chi'\sigma_l} b_{\chi'\sigma_{\rm I}} \qquad (92)\\ &+ \frac{8m_u}{\chi_c} b_{\chi'\sigma_l} \mathcal{J}^\Lambda_{2,0}[\bar{f}_{\sigma_{\rm I}}\bar{f}_\pi\bar{f}_\pi] \\ &+ \frac{8m_u}{\chi_c} b_{\chi'\sigma_{\rm I}} \mathcal{J}^\Lambda_{2,0}[\bar{f}_{\sigma_l}\bar{f}_\pi\bar{f}_\pi], \end{aligned}$$

where $\bar{f}_a$ are "physical" form factor functions defined in the Appendix. The pure quark contribution is calculated as described in the Appendix. The result is

$$A^{(2)}_{\sigma_l\to\sigma_{\rm I}2\pi} = -4\mathcal{J}^\Lambda_{2,0}[\bar{f}_{\sigma_l}\bar{f}_{\sigma_{\rm I}}\bar{f}_\pi\bar{f}_\pi]. \qquad (93)$$

The corresponding decay widths (in MeV) are negligibly small:

$$\Gamma_{\sigma_{\rm III}\to\sigma 2\pi} \approx 1, \qquad (94)$$
$$\Gamma_{\sigma_{\rm IV}\to\sigma 2\pi} \approx 2,$$
$$\Gamma_{\sigma_{\rm V}\to\sigma 2\pi} \approx 0.6.$$

Comparing the results obtained with experimental data (see Table 3), one can see that the decays $\sigma_{\rm I} \to \pi\pi$ and $\sigma_{\rm II} \to \pi\pi$ are in satisfactory agreement with experiment. For the states $\sigma_{\rm III}$, $\sigma_{\rm IV}$, and $\sigma_{\rm V}$, we have reliable values only for their total widths measured experimentally. Our results allow us to obtain just the order of magnitude for the decay widths, exceeding the experimental values by a factor of 2.0–3.0.

Concerning partial decay modes, the state $f_0(1500)$ decays mostly into 4π and 2π. According to the experimental data analysis given in [27], the ratio $\Gamma_{4\pi}/\Gamma_{2\pi} \approx 1.34$. We obtain $\Gamma_{4\pi}/\Gamma_{2\pi} \approx 2$, which is in qualitative agreement with [27]. The decays into 4π and 2π are suppressed for the state $f_0(1710)$. Its main decay mode is into kaons. This agrees with the analysis of experimental data given in [27] and corroborates our assumption that $f_0(1500)$ is a glueball.

The amplitudes describing decays of excited state $\hat{a}_0$ into $\eta\pi$, $\eta'\pi$, and $K\bar{K}$ are calculated through triangle quark loop diagrams and look as follows:

$$A_{\hat{a}_0\to\eta\pi} = 16m_u(\mathcal{J}_{2,0}^{\Lambda}[\bar{f}_{\hat{a}_0}\bar{f}_{\eta}^{u}\bar{f}_{\pi}] - P_1\cdot P_2\mathcal{J}_{3,0}^{\Lambda}[\bar{f}_{\hat{a}_0}\bar{f}_{\eta}^{u}\bar{f}_{\pi}]), \tag{95}$$

$$A_{\hat{a}_0\to\eta'\pi} = 16m_u(\mathcal{J}_{2,0}^{\Lambda}[\bar{f}_{\hat{a}_0}\bar{f}_{\eta'}^{u}\bar{f}_{\pi}] - P_1\cdot P_2\mathcal{J}_{3,0}^{\Lambda}[\bar{f}_{\hat{a}_0}\bar{f}_{\eta'}^{u}\bar{f}_{\pi}]), \tag{96}$$

$$A_{\hat{a}_0\to K\bar{K}} = 8m_u(C_{uu}\mathcal{J}_{2,0}^{\Lambda}[\bar{f}_{\hat{a}_0}\bar{f}_{K}\bar{f}_{K}] + C_{us}\mathcal{J}_{1,1}^{\Lambda}[\bar{f}_{\hat{a}_0}\bar{f}_{K}\bar{f}_{K}]) - P_1\cdot P_2 8m_s\mathcal{J}_{2,1}^{\Lambda}[\bar{f}_{\hat{a}_0}\bar{f}_{K}\bar{f}_{K}], \tag{97}$$

where the constants C are defined in the Appendix (see (A.18)). The momenta P_1 and P_2 are those of the secondary particles. Their product is expressed via masses of mesons (see (A.2) in the Appendix). As a result, we obtain (in MeV)

$$\Gamma_{\hat{a}_0\to\eta\pi} = 250, \quad \Gamma_{\hat{a}_0\to\eta'\pi} = 36, \quad \Gamma_{\hat{a}_0\to K\bar{K}} = 160. \tag{98}$$

The total width is thereby 446 MeV.

The decay amplitude of $K_0^*(1430)$ (denoted in formulas as $\hat{K}_0^*$) into $K\pi$ has the form

$$A_{\hat{K}_0^*\to K\pi} = 8m_s\mathcal{J}_{1,1}^{\Lambda}[\bar{f}_{\hat{K}_0^*}\bar{f}_{K}^{u}\bar{f}_{\pi}] - 8m_sP_1\cdot P_2\mathcal{J}_{2,1}^{\Lambda}[\bar{f}_{\hat{K}_0^*}\bar{f}_{K}^{u}\bar{f}_{\pi}]. \tag{99}$$

The decay width is

$$\Gamma_{\hat{K}_0^*\to K\pi} = 200\ \text{MeV}. \tag{100}$$

There is also the possibility of the state $\hat{K}_0^*$ to decay into $K3\pi$ via the processes $\hat{K}_0^* \to K_0^*\pi\pi \to K3\pi$, $\hat{K}_0^* \to K_0^*\sigma_{\rm I} \to K3\pi$ and $\hat{K}_0^* \to K\pi\sigma_{\rm I} \to K3\pi$. A rough estimate of the corresponding decay widths shows that it can add ~50 MeV to the total width of $\hat{K}_0^*$.

7. CONCLUSION AND DISCUSSION

In papers [9, 10], we suggested a chiral quark model with a scalar glueball. However, in these papers, only ground states of scalar quarkonia were considered. To describe the whole spectrum of a scalar mesons in the mass interval from 0.4 to 1.7 GeV, one needs to introduce radially excited meson states. This has already been done, though without the glueball, in papers [5–7]. The radially excited quarkonia were described by means of form factors. Each of these form factors was a polynomial in the momentum space and had two parameters: the external c_a and the slope parameter d_a. In general, the external parameters c_a can always be absorbed by the four-quark-interaction constant G, giving rise to four different interaction constants $\bar{G}_a$, connected with excited meson states. The constants determine only the masses of excited mesons and do not affect the interaction of mesons. Only the slope parameters d_a influence decay amplitudes. And they are fixed by conditions (55) and (56) and are not arbitrary.

In papers [5–7], we have shown for the first time that 18 scalar meson states with masses lying between 0.4 and 1.7 GeV can be considered as two nonets of scalar quarkonia. In the present work, we introduced a glueball into the Lagrangian investigated in [5–7] and described the mixing of five scalar–isoscalar meson states: $\sigma_{\rm I}$, $\sigma_{\rm II}$, $\sigma_{\rm III}$, $\sigma_{\rm IV}$, and $\sigma_{\rm V}$ with the following masses: 400, 1070, 1320, 1550, and 1670 MeV, respectively. We showed that $f_0(1500)$ is a glueball. This conclusion has followed the analysis of strong decays of the meson state $f_0(1500)$. Indeed, according to our calculations, the state $f_0(1500)$ decays mostly into 4π and 2π, the decay into 4π being more probable. This is in agreement with experiment [8, 27]. Meanwhile, the decays of $f_0(1710)$ into 4π and 2π are suppressed as compared with those into kaons and η mesons (see [8, 27]). On the other hand, if the model parameters were fixed from the supposition that $f_0(1710)$ was the glueball, the main decay mode of $f_0(1710)$ would be 4π ($\Gamma_{4\pi} = 150$ MeV) and the remaining partial widths would be too small: $\Gamma_{\pi\pi} = 3$ MeV, $\Gamma_{K\bar{K}} = 5$ MeV, $\Gamma_{\eta\eta} = 2$ MeV, and $\Gamma_{\eta\eta'} = 2$ MeV. For the state $f_0(1500)$ in this case, the main decay would be into kaons ($\Gamma_{K\bar{K}} = 250$ MeV) and the other modes would give $\Gamma_{\pi\pi} = 10$ MeV, $\Gamma_{\eta\eta} = 34$ MeV, $\Gamma_{4\pi} = 90$ MeV. This crucially disagrees with experiment [27].

Note that, after the glueball is introduced into the effective meson Lagrangian, the mass of $\sigma_{\rm I}$ noticeably decreased as compared with the result from [5–7]. This is a consequence of the noticeable mixing between the glueball and the ground and radially excited $\bar{u}u$ ($\bar{d}d$) quarkonia, $f_0(400–1200)$ and $f_0(1370)$. The obtained mass and decay width of $\sigma_{\rm I}$ are in satisfactory agreement with recent experimental data [8, 25, 26]. On the other hand, the $\bar{s}s$ quarkonia mix with the glueball in small proportion (see Table 1). Therefore, after introducing the glueball (compare with [5–7]), the masses of $\sigma_{\rm II}$ and $\sigma_{\rm V}$ change less than the mass of $\sigma_{\rm I}$. However, here we obtain better agreement with experiment for the mass of $\sigma_{\rm V}$ than in [5–7]. For $\sigma_{\rm IV}$, we obtain that the state contains 67% of the glueball, which is in agreement with [2]. After this analysis, we identify the five scalar–isoscalar states $\sigma_{\rm I}$, $\sigma_{\rm II}$, $\sigma_{\rm III}$, $\sigma_{\rm IV}$, and $\sigma_{\rm V}$ with physically observed meson states in the following sequence: $f_0(400–1200)$, $f_0(980)$, $f_0(1370)$, $f_0(1500)$, $f_0(1710)$ (see Table 2). We also have excited isovectors: $\hat{a}_0$ with a mass of 1530 MeV and strange scalar meson $\hat{K}_0^*$ with a mass of 1430 MeV.

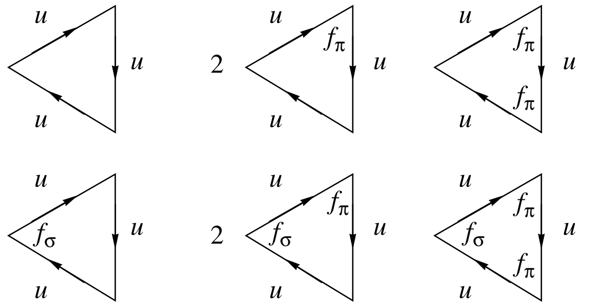

Fig. 3. The set of diagrams describing the decay of a scalar meson into a pair of pions. The vertices where a form factor occurs are marked by f. In this set of diagrams, the quark–meson vertices correspond to meson fields before taking into account mixing effects.

The chiral symmetry has played a crucial role in calculations. It allowed us to predict masses of scalar mesons, using masses of pseudoscalars.

Let us remind that our model is based on the $U(3)\times U(3)$ chiral symmetry and scale invariance of an effective meson Lagrangian. Both symmetries are very approximate for the energies under consideration. Therefore, our results are rather qualitative. As a result, the decay width obtained agrees with experiment only in order of magnitude. Nevertheless, we hope that the model gives, on the whole, a correct description of scalar meson properties.

ACKNOWLEDGMENTS

We are grateful to Drs. S.B. Gerasimov and A.E. Dorokhov for stimulating discussions.

The work was supported by the Russian Foundation for Basic Research, project no. 00-02-17190, and the Heisenberg–Landau program 2001.

APPENDIX

Calculation of the Quark Loop Contribution into the Strong Decay Amplitudes

In the calculation of the quark loop contributions to decay amplitudes, we follow our papers [5–7], where the external momentum dependence of decay amplitudes was taken into account.

It is convenient to take into account mixing effects before integration. To demonstrate how to do this, let us first calculate the decay of the state σ_{I} into pions. As one can see, eight[7)] diagrams (Fig. 3) contribute to this process. The expression for the amplitude is as follows (see (8) for the definition of form factor functions):

$$\begin{aligned}A^{(2)}_{\sigma_{\mathrm{I}}\to\pi\pi} = 8m_u\big[&g_{8,1}b_{\sigma_{8,1}\sigma_{\mathrm{I}}}(g^2_{1,1}Zb^2_{\pi_1\pi}\mathcal{J}^{\Lambda}_{2,0}[1] \\ &+ 2g_{1,1}g_{1,2}\sqrt{Z}b_{\pi_1\pi}b_{\pi_2\pi}\mathcal{J}^{\Lambda}_{2,0}[f^u_2] \\ &+ g^2_{1,2}b^2_{\pi_2\pi}\mathcal{J}_{2,0}[f^u_2f^u_2]) \\ &+ g_{8,2}b_{\sigma_{8,2}\sigma_{\mathrm{I}}}(g^2_{1,1}Zb^2_{\pi_1\pi}\mathcal{J}^{\Lambda}_{2,0}[f^u_2] \\ &+ 2g_{1,1}g_{1,2}\sqrt{Z}b_{\pi_1\pi}b_{\pi_2\pi}\mathcal{J}_{2,0}[f^u_2f^u_2] \\ &+ g^2_{1,2}b^2_{\pi_2\pi}\mathcal{J}^{\Lambda}_{2,0}[f^u_2f^u_2f^u_2]) \\ &- P_1\cdot P_2\,(g_{8,1}b_{\sigma_{8,1}\sigma_{\mathrm{I}}}(g^2_{1,1}Zb^2_{\pi_1\pi}\mathcal{J}^{\Lambda}_{3,0}[1] \\ &+ 2g_{1,1}g_{1,2}\sqrt{Z}b_{\pi_1\pi}b_{\pi_2\pi}\mathcal{J}^{\Lambda}_{3,0}[f^u_2] \\ &+ g^2_{1,2}b^2_{\pi_2\pi}\mathcal{J}^{\Lambda}_{3,0}[f^u_2f^u_2]) \\ &+ g_{8,2}b_{\sigma_{8,2}\sigma_{\mathrm{I}}}(g^2_{1,1}Zb^2_{\pi_1\pi}\mathcal{J}^{\Lambda}_{3,0}[f^u_2] \\ &+ 2g_{1,1}g_{1,2}\sqrt{Z}b_{\pi_1\pi}b_{\pi_2\pi}\mathcal{J}^{\Lambda}_{2,0}[f^u_2f^u_2] \\ &+ g^2_{1,2}b^2_{\pi_2\pi}\mathcal{J}^{\Lambda}_{2,0}[f^u_2f^u_2f^u_2]))\big].\end{aligned} \tag{A.1}$$

The product of the momenta of secondary particles can be expressed through masses of mesons:

$$P_1\cdot P_2 = \frac{1}{2}(M^2 - M_1^2 - M_2^2), \tag{A.2}$$

where M is the mass of the decaying meson and M_1 and M_2 are the masses of secondary particles ($M = M_{\sigma_{\mathrm{I}}}$, $M_1 = M_2 = M_\pi$ in this case). Let us continue (A.1) and calculate the sum before integration. The resulting expression becomes short:

$$\begin{aligned}A^{(2)}_{\sigma_{\mathrm{I}}\to\pi\pi} = 8m_u(&\mathcal{J}^{\Lambda}_{2,0}[\bar{f}_{\sigma\mathrm{I}}\bar{f}_\pi\bar{f}_\pi] \\ &- P_1\cdot P_2\mathcal{J}^{\Lambda}_{3,0}[\bar{f}_{\sigma\mathrm{I}}\bar{f}_\pi\bar{f}_\pi]),\end{aligned} \tag{A.3}$$

where $\bar{f}_a$ are form factor functions for the physical meson states, defined as follows:

$$\bar{f}_{\sigma_{\mathrm{I}}} = g_{8,1}b_{\sigma_{8,1}\sigma I} + g_{8,2}b_{\sigma_{8,2}\sigma_{\mathrm{I}}}f^u_2, \tag{A.4}$$

$$\bar{f}_\pi = g_{1,1}b_{\pi_1\pi}\sqrt{Z} + g_{1,2}b_{\pi_2\pi}f^u_2. \tag{A.5}$$

The coefficients $b_{\pi_1\pi}$ appear because of the mixing between the ground and excited pion states. Their values are $b_{\pi_1\pi}\approx 0.997$, $b_{\pi_2\pi}\approx 0.007$ [7]. Concerning the decays into the other pairs of pseudoscalars, the calculation of the corresponding contribution is carried out in the same manner. For strange pseudoscalar mesons, we have $b_{K_1K}\approx 0.96$, $b_{K_2K}\approx 0.09$ [7]. We will discriminate the form factor functions by the superscripts u and s, respectively. Below we give the physical form factors that were used in the calculation:

$$\bar{f}^u_{\sigma_l} = g_{8,1}b_{\sigma_{8,1}\sigma_l} + g_{8,2}(1 + d_u\mathbf{k}^2)b_{\sigma_{8,2}\sigma_l}, \tag{A.6}$$

$$\bar{f}^s_{\sigma_l} = g_{9,1}b_{\sigma_{9,1}\sigma_l} + g_{9,2}(1 + d_s\mathbf{k}^2)b_{\sigma_{9,2}\sigma_l}, \tag{A.7}$$

[7)] Two pairs of them are identical, which leads to the symmetry factor of 2.

$$\bar{f}_\pi = g_{1,1} b_{\pi_1\pi}\sqrt{Z} + g_{1,2}(1 + d_u \mathbf{k}^2) b_{\pi_2\pi}, \tag{A.8}$$

$$\bar{f}_K = g_{4,1} b_{K_1K}\sqrt{Z} + g_{4,2}(1 + d_{us} \mathbf{k}^2) b_{K_2K}, \tag{A.9}$$

$$\bar{f}_{\hat{a}_0} = g_{1,1} b_{a_{01}\hat{a}_0} + g_{1,2}(1 + d_u \mathbf{k}^2) b_{a_{02}\hat{a}_0}, \tag{A.10}$$

$$\bar{f}_{K_0^*} = g_{4,1} b_{{K_0^*}_1\hat{K}_0^*} + g_{4,2}(1 + d_{us} \mathbf{k}^2) b_{{K_0^*}_2\hat{K}_0^*}, \tag{A.11}$$

$$\bar{f}_\eta^u = g_{8,1} b_{\phi_{8,1}\eta}\sqrt{Z} + g_{8,2}(1 + d_u \mathbf{k}^2) b_{\phi_{8,2}\eta}, \tag{A.12}$$

$$\bar{f}_{\eta'}^u = g_{8,1} b_{\phi_{8,1}\eta'}\sqrt{Z} + g_{8,2}(1 + d_u \mathbf{k}^2) b_{\phi_{8,2}\eta'}, \tag{A.13}$$

$$\bar{f}_\eta^s = g_{9,1} b_{\phi_{9,1}\eta}\sqrt{Z} + g_{9,2}(1 + d_s \mathbf{k}^2) b_{\phi_{9,2}\eta}, \tag{A.14}$$

$$\bar{f}_{\eta'}^s = g_{9,1} b_{\phi_{9,1}\eta'}\sqrt{Z} + g_{9,2}(1 + d_s \mathbf{k}^2) b_{\phi_{9,2}\eta'}. \tag{A.15}$$

Let us write the quark loop contribution to the vertices of the effective meson Lagrangian in terms of physical meson states. Only the vertices describing the processes we are interested in are given below. For $l = \mathrm{I, II, III, IV, V}$, we have

$$\begin{aligned} &A^{(2)}_{\sigma_l\to\pi\pi}\sigma_l(2\pi^+\pi^- + \pi^0\pi^0) \\ &+ A^{(2)}_{\sigma_l\to K\bar{K}}\sigma_l(K^+K^- + K^0\tilde{K}^0) \\ &+ A^{(2)}_{\sigma_l\to\eta\eta}\sigma_l\eta\eta + A^{(2)}_{\sigma_l\to\eta\eta'}\sigma_l\eta\eta', \end{aligned} \tag{A.16}$$

$$\begin{aligned} A^{(2)}_{\sigma_l\to\pi\pi} &= 8m_u(\mathcal{J}_{2,0}^\Lambda[\bar{f}_{\sigma_l}^u\bar{f}_\pi\bar{f}_\pi] \\ &\quad - P_1\cdot P_2\mathcal{J}_{3,0}^\Lambda[\bar{f}_{\sigma_l}^u\bar{f}_\pi\bar{f}_\pi]), \\ A^{(2)}_{\sigma_l\to K\bar{K}} &= 8m_u(C_{uu}\mathcal{J}_{2,0}^\Lambda[\bar{f}_{\sigma_l}^u\bar{f}_K\bar{f}_K] \\ &\quad + C_{us}\mathcal{J}_{1,1}^\Lambda[\bar{f}_{\sigma_l}^u\bar{f}_K\bar{f}_K]) \\ &\quad - 8\sqrt{2}m_s(C_{ss}\mathcal{J}_{0,2}^\Lambda[\bar{f}_{\sigma_l}^s\bar{f}_K\bar{f}_K] \\ &\quad + C_{su}\mathcal{J}_{1,1}^\Lambda[\bar{f}_{\sigma_l}^s\bar{f}_K\bar{f}_K]) \\ &\quad - P_1\cdot P_2(8m_s\mathcal{J}_{2,1}^\Lambda[\bar{f}_{\sigma_l}^u\bar{f}_K\bar{f}_K] \\ &\quad - 8\sqrt{2}m_u\mathcal{J}_{1,2}^\Lambda[\bar{f}_{\sigma_l}^s\bar{f}_K\bar{f}_K]), \\ A^{(2)}_{\sigma_l\to\eta\eta} &= 8m_u\mathcal{J}_{2,0}^\Lambda[\bar{f}_{\sigma_l}^u\bar{f}_{\eta^u}\bar{f}_{\eta^u}] \\ &\quad - 8\sqrt{2}m_s\mathcal{J}_{0,2}^\Lambda[\bar{f}_{\sigma_l}^s\bar{f}_{\eta^s}\bar{f}_{\eta^s}] \\ &\quad - P_1\cdot P_2(8m_u\mathcal{J}_{3,0}^\Lambda[\bar{f}_{\sigma_l}^u\bar{f}_{\eta^u}\bar{f}_{\eta^u}] \\ &\quad - 8\sqrt{2}m_s\mathcal{J}_{0,3}^\Lambda[\bar{f}_{\sigma_l}^s\bar{f}_{\eta^s}\bar{f}_{\eta^s}]), \\ A^{(2)}_{\sigma_l\to\eta\eta'} &= 16m_u\mathcal{J}_{2,0}^\Lambda[\bar{f}_{\sigma_l}^u\bar{f}_{\eta^u}\bar{f}_{\eta'}^u] \\ &\quad - 16\sqrt{2}m_s\mathcal{J}_{0,2}^\Lambda[\bar{f}_{\sigma_l}^s\bar{f}_{\eta^s}\bar{f}_{\eta'}^s] \\ &\quad - P_1\cdot P_2(16m_u\mathcal{J}_{3,0}^\Lambda[\bar{f}_{\sigma_l}^u\bar{f}_{\eta^u}\bar{f}_{\eta'}^u] \\ &\quad - 16\sqrt{2}m_s\mathcal{J}_{0,3}^\Lambda[\bar{f}_{\sigma_l}^s\bar{f}_{\eta^s}\bar{f}_{\eta'}^s]), \end{aligned} \tag{A.17}$$

where

$$\begin{aligned} C_{uu} &= \frac{2m_u}{m_u + m_s}, \quad C_{us} = \frac{m_s(m_u - m_s)}{m_u(m_u + m_s)}, \\ C_{ss} &= \frac{2m_s}{m_u + m_s}, \quad C_{su} = \frac{m_u(m_s - m_u)}{m_s(m_u + m_s)}. \end{aligned} \tag{A.18}$$

Now we consider the decays of a scalar—isoscalar meson into a pair of σ_{I}. To calculate the quark loop contribution to the corresponding decay amplitudes, one should follow the method described above for pseudoscalar mesons. The quark loop contribution can be represented as a set of diagrams that result in a sum of integrals which can then be converted into a single integral over the physical form factors for scalar—isoscalar mesons. Thus, one obtains

$$A^{(2)}_{\sigma_l\to\sigma_{\mathrm{I}}\sigma_{\mathrm{I}}} \approx 8m_u\mathcal{J}_{2,0}^\Lambda[\bar{f}_{\sigma_l}^u\bar{f}_{\sigma\mathrm{I}}^u\bar{f}_{\sigma_{\mathrm{I}}}^u] \tag{A.19}$$

for $l = \mathrm{III, IV, V}$. In conclusion, we display the coefficients a_k that determine contact terms (89):

$$\begin{aligned} a_1 = -\frac{1}{\chi_c^3}\Bigg[&\frac{10}{3}\mathcal{C}_g + \sum_{a,b=8}^{9}\Big(-\frac{4}{3}\bar{\mu}_a^0 \\ &\times (G^{(-)})^{-1}_{ab}\mu_b + \frac{7}{3}\bar{\mu}_a^0\left(G^{(-)}\right)^{-1}_{ab}\bar{\mu}_b^0 \\ &+ \frac{1}{6}\mu_a^0\left(G^{(-)}\right)^{-1}_{ab}(\mu_b - \bar{\mu}_b^0)\Big) \\ &+ h_\sigma\big(16F_0^2 - 18F_0F_0^0 + 4(F_0^0)^2\big)\Bigg], \end{aligned} \tag{A.20}$$

$$\begin{aligned} a_2 = &-\frac{\sqrt{2}h_\sigma}{\sqrt{3}\chi_c^2}(14F_0 - 10F_0^0) \\ &- \frac{1}{\chi_c^2}\sum_{a=8}^{9} g_{8,1}\left(G^{(-)}\right)^{-1}_{8a}\bar{\mu}_a^0, \end{aligned} \tag{A.21}$$

$$\begin{aligned} a_3 = &\frac{4h_\sigma}{3\chi_c} \\ &- \frac{1}{\chi_c}\left(g_{8,1}^2\left((G^{(-)})^{-1}_{88} - 8\mathcal{J}_{1,0}^\Lambda[1]\right) + 4m_u^2\right), \end{aligned} \tag{A.22}$$

$$a_4 = \frac{1}{\chi_c}\left(g_{8,2}^2\left(1/\bar{G}_8 - 8\mathcal{J}_{1,0}^\Lambda[f_2^u f_2^u]\right) + 4m_u^2\right). \tag{A.23}$$

REFERENCES

1. M. Jaminon and B. Van den Bosche, Nucl. Phys. A **619**, 285 (1997).
2. V. V. Anisovich, D. V. Bugg, and A. V. Sarantsev, Phys. Rev. D **58**, 111503 (1998).
3. N. A. Törnqvist and M. Roos, Phys. Rev. Lett. **76**, 1575 (1996); A. Palano, Nucl. Phys. B (Proc. Suppl.) **39**, 287 (1995); Eef van Beveren and G. Rupp, hep-ph/9806246; S. Narison, Nucl. Phys. B **509**, 312 (1998); Yu. S. Surovtsev, D. Krupa, and M. Nagy, Acta Phys. Pol. **31**, 2697 (2000); Phys. Rev. D **63**, 054024 (2001).
4. W. Lee and D. Weingarten, Phys. Rev. D **59**, 094508 (1999).
5. M. K. Volkov and V. L. Yudichev, Int. J. Mod. Phys. A **14**, 4621 (1999).
6. M. K. Volkov and V. L. Yudichev, Yad. Fiz. **63**, 527 (2000) [Phys. At. Nucl. **63**, 455 (2000)].

7. M. K. Volkov and V. L. Yudichev, Fiz. Élem. Chastits At. Yadra **31**, 576 (2000) [Phys. Part. Nucl. **31**, 282 (2000)].
9. Particle Data Group (D. E. Groom *et al.*), Eur. Phys. J. C **15**, 1 (2000).
9. D. Ebert, M. Nagy, M. K. Volkov, and V. L. Yudichev, Eur. Phys. J. A **8**, 567 (2000); M. K. Volkov and V. L. Yudichev, Eur. Phys. J. A **10**, 109 (2001).
10. M. K. Volkov and V. L. Yudichev, Yad. Fiz. **64**, 2091 (2001) [Phys. At. Nucl. **64**, 2006 (2001)]; hep-ph/0011326.
11. M. Nagy, M. K. Volkov, and V. L. Yudichev, Acta Phys. Slov. **50**, 643 (2000).
12. M. K. Volkov and C. Weiss, Phys. Rev. D **56**, 221 (1997).
13. M. K. Volkov, Yad. Fiz. **60**, 2094 (1997) [Phys. At. Nucl. **60**, 1920 (1997)].
14. M. K. Volkov, D. Ebert, and M. Nagy, Int. J. Mod. Phys. A **13**, 5443 (1998); M. K. Volkov, D. Ebert, and V. L. Yudichev, J. Phys. G **25**, 2025 (1999); M. K. Volkov, V. L. Yudichev, and M. Nagy, Nuovo Cimento A **112**, 955 (1999).
15. K. Kusaka, M. K. Volkov, and W. Weise, Phys. Lett. B **302**, 145 (1993).
16. J. Ellis and J. Lánik, Phys. Lett. B **150B**, 289 (1985); **175**, 83 (1986); B. A. Campbell, J. Ellis, and K. A. Olive, Nucl. Phys. B **345**, 57 (1990).
17. A. A. Andrianov, V. A. Andrianov, V. Yu. Novozhilov, and Yu. V. Novozhilov, Pis'ma Zh. Éksp. Teor. Fiz. **43**, 557 (1986) [JETP Lett. **43**, 719 (1986)]; A. A. Andrianov and V. A. Andrianov, Z. Phys. C **55**, 435 (1992).
18. M. K. Volkov, M. Nagy, and V. L. Yudichev, Nuovo Cimento A **112**, 225 (1999).
19. H. Vogl and W. Weise, Prog. Part. Nucl. Phys. **27**, 195 (1991).
20. S. P. Klevansky, Rev. Mod. Phys. **64**, 649 (1992).
21. M. K. Volkov, Fiz. Élem. Chastits At. Yadra **17**, 433 (1986) [Sov. J. Part. Nucl. **17**, 186 (1986)]; M. K. Volkov, Ann. Phys. (N. Y.) **157**, 282 (1984).
22. D. J. Broadhurst *et al.*, Phys. Lett. B **329**, 103 (1994); B. V. Geshkenbein and V. I. Morgunov, Yad. Fiz. **58**, 1873 (1995) [Phys. At. Nucl. **58**, 1771 (1995)]; S. Narison, Phys. Lett. B **387**, 162 (1996).
23. K. Kikkawa, Prog. Theor. Phys. **56**, 947 (1976).
24. M. K. Volkov and D. Ebert, Yad. Fiz. **36**, 1265 (1982) [Sov. J. Nucl. Phys. **36**, 736 (1982)]; Z. Phys. C **16**, 205 (1983).
25. B. S. Zou and D. V. Bugg, Phys. Rev. D **50**, 591 (1994); Long Li, Bing-song Zou, and Guang-lie Li, hep-ph/0010196.
26. G. Janssen, B. C. Pearce, K. Holinde, and I. Speth, Phys. Rev. D **52**, 2690 (1995).
27. The WA102 Collab. (D. Barberis *et al.*), Phys. Lett. B **479**, 59 (2000).

Physics of Atomic Nuclei, Vol. 65, No. 9, 2002, pp. 1673–1677. Translated from Yadernaya Fizika, Vol. 65, No. 9, 2002, pp. 1717–1721.
Original Russian Text Copyright © 2002 by Tryasuchev.

ELEMENTARY PARTICLES AND FIELDS
Theory

The Isobar Model of the $\gamma N \to \eta N$ Processes in the Energy Range from the Threshold to 1200 MeV

V. A. Tryasuchev

Tomsk Polytechnical University, Tomsk, Russia

Received June 26, 2001; in final form, January 9, 2002

Abstract—The isobar model of the $\gamma N \to \eta N$ processes is constructed on the basis of the precision measurements of the cross section for the $\gamma p \to \eta p$ process near the threshold in Mainz (Germany) and the sensational results of recent measurements of the Σ beam asymmetry and $d\sigma/d\Omega$ for this process in Grenoble (France). The model involves six nucleon resonances (MeV): $S_{11}(1535)$, $S_{11}(1650)$, $P_{11}(1440)$, $P_{13}(1720)$, $D_{13}(1520)$, and $F_{15}(1680)$. The properties of these resonances are discussed. The $P_{13}(1720)$ and $F_{15}(1680)$ resonances are responsible for large positive values of the Σ beam asymmetry for the $\gamma p \to \eta p$ reaction at small angles. The contribution of the $S_{11}(1650)$ resonance must be taken into account in addition to the contribution of the $S_{11}(1535)$ resonance in order to describe the experimental dependence of the total cross section on the photon energy. The values characterizing the $\gamma n \to \eta n$ reaction are calculated on the basis of the available data on the amplitudes of electromagnetic excitation of these resonances on protons and neutrons. © *2002 MAIK "Nauka/Interperiodica".*

1. INTRODUCTION

Knowledge of the electromagnetic properties of the baryon resonances is indispensable for constructing the dynamical quark models of baryons. The information on these properties comes mostly from studies of the photoproduction of π mesons on nucleons or nuclei. Since the photoproduction of pions involves a rich variety of the Δ and N^* resonances, the relevant properties of the resonances of mass greater than 1500 MeV are still not clearly understood. In contrast to the photoproduction of pions, the photoproduction of η mesons

$$\gamma + p \to \eta + p \tag{1}$$

involves only the N resonances with the isospin $I = 1/2$, so that numerous Δ resonances with $I = 3/2$ and close masses are separated. It should be noted that process (1) differs fundamentally from the photoproduction of pions on nuclei: the η meson involves a strange quark, whereas the pions involve only ordinary u and d quarks.

A model of the photoproduction of η mesons on nucleons over a wide range of energies consistent with recent experimental data is required for two purposes: firstly, for deriving information about the electromagnetic properties of resonances and, second, for studying the photoproduction of η mesons on nuclei and evaluating various backgrounds in the current and future experiments.

2. DESCRIPTION OF MODEL

The models [1–5] for process (1) adequately describe behavior of the reaction cross section near the threshold. With an increase in the photon energy, the number of resonances with higher angular momenta involved in the process rapidly increases due to a relatively large mass of the η meson. Some of the aforementioned models [2, 3, 5] do not take into account such resonances. Because of this, our study relies on the isobar model of the photoproduction of η mesons on nucleons. This model takes into account the contribution of resonances only to the s channel. The contributions of the nucleons and vector mesons to the amplitude of the process under consideration are incorporated in this model by including the effective s-channel contributions of the resonances. Fortunately, the contributions of the nucleons and vector mesons are sufficiently small even in the near-threshold region [1–3]. In the case under study, the $P_{11}(1440)$ resonance with a mass below the threshold and large width is interpreted as the nonresonance background.

In the center-of-mass system, the amplitude of process (1) in the angular momentum representation was expressed in terms of the multipole amplitudes for the photoproduction of pseudoscalar mesons on nucleons [6]. In the proposed model, all multipole amplitudes of both electric ($E_{l\pm}$) and magnetic ($M_{l\pm}$) types are considered as resonance and, therefore, represented in the Breit–Wigner form

$$E_{l\pm} = \frac{ie^{i\phi_r}(\Gamma^E_{\gamma p}\Gamma_{\eta p})^{1/2}}{2[kqj(j+1)]^{1/2}(W_r - W - i\Gamma/2)}, \quad (2)$$

the same being true for the $M_{l\pm}$ amplitudes. Here, k and q are the momenta of the photon and meson in the center-of-mass system; l is the orbital momentum of the meson; $j = l \pm 1$ for $E_{l\pm}$ and $j = l$ for $M_{l\pm}$; subscripts of l indicate the total angular momentum $J = l \pm 1/2$ of the meson–nucleon system; W is the total energy of the system; and W_r is the mass of the resonance. The energy dependence of the total widths Γ of the resonances coincides with that in [7]:

$$\Gamma = \sum_\lambda \frac{p\nu_l(pR)}{p_\lambda \nu_l(p_\lambda R)}\Gamma_\lambda, \quad (3)$$

where Γ_λ are the partial widths of decay in the channel λ; p and p_λ are the momenta of the mesons produced in the two-body decay of the resonance (the former momentum corresponds to the energy W, and the latter, to $W = W_r$); $\nu_l(x)$ are the barrier factors for process (1) depending on the orbital momentum l of the meson [8]; and R is the range of the strong interactions (here it is fixed at the scale 1 fm). For all resonances except $S_{11}(1535)$, only π meson channel of the decay of the resonances was considered as contributing to the sum in formula (3), whereas, for the $S_{11}(1535)$ resonance, in view of its importance in process (1), we set

$$\Gamma = (0.5q/q_r + 0.4p/p_r + 0.1)\Gamma_r,$$

where $q(q_r)$ and $p(p_r)$ are, respectively, the momenta of the η and π mesons in the center-of-mass system with the total energy W ($W = W_r$) and Γ_r are the widths of the resonances in the rest frame. The electromagnetic $\Gamma^{E,M}_{\gamma p}$ and strong $\Gamma_{\eta p}$ vertices of the resonance multipole amplitudes (2) are parametrized as

$$(\Gamma^{E,M}_{\gamma p}\Gamma_{\eta p})^{1/2} \quad (4)$$
$$= \{[2kR\nu_n(kR)][2qR\nu_l(qR)\}^{1/2}\gamma^{E,M},$$

where $n = l - 2$ for the multipole amplitudes E_{l-} and $n = l$ for the others. The dimensional values $\gamma^{E,M}$ together with the energies W_r and the widths Γ_r of the resonances were considered as the fitting parameters of the model. Moreover, the phases of the multipole amplitudes ϕ_r [see formula (2)] have to be considered as the additional parameters.

Similar models involving three resonances—$S_{11}(1535)$, $P_{11}(1440)$, and $D_{13}(1520)$—were successfully employed for description of the $\gamma N \to \eta N$ processes near the threshold [1, 4, 9]. In order to reproduce the differential cross sections measured in Mainz [10], it was sufficient to set the phase factors of the multipole amplitudes equal to unity. Fortunately, these models provide for a satisfactory description of the data on the cross section $d\sigma/d\Omega$ and the asymmetry Σ caused by the linear polarization of the photons in reaction (1), which were obtained recently in the experiment at higher energies at the Grenoble facility [11, 12]. For this reason, our study is based on the model proposed in [9] with taking into account resonances with energies higher than 1535 MeV. We assumed that contributions to the amplitude of reaction (1) can come from resonances with the orbital momentum $L < 3$: $P_{13}(1720)$, $D_{13}(1700)$, and $D_{15}(1675)$. Based on the results of preliminary calculations, the $P_{13}(1720)$ resonance was preferred. Large positive values of $\Sigma(\theta)$ at small escape angles θ of mesons were obtained in the experimental studies of reaction (1) at a total energy of $W = 1687$ MeV and above. In our opinion, this fact indicates that the $F_{15}(1680)$ resonance has a profound effect on the process under consideration. Since coupling of this resonance to the electromagnetic field is reliably strong [13], it is natural to assume a strong coupling of this resonance with the ηN channel.

Experimental dependence of the total cross section of reaction (1) on the photon energy over the region under study [12] contradicts the fact that the contribution of the $S_{11}(1535)$ resonance slowly decreases with the energy. For this reason, we have to take into account the $S_{11}(1650)$ resonance in order to compensate for a large contribution of the $S_{11}(1535)$ resonance over the energy range under consideration.

3. RESULTS AND DISCUSSION

Using only six resonances indicated above and varying their properties as proposed in [13], we achieve a good agreement of our description with the data obtained in both Mainz [10] and Grenoble [11, 12]. For a comparison of the calculated values with the experimental data, we use the dependence of these values on the energy of the incident photons K_0 in the center-of-mass system at $\theta = 90°$ (as in [5]). Note that, for this escape angle of mesons, the experimental data are most exact. The result obtained by visual fitting is shown in Figs. 1–4 by solid curves in comparison with the experimental data. The required properties of the resonances are presented in the table.

It has been repeatedly pointed out that the dominant contribution to the cross section of process (1) is due to the $S_{11}(1535)$ resonance, which is most strongly coupled to the decay channel ηN. However, the experimental energy dependence of the total cross section of process (1) in the entire energy range studied cannot be explained in terms of this S-wave contribution only. An agreement with the data obtained

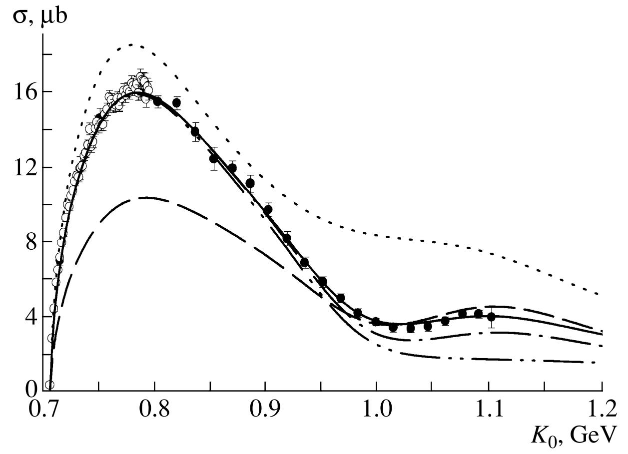

Fig. 1. Dependence of the integrated cross section for the processes $\gamma p \to \eta p$ (solid curve) and $\gamma n \to \eta n$ (dashed curve) on the photon energy in the laboratory system. The experimental data for the $\gamma p \to \eta p$ reaction are taken from [10] (○) and [12] (●). The energy dependences of the integrated cross section for the $\gamma p \to \eta p$ reaction with incomplete amplitudes were calculated with neglect of the $S_{11}(1650)$ resonance (dotted curve), $F_{15}(1680)$ resonance (dash-dotted curve), and $P_{13}(1720)$ resonance (dash-and-double-dot curve).

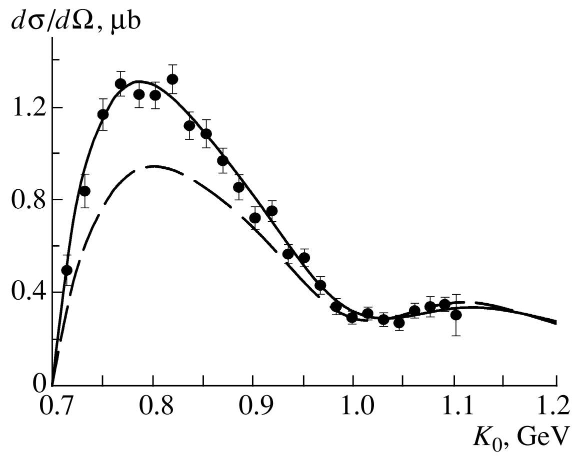

Fig. 2. Differential cross sections $d\sigma/d\Omega$ of the reactions $\gamma p \to \eta p$ (solid curve) and $\gamma n \to \eta n$ (dashed curve) as functions of the energy of the photon in the laboratory system at the meson escape angle $\theta_{\text{c.m.}} = 90°$. Dots show the experimental data for the $\gamma p \to \eta p$ process at $\theta_{\text{c.m.}} = (90 \pm 12)°$ [12].

in the two mentioned experiments (Figs. 1 and 2) was obtained only upon taking into account the contribution of the $S_{11}(1650)$ resonance "compensating" for the contribution of the dominant resonance. It should be noted that no such agreement with the experimental data was obtained in [14] despite the fact that the analysis performed in a similar model involved a greater number of resonances.

The calculated angular distributions $d\sigma(\theta)/d\Omega$ also agree well with the results of the other two experiments—MAMI (Germany) and GRAAL (France) at the energies of the incident photon up to $K_0 \approx 950$ MeV. At higher energies, the calculated distributions $d\sigma(\theta)/d\Omega$ show a pronounced decrease in the forward direction. A similar decrease takes place in the distributions predicted in [14] however, it is not observed experimentally [12].

Using the data from the table, we find that the $S_{11}(1535)$ resonance is characterized by the ratio

$$\Gamma_\gamma/\Gamma_r \approx 0.34\%$$

(Γ_γ is the total γ-width of the resonance), which coincides with the maximum value of this ratio recommended in [13]. This is partly explained by the fact that, in our model, some other, nonresonant, contributions (nucleon exchanges in the s and u channels and the vector-meson contributions in the t channel) to the amplitude of process (1) are implicitly included in the contribution of the $S_{11}(1535)$ resonance. The obtained results for this resonance (see table) can be represented in an illustrative form

$$\Gamma_{\eta p}\Gamma_\gamma/\Gamma_r = 0.27 \text{ MeV}.$$

At $\Gamma_{\eta p}/\Gamma_r = 0.50$, the invariant helicity amplitude for the photoexcitation of this resonance is $A_{1/2} = 0.1096$ GeV$^{-1/2}$. Conversely, given the value of the amplitude $A_{1/2} = 0.090$ GeV$^{-1/2}$ (as was proposed in [13]), we arrive at $\Gamma_{\eta p}/\Gamma_r = 0.74$. Both these values are much greater than those in [13]. However, our value of the photoexcitation amplitude $A_{1/2}$ of the $S_{11}(1535)$ resonance is in good agreement with the results of [14] ($A_{1/2} = 0.103$ GeV$^{-1/2}$). The same is valid for the ratio $\Gamma_\gamma/\Gamma_r \approx 0.4\%$ characterizing the $S_{11}(1650)$ resonance, which is determined from the data fitting. This ratio is twice as large as the upper limit of this value recommended in [13].

The dependence of the asymmetry Σ for process (1) on the energy of the γ quanta is shown in Fig. 3. This asymmetry is due to the linear polarization of photons parallel or transverse to the plane of the reaction. Large positive values of the asymmetry at small values of the angle θ ($\theta < 50°$) for $K_0 > 950$ MeV (which are not seen in Fig. 3) are obtained with regard for the contributions of the $P_{13}(1720)$ and $F_{15}(1680)$ resonances to the amplitude (see the figure in [15]). Taking these resonances into account makes it possible to reproduce the second, small and wide, maximum of the total cross section for process (1) (see Fig. 1). Note that the authors of [14] failed to reproduce this maximum. In our model, the maxima of the angular distribution $\Sigma(\theta)$ for $K_0 > 950$ MeV

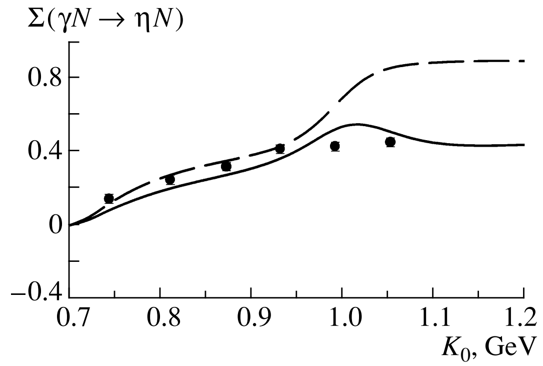

Fig. 3. Photon asymmetry Σ for the processes $\gamma p \to \eta p$ (solid curve) and $\gamma n \to \eta n$ (dashed curve) as a function of the photon energy in the laboratory system for the meson escape angle $\theta_{\text{c.m.}} = 90°$. Dots show experimental data for the $\gamma p \to \eta p$ process at $\theta_{\text{c.m.}} = (90 \pm 12)°$ [11].

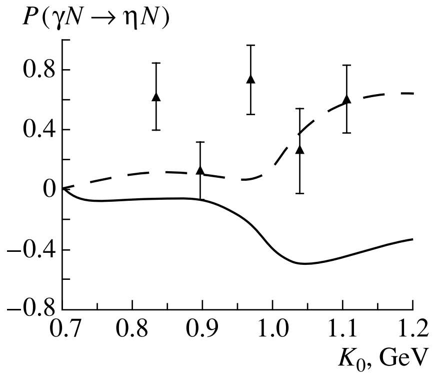

Fig. 4. Polarization $P(K_0)$ of the recoil nucleons in the reactions $\gamma p \to \eta p$ (solid curve) and $\gamma n \to \eta n$ (dashed curve) as a function of the photon energy in the laboratory system for the meson escape angle $\theta_{\text{c.m.}} = 90°$. Dots show experimental data for the $\gamma p \to \eta p$ reaction at $\theta_{\text{c.m.}} = (90 \pm 10)°$ [16].

and the maxima of $d\sigma(\theta)/d\Omega$ for the respective energies occur at the same angles ($\theta \approx 50°$). For this reason, the asymmetry Σ rapidly increases with the photon energies in the region of 1 GeV. The values of $\gamma^{E,M}$ characterizing the $P_{13}(1720)$ resonance are in both qualitative and quantitative agreement with the data reported in [13], whereas the electromagnetic properties of the $F_{15}(1680)$ resonance disagree with these data. The values from the table characterizing this resonance imply the following ratio between the helicity amplitudes $A_{1/2}$ and $A_{3/2}$:

$$\mid A_{1/2}/A_{3/2} \mid = 1.41.$$

This value is an order of magnitude greater than the value recommended in [13]. It is possible that replacement of the $F_{15}(1680)$ resonance with the $D_{15}(1675)$ resonance, which is close to the former resonance in mass and has the same angular momentum, will remove the discrepancy; however, our attempt to do this has failed. The calculated polarization of the recoil protons $P(K_0)$ and the asymmetry $T(K_0)$ caused by the polarization of the target protons in reaction (1) are shown in Figs. 4 and 5 by solid curves. It is seen that predictions of the model used disagree with the results of the measurements of $P(K_0)$ [16] made thirty years ago (see Fig. 4). Unfortunately, no prediction for this value was made in [14]. Our attempts to find an agreement of large positive values of Σ with the positive values of the polarization P have not met with success. In order to solve this problem, new experimental measurements are needed.

Properties of the resonances obtained from the phenomenological analysis of the $\gamma p \to \eta p$ process in the energy range from the threshold to 1200 MeV

N^* resonances	W_r, MeV	Γ_r, MeV	γ^E, MeV	γ^M, MeV	ϕ_r, deg
$S_{11}(1535)$	1535	158	2.15	–	0
$S_{11}(1650)$	1645	120	−0.550	–	4.0
$P_{11}(1440)$	1440	350	–	0.450	0
$P_{13}(1720)$	1718	140	−0.085	0.409	132.0
$D_{13}(1520)$	1520	120	0.200	0.330	0
$F_{15}(1680)$	1678	120	0.190	0.800	18.0

Using the estimates [13] of the helicity amplitudes for the photoexcitation of resonances on protons and neutrons and taking into account the charge independence of the hadronic vertices, we computed the cross sections and polarization characteristics for the photoproduction of η mesons on neutrons

$$\gamma + n \to \eta + n. \tag{5}$$

An exception from this rule is the multipole amplitude of the $S_{11}(1535)$ resonance, for which we set

$$E^n_{0+} \approx -0.81 E^p_{0+}, \tag{6}$$

on the basis of the experimental data [17] on the ratio of cross sections for the photoproduction of η mesons on the neutron and proton in the neighborhood of this resonance. Theoretical predictions for the observables of reaction (5) are shown by dashed curves in Figs. 1–5. It is of interest that the calculated dependences of $\Sigma(K_0)$ for processes (1) and (5) are in close proximity to each other (Fig. 3), whereas the calculated values of $P(K_0)$ and $T(K_0)$ for these processes are opposite in sign (Figs. 4 and 5).

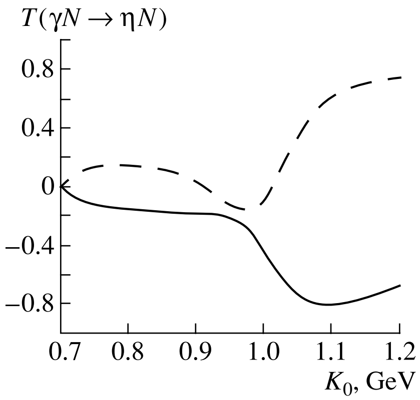

Fig. 5. Asymmetry $T(K_0)$ caused by the polarization of the target nucleons for the reactions $\gamma p \to \eta p$ (solid curve) and $\gamma n \to \eta n$ (dashed curve) versus the photon energy in the laboratory system for the meson escape angle $\theta_{\mathrm{c.m.}} = 90°$.

Introducing some additional N^* resonances in the proposed model could give better agreement with the results of the experiments under consideration (however, at the expense of complexity). For this reason, the proposed approach offers a 'minimal' model, that is, the model with a minimum of resonances taken into consideration in the energy range studied. New experimental data on reaction (1) at higher energies will force us to revise the role of the N^* resonances included in the model, because one has to introduce resonances of higher mass, whose contribution at $K_0 = 1200$ MeV is small. In conclusion, we note that a nonvanishing coupling of the $S_{11}(1650)$, $F_{15}(1680)$, and $P_{13}(1720)$ resonances to the ηN channel comes as no surprise to us but supports an ingenious conjecture of the authors of [8] made in the 1970s.

ACKNOWLEDGMENTS

The author is grateful to Dr. D. Rebreyend for kindly providing the experimental data from GRAAL (France).

REFERENCES

1. C. Bennhold and H. Tanabe, Nucl. Phys. A **530**, 625 (1991).
2. M. Benmerrouche and N. C. Mukhopadhyay, Phys. Rev. Lett. **67**, 1070 (1991).
3. A. Fix and H. Arenhovel, Nucl. Phys. A **620**, 457 (1997).
4. L. Tiator, C. Bennhold, and S. S. Kamalov, Nucl. Phys. A **580**, 455 (1994).
5. M. Benmerrouche, N. C. Mukhopadhyay, and J. F. Zhang, Phys. Rev. D **51**, 3237 (1995).
6. G. F. Chew, M. L. Goldberger, F. E. Low, and Y. Nambu, Phys. Rev. **106**, 1345 (1957).
7. H. R. Hicks, S. E. Deans, D. T. Jacobs, *et al.*, Phys. Rev. D **7**, 2614 (1973).
8. J. M. Blatt and V. F. Weisskopf, *Theoretical Nuclear Physics* (Wiley, New York, 1952; Inostrannaya Literatura, Moscow, 1954).
9. V. A. Tryasuchev, Fiz. Élem. Chastits At. Yadra **30**, 1391 (1999) [Phys. Part. Nucl. **30**, 606 (1999)].
10. B. Krusche, J. Ahrens, G. Anton, *et al.*, Phys. Rev. Lett. **74**, 3736 (1995).
11. J. Ajaka, M. Anghinolfi, V. Bellini, *et al.*, Phys. Rev. Lett. **81**, 1797 (1998).
12. F. Renard, M. Anghinolfi, O. Bartalini, *et al.*, hep-ex/0011098.
13. Particle Data Group, Eur. Phys. J. C **15**, 1 (2000).
14. W. T. Chiang, S. N. Yang, L. Tiator, and D. Drechsel, hep-th/0106006.
15. V. A. Tryasuchev, Izv. Vyssh. Uchebn. Zaved., Fiz., No. 7, 3 (2001).
16. C. A. Heusch, C. Y. Prescott, L. S. Rochester, *et al.*, Phys. Rev. Lett. **25**, 1381 (1970).
17. V. Hejny, P. Achenbach, J. Ahrens, *et al.*, Eur. Phys. J. A **6**, 83 (1999).

Translated by R. Rogalyov

Physics of Atomic Nuclei, Vol. 65, No. 9, 2002, pp. 1678–1691. Translated from Yadernaya Fizika, Vol. 65, No. 9, 2002, pp. 1722–1735.
Original Russian Text Copyright © 2002 by Alekseev.

ELEMENTARY PARTICLES AND FIELDS
Theory

Effective Method for Calculating the Analytic QCD Coupling Constant

A. I. Alekseev*

Institute for High Energy Physics, Protvino, Moscow oblast, 142284 Russia

Received April 27, 2001; in final form, December 21, 2001

Abstract—The analytic running coupling constant α_{an} for strong interactions is considered for approximations of standard perturbation theory up to the three-loop level. Nonperturbative contributions are singled out explicitly in α_{an}. They are represented in the form of an expansion in a series in inverse powers of the Euclidean momentum squared. It is shown that two- and three-loop corrections lead to a partial compensation of the nonperturbative one-loop contribution of order $1/q^2$, which is leading in the ultraviolet region. An efficient method for calculating the analytic running coupling constant for all $q > \Lambda$ is developed on the basis of the above expansion. A comparative analysis of perturbative and nonperturbative contributions is performed in the infrared region, where the latter play the most important role. A simultaneous consideration of the momentum dependence of α_{an} and its perturbative component for one- to three-loop cases leads to the conclusion that the analytic running coupling constant is stable with respect to higher corrections and that it depends only slightly on conditions imposed in matching solutions that involve different numbers n_f of active-quark flavors. *© 2002 MAIK "Nauka/Interperiodica".*

1. INTRODUCTION

Perturbation theory, which is the main tool of investigations within QCD, a theory that describes strong interactions at sufficiently high values of the energy scale, generates nonphysical singularities in the infrared region. It is commonly believed that these singularities must be canceled by nonperturbative contributions. Such contributions naturally arise in the analytic approach to QCD (see the review article of Solovtsov and Shirkov [1]). In exploring such issues, use is made of the so-called analyticization procedure employing the ideas that date back to the studies of Redmond [2] and Bogolyubov, Logunov, and Shirkov [3], who considered the problem of an nonphysical ghost pole in particle propagators. The procedure hinges on the principle of summing, under the sign of the Källén–Lehmann spectral integral, information obtained from perturbation theory. This yields expressions free from nonphysical singularities. By imposing the condition of analyticity on the QCD running coupling constant (invariant charge) as a function of the variable q^2 (q^2 is the square of the Euclidean momentum, $q^2 > 0$), a solution to the problem of a ghost pole in QCD was proposed in the recent studies of Shirkov and Solovtsov [4, 5]. Such a condition is imposed within the dispersion approach to QCD [6]. The value of the one-loop analytic running coupling constant at the origin proved to be finite and independent of Λ (universal), $\alpha^{(1)}_{\mathrm{an}}(0) = 4\pi/b_0$. Within the hypothesis that the interaction is frozen in the infrared region, the problem of the ghost pole in QCD is also solved. In [7, 8], the question of whether the coupling constant is frozen at low energies is considered within a specific computational scheme based on an expansion around the point $16\frac{1}{2} - n_f$. Within the model of a stochastic QCD vacuum [9, 10], the coupling constant is also frozen in the infrared region. There, perturbation theory is constructed with respect to a nonperturbative background field, and a dimensional parameter dependent on the process m_{B} being considered arises in the expression for the running coupling constant [$1/\ln(q^2/\Lambda^2) \to 1/\ln((q^2 + m_B^2)/\Lambda^2)$, $m_B \simeq 1$ GeV].

In [4, 5], it was found that the analyticization procedure possesses the important property that the analytic running coupling constant at the origin is stable with respect to higher order corrections: $\alpha^{(1)}_{\mathrm{an}}(0) = \alpha^{(2)}_{\mathrm{an}}(0) = \alpha^{(3)}_{\mathrm{an}}(0)$. Thus, higher order corrections do not change the value of the analytic running coupling constant at the origin. It should be noted that, although the derivative of the analytic running coupling constant at the origin is infinite, the quantity $\alpha_{\mathrm{an}}(q^2)$ proves to be stable with respect to higher order corrections over the entire infrared region.

For the standard and for the iterative two-loop solution, nonperturbative contributions to the analytic running coupling constant were calculated explicitly in [11]. Since the perturbative expressions corresponding to these two cases behave differently in the infrared region, the nonperturbative contributions

---

*e-mail: `alekseev@mx.ihep.su`

also behave differently there. It was shown that, in the ultraviolet region—more precisely, for $q > \Lambda$—the nonperturbative contributions can be represented as power series in inverse powers of q^2, where the expansion coefficients exhibit different dependences on the ordinal number. In [12, 13], the nonperturbative contributions to $\alpha_{\mathrm{an}}(q^2)$ were isolated explicitly for approximations of the perturbation theory up to the three-loop level. The method developed there for performing integration in the vicinity of the singularities of the original perturbation theory is more general than that which was used in [11].

In the present study, we will analyze the momentum dependence of the QCD running coupling constant and of its nonperturbative component, the one- to three-loop cases being considered simultaneously. This makes it possible to describe quantitatively stability of the analytic running coupling constant with respect to the number of loops (it has already been mentioned that this stability property was first discovered in [4, 5]).

2. ONE-LOOP ANALYTIC COUPLING CONSTANT

The fundamentals of the approach that is employed in the present study will be described here for the simple example of the QCD one-loop running coupling constant. The one-loop renormalization-group equation for the running coupling constant $\alpha_s(q^2)$ has the solution

$$\alpha_s(q^2) = \frac{\alpha_s(\mu^2)}{1 + \frac{b_0}{4\pi}\alpha_s(\mu^2)\ln(q^2/\mu^2)}, \tag{1}$$

where $b_0 = 11 - \frac{2}{3}n_f$, n_f is the number of flavors of active quarks, and μ is the normalization point. Introducing the renormalization-invariant parameter Λ,

$$\Lambda^2 = \mu^2 e^{-\frac{4\pi}{b_0\alpha_s(\mu^2)}}, \tag{2}$$

we can can recast Eq. (1) into the form

$$\alpha_s(q^2) = \frac{4\pi}{b_0}\,\frac{1}{\ln(q^2/\Lambda^2)}, \tag{3}$$

which involves an nonphysical pole at $q^2 = \Lambda^2$. The vanishing of expression (3) for $q^2 \to \infty$ corresponds to the remarkable property of asymptotic freedom [14] of non-Abelian gauge theories, while the growth of α_s (to some critical value or to infinity) with decreasing q^2 can have a bearing on a solution to the confinement problem. Let us estimate the parameter Λ. Assuming that, at $q = M_Z = 91.2$ GeV (M_Z is the Z-boson mass), $\alpha_s = 0.118$ [15] and setting $n_f = 5$, we obtain $\Lambda = 87.8$ MeV from Eq. (3). In the region of q values being considered, we have $d\Lambda/\Lambda \simeq 7d\alpha_s/\alpha_s$, so that a 1% uncertainty in α_s leads to an approximately 7% uncertainty in Λ.

Equation (1) can be represented as the result obtained by summing the following series:

$$\alpha_s(q^2) = \alpha_s(\mu^2)\sum_{n=0}^{\infty}\left(-\frac{b_0}{4\pi}\alpha_s(\mu^2)\right)^n \ln^n(q^2/\mu^2). \tag{4}$$

It is noteworthy that the sum of a finite number of terms in the series on the right-hand side of Eq. (4) is not a renormalization-invariant quantity. Thus, the renormalization-group method makes it possible to sum up an infinite class of diagrams, the renormalization invariance of the result being concurrently restored. However, the analytic structure in the complex plane of q^2 has changed significantly as a result. Each term in Eq. (4) is an analytic function in the complex plane of q^2 with a cut along the negative real semiaxis, but, in expressions (1) and (3), there is a pole at the point $q^2 = \Lambda^2$ in addition to this cut. If one wants to preserve analyticity in the complex plane of q^2 with a cut along the negative real semiaxis, it is possible to make an analytic continuation of the terms in the series on the right-hand side of (4) to the Minkowski space, $q^2 \to -\sigma - i0$, and, after that, to sum up the imaginary parts of all the imaginary parts of these terms. This yields

$$\begin{aligned}\mathrm{Im}\alpha_s(-\sigma - i0) &= \alpha_s(\mu^2) \\ &\times \sum_{n=0}^{\infty}\left(-\frac{b_0}{4\pi}\alpha_s(\mu^2)\right)^n \mathrm{Im}\left[\ln^n(-\sigma/\mu^2 - i0)\right] \\ &= \frac{1}{2i}\left\{\frac{\alpha_s(\mu^2)}{1 + \frac{b_0}{4\pi}\alpha_s(\mu^2)[\ln(\sigma/\mu^2) - i\pi]}\right. \\ &\left.- \frac{\alpha_s(\mu^2)}{1 + \frac{b_0}{4\pi}\alpha_s(\mu^2)[\ln(\sigma/\mu^2) + i\pi]}\right\} \\ &= \frac{4\pi}{b_0}\mathrm{Im}\frac{1}{\ln(\sigma/\Lambda^2) - i\pi} = \frac{4\pi}{b_0}\frac{\pi}{\ln^2(\sigma/\Lambda^2) + \pi^2}.\end{aligned} \tag{5}$$

Introducing the quantity $\tilde{\rho}(\sigma) = \mathrm{Im}\alpha_s(-\sigma - i0)$, we define a new analytic running coupling constant through the dispersion relation

$$\alpha_{\mathrm{an}}(q^2) = \frac{1}{\pi}\int_0^{\infty}\frac{d\sigma\,\tilde{\rho}(\sigma)}{\sigma + q^2 - i0}. \tag{6}$$

For the one-loop spectral density $\tilde{\rho}(\sigma)$, the integral in Eq. (6) can be taken explicitly, whereupon we arrive at

$$\alpha_{\mathrm{an}}(q^2) = \frac{4\pi}{b_0}\left[\frac{1}{\ln(q^2/\Lambda^2)} + \frac{\Lambda^2}{\Lambda^2 - q^2}\right]. \tag{7}$$

The ghost pole at the point $q^2 = \Lambda^2$ is canceled, so that the running coupling constant in (7) as a function of q^2 has the desired analytic structure. In order to ensure the manifest renormalization invariance of expression (7), one can solve the following equation for the parameter Λ:

$$\alpha_{\rm an}(\mu^2) = \frac{4\pi}{b_0}\left[\frac{1}{\ln(\mu^2/\Lambda^2)} + \frac{\Lambda^2}{\Lambda^2 - \mu^2}\right]. \qquad (8)$$

From a dimensional analysis, it follows that

$$\Lambda^2 = \mu^2 e^{-\phi\left(\alpha_{\rm an}(\mu^2)\right)}, \qquad (9)$$

where the function $\phi(z)$ is determined by the equation

$$\frac{b_0}{4\pi}z = \frac{1}{\phi(z)} + \frac{1}{1 - e^{\phi(z)}}. \qquad (10)$$

Over the interval from zero to $4\pi/b_0$, the function $\phi(z)$ decreases monotonically from $+\infty$ to $-\infty$. For $z \to 0$, the function $\phi(z)$ assumes the form $\phi(z) \simeq 4\pi/(b_0 z)$, so that $\Lambda^2 \simeq \mu^2 e^{-4\pi/\left(b_0\alpha_{\rm an}(\mu^2)\right)}$ for $\alpha_{\rm an}(\mu^2) \to 0$; therefore, the second term in the bracketed expression on the right-hand side of Eq. (7) must be treated as a nonperturbative one. The new β function can be represented in the form

$$\beta(\alpha_{\rm an}) = q\frac{\partial\alpha_{\rm an}(q^2)}{\partial q} \qquad (11)$$
$$= \frac{8\pi}{b_0}\left[-\frac{1}{\phi^2(\alpha_{an})} + \frac{e^{\phi(\alpha_{\rm an})}}{\left(1 - e^{\phi(\alpha_{\rm an})}\right)^2}\right].$$

For $\alpha_{\rm an} \to 0$, we have $\beta(\alpha_{\rm an}) \simeq -(b_0/2\pi)\alpha_{\rm an}^2$. For $z \to 4\pi/b_0$, the function $\phi(z)$ behaves as $\phi(z) \simeq 1/(b_0 z/4\pi - 1)$; accordingly, $\beta(\alpha_{\rm an}) \simeq -(b_0/2\pi)(\alpha_{\rm an} - 4\pi/b_0)^2$ for $\alpha_{\rm an} \to 4\pi/b_0$. The new β function has two second-order zeros. Of these, one is an ultraviolet-stable point, while the other is an infrared-stable point.

Thus, the QCD running coupling constant as obtained within the analytic approach possesses the following interesting properties:

(i) By construction, this running coupling constant as a function q^2 has an analytic structure that is compatible with the causality principle.

(ii) As a function of $\alpha_{\rm an}(\mu^2)$, it has an essential singularity at the origin; the asymptotic expansion of its nonperturbative part in $\alpha_{\rm an}(\mu^2)$ for $\alpha_{\rm an}(\mu^2) \to +0$ is equal to zero, which ensures conformity to the original perturbation theory.

(iii) Apart from fast decreasing power-law terms, it coincides with the usual result of perturbation theory in the ultraviolet region (with allowance for renormalization invariance).

(iv) In the infrared region, it does not have nonphysical singularities. Its value at the origin is finite and is independent of the normalization condition, $\alpha_{\rm an}(0) = 4\pi/b_0$.

As will be seen below, all these properties are preserved at the two- and at the three-loop level. It is important to note that, in the one-loop case, we have not only the spectral representation (6); in addition, there are, first, an expression where nonperturbative contributions are singled out explicitly from the running coupling constant,

$$\alpha_{\rm an}(q^2) = \alpha^{\rm pt}(q^2) + \alpha_{\rm an}^{\rm npt}(q^2), \qquad (12)$$

and, second, a simple formula for nonperturbative contributions. For $q > \Lambda$, these contributions can be represented as the series

$$\alpha_{\rm an}^{\rm npt}(q^2) = \frac{4\pi}{b_0}\sum_{n=1}^{\infty} c_n\left(\frac{\Lambda^2}{q^2}\right)^n, \qquad (13)$$

where $c_n = -1$. With an eye to a subsequent extension of the above analysis to multiloop cases, we will now try to assess the usefulness of the representation of nonperturbative contributions in the form (13). We will find the precision to which this series is approximated by the sum of its first N terms. The absolute error of this procedure,

$$\Delta^{(N)} = -\frac{4\pi}{b_0}\sum_{n=N+1}^{\infty}\left(\frac{\Lambda^2}{q^2}\right)^n \qquad (14)$$
$$= -\frac{4\pi}{b_0}\left(\frac{\Lambda^2}{q^2}\right)^N \frac{\Lambda^2}{q^2 - \Lambda^2},$$

depends on q and N at given n_f and Λ, an increase in q and N leading to a decrease in this error. The relative error of the approximation of $\alpha_{\rm an}$ is

$$\delta^{(N)} = \frac{\alpha_{\rm an}^{\rm approx} - \alpha_{\rm an}}{\alpha_{\rm an}} \qquad (15)$$
$$= \frac{-\Delta^{(N)}}{\alpha_{\rm an}} = \left(\frac{\Lambda^2}{q^2}\right)^N \frac{\ln(q^2/\Lambda^2)}{q^2/\Lambda^2 - 1 - \ln(q^2/\Lambda^2)}.$$

In the one-loop case, this quantity is independent of n_f explicitly. From Eq. (15), one can find the number of terms of the approximation that ensure the required precision:

$$N = \frac{1}{\ln(q^2/\Lambda^2)}\left[-\ln\delta - \ln\left(q^2/\Lambda^2\right.\right. \qquad (16)$$
$$\left.\left. -\ 1 - \ln(q^2/\Lambda^2)\right) + \ln\left(\ln(q^2/\Lambda^2)\right)\right].$$

For $\delta = 10^{-2}$ and $q = 1.1\Lambda$, this formula yields $N = 36.2$, so that the required precision is ensured by taking 37 terms of the series. For $q = 10\Lambda$, we obtain $N = 0.34$; therefore, one term is quite sufficient in this case. The approximation by one term is sufficient even for $q > 4.4\Lambda$. Thus, we see that, if the dependence of the coefficients c_n on n is "not very bad," the nonperturbative contributions can be found to a preset precision for q values rather close to Λ and that, at fairly large q, it is sufficient to retain only the first term of the series. For relative errors of the approximation of α_{an} that range between 10^{-2} and 10^{-8}, Fig. 1 shows the number N of terms in the power series (13) for $\alpha_{\text{an}}^{\text{npt}}$ as a function of q/Λ. This dependence proves to be useful in estimating the accuracy of the simple approximation of nonperturbative contributions by a partial sum of a power series in the case where the n dependence of the coefficients c_n in this series makes it possible to consider the one-loops series as a majorizing series.

In the two- and the three-loop case, we single out nonperturbative contributions from α_{an}, represent them as series in inverse powers of q^2, and explore the accuracy of the approximations obtained by truncating these series at finite numbers of terms.

3. THREE-LOOP ANALYTIC COUPLING CONSTANT

The QCD running coupling constant $\alpha_s(\mu^2)$ is a solution to the renormalization-group equation

$$\mu\frac{\partial\alpha_s(\mu^2)}{\partial\mu} = \beta(\alpha_s) = \beta_0\alpha_s^2 + \beta_1\alpha_s^3 + \beta_2\alpha_s^4 + \dots, \tag{17}$$

where the coefficients are

$$\beta_0 = -\frac{1}{2\pi}b_0, \quad b_0 = 11 - \frac{2}{3}n_f, \tag{18}$$
$$\beta_1 = -\frac{1}{4\pi^2}b_1, \quad b_1 = 51 - \frac{19}{3}n_f,$$
$$\beta_2 = -\frac{1}{64\pi^3}b_2, \quad b_2 = 2857 - \frac{5033}{9}n_f + \frac{325}{27}n_f^2.$$

The first two coefficients β_0 and β_1 are independent of the choice of renormalization scheme, whereas the next coefficients in expansion (17) are scheme-dependent. The coefficient β_2 in (18) corresponds to the $\overline{MS}$ scheme [16]. The standard three-loop solution to the renormalization-group equation for the running QCD coupling constant is represented as an expansion in inverse powers of the logarithm $\ln(\mu^2/\Lambda^2)$ (where $\Lambda = \Lambda_{\overline{MS}}$) [15]; that is,

$$\alpha_s(\mu^2) = \frac{4\pi}{b_0\ln(\mu^2/\Lambda^2)} \tag{19}$$
$$\times\left[1 - \frac{2b_1}{b_0^2}\frac{\ln[\ln(\mu^2/\Lambda^2)]}{\ln(\mu^2/\Lambda^2)} + \frac{4b_1^2}{b_0^4\ln^2(\mu^2/\Lambda^2)}\right.$$
$$\left.\times\left(\left(\ln[\ln(\mu^2/\Lambda^2)] - \frac{1}{2}\right)^2 + \frac{b_2 b_0}{8b_1^2} - \frac{5}{4}\right)\right].$$

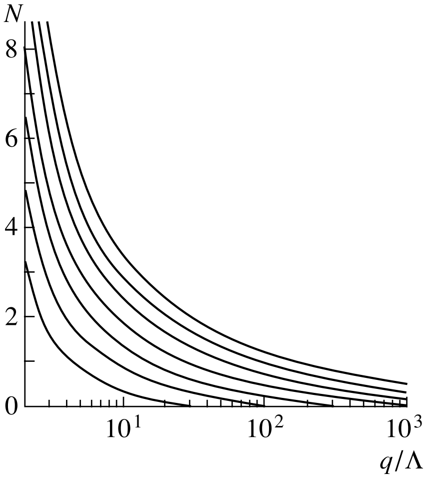

Fig. 1. Number of terms in the power series in (13) for $\alpha_{\text{an}}^{\text{npt}}$ as a function of q/Λ at the one-loop level for preset values of the relative error δ in the approximation of α_{an} that range between (lower curve) 10^{-2} and (upper curve) 10^{-8}.

The first two terms in square brackets in Eq. (19) corresponds to the two-loop solution, where there is no term of the form $1/\ln^2(\mu^2/\Lambda^2)$. It should be noted that the expansion of the iterative two-loop solution from [5] in inverse powers of the above logarithm generates such a term; it can be canceled by redefining the parameter Λ. We introduce the function $a(x) = (b_0/4\pi)\alpha_s(q^2)$, where $x = q^2/\Lambda^2$. Instead of Eq. (19), we then obtain

$$a(x) = \frac{1}{\ln x} - b\frac{\ln(\ln x)}{\ln^2 x} \tag{20}$$
$$+ b^2\left(\frac{\ln^2(\ln x)}{\ln^3 x} - \frac{\ln(\ln x)}{\ln^3 x} + \frac{\kappa}{\ln^3 x}\right).$$

The coefficients b and κ are

$$b = \frac{2b_1}{b_0^2} = \frac{102 - \frac{38}{3}n_f}{(11 - \frac{2}{3}n_f)^2}, \quad \kappa = \frac{b_0 b_2}{8b_1^2} - 1. \tag{21}$$

At $n_f = 3$, the coefficients b and κ take the values of $b = 64/81 \simeq 0.7901$ and $\kappa \simeq 0.4147$. At large values of x, the one-loop term in Eq. (20) is a leading one, the terms that follow it yielding corrections to this one-loop term. At small values of x, these corrections become dominant, which is due to the presence of singularities at the point $x = 1$ that have different analytic structures. Namely, we have the following types of behavior at $x \simeq 1$:

$$a^{(1)}(x) \simeq \frac{1}{x-1}, \tag{22}$$
$$a^{(2)}(x) \simeq -\frac{b}{(x-1)^2}\ln(x-1),$$

$$a^{(3)}(x) \simeq \frac{b^2}{(x-1)^3}\ln^2(x-1).$$

The analytic approach makes it possible to get rid of these nonphysical singularities without spoiling the ultraviolet behavior of the coupling constant.

By definition, the analytic running coupling constant can be calculated with the aid of the spectral representation

$$a_{\mathrm{an}}(x) = \frac{1}{\pi}\int\limits_0^\infty \frac{d\sigma}{x+\sigma}\rho(\sigma), \tag{23}$$

the spectral density satisfying the conditions $\rho(\sigma) = \mathrm{Im} a_{\mathrm{an}}(-\sigma - i0) = \mathrm{Im} a(-\sigma - i0)$. Performing an analytic continuation of Eq. (20) to the Minkowski space, $x = -\sigma - i0$, we obtain

$$\begin{aligned} a(-\sigma - i0) = {} & \frac{1}{\ln\sigma - i\pi} - \frac{b}{(\ln\sigma - i\pi)^2} \\ & \times \ln(\ln\sigma - i\pi) + b^2\left\{\frac{\ln^2(\ln\sigma - i\pi)}{(\ln\sigma - i\pi)^3}\right. \\ & \left. - \frac{\ln(\ln\sigma - i\pi)}{(\ln\sigma - i\pi)^3} + \frac{\kappa}{(\ln\sigma - i\pi)^3}\right\}. \end{aligned} \tag{24}$$

Calculating the imaginary part of expression (24), we find the spectral density in the form

$$\begin{aligned} \rho(\sigma) = {} & \frac{\pi}{t^2+\pi^2} - \frac{b}{(t^2+\pi^2)^2} \\ & \times \left[2\pi t F_1(t) - \left(t^2 - \pi^2\right)F_2(t)\right] \\ & + \frac{b^2}{(t^2+\pi^2)^3}\left[\pi\left(3t^2 - \pi^2\right)\left(F_1^2(t) - F_2^2(t)\right)\right. \\ & - 2t\left(t^2 - 3\pi^2\right)F_1(t)F_2(t) \\ & - \pi\left(3t^2 - \pi^2\right)F_1(t) + t\left(t^2 - 3\pi^2\right) \\ & \left. \times F_2(t) + \pi\kappa\left(3t^2 - \pi^2\right)\right], \end{aligned} \tag{25}$$

where $t = \ln(\sigma)$ and

$$F_1(t) \equiv \frac{1}{2}\ln(t^2+\pi^2), \quad F_2(t) \equiv \arccos\frac{t}{\sqrt{t^2+\pi^2}}. \tag{26}$$

With the aid of (23), (25), and (26), the analytic running coupling constant can be explored, for example, by numerical methods. In order to calculate α_{an}, we will develop an alternative method that is more convenient and more efficient than that and which does not involve numerical integration.

The function $a(x)$ in Eq. (20) is analytic in the complex plane of the variable x with a cut along the real axis from 1 to $-\infty$ and is real at real $x > 1$. In order to find the spectral density $\rho(\sigma)$, we can therefore use the Schwarz reflection principle, according to which $(a(x))^* = a(x^*)$. We then have

$$\rho(\sigma) = \frac{1}{2i}(a(-\sigma - i0) - a(-\sigma + i0)). \tag{27}$$

Making a change of variable of the form $\sigma = \exp(t)$ and using formulas (23), (24), and (27), we obtain the representation

$$\begin{aligned} a_{\mathrm{an}}(x) = {} & \frac{1}{2\pi i}\int\limits_{-\infty}^{\infty} dt\,\frac{e^t}{x+e^t} \\ & \times\left\{\frac{1}{t-i\pi} - \frac{1}{t+i\pi} - b\left[\frac{\ln(t-i\pi)}{(t-i\pi)^2}\right.\right. \\ & \left. - \frac{\ln(t+i\pi)}{(t+i\pi)^2}\right] + b^2\left[\frac{\ln^2(t-i\pi)}{(t-i\pi)^3} - \frac{\ln^2(t+i\pi)}{(t+i\pi)^3}\right. \\ & - \frac{\ln(t-i\pi)}{(t-i\pi)^3} + \frac{\ln(t+i\pi)}{(t+i\pi)^3} \\ & \left.\left. + \frac{\kappa}{(t-i\pi)^3} - \frac{\kappa}{(t+i\pi)^3}\right]\right\}. \end{aligned} \tag{28}$$

Let us now explore the singularities of the integrand on the right-hand side of (28)—we denote this integrand by $F(t)$—in the complex plane of the variable t. First of all, there are simple poles at $t = \ln x \pm i\pi(1+2n)$, $n = 0, 1, 2, \ldots$. All residues of the function $\exp(t)/(x+\exp(t))$ at these poles are equal to unity. In addition, the integrand $F(t)$ has singularities at the points $t = \pm i\pi$; these are a simple pole; a third-order pole; and logarithmic branch points, which coincide with a second- and a third-order pole. In a standard way, we draw, in the complex plane of the variable t, the cuts $t = \pm i\pi - \lambda$, where λ is a real-valued parameter, $0 < \lambda < \infty$. The expression obtained by multiplying the integrand $F(t)$ by t tends to zero for $|\,t\,| \to \infty$. Without changing the value of the integral being considered, we can therefore include in it integration along an arc of infinite radius. Specifically, we close up the integration contour C_1 in the upper half-plane of the variable t, eliminating the singularity at $t = i\pi$. This leads to the emergence of the additional contributions from integration along the banks of the cut and from integration around the singularities at the point $t = i\pi$. We denote the corresponding contour by C_2.

Let us now consider the integral along the contour C_1. The residues of the function $F(t)$ at the points $t = \ln(x) + i\pi(1+2n)$, $n = 0, 1, 2, \ldots$, are

$$\begin{aligned} & \mathrm{Res}\,F(t)\,|_{t=\ln(x)+i\pi(1+2n)} \\ & = \frac{1}{\ln(x) + 2\pi i n} - \frac{1}{\ln(x) + 2\pi i(n+1)} \end{aligned} \tag{29}$$

$$- b\left[\frac{\ln(\ln(x)+2\pi in)}{(\ln(x)+2\pi in)^2} - \frac{\ln(\ln(x)+2\pi i(n+1))}{(\ln(x)+2\pi i(n+1))^2}\right]$$
$$+ b^2\left[\frac{\ln^2(\ln(x)+2\pi in)}{(\ln(x)+2\pi in)^3}\right.$$
$$- \frac{\ln^2(\ln(x)+2\pi i(n+1))}{(\ln(x)+2\pi i(n+1))^3}$$
$$- \frac{\ln(\ln(x)+2\pi in)}{(\ln(x)+2\pi in)^3} + \frac{\ln(\ln(x)+2\pi i(n+1))}{(\ln(x)+2\pi i(n+1))^3}$$
$$\left. + \frac{\kappa}{(\ln(x)+2\pi in)^3} - \frac{\kappa}{(\ln(x)+2\pi i(n+1))^3}\right].$$

By using the Cauchy residue theorem, we evaluate the contribution $\Delta(x)$ to the integral in (28) from integration along the contour C_1. The result is

$$\Delta(x) = \frac{1}{2\pi i}\int\limits_{C_1} F(t)\,dt \tag{30}$$
$$= \sum_{n=0}^{\infty} \operatorname{Res} F(t = \ln(x) + i\pi(1+2n)) =$$
$$= \frac{1}{\ln x} - b\frac{\ln(\ln x)}{\ln^2 x}$$
$$+ b^2\left(\frac{\ln^2(\ln x)}{\ln^3 x} - \frac{\ln(\ln x)}{\ln^3 x} + \frac{\kappa}{\ln^3 x}\right).$$

We can see that this contribution is exactly equal to the original expression (20). Therefore, we call it the perturbative part of $a_{\rm an}(x)$, $a^{\rm pt}(x) = \Delta(x)$. It is natural to refer to the remaining part of integration along the contour C_2 as the nonperturbative part of $a_{\rm an}(x)$,

$$a_{\rm an}(x) = a^{\rm pt}(x) + a^{\rm npt}_{\rm an}(x). \tag{31}$$

Let us now proceed to calculate $a^{\rm npt}_{\rm an}(x)$. In performing integration along the contour C_2, we can discard terms in the integrand on the right-hand side of (28) that do not involve singularities at $t = i\pi$. We further make the change of variable $t = z + i\pi$ and introduce the function

$$f(z) = \frac{1}{1 - x\exp(-z)}. \tag{32}$$

For the nonperturbative contributions, we then arrive at the representation

$$a^{\rm npt}_{\rm an}(x) = \frac{1}{2\pi i}\int\limits_{C} dz\, f(z) \tag{33}$$
$$\times\left\{\frac{1}{z} - b\frac{\ln(z)}{z^2} + b^2\frac{\ln^2(z)}{z^3} - b^2\frac{\ln(z)}{z^3} + \frac{\kappa b^2}{z^3}\right\}.$$

In the complex plane of the variable z with a cut along the negative real semiaxis, the contour C goes from the point $z = -\infty - i0$ along the lower bank of the cut, circumvents the point $z = 0$, and then goes along the upper bank of the cut to the point $z = -\infty + i0$. Here, x is treated as a real variable satisfying the condition $x > 1$. The contour C can then be drawn in such a way as to avoid circumventing extra singularities and to ensure fulfillment of conditions that are used in the Appendix to calculate relevant integrals. For $x \neq 0$, the function given by (32), along with its derivatives, decreases exponentially for $z \to -\infty$; therefore, we can omit boundary terms in formulas presented in the Appendix. Using formulas from the Appendix and Eq. (33), we obtain

$$a^{\rm npt}_{\rm an}(x) = -\frac{1}{2\pi i}\int\limits_{C} dz\left\{f'(z)\ln(z)\right. \tag{34}$$
$$- bf''(z)\left(\ln(z) + \frac{1}{2}\ln^2(z)\right)$$
$$+ b^2 f'''(z)\left[\left(1 + \frac{1}{2}\kappa\right)\ln(z)\right.$$
$$\left.\left. + \frac{1}{2}\ln^2(z) + \frac{1}{6}\ln^3(z)\right]\right\}.$$

The function $f(z)$, along with its derivatives, is regular on the negative real semiaxis of the variable z; therefore, Eq. (34) can be recast into the form

$$a^{\rm npt}_{\rm an}(x) = -\int\limits_{0}^{-\infty} du\left[f'(u)\bar{\Delta}_1(u)\right. \tag{35}$$
$$- bf''(u)\left(\bar{\Delta}_1(u) + \frac{1}{2}\bar{\Delta}_2(u)\right)$$
$$+ b^2 f'''(u)\left(\left(1 + \frac{1}{2}\kappa\right)\bar{\Delta}_1(u)\right.$$
$$\left.\left. + \frac{1}{2}\bar{\Delta}_2(u) + \frac{1}{6}\bar{\Delta}_3(u)\right)\right],$$

where u is a real variable, while $u < 0$ and $\bar{\Delta}_i(u)$ are the discontinuities of the powers of the logarithms involved; that is,

$$\bar{\Delta}_1(u) = \frac{1}{2\pi i}(\ln(u+i0) - \ln(u-i0)) = 1, \tag{36}$$
$$\bar{\Delta}_2(u) = \frac{1}{2\pi i}\big(\ln^2(u+i0)$$
$$- \ln^2(u-i0)\big) = 2\ln(-u),$$
$$\bar{\Delta}_3(u) = \frac{1}{2\pi i}\big(\ln^3(u+i0)$$
$$- \ln^3(u-i0)\big) = 3\ln^2(-u) - \pi^2.$$

Let us introduce the variable $\sigma = \exp(u)$. From Eqs. (32), (35), and (36), we obtain the following expression for the nonperturbative contributions:

$$a^{\mathrm{an}}_{\mathrm{an}}(x) = \frac{1}{1-x} + b\Biggl\{\frac{x}{(1-x)^2} + x\int\limits_0^1 d\sigma\,\ln(-\ln(\sigma))\frac{x+\sigma}{(x-\sigma)^3}\Biggr\} + b^2\Biggl\{\left(1+\frac{\kappa}{2}-\frac{\pi^2}{6}\right)\frac{x(1+x)}{(1-x)^3} - x\int\limits_0^1 d\sigma\left[\ln(-\ln(\sigma)) + \frac{1}{2}\ln^2(-\ln(\sigma))\right] \times \frac{x^2+4x\sigma+\sigma^2}{(x-\sigma)^4}\Biggr\}. \tag{37}$$

Let us prove that $a_{\mathrm{an}}(0) = 1$. Setting $x = 0$ in Eq. (28), we obtain

$$a_{\mathrm{an}}(0) = \frac{1}{2\pi i}\int\limits_{-\infty}^{\infty} dt\,\Biggl\{\frac{1}{t-i\pi} - \frac{1}{t+i\pi} - b\left[\frac{\ln(t-i\pi)}{(t-i\pi)^2} - \frac{\ln(t+i\pi)}{(t+i\pi)^2}\right] + b^2\left[\frac{\ln^2(t-i\pi)}{(t-i\pi)^3} - \frac{\ln^2(t+i\pi)}{(t+i\pi)^3} - \frac{\ln(t-i\pi)}{(t-i\pi)^3} + \frac{\ln(t+i\pi)}{(t+i\pi)^3} + \frac{\kappa}{(t-i\pi)^3} - \frac{\kappa}{(t+i\pi)^3}\right]\Biggr\}. \tag{38}$$

In the complex plane of the variable t, there are now no singularities corresponding to perturbative contributions. Following the same line of reasoning as above, we obtain the following expression instead of (33):

$$a_{\mathrm{an}}(0) = \frac{1}{2\pi i}\int\limits_C dz\,\Biggl\{\frac{1}{z} - b\frac{\ln(z)}{z^2} + b^2\frac{\ln^2(z)}{z^3} - b^2\frac{\ln(z)}{z^3} + \frac{\kappa b^2}{z^3}\Biggr\}. \tag{39}$$

Here, the contour C is identical to that in (33). Let us make use of formulas from the Appendix for $f(z) = 1$. There are now no integrals on the right-hand sides, but it is necessary to take into account boundary terms. Setting $z_1 = -\lambda - i\varepsilon$ and $z_2 = -\lambda + i\varepsilon$, $\lambda \to +\infty$, we can see that only the first term in expression (39) makes a nonzero contribution, $\int_C dz/z = 2\pi i$. Thus, we have $a_{\mathrm{an}}(0) = 1$.

4. NONPERTURBATIVE CONTRIBUTIONS AT $q > \Lambda$

The perturbative function $a(x)$ has nonphysical singularities at $x = 1$, the leading singularities being given by (22). The nonperturbative contributions (37) also have singularities at $x = 1$, which cancel the singularities of the perturbative function $a(x)$. For $x > 1$, we can expand expression (37) in a series in inverse powers of x; that is,

$$a^{\mathrm{an}}_{\mathrm{npt}}(x) = \sum_{n=1}^{\infty}\frac{c_n}{x^n}, \tag{40}$$

where

$$c_n = -1 + bn\left[1 + n\int\limits_0^1 d\sigma\,\sigma^{n-1}\ln(-\ln(\sigma))\right] - b^2n^2\Biggl\{1 - \frac{\pi^2}{6} + \frac{\kappa}{2} + n\int\limits_0^1 d\sigma\,\sigma^{n-1} \times \left[\ln(-\ln(\sigma)) + \frac{1}{2}\ln^2(-\ln(\sigma))\right]\Biggr\}. \tag{41}$$

Making the change of variable according to the relation $\sigma = \exp(-t)$ and performing integration with respect to t by using the results presented in [17, 18], we obtain

$$c_n = -1 + bn(1-\gamma-\ln(n)) - \frac{1}{2}b^2n^2\left[1 - \frac{\pi^2}{6} + \kappa + (1-\gamma-\ln(n))^2\right], \tag{42}$$

where γ is the Euler constant ($\gamma \simeq 0.5772$). From Eq. (42), it follows that the power series in (40) converges uniformly for $x > 1$, the radius of convergence being equal to unity. In the approximation being considered, the coefficients c_n are given in Table 1 for various values of n and n_f and for various numbers of loops from one to three. The one-loop contribution to c_n is equal to -1 for all n and n_f. The two-loop corrections to c_n decrease monotonically with increasing n for all physically interesting values of n_f, including $n_f = 0, 3, 4, 5, 6$; with increasing n, the three-loop corrections to c_n first increase and then decrease monotonically for all of the above values of n_f. In the ultraviolet region, the nonperturbative contributions are determined by the first term of the series in (40). The two-loop correction to the leading term for $x \to \infty$ is positive (it changes from 0.36 at $n_f = 0$ to 0.22 at $n_f = 6$), whereas corrections to the next terms are negative. For $n_f \leq 4$, the three-loop correction to the leading term changes the two-loop result for the nonperturbative contributions only slightly. At $n_f = 5$, the three-loop correction is 2.4

Table 1. Coefficients c_n and loop corrections Δ_n for various values of n and n_f at the one- to the three-loop level

n_f	n	$c_n^{\text{1-loop}}$	$\Delta_n^{\text{2-loop}}$	$\Delta_n^{\text{3-loop}}$	$c_n^{\text{2-loop}}$	$c_n^{\text{3-loop}}$
0	1	−1.0	0.35640	−0.01568	−0.64360	−0.65929
	2	−1.0	−0.45582	0.08741	−1.45582	−1.36841
	3	−1.0	−1.70912	−1.03012	−2.70912	−3.73924
	4	−1.0	−3.24886	−4.51236	−4.24886	−8.76122
	5	−1.0	−5.00160	−11.31238	−6.00160	−17.31398
3	1	−1.0	0.33405	0.01608	−0.66595	−0.64987
	2	−1.0	−0.42724	0.19623	−1.42724	−1.23101
	3	−1.0	−1.60196	−0.63626	−2.60196	−3.23823
	4	−1.0	−3.04517	−3.48652	−4.04517	−7.53168
	5	−1.0	−4.68801	−9.19185	−5.68801	−14.87987
4	1	−1.0	0.31252	0.04949	−0.68748	−0.63799
	2	−1.0	−0.39970	0.31340	−1.39970	−1.08630
	3	−1.0	−1.49872	−0.23818	−2.49872	−2.73690
	4	−1.0	−2.84891	−2.48499	−3.84891	−6.33389
	5	−1.0	−4.38587	−7.15989	−5.38587	−12.54576
5	1	−1.0	0.27813	0.11653	−0.72187	−0.60535
	2	−1.0	−0.35571	0.55755	−1.35571	−0.79817
	3	−1.0	−1.33377	0.50736	−2.33377	−1.82641
	4	−1.0	−2.53536	−0.73077	−3.53536	−4.26613
	5	−1.0	−3.90317	−3.73728	−4.90317	−8.64045
6	1	−1.0	0.22433	0.25378	−0.77567	−0.52189
	2	−1.0	−0.28692	1.07460	−1.28692	−0.21231
	3	−1.0	−1.07581	1.93179	−2.07581	−0.14402
	4	−1.0	−2.04500	2.37205	−3.04500	−0.67296
	5	−1.0	−3.14826	2.01775	−4.14826	−2.13052

times less than the two-loop correction, but, at $n_f = 6$, it exceeds the two-loop correction. We note that, as n_f is increased, a decrease in the two-loop corrections is more than compensated by the growth of three-loop corrections. It is of interest that the inclusion of the two-loop corrections compensates, to some extent, the $1/x$ leading term at large x, this remaining in force upon taking into account three-loop terms.

For $n_f \geq 3$, the three-loop coefficient $|c_1^{\text{3-loop}}|$ is somewhat less than the two-loop coefficient $|c_1^{\text{2-loop}}|$. From this, it does not follow, however, that, in the analytic approach, higher corrections lead to a complete compensation of nonperturbative contributions in the ultraviolet region.

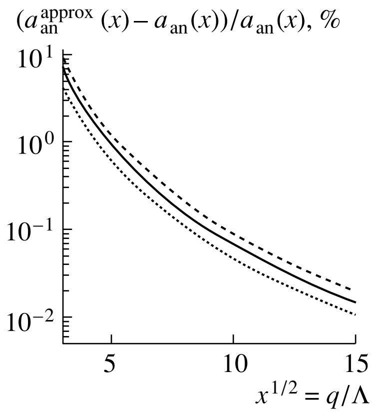

Fig. 2. Relative error in calculating the analytic running coupling constant versus momentum for the case where the nonperturbative ultraviolet tail is approximated by one term. The results obtained at the one-, the two-, and the three-loop level are represented by the dotted, the dashed, and the solid curve, respectively.

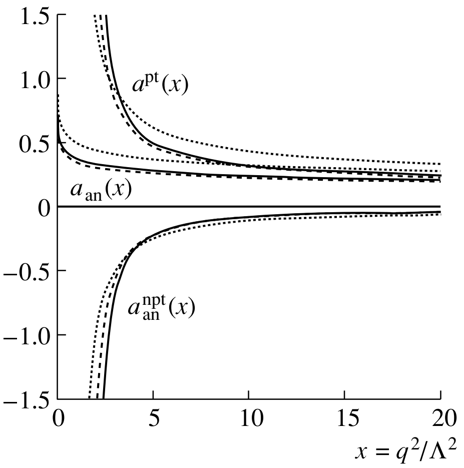

Fig. 3. Analytic running coupling constant $a_{\rm an}$ and its components $a^{\rm pt}$ and $a_{\rm an}^{\rm npt}$ (the perturbative and the nonperturbative one, respectively) versus $x = q^2/\Lambda^2$ for the one- to the three-loop case (the notation for the curves is identical to that in Fig. 2). The number of active-quark flavors was set to $n_f = 3$.

5. MOMENTUM DEPENDENCE OF $\alpha_{\rm an}$ AND $\alpha_{\rm an}^{\rm npt}$

Let us explore the convergence properties of the series in (40). Since $n > \ln^2(n)$ for $n \geq 1$, the series

$$S_3 = \sum_{n=1}^{\infty} \frac{n^3}{x^n} = \frac{x(x^2+4x+1)}{(x-1)^4} \tag{43}$$

is of use in estimating the accuracy of the approximation of the nonperturbative contribution by a partial sum of the series in (40) with coefficients (42), the convergence properties of the series in (40) not being worse than those of the series in (43). The absolute error of the approximation of the series in (43) by the sum of the first N terms is

$$\Delta_3^{(N)} = \frac{1}{x^N(x-1)}\left[\frac{x(x^2+4x+1)}{(x-1)^4} + \frac{3x(x+1)N}{(x-1)^3} + \frac{3xN^2}{x-1} + N^3\right]. \tag{44}$$

Formula (44) is qualitatively similar to the one-loop formula (14). The absolute error depends on x and N, becoming smaller for greater values of x and N. For the value of $x = 2$ ($q = 1.4\Lambda$), which is rather small, we find from Eqs. (43) and (44) that the relative error of the approximation of the series in (43) for $N = 30$ is equal to $\bar{\delta}^{(N)} \simeq 10^{-10}$. In our investigation of the series in (40), we will therefore retain 30 terms ($N_\infty = 30$). At large values of q, it is not necessary to sum up many terms of the series. For the one- to the three-loop case, the relative error of the approximation of the analytic running coupling constant is shown in Fig. 2 for the approximation of the nonperturbative contributions by the first term of the series in (40),

$$\alpha_{\rm an}(q^2) \simeq \alpha^{\rm pt}(q^2) - \frac{4\pi}{b_0}\left[1 - b\,(1-\gamma) + \frac{1}{2}b^2\left(1 - \frac{\pi^2}{6} + \kappa + (1-\gamma)^2\right)\right]\frac{\Lambda^2}{q^2}. \tag{45}$$

For the above region of q, we have chosen $n_f = 4$.

Let us now consider the behavior of the nonperturbative contributions in the infrared region, where these contributions are the most significant. In performing calculations in this region, we set $n_f = 3$. For the one- to the three-loop case, Fig. 3 displays the quantities $a^{\rm pt}$, $a_{\rm an}^{\rm npt}$, and $a_{\rm an}$ versus x. Here, the nonperturbative contributions were computed by summing the series in (40), while the analytic running coupling constant was determined with the aid of the dispersion relation (23) and formulas (25) and (26). It turned out that, in the cases being considered, numerical integration must be performed with caution. An insufficiently high precision of integration may manifest itself as excessively high stability of the running coupling constant with respect to an increase in the number of loops in the approximation used. As a criterion of the accuracy of integration in our calculations, we imposed the condition requiring that the analytic running coupling constant $a_{\rm an}(x)$ as obtained by numerically integrating the spectral density according to formulas (23), (25), and (26) be consistent (to within $2 \times 10^{-3}\%$) with the quantity $a_{\rm an}(x)$ defined as the sum of its components $a^{\rm pt}(x)$ and $a_{\rm an}^{\rm npt}(x)$, the nonperturbative component being calculated by summing 30 terms of the series in (40).

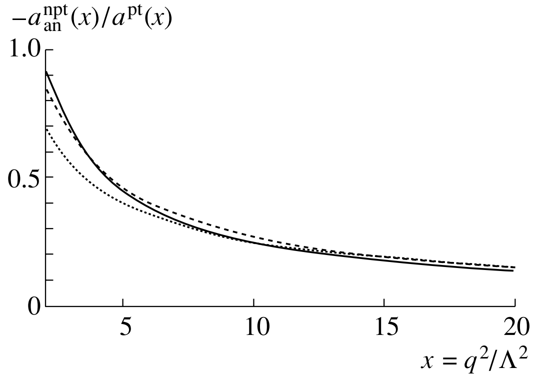

Fig. 4. Ratio of the nonperturbative component of the analytic running coupling constant to its perturbative component as a function of $x = q^2/\Lambda^2$ for the one- to the three-loop case (the notation for the curves is identical to that in Fig. 2). The number of active-quark flavors was set to $n_f = 3$.

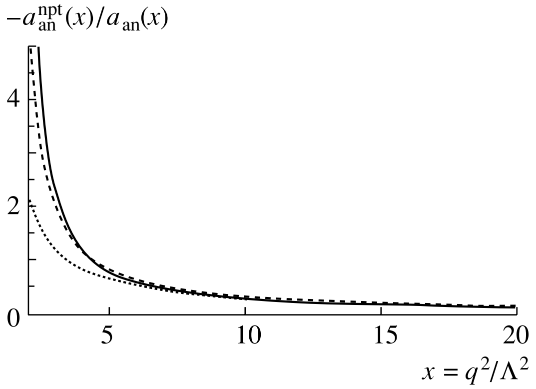

Fig. 5. Ratio of the nonperturbative component of the running coupling constant $a_{\rm an}^{\rm npt}$ to this coupling constant as a function of $x = q^2/\Lambda^2$ for the one- to the three-loop case (the notation for the curves is identical to that in Fig. 2). The number of active-quark flavors was set to $n_f = 3$.

The calculations in question were performed for values of the variable x that span the interval between 2 and 20. With decreasing x, the perturbative component $a^{\rm pt}$ grows, reaching unity at $q \sim 1.7\Lambda$. The nonperturbative component is negative; with decreasing x, it decreases, compensating for the growth of the perturbative component. The quantity $a_{\rm an}$ is regular for $x > 0$ and $a_{\rm an}^{(l)}(0) = 1$ (l is the number of loops). As can be seen from Fig. 3, the curve representing the two-loop analytic result is rather close to that representing the three-loop analytic result, whence we conclude that, even at this stage (that is, prior to imposing normalization conditions), the results are indicative of stability of solutions to changes in the number of loops. As to the corresponding perturbative curves, which do not have a common point at the origin, they are not close to each other for $x < 5$.

Let us assess the magnitude of the nonperturbative contributions. For the one- to the three-loop case, the ratio of nonperturbative component of the analytic running coupling constant to its perturbative component is given in Fig. 4 as a function of $x = q^2/\Lambda^2$. At $x = 20$, this ratio is about -0.15; with decreasing x ($x > 1$), it tends to -1. For the same numbers of loops, Fig. 5 shows the ratio of the nonperturbative component of the analytic running cou-

Table 2. Parameters $\Lambda_{\rm pt}^{(l,n_f)}$ and $\Lambda_{\rm an}^{(l,n_f)}$ (in MeV), where l is the number of loops and $n_f = 3$, under the normalization condition $\alpha(M_\tau) = 0.35$ at $M_\tau = 1777.03$ MeV

	$l = 1$	$l = 2$	$l = 3$
$\Lambda_{\rm pt}^{(l,3)}$	241.78	431.54	400.75
$\Lambda_{\rm an}^{(l,3)}$	296.75	748.64	612.52

Table 3. Analytic running coupling constant $\alpha_{\rm an}^{(l)}$ versus q, where l is the number of loops and $n_f = 3$, under the normalization condition $\alpha(M_\tau) = 0.35$ at $M_\tau = 1777.03$ MeV

q, MeV	$\alpha_{\rm an}^{(1)}$	$\alpha_{\rm an}^{(2)}$	$\alpha_{\rm an}^{(3)}$
2000.0	0.3345	0.3354	0.3348
1900.0	0.3411	0.3416	0.3413
1800.0	0.3483	0.3484	0.3483
1700.0	0.3561	0.3557	0.3559
1600.0	0.3646	0.3635	0.3642
1500.0	0.3740	0.3721	0.3731
1400.0	0.3843	0.3815	0.3830
1300.0	0.3958	0.3919	0.3938
1200.0	0.4087	0.4034	0.4058
1100.0	0.4233	0.4162	0.4192
1000.0	0.4398	0.4306	0.4343
900.0	0.4589	0.4470	0.4513
800.0	0.4812	0.4659	0.4709
700.0	0.5076	0.4880	0.4935
600.0	0.5395	0.5143	0.5202
500.0	0.5789	0.5465	0.5523
400.0	0.6291	0.5870	0.5919
300.0	0.6956	0.6405	0.6425
200.0	0.7890	0.7157	0.7114
100.0	0.9333	0.8356	0.8189
0.0	1.3963	1.3962	1.3962

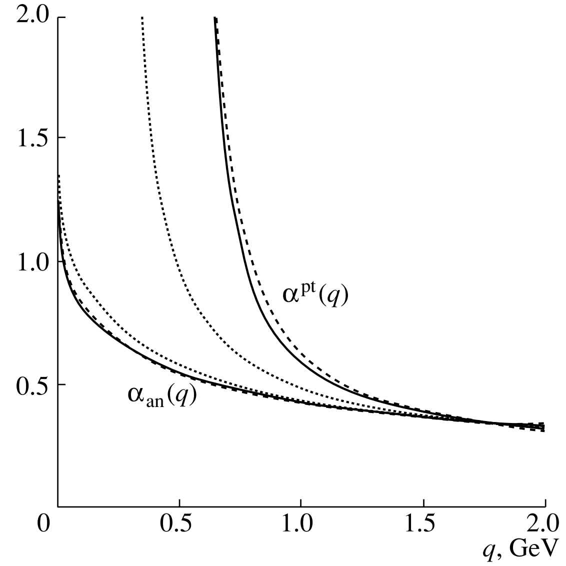

Fig. 6. Analytic running coupling constant α_{an} and its perturbative component α^{pt} versus momentum for the one- to the three-loop case (the notation for the curves is identical to that in Fig. 2) under the normalization condition $\alpha(M_\tau) = 0.35$ at $M_\tau = 1777.03$ MeV. The number of active-quark flavors was set to $n_f = 3$.

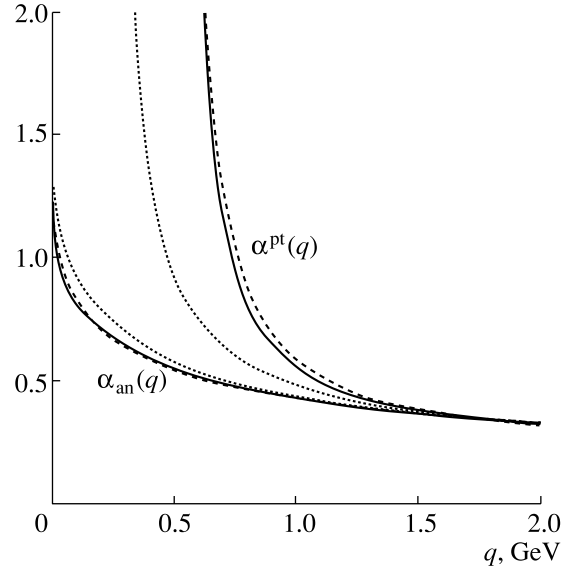

Fig. 7. Analytic running coupling constant α_{an} and its perturbative component α^{pt} versus momentum for the one- to the three-loop case (the notation for the curves is identical to that in Fig. 2) under the normalization conditions $\alpha(M_\tau) = 0.35$ at $M_\tau = 1777.03$ MeV with $n_f = 4$ and $\alpha^{n_f=4}(m_c) = \alpha^{n_f=3}(m_c)$ at $m_c = 1.3$ GeV.

pling constant to this coupling itself as a function of $x = q^2/\Lambda^2$. This ratio is equal to -0.18 at $x = 20$, but it decreases infinitely with decreasing x $(x > 1)$.

If we impose a normalization condition on the functions being considered, for example, at the q value equal to the τ-lepton mass M_τ, the curves representing the two-loop and the three-loop result for α_{an} become still closer to each other. This can be seen from Fig. 6. The normalization condition used for all functions displayed in this figure is $\alpha(M_\tau) = 0.35$ at $M_\tau = 1777.03$ MeV [15]. In just the same way as in [4, 5], the number n_f of active-quark flavors is treated here as an effective parameter and is set to three. Table 2 gives the values of the parameter Λ that correspond to the above normalization condition, while Table 3 presents the values of α_{an} for q changing from 2 GeV to zero. The values of the parameter Λ in the two- and three-loop approximation for the analytic running coupling constant prove to be much greater (by a factor ranging between 1.5 and 2) than those for the perturbative coupling constant. This is because the nonperturbative contributions are rather large at the normalization point. The values of α_{an} in the two- and the three-loop case are close to each other in the interval of q values being considered. At $q = 100$ MeV, the distinction between them reaches a maximum value of 2%. The values of $\alpha_{\mathrm{an}}^{(l)}(0)$ in Table 3 enable us to check the accuracy of integration, since it is known from the outset that $\alpha_{\mathrm{an}}^{(l)}(0) = 1.396263$.

Within perturbation theory, there is a recipe [19] for matching solutions corresponding to different values of n_f. According to this recipe, the quantity α_s can be discontinuous at the matching point $\mu^{(n_f)}$. Since the coefficient c_2 from [19] is positive and since C_2 is negative, the matching condition can nevertheless be treated as the continuity condition at some point $\tilde{\mu}^{(n_f)}$. For the c quark, the value of the running quark mass in the $\overline{MS}$ scheme is $m_c \simeq 1.3$ GeV and the pole mass is $M_c \simeq 1.5$ GeV; taking this into account, we find that the point $\mu_c \equiv \tilde{\mu}^{(n_f=4)}$ of matching according to the continuity condition lies in the interval $m_c < \mu_c < M_c$. For the analytic coupling constant, the requirement of continuity at the point where the solutions in question are matched is natural. Let us consider normalization conditions that take into account the presence of the threshold corresponding to the c quark. For the normalization conditions $\alpha(M_\tau) = 0.35$ at $M_\tau = 1777.03$ MeV with $n_f = 4$ and $\alpha^{n_f=4}(m_c) = \alpha^{n_f=3}(m_c)$ at $m_c = 1.3$ GeV, Fig. 7 displays α^{pt} and α_{an} versus momentum. The corresponding set of values of the parameter Λ is given in Table 4, while the values of α_{an} for the values of the momentum q that were considered in the preceding case are presented in Table 5. As in the preceding case, the values of $\alpha_{\mathrm{an}}^{(2)}$ and $\alpha_{\mathrm{an}}^{(3)}$ are close to each other, the maximum distinction of 2% between them being observed at $q = 100$ MeV.

Table 4. Parameters $\Lambda_{\rm pt}^{(l,n_f)}$ and $\Lambda_{\rm an}^{(l,n_f)}$ (in MeV), where l is the number of loops and n_f is the number of active-quark flavors, under the normalization conditions $\alpha^{n_f=4}(M_\tau) = 0.35$ at $M_\tau = 1777.03$ MeV and $\alpha^{n_f=4}(m_c) = \alpha^{n_f=3}(m_c)$ at $m_c = 1.3$ GeV

	$l = 1$	$l = 2$	$l = 3$
$\Lambda_{\rm pt}^{(l,3)}$	236.25	413.88	385.28
$\Lambda_{\rm pt}^{(l,4)}$	206.12	368.17	347.28
$\Lambda_{\rm an}^{(l,3)}$	294.68	750.18	613.02
$\Lambda_{\rm an}^{(l,4)}$	242.61	560.50	479.65

It is important to note that the values of $\alpha_{\rm an}^{(2)}$ and $\alpha_{\rm an}^{(3)}$ in Tables 3 and 5 differ by not more than 0.1% for any value of q. As to $\alpha^{\rm pt}$, the change in the normalization condition changed significantly its momentum dependence. This can be seen from a comparison of the graphs of $\alpha^{\rm pt}(q)$ in Figs. 6 and 7. For example, the three-loop perturbative curves at $q = 0.7$ GeV differ by 15%. The data in Tables 2 and 4 demonstrate that, in relation to the preceding case, the values of $\Lambda_{\rm pt}^{(l,3)}$ became somewhat smaller, while the values of $\Lambda_{\rm an}^{(l,3)}$ underwent virtually no change. Thus, we see that not only is the analytic running coupling constant stable with respect to the inclusion of higher approximations, but it also possesses threshold stability. It should also be noted that, in response to the change in n_f, $\Lambda_{\rm an}$ changes much more significantly than Λ_{pt}.

CONCLUSION

The representation of the QCD analytic running coupling constant in the form

$$\alpha_{\rm an}(q^2) = \alpha^{\rm pt}(q^2) + \frac{4\pi}{b_0}\sum_{n=1}^{\infty} c_n \left(\frac{\Lambda^2}{q^2}\right)^n \qquad (46)$$

with calculable coefficients c_n provides an efficient method for calculating $\alpha_{\rm an}$ for $q > \Lambda$ to a precision at the level of precision in calculating standard mathematical functions. In applying this method, it is not necessary to sum a large number of terms of the series in (46). Even at $q \sim 5\Lambda$, the approximation of the nonperturbative tail by the leading term of this series ensures a 1% precision in calculating $\alpha_{\rm an}$. For the standard three-loop solution (19), the explicit expressions for the coefficients c_n are given by the simple formula (42). Owing to this, it is convenient to analyze experimental data in terms of $\alpha_{\rm an}$.

Table 5. Analytic running coupling constant $\alpha_{\rm an}^{(l)}$ versus q, where l is the number of loops, under the normalization conditions $\alpha^{n_f=4}(M_\tau) = 0.35$ at $M_\tau = 1777.03$ MeV and $\alpha^{n_f=4}(m_c) = \alpha^{n_f=3}(m_c)$ at $m_c = 1.3$ GeV

q, MeV	$\alpha_{\rm an}^{(1)}$	$\alpha_{\rm an}^{(2)}$	$\alpha_{\rm an}^{(3)}$
2000.0	0.3349	0.3354	0.3349
1900.0	0.3413	0.3416	0.3413
1800.0	0.3483	0.3484	0.3483
1700.0	0.3559	0.3557	0.3559
1600.0	0.3642	0.3636	0.3641
1500.0	0.3734	0.3722	0.3731
1400.0	0.3835	0.3817	0.3830
1300.0	0.3947	0.3922	0.3940
1200.0	0.4076	0.4037	0.4060
1100.0	0.4221	0.4165	0.4194
1000.0	0.4386	0.4309	0.4344
900.0	0.4576	0.4473	0.4515
800.0	0.4798	0.4662	0.4710
700.0	0.5062	0.4883	0.4937
600.0	0.5380	0.5147	0.5204
500.0	0.5773	0.5469	0.5525
400.0	0.6275	0.5874	0.5920
300.0	0.6940	0.6408	0.6426
200.0	0.7874	0.7161	0.7115
100.0	0.9320	0.8359	0.8190
0.0	1.3963	1.3962	1.3962

The coefficients c_n in the representation given by (46) depend on the input approximate solution within perturbation theory. By way of example, we take the two-loop iterative solution presented by Shirkov and Solovtsov [4] in the form

$$a^{\rm it}(x) = \frac{1}{\ln x + b\ln(\ln x)}. \qquad (47)$$

The analytic expression corresponding to this solution can be represented in the form

$$a_{\rm an}(x) = a^{\rm it}(x) - \frac{1}{1 + b x_0^{1/b}}\frac{x_0}{x - x_0} \qquad (48)$$

$$+ b\int\limits_0^\infty d\xi\, \frac{1}{1 - x\exp(\xi)}\frac{1}{[\xi - b\ln\xi]^2 + b^2\pi^2},$$

where x_0 is the solution to the equation $\ln x_0 = x_0^{-1/b}$. The coefficients of the expansion in $1/x^n$ are given by

$$c_n = -\frac{x_0^n}{1 + b x_0^{1/b}} - b \int\limits_0^\infty d\xi \, \frac{\exp(-\xi n)}{[\xi - b\ln\xi]^2 + b^2\pi^2}. \tag{49}$$

At $n_f = 3$, this yields $c_1 = -0.762$, $c_2 = -1.166$, and $c_3 = -1.909$. These values differ significantly from the corresponding values in Table 1 for standard nonperturbative contributions. In this connection, we would like to mention the study of Magradze [20]; in constructing the analytic coupling constant, he took, for an input expression, that which is obtained as an exact solution to the two-loop renormalization-group equation and which is expressed in terms of the Lambert function $W(y)$ specified by the equation $y = W(y)\exp\{W(y)\}$. It can be expected that the corresponding nonperturbative contributions can be represented in the form of expansion (40), where the dependence of the coefficients c_n on n and n_f is peculiar to the choice of the input.

In addition to the above ambiguity, there is the ambiguity [21] that is inherent in the Redmond procedure and which is not removed by the requirement of renormalization invariance. In studying the photon propagator in QED, it was shown in [22] that, for the ambiguity in summing a diagrammatic series to be removed, it is necessary to require not only the presence of spectral representations but also fulfillment of the equations of motion. An approach to studying nonperturbative contributions in QCD on the basis of dynamical Dyson–Schwinger equations was employed in [23]. As an example of going beyond perturbation theory in models like massless QED and the asymptotically free $\lambda\phi_6^3$ model, we would like to indicate the studies of Klimenko [24].

ACKNOWLEDGMENTS

I am grateful to B.A. Arbuzov, V.A. Petrov, V.E. Rochev, and D.V. Shirkov for stimulating discussions.

This work was supported in part by the Russian Foundation for Basic Research (project no. 02-01-00601).

APPENDIX

Suppose that $f(z)$ is regular in a simply connected region D and that $z = 0 \in D$. Since we have to deal with integrands that have pole and logarithmic singularities at the origin, we draw a cut in the region D along the negative real axis. For any contour C that lies in the region $\tilde{D}$ cut in the way indicated above and which goes from the point $z_1 \neq 0$ to the point $z_2 \neq 0$, the following relations hold:

$$\int\limits_C \frac{dz}{z} f(z) = -\int\limits_C dz\, \ln(z) f'(z) + \ln(z) f(z)\Big|_{z_1}^{z_2},$$

$$\int\limits_C \frac{dz}{z^3} f(z) = -\frac{1}{2}\int\limits_C dz\, \ln(z) f'''(z)$$
$$+ \left\{-\frac{1}{2z^2} f(z) - \frac{1}{2z} f'(z) + \frac{1}{2}\ln(z) f''(z)\right\}\Big|_{z_1}^{z_2},$$

$$\int\limits_C \frac{dz}{z^2} \ln(z) f(z) = -\int\limits_C dz \left(\ln(z) + \frac{1}{2}\ln^2(z)\right)$$
$$\times f''(z) + \left\{-\frac{1}{z} f(z) - \frac{\ln(z)}{z} f(z)\right.$$
$$\left. + \ln(z) f'(z) + \frac{1}{2}\ln^2(z) f'(z)\right\}\Big|_{z_1}^{z_2},$$

$$\int\limits_C \frac{dz}{z^3} \ln(z) f(z) = -\int\limits_C dz \left(\frac{3}{4}\ln(z) + \frac{1}{4}\ln^2(z)\right)$$
$$\times f'''(z) + \left\{-\frac{1}{4z^2} f(z) - \frac{3}{4z} f'(z)\right.$$
$$- \frac{\ln(z)}{2z^2} f(z) - \frac{\ln(z)}{2z} f'(z)$$
$$\left. + \frac{3\ln(z)}{4} f''(z) + \frac{\ln^2(z)}{4} f''(z)\right\}\Big|_{z_1}^{z_2},$$

$$\int\limits_C \frac{dz}{z^3} \ln^2(z) f(z) = -\int\limits_C dz \left(\frac{7}{4}\ln(z)\right.$$
$$\left. + \frac{3}{4}\ln^2(z) + \frac{1}{6}\ln^3(z)\right) f'''(z)$$
$$+ \left\{-\frac{1}{4z^2} f(z) - \frac{7}{4z} f'(z) - \frac{\ln(z)}{2z^2} f(z)\right.$$
$$- \frac{3\ln(z)}{2z} f'(z) + \frac{7\ln(z)}{4} f''(z) - \frac{\ln^2(z)}{2z^2} f(z)$$
$$\left. - \frac{\ln^2(z)}{2z} f'(z) + \frac{3\ln^2(z)}{4} f''(z) + \frac{\ln^3(z)}{6} f''(z)\right\}\Big|_{z_1}^{z_2}.$$

REFERENCES

1. I. L. Solovtsov and D. V. Shirkov, Teor. Mat. Fiz. **120**, 482 (1999).
2. P. J. Redmond, Phys. Rev. **112**, 1404 (1958).
3. N. N. Bogolyubov, A. A. Logunov, and D. V. Shirkov, Zh. Éksp. Teor. Fiz. **37**, 805 (1959) [Sov. Phys. JETP **10**, 574 (1960)].

4. D. V. Shirkov and I. L. Solovtsov, JINR Rapid Commun., No. 2[76]-96, 5 (1996).
5. D. V. Shirkov and I. L. Solovtsov, Phys. Rev. Lett. **79**, 1209 (1997).
6. Yu. L. Dokshitzer, G. Marchesini, and B. R. Webber, Nucl. Phys. B **469**, 93 (1996).
7. A. C. Mattingly and P. M. Stevenson, Phys. Rev. D **49**, 437 (1994).
8. P. M. Stevenson, Phys. Lett. B **331**, 187 (1994).
9. Yu. A. Simonov, Pis'ma Zh. Éksp. Teor. Fiz. **57**, 513 (1993) [JETP Lett. **57**, 525 (1993)].
10. Yu. A. Simonov, Yad. Fiz. **58**, 113 (1995) [Phys. At. Nucl. **58**, 107 (1995)].
11. A. I. Alekseev, Phys. Rev. D **61**, 114005 (2000).
12. A. I. Alekseev, Teor. Fiz. **1**, 10 (2000).
13. A. I. Alekseev, Preprint No. 2000-40, IHEP (Protvino, 2000); hep-ph/0011178.
14. D. J. Gross and F. Wilczek, Phys. Rev. Lett. **30**, 1342 (1973); H. D. Politzer, Phys. Rev. Lett. **30**, 1346 (1973).
15. Review of Particle Physics, Eur. Phys. J. C **15**, 85 (2000).
16. W. A. Bardeen, A. J. Buras, D. W. Duke, and T. Muta, Phys. Rev. D **18**, 3998 (1978).
17. *Higher Transcendental Functions (Bateman Manuscript Project),* Ed. by A. Erdelyi (McGraw-Hill, New York, 1953; Nauka, Moscow, 1965), Vol. 1.
18. A. P. Prudnikov, Yu. A. Brychkov, and O. I. Marichev, *Integrals and Series* (Nauka, Moscow, 1981; Gordon and Breach, New York, 1986), Vol. 1.
19. K. G. Chetyrkin, B. A. Kniehl, and M. Steinhauser, Phys. Rev. Lett. **79**, 2184 (1997).
20. B. A. Magradze, Int. J. Mod. Phys. A **15**, 2715 (2000).
21. D. A. Kirzhnits, V. Ya. Faĭnberg, and E. S. Fradkin, Zh. Éksp. Teor. Fiz. **38**, 239 (1960) [Sov. Phys. JETP **11**, 174 (1960)].
22. B. A. Arbuzov, Dokl. Akad. Nauk SSSR **128**, 1149 (1959) [Sov. Phys. Dokl. **4**, 1066 (1959)].
23. A. I. Alekseev and B. A. Arbuzov, Yad. Fiz. **61**, 314 (1998) [Phys. At. Nucl. **61**, 264 (1998)]; A. I. Alekseev and B. A. Arbuzov, Mod. Phys. Lett. A **13**, 1747 (1998); A. I. Alekseev, in *Proceedings of the Workshop on Nonperturbative Methods in Quantum Field Theory, Adelaide, Australia, 1998,* Ed. by A. W. Schreiber, A. G. Williams, and A. W. Thomas (World Sci., Singapore, 1998), p. 104; hep-ph/9808206.
24. K. G. Klimenko, Teor. Mat. Fiz. **37**, 416 (1978); **40**, 38 (1979).

Translated by A. Isaakyan

Physics of Atomic Nuclei, Vol. 65, No. 9, 2002, pp. 1692–1710. Translated from Yadernaya Fizika, Vol. 65, No. 9, 2002, pp. 1736–1754.
Original Russian Text Copyright © 2002 by Kiselev, Kovalsky, Onishchenko.

ELEMENTARY PARTICLES AND FIELDS
Theory

Potential of Heavy Quarks in the Static Limit of QCD

V. V. Kiselev*, A. E. Kovalsky[1], and A. I. Onishchenko[2]*****

Institute for High Energy Physics, Protvino, Moscow oblast, 142284 Russia

Received December 5, 2000; in final form, November 29, 2001

Abstract—The potential of static quarks that is consistent both with the three-loop QCD running coupling constant, the two-loop perturbative matching of the $\overline{MS}$ and V schemes being taken into account here, and with the regime of quark confinement at long distances is derived on the basis of the procedure and arguments proposed by Richardson, Buchmüller, and Tye. Applications of this approach are discussed for the masses of heavy quarks, for the mass spectra of heavy quarkonia, and for the leptonic widths of vector states. © *2002 MAIK "Nauka/Interperiodica"*.

1. INTRODUCTION

The potential of static heavy quarks reflects the most important features of QCD dynamics, including asymptotic freedom and confinement. In studying subtle and rare electromagnetic processes in the heavy-quark sector of the Standard Model, it is necessary to understand profoundly strong-interaction-induced effects. For hard processes, there are, in addition to perturbative calculations, three general approaches to obtaining comprehensive answers to the question of how heavy quarks are bound within hadrons and the question of how the measured properties of hadrons are related to the features of heavy quarks with respect to their electroweak interactions and QCD forces. These are an operator-product expansion in inverse powers of the heavy-quark mass, QCD sum rules, and potential models that employ various approximations of the Bethe–Salpeter equation with a static potential. The first method is usually used to deduce inclusive estimates, whereas the second and the third one are invoked for exclusive calculations. It is of paramount importance to find out whether the results of calculations based on these methods are consistent; therefore, a comparative analysis of such results is urgently needed for this. Obviously, the wider the set of systems and processes involved in such an analysis, the more profound the qualitative and quantitative understanding of the dynamics of heavy quarks.

In the leading order of perturbative QCD at short distances and with a linear confining interaction in the infrared region, the potential of static heavy quarks was considered within the Cornell model [1], where a simple superposition of two asymptotic limits was introduced (an effective Coulomb interaction and a stringlike interaction). The observed heavy quarkonia occur in the intermediate region of distances, where the contribution of either potential term is of importance in determining the mass spectra. For this reason, phenomenological approximations of the potential (a logarithmic and a power-law dependence [2, 3]) that were constructed with allowance for regularities observed in the mass spectra [4] could be successfully used. In relation to the masses of bound heavy-quark states, the quarkonium wave functions at the origin, which determine leptonic coupling constants and normalizations of the cross sections for the production of quarkonia, are more sensitive to the global properties of the potential. Potentials that are consistent both with asymptotic freedom and with a linear form of confinement were proposed by Richardson [5] within the one-loop approximation and by Buchmüller and Tye [6] at the two-loop level. Technically, it is necessary to calculate, within a specific regularization scheme—say, the modified minimal-subtraction ($\overline{MS}$) scheme—the perturbative expansion of the potential of static quarks by representing this potential in the form of a Coulomb potential with a running coupling constant in the V scheme. As a result, calculations within perturbation theory yield conditions that ensure the matching of the $\overline{MS}$ and V schemes. Calculations with the running coupling constant $\alpha_s^{\overline{MS}}$ at the n-loop level require matching with α_V at the $(n-1)$-loop level. We note that two input coefficients corresponding to the β function are quantities that are independent of either the regu-

---

[1] Moscow Institute for Physics and Technology, Institutskiĭ pr. 9, Dolgoprudnyĭ, Moscow oblast, 141700 Russia.

[2] Institute of Theoretical and Experimental Physics, Bol'shaya Cheremushkinskaya 25, Moscow, 117259 Russia.

*e-mail: `kiselev@th1.ihep.su`

**e-mail: `kovalsky_a_e@mail.ru`

***e-mail: `onischen@heron.itep.ru`

larization scheme or the computational procedure, whereas the remaining coefficients do generally depend on the computational procedure. The V scheme is defined for an observable, so that its β function is gauge-invariant. For α_V, Buchmüller and Tye introduced a β function such that it is consistent with the known asymptotic regimes at short and long distances. They proposed a functional form leading to an effective charge that is specified by only two parameters, a perturbative and a nonperturbative one (scale in the running coupling constant at large virtualities and tension of the quark–gluon string, respectively). A full characterization also requires specifying the coefficients in the β function. Only the two-loop β function and the conditions of one-loop matching with the potential had been known by the instant at which the article of Buchmüller and Tye appeared. In recent years, considerable advances have been been in relevant computations: the two-loop conditions of matching of the V and $\overline{MS}$ schemes [7, 8] can be combined with the three-loop running coupling constant $\alpha_s^{\overline{MS}}$. Thus, it would be of great interest to modify the Buchmüller–Tye potential for static quarks in accordance with the present-day status of perturbative calculations. Moreover, two questions remain open at present. First, the asymptotic perturbative expansion of the Buchmüller–Tye β function to the third order leads to the three-loop coefficient that differs drastically from the exact result—even its sign is incorrect. Second, the parameter $\Lambda_{\overline{MS}}$ used in the Buchmüller–Tye potential is at odds with the results of recent measurements reported in [9]. In order to clarify these points, we will derive the potential of static quarks that is consistent with the current state of affairs in this realm of investigations.

Yet another facet of this study is associated with the masses of heavy quarks. Once the potential has been specified, the pole masses define the mass spectra of heavy quarkonia without any arbitrariness.[3] Therefore, it is necessary to check the consistency of mass estimates within this approach with the QCD potential for static quarks and within QCD sum rules.

The ensuing exposition is organized as follows. In Section 2, we generalize the Buchmüller–Tye procedure to the case of three loops and derive the potential of static quarks. We consider numerical values of the potential parameters and their consistency with the corresponding values known from other approaches. In Section 3, we discuss the implications of this approach for the masses of heavy quarks, for the spectra of heavy quarkonia, and for the leptonic coupling constants. The results that we have obtained are summarized in the Conclusion.

2. QCD AND POTENTIAL OF STATIC QUARKS

In this section, we discuss two regimes for QCD forces between static heavy quarks: asymptotic freedom and confinement. Further, we present a construction that combines these two regimes in a unified β function that is consistent with both limits at small and large values of the QCD coupling constant.

2.1. Perturbative Results at Short Distances

The static potential is defined in a manifestly gauge-invariant form in terms of the vacuum expectation value of the Wilson loop as [10]

$$V(r) = -\lim_{T\to\infty}\frac{1}{iT}\ln\langle\mathcal{W}_\Gamma\rangle, \qquad (1)$$

$$\mathcal{W}_\Gamma = \widetilde{\mathrm{tr}}\,\mathcal{P}\exp\left(ig\oint_\Gamma dx_\mu A^\mu\right),$$

where Γ is a rectangular contour with sides T in time and r in space. The gauge fields A_μ of charge g are ordered along the path (this is denoted by the symbol $\mathcal{P}$), and the color trace is normalized according to the condition $\widetilde{\mathrm{tr}}(...) = \mathrm{tr}(...)/\mathrm{tr}\hat{1}$.

It is common practice to consider the V scheme for the QCD coupling constant. This scheme is usually introduced by defining the potential of static quarks in momentum space via the relation

$$V(\mathbf{q}^2) = -C_F\frac{4\pi\alpha_V(\mathbf{q}^2)}{\mathbf{q}^2}, \qquad (2)$$

where α_V can be matched with $\alpha_s^{\overline{MS}}$ specified at an arbitrary normalization point μ; that is,

$$\alpha_V(\mathbf{q}^2) = \alpha_s^{\overline{MS}}(\mu^2)\sum_{n=0}^{\infty}\tilde{a}_n(\mu^2/\mathbf{q}^2)\left(\frac{\alpha_s^{\overline{MS}}(\mu^2)}{4\pi}\right)^n \qquad (3)$$

$$= \alpha_s^{\overline{MS}}(\mathbf{q}^2)\sum_{n=0}^{\infty}a_n\left(\frac{\alpha_s^{\overline{MS}}(\mathbf{q}^2)}{4\pi}\right)^n.$$

At present, our knowledge of this expansion[4] does not go beyond the tree, the one-loop, and the two-loop matching condition, so that we have

$$a_0 = \tilde{a}_0 = 1, \quad a_1 = \frac{31}{9}C_A - \frac{20}{9}T_F n_f, \qquad (4)$$

---

[3] We are dealing here with so-called spin-averaged spectra, since the inclusion of a spin-dependent splitting would lead to the emergence of additional parameters that are beyond the static approximation.

[4] For an analysis of the possible special features of the expansion, the reader is referred to [10].

$$\tilde{a}_1 = a_1 + \beta_0 \ln \frac{\mu^2}{\mathbf{q}^2},$$

$$a_2 = \left(\frac{4343}{162} + 4\pi^2 - \frac{\pi^4}{4} + \frac{22}{3}\zeta(3)\right) C_A^2 \quad (5)$$
$$- \left(\frac{1798}{81} + \frac{56}{3}\zeta(3)\right) C_A T_F n_f$$
$$- \left(\frac{55}{3} - 16\zeta(3)\right) C_F T_F n_f + \left(\frac{20}{9} T_F n_f\right)^2,$$

$$\tilde{a}_2 = a_2 + \beta_0^2 \ln^2 \frac{\mu^2}{\mathbf{q}^2} + (\beta_1 + 2\beta_0 a_1) \ln \frac{\mu^2}{\mathbf{q}^2}. \quad (6)$$

Here, we have employed the usual notation for the $SU(N_c)$ gauge group: $C_A = N_c$, $C_F = (N_c^2 - 1)/(2N_c)$, and $T_F = 1/2$. The number of active quark flavors is denoted by n_f.

Upon setting $\mathfrak{a} = \alpha/(4\pi)$, the β function is defined as

$$\frac{d\mathfrak{a}(\mu^2)}{d \ln \mu^2} = \beta(\mathfrak{a}) = -\sum_{n=0}^{\infty} \beta_n \mathfrak{a}^{n+2}(\mu^2), \quad (7)$$

so that we have $\beta_{0,1}^V = \beta_{0,1}^{\overline{MS}}$ and

$$\beta_2^V = \beta_2^{\overline{MS}} - a_1 \beta_1^{\overline{MS}} + (a_2 - a_1^2)\beta_0^{\overline{MS}} \quad (8)$$
$$= \left(\frac{618 + 242\zeta(3)}{9} + \frac{11(16\pi^2 - \pi^4)}{12}\right) C_A^3$$
$$- \left(\frac{445 + 704\zeta(3)}{9} + \frac{16\pi^2 - \pi^4}{3}\right) C_A^2 T_F n_f$$
$$+ \frac{2 + 224\zeta(3)}{9} C_A (T_F n_f)^2$$
$$- \frac{686 - 528\zeta(3)}{9} C_A C_F T_F n_f$$
$$+ 2 C_F^2 T_F n_f + \frac{184 - 192\zeta(3)}{9} C_F (T_F n_f)^2.$$

The coefficients in the β function that were calculated in the $\overline{MS}$ scheme [11] are given by

$$\beta_0^{\overline{MS}} = \frac{11}{3} C_A - \frac{4}{3} T_F n_f, \quad (9)$$

$$\beta_1^{\overline{MS}} = \frac{34}{3} C_A^2 - 4 C_F T_F n_f - \frac{20}{3} C_A T_F n_f, \quad (10)$$

$$\beta_2^{\overline{MS}} = \frac{2857}{54} C_A^3 + 2 C_F^2 T_F n_f \quad (11)$$
$$- \frac{205}{9} C_A C_F T_F n_f - \frac{1415}{27} C_A^2 T_F n_f$$
$$+ \frac{44}{9} C_F (T_F n_f)^2 + \frac{158}{27} C_A (T_F n_f)^2.$$

The expression for the potential in coordinate space is obtained by applying the Fourier transformation. The result is [7]

$$V(r) = -C_F \frac{\alpha_s^{\overline{MS}}(\mu^2)}{r} \quad (12)$$
$$\times \left(1 + \frac{\alpha_s^{\overline{MS}}(\mu^2)}{4\pi} \left(2\beta_0 \ln(\mu r') + a_1\right)\right.$$
$$+ \left(\frac{\alpha_s^{\overline{MS}}(\mu^2)}{4\pi}\right)^2 \left(\beta_0^2 \left(4 \ln^2(\mu r') + \frac{\pi^2}{3}\right)\right.$$
$$\left.\left. +\ 2(\beta_1 + 2\beta_0 a_1) \ln(\mu r') + a_2\right) + \ldots\right),$$

where $r' \equiv r \exp(\gamma_{\mathrm{E}})$, with γ_{E} being the Euler constant. Defining a new distance-dependent running coupling constant via the relation

$$V(r) = -C_F \frac{\bar{\alpha}_V(1/r^2)}{r}, \quad (13)$$

one can calculate its β function with the aid of (12); as a result, it turns out that [7]

$$\bar{\beta}_2^V = \beta_2^V + \frac{\pi^2}{3} \beta_0^3 \quad (14)$$

and that the low-order coefficients $\bar{\beta}_{0,1}^V$ are equal to the scheme-invariant values presented above.

In order to normalize the coupling constants, we use relations (3) at $\mathbf{q}^2 = m_Z^2$.

2.2. Quark Confinement

The nonperturbative behavior of QCD forces between static heavy quarks at long distances r is usually represented by the linear potential (see the relevant discussion in [12])

$$V^{\mathrm{conf}}(r) = k \cdot r, \quad (15)$$

which corresponds to the area law for the Wilson loop.

This potential can be expressed in terms of a constant chromoelectric field between sources that occur in the fundamental representation of the $SU(N_c)$ group. By way of example, we indicate that, in the Schwinger–Fock fixed-point gauge

$$x_\mu \cdot A^\mu(x) = 0,$$

the gluon field is expressed in terms of the strength tensor as

$$A_\mu(x) \approx -\frac{1}{2} x^\nu G_{\nu\mu}(0).$$

For static quarks separated by a distance $\mathbf{r}$, one can then obtain the following relation in terms of components (the subscripts m and 0 are associated with spatial and time components)

$$\bar{Q}_i(0) G_{m0}^a(0) Q_j(0) = \frac{\mathbf{r}_m}{r} E T_{ij}^a.$$

Here, the fields of heavy quarks are normalized to unity; T^a_{ij} are the generators of the color-symmetry group in the fundamental representation; i and j are color indices of the quarks involved; and E is the chromoelectric-field normalization, which is expressed in terms of the gluon condensate (see below). The potential that confines quarks can then be represented as

$$V^{\rm conf}(r) = \frac{1}{2} g\, C_F\, E\cdot r.$$

Assuming that the same field strength corresponds to the formation of the gluon condensate and introducing stochastic color sources n_i, which must be averaged over a vacuum, we can easily obtain

$$\langle G^2_{\mu\nu}\rangle = -4\,\langle G^a_{m0}(0) G^a_{m0}(0)\rangle = 4\, C_F\, E^2 \langle \bar n n\rangle,$$

where we have used the relation

$$\langle \bar n T^a T^b n\rangle = -\langle \bar n T^a n\cdot \bar n T^b n\rangle, \tag{16}$$

which guarantees that the sources do not violate gauge invariance, since they do not generate a gluon mass.[5] Further, it is obvious that

$$\langle \bar n T^a T^b n\rangle = C_F \frac{\delta^{ab}}{N_c^2-1}\langle \bar n n\rangle.$$

We then conclude that the relation between the field strength E and the string tension depends on the normalization of the vacuum sources n_i. We set

$$\langle \bar n_i n_j\rangle = n_l \delta_{ij},$$

where n_l stands for the mean number of stochastic light flavors, which is a free parameter of the present consideration. Needless to say, the quantity n_l must be finite even in the case of pure gluodynamics featuring no light quarks in the infrared region. Moreover, light-quark loops can generate ruptures of a gluon string—that is, strong decays of higher excitations. We assume that n_l is determined primarily by gluon dynamics (that is, it depends on the number of colors), weakly correlating with the number of quark flavors. A simple consideration of the potential force between two color sources in the fundamental and the adjoint representation—that is, a comparison of color factors for one-gluon Coulomb potentials—makes it possible to determine the number of stochastic sources replacing, in the approach adopted here, vacuum gluons for pure gluodynamics. The result is

$$n_l = \frac{1}{N_c}\frac{C_A}{C_F} = \frac{3}{4},$$

where the factor $1/N_c$ ensures the normalization of a source to unity and C_A/C_F is the corresponding ratio of color charges. A shift of n_l in QCD featuring light quarks is not fixed explicitly; however, lattice calculations revealed that the dependence of the string tension on the number of light quarks is rather weak [13]. Finally, the coefficient in the linear term of the potential assumes the form

$$k = \frac{\pi}{2\sqrt{N_c}} C_F \sqrt{\left\langle \frac{\alpha_s}{\pi} G^2_{\mu\nu}\right\rangle}. \tag{17}$$

The quantity k is usually expressed in terms of $\alpha'_{\mathbb P}$ as

$$k = \frac{1}{2\pi\alpha'_{\mathbb P}}.$$

Buchmüller and Tye set $\alpha'_{\mathbb P} = 1.04$ GeV^{-2}; here, we will also use this string-tension value, which is related to the slope of Regge trajectories and which can be compared with the estimate following from (17). At $\langle \frac{\alpha_s}{\pi} G^2_{\mu\nu}\rangle = (1.6\pm 0.1)\times 10^{-2}$ GeV^4 [14], we have

$$\alpha'_{\mathbb P} = 1.04 \pm 0.03\ \text{GeV}^{-2},$$

which complies well with the fixed value given above.[6]

The form of the confining potential in (15) corresponds to the limit where, for small virtualities, $\mathbf q^2 \to 0$, the limiting behavior of the coupling constant α_V is

$$\alpha_V(\mathbf q^2) \to \frac{K}{\mathbf q^2}, \tag{18}$$

whence it follows that

$$\frac{d\alpha_V(\mathbf q^2)}{d\ln \mathbf q^2} \to -\alpha_V(\mathbf q^2). \tag{19}$$

For the function β_V, this yields the asymptotic behavior corresponding to confinement.

2.3. Unified β Function and Potential

Buchmüller and Tye proposed a procedure for reconstructing the β function in the entire region of the charge variation on the basis of the known limits in the regime of asymptotic freedom in a given order of perturbation theory in α_s and in the confining regime. For example, the function $\beta_{\rm PT}$ found within asymptotic perturbation theory at the one-loop level transforms into the Richardson β function; that is,

$$\frac{1}{\beta_{\rm PT}(\mathfrak a)} = -\frac{1}{\beta_0 \mathfrak a^2} \to \frac{1}{\beta_{\rm Rich}(\mathfrak a)} \tag{20}$$
$$= -\frac{1}{\beta_0 \mathfrak a^2\,(1-\exp[-1/(\beta_0\mathfrak a)])}.$$

The Richardson function has an essential singularity for $\mathfrak a \to 0$, with the result that the relevant expansion

---

[5] The mass term generated by the sources must have had the form $\mathcal L \sim A^a_\nu A^b_\nu [\bar n T^a T^b n + \bar n T^a n\cdot \bar n T^b n]$, which vanishes, by virtue of Eq. (16), upon averaging over the sources.

[6] Arbitrariness in choosing n_l can change the appropriate value of the gluon condensate.

leads to an asymptotic series in $\mathfrak{a}$. For $\mathfrak{a} \to \infty$, the function β_{Rich} tends to the confining-regime limit, as is seen in (19).

At the two-loop level, an analysis based on the same method leads to the Buchmüller–Tye β function,

$$\frac{1}{\beta_{\rm PT}(\mathfrak{a})} = -\frac{1}{\beta_0\mathfrak{a}^2} + \frac{\beta_1}{\beta_0^2\mathfrak{a}} \to \frac{1}{\beta_{\rm BT}(\mathfrak{a})} \tag{21}$$
$$= -\frac{1}{\beta_0\mathfrak{a}^2\left(1-\exp\left[-1/(\beta_0\mathfrak{a})\right]\right)} + \frac{\beta_1}{\beta_0^2\mathfrak{a}}\exp[-l\mathfrak{a}].$$

The exponential factor in the second term contributes in the next-to-leading order in $\mathfrak{a}$ at small $\mathfrak{a}$, so that the perturbative limit is restored. However, we can easily find that, when the relevant series expansion is constructed, the third coefficient in the function $\beta_{\rm BT}$ is given by

$$\beta_{2,\rm BT} = \frac{\beta_1}{\beta_0}(\beta_1 - l\beta_0).$$

We see that, at the chosen value of $l = 24$, it is negative [6], which is at odds with the new result obtained in [7, 8] and presented in (8).

In order to make use of the three-loop results for the perturbative β function, we introduce the transformation

$$\frac{1}{\beta_{\rm PT}(\mathfrak{a})} = -\frac{1}{\beta_0\mathfrak{a}^2} + \frac{\beta_1 + \left(\beta_2^V - \beta_1^2/\beta_0\right)\mathfrak{a}}{\beta_0^2\mathfrak{a}} \tag{22}$$
$$\to \frac{1}{\beta(\mathfrak{a})} = -\frac{1}{\beta_0\mathfrak{a}^2\left(1-\exp\left[-1/(\beta_0\mathfrak{a})\right]\right)}$$
$$+ \frac{\beta_1 + \left(\beta_2^V - \beta_1^2/\beta_0\right)\mathfrak{a}}{\beta_0^2\mathfrak{a}}\exp\left[-\frac{l^2\mathfrak{a}^2}{2}\right],$$

where, as before, the exponential factor in the second term contributes only in the order that follows, in accuracy, the order of the three-loop consideration for $\mathfrak{a} \to 0$. In the perturbative limit, the usual solution for the running coupling constant,

$$\mathfrak{a}(\mu^2) = \frac{1}{\beta_0\ln(\mu^2/\Lambda^2)} \tag{23}$$
$$\times\left[1 - \frac{\beta_1}{\beta_0^2}\frac{1}{\ln(\mu^2/\Lambda^2)}\ln\ln\frac{\mu^2}{\Lambda^2} + \frac{\beta_1^2}{\beta_0^4}\frac{1}{\ln^2\frac{\mu^2}{\Lambda^2}}\right.$$
$$\left.\times\left(\ln^2\ln(\mu^2/\Lambda^2) - \ln\ln\frac{\mu^2}{\Lambda^2} - 1 + \frac{\beta_2^V\beta_0}{\beta_1^2}\right)\right],$$

remains valid, where, as usual, we have introduced the dimensional constant Λ that appears as the constant of integration of the relevant renormalization-group equation and which specifies the point of the infrared singularity in the running coupling constant. By using the asymptotic limits in (18) and (23), we can find an equation for any β function satisfying given boundary conditions. For example, we have

$$\ln\frac{\mu^2}{\Lambda^2} = \frac{1}{\beta_0\mathfrak{a}(\mu^2)} + \frac{\beta_1}{\beta_0^2}\ln\beta_0\mathfrak{a}(\mu^2) \tag{24}$$
$$+ \int\limits_0^{\mathfrak{a}(\mu^2)} dx\left[\frac{1}{\beta_0 x^2} - \frac{\beta_1}{\beta_0^2 x} + \frac{1}{\beta(x)}\right],$$

$$\ln\frac{K}{\mu^2} = \ln\mathfrak{a}(\mu^2) + \int\limits_{\mathfrak{a}(\mu^2)}^{\infty} dx\left[\frac{1}{x} + \frac{1}{\beta(x)}\right]. \tag{25}$$

At a given β function, Eqs. (24) and (25) generally specify the relationship between the scale Λ and the parameter K of the linear potential [see Eq. (18)],

$$k = 2\pi C_F K.$$

With the aid of (22), Eq. (24) can easily be integrated, whereby one obtains an implicit solution for the scale dependence of the charge. Specifically, we have

$$\ln\frac{\mu^2}{\Lambda^2} = \ln\left[\exp\left(\frac{1}{\beta_0\mathfrak{a}(\mu^2)}\right) - 1\right] \tag{26}$$
$$+ \frac{\beta_1}{\beta_0^2}\left[\ln\frac{\beta_0\sqrt{2}}{l} - \frac{1}{2}\left(\gamma_{\rm E} + {\rm E}_1\left[\frac{l^2\mathfrak{a}^2(\mu^2)}{2}\right]\right)\right]$$
$$+ \frac{\beta_2^V\beta_0 - \beta_1^2}{\beta_0^3}\frac{\sqrt{\pi/2}}{l}\,{\rm Erf}\left[\frac{l\,\mathfrak{a}(\mu^2)}{\sqrt{2}}\right],$$

where

$${\rm E}_1[x] = \int\limits_x^{\infty} dt\, t^{-1}\exp[-t]$$

is the exponential integral and

$${\rm Erf}[x] = \frac{2}{\sqrt{\pi}}\int\limits_0^x dt\,\exp[-t^2]$$

is the error function.

Equation (26) can be inverted by applying the method of iterations, as was done in deriving Eq. (23). As a result, an approximate solution to Eq. (26) takes the form

$$\mathfrak{a}(\mu^2) = \frac{1}{\beta_0\ln\left[1 + \eta(\mu^2)(\mu^2/\Lambda^2)\right]}, \tag{27}$$

where

$$\eta(\mu^2) = \left(\frac{l}{\beta_0\sqrt{2}}\right)^{\beta_1/\beta_0^2} \tag{28}$$
$$\times\exp\left[\frac{\beta_1}{2\beta_0^2}\left(\gamma_{\rm E} + {\rm E}_1\left[\frac{l^2\mathfrak{a}_1^2(\mu^2)}{2}\right]\right)\right.$$

$$-\frac{\beta_2^V\beta_0-\beta_1^2}{\beta_0^3}\,\frac{\sqrt{\pi/2}}{l}\,\mathrm{Erf}\left[\frac{l\,\mathfrak{a}_1(\mu^2)}{\sqrt{2}}\right]\Bigg],$$

with $\mathfrak{a}_1$ being obtained in two iterations:

$$\mathfrak{a}_1(\mu^2)=\frac{1}{\beta_0\ln\left[1+\eta_1(\mu^2)(\mu^2/\Lambda^2)\right]}, \tag{29}$$

$$\eta_1(\mu^2)=\left(\frac{l}{\beta_0\sqrt{2}}\right)^{\frac{\beta_1}{\beta_0^2}} \tag{30}$$

$$\times\exp\left[\beta_1/2\beta_0^2\left(\gamma_{\mathrm{E}}+\mathrm{E}_1\left[\frac{l^2\mathfrak{a}_0^2(\mu^2)}{2}\right]\right)\right],$$

$$\mathfrak{a}_0(\mu^2)=\frac{1}{\beta_0\ln\left[1+(\mu^2/\Lambda^2)\right]}. \tag{31}$$

Going over to the limit $\mu^2\to 0$, we arrive at the relation

$$\ln 4\pi^2 C_F\alpha'_P\Lambda^2=\ln\beta_0 \tag{32}$$

$$+\frac{\beta_1}{2\beta_0^2}\left(\gamma_{\mathrm{E}}+\frac{l^2}{2\beta_0^2}\right)-\frac{\beta_2^V\beta_0-\beta_1^2}{\beta_0^3}\,\frac{\sqrt{\pi/2}}{l},$$

which fixes completely the parameters in the β function and the charge in terms of the scale Λ and the slope $\alpha'_{\mathbb{P}}$, since the parameter l is specified, in the form of an explicit function, by these two quantities in (32) .

We recall that, for $\mu^2\to\infty$, the perturbative expression (23) becomes valid as the limit of the effective charge in (27).

We can now proceed to discuss the numerical values of the potential parameters.

2.4. Choice of Scales

As was mentioned above, the slope of Regge trajectories, which specifies the linear part of the potential is fixed:

$$\alpha'_{\mathbb{P}}=1.04\ \ \mathrm{GeV}^{-2}.$$

We also use the measured QCD coupling constant [9] and take

$$\alpha_s^{\overline{MS}}(m_Z^2)=0.123$$

for the basic parameter controlling the potential. For this choice of normalization value for the QCD coupling constant, the scale is $\Lambda^{\overline{MS}}_{n_f=5}\approx 273$ MeV; this differs somewhat from the averaged value of $\Lambda^{\overline{MS}}_{n_f=5}\approx 208^{+25}_{-23}$ MeV, which is presented by the Particle Data Group [9] and which corresponds to the value of $\alpha_s^{\overline{MS}}(m_Z^2)=0.1181\pm 0.002$. However, this averaged value, which includes various data, is determined primarily by the most precise measurements—specifically, by LEP data on hadronic events at the Z-boson peak (hadronic width), by τ-lepton decays, by data on deep-inelastic scattering, and by lattice calculations for systems of heavy quarkonia. In these quantities, high-energy measurements at LEP for Z and at HERA for the evolution of the nucleon structure functions yield the average values of $\alpha_s^{\overline{MS}}(m_Z^2)=0.123\pm 0.004$ and $\alpha_s^{\overline{MS}}(m_Z^2)=0.122\pm 0.004$, respectively, and only the evolution of the structure functions at low virtualities, where the evolution is affected by poorly defined nonperturbative effects and by the contributions of higher twists, and the energy-dependent sum rules for structure functions at low energies shift sizably the average value of the coupling constant in deep-inelastic lepton–nucleon scattering. Thus, we conjecture that the methodological uncertainty in the above average value is somewhat underrated, since, in this case, low-energy data involve theoretical sources of uncertainty, which are difficult to assess. Data on τ-lepton decays lead to $\alpha_s^{\overline{MS}}(m_Z^2)=0.121\pm 0.003$. This result is based on sum rules, where knowledge of nonperturbative corrections is much more precise than in deep-inelastic scattering, although there are theoretical problems even here that are associated with the formulation of sum rules in the region of physical states, where there are distinctions from the classical version of sum rules at negative virtualities of large magnitude. Finally, lattice calculations investigate the splitting of states of heavy quarkonia that is determined by dynamics in the infrared region; at the same time, such calculations employ approximations featuring zero number of light quarks or $n_f=2$, relying on a subsequent extrapolation to $n_f=3$, as well as to the region of large virtualities owing to evolution. Nevertheless, a high accuracy of such estimates is declared. As we have seen, spectroscopic data on systems of heavy quarks should be interpreted with great caution, since the evolution of the potential parameters from the region of bound states to high virtualities is affected by nonperturbative factors. Thus, we can see that the normalization value adopted here for the QCD coupling constant agrees well with the results of direct high-energy measurements; at the same time, indirect data obtained at low energies prove to be compatible with it if we take into consideration their poorly controllable systematic uncertainties.

We note that the reduction of the normalization value—for example, down to $\alpha_s^{\overline{MS}}(m_Z^2)=0.120$—results in the fact that it becomes impossible to describe data on the mass splitting in heavy quarkonia between the $1S$ and $2S$ levels, which is very sensitive to variations in the normalization of the QCD running coupling constant: instead of $M(2S)-M(1S)\approx 580$ MeV, there arises a result that is about 100 MeV less than that. Concurrently, a change in

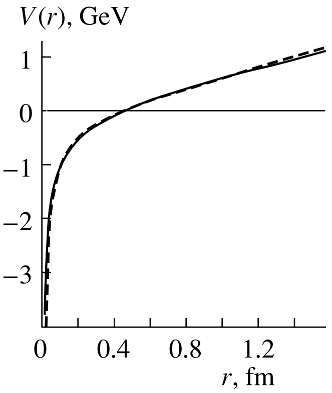

Fig. 1. Potential of static heavy quarks in QCD (solid curve) along with that in the Cornell model (dashed curve), an additive shift being made here along the energy scale.

the other dimensional parameter, the slope of the Regge trajectory, from the adopted value of $\alpha'_{\mathbb{P}} = 1.04$ GeV^{-2} down to $\alpha'_{\mathbb{P}} = 0.87$ GeV^{-2} leads to an insignificant variation both in the splitting and in the corresponding value of the coupling-constant scale associated with its evolution toward low virtualities.

We then obtain

$$\alpha_V(m_Z^2) \approx 0.1306$$

and use this value as the normalization condition for $\mathfrak{a}(m_Z^2)$. We then determine the values of the parameter Λ for the effective charge versus the number of active flavors. We have

$$\Lambda_{n_f=3} = 643.48\ MeV, \quad l = 56, \tag{33}$$

$$\Lambda_{n_f=4} = 495.24\, MeV, \quad l = 37.876, \tag{34}$$

$$\Lambda_{n_f=5} = 369.99\, MeV, \quad l = 23.8967, \tag{35}$$

where we set the threshold values for the changeover of the number of flavors to $m_5 = 4.6$ GeV and $m_4 = 1.5$ GeV. Having determined the momentum dependence of the charge, we make a Fourier transformation and arrive at

$$V(r) = k \cdot r - \frac{8C_F}{r} u(r), \tag{36}$$

$$u(r) = \int_0^\infty \frac{dq}{q} \left(\mathfrak{a}(q^2) - \frac{K}{q^2}\right) \sin(q \cdot r),$$

where the function $u(r)$ has been determined numerically for $r > 0.01$ fm and is presented as a file of the MATHEMATICA system in the notebook format on the site quoted in [15].

We note that, at short distances, the behavior of the potential is purely perturbative; in view of this, it is legitimate, for $r < 0.01$ fm, to set [see Eq. (13)]

$$V(r) = -C_F \frac{\bar{\alpha}_V(1/r^2)}{r},$$

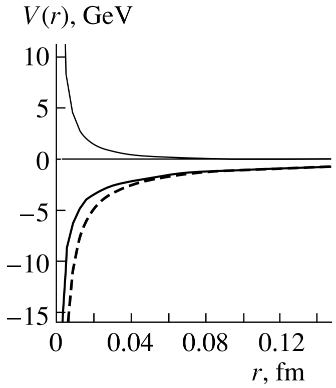

Fig. 2. Potential of static heavy quarks in QCD (thick solid curve) along with that in the Cornell model (dashed curve), an additive shift being made here along the energy scale, and their difference (thin solid curve) at short distances, which is due to the scale dependence of the QCD coupling constant.

where the running coupling constant $\bar{\alpha}_V(1/r^2)$ is given in Eq. (23) with the corresponding value of $\bar{\beta}_2^V$ at $n_f = 5$ and is normalized by the condition that requires matching with the potential (36) at the point $r_s = 0.01$ fm; as a result, the numerical calculations based on (36) and (13) appear to be consistent at

$$\bar{\alpha}_V(1/r_s^2) = 0.22213,$$

which leads to $\Lambda^{\overline{V}}_{n_f=5} = 617.42$ MeV.

Thus, we have completely specified the model of the potential of heavy quarks in QCD. Figure 1 shows the potential as a function of the interquark spacing. It can be seen that the calculated potential is close in shape to the Cornell model potential, which was obtained phenomenologically by fitting the mass spectra of heavy quarkonia.

A noticeable distinction between the QCD potential that we derived and that in the Cornell model at long distances is due to a mere numerical difference of values chosen for the string tension: we adopted the value from the study of Buchmüller and Tye, whereas the Cornell model employs a greater string tension. The distinction between these two potentials at short distances is much more significant (see Fig. 2), which is caused by a clear physical reason: the QCD coupling constant is running in our approach, but it is fixed in the Cornell model.

For the sake of comparison, the differences of the β functions in (20), (21), and (22) are displayed in Fig. 3 at fixed values of the parameters l and $n_f = 3$. From this figure, it can be seen that the asymptotic perturbative expansion of β for $\mathfrak{a} \to 0$ plays a dominant role for $\mathfrak{a} < \mathfrak{a}_0$, where $\mathfrak{a}_0 \approx 0.03$ corresponds to $\alpha_{V,0} \approx 0.37$. This value of the coupling constant $\alpha_{V,0}$ coincides with the effective Coulomb constant in the Cornell model. At greater values of the coupling constant, contributions associated with the confining regime become significant.

At this point, two comments are in order. First, the potential that we derived was obtained by employing a perturbative normalization to the measured value of $\alpha_s^{\overline{MS}}(m_Z^2)$ and the three-loop form of evolution to lower virtualities. Second, the variation in the running coupling constant is modified (numerically, the deviation from the perturbative regime becomes sizable at virtualities in the region $\mu < 3$–4 GeV) in such a way that the limiting value characteristic of the confining regime is achieved for $\mu \to 0$, in which case the perturbative relationship between the scales Λ and $\Lambda^{\overline{MS}}$ is violated at virtualities specifying the physical scale of strong interactions in systems involving charmed and beauty quarks. It was the reason why Buchmüller and Tye determined $\Lambda^{\overline{MS}}$ incorrectly.

3. MASSES OF HEAVY QUARKS AND LEPTONIC CONSTANTS

In considering the features of bound states of heavy quarks, it should be noted first of all that one must clearly separate two theoretical problems. The first is the problem of calculating the potential of heavy quarks. This problem, where the static limit $m_Q \to \infty$ is the leading-order approximation of the operator-product expansion in the inverse heavy-quark mass, was considered in the preceding section. The second problem is that of calculating the masses of bound states. In heavy quarkonia, the kinetic energy of quark motion is commensurate with the potential energy; therefore, the sum of the nonrelativistic kinetic term and the static potential—these two terms are precisely those that specify the dominant term in the Schrödinger equation for bound states—represents the leading approximation for the effective Lagrangian in the operator-product expansion in the inverse heavy-quark mass. Corrections to bound-state masses computed on the basis of the nonrelativistic Schrödinger equation with the static potential stem from relativistic terms in the kinetic energy and from operators that are dependent on the quark spins and interquark spacings and which are suppressed by inverse powers of the heavy-quark mass, as well as from nonpotential effects of the retardation of interaction. It will be shown below that the magnitude of such corrections can be restricted numerically, with the result that there arises a methodological uncertainty in calculating the mass spectra of heavy quarkonia within the potential approach featuring a static potential.

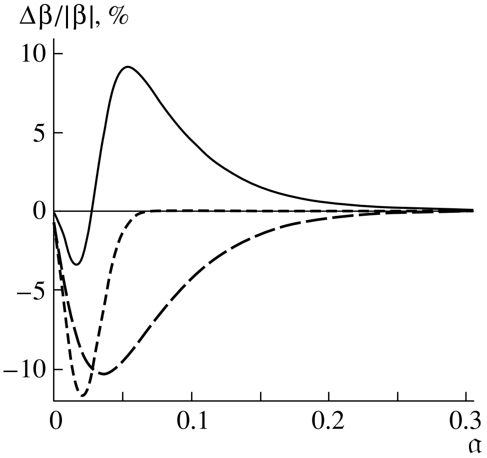

Fig. 3. Differences of the β functions versus the effective charge: (solid curve) $(\beta - \beta_{\rm BT})/|\beta|$, (short dashes) $(\beta - \beta_{\rm Rich})/|\beta|$, and (long dashes) $(\beta_{\rm BT} - \beta_{\rm Rich})/|\beta_{\rm BT}|$.

3.1. Masses

For a potential that is specified in the static approximation, we can determine the masses of heavy quarks from a comparison of the mass spectra of heavy quarkonia with the calculated values. The predicted charmonium and bottomonium masses are given in Table 1[7] at

$$m_c = 1.468 \text{ GeV}, \quad m_b = 4.873 \text{ GeV} \qquad (37)$$

without taking into account relativistic effects, which may prove to be of importance for charmonium [for example, $\Delta M(\bar{c}c) \sim 40$ MeV]. At present, the only measured splitting of nS levels is the splitting of η_c and J/ψ, which makes it possible to estimate the so-called spin-averaged mass of a state:

$$\overline{M}(1S) = (3M_{J/\psi} + M_{\eta_c})/4.$$

Assuming that the simple relation $\overline{M}(nS) = M_{\psi(nS)} - (M_{J/\psi} - M_{\eta_c})/4n$ is valid [4], we also estimate the expected splittings for excited states to a precision that we believe to be higher than 10 MeV. For the P-wave levels, we use the masses

$$\overline{M}(P) = M_1 + \frac{1}{3}(M_2 - M_0) + \frac{2}{9}(M_2 - M_1 + 2(M_0 - M_1)),$$

where M_J is the mass of the state that is characterized by the total spin J and by the sum of the quark spins that is equal to $S = 1$. Here, we assumed that

---

[7] We assume that the $\psi(3770)$ charmonium state is a mixture of the $3S$ and $3D$ levels, the $3D$ mass being insignificantly shifted.

Table 1. Charmonium, bottomonium, and quarkonium ($\bar{b}c$) masses predicted in the present study, along with experimental data treated according to the procedure described in the main body of the text

$\bar{Q}Q(nL)$	M, GeV	$\overline{M}_{\text{expt}}$, GeV	$\bar{Q}Q(nL)$	M, GeV	$\overline{M}_{\text{expt}}$, GeV
$\bar{c}c(1S)$	3.068	3.068	$\bar{c}c(2P)$	3.493	3.525
$\bar{c}c(2S)$	3.670	3.671	$\bar{c}c(3P)$	3.941	–
$\bar{c}c(3S)$	4.092	4.040	$\bar{c}c(3D)$	3.785	3.770
$\bar{b}b(1S)$	9.446	9.446	$\bar{b}b(2P)$	9.879	9.900
$\bar{b}b(2S)$	10.004	10.013	$\bar{b}b(3P)$	10.239	10.260
$\bar{b}b(3S)$	10.340	10.348	$\bar{b}b(3D)$	10.132	–
$\bar{b}b(4S)$	10.606	10.575	$\bar{b}b(5S)$	10.835	10.865
$\bar{b}c(1S)$	6.322	6.40	$\bar{b}c(2P)$	6.739	–
$\bar{b}c(2S)$	6.895	–	$\bar{b}c(3P)$	7.148	–
$\bar{b}c(3S)$	7.279	–	$\bar{b}c(3D)$	7.013	–

the spin-dependent forces are given by

$$V_{\text{SD}} = A(\mathbf{L}\cdot\mathbf{S}) + B(\mathbf{L}\cdot\mathbf{S})^2 - \frac{1}{3}B\mathbf{L}^2\cdot\mathbf{S}^2,$$

where the third term corresponds to the third term in the expression for the mass $\overline{M}(P)$ and leads to a shift of the levels that is proportional to the orbital angular momentum L.

We also assumed that

$$M_\Upsilon - M_{\eta_b} \approx \frac{\alpha_s(m_b)}{\alpha_s(m_c)}\frac{m_c^2}{m_b^2}\frac{|R_{\bar{b}b}(0)|^2}{|R_{\bar{c}c}(0)|^2} \times (M_{J/\psi} - M_{\eta_c}) \approx 56\ MeV,$$

where $R_{\bar{b}b}(0)$ and $R_{\bar{c}c}(0)$ are the radial wave functions at the origin calculated for the $1S$-wave states of the $\bar{b}b$ and $\bar{c}c$ quarkonia in solving the Schrödinger equation with the static potential. In such calculations, the dimensions of the quarkonia prove to be approximately equal to those in the model proposed by Buchmüller and Tye, although the state masses that we obtained are slightly different from those in their model, since we have used, for the input parameters, the different ground-state masses

$$M_{\bar{c}c}(1S) = 3.068\ \text{GeV}, \quad M_{\bar{b}b}(1S) = 9.446\ \text{GeV}.$$

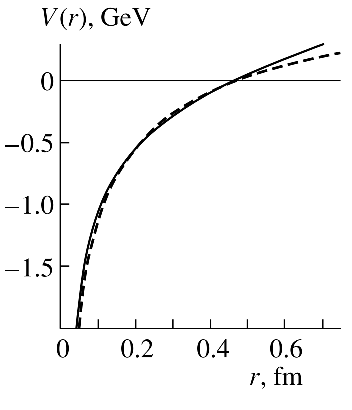

Fig. 4. Potential of static heavy quarks in QCD (solid curve) along with the representation of the perturbative expression (12) at $\mu = 1.5$ GeV (dashed curve), an additive shift being made here along the energy scale.

Further, we predict the mass of the heavy quarkonium $\bar{b}c$,[8] as is given in Table 1. The computed mass values are seen to comply well with the values obtained for the Buchmüller–Tye and for the Martin potential [17].

The quarkonium wave functions at the origin are related to the normalization of the cross sections for quarkonium production. The computed values are close to those that were obtained for the Buchmüller–Tye potential, but they are somewhat less for two reasons, that which is associated with the change in the heavy-quark mass and that which is associated with the distinction in the asymptotic behavior of the potential for $r \to 0$.

In the proposed approach, we fixed the pole heavy-quark masses (37) as quantities that are independent of the scale. In order to compare these values with those that were obtained within QCD sum rules, we note above all that, in QCD sum rules, use is usually made of nonrelativistic QCD (NRQCD) [18] with the nonperturbative potential (12), which explicitly depends on the normalization point μ (the conventional notation in the sum rules is μ_{soft}). We have

---

[8] The current experimental error in the measurements of the ground-state mass is still high, $\delta M = \pm 0.39$ GeV [16].

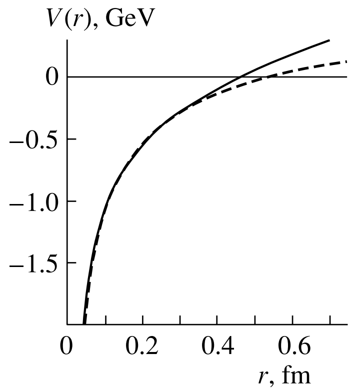

Fig. 5. As in Fig. 4, but for $\mu = 2.0$ GeV.

verified that, at short distances and large $\mu_{\rm soft}$, the perturbative potential (12) reproduces the form of the potential derived in the present study, but that there is a deviation at $r \gg 1/\mu_{\rm soft}$. At distances characteristic of the ground states of heavy quarkonia, $\langle r_{\bar{b}b(1S)}\rangle \approx 0.22$ fm and $\langle r_{\bar{c}c(1S)}\rangle \approx 0.42$ fm, the potential can be approximated by the perturbative expression at $\mu_{\rm soft} = 1.5 - 2.0$ GeV (see Figs. 4, 5) with an additive energy shift $\delta V(\mu_{\rm soft})$ that is shown in Fig. 6. Thus, we can see that the masses of the charmonium and bottomonium ground states can be computed by using the perturbative potential (12).

In order to illustrate the scale dependence of the region where the total and the perturbative static potential in QCD coincide, we choose the scale values of $\mu_{\rm soft} = 1.5$ GeV and $\mu_{\rm soft} = 2$ GeV in Figs. 4 and 5, respectively. From these figures, it can be seen that, as the scale $\mu_{\rm soft}$ of normalization of the perturbative potential is reduced, the region where this potential coincides with the total static QCD potential introduced above is shifted toward longer distances. If we assume that characteristic distances are determined by the inverse normalization scale, $r \sim 1/\mu_{\rm soft}$, this result becomes quite expectable. By way of example, we indicate that, at $\mu_{\rm soft} = 1.5$ GeV, one has $r \approx 0.15$ fm for a typical interquark distance at which the perturbative potential is expected to be consistent with the total potential. However, the linear component of the QCD potential grows rather slowly in relation to the rate of variation of the Coulomb contribution, with the result that the distinction between the total potential and the perturbative one becomes sizable not at $r \approx 0.15$ fm but at longer distances of $r \approx 0.5$ fm. At scale values in the region $\mu_{\rm soft} < 1.5$ GeV, the shape of the perturbative potential begins to deviate significantly from the shape of the potential including nonperturbative contributions.

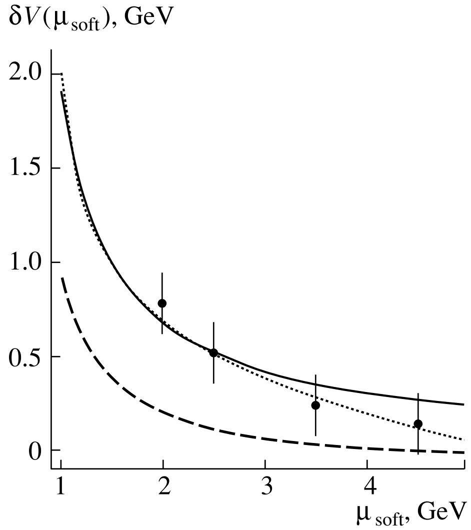

Fig. 6. Additive shift that must be made along the energy scale in order to match the μ-dependent perturbative potential with the potential calculated in this study on the basis of QCD. The solid and the dashed curve correspond to the two- and the three-loop matching. The points represent the results obtained within QCD sum rules for bottomonium. The dotted curve was calculated according to the relation between the running and the pole mass at the scale μ.

It follows that, if we redefine the heavy-quark masses as[9]

$$m^{\rm pole}(\mu)_{b,\,c} = m_{b,\,c} + \frac{1}{2}\delta V(\mu),$$

masses that are rather close to the experimental values will be obtained by solving the Schrödinger equation with the perturbative potential. Thus, the pole masses obtained within the potential QCD approach have been matched with the pole masses of perturbation theory that were calculated at the two-loop level.

We have numerically estimated the running masses $\bar{m}(\bar{m})$ within the $\overline{MS}$ scheme by using two-loop relations[10] to establish the relationship with the pole mass [20, 21] and by setting the normalization scale $\mu_{\rm soft}$ to $\bar{m}$. As a result, we arrived at

$$\bar{m}_c(\bar{m}_c) = 1.40 \pm 0.09 \ \ {\rm GeV},$$

---

[9] This redefinition is indicative of a perturbative renormalon (see the review article of Beneke [19]). Indeed, there are two sources of the deviation δV. The first is represented by the linear confining potential of static quarks. However, this source makes an insignificant contribution to δV. The second source is associated with the infrared divergence in the running QCD coupling constant obtained within perturbation theory. It can easily be shown that a small residual term that is weakly dependent on $\mu_{\rm soft}$ arises upon subtracting, from δV, the singular term, which is proportional to $\sim 1/(\mu_{\rm soft} - \Lambda)$.

[10] Here, we have not applied recent results from [20] for the three-loop mass matching, since this would lead us beyond the accuracy adopted in the present consideration.

$$\bar{m}_b(\bar{m}_b) = 4.20 \pm 0.06 \ \text{GeV},$$

which is in good agreement with various sum-rule estimates of m_b [22–25] and m_c [26].[11)]

In [24], the dependence of the pole mass on the scale μ_{soft} was calculated to the third order of perturbation theory. The uncertainty in estimating the heavy-quark mass from QCD sum rules for bottomonium was 0.1 GeV for the running mass in the $\overline{MS}$ scheme and 0.06 GeV for the low-energy mass (kinetic mass). The b-quark pole mass depends both on the normalization scale and on the order of perturbative QCD in α_s. In order to compare the sum-rule results with the values obtained within the potential approach developed in the present study, we fixed the order in α_s and restricted our consideration to the two-loop approximation. At the value of $\mu_{\text{soft}} =$ 2.5 GeV, taken by way of example, the estimates obtained on the basis of the perturbative-potential method and on the basis of sum rules then agree within the uncertainties of the two methods. Taking the above scale value for the initial-normalization point, we present the sum-rule results in Fig. 6 in the form of a shift along the energy scale. For the sake of clarity, the μ-dependent pole mass as calculated from the analysis in [24] is displayed in Fig. 6 with an uncertainty of $\delta m = 80$ MeV, which is a characteristic error inherent in the running-mass estimates given in [24]. Despite the different choices of normalization for the QCD coupling constant $\alpha_s^{\overline{MS}}(m_Z^2) = 0.118$ in [24], we can see fairly good agreement between the shapes of the μ dependences both for the energy shift of the perturbative potential with respect to the potential adopted in QCD and for the change in the perturbative pole mass of the b quark within QCD sum rules. As to the one-loop matching of the perturbative potential, we only note that the corresponding sum rules yield, in the same order, an energy shift that is close to zero for $\mu_{\text{soft}} > 2$ GeV within the accuracy of the method, and this estimate is consistent with the result obtained on the basis of the potential approach, as is shown in Fig. 6. Thus, we can see that, in the case of the two-loop matching of the V and $\overline{MS}$ schemes, the shift of the energy scale in the perturbative potential indicates that the shape of the QCD potential corresponds to the soft-normalization-scale dependence in the perturbative pole mass within QCD sum rules for bottomonium.

The μ dependence obtained in the pole mass can now be compared with the equation relating the running heavy-quark mass in the $\overline{MS}$ scheme to the pole mass, as was derived in [27], where we find that

$$m^{\text{pole}} = \bar{m}(\mu)\left(1 + c_1(\mu)\frac{\alpha_s^{\overline{MS}}(\mu^2)}{4\pi} + c_2(\mu)\left(\frac{\alpha_s^{\overline{MS}}(\mu^2)}{4\pi}\right)^2\right) \tag{38}$$

at

$$c_1(\mu) = C_F(4 + 3L), \tag{39}$$

$$\begin{aligned} c_2(\mu) = {} & C_F C_A\left(\frac{1111}{24} - 8\zeta(2) - 4I_3(1) + \frac{185}{6}L + \frac{11}{2}L^2\right) \\ & - C_F T_F n_f\left(\frac{71}{6} + 8\zeta(2) + \frac{26}{3}L + 2L^2\right) \\ & + C_F^2\left(\frac{121}{8} + 30\zeta(2) + 8I_3(1) + \frac{27}{2}L + \frac{9}{2}L^2\right) \\ & - 12C_F T_F(1 - 2\zeta(2)). \end{aligned} \tag{40}$$

Here, we have $I_3(1) = (3/2)\zeta(3) - 6\zeta(2)\ln 2$ and $L = 2\ln(\mu/m^{\text{pole}})$. The result obtained in [21] is reproduced at $\mu = m^{\text{pole}}$. It can easily be verified that the logarithms can be eliminated from the definition of $c_{1,2}$ by expressing the running values $\bar{m}(\mu)$ and $\alpha_s^{\overline{MS}}(\mu)$ in Eq. (38) in terms of $\bar{m}(m^{\text{pole}})$ and $\alpha_s^{\overline{MS}}(m^{\text{pole}})$. Nevertheless, we find that the explicit dependence on μ in (38) replicates the form of the renormalon contribution, as can be seen in the perturbative potential, where there is a similar effect because of the truncation of the perturbation-theory series and because of the infrared pole in the QCD running coupling constant. The difference $2(m_b^{\text{pole}}(\mu) - m_b)$ is displayed in Fig. 6 according to Eq. (38) at $\bar{m}(\bar{m}) = 4.3$ GeV. From this figure, we can see that the results obtained in [24] on the basis of QCD sum rules agree with those expected from Eq. (38) and that the μ-dependent shift of the pole mass approximately coincides with the shift of the perturbative potential with respect to the static QCD potential, which is free from the renormalon arbitrariness associated with the infrared singularity in the coupling constant at a finite energy scale in perturbation theory. This fact implies cancellation of infrared indeterminacies in the sum of the perturbative potential and the perturbative heavy-quark masses, and it is precisely this sum that specifies the energy of the heavy-quarkonium bound state. Thus, we can define the pole mass

$$\hat{m}^{\text{pole}} = m^{\text{pole}}(\mu) - \frac{1}{2}\delta V(\mu), \tag{41}$$

[11)] We note that there are distinctions between the values usually quoted in the literature for $\bar{m}(\bar{m})$ and $\bar{m}(m^{\text{pole}})$.

which is free from this arbitrariness in taking into account infrared contributions to the pole mass and which involves, on the right-hand side, the pole mass given by (38). For the beauty quark, the pole mass defined according to (41) agrees, to within 80 MeV, with the mass obtained on the basis of the potential approach proposed in the present study:

$$\hat{m}_b^{\rm pole} \approx m_b.$$

3.2. Heavy-Quark Masses and Potential Nonrelativistic QCD

In this subsection, we discuss the line of investigation that is being developed at present in the theory of the heavy quarkonia $Q\bar{Q}'$ on the basis of an effective theory referred to as potential nonrelativistic QCD (pNRQCD) [28]. This theory describes, in a natural way, both the interaction of heavy quarks in terms of a potential and the interaction with external ultrasoft fields within QCD.[12] We compare the results of pNRQCD calculations for the masses of heavy quarks with the analogous results that were obtained above within the approach employing the static QCD potential.

First, the fact that the motion of heavy quarks in heavy quarkonia is nonrelativistic makes it possible to introduce, within pNRQCD, three important physical scales in such systems. These are m, the heavy-quark mass; mv, the soft scale of the heavy-quark momentum in a hadron; and mv^2, the ultrasoft energy scale. The parameters in question are well separated because of the smallness of v, which is the velocity of a heavy quark in a hadron. Upon matching the effective theory with full QCD at the hard scale $\mu_{\rm hard} \sim m$, fields involving high virtualities of about the heavy-quark mass are eliminated from consideration within NRQCD. This leads to the introduction of perturbative Wilson coefficients in the operator-production expansion of the effective theory, and we are dealing with heavy quarks interacting with gluons at virtualities $\mu_{\rm fact,\,soft}$ of about mv. In order that heavy-quark fields could be considered at smaller values of the normalization scale μ down to mv^2, it is necessary to introduce the effective pNRQCD Lagrangian from which soft fields are eliminated, whereupon there remain the potential interaction of heavy quarks with each other and the interaction with ultrasoft gluon fields within a multipole expansion. The matching of pNRQCD and NRQCD must be performed at the scale $\mu_{\rm fact} \sim mv$. There is also an effective nonrelativistic QCD theory (see [30]) involving a renormalization-group summation over velocities (vNRQCD). In this theory, the relevant renormalization group [31] is used to match vNRQCD operators with full QCD at the scale of about m and to trace the evolution toward a small scale, where one may arrive at either mv or mv^2. Presently, the development of vNRQCD is at the stage of the one-loop matching of the potential of heavy quarks to the second order in the velocity (v^2)—that is, to spin-dependent terms of order $1/m^2$, which are beyond the present analysis. Therefore, we focus on discussing pNRQCD.

The pNRQCD Lagrangian has the form

$$\begin{aligned}\mathcal{L}_{\rm pNRQCD} = {\rm tr}\Bigg\{ & S^\dagger \left(i\partial_0 - \frac{\mathbf{P}^2}{4m} - \frac{\mathbf{p}^2}{m} + \frac{\mathbf{p}^4}{4m^3} \right. \\ & \left. - V_s(r) - \frac{V_s^{(1)}}{m} - \frac{V_s^{(2)}}{m^2} + \ldots \right) S \\ & + O^\dagger \left(iD_0 - \frac{\mathbf{P}^2}{4m} - \frac{\mathbf{p}^2}{m} + \frac{\mathbf{p}^4}{4m^3} \right. \\ & \left. - V_o(r) - \frac{V_o^{(1)}}{m} - \frac{V_o^{(2)}}{m^2} + \ldots \right) O \Bigg\} \\ & + gV_A(r){\rm tr}\left\{ O^\dagger \mathbf{r}\cdot\mathbf{E}S + S^\dagger \mathbf{r}\cdot\mathbf{E}O \right\} \\ & + g\frac{V_B(r)}{2}{\rm tr}\left\{ O^\dagger \mathbf{r}\cdot\mathbf{E}O + O^\dagger O\mathbf{r}\cdot\mathbf{E} \right\} \\ & - \frac{1}{4}G^a_{\mu\nu}G^{\mu\nu a},\end{aligned} \tag{42}$$

where $\mathbf{P}$ is the momentum canonically conjugate to the c.m. coordinate; $\mathbf{p}$ is the heavy-quark momentum in the c.m. frame; $\mathbf{E}$ is the external chromoelectric field of ultrasoft gluons, its strength tensor being $G^a_{\mu\nu}$; and $V_{s,o,A,B}$ are Wilson coefficients, which have the meaning of potentials in different orders in the inverse heavy-quark mass m. Equation (42) does not include power-law corrections in $1/m$ to V_A and V_B and to purely gluon operators or higher terms of the multipole expansion. In the leading order, the singlet and the octet operator (S and O, respectively) are represented as the relevant bilinear products of the nonrelativistic heavy-quark and heavy-antiquark spinors. The matching of the operators S and O with the NRQCD spinors was performed in [28] up to the three-loop level both for the potential and for the normalization factors in the operator-product expansion of the corresponding Wilson loop. In this Lagrangian,

---

[12] As a matter of fact, one elaborates here, in a formal way, on the approach proposed long ago by Voloshin and Leutwyler [29] for Coulomb-like systems whose interaction Hamiltonian involves a perturbation that is expressed in terms of slowly varying external fields and corrections leading to the Coulomb term.

the singlet potential $V_s(r)$ and the octet potential $V_o(r)$ are the Wilson coefficients of the bilinear forms in S and O, respectively, in the leading order in $1/m$. In [28], it is shown that this definition of the potential of static quarks is consistent with the definition in terms of the Wilson loop (1).

Cancellation of the renormalon arbitrariness in the sum of the perturbative pole masses of heavy quarks and the potential up to two loops is yet another important result within pNRQCD.

It should be emphasized that, for the running coupling constant in coordinate space, the three-loop matching of the V and $\overline{MS}$ schemes within pNRQCD leads, in the leading-logarithm approximation, to the result

$$\alpha_V(1/r^2,\mu) = \alpha_s^{\overline{MS}}(1/r^2) \tag{43}$$

$$\times \left\{ 1 + (a_1 + 2\gamma_E\beta_0)\,\frac{\alpha_s^{\overline{MS}}(1/r^2)}{4\pi} \right.$$

$$+ \left[\gamma_{\mathrm{E}}\,(4a_1\beta_0 + 2\beta_1) + \left(\frac{\pi^2}{3} + 4\gamma_{\mathrm{E}}^2 \right) \beta_0^2 + a_2 \right]$$

$$\left. \times \frac{\left(\alpha_s^{\overline{MS}}(1/r^2) \right)^2}{16\,\pi^2} + \frac{C_A^3}{12}\,\frac{\left(\alpha_s^{\overline{MS}}(1/r^2) \right)^3}{\pi}\,\ln(r\mu) \right\},$$

which, as can be seen, reduces to (12) in the two-loop approximation. However, the three-loop contribution generates an explicit scale dependence of perturbative calculations in pNRQCD. This dependence was discussed in [28] for two cases where the confinement scale Λ_{QCD} and the binding energy mv^2 are ordered in such a way that either (a) $\Lambda_{\mathrm{QCD}} \gg mv^2$ or (b) $mv^2 \gg \Lambda_{\mathrm{QCD}}$. If case (a) is realized, then nonperturbative effects are significant in the singlet potential of static quarks; therefore, it can be calculated only upon introducing model-dependent terms caused by ultrasoft gluons that form the gluon sea in heavy quarkonia. The excitations of this sea, which are referred to as gluelumps, have a characteristic excitation energy appearing to be the nonperturbative scale μ on which the potential depends.[13] In case (b), the potential is a purely perturbative quantity. It should be noted, however, that, in calculating observable physical quantities, such as the masses of bound states, it is necessary to take into account the contributions from ultrasoft perturbative gluons whose virtualities are less than μ; this must lead to a μ-dependent shift of energy, but this shift is of course bound to be canceled by the contribution originating from the μ-dependent term in the potential with the effective coupling constant (43) and possibly appearing in the heavy-quark masses. In either case, calculations within perturbative NRQCD for the singlet operator[14] explicitly indicate that it is necessary to take into account gluon degrees of freedom in heavy quarkonia. It was emphasized in [28] that, obviously, this feature is peculiar precisely to a non-Abelian theory [see the factor C_A in front of the logarithmic term in (43)].

In our opinion, this dependence on ultrasoft gluon fields in the heavy-quarkonium potential reflects, in a natural way, the fact of formation of a gluon string between heavy quarks at long distances. Without considering the ordering of the confinement scales and the quark binding energy, the introduction of such a string must eliminate the explicit dependence of the total potential on an extra unphysical scale that is associated with a computational method. In the present article, this was done above by introducing a unified beta function for the coupling constant within the V scheme. This solution to the problem is qualitatively consistent with pNRQCD, because, in the perturbative regime, the contribution of the logarithmic term is negligible, as can be seen for the confining linear term in the potential at short distances, and because, at long distances, the nonperturbative contribution confining quarks is significant, the string tension being a natural physical scale of such an interaction. In the static QCD potential derived above, we have not considered the possible nontrivial excitations corresponding to a polygonal shape of the string, where a cusp moves along the string at a speed equal to the speed of light. Such excitations could be associated with hybrid states featuring gluelumps. Thus, we can see that the QCD potential for static quarks that was proposed in the present study does not come into conflict with the current status of pNRQCD.

A particular comment on the linear term in the potential is in order here. In [28], Brambilla *et al.* employed a specific model of infrared behavior, whereby they obtained, at long distances between heavy quarks, an ultrasoft correction in a form involving a constant shift δV_0 of energy and a quadratic term $\sigma_2 r^2$. On this basis, those authors concluded that a linear term could nevertheless appear in a more involved model of infrared behavior. In the preceding section, we have demonstrated how one can obtain a similar linear regime of confinement.

Some recent studies (see [32, 33]) were devoted to calculating the lowest bound state of a heavy quarkonium by a method that combines the potential approach in pNRQCD with nonperturbative corrections

---

[13] The possible nonpotential interaction terms are discussed in [28].

[14] Here, we do not dwell upon the octet potential of static quarks, although some qualitative conclusions could be directly extended from the singlet to the octet state.

to the binding energy that arise upon performing a multipole expansion in QCD [29] [this expansion is explicitly presented in (42)]. For example, the perturbative B_c-meson mass was calculated in [32] on the basis of a perturbative expansion for the static potential, the leading approximation being taken there in the form of Coulomb wave functions. As we have already seen, the perturbative potential is plagued by renormalon indefiniteness. In order to eliminate this dependence on the choice of scale μ in the potential, Brambilla and Vairo [32] calculated the masses of J/ψ and Υ within the same approach at the same point μ and inverted the problem of calculating the heavy-quark masses by equating the computed perturbative masses of the charmonium and bottomonium ground states to the known experimental values. This procedure leads to μ-dependent pole heavy-quark masses that are represented in the form of series in $\alpha_s(\mu)$. It is assumed that this procedure can ensure cancellation of the renormalon in the hadron mass to a precision of 50 MeV. As a result, the perturbative mass of the B_c meson takes the value

$$M_{B_c}^{\rm pert} = 6326^{+29}_{-9}\ \ {\rm MeV}, \qquad (44)$$

which is rather stable against variations of μ over the region $1.2 < \mu < 2.0$ GeV. It is natural to compare this result with the value in Table 1 and with the μ region described above in studying the matching of the perturbative potential with the total QCD potential. Brambilla and Vairo [32] did not present the μ-dependent heavy-quark masses. In view of nearly perfect agreement between the estimates of the B_c mass in (44) and in Table 1, we can nevertheless expect that such a dependence is close in shape to the computed shift $\delta V(\mu)$.

In [33], the same perturbative method allowing both for corrections from the gluon condensate in the multipole expansion of QCD and for an additional small contribution of the $\alpha_s^5 \log \alpha_s$ type was used to calculate the heavy-quark masses on the basis of a comparison of the resulting theoretical expressions with experimental data on the masses of the charmonium and bottomonium ground states. This procedure yielded the pole masses, which in fact depend on the normalization scale since use was made of the substitution $\mu = C_F \alpha_s m_Q$ in the potential. Obviously, this led to a mass that is plagued by a renormalon indefiniteness, and the result was

$$m_b = 5022 \pm 58\ \ {\rm MeV},$$

which is much greater than our estimate. The reason behind this discrepancy is quite clear. This is the shift $\delta V(\mu)$ of energy. The running mass in the $\overline{MS}$ scheme from [33] is in excess of our estimate by approximately 260 MeV in the same order in α_s for the relation between the running and the pole mass. The distinction becomes minor upon employing the three-loop relation for the masses, as was done in [33]. However, the same correction reduces our estimate in spectroscopic calculations based on the total static potential within QCD. In our opinion, all the aforesaid casts some doubt on the values obtained in [33] for the heavy-quark masses.

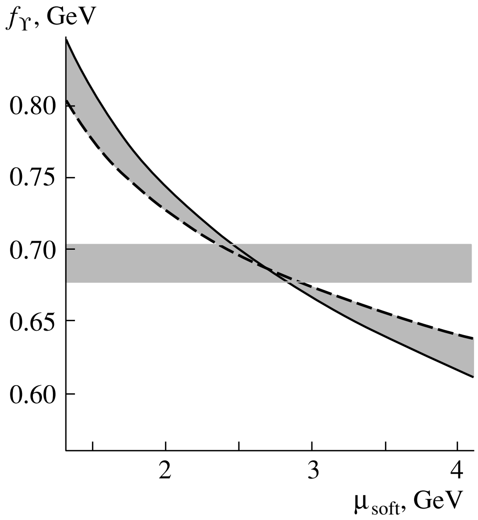

Fig. 7. Leptonic coupling constant for the bottomonium vector ground state as a function of the soft normalization scale. The dashed and the solid curve correspond to $\mu_{\rm hard} = 2m_b$ and $\mu_{\rm hard} = m_b$, respectively. The horizontal band is bounded by the experimental limits on the leptonic constant.

The dependence of the static potential on finite heavy-quark masses was considered in [34]. This dependence arises from a smooth variation in the number of active flavors in the expressions for the coefficients in the perturbative beta function and in the conditions of matching for α_V. As was described above, we make use of a stepwise change in the number of active flavors. In view of this, our analysis suffers from an implicit model dependence, which can hardly be removed from the problem under consideration.

As to QCD lattice calculations for problems featuring a potential, they are surveyed in [35]. Here, we would like to emphasize that the potential of static quarks on a lattice is very close in shape to the potential in the Cornell model. However, the analysis in [35] ignores the possible additive shift of the energy of the perturbative potential with respect to the total QCD potential. This led to the conclusion that the total potential on a lattice differs significantly from the perturbative potential in the region where lattice calculations are applicable, which is bounded by the lattice dimensions (asymptotically short distances are beyond reach of such calculations). An up-to-date review of phenomenological potential models is given

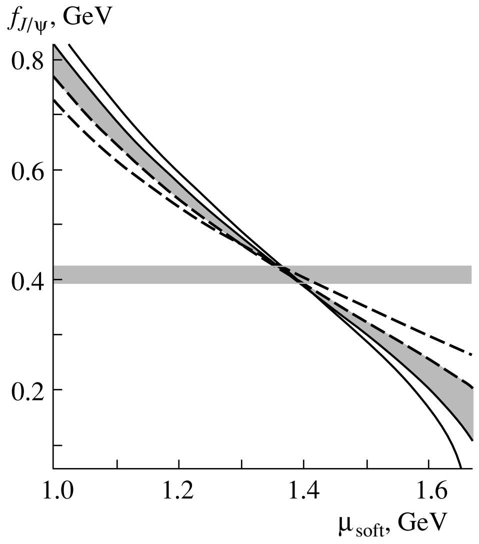

Fig. 8. Leptonic coupling constant for the vector ground state of the charmonium as a function of the soft normalization scale. The shaded region bounded by curves corresponds to changing the hard scale from (dashed curve) $\mu_{\rm hard} = 1.07m_c$ to (solid curve) $\mu_{\rm hard} = 0.93m_c$. The horizontal band corresponds to the experimental limits on the constant. Also presented are the results for (dashed curve) $\mu_{\rm hard} = 1.26m_c$ and (solid curve) $\mu_{\rm hard} = 0.87m_c$.

in the lectures of Brambilla and Vairo [36]. Effects associated with finite values of the quark masses in nonrelativistic bound states are considered in [37]. Some applications of pNRQCD to heavy quarkonia are described in [38].

3.3. Leptonic Constants

For heavy nonrelativistic quarks, the leptonic coupling constant of a heavy quarkonium can be expressed in terms of the wave function at the origin as

$$f_{\rm NR} = \sqrt{\frac{12}{M}}\,|\Psi(0)|,$$

where M is the bound-state mass and where the leading approximation to the wave function is found in solving the Schrödinger equation with the static potential.

In the approximation of NRQCD for heavy quarks, the calculation of leptonic coupling constants for heavy quarkonia at the two-loop levels requires the matching of the quark currents in NRQCD with the currents in full QCD,

$$J_\nu^{\rm QCD} = \bar{Q}\gamma_\nu Q, \quad \mathcal{J}_\nu^{\rm NRQCD} = \chi^\dagger \sigma_\nu^\perp \phi.$$

Here, we have introduced the following notation: Q stands for relativistic quark fields; χ and ϕ are the nonrelativistic quark and antiquark spinors; and $\sigma_\nu^\perp = \sigma_\nu - v_\nu(\sigma\cdot v)$, where v is the heavy-quarkonium 4-velocity. We have

$$J_\nu^{\rm QCD} = \mathcal{K}(\mu_{\rm hard};\mu_{\rm fact})\cdot \mathcal{J}_\nu^{\rm NRQCD},$$

where $\mu_{\rm hard}$ specifies the normalization point for the matching of NRQCD with full QCD, while $\mu_{\rm fact}$ is the normalization point for perturbative calculations within NRQCD. On the basis of matching the potential for static quarks in QCD with the two-loop perturbative potential, we assume that the most appropriate choice of scale in describing bottomonium and charmonium is

$$\mu_{\rm fact} = \mu_{\rm soft} = 1.3{-}2\ \text{GeV}. \qquad (45)$$

For heavy quarkonia formed by quarks of the same flavor, the two-loop expression for the Wilson coefficient $\mathcal{K}$ is known to be [24, 39, 40]

$$\mathcal{K}(\mu_{\rm hard};\mu_{\rm fact}) = 1 - \frac{8}{3}\frac{\alpha_s^{\overline{MS}}(\mu_{\rm hard})}{\pi} \qquad (46)$$
$$+ \left(\frac{\alpha_s^{\overline{MS}}(\mu_{hard})}{\pi}\right)^2 c_2(\mu_{\rm hard};\mu_{\rm fact}).$$

The explicit expression for c_2 can be found in [39, 40]. Here, an additional problem is presented by the convergence of (46) at a preset choice of scales. Setting $\mu_{\rm hard} = (1-2)m_b$ and employing (45), we find that the convergence of QCD corrections for bottomonium is good and estimate its leptonic coupling constant defined as

$$\langle 0|J_\nu^{\rm QCD}|\Upsilon,\lambda\rangle = \epsilon_\nu^\lambda f_\Upsilon M_\Upsilon,$$

where λ is the polarization of the vector state ϵ_ν. As a result, we obtain

$$f_\Upsilon = 685 \pm 30\ \text{MeV},$$

while the experimental value is $f_\Upsilon^{\rm expt} = 690 \pm 13$ MeV [9].

As can be seen from Fig. 7, a variation of the hard scale over a wide region leads to the presence of a stable point at which the result is weakly sensitive to such a variation. Stability is observed at $\mu_{\rm soft} \approx 2.6$ GeV, in which case the perturbative potential is rather close to the potential of static quarks in QCD at distances characteristic of the dimensions of the $1S$ level in the $\bar{b}b$ system.

Results obtained by applying the above procedure to estimate the leptonic coupling constant for the charmonium J/ψ are more sensitive to the choice of factorization scale. Indeed, the dimension of this system is $\langle r_{\bar{c}c(1S)}\rangle \approx 0.42$ fm, which imposes more stringent constraints on $\mu_{\rm fact} \approx 1.3{-}1.5$ GeV, since, at larger scale values, the perturbative potential deviates noticeably from the QCD potential of static quarks in the region of the $\bar{c}c$ state, while, at smaller

Table 2. Ratios of the leptonic coupling constants of heavy quarkonia according to the predictions of our present study, along with experimental data

nS	$f^2_{\psi(nS)}/f^2_{\psi}$		$f^2_{\Upsilon(nS)}/f^2_{\Upsilon}$	
	QCD	experiment	QCD	experiment
$2S$	0.55	0.48 ± 0.07	0.47	0.47 ± 0.03
$3S$	0.32	0.25 ± 0.06	0.34	0.36 ± 0.02

values of the soft normalization scale, the perturbative potential calculated at the two-loop level may have a functional form totally different from that of the QCD potential even within a limited range of interquark distances. Yet another problem is that which is associated with the energy shift $\delta V(\mu) = 1.0$–1.2 GeV, which renormalizes significantly the pole mass of the charmed quark: $m_c^{\rm pole} = 1.968$–2.068 GeV. This shift does not introduce a perturbation in the bound-state mass, but it is of importance for the wave-function value at the origin. If, for example, following the fairly accurate scaling relationship for the leptonic coupling constants from [41], we introduce, in the equation for the leptonic coupling constant of the bound state of nonrelativistic quarks, the quantity $P(\mu) = \kappa\Psi(0)\, m_c^{\rm pole}(\mu)/m_c$[15] instead of the wave function $\Psi(0)$, then the result obtained numerically will be

$$f_{J/\psi} = 400 \pm 35 \;\; \text{MeV},$$

which can be compared with the experimental value of $f^{\rm exp}_{J/\psi} = 409 \pm 15$ MeV.

From Fig. 8, we can see that the point of stability with respect to variations in $\mu_{\rm hard}$ occurs at soft-factorization-scale values ($\mu_{\rm soft} \approx 1.35$ GeV) that could be expected on the basis of the estimate of the mean charmonium radius, so that $\mu_{\rm soft} \sim 1/\langle r_{\bar{c}c(1S)}\rangle$. However, stability occurs in a narrow range of $\mu_{\rm hard}$ near the charmed-quark mass.

At present, the conditions of matching of the quark currents for a heavy quarkonium formed by quarks of different flavors, $\bar{b}c$, are known only at the one-loop level [41, 42]. By way of example, we indicate that the result for the pseudoscalar state has the form

$$\mathcal{K}(\mu_{\rm hard};\mu_{\rm fact}) \qquad (47)$$
$$= 1 - \frac{\alpha_s^{\overline{MS}}(\mu_{\rm hard})}{\pi}\left(2 - \frac{m_b - m_c}{m_b + m_c}\ln\frac{m_b}{m_c}\right),$$

which is independent of the factorization scale. The one-loop matching of the perturbative potential with the QCD potential of static quarks at $r \sim 0.3$–0.4 fm, which is a typical interquark distance for the B_c-meson ground state [43], leads to results that can be considered as a mere illustration, because deviations in the form of potentials are quite sizable. Moreover, it is mandatory to set $\mu_{\rm fact} = \mu_{\rm hard}$, since these scales are indistinguishable as long as a nonzero anomalous dimension is disregarded at the two-loop level. Nonetheless, we set $\mu_{\rm hard} = 1.3$–1.8 GeV and neglect the shift δV, which is so small at the one-loop level that the inclusion of it would lead to going beyond the level of precision adopted here. Indeed, one can see from Fig. 6 that the value of the shift along the energy scale in the one-loop approximation is small at high virtualities of about 2 GeV, so that it can be disregarded; at the same time, the form of the perturbative potential at low virtualities approaches the form of the QCD potential only for distances in the narrow range $r = 0.1$–0.25 fm; therefore, the results that are based on the matching the perturbative and the total potential at the one-loop level are unreliable in evaluating the heavy-quark masses on the basis of the parameters of the bound state that were calculated with the perturbative potential. Eventually, our estimate of the B_c leptonic constant is

$$f_{B_c} = 400 \pm 45 \;\; \text{MeV},$$

which can be compared with the sum-rule estimate $f^{\rm SR}_{B_c} = 400 \pm 25$ MeV [41, 44].

Finally, Table 2 displays the ratios of the leptonic coupling constants for excited nS-wave levels of the $\bar{b}b$ and $\bar{c}c$ levels, along with experimental data. We can see that the predictions are in good agreement with the measured values. For the sake of completeness, we made an attempt at estimating the leptonic coupling constant for the $2S$-wave level in the $\bar{b}c$ system. The result is

$$f_{B_c(2S)} = 280 \pm 50 \;\; \text{MeV},$$

which agrees with the scaling relationship from [41].

Thus, we have analyzed the estimates that follow from the method of QCD potential of static quarks for the masses of heavy quarks and heavy quarkonia, as well as for the leptonic coupling constants, and

---

[15] By solving the Schrödinger equation with shifted masses and a shifted potential, we have verified that this mass dependence of the wave functions is valid to a precision better than 6%, so that we set $\kappa = 0.95$.

have found that these estimates are in good agreement both with experimental data and with the results obtained previously on the basis of QCD sum rules.

4. CONCLUSION

We have derived the QCD potential for static heavy quarks from the known boundary regimes at short and long distances—that is, asymptotic freedom at the three-loop level and confinement. The potential is determined by the following quantities: the perturbative beta function; the coefficients determined by matching the $\overline{MS}$ scheme with the V scheme; the normalization of the QCD running coupling constant at $\mu^2 = m_Z^2$; and the slope of Regge trajectories, which controls the linear term in the potential. As a result, we have modified the Buchmüuller–Tye method in accordance with the modern status of perturbative calculations.

In the static limit, a two-loop treatment of the Coulomb potential leads to significant corrections to the beta function for the effective charge, $\Delta\beta/\beta \sim 10\%$, as can be seen from Fig. 3. Such a correction is of importance for determining the critical charge value—that is, a value that specifies a transition region between the regime of perturbation theory and the nonperturbative limit. Moreover, the two-loop matching condition and three-loop evolution of the running coupling constant normalized according to high-energy data on m_Z determine the energy-scale region, where the changeover of these regimes occurs. This scale is strongly correlated with data on the mass spectra of heavy quarkonia. Indeed, it is related to the splitting between the $1S$ and $2S$ levels. It should be emphasized that a consistent two-loop consideration leads to precisely that value of the effective Coulomb constant which was obtained by fitting the potential within the Cornell model. In relation to the one-loop analysis of Buchmüller and Tye, who determined a $\Lambda_{\rm QCD}$ value that is at odds with the modern normalization of the coupling constant at high energies, this is an achievement of the present study. As a result, the two-loop modification introduced here results in a correct normalization of the effective Coulomb charge at interquark distances characteristic of the mean dimensions of heavy quarkonia and determines the evolution at short distances of $r < 0.08$ fm (see Fig. 2). The latter is of importance in calculating the relevant leptonic coupling constants, which are related to the wave functions at the origin.

Other corrections to the potential of heavy quarks are associated with effects due to finite quark masses, whence it follows that they cannot be interpreted within the static approximation. For example, spin-dependent forces, relativistic corrections, and specific non-Abelian terms of the potential[16) in heavy quarkonia must generally be taken into account in analyzing relevant mass spectra. The order of magnitude of the leading nonstatic corrections can be estimated by associating them with the characteristic shift of levels due to, say, the hyperfine splitting of the S-wave levels in heavy quarkonia.[17) In this way, we find that the uncertainty in the analysis of the heavy-quark masses can be conservatively estimated at $\delta m \simeq 80$ MeV.

Thus, the non-Abelian term in the potential α_s^2/r^2 involves a coefficient of the form $1/m_Q$; therefore, it vanishes in the static limit $m_Q \to \infty$. The uncertainty in the heavy-quark masses that arises because of the disregard of such contributions has been assessed above. If we formally consider perturbation theory in order to compute the bound-state levels in a heavy quarkonium with Coulomb functions taken for a leading approximation—recall that this is beyond the scope of our approach—the aforementioned non-Abelian potential makes a contribution of the same order in α_s, α_s^4, as the two-loop corrections to the matching of the perturbative static potential, since the averaging of $1/r^2$ leads to a coefficient of the form $\alpha_s^2 m_Q^2$. However, two-loop effects are of importance for a consistent analysis of the static potential itself and its normalization at high energies—that is, even in the static limit, these correction play a significant role in the evolution of the running effective charge in the potential from high energies to the scale typical of heavy-quark bound states; at the same time, nonstatic contributions can everywhere be disregarded in a numerical analysis. One can see that our consideration is quite consistent in the static approximation, and it is the approximation that we wanted to study in this article.

The two-loop perturbative potential has been matched here with the QCD potential of heavy quarks in order to compute the heavy-quark masses and to compare the values obtained within this approach with the results based on QCD sum rules. It has been found that the agreement between these two approaches is good.

In recent years, the heavy-quark masses were determined in [23–25] by using QCD sum rules, which implement a consistent approach having a sound

---

[16) They have the α_s^2/r^2 form and involve a factor of the inverse-quark-mass type.

[17) This splitting is about 100 MeV or even less.

theoretical basis. They rely on separating the contributions of interactions at short distances from nonperturbative effects by appropriately choosing values of the parameters that determine the scheme of sum-rule calculations. In this approach, the nonperturbative contributions are specified in the form of quark–gluon condensates with relevant Wilson coefficients of a factorized form, which are calculable perturbatively since they depend on high virtualities at short distances. However, it would be incorrect to believe that these explicit contributions, which are suppressed in some region of the scheme parameters, are the only terms that are caused by nonperturbative infrared dynamics within QCD. By disregarding the condensate contributions, we can indeed find that correlation functions in perturbative QCD suffer from the renormalon arbitrariness, which means that the perturbation-theory expansion in a series in α_s is asymptotic and that the sum of this series depends on the method of summation. The physical reason behind this divergence and this arbitrariness is that there is an infrared singularity in the perturbative QCD coupling constant. As a matter of fact, such a singularity may possibly be regularized in an implicit form because of nonperturbative dynamics associated with quark–gluon condensates.[18] As a result, the perturbative pole mass in QCD sum rules is not a well-defined quantity; in view of this, some more appropriate quantities were introduced in the analysis by the authors of [23–25]. They were constructed from the pole mass with the aid of specific infrared subtractions, which are interpreted independently of quark–gluon condensates. This constructions depend on the subtraction methods proposed by their authors, who present various physical arguments, more or less rigorous and justified. Such infrared subtractions imply the introduction of nonperturbative regulators in the consideration. In the present study, we have considered a unified beta function for the effective charge in the potential, and the definition of this function presumes infrared stability. Thus, we can see that an analysis of the heavy-quark masses, both within sum rules and within the potential approach, invokes effects caused by infrared QCD dynamics; although the constructive procedures used have different explicit forms, they have the same physical meaning and the same irremovable methodological uncertainties.

The calculated mass spectra of heavy quarkonia and the leptonic coupling constants of the nS-wave levels are in good agreement with the measured values. The features of the B_c mesons have been predicted.

ACKNOWLEDGMENTS

We are grateful to A.K. Likhoded and A.L. Kataev for stimulating discussions and to A.A. Pivovarov for enlightening comments on the results that QCD sum rules produce for the b-quark mass. We are also indebted to Antonio Vairo for important comments, indications of references that were useful in discussing our results, and explanations concerning methods used within pNRQCD, as well as for discussions.

This work was supported in part by the Russian Foundation for Basic Research (project nos. 01-02-99315, 01-02-16585, and 00-15-96645).

REFERENCES

1. E. Eichten *et al.*, Phys. Rev. D **17**, 3090 (1978); **21**, 203 (1980).
2. C. Quigg and J. L. Rosner, Phys. Lett. B **71B**, 153 (1977).
3. A. Martin, Phys. Lett. B **93B**, 338 (1980).
4. C. Quigg and J. L. Rosner, Phys. Rep. **56**, 167 (1979).
5. J. L. Richardson, Phys. Lett. B **82B**, 272 (1979).
6. W. Buchmüller and S.-H. H. Tye, Phys. Rev. D **24**, 132 (1981).
7. M. Peter, Nucl. Phys. B **501**, 471 (1997); Phys. Rev. Lett. **78**, 602 (1997).
8. Y. Schröder, Phys. Lett. B **447**, 321 (1999).
9. C. Caso *et al.*, Eur. Phys. J. C **3**, 1 (1998).
10. L. Susskind, *Coarse-Grained QCD in Weak and Electromagnetic Interactions at High Energy,* Ed. by R. Balian and C. H. Llewellyn Smith (North-Holland, Amsterdam, 1977); W. Fischler, Nucl. Phys. B **129**, 157 (1977); T. Appelquist, M. Dine, and I. J. Muzinich, Phys. Lett. B **69B**, 231 (1977); Phys. Rev. D **17**, 2074 (1978); A. Billoire, Phys. Lett. B **92B**, 343 (1980); E. Eichten and F. L. Feinberg, Phys. Rev. Lett. **43**, 1205 (1979); Phys. Rev. D **23**, 2724 (1981).
11. O. V. Tarasov, A. A. Vladimirov, and A. Yu. Zharkov, Phys. Lett. B **93B**, 429 (1980); S. A. Larin and J. A. M. Vermaseren, Phys. Lett. B **303**, 334 (1993).
12. Yu. A. Simonov, Phys. Rep. **320**, 265 (1999); Yu. A. Simonov, Usp. Fiz. Nauk **166**, 337 (1996) [Phys. Usp. **39**, 313 (1996)]; Yu. A. Simonov, S. Titard, and F. J. Yndurain, Phys. Lett. B **354**, 435 (1995).
13. C. Bernard *et al.*, Phys. Rev. D **62**, 034503 (2000).
14. M. A. Shifman, A. I. Vainshtein, and V. I. Zakharov, Nucl. Phys. B **147**, 385 (1979); L. J. Reinders, H. R. Rubinstein, and S. Yazaki, Phys. Rep. **127**, 1 (1985); V. A. Novikov *et al.*, Phys. Rep. C **41**, 1 (1978).
15. http://www.ihep.su/~kiselev/Potential.nb
16. CDF Collab. (F. Abe *et al.*), Phys. Rev. Lett. **81**, 2432 (1998); Phys. Rev. D **58**, 112004 (1998).
17. E. Eichten and C. Quigg, Phys. Rev. D **49**, 5845 (1994); S. S. Gershtein *et al.*, Phys. Rev. D **51**, 3613 (1995).

---

[18] By way of example, we indicate that the perturbative heavy-quark mass shell becomes physically meaningless in the presence of nonperturbative condensates.

18. G. T. Bodwin, E. Braaten, and G. P. Lepage, Phys. Rev. D **51**, 1125 (1995); T. Mannel and G. A. Schuller, Z. Phys. C **67**, 159 (1995).
19. M. Beneke, Phys. Rep. **317**, 1 (1999).
20. K. Melnikov and T. van Ritbergen, hep-ph/9912391.
21. N. Gray, D. J. Broadhurst, W. Grafe, and K. Schilcher, Z. Phys. C **48**, 673 (1990); D. J. Broadhurst, N. Gray, and K. Schilcher, Z. Phys. C **52**, 111 (1991).
22. A. A. Penin and A. A. Pivovarov, Nucl. Phys. B **549**, 217 (1999).
23. M. Beneke, hep-ph/9911490; M. Beneke and A. Signer, Phys. Lett. B **471**, 233 (1999).
24. K. Melnikov and A. Yelkhovsky, Phys. Rev. D **59**, 114009 (1999).
25. A. H. Hoang, Phys. Rev. D **61**, 034005 (2000).
26. C. A. Dominguez, G. R. Gluckman, and N. Paver, Phys. Lett. B **333**, 184 (1994); S. Narison, Phys. Lett. B **341**, 73 (1994); Nucl. Phys. B (Proc. Suppl.) **74**, 304 (1999).
27. J. Fleischer, F. Jegerlehner, O. V. Tarasov, and O. L. Veretin, Nucl. Phys. B **539**, 671 (1999).
28. N. Brambilla, A. Pineda, J. Soto, and A. Vairo, Nucl. Phys. B **566**, 275 (2000); Phys. Rev. D **60**, 091502 (1999).
29. M. B. Voloshin, Nucl. Phys. B **154**, 365 (1979); H. Leutwyler, Phys. Lett. B **98B**, 447 (1981).
30. A. V. Manohar and I. W. Stewart, Preprint UCSD/PTH 00-04 (2000); hep-ph/0003032.
31. M. E. Luke, A. V. Manohar, and I. Z. Rothstein, hep-ph/9910209.
32. N. Brambilla and A. Vairo, Preprint CERN-TH/2000-036 (2000); hep-ph/0002075.
33. F. J. Yndurain, Preprint FTUAM-00-07 (2000); hep-ph/0002237; S. Titard and F. J. Yndurain, Phys. Rev. D **49**, 6007 (1994); **51**, 6348 (1995); A. Pineda and F. J. Yndurain, Phys. Rev. D **58**, 094022 (1998); **61**, 077505 (2000).
34. M. Melles, hep-ph/0001295.
35. G. S. Bali, hep-ph/0001312.
36. N. Brambilla and A. Vairo, *Lectures given at HUGS at CEBAF, 13th Annual Hampton University Graduate Studies at the Continuous Electron Beam Facility, 1998;* hep-ph/9904330.
37. D. Eiras and J. Soto, hep-ph/0005066.
38. B. A. Kniehl and A. A. Penin, Nucl. Phys. B **563**, 200 (1999); N. Brambilla, A. Pineda, J. Soto, and A. Vairo, Phys. Lett. B **470**, 215 (1999).
39. M. Beneke, A. Signer, and V. A. Smirnov, Phys. Rev. Lett. **80**, 2535 (1998).
40. A. Czarnecki and K. Melnikov, Phys. Rev. Lett. **80**, 2531 (1998).
41. V. V. Kiselev, Int. J. Mod. Phys. A **11**, 3689 (1996); Nucl. Phys. B **406**, 340 (1993).
42. E. Braaten and S. Fleming, Phys. Rev. D **52**, 181 (1995).
43. S. S. Gershtein *et al.*, Preprint IHEP 98-22 (Protvino, 1998); hep-ph/9803433; Usp. Fiz. Nauk **165**, 3 (1995) [Phys. Usp. **38**, 1 (1995)].
44. S. Narison, Phys. Lett. B **210**, 238 (1988); V. V. Kiselev and A. V. Tkabladze, Yad. Fiz. **50**, 1714 (1989) [Sov. J. Nucl. Phys. **50** 1063 (1989)]; T. M. Aliev and O. Yilmaz, Nuovo Cimento A **105**, 827 (1992); S. Reinshagen and R. Rückl, Preprints CERN-TH. 6879/93, MPI-Ph/93-88 (1993); M. Chabab, Phys. Lett. B **325**, 205 (1994).

Translated by A. Isaakyan

Physics of Atomic Nuclei, Vol. 65, No. 9, 2002, pp. 1711–1721. Translated from Yadernaya Fizika, Vol. 65, No. 9, 2002, pp. 1755–1765.

ELEMENTARY PARTICLES AND FIELDS
Theory

Phenomenological Analysis of the Experimental Data on the Photoproduction of η Mesons off Nucleons

E. V. Balandina, E. M. Leĭkin, and N. P. Yudin*

Institute of Nuclear Physics, Moscow State University, Vorob'evy gory, Moscow, 119899 Russia

Received July 5, 2001

Abstract—The initial stage of a phenomenological analysis of experimental data on the η meson photoproduction off nucleons in the energy range from the threshold to 1.1 GeV is carried out based on a linear nonparametric model. The goal of this stage of the analysis is to obtain statistically reliable information about the partial waves that form the main characteristics of the process. The analysis uses the data of three laboratories about the angular distributions of η-mesons and their Σ and T asymmetries. The results of the analysis of the angular distributions demonstrate the presence of contradictions in the data obtained by different laboratories. The results of the analysis of the energy dependences of the polarization observables Σ and T show that the process regime probably changes in the vicinity of 0.9 GeV, which may be caused by the transition from the region of the $S_{11}(1535)$ and $D_{13}(1520)$ resonances to the region of the $D_{15}(1675)$ and $F_{15}(1630)$ resonances. *© 2002 MAIK "Nauka/Interperiodica".*

1. INTRODUCTION

Investigation of the meson photoproduction processes off nucleons makes it possible to extract important information about the electromagnetic and strong decay properties of nucleon resonances from the characteristics of these processes. An increase in the interaction energy is accompanied by strong overlap of the resonances related to their large hadronic widths, which hinders reliable estimation of the resonance parameters. A unique possibility of avoiding these difficulties is offered by the study of the η-meson photoproduction process. This is related to the existence of a small number of resonances that decay into the $p\eta$ channel. We can believe that three resonances—$P_{11}(1440)$, $D_{13}(1520)$, and $S_{11}(1535)$—will play the dominating role immediately above the threshold of the $\gamma p \to \eta p$ reaction ($E_\gamma =$ 706.92 MeV). The available data [1] indicate the possibility of determining, first of all, the characteristics of the $S_{11}(1535)$ and $D_{13}(1520)$ resonances.

The main goal of the analysis is to extract estimates of the photoproduction amplitudes, usually the multipole amplitudes, from the experimentally measured characteristics. This is justified by the fact that these amplitudes are directly related to the production of a nucleon resonance with certain quantum numbers corresponding to the given partial wave.

It is well known that the experimentally measured characteristics, namely, the differential cross sections $d\sigma/d\Omega$ of the process and the polarization properties (asymmetry Σ for the linearly polarized beam of gamma radiation, asymmetry T for the polarized proton target, polarization P of the recoil nucleons), are bilinear forms of the complex amplitudes of the photoproduction process. Therefore, the analysis is naturally separated into two stages. The first stage is a linear regression problem. Solution of the problem gives information about the partial waves that contribute to the process. The problem is solved through expanding the observables into series, in this case, over the orthogonal Legendre polynomials, by the standard procedures [2] in order to determine the statistically significant terms of the expansion. In contrast to the expansion in power series with respect to $\cos\theta$, where θ is the meson emission angle in the center-of-mass frame (c.m.f.), the expansion with respect to the Legendre polynomials is related to their orthogonality. When the results of measurements for a sufficiently large number of emission angles are available, this property simplifies determination of the number of terms in the series providing the best description of data. The orthogonal polynomials give lower nondiagonal elements in the error matrix, which is important for interpretation of the diagonal elements as the errors of the regression coefficients. Thus, the first stage of the analysis determines the set of the linear regression coefficients that ensures the best (with respect to statistics) description of the experimental data. The data, obtained by various laboratories and used in the analysis, should be compatible—this fac-

---

*e-mail: `yudin@helene.npi.msu.su`

tor is important for obtaining reliable estimates of the photoproduction amplitudes.[1]

The second stage consists in solving a system of nonlinear (quadratic) equations with respect to real and imaginary parts of the multipole amplitudes. The number and the type of equations are determined by the results of the first stage. The right-hand sides of the equations with respect to the amplitudes represent the obtained estimates of the regression coefficients. Determination of the multipole amplitudes usually requires removing continuous and discrete ambiguities of the solutions caused by the individual specific features of the system of nonlinear equations, which, generally, make the system inconsistent.

2. THE ANALYSIS PROCEDURE

At the first stage of the phenomenological analysis of the experimental data, we used a nonparametric linear model where the observables are represented in terms of the expansion into series with respect to the Legendre polynomials $P_l(\cos\theta)$. For the differential cross section $d\sigma(\theta)/d\Omega$, the expansion assumes the form

$$\frac{k}{q}\frac{d\sigma(\theta)}{d\Omega} = \sum a_l P_l(\cos\theta), \qquad (1)$$

where k and q are the momenta (in the c.m.f.) of the γ quantum and η meson, respectively. The regression coefficients a_l are bilinear forms with respect to the real and imaginary parts of $E_{l\pm}$ and $M_{l\pm}$, which are, respectively, the electric and magnetic transition amplitudes to the final states with the total momenta $l \pm 1/2$. The amplitudes depend on the γ quantum energy E_γ. The nonparametric model provides, generally, unbiased estimates of the regression coefficients, which ensures reliability of the further estimates of the multipole amplitudes of the process.

For the polarization observables, a similar expansion is applied to the statistics that include the observables. In general, the first stage of the analysis should provide statistically reliable information about the partial waves that form the main characteristics of the process. Reliability of the conclusions obtained at this stage determines reliability of the final estimates of the multipole amplitudes. We determined the number of the expansion terms providing the best description of the data on the basis of two statistical criteria. The expansion was restricted to the terms for which the coefficients at the Legendre polynomials significantly differ from zero. Here, we also checked that subsequent terms introduce no nonvanishing coefficients. Then, we determined the possibility of improving the quality of description by increasing the number of terms, as evaluated by the Fisher criterion [2]. Usually, both criteria led to the same conclusions.

The experimental data included the observables measured at a specified energy of the gamma quanta; that is, we performed a so-called energy-independent analysis. The energy-dependent analysis is based, as a rule, on the parametric models which do not ensure the obtainment of unbiased estimates. Of special importance is the question whether the experimental data measured by various laboratories form a unique general massive and therefore can be used to obtain final unbiased estimates of the multipole amplitudes of the process.

3. RESULTS OF THE ANALYSIS OF THE DIFFERENTIAL CROSS SECTION

First, we analyzed the results of measurements of the differential cross sections for the photoproduction of η mesons off protons carried out at the Mainz accelerator [1]. These results include ten angular distributions measured at ten angles in the energy interval of the gamma-quanta from 715 to 790 MeV. Retaining only terms in the expansion with the coefficients at the Legendre polynomials significantly different from zero, we arrived at a three-term approximation that provided the best description of the complete set of experimental data on the differential cross sections. The Fisher criterion confirmed the correct choice of the three-term expansion. Table 1 presents the results of the three-term approximation. The errors of the individual regression coefficients are obtained from the diagonal elements of the error matrix with an allowance for the errors of the input data and the residual sum of squares that characterizes the quality of data description by the chosen model. The values of χ^2/n, where n is the number of degrees of freedom, characterize the statistical substantiation of the chosen linear model.

When analyzing the results in Table 1, attention should be paid to the following facts. First of all, the coefficient a_0 exceeds the coefficients a_1 and a_2 by one order of magnitude. Moreover, virtually all values of a_1 insignificantly differ from zero. This is clearly illustrated by the expansion in which the term with a_1 is omitted. It is clear from Table 2 that the absence of the term with a_1 does not spoil the description. The interpretation of these results requires consideration of the expressions for the regression coefficients in terms of the multipole amplitudes. When we use the

---

[1] A similar analysis procedure was used in a series of papers aimed at the determination of the isotopic components of the multipole amplitudes for the $\gamma p \longrightarrow \pi N$ process in the energy region of 300–400 MeV from experimental data on the pion photoproduction only (see, e.g., [3]).

Table 1. The values of coefficients a_0, a_1, a_2 [μb/sr] in the three-term expansion (1) for the angular distributions from [1]

E_γ, MeV	χ^2/n	a_0	a_1	a_2
715.69	1.41	5.10 ± 0.06	0.03 ± 0.11	0.07 ± 0.14
723.92	0.48	4.59 ± 0.03	-0.14 ± 0.05	-0.19 ± 0.07
732.00	1.82	4.30 ± 0.05	0.01 ± 0.09	0.02 ± 0.12
739.95	1.47	4.18 ± 0.05	-0.09 ± 0.08	-0.30 ± 0.10
748.16	0.67	3.99 ± 0.03	-0.03 ± 0.05	-0.28 ± 0.07
757.03	0.73	3.86 ± 0.03	-0.05 ± 0.05	-0.16 ± 0.06
766.22	0.71	3.68 ± 0.03	-0.06 ± 0.05	-0.31 ± 0.06
775.05	1.86	3.54 ± 0.05	-0.11 ± 0.08	-0.22 ± 0.10
782.98	0.67	3.46 ± 0.03	-0.11 ± 0.05	-0.37 ± 0.07
789.73	1.39	3.33 ± 0.05	-0.17 ± 0.07	-0.37 ± 0.10

expansion (1) with respect to the Legendre polynomials, these expressions up to the terms with E_{3-}, M_{3-} assume the form

$$\begin{aligned} a_0 = {} & |E_{0+}|^2 + 6|E_{1+}|^2 + |M_{1-}|^2 + 2|M_{1+}|^2 \\ & + 2|E_{2-}|^2 + 6|M_{2-}|^2 + 18|E_{2+}|^2 \\ & + 9|M_{2+}|^2 + 9|E_{3-}|^2 + 18|M_{3-}|^2, \end{aligned} \tag{2}$$

$$\begin{aligned} a_1 = 2\mathrm{Re}\Big[& E_{0+}^*(3E_{1+} + M_{1+} - M_{1-}) \\ & + M_{1-}^*(3M_{2-} - E_{2-}) \\ & + \frac{3}{5}E_{1+}^*(24E_{2+} + 3M_{2+} - E_{2-} - 3M_{2-}) \\ & + M_{1+}^*\left(\frac{3}{5}M_{2-} + E_{2-} + \frac{27}{5}M_{2+}\right) \\ & + \frac{9}{5}E_{3-}^*\left(3E_{2-} - \frac{4}{7}E_{2+} - M_{2-} + M_{2+}\right) \\ & + \frac{18}{35}M_{3-}^*(2M_{2+} + 28M_{2-} - 5E_{2+})\Big], \end{aligned}$$

$$\begin{aligned} a_2 = {} & 3|E_{1+}|^2 - |M_{1+}|^2 - |E_{2-}|^2 + 3|M_{2-}|^2 \\ & + \frac{108}{7}|E_{2+}|^2 + \frac{36}{7}|M_{2+}|^2 + \frac{36}{7}|E_{3-}|^2 \\ & + \frac{108}{7}|M_{3-}|^2 + 2\mathrm{Re}\Big[E_{0+}^*(E_{2-} - 3M_{2-} \\ & + 6E_{2+} + 3M_{2+}) - M_{1-}^*(3E_{1+} + M_{1+}) \\ & + 3E_{1+}^*M_{1+} + 3E_{2-}^*\left(M_{2+} - \frac{4}{7}E_{2+} - M_{2-}\right) \\ & + \frac{9}{7}M_{2-}^*(M_{2+} - 4E_{2+}) + \frac{36}{7}E_{2+}^*M_{2+} \\ & + 3E_{3-}^*\left(M_{1+} - M_{1-} - \frac{3}{7}E_{1+}\right) \\ & + 6M_{3-}^*\left(M_{1-} + \frac{2}{7}M_{1+} - \frac{6}{7}E_{3-} - \frac{6}{7}E_{1+}\right)\Big]. \end{aligned}$$

Table 2. The values of coefficients a_0 and a_2 [μb/sr] in the two-term expansion (1) for the angular distributions from [1]

E_γ, MeV	χ^2/n	a_0	a_2
715.69	1.24	5.10 ± 0.06	0.07 ± 0.13
723.92	0.89	4.59 ± 0.04	-0.20 ± 0.09
732.00	1.59	4.30 ± 0.05	0.02 ± 0.11
739.95	1.55	4.17 ± 0.05	-0.31 ± 0.10
748.16	0.63	3.99 ± 0.03	-0.29 ± 0.06
757.03	0.72	3.86 ± 0.03	-0.17 ± 0.06
766.22	0.74	3.68 ± 0.03	-0.32 ± 0.06
775.05	2.12	3.53 ± 0.05	-0.23 ± 0.11
782.98	1.07	3.45 ± 0.04	-0.38 ± 0.08
789.73	2.17	3.32 ± 0.06	-0.39 ± 0.12

Previous papers devoted to the analysis of the η-meson photoproduction off protons in the energy region above the threshold [1, 4] emphasized the dominating role of the s wave, that is, of the amplitude E_{0+} responsible for the formation of $S_{11}(1535)$; The manifestation of p and d waves, corresponding to the amplitudes E_{1+}, $M_{1\pm}$ and $E_{2\pm}$, $M_{2\pm}$, was attributed to their interference with the s wave.

Thus, the results of this analysis of the data on the differential cross sections for the $\gamma p \to \eta p$ process, obtained at the Mainz accelerator, confirm the

Table 3. The values of coefficients a_0, a_1, and a_2 (in μb/sr) in the three-term expansion (1) for the angular distribution from [5]

E_γ, MeV	χ^2/n	a_0	a_1	a_2
710.3	2.37	4.89 ± 0.71	-0.86 ± 1.23	0.57 ± 2.01
716.5	1.18	3.58 ± 0.16	-0.79 ± 0.31	0.72 ± 0.39
722.6	2.03	4.39 ± 0.16	-0.53 ± 0.32	0.16 ± 0.40
729.0	1.05	3.64 ± 0.13	-0.48 ± 0.24	0.15 ± 0.31
735.1	0.74	3.42 ± 0.09	-0.61 ± 0.18	-0.08 ± 0.23
747.4	0.60	3.42 ± 0.09	-0.30 ± 0.16	-0.11 ± 0.21
753.2	0.82	3.37 ± 0.09	-0.65 ± 0.18	-0.34 ± 0.23
759.2	0.82	3.20 ± 0.09	-0.21 ± 0.18	-0.14 ± 0.23
765.2	0.85	3.01 ± 0.09	-0.62 ± 0.17	-0.05 ± 0.22
771.0	1.47	3.14 ± 0.10	-0.41 ± 0.17	0.10 ± 0.22
776.9	0.72	3.15 ± 0.07	-0.19 ± 0.13	-0.17 ± 0.16
782.5	1.15	2.92 ± 0.09	-0.48 ± 0.16	-0.37 ± 0.20
788.2	0.94	2.85 ± 0.07	-0.40 ± 0.14	0.14 ± 0.18
793.8	2.01	2.96 ± 0.12	-0.21 ± 0.22	-0.14 ± 0.27
799.3	2.68	2.67 ± 0.13	-0.31 ± 0.26	0.27 ± 0.29
805.0	0.67	2.80 ± 0.07	-0.41 ± 0.13	0.04 ± 0.15
810.4	1.50	2.61 ± 0.10	-0.30 ± 0.19	-0.11 ± 0.20
815.8	1.55	2.65 ± 0.10	-0.33 ± 0.20	-0.28 ± 0.23
821.0	1.20	2.56 ± 0.10	-0.47 ± 0.20	0.52 ± 0.22
826.3	2.66	2.25 ± 0.15	-0.59 ± 0.28	-0.09 ± 0.31
832.6	0.73	2.36 ± 0.07	-0.35 ± 0.13	-0.17 ± 0.15
839.6	4.32	2.18 ± 0.15	-0.46 ± 0.29	-0.08 ± 0.36
846.7	2.53	2.21 ± 0.19	-0.57 ± 0.39	-0.39 ± 0.38
853.6	1.06	2.08 ± 0.12	-0.48 ± 0.21	0.28 ± 0.28
860.4	4.13	1.95 ± 0.19	-0.42 ± 0.37	0.29 ± 0.39
867.0	3.36	1.58 ± 0.13	-1.01 ± 0.25	-0.50 ± 0.29
873.6	1.17	1.86 ± 0.11	-0.40 ± 0.19	-0.19 ± 0.18
880.1	0.74	1.94 ± 0.08	-0.13 ± 0.17	0.04 ± 0.15
886.4	1.32	1.89 ± 0.13	-0.04 ± 0.26	0.12 ± 0.22
892.7	1.86	1.84 ± 0.20	0.20 ± 0.39	0.37 ± 0.29
898.8	1.14	1.37 ± 0.07	-0.47 ± 0.14	0.06 ± 0.12

manifestation of the contributions from resonances $S_{11}(1535)$ (with the amplitude E_{0+}) and $D_{13}(1520)$ (with the amplitudes E_{2-} and M_{2-}), and the absence of the effects from the p-wave resonances (with the amplitudes E_{1+} and $M_{1\pm}$) in the process under consideration.

We performed a similar analysis with the experimental data on the differential cross sections for the $\gamma p \to \eta p$ process, measured at the Bonn accelera-

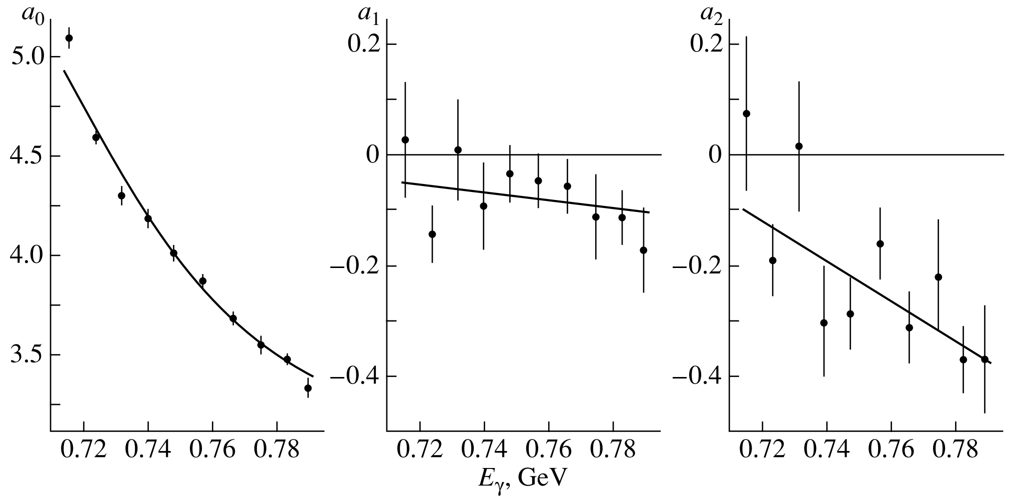

Fig. 1. The coefficients a_0, a_1, and a_2 (in μb/sr) for the three-term expansion (1) by the data from [1]; the curves (here and on) represent the results of fitting.

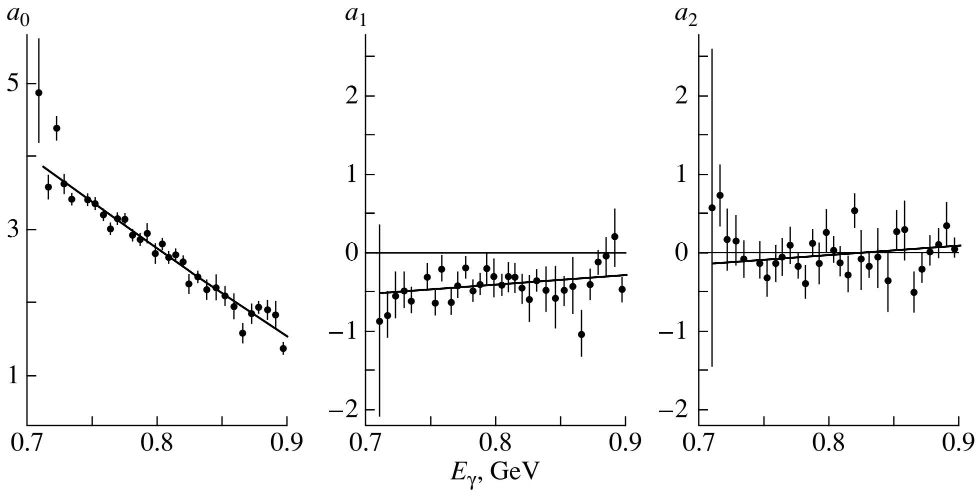

Fig. 2. Same that in Fig. 1 for the data from [5].

tor [5]. The analysis uses the results corresponding to the energy range from the photoproduction threshold up to 900 MeV. The data measured at higher energies were not used owing to their low statistical accuracy and low number of the measurement angles. Similarly to the analysis of the angular distributions measured in Mainz, it turned to be sufficient to leave the three lowest terms in the expansion with respect to the Legendre polynomials, that is, to use a three-term approximation of the differential cross sections. Table 3 displays the corresponding regression coefficients. A comparison of the results in Tables 1 and 3 clearly demonstrates their inconsistency. In contrast to the Mainz data, the approximation of the Bonn data results in an insignificant contribution of the interference between s and d waves up to an energy of 0.9 GeV; at the same time, the contribution of the sp interference virtually absent from the previous analysis is significantly different from zero, which is confirmed by the description of the data from [5] by a two-term expression containing only a_0 and a_1 (see Table 4). Inconsistency of the experimental data measured in two laboratories is illustrated in Figs. 1 and 2, which present the energy dependences of the regression coefficients a_0, a_1, and a_2 describing the experimental angular distributions.

In this respect, an analysis of the angular distributions in the $\gamma p \to \eta p$ process measured in Grenoble [6] in the energy range from the threshold to 1.1 GeV is of special interest. Table 5 and Fig. 3 present the results of the analysis of these angular distributions. Similarly to two previous cases, a sat-

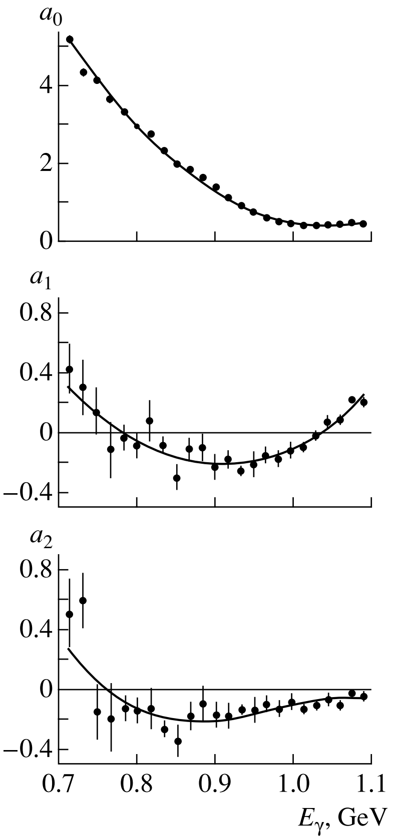

Fig. 3. The coefficients a_0, a_1, and a_2 (in μb/sr) for the data from [6].

isfactory description of the data is reached with the three lowest terms left in the expansion with respect to the Legendre polynomials. This result confirms the dominating role of the s wave, or the coefficient a_0. However, in contrast to the results of analysis for the angular distributions [1, 5], the values of a_1 and a_2 are approximately on the same order of magnitude. Therefore, the contributions of p- and d-wave amplitudes in the results of three experiments qualitatively disagree with each other. This means inconsistency of the estimates of a_1 and a_2, obtained from the experimental data [1, 5, 6].

4. THE RESULTS OF THE ANALYSIS OF THE POLARIZATION OBSERVABLES

At the moment, there are relatively systematic data only for two polarization observables: asymmetry $\Sigma(\theta)$ of the linearly polarized beam of gamma radiation measured in Grenoble [7] and the asymmetry $T(\theta)$ for the polarized proton beam measured in Bonn [8]. The analysis of the polarization observables reduces to the Legendre expansion of the following statistics:

$$\frac{k}{q}\frac{d\sigma}{d\Omega}\frac{1}{\sin^2\theta}\Sigma = \sum b_l P_l(\cos\theta), \qquad (3a)$$

$$\frac{k}{q}\frac{d\sigma}{d\Omega}\frac{1}{\sin\theta}T = \sum c_l P_l(\cos\theta). \qquad (3b)$$

Since the observables $d\sigma/d\Omega$, Σ, and T are measured, generally, at different values of angles and energies, we formed the statistics using the interpolated values of $d\sigma/d\Omega$ calculated from the coefficients a_0, a_1, a_2, obtained in the analysis of the angular distributions. We used the sets of parameters obtained in the analysis of three experiments [1, 5, 6]. In other words, we analyzed both the statistics (3) formed from the data of one laboratory and the statistics for $d\sigma/d\Omega$ formed from the data of two other laboratories. Tables 6–11 present the values of coefficients b_l and c_l obtained as a result of this analysis. Figures 4 and 5 display the energy dependences of the coefficients. It is clear from these figures that using the inconsistent angular distributions in statistics (3) does not affect the general behavior of the corresponding coefficients b_l and c_l which exhibit evident similarity. In other words, the differences in $d\sigma/d\Omega$ are not explicitly reflected in the polarization observables.

The coefficients b_l and c_l are expressed in terms of the multipole amplitudes up to the terms with E_{3-}, M_{3-}:

$$\begin{aligned} b_0 = {} & \frac{3}{2}|M_{1+}|^2 - \frac{9}{2}|E_{1+}|^2 + \frac{3}{2}|E_{2-}|^2 \qquad (4) \\ & + 12|M_{2+}|^2 - 24|E_{2+}|^2 - 12|E_{3-}|^2 \\ & + 24|M_{3-}|^2 + 3\mathrm{Re}[E^*_{0+}(E_{2-} + E_{2+} \\ & + M_{2-} - M_{2+}) + M^*_{1-}(M_{1+} - E_{1+}) \\ & + E^*_{1+}M_{1+} + E^*_{2-}(M_{2-} + 4E_{2+} - M_{2+}) \\ & + M^*_{2-}(7M_{2+} - 4E_{2+}) + 4E^*_{2+}M_{2+} \\ & + E^*_{3-}(7E_{1+} + M_{1+} - M_{1-} + 4M_{3-}) \\ & + M^*_{3-}(4E_{1+} + 4M_{1+} - M_{1-})], \end{aligned}$$

$$\begin{aligned} b_1 = {} & 3\mathrm{Re}[5E^*_{0+}(E_{3-} + M_{3-}) + 3E^*_{1+}(2E_{2-} - 3E_{2+}) \\ & + M^*_{1+}(6M_{2-} + 4M_{2+} + 5E_{2+}) \\ & + 5M^*_{1-}(M_{2+} - E_{2+}) + 4E^*_{3-}(9E_{2+} - E_{2-}) \\ & + M^*_{3-}(9M_{2-} + 5E_{2-} + 36M_{2+})], \end{aligned}$$

$$\begin{aligned} b_2 = {} & -30|E_{2+}|^2 + 15|M_{2+}|^2 - 15|E_{3-}|^2 + 30|M_{3-}|^2 \\ & + 15\mathrm{Re}[E^*_{2+}(3E_{2-} + M_{2+} - M_{2-}) + 4M^*_{2+}M_{2-} \\ & + E^*_{3-}(M_{3-} + 4E_{1+}) + M^*_{3-}(E_{1+} + 3M_{1+})]; \end{aligned}$$

$$\begin{aligned} c_0 = {} & \mathrm{Im}[E^*_{0+}(3E_{1+} - 3M_{1+} - 2E_{3-} - 2M_{3-}) \qquad (5) \\ & + M^*_{1-}(2M_{2+} - 2E_{2+} + 3E_{2-} + 3M_{2-}) \\ & + 5(M^*_{1+} + 3E^*_{1+})(E_{2+} - M_{2+}) \\ & + 5(3M^*_{2-} - E^*_{2-})(E_{3-} + M_{3-})], \end{aligned}$$

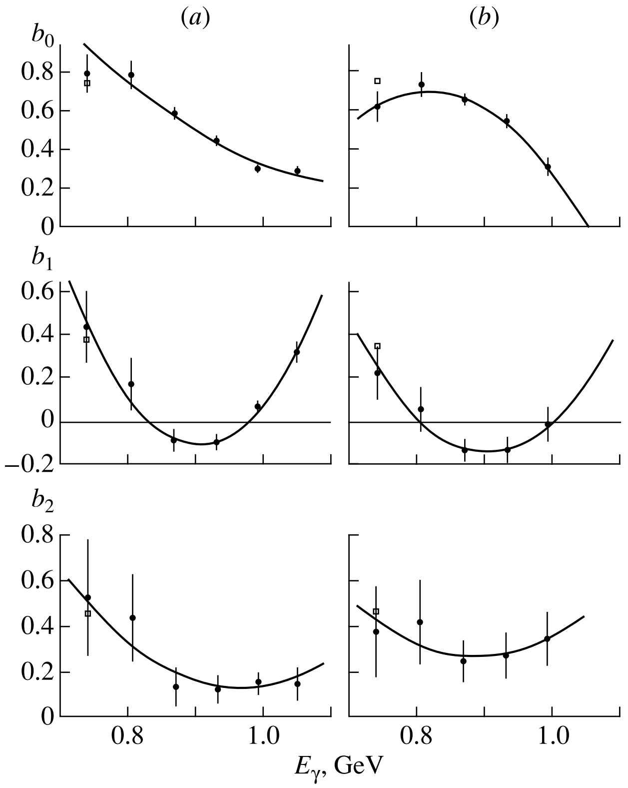

Fig. 4. The coefficients b_0, b_1, and b_2 (in μb/sr) for statistics (3a): (*a*) cross sections from [6]; (*b*) cross sections from [5]; (□) cross sections from [1].

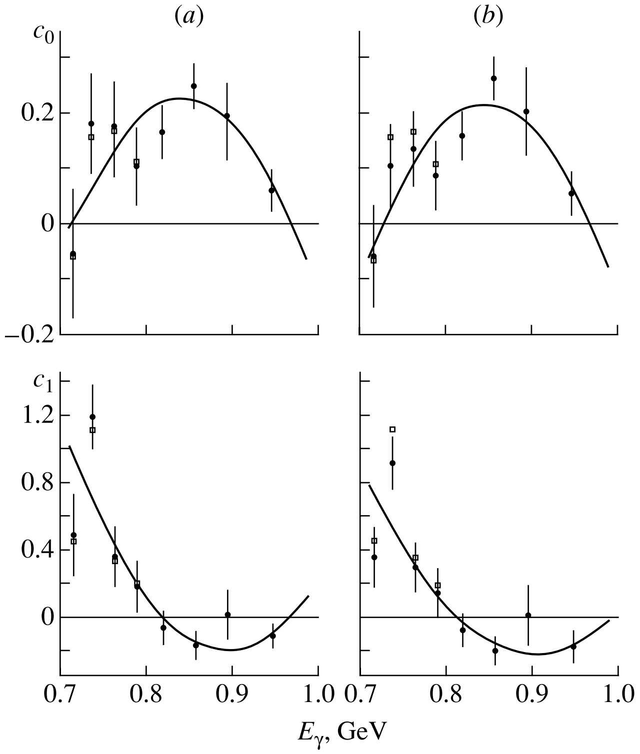

Fig. 5. The coefficients c_0 and c_1 (in μb/sr) for statistics (3b): (*a*) cross sections from [6]; (*b*) cross sections from [5]; (□) cross sections from [1].

Table 4. The values of coefficients a_0 and a_1 (in μb/sr) in the two-term expansion (1) for the angular distribution from [5]

E_γ, MeV	χ^2/n	a_0	a_1
710.3	2.01	4.74 ± 0.44	-0.80 ± 1.11
716.5	1.54	3.43 ± 0.16	-0.71 ± 0.35
722.6	1.82	4.36 ± 0.13	-0.55 ± 0.30
729.0	0.95	3.62 ± 0.11	-0.50 ± 0.23
735.1	0.66	3.43 ± 0.08	-0.61 ± 0.17
747.4	0.55	3.43 ± 0.08	-0.29 ± 0.15
753.2	0.94	3.41 ± 0.10	-0.63 ± 0.19
759.2	0.76	3.22 ± 0.09	-0.19 ± 0.17
765.2	0.75	3.02 ± 0.09	-0.62 ± 0.16
771.0	1.32	3.13 ± 0.09	-0.42 ± 0.16
776.9	0.74	3.17 ± 0.07	-0.14 ± 0.13
782.5	1.52	2.94 ± 0.10	-0.42 ± 0.18
788.2	0.90	2.83 ± 0.07	-0.43 ± 0.13
793.8	1.82	2.97 ± 0.11	-0.17 ± 0.20
799.3	2.62	2.62 ± 0.12	-0.44 ± 0.22
805.0	0.59	2.80 ± 0.06	-0.43 ± 0.11
810.4	1.37	2.63 ± 0.09	-0.26 ± 0.17
815.8	1.65	2.68 ± 0.10	-0.22 ± 0.18
821.0	1.86	2.44 ± 0.11	-0.70 ± 0.21
826.3	2.25	2.26 ± 0.13	-0.56 ± 0.24
832.6	0.76	2.39 ± 0.06	-0.27 ± 0.11
839.6	3.73	2.19 ± 0.13	-0.43 ± 0.24
846.7	2.55	2.32 ± 0.16	-0.27 ± 0.27
853.6	1.06	2.01 ± 0.08	-0.57 ± 0.19
860.4	3.90	1.87 ± 0.15	-0.60 ± 0.28
867.0	4.21	1.65 ± 0.14	-0.76 ± 0.23
873.6	1.19	1.89 ± 0.10	-0.30 ± 0.17
880.1	0.65	1.92 ± 0.06	-0.16 ± 0.11
886.4	1.19	1.84 ± 0.09	-0.15 ± 0.16
892.7	2.06	1.63 ± 0.12	-0.23 ± 0.21
898.8	1.00	1.35 ± 0.06	-0.52 ± 0.10

$$\begin{aligned} c_1 = 3\mathrm{Im}[&E^*_{0+}(4E_{2+} - 4M_{2+} - E_{2-} - M_{2-}) \\ &+ M^*_{1-}(M_{1+} - E_{1+}) - 4E^*_{1+}M_{1+} \\ &+ E^*_{2-}(E_{2+} - M_{2+} - 4M_{2-}) \\ &+ 3M^*_{2-}(M_{2+} - E_{2+}) - 18E^*_{2+}M_{2+} \\ &+ (E^*_{3-} + M^*_{3-})(4M_{1-} - 3E_{1+} - M_{1+}) \\ &- 18E^*_{3-}M_{3-}]. \end{aligned}$$

5. DISCUSSION

It is necessary to emphasize that the following conclusions from the results of analysis are obtained from qualitative considerations and require quantitative confirmation.

Note the following facts: irrespective of the data on $d\sigma/d\Omega$, the description of statistics (3a), which includes Σ, requires the three-term expansion with the coefficients (4), while the statistics (3b) is satisfactorily described by the two-term expansion with the coefficients (5). One should also pay attention to the energy dependence of the coefficient a_1. According to Eqs. (2), a change in this quantity in the energy interval from the threshold up to approximately 0.9 GeV can be related to a decrease in the s-wave amplitude and the corresponding reduction of the sp

Table 5. The values of coefficients a_0, a_1, and a_2 (in μb/sr) for the angular distributions from [6]

E_γ, MeV	χ^2/n	a_0	a_1	a_2
714.2	0.17	5.17 ± 0.09	0.42 ± 0.16	0.51 ± 0.23
731.7	0.26	4.32 ± 0.09	0.29 ± 0.18	0.59 ± 0.18
749.1	0.44	4.12 ± 0.06	0.14 ± 0.16	-0.16 ± 0.18
766.3	1.39	3.64 ± 0.09	-0.12 ± 0.19	-0.18 ± 0.22
784.6	0.27	3.32 ± 0.03	-0.03 ± 0.07	-0.13 ± 0.08
800.6	0.36	2.97 ± 0.03	-0.09 ± 0.07	-0.14 ± 0.08
817.6	0.97	2.75 ± 0.06	0.07 ± 0.12	-0.12 ± 0.13
834.5	0.16	2.33 ± 0.02	-0.08 ± 0.05	-0.26 ± 0.05
851.2	0.68	1.99 ± 0.04	-0.31 ± 0.09	-0.34 ± 0.10
867.9	0.65	1.83 ± 0.04	-0.12 ± 0.08	-0.18 ± 0.09
884.0	1.06	1.64 ± 0.05	-0.10 ± 0.09	-0.10 ± 0.11
900.4	0.81	1.39 ± 0.03	-0.25 ± 0.07	-0.17 ± 0.08
917.2	0.76	1.13 ± 0.03	-0.18 ± 0.07	-0.18 ± 0.08
933.3	0.13	0.92 ± 0.01	-0.27 ± 0.02	-0.14 ± 0.03
949.4	1.29	0.77 ± 0.03	-0.22 ± 0.06	-0.14 ± 0.08
965.5	0.65	0.64 ± 0.02	-0.16 ± 0.04	-0.10 ± 0.05
981.3	1.00	0.53 ± 0.02	-0.19 ± 0.04	-0.13 ± 0.05
997.2	1.43	0.46 ± 0.02	-0.12 ± 0.04	-0.09 ± 0.05
1012.9	0.48	0.41 ± 0.01	-0.10 ± 0.03	-0.14 ± 0.03
1028.6	0.45	0.40 ± 0.01	-0.02 ± 0.02	-0.11 ± 0.03
1044.1	0.91	0.41 ± 0.02	0.06 ± 0.04	-0.07 ± 0.04
1059.4	0.35	0.44 ± 0.01	0.08 ± 0.02	-0.11 ± 0.02
1074.8	0.08	0.47 ± 0.01	0.21 ± 0.01	-0.03 ± 0.01
1089.2	0.37	0.47 ± 0.01	0.20 ± 0.03	-0.05 ± 0.03
1100.4	0.07	0.45 ± 0.01	0.12 ± 0.03	-0.11 ± 0.03

Table 6. The values of coefficients b_0, b_1, and b_2 (in μb/sr) for statistics (3a): Σ from [7], $d\sigma/d\Omega$ from [6]

E_γ, MeV	χ^2/n	b_0	b_1	b_2
742.5	0.69	0.80 ± 0.10	0.44 ± 0.17	0.52 ± 0.26
807.0	1.07	0.79 ± 0.07	0.17 ± 0.12	0.43 ± 0.19
870.0	1.05	0.59 ± 0.03	-0.09 ± 0.05	0.13 ± 0.08
932.0	1.18	0.44 ± 0.02	-0.10 ± 0.04	0.12 ± 0.06
992.0	1.74	0.31 ± 0.02	0.06 ± 0.03	0.14 ± 0.05
1050.5	6.73	0.28 ± 0.03	0.32 ± 0.05	0.14 ± 0.07

interference. The increase in a_1 in the energy interval 0.9–1.1 GeV is most likely caused by an increase in the contribution from the higher partial waves, because there are no known p-wave resonances in this region [9]. Next, the energy dependence of b_2 is qualitatively similar to a_1 and b_1, although b_2, in contrast to a_1 and b_1, does not include a contribution from the s wave. This probably means that the decrease in b_2, at energies below 0.9 GeV, is related to the $D_{13}(1520)$ resonance; the increase in b_2 in the energy region 0.9–1.1 GeV might be caused by

Table 7. The values of coefficients b_0, b_1, and b_2 (in μb/sr) for statistics (3a): Σ from [7], $d\sigma/d\Omega$ from [5]

E_γ, MeV	χ^2/n	b_0	b_1	b_2
742.5	0.67	0.62 ± 0.08	0.25 ± 0.13	0.37 ± 0.20
807.0	1.11	0.74 ± 0.07	0.07 ± 0.12	0.41 ± 0.19
870.0	0.95	0.65 ± 0.03	-0.13 ± 0.06	0.24 ± 0.09
932.0	0.97	0.54 ± 0.04	-0.13 ± 0.07	0.26 ± 0.10
992.0	0.42	0.31 ± 0.05	-0.01 ± 0.08	0.34 ± 0.12

Table 8. The values of coefficients b_0, b_1, and b_2 (in μb/sr) for statistics (3a): Σ from [7], $d\sigma/d\Omega$ from [1]

E_γ, MeV	χ^2/n	b_0	b_1	b_2
742.5	0.66	0.75 ± 0.09	0.38 ± 0.16	0.45 ± 0.24

Table 9. The values of coefficients c_0 and c_1 (in μb/sr) for statistics (3b): T from [8], $d\sigma/d\Omega$ from [6]

E_γ, MeV	χ^2/n	c_0	c_1
717.0	0.69	-0.05 ± 0.12	0.48 ± 0.25
738.0	0.51	0.18 ± 0.09	1.19 ± 0.20
765.0	0.96	0.17 ± 0.09	0.36 ± 0.18
790.0	0.95	0.10 ± 0.07	0.18 ± 0.15
820.0	0.69	0.16 ± 0.05	-0.07 ± 0.10
857.0	0.44	0.25 ± 0.04	-0.17 ± 0.09
895.0	1.12	0.18 ± 0.07	0.01 ± 0.15
947.0	0.50	0.06 ± 0.04	-0.11 ± 0.08

the effect of $D_{15}(1675)$ and $F_{15}(1680)$ resonances. In this case, the interference of d and f waves should be manifested at energies of 1.0–1.1 GeV as a shift of the angular distribution $\Sigma(\theta)$ toward small angles relative to 90° in the c.m.f., which is observed in experiment [7].

It is clear from expression (4) that behavior of the parameter b_1 at energies above 0.9 GeV can be caused by the sf interference. However, in this case, it is necessary to explain the absence of the term with $P_3(\cos(\theta))$ from the expansion of $(k/q)\,(d\sigma/d\Omega)$: the coefficient a_3 at this term contains a similar interference contribution:

$$a_3 \sim 6\mathrm{Re}[E^*_{0+}(E_{3-} - 2M_{3-})]. \qquad (6)$$

Table 10. The values of coefficients c_0 and c_1 (in μb/sr) for statistics (3b): T from [8], $d\sigma/d\Omega$ from [5]

E_γ, MeV	χ^2/n	c_0	c_1
717.0	0.74	-0.06 ± 0.09	0.35 ± 0.19
738.0	0.56	0.11 ± 0.08	0.91 ± 0.16
765.0	0.90	0.13 ± 0.07	0.29 ± 0.15
790.0	0.96	0.09 ± 0.06	0.14 ± 0.14
820.0	0.66	0.16 ± 0.05	-0.09 ± 0.10
857.0	0.40	0.26 ± 0.04	-0.21 ± 0.09
895.0	1.16	0.20 ± 0.08	0.01 ± 0.18
947.0	0.52	0.06 ± 0.04	-0.18 ± 0.10

It is possible that the absence of a_3 is explained by the fact that the amplitudes E_{3-} and M_{3-} enter b_1 and a_3 with opposite signs, leading to summation in b_1 and subtraction in a_3.

Table 11. The values of coefficients c_0 and c_1 (in μb/sr) for statistics (3b): T from [8], $d\sigma/d\Omega$ from [1]

E_γ, MeV	χ^2/n	c_0	c_1
717.0	0.72	-0.06 ± 0.12	0.45 ± 0.24
738.0	0.56	0.16 ± 0.09	1.10 ± 0.19
765.0	0.92	0.16 ± 0.08	0.34 ± 0.17
790.0	0.95	0.11 ± 0.08	0.19 ± 0.16

In conclusion, we emphasize that the energy behavior of the coefficients a_1, b_1, b_2, c_0, and c_1 revealed by this analysis is probably indicative of a change in the process regime in the vicinity of 0.9 GeV, which is caused by the transition from the region of $S_{11}(1535)$ and $D_{13}(1520)$ resonances to the region of $D_{15}(1675)$ and $F_{15}(1680)$ resonances.

Further progress requires improvement of the experimental data on the known observables and extension of the database by including other observables, first of all, the polarization of the recoil protons.

REFERENCES

1. B. Krusche *et al.*, Phys. Rev. Lett. **74**, 3736 (1995).
2. D. J. Hudson, *Statistics. Lectures on Elementary Statistics and Probability* (Geneva, 1964; Mir, Moscow, 1970); C. R. Rao, *Linear Statistical Inference and Its Applications* (Wiley, New York, 1965; Mir, Moscow. 1968).
3. V. F. Grushin *et al.*, Yad. Fiz. **38**, 1448 (1983) [Sov. J. Nucl. Phys. **38**, 881 (1983)].
4. L. Tiator *et al.*, Phys. Rev. C **60**, 35210 (1999).
5. L. Soezueer *et al.*, http://gwdac.phys.gwu.edu./
6. F. Renard *et al.*, hep-ex/0011098.
7. J. Ajaka *et al.*, Phys. Rev. Lett. **81**, 1797 (1998).
8. A. Bock *et al.*, Phys. Rev. Lett. **81**, 534 (1998).
9. Review of Particle Physics, Eur. Phys. J. C **4** (1–4) (2000).

Translated by M. Kobrinsky

Physics of Atomic Nuclei, Vol. 65, No. 9, 2002, pp. 1722–1732. Translated from Yadernaya Fizika, Vol. 65, No. 9, 2002, pp. 1766–1776.

ELEMENTARY PARTICLES AND FIELDS
Theory

Analysis of Charged-Particle Production in Nucleus–Nucleus Interactions near and beyond the Kinematical Limit for Free NN Collisions within the FRITIOF Model

A. S. Galoyan[1)]*, **G. L. Melkumov**, and **V. V. Uzhinskii**

Joint Institute for Nuclear Research, Dubna, Moscow oblast, 141980 Russia

Received May 10, 2001; in final form, September 7, 2001

Abstract—The production of charged particles ($\pi^{\pm}$ mesons and protons) in nucleus–nucleus interactions at energies in the range 3.3–3.7 GeV/nucleon is considered. It is shown that the FRITIOF model adapted to moderately high energies reproduces satisfactorily the energy spectra of mesons emitted into the backward hemisphere in the laboratory frame, as well as their dependence on the masses of colliding nuclei. The FRITIOF model supplemented with the Reggeon model of nuclear breakup allows one to describe the soft part of the spectra of backward-emitted protons. Other approaches are required for describing the hard part of the spectra. *© 2002 MAIK "Nauka/Interperiodica".*

The mechanism of cumulative-particle production in hadron–nucleus (hA) interactions was widely discussed in the literature [1–10]. Much less attention was and is presently paid to nucleus–nucleus (AA) interactions. This is because hA interactions are analyzed by methods that do not require large computational work, which involve explicitly specifying fragmentation functions, structure functions, cross sections, etc. In the case of AA interactions, only within the simplest approximation similar to that of Czyz–Maximon [11] can cross sections be obtained in the form of analytic expressions or single and double integrals. Within the correct Glauber approach, this is virtually impossible. In addition, according to the Glauber approach, the variety of elementary processes in AA interactions is much broader than that in the case of hA interactions. Even listing possible processes is quite a complicated mathematical problem, but it can be effectively solved by stochastic-simulation methods, that is, well-known Monte Carlo programs generating simulated events. At present, various computational algorithms have been suggested. For example, the DIAGEN program [12] makes it possible to generate random samples of processes (diagrams of AA interactions). Similar subprograms are included in all generator programs. Simulation of a particle-production process corresponding to a given interaction diagram presents another problem, which can be solved by using models like FRITIOF [13], RQMD [14–16], and VENUS [17]. As a rule, these models are employed to analyze the general characteristics of hA and AA interactions. The use of these models in analyzing cumulative-particle production provides additional possibilities for verifying general statements of the models and for clarifying the mechanisms of the processes.

In contrast to analytic models, generator programs provide an exclusive description of interactions, which is needed for modern experiments in order to take into account background conditions, setup geometry, particle-detection efficiencies, etc. However, simulation of rare processes requires considerable computational work (reduced by applying special methods of weighted modeling), but this work can in principle be done by using modern facilities. The production of cumulative particles is not a rare process; therefore, generator programs can efficiently be used to analyze it.

Previously [18], we showed that the FRITIOF model reproduces the main characteristics of the production of cumulative π^0 mesons in the process of fragmentation of helium and carbon projectile nuclei interacting with helium and carbon nuclei at an energy of 3.6 GeV/nucleon. Here, we study the possibility of employing the FRITIOF model to describe the charged-particle yield in hA and AA interactions near and beyond the kinematical limit for free NN collisions.

[1)] Yerevan Physics Institute, ul. Brat'ev Alikhanian 2, AM-37503 Yerevan, Armenia.

*e-mail: `galoyan@cv.jinr.ru`

1. FUNDAMENTALS OF THE FRITIOF MODEL

The FRITIOF model assumes the two-particle kinematics of inelastic hh interactions, $a + b \longrightarrow a' + b'$, where a' and b' are excited states of initial hadrons a and b, respectively. The excited states are characterized by their masses. In order to chose hadron masses, we employ the approach presented in [13] (see also [19]). The model parameters were refined in [20].

In the case of hA and AA interactions, it is assumed that nucleons excited in primary collisions can interact with each other and with other nucleons, thus increasing their mass. The probability of multiple collisions is calculated within the Glauber approach.

Excited hadrons are considered as QCD strings whose fragmentation produces hadrons. As the string mass grows, the multiplicity of secondary particles also increases. These factors are also responsible for a higher multiplicity of AA collisions as compared to that in hA and hh ones; the same factors control cumulative-particle production.

In order to determine the time sequence of nucleon—nucleon collisions in the case of hA and AA interactions within the FRITIOF model, the Glauber approximation is used. Since cascade processes involving secondary particles are disregarded, the characteristics of slow particles produced in the breakup of a nucleus are not described within the model. In order to eliminate this drawback, it was suggested to supplement the FRITIOF model with the Reggeon model of nuclear breakup [22].

We take into account nuclear breakup in two steps. At the first step, we determine, by means of the Glauber approximation [12], the number of inelastically interacting nucleons, that is, the number of so-called hit ones. At the second step, we consider noninteracting nucleons. It is assumed that a noninteracting nucleon that is at an impact distance r from a hit nucleon can be involved in a Reggeon cascade with the probability $W = C_{\mathrm{nd}} e^{-r^2/r^2_{\mathrm{nd}}}$. Such a nucleon can involve another spectator nucleon, and so on. It is assumed that all hit and involved nucleons leave the nucleus.

In order to describe the multiplicity of protons participating in the collisions of nuclei with carbon nuclei, the following parameter values were chosen: $C_{\mathrm{nd}} = 1$ and $r_{\mathrm{nd}} = 1.2$ fm.

The excitation energy of the residual nucleus was calculated according to the method presented in detail in [19]. To simulate the relaxation of excited nuclei, we used the evaporation model [23] (see also [24]).

Within the modified FRITIOF model [19], it is suggested that the distribution of nucleons emitted, for example, from the target nucleus with respect to kinematical variables has the form

$$P\{x_i^-\}, \{\mathbf{p}_{i\perp}\}$$

$$\propto \prod_{i=1}^{N_T} \exp[-\mathbf{p}^2_{i\perp}/\langle p^2_\perp \rangle] \exp[-(x_i^- - 1/N_T)^2/(d_x/N_T)^2],$$

$$\sum_{i=1}^{N_T} \mathbf{p}_{i\perp} = 0, \quad \sum_{i=1}^{N_T} x_i^- = 1,$$

where N_T is the multiplicity of emitted nucleons, $\mathbf{p}_{i\perp}$ is the transverse momentum of the ith emitted nucleon, and $x_i^- = (E_i - p_{iz})/W_T^-$ is the longitudinal-momentum fraction carried away by the nucleon. The law of energy—momentum conservation is used to determine the quantity W_T^- and the analogous quantity W_P^+ for nucleons ejected from the projectile nucleus [19].

The values of $\langle p^2_\perp \rangle = 0.17$ (GeV/c)^2 and $d_x = 0.282$ were determined from an analysis of the spectra of particles emitted into the backward hemisphere in hA and AA interactions. Below, this procedure will be referred to as the method for taking into account Fermi motion.

2. ANALYSIS OF PARTICLE PRODUCTION INTO BACKWARD HEMISPHERE IN THE AA INTERACTIONS

Figures 1 and 2 present experimental data from [25] on invariant exclusive cross sections for π^--meson production into the backward hemisphere in AA interactions at an energy of 3.36 GeV/nucleon, together with the results of the FRITIOF model calculations [21]. It is seen that the model reproduces qualitatively the dependences of the cross sections on T (the kinetic energy of π^- mesons), θ (the meson emission angle with respect to the beam direction), and the masses of the projectile and target nuclei. In general, the calculated values are higher than the experimental data. For θ varying from 90° to 110° and from 110° to 130°, the slopes of the calculated spectra agree well with the experimental ones. For $\theta > 130°$, the model predicts a somewhat smaller slope than that which is needed to fit the experimental data.

There arises the natural problem of disclosing factors that made it possible to attain qualitative agreement between the experimental data and our model calculations. According to Fig. 3, the spectra of π^- mesons in AA interactions are similar to those in NN collisions. To describe the latter spectra, considerable efforts were made in [20]. As a result, the meson spectra in AA interactions were described without using fitting parameters.

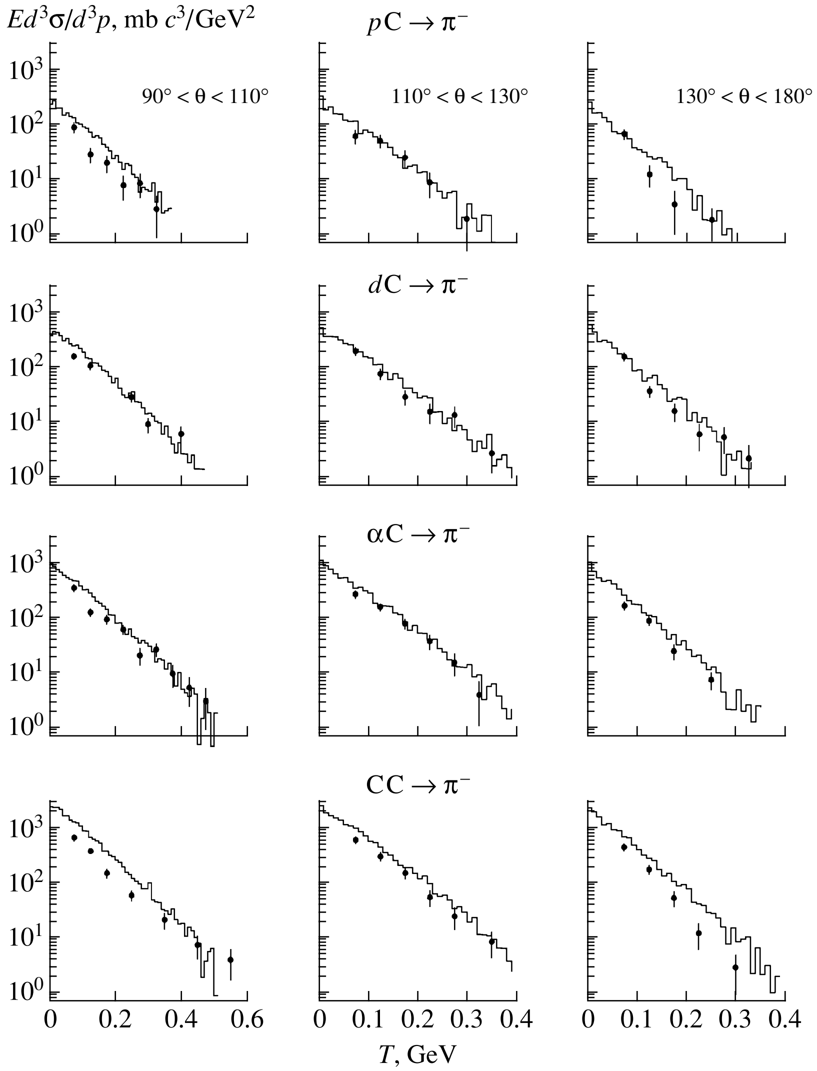

Fig. 1. Invariant inclusive cross sections for the production of π^- mesons in pC, dC, αC, and CC interactions at an energy of 3.36 GeV/nucleon. Here, T is the kinetic energy of π^- mesons, while θ is the meson emission angle with respect to the beam direction. Points stand for experimental data from [25], while the histograms (here and below) represent the results of our calculations within the FRITIOF model.

The absolute normalization of the spectra is determined by the Glauber cross sections. In order to calculate these cross sections [12], one needs to specify certain characteristics of NN interactions, namely, the total cross section ($\sigma^{\rm tot}_{NN}$), the slope of the differential cross section for elastic scattering (B_{NN}), and the ratio of the real to the imaginary part of the elastic scattering amplitude at zero momentum transfer [$\rho_{NN} = {\rm Re} f_{NN}(0)/{\rm Im} f_{NN}(0)$].

The amplitude of elastic NN scattering in the impact-parameter representation was parametrized in the form standard for the Glauber approximation,

$$f_{NN}(\mathbf{b}) = \frac{\sigma^{\rm tot}_{NN}(1 - i\rho_{NN})}{4\pi B_{NN}} e^{-\mathbf{b}^2/2B_{NN}}, \qquad (1)$$

by using the parameter values [26]

$$\sigma^{\rm tot}_{NN} = 42 \text{ mb}, \quad B_{NN} = 7.8\,({\rm GeV}/c)^{-2},$$
$$\rho_{NN} = -0.23.$$

The single-particle densities of nuclei heavier than helium were parametrized in the form

$$\rho(r) = {\rm const}/[1 + e^{\frac{r-R_A}{c}}], \qquad (2)$$
$$R_A = 1.07A^{1/3} \text{ fm}, \quad c = 0.545 \text{ fm}.$$

Center-of-mass correlations were taken into account as in [27]. The densities of light nuclei were parametrized as in [12]. No modification of the characteristics of NN interactions in the nuclear medium was introduced.

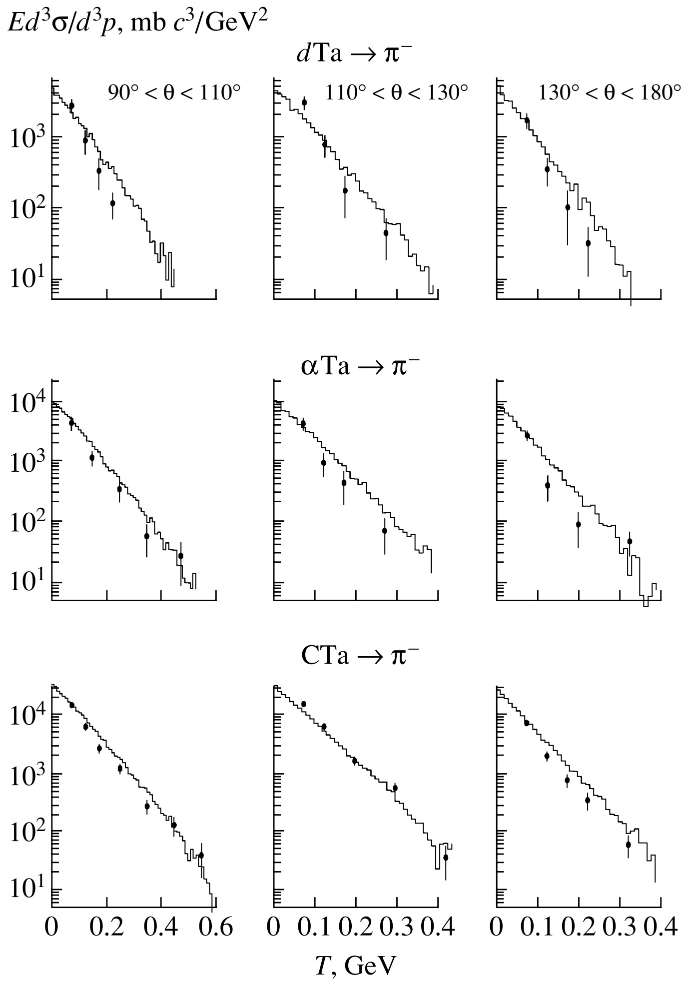

Fig. 2. As in Fig. 1, but for dTa, αTa, and CTa interactions. Points represent experimental data from [25].

Within the approach considered, the similarity of the particle spectra in hA and NN collisions admits a simple explanation. In NN collisions at sufficiently high energies, the spectra in the fragmentation regions do not depend on the interaction energy. In hA collisions, intranuclear nucleons involved in the collision process undergo fragmentation irrespective of the projectile particle—in the same way, as in NN interactions. Since each participant nucleon contributes to the cross section independently and since the average number of these nucleons is $\langle\nu\rangle \sim A^{1/3}$, the cross section is

$$\sigma \sim \langle\nu\rangle\sigma_{hA}^{\text{in}} \sim A^{1/3}A^{2/3} = A^1.$$

In AA interactions, the similarity can take place only if the nucleons of the target nucleus are involved in a single collision. In the interactions between two light nuclei and between light and heavy ones, this is precisely so. It follows that the inclusive cross sections should be proportional to A^1 and that the Glauber approximation (applied to determine the multiplicity of participant nucleons of the target nucleus and the interaction cross sections) is responsible for reproducing the absolute values of the cross sections. Since the analysis of general characteristics of AA interactions in this model leads to underestimating the multiplicity of mesons [28], it is reasonable to suggest that the overestimation of the inclusive cross sections is caused by certain drawbacks of the Glauber approximation.

The spectra of mesons in NN and AA interactions can be treated as similar ones only for a first approximation. A more careful analysis shows that the spectra of mesons produced in NN collisions cannot be described by a simple exponential dependence, but that the spectra of AA collisions are described well by such a dependence. The distinctions between the spectra are caused by features of the proposed interaction mechanism.

Of course, the main distinction between the spectra is associated with the fact that the spectra of

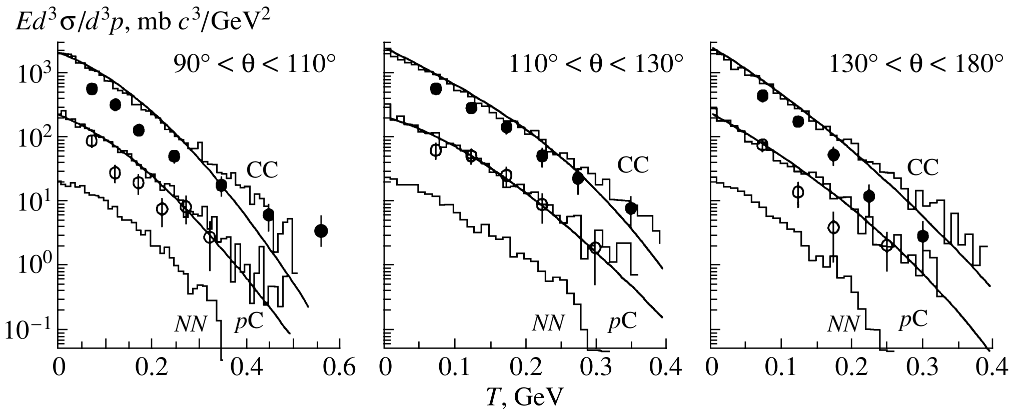

Fig. 3. Invariant inclusive cross sections for π^--meson production in NN, pC, and CC interactions at an energy of 3.36 GeV/nucleon. Points correspond to experimental data from [25]. The curves represent the results of the calculations disregarding the Fermi motion of nucleons.

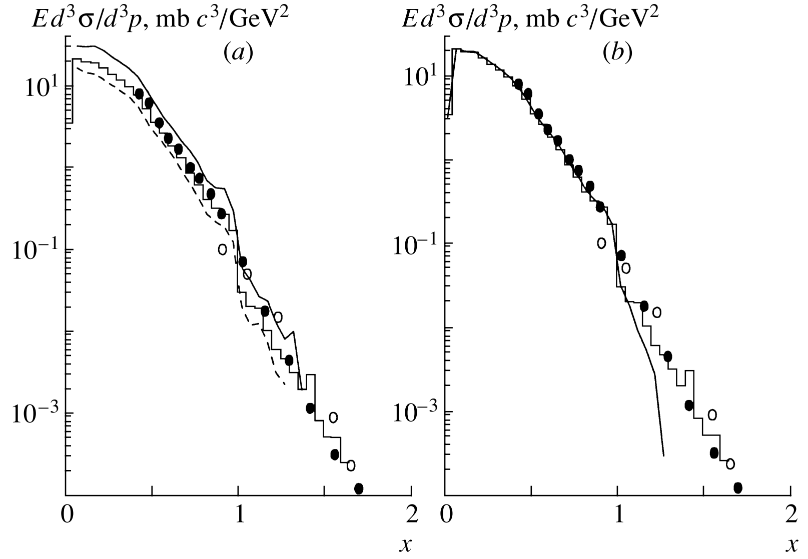

Fig. 4. Invariant inclusive cross sections for π^--meson production in dp interactions. Points correspond to experimental data from [29, 30]; the curves represent the results of our calculation (see main body of the text).

mesons in NN interactions are limited by the accessible kinematical region, while those in AA interactions are not limited by this factor. In the experimental data considered, only the last points lie outside the kinematical region for free NN collisions.

According to Fig. 3, the π^--meson spectra change slightly after taking into account the Fermi motion of nucleons within the kinematical region allowed for NN interactions. The meson yield outside this region, even without taking into account the Fermi motion of nucleons, is described by the nucleon-mass-increasing mechanism. By way of example, we indicate that, in multiple hA interactions, the majority of intranuclear nucleons interact with a fast excited nucleon, which has a mass different from that of the projectile particle. This is the effect that leads to a change in the boundaries of the kinematical region.

3. ANALYSIS OF $d + A \to \pi^-(0°) + X$ PROCESSES AT $P_d = 8.9$ GeV/c

Let us consider the dependence of the particle-production cross section on the mass of the nucleus on which the fragmentation process occurs. In order to do this, we analyze the data from [29] on $d + A \to \pi^-(0°) + X$ reactions at a momentum of $P_d = 8.9$ GeV/c. The experimental data from [29, 30] are presented in Fig. 4 versus the variable x defined as

$$x = \frac{M_N E_{\pi^-} - \frac{1}{2}M_{\pi^-}^2}{E_N M_N - E_N E_{\pi^-} - M_N^2 + P_N P_{\pi^-} \cos\theta_{\pi^-}},$$

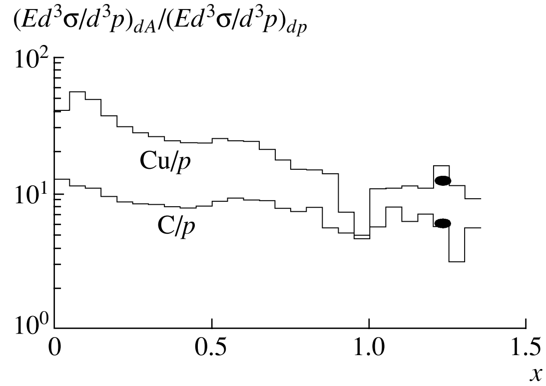

Fig. 5. Ratio of the invariant cross sections for π^--meson production on a nucleus A and on a proton. Points correspond to experimental data from [29].

where M_N, P_N, and E_N are, respectively, the nucleon mass, momentum, and energy; M_{π^-}, P_{π^-}, and E_{π^-} are, respectively, the π^--meson mass, momentum, and energy; θ_{π^-} is the pion emission angle in the laboratory frame; and $P_N = 4.45$ GeV/c.

In Fig. 4a, the solid curve shows the cross sections for the reaction $d + p \to \pi^-(0°) + X$ calculated within the standard version of the model. This curve exhibits an irregularity at $x \sim 1$ caused by the neglect of the Fermi motion of nucleons inside the deuteron (this problem appears to be nontrivial). Outside this region, we see that the shape of the calculated spectrum is similar to that of the experimental distribution, but that there is some overestimation in magnitude.

The simplest way to fit the experimental data is to reduce the calculated cross section for inelastic interactions. An alternative possibility (that is, variation of the FRITIOF model parameters) leads to a change in the spectrum slopes. As an example, the solid curve in Fig. 4b shows the results of the calculation according to the model version that neglects the deexcitation of nucleons. In this case, the only possibility is to reduce the inelastic cross section. For this purpose, we replaced the function g in the Glauber expressions,

$$g(\mathbf{b}) = f_{NN}(\mathbf{b}) + f^*_{NN}(\mathbf{b}) - f_{NN}(\mathbf{b})f^*_{NN}(\mathbf{b}),$$

by

$$g(\mathbf{b}) = \theta(r_{NN} - |\mathbf{b}|), \quad r_{NN} = \sqrt{\sigma/\pi}.$$

Taking σ to be less than $\sigma^{\rm in}_{NN}$ by 50%, we obtained the lower curve in Fig. 4a. The histogram that represents the best fit to the experimental data and which is reproduced in Fig. 4b was calculated with the cross section reduced by 30%. In this way, we achieved a satisfactory description of the dependence of the cross section not only on x, but also on the mass of the nucleus on which the fragmentation process occurs (see Fig. 5).

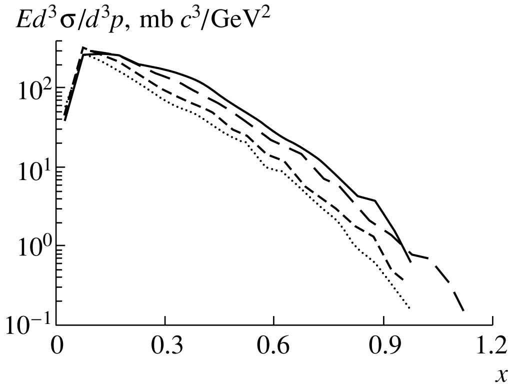

Fig. 6. Invariant cross sections for π^--meson production in dCu interactions featuring various number of collisions inside the nucleus. The solid curve corresponds to single interactions; the long-dashed and short-dashed curves correspond to double and triple ones, respectively; and the dotted curve corresponds to fourfold collisions.

Figure 5 presents the ratio of the calculated cross section for π^--meson production on nucleus A to that on a proton $(Ed^3\sigma/d^3p)_{dA}/(Ed^3\sigma/d^3p)_{dp}$ upon a 30% decrease in $\sigma^{\rm in}$. The points correspond to experimental data from [29] at $x = 1.23$. It is seen that the model version featuring a reduced cross section reproduces the weak dependence of the spectra on the mass of the nucleus on which fragmentation occurs.

Presently, it is not clear what causes the need for reducing the cross section. It could be either a drawback of the Glauber approximation, or an incorrect parametrization of the deuteron wave function [12], or errors in the experimental data. The problem requires a more careful experimental and theoretical consideration. However, even at this stage, we can describe a weak A dependence of the cross section.

In Fig. 6, we present the spectra of π^- mesons in dCu interactions for various numbers of collisions inside the nucleus. In the case of a single interaction, there is naturally no production of cumulative particles. Double collisions make the main contribution at $x > 1$. The contributions of collisions of higher multiplicities are negligible in this region. In the case of double interactions at $x > 1$, dominant processes are those in which one nucleon of the nucleus collides with two nucleons of the deuteron. Within the approximation of a hard projectile nucleus [31], the cross section for such processes is given by the expression

$$E\frac{d^3\sigma}{d^3p} = (E\frac{d^3\sigma}{d^3p})_{dp} \int d^2bT_A(\mathbf{b})e^{-\sigma_{dN}T_A(\mathbf{b})}, x > 1,$$

where T_A is a function of the nucleus thickness. The cross section is proportional to $A^{1/3}$.

It is evident that the double collisions in question occur on the nuclear periphery. However, in contrast

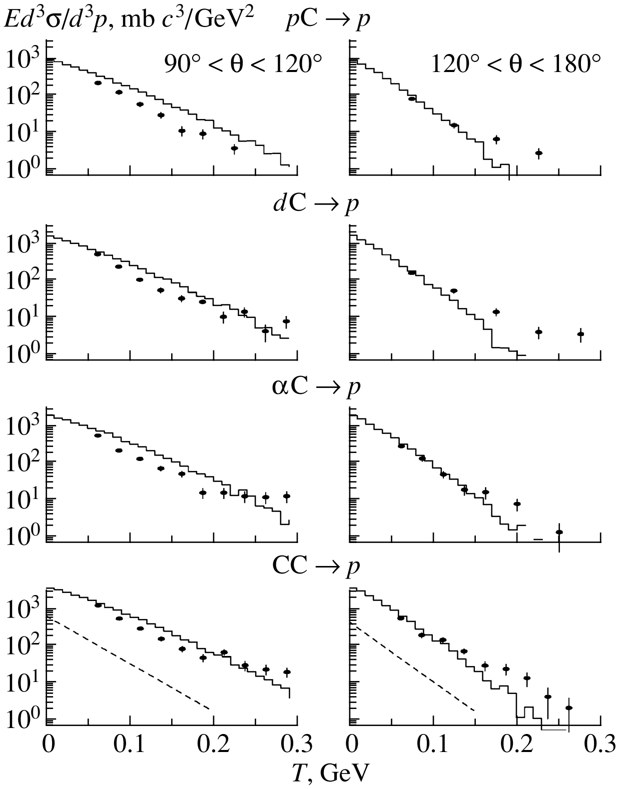

Fig. 7. Invariant cross sections for proton production in AC interactions at a momentum of 4.2 GeV/c per nucleon. Points correspond to experimental data from [32] (see main body of the text).

to the concepts developed in [29], the peripheral character is caused by an increase in the longitudinal momentum of hit nucleons of the deuteron in multiple collisions (this results in the “softness” of the spectrum) rather than by the absence of absorption of projectile deuterons and cumulative mesons in the nucleus. Effectively, multiple interactions can be considered as processes that remove deuterons from the double-collision channel.

Thus, within the approach considered, we can explain the strong dependence of the cross sections for cumulative-particle production on the mass of the nucleus on which the fragmentation process occurs.

4. DESCRIPTION OF THE PROTON SPECTRA

The results of the calculations of the invariant inclusive cross sections for proton production in AA interactions and experimental data from [32] are presented in Fig. 7. It is seen from the figure that the model reproduces the slopes of the experimental spectra in the angular interval $90° \leq \theta < 120°$. In the region $\theta \geq 120°$, the results of the calculations are close to the experimental points for $T \leq 150$ MeV. At greater values of T, there is a systematic distinction between the results of the calculation and the experimental data. The model reproduces the dependence of the cross section on the projectile-nucleus mass. In Fig. 7, the dashed curves correspond to the results of the calculation of the proton spectra in CC interactions that disregards the nucleons involved (that is, $C_{\mathrm{nd}} = 0$). It is seen that, in order to describe the proton yield, it is necessary to go beyond the Glauber approximation in taking into account the breakup of nuclei.

The description of the proton yield in collisions with heavy nuclei requires varying the parameter C_{nd}. In Figs. 8 and 9, we present the experimental data from [33] on the characteristics of protons in nTa and CTa interactions at a momentum of $P = 4.2$ GeV/c per nucleon. In these figures, we also give the results of the calculations (solid curves) with the parameter $C_{\mathrm{nd}} = 0.2$ and, for the sake of comparison, the results of the calculations (dashed curves) within the cascade–evaporation model, where the multiplicity of mesons in CTa interactions is considerably overestimated. It should be noted that, within the FRITIOF model disregarding the elastic rescattering of nucleons, we were unable to describe the proton multiplicities in pC, nTa, CC, and CTa interactions with a constant parameter C_{nd}. Allowance for elastic rescattering enabled us to unify the calculations. However, different target nuclei are to be described with different values of the parameter C_{nd}. Attempts at describing all data with a common parameter C_{nd} failed. Of course, this is a disadvantage of the model. Nevertheless, the chosen value of the parameter enables us to reproduce the soft part of the spectrum of protons emitted into the backward hemisphere.

Figure 10 presents experimental data on the invariant cross sections for proton production in ATa interactions at a momentum of 4.2 GeV/c per nucleon, together with the results of the calculation within the FRITIOF model at $C_{\mathrm{nd}} = 0.2$. It is seen that the model reproduces the slope of the spectrum in the angular interval $90° \leq \theta < 120°$ for the kinetic energy T ranging from zero to 250 MeV and in the interval $120° \leq \theta \leq 180°$ for T values from zero to 150 MeV. In these regions of T, the model leads to a correct dependence on the projectile-nucleus mass.

We emphasize that the experimental distributions change their behavior at high T. The model does not reproduce this effect, although the number of simulated events exceeds experimental statistics by a factor of 10. Apparently, it is necessary to take into account some other proton-production mechanisms.

Analogous results supplementing to those presented above were obtained from an analysis of pC interactions at momenta of $P_p = 18$, 34, and

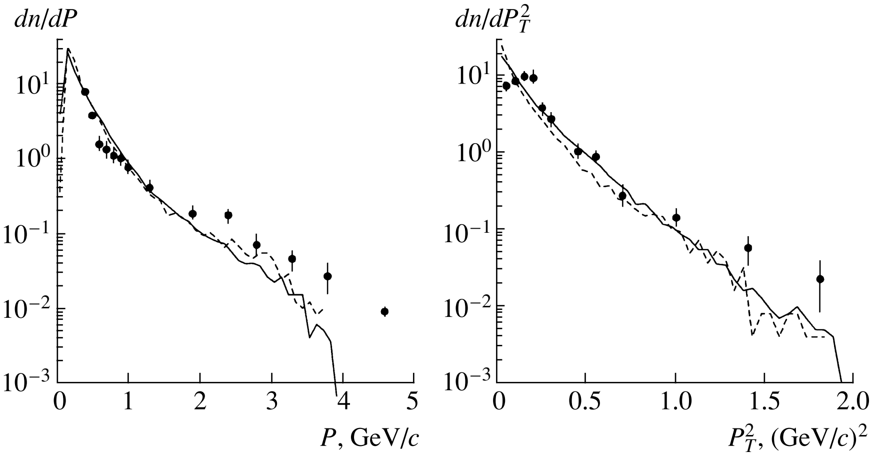

Fig. 8. Total- and transverse-momentum distributions of protons produced in nTa interactions. Points correspond to experimental data from [33]. The dashed and solid curves represent the results of the calculations within the cascade–evaporation and the FRITIOF model, respectively.

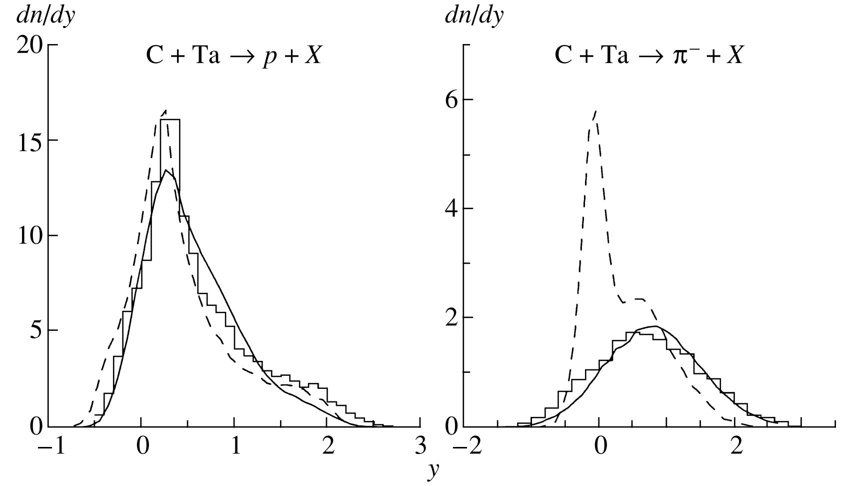

Fig. 9. Rapidity distributions of protons and π^- mesons produced in CTa interactions. The histograms correspond to experimental data from [33]. The dashed and solid curves represent the results of the calculations within the cascade–evaporation and the FRITIOF model, respectively.

57 GeV/c [35] and pC and pTa interactions at $P_p =$ 400 GeV/c [36]. As an example, Fig. 11 shows experimental data and the results of the calculations for $P_p = 400$ GeV/c. The model predicts the production of rather hard mesons and protons. For mesons, the results of the calculations agree with experimental data for $\theta \sim 70^\circ$ and $\theta > 130^\circ$. At $\theta \sim 90^\circ$, the slope of the spectrum exceeds the experimental values. As for protons, the situation is different: the calculated and experimental spectra agree at $\theta \sim 70^\circ$. For larger angles, the calculations reproduce the soft part of the spectrum. The yield of hard protons is underestimated. Moreover, the model does not predict an exponential decrease of the spectra.

The meson spectra, as was shown above, slightly change after taking into account the Fermi motion of nucleons. The spectra and their dependence on the meson emission angle are controlled mainly by the meson-production mechanism—in particular, by the mass-increase mechanism and the mechanism of hit-nucleon fragmentation. Further investigations are to demonstrate which of these is responsible for the angular dependence. It is reasonable to assume that an analysis of the great amount of available experimental data on hA interactions would help to solve this problem.

As to protons, their absolute yield, as mentioned above, is controlled by the nuclear-breakup model, while the spectrum depends on the method for taking into account the Fermi motion of nucleons. Probably, allowances for the interplay of the transverse and

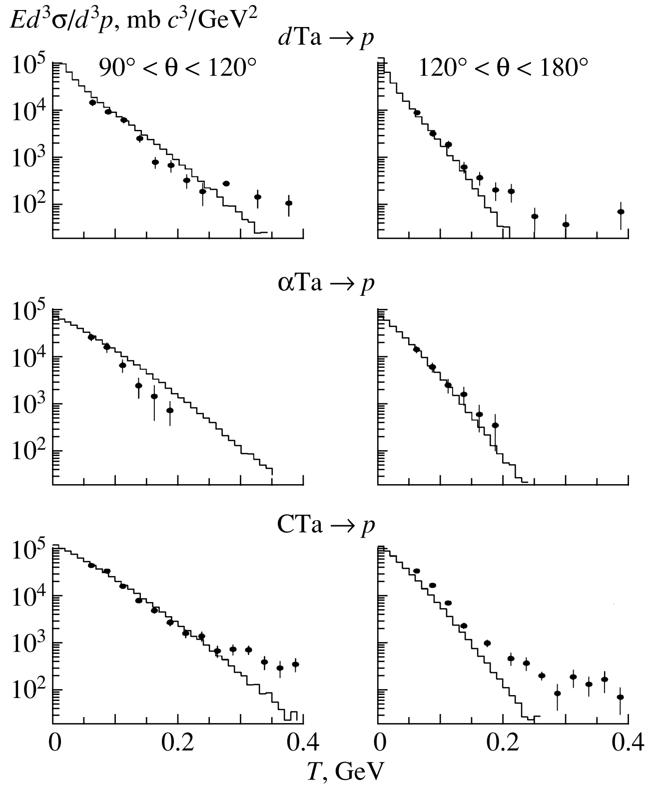

Fig. 10. Invariant cross sections for proton production in ATa interactions at a momentum of 4.2 CeV/c per nucleon. Points represent experimental data from [32].

longitudinal momenta of ejected nucleons would help to improve the model.

Summarizing this consideration, we can conclude that the standard Reggeon model of nuclear breakup does not allow us to describe the proton yield in collisions of light and heavy nuclei with a constant parameter $C_{\rm nd}$. This is probably because of the neglect of a specific structure of light nuclei. However, the method employed to take into account Fermi motion makes it possible to describe the soft part of the spectra of protons emitted into the backward hemisphere. Other approaches are required for describing the hard part of the spectra.

Probably, the most promising way is to take into account the presence of multiquark configurations in nuclei. Here, many problems arise. These include the following: What multiquark bags can appear in nuclei? What is the multiplicity distribution for these bags? What is their spatial distribution? In what way do these bags interact with each other and with the nucleons? All these problems must be solved in constructing the Monte Carlo program. The majority of them were considered in [37].

Komarov and Müller [37] used an uncorrelated nucleon distribution in nuclei and took into account the nucleon core (0.4 fm). By analogy with the majority of approaches, they assumed that nucleons form a flucton if their centers fall within a small volume V_c. The cross section for the interaction of the projectile hadron with a flucton was deduced within the geometric approach. It was suggested that, in a hadron–flucton collision, the excitation-energy transfer to the flucton is distributed as

$$P(-E_{\rm exc}) \propto \exp(-E_{\rm exc}/\langle E_{\rm exc}\rangle),$$
$$0.2 \le E_{\rm exc} \le 3 \text{ GeV}.$$

It was also assumed that the excited flucton decays either into nucleons or into nucleons and one meson, with the matrix element for the decay process being constant. This provides the possibility of reproducing the proton spectra in pA interactions for energies in the range from 0.64 to 400 GeV by using only three parameters: $E_{\rm exc} = 0.14$ GeV; a parameter that specifies the flucton radius, $r_k = k^{1/3} r_c$ (where $r_c = 0.8$ fm and k is the number of nucleons inside the cluster); and the probability of flucton decay via a mesonless channel.

Efremov *et al.* [38] used the standard concept of fluctons that is close to that presented above. However, the decay matrix element was not assumed to be constant—it was constructed according to the model of quark–gluon strings. The consideration in [38] was

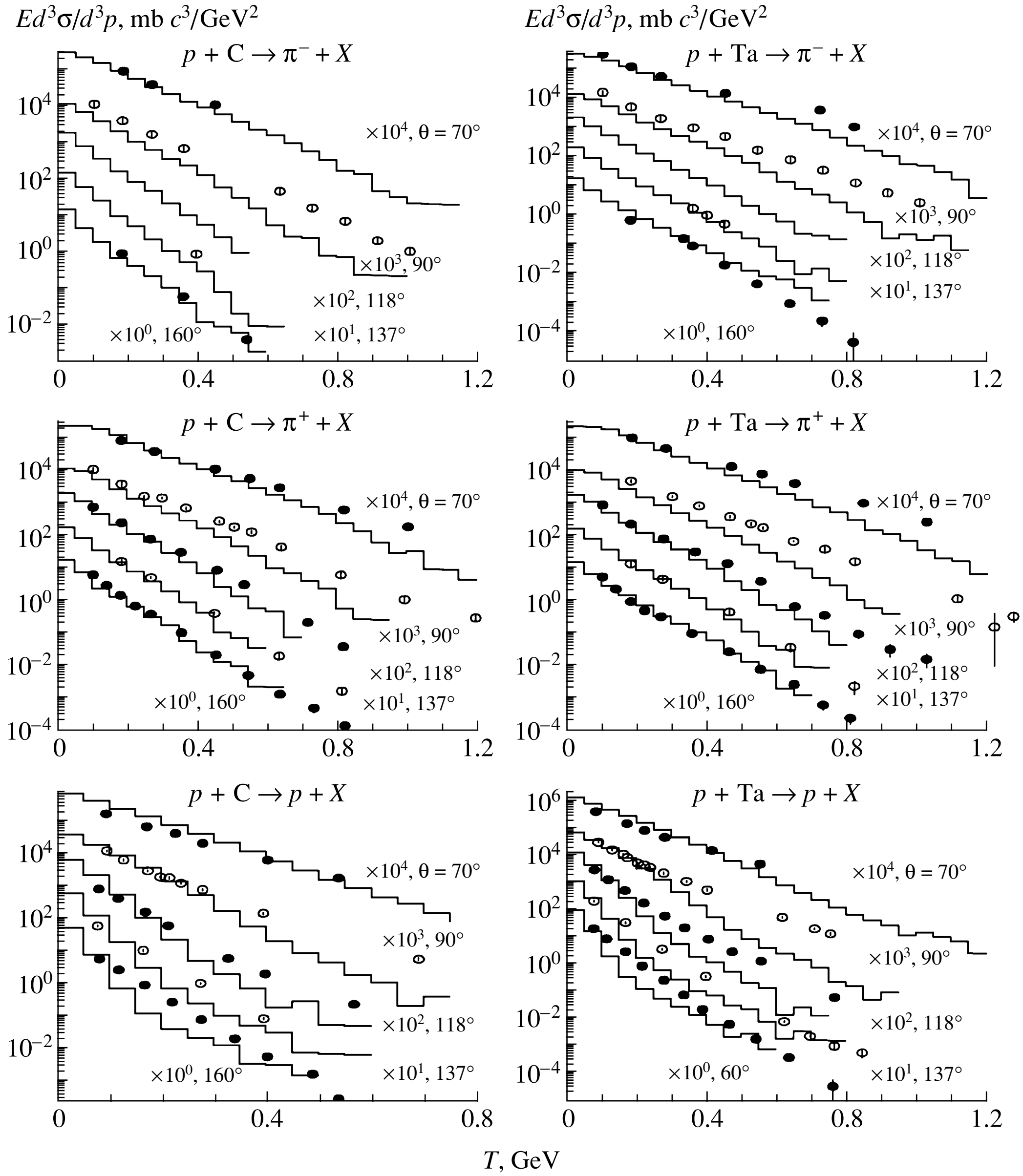

Fig. 11. Invariant cross sections for the production of π^+ mesons and protons in pA interactions at a momentum of 400 GeV/c (the results are normalized to the masses of fragmenting nuclei). Points correspond to experimental data from [36].

restricted to the $\pi^\pm$- and $K^\pm$-meson spectra in pBe interactions at $E = 40$ GeV and to the ratio of the spectra of K^- mesons and antiprotons.

The scheme suggested in [37] can be included in a Monte Carlo program of the FRITIOF type, probably supplemented with the results obtained within the quark–gluon approach [38]. Undoubtedly, this would provide a description of the proton spectra; however, this requires an independent study. Thus, investigation of hard cumulative protons can clarify in general the role of multinucleon configurations in nuclei.

ACKNOWLEDGMENTS

We are grateful to A.G. Litvinenko and V.K. Bondarev for interest in this study.

The work of V.V. Uzhinskii was supported in part by the Russian Foundation for Basic Research, project no. 00-01-00307.

REFERENCES

1. A. M. Baldin, Fiz. Élem. Chastits At. Yadra **8**, 429 (1977) [Sov. J. Part. Nucl. **8**, 175 (1977)].
2. V. S. Stavinskiĭ, Fiz. Élem. Chastits At. Yadra **10**, 949 (1979) [Sov. J. Part. Nucl. **10**, 373 (1979)].

3. V. K. Bondarev, Fiz. Élem. Chastits At. Yadra **28**, 13 (1997) [Phys. Part. Nucl. **28**, 5 (1997)].
4. M. I. Strikman and L. L. Frankfurt, Fiz. Élem. Chastits At. Yadra **11**, 571 (1980) [Sov. J. Part. Nucl. **11**, 221 (1980)]; L. L. Frankfurt and M. I. Strikman, Phys. Rep. **76**, 215 (1981); **160**, 235 (1988).
5. V. K. Luk'yanov and A. I. Titov, Fiz. Élem. Chastits At. Yadra **10**, 815 (1979) [Sov. J. Part. Nucl. **10**, 321 (1979)].
6. B. Z. Kopeliovich and F. Niedermayer, Phys. Lett. B **117B**, 101 (1981); B. Z. Kopeliovich, Yad. Fiz. **39**, 606 (1984) [Sov. J. Nucl. Phys. **39**, 383 (1984)]; B. Z. Kopeliovich and F. Nidermayer, Zh. Éksp. Teor. Fiz. **87**, 1121 (1984) [Sov. Phys. JETP **60**, 640 (1984)].
7. V. B. Kopeliovich, Phys. Rep. **139**, 51 (1986).
8. M. I. Gorenstain, G. M. Zinovjev, and V. P. Shelest, Phys. Lett. B **67B**, 100 (1977); M. I. Gorenshteĭn, G. M. Zinov'ev, and V. P. Shelest, Yad. Fiz. **26**, 788 (1977) [Sov. J. Nucl. Phys. **26**, 414 (1977)].
9. I. G. Bogatskaya *et al.*, Yad. Fiz. **27**, 856 (1978) [Sov. J. Nucl. Phys. **27**, 454 (1978)]; I. G. Bogatskaya *et al.*, Phys. Rev. C **22**, 209 (1980).
10. B. N. Kalinkin and V. L. Shmonin, Phys. Scr. **42**, 393 (1990); B. N. Kalinkin and Yu. F. Gagarin, Phys. Scr. **57**, 621 (1998).
11. W. Czyz and L. C. Maximon, Ann. Phys. (N.Y.) **52**, 59 (1969).
12. S. Yu. Shmakov, V. V. Uzhinskii, and A. M. Zadorojny, Comput. Phys. Commun. **54**, 125 (1989).
13. B. Andersson *et al.*, Nucl. Phys. B **281**, 289 (1987); B. Nilsson-Almquist and E. Stenlund, Comput. Phys. Commun. **43**, 387 (1987).
14. H. Sorge, H. Stöcker, and W. Greiner, Ann. Phys. (N.Y.) **192**, 266 (1989); Nucl. Phys. A **498**, 567 (1989).
15. H. Sorge, A. V. Keitz, R. Mattiello, *et al.*, Z. Phys. C **47**, 629 (1990).
16. H. Sorge, Phys. Rev. C **52**, 3291 (1995); G. Q. Li, C. M. Ko, G. E. Brown, and H. Sorge, Nucl. Phys. A **611**, 539 (1996); R. Mattiello, H. Sorge, H. Stöcker, and W. Greiner, Phys. Rev. C **55**, 1443 (1997).
17. K. Werner, Phys. Rep. **232**, 87 (1993).
18. A. S. Galoyan and V. V. Uzhinskii, Kratk. Soobshch. Ob'edin. Inst. Yad. Issled., No. 2[94]-99, 30 (1999).
19. EMU-01 Collab. (M. I. Adamovich *et al.*), Z. Phys. A **358**, 337 (1997).
20. B. Gankhuyag and V. V. Uzhinskii, Soobshch. Ob'edin. Inst. Yad. Issled., No. R1-97-315 (Dubna, 1997); No. R2-97-397 (Dubna, 1997).
21. V. V. Uzhinskii, Preprint No. E2-96-192, OIYaI (Joint Inst. for Nuclear Research, Dubna, 1996).
22. Kh. El-Waged and V. V. Uzhinskii, Yad. Fiz. **60**, 925 (1997) [Phys. At. Nucl. **60**, 828 (1997)].
23. V. Weisskopf, Phys. Rev. **52**, 295 (1937).
24. V. S. Barashenkov and V. D. Toneev, *Interactions of High-Energy Particles and Nuclei with Nuclei* (Atomizdat, Moscow, 1972).
25. G. N. Agakishiev *et al.*, Yad. Fiz. **55**, 736 (1992) [Sov. J. Nucl. Phys. **55**, 408 (1992)].
26. V. Flaminio *et al.*, Preprint No. 84-01, CERN-HERA (1984).
27. V. V. Uzhinskii and S. Yu. Shmakov, Yad. Fiz. **57**, 1532 (1994) [Phys. At. Nucl. **57**, 1459 (1994)].
28. A. I. Bondarenko, R. A. Bondarenko, A. S. Galoyan, *et al.*, Preprint No. P1-2000-138, OIYaI (Joint Inst. for Nuclear Research, Dubna, 2000); Yad. Fiz. **65**, 95 (2002) [Phys. At. Nucl. **65**, 90 (2002)].
29. Yu. S. Anisimov *et al.*, Yad. Fiz. **60**, 1070 (1997) [Phys. At. Nucl. **60**, 957 (1997)].
30. A. M. Baldin *et al.*, Soobshch. Ob'edin. Inst. Yad. Issled., No. 1-82-28 (Dubna, 1982).
31. G. D. Alkhazov *et al.*, Nucl. Phys. A **280**, 365 (1977); V. S. Barashenkov and Zh. Zh. Musul'manbekov, Preprint No. R2-11453, OIYaI (Joint Inst. for Nuclear Research, Dubna, 1978); Acta Phys. Pol. B **10**, 373 (1979).
32. S. Batskovich *et al.*, Yad. Fiz. **56** (4), 211 (1993) [Phys. At. Nucl. **56**, 540 (1993)].
33. R. N. Bekmirzaev *et al.*, Yad. Fiz. **49**, 488 (1989) [Sov. J. Nucl. Phys. **49**, 305 (1989)].
34. R. N. Bekmirzaev *et al.*, Yad. Fiz. **58**, 1822 (1995) [Phys. At. Nucl. **58**, 1721 (1995)].
35. I. M. Belyaev *et al.*, Yad. Fiz. **56** (10), 135 (1993) [Phys. At. Nucl. **56**, 1378 (1993)].
36. N. A. Nikiforov *et al.*, Phys. Rev. C **22**, 700 (1980); Yu. D. Bayukov *et al.*, Phys. Rev. C **20**, 764 (1979).
37. V. I. Komarov, H. Müller, and S. Tesch, Fortschr. Phys. **33**, 595 (1985).
38. A. V. Efremov, A. B. Kaidalov, G. I. Lykasov, and N. V. Slavin, Yad. Fiz. **57**, 932 (1994) [Phys. At. Nucl. **57**, 874 (1994)].

Translated by O. Chernavskaya

Physics of Atomic Nuclei, Vol. 65, No. 9, 2002, pp. 1733–1742. Translated from Yadernaya Fizika, Vol. 65, No. 9, 2002, pp. 1777–1787.

ELEMENTARY PARTICLES AND FIELDS
Theory

Production and Rescattering of Heavy Quarks in Ultrarelativistic Nucleus–Nucleus Collisions

I. P. Lokhtin[*] **and A. M. Snigirev**

Institute of Nuclear Physics, Moscow State University, Vorob'evy gory, Moscow, 119899 Russia

Received May 21, 2001; in final form, August 28, 2001

Abstract—Contributions of various mechanisms to the heavy-quark-production cross section in ultrarelativistic nucleus–nucleus collisions, including the direct pair production $b\bar{b}$ and $c\bar{c}$ as a result of hard primary collisions and pair production in showers induced by hard-produced partons in the initial and final states, are investigated. The sensitivity of the muon pair spectra with large invariant masses (from semileptonic $B\bar{B}$ decays) and spectra of the secondary J/ψ (from individual B decays) to the multiple scattering and the energy losses of b quarks in dense quark–gluon matter is studied. The formation of such matter is expected in heavy-ion collisions at the LHC. © *2002 MAIK "Nauka/Interperiodica"*.

1. INTRODUCTION

Production of the heavy b and c quarks in high-energy hadron collisions is interesting in view of the possibility of studying the dynamics of the hard processes applicable to the description of the standard and new QCD physics [1–3] of these processes. As is known, the light u, d, and s quarks can be produced as a result of both hard QCD processes and the nonperturbative hadronization or fragmentation of valence quarks—constituents of the initial hadrons. At the same time, since the heavy b and c quarks are absent from the initial flavor content of hadrons and their production in the nonperturbative processes is negligible [1], the production of b and c quarks can be completely described in the QCD perturbation theory provided that the mass of the heavy quark M_Q significantly exceeds the characteristic QCD confinement scale ($M_Q \gg \Lambda_{\rm QCD}$). In this case, the heavy quark production cross section is the product of the parton cross section for $Q\bar{Q}$ pair production and the structure function of the distribution of quarks or gluons, which produce the $Q\bar{Q}$ pairs in their collision.

The specific interest in heavy-quark production in ultrarelativistic nucleus–nucleus collisions is caused mainly by the possibility of studying the behavior (interaction) of the massive color charge in a superheavy QCD matter represented by the quark–gluon plasma (QGP). The search for and characterization of the QGP is one of the most interesting problems in modern high-energy physics (see, e.g., reviews [4–8]). The experimental data obtained on the SPS accelerator in CERN at the c.m. energy $\sqrt{s} \simeq$ 20 GeV per nucleon pair (anomalous suppression of the J/ψ quarkonium production [9], enhanced yield of strange particles [10]) and on the recently commissioned RHIC collider in the Brookhaven National Laboratory at $\sqrt{s} = 130$ GeV per nucleon pair (suppression of hard hadron production [11]) make it possible to assume that the QGP might be produced in the most central heavy-ion collisions (Pb–Pb, Au–Au). However, other interpretations still cannot be excluded [12, 13].

The Large Hadron Collider, which is now under construction in CERN, is expected to provide lead ion interaction at significantly higher energy $\sqrt{s} = 5.5$ TeV per nucleon pair. This may result in the production of virtually "ideal" quark–gluon (or gluon) plasma with an initial energy density significantly exceeding the critical value for the quark–hadron phase transition $\varepsilon_0 \simeq 0.5$ TeV/fm$^3 \gg \varepsilon_{\rm cr} \sim 1$ GeV/fm^3 [14]. In this case, the inclusive cross section for the production of b quarks will be sufficiently high for the systematic study of various aspects of "b physics," while at the RHIC energy we can merely expect to observe effects related to the production of lighter c quarks. The quark pairs produced at the very beginning of nucleus–nucleus collisions as a result of heavy QCD scattering propagate through the dense matter and interact with the medium constituents, thus providing information about the early stages of the matter evolution. We emphasize that partons in the superdense quark–gluon medium ($\rho^{1/3} \gg \Lambda_{\rm QCD}$, where ρ is the particle number density), where the color interaction is screened owing to the collective effects, are asymptotically free. Therefore, it is possible to consider

---

[*] e-mail: `igor@lav01.sinp.msu.ru`

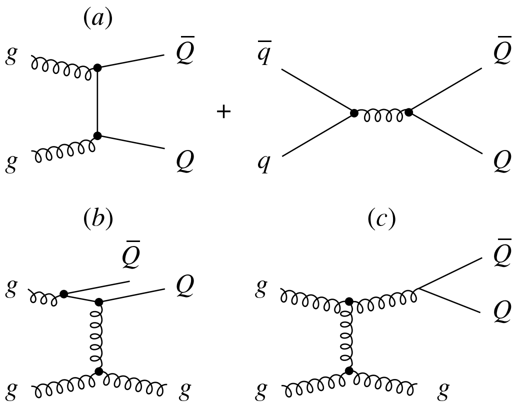

Fig. 1. Examples of the diagrams for various mechanisms of the heavy quark production in the hadron collisions: (*a*) with two heavy quarks ("pair production"); (*b*) with one heavy quark ("flavor excitation"); (*c*) without heavy quarks ("gluon splitting") in the vertices of the hard subprocess.

the problem of hard parton scattering in the QGP within perturbative QCD [15, 16], where the Debye screening mass $\mu_{\rm D}$ is the natural regularization parameter for the parton–parton interaction.

Investigation of the energy loss mechanism for partons in dense QCD matter [17] is a relevant problem. The parton energy losses can be divided into radiative losses related to emission of "bremsstrahlung" gluons [15, 16, 18–21] and collision losses caused by elastic rescattering [22–25]. The rescattering intensity is an increasing function of the temperature (energy density). Therefore, the formation of superdense and "hot" parton matter in heavy-ion collisions (with the initial temperature estimated as $T_0 \sim 1$ GeV at the LHC [14]) should result in significantly greater energy losses for the hard partons as compared to the case of a "cool" nuclear matter or a hadron gas with $T \lesssim 0.2$ GeV. In particular, an interesting prediction related to the coherent nature of the radiation induced by the QCD medium is the dependence of the energy losses per unit length dE/dx on the total distance traveled in the dense medium L and a nontrivial energy dependence of the effect [18, 19]. Experimental study of the L-dependence of the energy losses can be carried out in various bins of the impact parameter of the nucleus–nucleus collision, which determines the effective volume of the dense area of the initial overlap of the nuclei [26].

Considering the possibility of experimental observation of the aforementioned effects, we would like to note that the energy losses of (mainly) gluon jets can lead to suppression of the yield of hard hadron jets [25–27] and hard hadrons [28], while the energy losses of the jets induced mainly by the light u and d quarks result in the p_T disbalance in the $Z+$jet [29] and $\gamma+$jet [30] processes. At the same time, the mass spectrum of muon pairs with large invariant masses from the semileptonic decays of B and D mesons is sensitive to rescattering of the heavy b and c quarks [31–33]. The aforementioned production processes can be investigated in heavy-ion collisions [34] at the LHC with the Compact Muon Solenoid (CMS) detector, which is now under design. The detector is optimized for the precise measurement of characteristics of the high-energy muons, photons, electrons, and hadron jets [35].

The main purpose of this work was to study sensitivity of the mass spectra of the muon pairs with large invariant masses (from semileptonic $B\bar{B}$ decay) and the spectra of the secondary J/ψ (from individual B decays) to the multiple scattering and the energy losses of b quarks from various sources in heavy-ion collisions at the LHC. In Section 2, we analyze various mechanisms of the heavy quark production at the LHC energy and estimate their contributions to the cross section for the kinematic acceptance of the CMS experiment. In Section 3, we consider the difference between the medium-induced gluon radiation of massive quarks and the case of massless quarks. Section 4 briefly describes a model for heavy quark rescattering in the QCD medium. In Section 5, we present and discuss our results. In the Conclusion, we formulate the conclusions of this study.

2. MECHANISMS OF HEAVY QUARK PRODUCTION AND SPECTRA OF MUON PAIRS IN ULTRARELATIVISTIC HEAVY-ION COLLISIONS

The $b\bar{b}$ and $c\bar{c}$ pairs are produced at the very beginning of the nucleus–nucleus collision as a result of hard, mainly gluon–gluon collisions. They propagate through the dense medium and "capture" u, d, or s quarks at the hadronization stage, thus forming B and D mesons. The latter decay into hadrons and leptons in the time period on the order of the mean lifetime ($c\tau_{B^\pm} = 496$ μm, $c\tau_{B^0} = 464$ μm, $c\tau_{D^\pm} = 315$ μm, $c\tau_{D^0} = 124$ μm). In particular, $\approx$20% of B mesons and $\approx$12% of D mesons give muons; approximately one-half of muons from B mesons are produced through the intermediate D mesons [36].

There are several mechanisms for the heavy quark production in high-energy hadron collisions [3]; Fig. 1 displays the corresponding diagrams. Following the classification and terminology of the authors of [3], we distinguish three classes of such processes, depending on the number of the heavy quarks in the vertices of the hard subprocess (2, 1, or 0, respectively):

1. "Pair production," $gg \to Q\bar{Q}$ and $q\bar{q} \to Q\bar{Q}$ in the leading $\mathcal{O}(\alpha_s^2)$ order of the QCD perturbation

theory (Fig. 1*a*) (allowance for the corrections $\mathcal{O}(\alpha_s^3)$ missing from Fig. 1*a* is possible, for example $gg \to Q\bar{Q}g$, $qg \to Q\bar{Q}q$, $q\bar{q} \to Q\bar{Q}g$).

2. "Flavor excitation," whereby one heavy quark is produced in the vertex of the heavy process $Qq \to Qq$ or $Qg \to Qg$, while another heavy quark $\bar{Q}$ is produced as a result of the parton shower in the initial state (Fig. 1*b*).

3. "Gluon splitting," whereby both heavy quarks are produced in the shower induced by the hard-produced gluon in the final state $g \to Q\bar{Q}$ (Fig. 1*c*).

Note that, at an intermediate energy, most of the heavy quarks are produced directly as a result of the hard initial scatterings ("pair production"), while, at the LHC energy, we expect that the contribution from the $Q\bar{Q}$ pairs produced in the parton showers in the initial and final states ("flavor excitation" and "gluon splitting") will dominate (up to 90%). Despite a large probability for the events with high transferred momentum (p_T) to involve at least one $b\bar{b}$ or $c\bar{c}$ pair, most such quarks carry away a small part of the total transverse momentum of the jet. As a result, quarks are concentrated in the region of relatively small invariant masses and p_T. Nevertheless, as we shall see later, even for sufficiently large invariant masses of muon pairs from the decays of heavy quarks

$$M_{\mu^+\mu^-} = \sqrt{(E_{\mu^+} + E_{\mu^-})^2 - (\mathbf{p}_{\mu^+} + \mathbf{p}_{\mu^-})^2},$$

the contributions of the three mechanisms are comparable in order of magnitude.

In order to estimate the spectra of muon pairs from the heavy quarks in Pb–Pb collisions at the LHC, we used the heavy quark production cross section $\sigma_{NN}^{Q\bar{Q}}$ for the nucleon–nucleon interactions at $\sqrt{s} = 5.5$ TeV, their spectra of initial momentum, the hadronization and fragmentation schemes of B and D mesons obtained in the PYTHIA5.7 model [37] with the STEQ2L parametrization of the structure function and included parton showers in the initial and final states, which effectively allow for higher (with respect to α_s) corrections. We used the following masses of b and c quarks: $M_b = 5$ GeV/c^2 and $M_c = 1.35$ GeV/c^2. The corresponding cross sections in Pb–Pb collisions are obtained by multiplying $\sigma_{NN}^{Q\bar{Q}}$ by the number of binary nucleon–nucleon collisions. Then, the initial distribution for the yield of $Q\bar{Q}$ pairs with respect to the impact parameter b of the AA collision assumes the form [26, 38]

$$\frac{d^2\sigma_{AA}^{Q\bar{Q}}}{d^2b}(b,\sqrt{s}) = T_{AA}(b)\sigma_{NN}^{Q\bar{Q}}(\sqrt{s})\frac{d^2\sigma_{AA}^{\text{in}}}{d^2b}(b,\sqrt{s}), \quad (1)$$

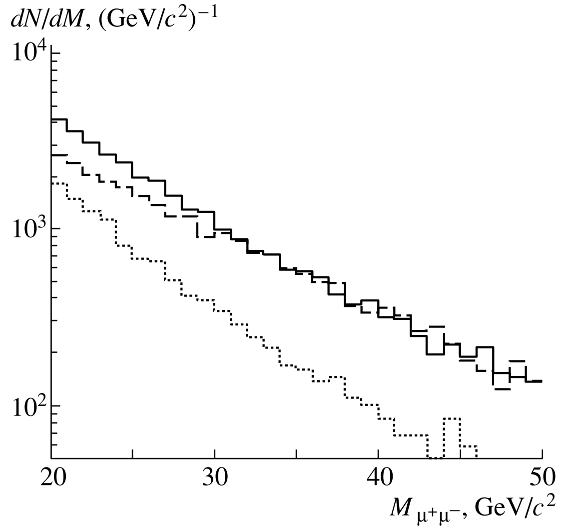

Fig. 2. The initial distribution of $\mu^+\mu^-$ pairs from a correlated semileptonic decay of the $B\bar{B}$ meson pairs with respect to the invariant mass for various b quark production mechanisms: "pair production" (solid histogram), "flavor excitation" (dashed histogram), and "gluon splitting" (dotted histogram); $p_T^\mu > 5$ GeV/c and $|\eta^\mu| < 2.4$. The histograms are normalized to the number of events in the Pb–Pb collisions for two weeks of LHC operation with the luminosity $L = 10^{27}$ cm^{-2} s^{-1}.

where the AA inelastic differential cross section is

$$\frac{d^2\sigma_{AA}^{\text{in}}}{d^2b}(b,\sqrt{s}) = \left[1 - \left(1 - \frac{1}{A^2}T_{AA}(b)\sigma_{NN}^{\text{in}}(\sqrt{s})\right)^{A^2}\right], \quad (2)$$

and the inelastic nondiffraction nucleon–nucleon cross section is $\sigma_{NN}^{\text{in}} \simeq 60$ mb at $\sqrt{s} = 5.5$ TeV. The standard nuclear overlap function is $T_{AA}(b) = \int d^2sT_A(s)T_A(|\mathbf{b} - \mathbf{s}|)$, where $T_A(s) = A\int dz\rho_A(s,z)$ is the nuclear thickness function for the nucleon density in the nucleus $\rho_A(s,z)$ [39]. It should be emphasized that the obtained cross sections $\sigma_{AA}^{Q\bar{Q}} = A^2\sigma_{NN}^{Q\bar{Q}}$ for the quark yield are merely estimates which do not allow for the nuclear effects in the initial ("nuclear screening") and final (rescattering and energy loss) states. We shall consider these effects in Section 5.

Figure 2 displays the initial distribution of $\mu^+\mu^-$ pairs from the dominating source—fragmentation of $b\bar{b}$—with respect to the invariant mass ($M_{\mu^+\mu^-} = 20$–50 GeV/c^2) with allowance for the kinematic acceptance of the CMS experiment at the LHC, $p_T^\mu > 5$ GeV/c and $|\eta^\mu| < 2.4$ [34, 35]. The histograms are normalized to the expected number of events in Pb–Pb collisions for two operation weeks ($R = 1.2 \times 10^6$ s) of the LHC accelerator with the luminosity

$L = 10^{27}$ cm^{-2} s^{-1} [35], that is

$$\int dM \frac{dN_{\mu^+\mu^-}}{dM} = R\sigma_{AA}^{\mu^+\mu^-} L.$$

Figure 2 demonstrates that the contributions from the "pair production" and "flavor excitation" at large invariant masses are approximately equal, while the relative contribution of the "gluon splitting" decreases with increasing M. The cross sections integrated over $M_{\mu^+\mu^-} > 20$ GeV$/c^2$ are 26.5, 20.5, and 9.5 μb for the "pair production," "flavor excitation," and "gluon splitting," respectively. This corresponds to the total numbers of $\mu^+\mu^-$ pairs 3.2×10^4, 2.5×10^4, and 1.15×10^4, respectively, in the mass range $M_{\mu^+\mu^-} =$ 20–50 GeV$/c^2$.

We found that the initial number of $\mu^+\mu^-$ pairs from $c\bar{c}$ decay is lower approximately by a factor of 5 than the signal from $b\bar{b}$. Therefore, hereafter we shall consider only the signal from the dominating channel ($b\bar{b} \to B\bar{B} \to \mu^+\mu^- X$). Moreover, the energy losses of c quarks induced by the medium can significantly exceed the energy losses of b quarks owing to the mass difference (see the next section); this would result in additional suppression of the $c\bar{c} \to \mu^+\mu^-$ yield.

In the analysis of the contribution of background dimuons, we distinguish the correlated and uncorrelated sources. The main uncorrelated background is the direct production of the Drell–Yan muon pairs, $q\bar{q} \to \mu^+\mu^-$, the corresponding production cross section in the kinematic region studied being $\sim$5.5 μb. Such dimuons do not interact with the medium in the final state. The main difference in the production geometry of the Drell–Yan dimuons and those from the decays of B and D mesons is that the former are emitted directly from the primary vertex of the nuclear interaction, while the latter are produced at a certain distance from the primary vertex (at the "secondary vertex") determined by the lifetime and the meson γ-factor. Therefore, it is possible to suppress the yield of the Drell–Yan dimuons by an algorithm of dimuon reconstruction, which uses the tracker information about the position of the secondary vertex of the muon pair [34].

In addition, there is a contribution from the uncorrelated decays of pions and kaons, $\pi^{\pm}, K^{\pm} \to \mu^{\pm}\nu(\bar{\nu})$, and from muon pairs of the "mixed" type (for example, one muon from the hadron decay and another one from $b \to B$, and so on). This contribution is on the same order of magnitude as that from $b\bar{b}$. A standard method for the subtraction of the uncorrelated part of the spectrum uses the spectrum of the muon pair with the same charge sign:

$$\frac{dN^{\text{uncor}}_{\mu^+\mu^-}}{dM} = 2\sqrt{\frac{dN_{\mu^+\mu^+}}{dM}\frac{dN_{\mu^-\mu^-}}{dM}}. \quad (3)$$

One more process that can also give information about the production and rescattering of b quarks in ultrarelativistic collisions of heavy ions is the production of secondary charmoniums. The decay of the B meson gives J/ψ with a probability of 1.15%; the so produced J/ψ decays into a muon pair with a probability of 5.9% [36]:

$$b\bar{b} \to B\bar{B}\,X \to J/\psi\,Y \to \mu^+\mu^- Y.$$

The cross section for the production of the secondary $J/\psi(\to \mu^+\mu^-)$ from the $b\bar{b}$ "pair production" estimated for the same acceptance is $\sim$10.5 μb and reaches only $\approx$17% of the total production cross section for the secondary J/ψ, while the contributions of the "flavor excitation" and "gluon splitting" are approximately equal, being about 25.5 μb each. A difference from the picture of the relative contributions from various mechanisms for the dimuons from the semileptonic decays of $B\bar{B}$ is explained by the fact that, in the case of J/ψ, we consider the region of significantly lower invariant masses, $M_{\mu^+\mu^-} = M_{J/\psi} =$ 3.1 GeV$/c^2$. In this region, the contribution due to the quarks from the parton showers is more significant. At the same time, we emphasize that the spectrum shapes of the secondary J/ψ with respect to the transverse momentum and rapidity are virtually the same for the different sources of b quark production. The reason is that the spectra carry information about the spectra of the individual b quarks, which weakly depend on the production mechanism [3]. Significantly different are the quark–antiquark correlations, which leads to differences in the distributions with respect to the quantities sensitive to the $Q\bar{Q}$ correlation, in particular, with respect to the invariant mass of the muon pair, their azimuthal correlation, and so on.

The main background signal for the production of the secondary J/ψ is the primary J/ψ produced at the first stage of nucleus–nucleus interaction as a result of gluon fission. The estimated initial cross section for the muon production from the primary J/ψ under the same kinematic conditions is $\approx$4 μb. However, the estimate of the actual cross section is a difficult task: on the one hand, the yield of the primary J/ψ might be suppressed owing to the color screening [40] and/or dynamical dissociation [41] in the QGP; on the other hand, the "thermal" models predict a certain additional yield of J/ψ from the QGP (see review [42] and references therein). In some models, the authors assume that J/ψ can be regenerated at the hadron stage as a result of the $D\bar{D}$ interactions [43]. In any case, there is a problem of separating the signals from the primary and secondary J/ψ. The spacetime scale of the primary J/ψ production is significantly smaller than that of the secondary J/ψ produced as a result of the B meson decays. Therefore, the dimuon separation can be performed in the same manner as was suggested for the Drell–Yan dimuons and the dimuons from $B\bar{B}$ fragmentation, that is, using information from the tracking system about the geometric position of the vertex of the muon pair production.

Concluding this section, we emphasize that there are theoretical ambiguities related to the calculation of cross sections for the heavy quark production in nucleon–nucleon collisions at LHC energies. The total cross sections and the corresponding spectra of $\mu^+\mu^-$ pairs depend on the choice of parton structure functions, quark masses, B meson fragmentation schemes, higher (with respect to α_s) corrections to the cross section, and so on. Therefore, it is highly desirable to measure the dimuon spectra at large invariant masses for the secondary J/ψ in pp or dd collisions at the same or close energy per nucleon as that in the case of the heavy-ion collisions.

3. GLUON RADIATION OF HEAVY QUARKS IN A DENSE MEDIUM

As was mentioned in the Introduction, the results of recent investigations of the impact of the coherent effects (QCD analog of the Landau–Pomeranchuk–Migdal effect in QED—the LPM effect) on the spectrum of the gluon radiation induced by the medium [18, 19] are applicable only in the ultrarelativistic limit of massless quarks. Mustafa *et al.* [44] made an attempt to calculate the energy losses of a quark with a nonzero mass M_q; however, in the limit $M_q \to 0$, the obtained dependence of energy losses on the initial quark energy E is qualitatively different from the results of [18, 19]. Thus, the problem of the correct description of the coherent picture of the radiation energy losses by heavy quarks in the entire range of momentum is still unsolved. We can distinguish two limiting cases of the energy losses by heavy quarks. There are grounds to assume that the medium-induced gluon radiation of slow quarks with $p_T \lesssim M_q$ should be suppressed [44]. At the same time, the limiting ultrarelativistic case of $p_T \gg M_q$ corresponds to the gluon radiation of massless quarks.

The approximation used in [44] is based on the factorization of the matrix element into elastic scattering and gluon emission [45], when the distribution with respect to the number of the emitted gluons assumes the form

$$\frac{dN_g}{d\eta d^2q_T} = \frac{3\alpha_s}{\pi^2}\frac{l_T^2}{q_T^2(\mathbf{q}_T - \mathbf{l}_T)^2}, \qquad (4)$$

where $q = (q_0, \mathbf{q}_T, q_3)$ and $l = (l_0, \mathbf{l}_T, l_3)$ correspond to the 4-momenta of the emitted and intermediate gluons, and $\eta = (1/2)\ln\left[(q_0 + q_3)/(q_0 - q_3)\right]$ is the rapidity of the emitted gluon along the momentum direction of the incident quark. Such an approximation is applicable in the limited q_T interval for the low rapidities $\eta \sim 0$ and $l_T(q_0/E) \ll q_T$. The authors of [44] allowed for the coherent LPM effect for the gluons with the formation time below the free path length of the quark in the medium through restricting the emission of such gluons by a step function [16]. However, we have already mentioned that this results in a qualitative difference of the energy dependence of the quark energy losses in the massless limit as compared to that obtained from a more detailed consideration in [18, 19].

In our case, the main contribution to the region of the dimuon invariant masses $M_{\mu^+\mu^-} \gtrsim 20$ GeV$/c^2$ and the secondary J/ψ comes from the b quarks with the "intermediate" values of $p_T \gtrsim 5$ GeV$/c$, the radiation spectrum of which is rather close to the incoherent regime. Hereafter, in order to estimate the sensitivity of the dimuon spectra to the medium-induced effects, we consider two limiting cases: (1) the "minimum" effect with energy losses only by collisions and (2) the "maximum" effect with energy losses by collisions and radiation in the limit of the incoherent radiation with no account for the coherent LPM suppression of radiation (that is, $dE/dx \propto E$ and does not depend on the traveled distance L). In the latter case, we used the Bethe–Heitler cross section obtained in the relativistic kinematics and estimated the medium-induced energy losses by radiation per unit length [19] as the integral over the complete spectrum of emitted gluons:

$$\frac{dE}{dx} = E\rho \int\limits_0^{1-M_q/E} dy \frac{4\alpha_s C_3(y)(4 - 4y + 2y^2)}{9\pi y\left[M_q^2 y^2 + m_g^2(1-y)\right]}, \qquad (5)$$

$$C_3(y) = \frac{9\pi\alpha_s^2 C_{ab}}{4}\left[1 + (1-y)^2 - y^2\right] \times \ln\frac{2\left(\alpha_s^2\rho E y(1-y)\right)^{1/4}}{\mu_{\rm D}},$$

where $m_g \sim 3T$ is the effective "mass" of the emitted gluon at the temperature T; $y = q_0/E$ is the fraction of the initial quark energy carried by the emitted gluon; $\rho \propto T^3$ is the medium density; $\mu_{\rm D}^2 = 4\pi\alpha_s T^2(1 + N_f/6)$ is the squared Debye mass, which regularizes the integral parton scattering cross section at the lower limit; and $C_{ab} = 9/4$, 1, and $4/9$ for gg, gq, and qq scattering, respectively.

4. RESCATTERING OF HEAVY QUARKS IN THE DENSE MEDIUM

We carried out the Monte Carlo modeling of the free path length of b quarks with the mass $M_b =$

5 GeV/c^2 in the expanding QGP produced in Pb–Pb collisions in the region of the initial overlap of the nuclei. In [26], we presented the details of the geometric production model and propagation of the hard parton through the dense matter. In the general case, the rescattering intensity and the energy losses are sensitive to the initial conditions (energy density ε_0 and formation time τ_0) and to the spacetime evolution of the medium, which is described by the equations for the longitudinally expanding quark–gluon liquid, where partons are formed at the hypersurface of the constant proper time $\tau = \sqrt{t^2 - z^2}$ [46].

The rescatterings can be considered as independent [16] when the free path length of the hard parton exceeds the radius of the color screening in the QCD medium, $\lambda \gg \mu_{\rm D}^{-1}$. The transverse (with respect to the collision axis z) distance between two successive collisions in the model, $\Delta x_i = (\tau_{i+1} - \tau_i) v_T = (\tau_{i+1} - \tau_i) p_T / E$, corresponds to the probability density

$$\frac{dP}{d(\Delta x_i)} = \frac{1}{\lambda(\tau_{i+1})} \exp\left(- \int\limits_0^{\Delta x_i} \frac{ds}{\lambda(\tau_i + s)} \right), \quad (6)$$

where the free path length is $\lambda = 1/(\sigma\rho)$. The medium density $\rho(\tau)$ and the cross section for the quark scattering $\sigma(\tau)$ are functions of the proper time. Then, the main kinetic integral equations for the energy loss ΔE as a function of the initial energy E and the covered distance L assumes the form

$$\Delta E(L, E) = \int\limits_0^L dx \frac{dP(x)}{dx} \lambda(x) \frac{dE(x, E)}{dx}, \quad (7)$$

$$\frac{dP(x)}{dx} = \frac{1}{\lambda(x)} \exp\left(-x/\lambda(x)\right),$$

where the current transverse coordinate of the quark $x(\tau)$ is determined from the equation $dx/d\tau = v_T$, and $x = \tau$ at $v_T = 1$.

The dominating contribution to the differential cross section $d\sigma/dt$ for the quark scattering with the energy E and momentum $p = \sqrt{E^2 - M_q^2}$ off the "thermal" parton with the energy (or effective mass) $m_0(\tau) \sim 3T(\tau) \ll E$ at the temperature T can be calculated in the target reference frame as [16, 44]

$$\frac{d\sigma_{ab}}{dt} \simeq C_{ab} \frac{2\pi\alpha_s^2(t)}{t^2} \frac{E^2}{p^2}. \quad (8)$$

The running QCD coupling constant is

$$\alpha_s(t) = \frac{12\pi}{(33 - 2N_f)\ln\left(t/\Lambda_{\rm QCD}^2\right)} \quad (9)$$

for N_f active quark flavors, and the scale QCD parameter $\Lambda_{\rm QCD}$ is on the order of the critical temperature T_c. The integral parton cross section is regularized by the Debye screening mass $\mu_{\rm D}^2$:

$$\sigma_{ab}(\tau) = \int\limits_{\mu_{\rm D}^2}^{t_{\rm max}} dt \frac{d\sigma_{ab}}{dt}, \quad (10)$$

where $t_{\rm max} = [s - (M_q + m_0)^2][s - (M_q - m_0)^2]/s$ and $s = 2m_0 E + m_0^2 + M_q^2$.

In the next ith rescattering with the squared transferred momentum t_i off the accompanying (moving with the same longitudinal rapidity y) medium constituent with the effective mass m_{0i}, the quark loses the transverse energy $\Delta\mathcal{E}_T$ and changes its rapidity by Δy:

$$\Delta\mathcal{E}_T = E_T \quad (11)$$
$$- \sqrt{\left(p_T - \frac{E_T}{p_T}\frac{t_i}{2m_{0i}} - \frac{t_i}{2p_T}\right)^2 + \Delta k_t^2 \sin^2\phi + M_q^2},$$

$$\operatorname{sh}(\Delta y) = \frac{k_t \cos\phi}{E_T - \Delta\mathcal{E}_T}, \quad (12)$$

where the additional (with respect to the current) transverse $\mathbf{p}_T$) momentum

$$\Delta k_t \quad (13)$$
$$= \sqrt{\left(E_T - \frac{t_i}{2m_{0i}}\right)^2 - \left(p_T - \frac{E_T}{p_T}\frac{t_i}{2m_{0i}} - \frac{t_i}{2p_T}\right)^2 - M_q^2},$$

and ϕ is the angle between the direction of the vector $\Delta\mathbf{k}_t$ and the z axis (the distribution is uniform with respect to this angle). The radiation energy losses induced by the medium are calculated through expression (5) without any additional change in the longitudinal rapidity of the quark.

Our calculation used the well known scaling Bjorken solution [46] for the energy density, temperature, and the QGP density:

$$\varepsilon(\tau)\tau^{4/3} = \varepsilon_0 \tau_0^{4/3}, \quad (14)$$

$$T(\tau)\tau^{1/3} = T_0 \tau_0^{1/3}, \quad (15)$$

$$\rho(\tau)\tau = \rho_0 \tau_0. \quad (16)$$

For definiteness, we accepted the initial conditions for the formation of the gluon-excessive plasma, which are expected for the central Pb–Pb collisions at the LHC [14]: $\tau_0 \approx 0.1$ fm/c, $T_0 \approx 1$ GeV, $N_f \approx 0$, $\rho_g \approx 1.95T^3$. We emphasize that the initial energy density ε_0 in the dense area of the nuclear overlap weakly depends on the impact parameter b ($\delta\varepsilon_0/\varepsilon_0 \lesssim 10\%$) at $b \lesssim R_A$, but rapidly decreases for $b \gtrsim R_A$ [26]. At the same time, the distance traveled by a hard parton in the dense medium, averaged over all possible production vertices $\langle L\rangle$, decreases virtually linearly with the b growth. Hence, for the impact parameter $b < R_A$, where $\approx$60% of the heavy quark pairs are produced [34], the difference in the rescattering intensity and the corresponding energy losses is determined mainly by the traveled distance, rather than by different values of the initial energy.

We stopped generation of the quark rescatterings when one of the following conditions become valid:

(1) Quark leaves the dense matter; that is, the traveled distance exceeds the transverse dimension of the dense area from the quark production vertex to the left point. The details of the geometric calculations of these values for the specified value of the impact parameter b can be found in [26].

(2) Plasma is cooled to the critical temperature $T_c = 200$ MeV. Therefore, we neglect the additional small contribution to the energy loss from the quark rescattering in the hadron gas.

(3) Quark loses so much energy that its transverse momentum upon the next scattering becomes lower than the average transverse momentum of the "thermal" constituent of the medium at the temperature T. Such quark becomes a part of the "thermalized" system, and its momentum is generated in the rest frame of the accompanying medium element from the thermal distribution $dN/d^3p \propto \exp(-E/T)$ and transformed to the c.m. frame of the nucleus–nucleus collision [32, 33].

5. MUON PAIR SPECTRA: NUMERICAL RESULTS

In order to estimate the sensitivity of the dimuon spectra to the nuclear effects, we carried out the calculations for four scenarios:

(1) The heavy quark spectra and the corresponding dimuon spectra from the decays of B mesons are linear superpositions of the independent nucleon–nucleon collisions [see expressions (1) and (2)]. In other words, all nuclear effects are switched off and the $Q\bar{Q}$ production cross section in AA collisions integrated over all impact parameters is determined by the corresponding cross section in the nucleon–nucleon collisions just as $\sigma_{AA}^{Q\bar{Q}} = A^2\sigma_{NN}^{Q\bar{Q}}$ (the obtained results correspond to Fig. 2).

(2) We allow for the nuclear effect in the initial state by modifying the nucleon structure functions in the nucleus (nuclear screening) with the phenomenological parametrization suggested by Eskola *et al.* [47]; in this case, $\sigma_{AA}^{Q\bar{Q}} = A^{2\beta}\sigma_{NN}^{Q\bar{Q}}$, where the exponent $\beta(x, Q^2) \le 1$ has a rather complex dependence on the fraction of the carried 4-momentum x and the square of the momentum transferred in the hard subprocess Q^2 involved in the evolution of the structure function [47].

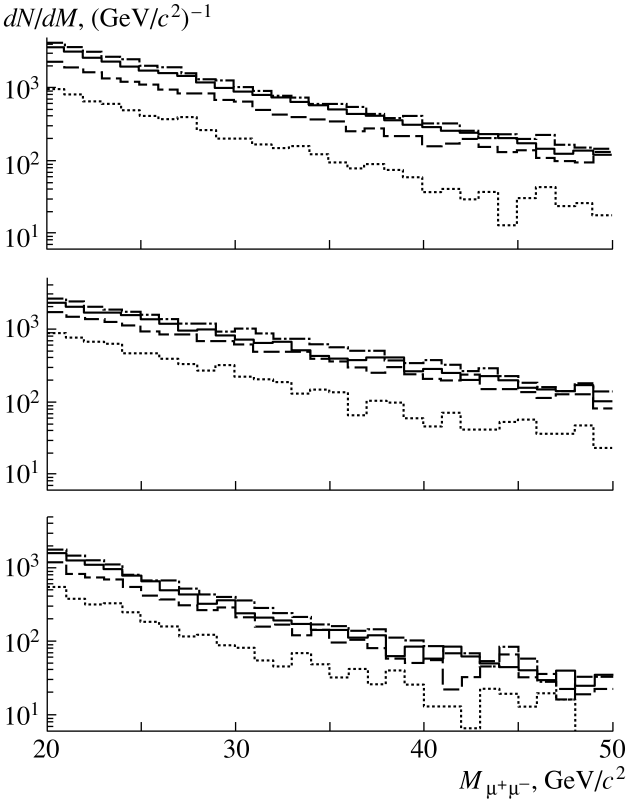

Fig. 3. The distribution of $\mu^+\mu^-$ pairs from a semileptonic decay of the $B\bar{B}$ meson pairs: without nuclear screening and the energy losses of b quarks (dash-dotted histogram); with nuclear screening without energy losses (solid histogram); with nuclear screening and collision energy losses (dashed histograms); with nuclear screening, collision and radiation energy losses (dotted histogram). The three figures stand for various b quark production mechanisms (from above): "pair production," "flavor excitation," and "gluon splitting." The kinematic restrictions and the histogram normalization are the same as in Fig. 2.

(3) In addition to the nuclear screening, we allow for the minimum effect of the quark rescattering in the final state, that is, for the collision energy losses (see Section 4).

(4) In addition to the nuclear screening, we allow for the maximum effect of the quark rescattering in the final state, that is, for the collision and radiation energy losses in the incoherent limit (see Section 3).

Figure 3 shows the distributions of $\mu^+\mu^-$ pairs from various sources of the $b\bar{b}$ pair fragmentation ("pair production," "flavor excitation," "gluon splitting") with respect to the invariant mass $M_{\mu^+\mu^-} \ge 20$ GeV/c^2 (kinematical acceptance $p_T^\mu > 5$ GeV/c,

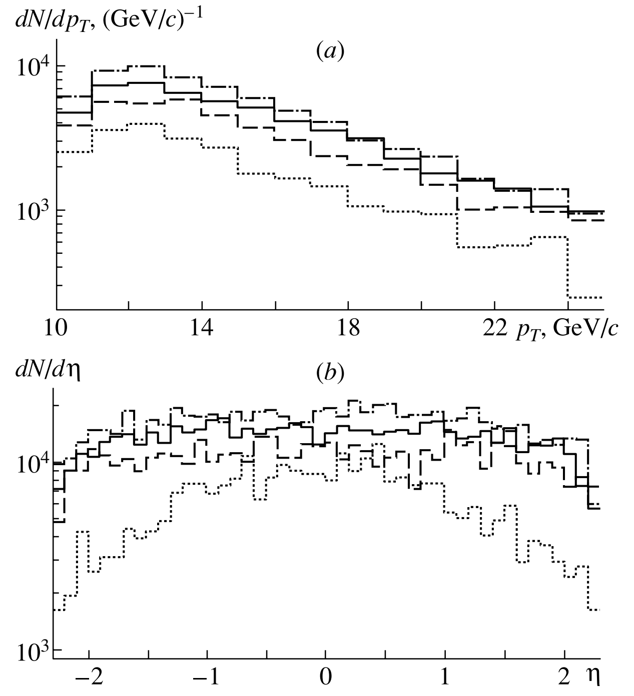

Fig. 4. Total (from all three production mechanisms) distributions of the secondary $J/\psi(\to\mu^+\mu^-)$ from decays of the individual B mesons with respect to (a) the transverse momentum and (b) pseudorapidity. The kinematical restrictions, notation, and histogram normalization is the same as in Fig. 2; the histogram notation is the same as in Fig. 3.

$|\eta^\mu| < 2.4$) for the four scenarios described above. As in Fig. 2, the histograms are normalized to the expected number of events in Pb–Pb collisions for two weeks of LHC operation. For all three sources, the effect of nuclear screening in the considered region is not very significant and results in the weak (about 15%) reduction in the yield of the $\mu^+\mu^-$ pairs. The suppression of the dimuon yield owing to the rescattering and the energy loss is more significant, by a factor of 1.3–1.6 in scenario 3 (only collision energy losses) and by a factor of 3.2–4.2 for scenario 4 (collision and radiation energy losses).

Note that the number of the muon pairs integrated over the whole phase space is, of course, conserved, while the suppression occurs in a restricted phase space owing to the implication of the kinematic restrictions. As the collision energy losses are virtually independent of the initial quark energy, the suppression of the dimuon yield is most significant for relatively low invariant masses. At the same time, the relative contribution of the gluon radiation to the total energy losses increases with growing mass $M_{\mu^+\mu^-}$, because the radiation energy losses are described by an increasing function of the initial quark energy ($\propto E$ in the incoherent limit used in our calculations) and affect the whole interval of the invariant masses, in particular, the most energetic part of the spectrum. The suppression effect for the dimuon yield owing to the energy losses by b quarks is more pronounced for quarks from“pair production” and is less pronounced for quarks from “flavor excitation.” This is related to the difference in the quark–antiquark correlations for various production mechanisms. In particular, the quark distributions from “pair production” with respect to the difference in the transverse momenta and azimuthal angles of the pairs $Q\bar{Q}$ have a pronounced maximum at $\Delta p_T = 0$ and $\Delta\varphi = \pi$. That is, such pairs have a strong azimuthal “backward–backward” correlation and mutually compensating p_T, while the distribution of the quark pairs with respect to Δp_T and $\Delta\varphi$ for other mechanisms is smoother [3].

The quantitative picture of the suppression of the secondary J/ψ from the decays of individual B mesons is somewhat different from the suppression picture for the dimuons from a correlated semileptonic decay of $B\bar{B}$ meson pairs. As the spectra of the secondary J/ψ carry information about the spectra of individual b quarks, which are virtually the same for various production mechanisms [3], the suppression factor of the secondary J/ψ is virtually the same for the considered production mechanisms and reaches $\approx$1.3 in the case of collision losses and $\approx$2.2 in the case of collision and radiation losses. Figure 4 displays the total (for all three production mechanisms) distributions of the secondary $J/\psi(\to\mu^+\mu^-)$ with respect to the transverse momentum and the pseudorapidity for the indicated model scenarios and the kinematic conditions. The lower sensitivity of the yield of the secondary J/ψ to the rescattering and the energy loss of b quarks as compared to the large-mass dimuons is explained by the fact that the secondary J/ψ reproduce the information about only one b quark from the pair. Indeed, according to the geometry, there exists (and is determined by the position of the production vertex of the quark pair) sufficiently large probability for one quark to (virtually) avoid the rescattering and not (virtually) lose energy. At the same time, the probability that both quarks will lose a small part of the energy is close to zero, in particular, in the case of their strong azimuthal correlation. We also emphasize that the effect of nuclear screening is somewhat more significant for the secondary J/ψ from “pair production” ($\approx$25%) than for the secondary J/ψ from the shower production mechanisms of b quarks and dimuons with large invariant masses ($\approx$15%). This is related to a stronger nuclear screening for the lower values of x and Q^2 involved in the evolution of the structure function.

6. CONCLUSION

We considered various mechanisms of heavy quark production in ultrarelativistic nucleus–nucleus collisions, including direct pair production as a result of hard initial collisions and in showers induced by hard-produced partons in the initial and final states. Various mechanisms can be classified according to the number of heavy quarks present in the vertices of the hard subprocess (2, 1, or 0, respectively). The processes that can give information about the production of heavy quarks in hadron–hadron and nucleus–nucleus interaction are the production of $\mu^+\mu^-$ pairs with large invariant masses ($M_{\mu^+\mu^-} \gtrsim 20$ GeV/c^2) from correlated semileptonic decays of meson pairs (predominantly $B\bar{B}$), and the production of secondary $J/\psi(\to \mu^+\mu^-)$ from the decays of individual B mesons. Most the "shower" b quarks are concentrated in the region of relatively small invariant masses and p_T. Despite this, at the LHC energy they give the contribution to the dimuon spectra at large invariant masses on the same order of magnitude as that of the b quarks produced directly in result of the hard subprocesses; the contribution of the shower b quarks to the spectra of the secondary J/ψ is the dominating contribution.

We studied sensitivity of the muon pair spectra with large invariant masses and the spectra of the secondary J/ψ to multiple scattering and energy losses by b quarks owing to various sources in hot gluon matter, which is expected to appear in heavy-ion collisions at the LHC. The problem of correct description of the coherent picture of the radiation energy losses by heavy quarks is still unsolved. Therefore, in our numerical calculations, we considered two limiting cases: minimum effect with energy losses only by collisions and maximum effect with collision and radiation energy losses in the incoherent limit.

We found that the rescattering and the collision energy losses of b quarks induced by the dense medium can reduce the yield of $\mu^+\mu^-$ pairs in the interval of the invariant mass $20 < M_{\mu^+\mu^-} < 50$ GeV/c^2 by a factor of 1.3–1.6 (depending on the quark production mechanism), while the additional allowance for the radiation energy losses can suppress such dimuons by a factor of 3.2–4.2. The relative contribution of the radiation energy losses to the suppression of the dimuons from $B\bar{B}$ decay increases with the invariant mass and p_T owing to more pronounced energy dependence of the radiation energy losses compared to the collision losses. The dimuon spectra from the $b\bar{b}$ pairs produced directly in the primary hard collisions are slightly more sensitive to the energy losses as compared to the shower pairs. The reason is that the former pairs feature strong "backward–backward" correlation and mutually compensating p_T. The effect of nuclear screening in the indicated mass region is not very significant and results in a weak (on a level of $\approx 15\%$) suppression of the yield of $\mu^+\mu^-$ pairs.

The spectra of the secondary J/ψ carry information about the medium-induced energy losses of only one b quark from the pair. As a result, the corresponding suppression factor is lower than that for dimuons from $b\bar{b}$ fragmentation and varies from ≈ 1.3 (with only collision losses) to ≈ 2.2 (with collision and radiation losses), irrespectively of the quark production mechanism. At the same time, the effect of nuclear screening on the yield of the secondary J/ψ from "pair production" is somewhat more significant ($\approx 25\%$) compared to the case of the secondary J/ψ from the shower production mechanism of b quarks and heavy-mass dimuons. This is related to a stronger nuclear screening for the lower values of x and Q^2 involved in the evolution of the structure function. We assume that the future experimental comparison of the yields of the heavy-mass dimuons and secondary J/ψ can help to clarify the nature of the effects under consideration.

We also emphasize that the experimental resolution of the dimuon signal from $B\bar{B}$ decay and from direct Drell–Yan dimuons, as well as dimuons from the primary and secondary J/ψ, can be carried out using information from the tracking system about the geometric position of the muon pair production vertex.

Thus, the dimuon spectra are sensitive to the rescattering and energy losses of heavy quarks in dense QCD matter. These effects exceed the effect of nuclear screening and suppress the yield of $\mu^+\mu^-$ pairs with large invariant masses and secondary J/ψ in heavy-ion collisions as compared to the yields expected from the picture of independent nucleon–nucleon collisions. However, there are theoretical ambiguities related to the calculation of the production cross sections and the spectra of heavy quarks in nucleon–nucleon collisions at LHC energies. Therefore, it is desirable to carry out measurements in pp or dd collisions at the same or higher energy per nucleon that for heavy-ion collisions.

ACKNOWLEDGMENTS

The authors are grateful to E.E. Boos, U. Wiedemann, R. Vogt, D. Denegri, R. Kvatadze, O.L. Kodolova, L.I. Sarycheva, and S.V. Shmatov for fruitful discussions.

REFERENCES

1. B. Andersson, G. Gustafson, G. Ingelman, and T. Söstrand, Phys. Rep. **97**, 31 (1983).
2. A. V. Berezhnoĭ, V. V. Kiselev, and A. K. Likhoded, Yad. Fiz. **60**, 353 (1997) [Phys. At. Nucl. **60**, 289 (1997)]; **61**, 302 (1998) [**61**, 252 (1998)].
3. E. Norrbin and T. Sjöstrand, Eur. Phys. J. C **17**, 137 (2000).
4. H. Satz, Phys. Rep. **88**, 349 (1982).
5. I. L. Rozental' and Yu. A. Tarasov, Usp. Fiz. Nauk **163** (7), 29 (1993) [Phys. Usp. **36**, 572 (1993)].
6. J. W. Harris and B. Müller, Annu. Rev. Nucl. Part. Sci. **46**, 71 (1996).
7. I. P. Lokhtin, L. I. Sarycheva, and A. M. Snigirev, Fiz. Élem. Chastits At. Yadra **30**, 660 (1999) [Phys. Part. Nucl. **30**, 279 (1999)].
8. S. A. Bass, M. Gyulassy, H. Stocker, and W. Greiner, J. Phys. G **25**, R1 (1999).
9. M. C. Abreu *et al.* (NA 50 Collab.), Phys. Lett. B **410**, 337 (1997); **450**, 456 (1999).
10. S. Margetis *et al.* (NA 49 Collab.), Heavy Ion Phys. **4**, 63 (1996); F. Antinori *et al.* (WA 97 Collab.), J. Phys. G **25**, 423 (1999).
11. B. B. Back *et al.* (PHOBOS Collab.), Phys. Rev. Lett. **85**, 3100 (2000); K. Adcox *et al.* (PHENIX Collab.), nucl-ex/0012008.
12. *Proceedings of 14th International Conference on Ultrarelativistic Nucleus—Nucleus Collisions "Quark Matter'99," Torino, Italy, 1999,* Nucl. Phys. A **661** (1999).
13. *Proceedings of 15th International Conference on Ultrarelativistic Nucleus—Nucleus Collisions "Quark Matter'2001," New York, USA, 2001*, Nucl. Phys. A **698** (2002).
14. K. J. Eskola, K. Kajantie, and P. V. Ruuskanen, Phys. Lett. B **332**, 191 (1994); Eur. Phys. J. C **1**, 627 (1998); K. J. Eskola, Prog. Theor. Phys. Suppl. **129**, 1 (1997); Comments Nucl. Part. Phys. **22**, 185 (1998); K. J. Eskola and K. Tuominen, Phys. Lett. B **489**, 329 (2000); K. J. Eskola, K. Kajantie, P. V. Ruuskanen, and K. Tuominen, Nucl. Phys. B **570**, 379 (2000).
15. M. G. Ryskin, Yad. Fiz. **52**, 219 (1990) [Sov. J. Nucl. Phys. **52**, 139 (1990)].
16. M. Gyulassy and X.-N. Wang, Nucl. Phys. B **420**, 583 (1994); M. Gyulassy, M. Plümer, and X.-N. Wang, Phys. Rev. D **51**, 3436 (1995).
17. R. Baier, D. Schiff, and B. G. Zakharov, Annu. Rev. Nucl. Part. Sci. **50**, 37 (2000).
18. R. Baier *et al.*, Phys. Lett B **345**, 277 (1995); Nucl. Phys. B **483**, 291 (1997); **531**, 403 (1998); Phys. Rev. C **58**, 1706 (1998).
19. B. G. Zakharov, Pis'ma Zh. Éksp. Teor. Fiz. **64**, 737 (1996) [JETP Lett. **64**, 781 (1996)]; Pis'ma Zh. Éksp. Teor. Fiz. **65**, 585 (1997) [JETP Lett. **65**, 615 (1997)]; B. G. Zakharov, Yad. Fiz. **61**, 924 (1998) [Phys. At. Nucl. **61**, 838 (1998)]; B. G. Zakharov, Pis'ma Zh. Éksp. Teor. Fiz. **70**, 181 (1999) [JETP Lett. **70**, 176 (1999)].
20. U. Wiedemann and M. Gyulassy, Nucl. Phys. B **560**, 345 (1999); U. Wiedemann, Nucl. Phys. B **588**, 303 (2000); hep-ph/0008241.
21. M. Gyulassy, P. Levai, and I. Vitev, Nucl. Phys. B **594**, 371 (2001).
22. J. D. Bjorken, Fermilab Preprint 82/29-THY (1982).
23. S. Mrówczyński, Phys. Lett. B **269**, 383 (1991).
24. M. Thoma, Phys. Lett. B **273**, 128 (1991).
25. I. P. Lokhtin and A. M. Snigirev, Yad. Fiz. **60**, 360 (1997) [Phys. At. Nucl. **60**, 295 (1997)].
26. I. P. Lokhtin and A. M. Snigirev, Yad. Fiz. **64**, 1563 (2001) [Phys. At. Nucl. **64**, 1487 (2001)].
27. M. Gyulassy and M. Plumer, Phys. Lett. B **243**, 432 (1990).
28. M. Gyulassy and X.-N. Wang, Phys. Rev. Lett. **68**, 1480 (1992).
29. V. Kartvelishvili, R. Kvatadze, and R. Shanidze, Phys. Lett. B **356**, 589 (1995).
30. X.-N. Wang, Z. Huang, and I. Sarcevic, Phys. Rev. Lett. **77**, 231 (1996); X.-N. Wang and Z. Huang, Phys. Rev. C **55**, 3047 (1997).
31. E. Shuryak, Phys. Rev. C **55**, 961 (1997).
32. Z. Lin, R. Vogt, and X.-N. Wang, Phys. Rev. C **57**, 899 (1998); Z. Lin and R. Vogt, Nucl. Phys. B **544**, 339 (1999).
33. B. Kampfer, O. P. Pavlenko, and K. Gallmeister, Phys. Lett. B **419**, 412 (1998).
34. M. Bedjidian *et al.*, *Heavy Ion Physics Programme in CMS,* CERN CMS Note 2000/060.
35. CMS Collaboration Technical Proposal, CERN/LHCC 94-38 (1994).
36. Particle Data Group (D. E. Groom *et al.*), Eur. Phys. J. C **15**, 1 (2000).
37. T. Sjostrand, Comput. Phys. Commun. **82**, 74 (1994).
38. R. Vogt, Heavy Ion Phys. **9**, 339 (1999).
39. C. W. de Jager, H. de Vries, and C. de Vries, At. Data Nucl. Data Tables **14**, 485 (1974).
40. T. Matsui and H. Satz, Phys. Lett. B **178**, 416 (1986).
41. D. Kharzeev and H. Satz, Phys. Lett. B **334**, 155 (1994).
42. R. Vogt, Phys. Rep. **310**, 197 (1999).
43. P. Braun-Munzinger and K. Redlich, Eur. Phys. J. C **16**, 519 (2000).
44. M. G. Mustafa, D. Pal, D. K. Srivastava, and M. Thoma, Phys. Lett. B **428**, 234 (1998).
45. J. F. Gunion and G. Bertch, Phys. Rev. D **25**, 746 (1982).
46. J. D. Bjorken, Phys. Rev. D **27**, 140 (1983).
47. K. J. Eskola, V. J. Kolhinen, and C. A. Salgado, Eur. Phys. J. C **9**, 61 (1999).

Translated by M. Kobrinsky

Physics of Atomic Nuclei, Vol. 65, No. 9, 2002, pp. 1743–1745. From Yadernaya Fizika, Vol. 65, No. 9, 2002, pp. 1788–1790.
Original English Text Copyright © 2002 by Shabalin.

ELEMENTARY PARTICLES AND FIELDS
Theory

The Role of the Intermediate Resonance $a_0(980)$ in the Decay $\eta \to \pi\gamma\gamma$ *

E. P. Shabalin

Institute of Theoretical and Experimental Physics, Bol'shaya Cheremushkinskaya ul. 25, Moscow, 117259 Russia

Received December 4, 2000; in final form, August 6, 2001

Abstract—It is shown that if the $a_0(980)$ boson is the scalar chiral partner of a π meson, its contribution to the transition $\eta \to \pi\gamma\gamma$ has a value comparable to that originated by vector meson exchange. Together, these two mechanisms give the decay probability consistent with the experimental observation.

For the decay $\eta \to \pi\gamma\gamma$, the measured width [1]

$$\Gamma^{\mathrm{exp}}(\eta \to \pi\gamma\gamma) = 0.84 \pm 0.19 \ \mathrm{eV} \tag{1}$$

is twice that predicted by chiral perturbation theory (ChPT) in the leading $1/N_c$ approximation,

$$\Gamma^{\mathrm{ChPT}}(\eta \to \pi\gamma\gamma) = 0.42 \pm 0.20 \ \mathrm{eV} \quad [2], \tag{2}$$

and is more than twice that predicted by the Vector Meson Dominance (VMD) model:

$$\Gamma^{\mathrm{VMD}}(\eta \to \pi\gamma\gamma) = \begin{cases} 0.31 \ \mathrm{eV} & [2], \\ 0.30^{+0.16}_{-0.13} \ \mathrm{eV} & [3]. \end{cases} \tag{3}$$

Note that the mean value of $\Gamma^{\mathrm{ChPT}} = 0.42$ eV turns out to be slightly larger than what follows from the data [1] for the rates of $\rho \to \pi\gamma$, $\rho \to \eta\gamma$, and $\omega \to \eta\gamma$ decays. This point will be elucidated later.

Incorporation of the C-odd axial-vector resonances makes an additional contribution of 0.07 eV to $\Gamma(\eta \to \pi\gamma\gamma)$ [4] and does not change the situation. Therefore, some other contributions are necessary.

The purpose of this paper is to show that, if the $a_0(980)$ boson is the scalar partner of a π meson, its contribution to $\eta \to \pi\gamma\gamma$ decay is much larger than that estimated in [2, 3] and eliminates a disagreement between the experimental and theoretical widths. The main feature of the present calculation is the theoretically reasonable definition of the coupling constants $g_{a_0\eta\pi}$ and $g_{a_0\gamma\gamma}$, which turn out to be considerably larger than the ones in [2, 3]. Before discussing this point, let us represent formulas allowing one to separate out the a_0 contribution to Γ.

The most general form of the gauge invariant matrix element of the decay $\eta(p) \to \pi(k)\gamma(q_1)\gamma(q_2)$ is

$$M = \epsilon_\mu(q_1)\epsilon_\nu(q_2)M_{\mu\nu}, \tag{4}$$

where [5]

$$M_{\mu\nu} = A[q_{1\nu}q_{2\mu} - (q_1q_2)\delta_{\mu\nu}] + B[-(pq_1)(pq_2)\delta_{\mu\nu} - (q_1q_2)p_\mu p_\nu + (pq_1)q_{2\mu}p_\nu + (pq_2)q_{1\nu}p_\mu] \tag{5}$$

and

$$A_{\mathrm{VMD}} = \sum_{V=\rho,\omega,\phi} g_{V\eta\gamma}g^*_{V\pi\gamma} \times \left\{ \frac{p(p-q_1)}{M_V^2 - (p-q_1)^2} + \frac{p(p-q_2)}{M_V^2 - (p-q_2)^2} \right\}, \tag{6}$$

$$B_{\mathrm{VMD}} = -\sum_{V=\rho,\omega,\phi} g_{V\eta\gamma}g^*_{V\pi\gamma} \times \left\{ \frac{1}{M_V^2 - (p-q_1)^2} + \frac{1}{M_V^2 - (p-q_2)^2} \right\}, \tag{7}$$

$$A_{a_0} = \frac{g_{a\eta\pi}g_{a\gamma\gamma}}{M_a^2 - (q_1+q_2)^2}. \tag{8}$$

Using the approximation $M_V = M_\rho \simeq M_\omega$ and neglecting the ϕ-exchange contribution, we come to the following expression for the total width:

$$\Gamma = \Gamma^{\mathrm{VMD}} + (1024\pi^3 m_\eta^3)^{-1} \int\limits_0^{(m_\eta - m_\pi)^2} s^2 f(s) \times \left[A_{a_0}^2 + 2A_{a_0} \left(\sum_{V=\rho,\omega} g_{V\eta\gamma}g^*_{V\pi\gamma} \right) \times \left(1 - \frac{M_\rho^2}{f(s)} \ln \frac{2M_\rho^2 - m_\eta^2 - m_\pi^2 + s + f(s)}{2M_\rho^2 - m_\eta^2 - m_\pi^2 + s - f(s)} \right) \right] ds, \tag{9}$$

where $s = (q_1+q_2)^2$ and $f(s) = [(m_\eta^2 + m_\pi^2 - s)^2 - 4m_\eta^2 m_\pi^2]^{1/2}$. The constants $g_{VP\gamma}$ can be evaluated from the data for the rates of $V \to P\gamma$ decays:

$$g^2_{VP\gamma} = \frac{96\pi\Gamma_{VP\gamma}}{M_V^3(1 - m_P^2/M_V^2)^3}; \tag{10}$$

---

[*] This article was submitted by the author in English.

1063-7788/02/6509-1743$22.00 © 2002 MAIK "Nauka/Interperiodica"

The constants $g_{VP\gamma}$ predicted by the theory with $\theta_P = -\arcsin(1/3)$ and the ones evaluated from the data [1] for the $V \to P\gamma$-decay rates

$g^{\rm th}_{VP\gamma}(\sin\theta_P = -1/3)$	$g^{\rm th}_{VP\gamma}$, 10^{-4}/MeV	$g^{\rm exp}_{VP\gamma}$, 10^{-4}/MeV
$g_{\omega\pi\gamma}$ (input)	$7.04(1 \pm 0.03)$ (input)	$7.04(1 \pm 0.03)$
$g_{\omega\eta\gamma} = \sqrt{\frac{2}{27}} g_{\omega\pi\gamma}$	$1.915(1 \pm 0.03)$	$1.61(1 \pm 0.08)$
$g_{\rho\pi\gamma} = \frac{1}{3} g_{\omega\pi\gamma}$	$2.35(1 \pm 0.03)$	$2.72(1^{+0.12}_{-0.13})$
$g_{\rho\eta\gamma} = \sqrt{\frac{2}{3}} g_{\omega\pi\gamma}$	$5.74(1 \pm 0.03)$	$4.42(1^{+0.17}_{-0.21})$

some of them turn out to be smaller than those theoretically expected for the case

$$\eta = \eta_8 \cos\theta_P - \eta_0 \sin\theta_P = \frac{u\bar{u} + d\bar{d} - s\bar{s}}{\sqrt{3}} \tag{11}$$

considered in [2] and corresponding to $\sin\theta_P = -1/3$ (that is, $\theta_P \approx -20°$). The table illustrates the situation. Using the magnitudes of $g_{VP\gamma}$ from the table, we find

$$\left(\sum_{V=\rho,\omega} g_{V\eta\gamma} g^*_{V\pi\gamma}\right)^{\rm exp} \Bigg/ \left(\sum_{V=\rho,\omega} g_{V\eta\gamma} g^*_{V\pi\gamma}\right)^{\rm th} \tag{12}$$
$$= 0.87\left(1^{+0.15}_{-0.18}\right).$$

Then, the VMD result obtained in [2], $\Gamma^{\rm VMD}(\eta \to \pi\gamma\gamma) = 0.31$ eV, must be replaced by

$$\Gamma^{\rm VMD}_{\rm new} = 0.31 \cdot \left[0.87\left(1^{+0.15}_{-0.18}\right)\right]^2 \text{ eV} \simeq 0.23^{+0.077}_{-0.078} \text{ eV} \tag{13}$$

and $\Gamma(\eta \to \pi\gamma\gamma)$ in (2) must be replaced by 0.34 ± 0.20 eV.

Now, let us turn to the contribution of the a_0 boson. The experimental determination of the constants $g_{a\eta\pi}$ and $g_{a\gamma\gamma}$ is ambiguous, because it depends on the true width of a_0 decay. The true width may be as large as 300 MeV [6, 7], although the visible width in the $K^- p \to a_0\Sigma^-(1385)$ reaction is $\Gamma_{a\eta\pi} = 54 \pm 7$ MeV [8].

If $\Gamma_{a\eta\pi} \simeq 300$ MeV, irrespective of the nature of a_0 resonance, we have

$$|g_{a\eta\pi}| \approx 4.8 \text{ GeV}. \tag{14}$$

The constant $g_{a\gamma\gamma}$ can be evaluated in the same manner as $g_{\pi^0\gamma\gamma}$, that is, by calculating the triangle quark diagram. Such an evaluation does not depend on the unknown parameters. Then, $g_{a\gamma\gamma}$ differs from $g_{\pi^0\gamma\gamma}$ by a factor of 2/3, which was first found by Schwinger [9]. The matrix element of the $a_0 \to \gamma\gamma$ decay has the form [10, 11]

$$M(a_0 \to \gamma(q_1)\gamma(q_2)) = i\frac{2\alpha}{3\pi F_\pi} \tag{15}$$
$$\times (q_{2\mu}q_{1\nu} - (q_1q_2)\delta_{\mu\nu})\epsilon_\mu(q_1)\epsilon_\nu(q_2),$$

where $F_\pi \approx 93$ MeV.

Assuming that

$$g_{a\gamma\gamma} = \frac{2\alpha}{3\pi F_\pi} \tag{16}$$

and taking

$$g_{a\eta\pi} = -4.8 \text{ GeV}, \tag{17}$$

we come to the final estimate of the role of a_0 in $\eta \to \pi\gamma\gamma$ decay:

$$\Gamma(\eta \to \pi\gamma\gamma) = (0.31)^{\rm old}_{\rm VMD} \cdot 0.75(1^{+0.32}_{-0.41}) \tag{18}$$
$$+ [0.31(1^{+0.15}_{-0.18})]_{{\rm VMD}\times a_0} + (0.29)_{a_0} = 0.83^{+0.09}_{-0.11} \text{ eV}.$$

This result is very close to the one obtained by calculating the quark-box diagrams in the framework of the constituent quark model,

$$\Gamma^{\rm (box)}(\eta \to \pi\gamma\gamma) = 0.70 \text{ eV}, \quad [12] \tag{19}$$

and to the one obtained by collecting all (not only the leading $1/N_c$) contributions up to order p^6 in ChPT:

$$\Gamma^{(p^6)}_{\rm all}(\eta \to \pi\gamma\gamma) = 0.77 \pm 0.16 \text{ eV} \quad [13]. \tag{20}$$

However, the number 0.77 in this relationship must be reduced to ≈0.70, because in [13] the theoretical value 0.31 eV was used for the VMD contribution instead of 0.24 eV as follows from the above discussion.

The contribution of a_0 to $\Gamma(\eta \to \pi\gamma\gamma)$ found is also close to 0.27 eV, which was obtained in [10] in the framework of the model incorporating the constituent quarks together with scalar and vector resonances. We conclude that within the limits of experimental error, there is no contradiction between the experimental result and theoretical prediction for

$\Gamma(\eta \to \pi\gamma\gamma)$. Our approach clearly shows the effect of the intermediate bosons in this process. Contrary to the existing opinion [2, 3, 13], the scalar and vector bosons contribute to this transition with comparable strengths.

ACKNOWLEDGMENTS

I thank V.P. Chernyshev for drawing my attention to this topic.

REFERENCES

1. Particle Data Group (D. E. Groom *et al.*), Eur. Phys. J. C **15**, 1 (2000).
2. Ll. Ametler *et al.*, Phys. Lett. B **276**, 185 (1992).
3. J. N. Ng and D. J. Peters, Phys. Rev. D **46**, 5034 (1992).
4. P. Ko, Phys. Rev. D **47**, 3933 (1993).
5. G. Ecker, A. Pich, and E. de Rafael, Nucl. Phys. B **303**, 665 (1988).
6. S. Flatte, Phys. Lett. B **63B**, 224 (1976).
7. N. N. Achasov, S. A. Devyanin, and G. N. Shestakov, Usp. Fiz. Nauk **142**, 361 (1984) [Sov. Phys. Usp. **27**, 161 (1984)].
8. J. B. Gay *et al.*, Phys. Lett. B **63B**, 220 (1976).
9. J. Schwinger, Phys. Rev. **82**, 664 (1951).
10. M. K. Volkov and D. V. Kreopalov, Yad. Fiz. **37**, 1297 (1983) [Sov. J. Nucl. Phys. **37**, 770 (1983)].
11. E. P. Shabalin, Yad. Fiz. **46**, 852 (1987) [Sov. J. Nucl. Phys. **46**, 486 (1987)].
12. J. N. Ng and D. J. Peters, Phys. Rev. D **47**, 4939 (1993).
13. M. Jetter, Nucl. Phys. B **459**, 283 (1996).

Physics of Atomic Nuclei, Vol. 65, No. 9, 2002, pp. 1746–1747. Translated from Yadernaya Fizika, Vol. 65, No. 9, 2002, pp. 1791–1792.
Original Russian Text Copyright © 2002 by the Editorial Board.

CHRONICLE
Theory

On the 80th Anniversary of Karen Avetikovich Ter-Martirosyan

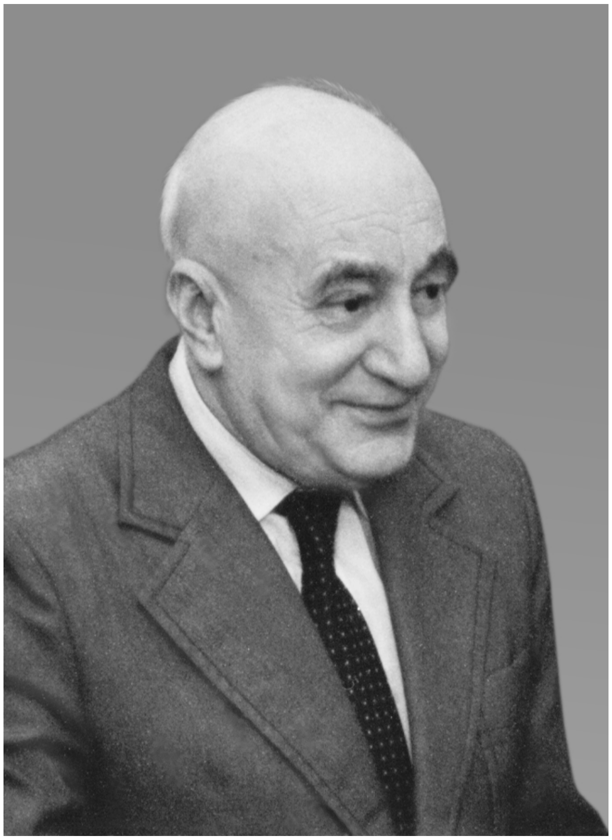

The world-famous theoretical physicist Karen Avetikovich Martirosyan, winner of the State and Pomeranchuk prizes, Soros professor, an outstanding scientist and a remarkable teacher, corresponding member of the Russian Academy of Sciences, will turn 80 this year on September 28.

Ter-Martirosyan was born in 1922 in Tbilisi. Having graduated from the Tbilisi State University in 1943, he became a postgraduate student of the Leningrad Physicotechnical Institute under the guidance of Yakov Il'ich Frenkel in 1945. After defending his PhD dissertation in 1949, he joined the theoretical department of the Leningrad Physicotechnical Institute, where he worked until 1955.

After moving to Moscow in 1955, Ter-Martirosyan started working at the Institute of Theoretical and Experimental Physics, where he continued collaboration with L.D. Landau, I.Ya. Pomeranchuk, V.B. Berestetskiĭ, and other physicists who determined the trends in the development of nuclear and particle physics.

Subsequent scientific activity of Ter-Martirosyan has been associated with the Institute of Theoretical and Experimental Physics. At this institute, he obtained brilliant results and founded new scientific trends, organized the laboratory of hadron physics, and formed his scientific school. More than 40 years ago, the Department Elementary Particle Physics of the Moscow Institute for Physics and Technology was created on the basis of the Institute of Theoretical and Experimental Physics and was headed by Ter-Martirosyan.

Ter-Martirosyan is the author of more than 150 papers in the field of nuclear physics, elementary particle physics, and quantum field theory. In 1952, he constructed the theory of Coulomb excitations of nuclei, leading to the discovery of nonsphericity of a number of heavy nuclei; in 1968, this work won the State Prize for the author. In 1952–1954, Karen Avetikovich constructed the solution of quantum-mechanical three-body problem for the case of a short-range potential. One of his greatest achievements in the field of quantum field theory at that time was the creation of the method of parquet equations for summation of planar graphs. Together with Pomeranchuk and his student V.N. Gribov, Ter-Martirosyan developed the theory of branching points in the angular-momentum plane. He is also the author of the theory of points of multi-Reggeon processes, the theory of growing cross sections, and the theory of critical and supercritical Pomeron.

Subsequent studies carried out by Ter-Martirosyan were devoted to hadron physics. He constructed the theory of hadron multiplicity distribution at high energies and proposed (together with A.B. Kaidalov) a model of creation and decay of quark–gluon strings. On the basis of this model, a realistic theory of generation of hadrons at high energies was constructed, which provides a correct description of experimental data. At the present time, topical investigations in the field of supersymmetric theories, Higgs particles, and the properties of heavy hadrons are being carried out in the hadron physics laboratory under the guidance of Ter-Martirosyan.

As before, the pedagogical activity occupies an important place in the life of Karen Avetikovich. Throughout his almost four decades of activity at the

Moscow Institute for Physics and Technology, hundreds of physicists have passed through his hands. His unique scientific school of theoretical physics includes world-recognized scientists who, in turn, have brought up a new generation of theorists. The courses of lectures on quantum mechanics and field theory delivered by Ter-Martirosyan to the students of the Moscow Institute for Physics and Technology formed the basis of the monograph *Gauge Theory of Particle Interaction* by K.A. Ter-Martirosyan and M.B. Voloshin, which was published in 1981 and remains one of the best textbook in quantum field theory.

In 2000, Prof. Ter-Martirosyan was elected a corresponding member of the Russian Academy of Sciences in the Department of Nuclear Physics. Karen Avetikovich continues his scientific activity and still delivers lectures to students and postgraduate students of the Moscow Institute for Physics and Technology and Institute of Theoretical and Experimental Physics with diligence. Being exceptionally attentive to his colleagues, he is always accessible for discussing any problems, both scientific and humanitarian.

Dear Karen Avetikovich, we congratulate you on the occasion of your jubilee and wish you long years of fruitful life and further achievements in your scientific activity!

Your students and colleagues